MECHANICAL PROPERTIES OF CERAMICS

Second Editon

JOHN B. WACHTMAN
W. ROGER CANNON
M. JOHN MATTHEWSON
Rutgers University

MECHANICAL PROPERTIES OF CERAMICS

MECHANICAL PROPERTIES OF CERAMICS

Second Editon

JOHN B. WACHTMAN
W. ROGER CANNON
M. JOHN MATTHEWSON
Rutgers University

For general information on our other products and services or for technical support, please contact our Customer Care Department within the United States at 877-762-2974, outside the United States at 317-572-3993 or fax 317-572-4002.

Wiley also publishes its books in a variety of electronic formats. Some content that appears in print may not be available in electronic formats. For more information about Wiley products, visit our web site at www.wiley.com.

CONTENTS

PREFACE

The second edition makes an attempt to improve the clarity of explanations in all chapters, update the coverage, and add problem sets at the end of chapters. These improvements should make this a better textbook for use in the classroom as well as a more readable text as a reference. Two new chapters have been added to fill important deficiencies in the first edition. Chapter 11 relates fracture strength and fracture toughness to the ceramic microstructures and Chapter 22 discusses hardness and the related subject, wear resistance. Chapter 17 has been expanded to give a description of fractographic markings and their origin. Several portions of chapters have also been deleted from the first edition because they were deemed unnecessary to a fundamental understanding of the subject and were often difficult to follow. Chapters 23–27, which dealt with specific materials, were eliminated and some of the information was incorporated into other chapters.

The second edition maintains the same objectives as the first edition. In fact, its intention to be used as a textbook has been enhanced by the clearer explanations and the addition of problem sets at the end of the chapters. These improvements are based on more than 20 years of teaching the subject by the two new coauthors to both graduate and undergraduate students. The text assumes only a general background in physics and calculus. It proceeds from the fundamental topics of stresses and strains (Chapters 1–3) and then moves on to more advanced and specific topics in mechanical properties of ceramics. Some of these topics are still under development, but the greater portion are quite mature since they were developed from the 1960s through 1996 when the first edition came out. While other textbooks may concentrate on elastic, viscoelastic, or plastic deformation, this text clearly emphasizes fracture behavior, a topic most important for the structural applications of brittle ceramics.

The text is also intended for use by professional materials scientists and engineers who have a general background in mechanical properties but need a more in-depth knowledge of the subject. Specific chapters may help the

processing scientist to develop and improve a ceramic. The discussion of microstructures in Chapter 11, for instance, will help the engineer develop a stronger, more flaw tolerant ceramic.

Another intended purpose of the book is as an aid for engineers of other disciplines outside of materials science in designing the proper stress level for a part. For instance, engineers dealing with glass under stress will find methods of predicting the lifetime of a glass structure and calculating its probability to failure. As with any very long term prediction, however, there are assumptions upon which the data are extrapolated. The text therefore discusses safety factors and how they will increase the probability of survival.

JOHN B. WACHTMAN
W. ROGER CANNON
M. JOHN MATTHEWSON

New Brunswick, New Jersey

ACKNOWLEDGMENTS

1

STRESS AND STRAIN

1.1 INTRODUCTION

Quantitative treatment of the mechanical behavior of ceramics (or any solid) requires the mathematical description of stress and strain. Each of these quantities is a second-rank tensor. The full three-dimensional treatment of stress and strain will be presented, but it is convenient to begin with a simple two-dimensional treatment and discuss types of mechanical behavior in terms of these. This approach permits qualitative ideas about the mechanical behavior of ceramics to be explained without obscuring them within the complexity of a full three-dimensional treatment. The scheme followed here is to introduce stress and strain in terms of an easily visualized picture of deforming a bar.

Consider a rectangular bar [as shown in Figure 1.1(a)] of length L, height h, and width w with a force F acting parallel to the length on each end (i.e., uniaxial loading). (The force is denoted by an arrow; however, it is distributed uniformly over the surface to which it is applied.) The bar will deform under the action of the forces. Accordingly, the bar is taken to deform by an amount δL

(a)

(b)

(c)

(d)

(e)
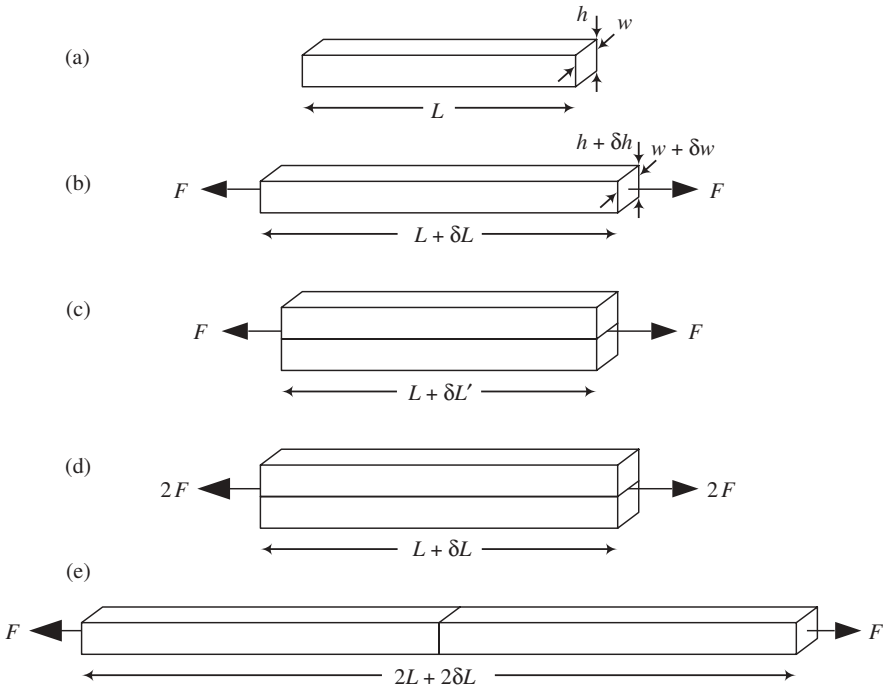
FIGURE 1.1   Bars subjected to tensile force.

in the direction of the force F and to deform an amount δh in the direction of the height h and δw in the direction of the width w, as shown in Figure 1.1(b). For a tensile force F as shown, the deformation δL is an extension, but the deformation at right angles to F is usually a contraction; δw and δh are generally negative for an applied tensile force. For certain directions in certain single crystals, the deformation δw or δh can actually be positive for an applied tensile stress. These are exceptional and rather rare cases.

Consider the two identical bars shown in Figure 1.1(c) subjected to the same force F. These bars are connected side by side in such a way that the load is shared equally between them. Each bar therefore supports only $F/2$ so that the deformations will be smaller in magnitude: that is, $\delta L' < \delta L$, $|\delta h'| < |\delta h|$, and $|\delta w'| < |\delta w|$. Absolute values are used for δh and δw since they are usually negative. For a linear elastic material (Chapter 3) these deformations will be exactly one-half of those for the single bar because the force supported by each bar is halved. However, if the force applied to the composite bars is $2F$, as shown in Figure 1.1(d), it is intuitively obvious that the deformations of each bar will be the same as the single bar in Figure 1.1(b).

Comparing the deformations in Figure 1.1(b)–(d) shows that the applied force is not a particularly useful way of quantifying the driving force for the deformation: for a fixed applied force the resulting deformation changes if the

cross-sectional area of the bar is changed. However, we see that doubling the cross-sectional area while at the same time doubling the force does result in the same deformation. This suggests that the variable controlling the deformation behavior is not total load but load per unit area. Accordingly, the **tensile stress** or **normal stress** σ is defined as the force F divided by the cross-sectional area A, so that

$$\sigma = \frac{F}{A} = \frac{F}{wh} \tag{1.1}$$

This is the definition of **engineering stress**, in contrast to the quantity termed **true stress**, which will be discussed in a later section. However, ceramics usually will fail at small strain when the difference between engineering stress and true stress is not significant. Unless otherwise stated, the term "stress" will refer to engineering stress in this book.

Comparing now the deformation of two bars connected end to end [Figure 1.1(e)] with the deformation of a single bar, the force F produces twice the extension of the latter case. The deformation inside the material is accommodated by stretching and bending of the interatomic bonds; comparing Figures 1.1(b) and (e) suggests that the deformation at the atomic level is the same in both cases. Doubling the length of the specimen results in double the extension. The deformation is therefore specified by the strain, which is defined as the ratio of the extension to the original length:

$$\varepsilon = \frac{\delta L}{L} \tag{1.2}$$

This is the definition of **engineering strain**, in contrast to the quantity termed **true strain**, which will be discussed in a later section. Unless otherwise stated, the term "strain" will refer to engineering strain in this book.

By using stress and strain instead of force and deformation, for the bar of Figure 1.1 we find that for a given applied stress the strain will always be the same, irrespective of the length or cross-sectional area of the bar.

In addition to forces normal to the end faces of the bar, surface tractions or shear forces might also be applied. Figure 1.2 shows an initially rectangular body subjected to tractions T applied to its upper and lower surfaces. The tractions tend to cause the body to deform into a parallelepiped whose adjacent sides have rotated by an angle ϕ with respect to each other. The shear forces give rise to a **shear stress** τ, which is defined in an analogous fashion to the tensile stress; that is, the stress is the force divided by the area over which the force is applied:

$$\tau = \frac{T}{A} = \frac{T}{wL} \tag{1.3}$$

but in this case the force is applied parallel to the area. Similarly to tensile strain, the shear strain γ is defined as the ratio of the deformation to the original
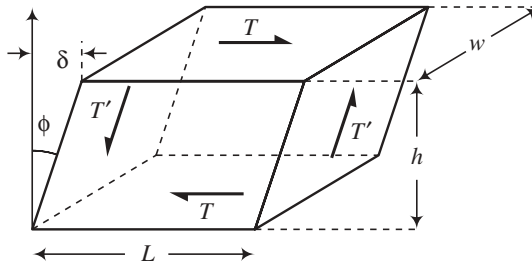
FIGURE 1.2 Rectangular body subjected to surface shear tractions.

dimension, which in this case is

$$\gamma = \frac{\delta}{h} = \tan \phi \approx \phi \tag{1.4}$$

It will be seen later that there are two different definitions of shear strain. Equation (1.4) defines the **engineering shear strain**. Note that this use of the term engineering strain is different from the context of using "engineering strain" to distinguish from "true strain"; see Section 1.7 for a discussion this topic. The engineering shear strain is related to the relative rotation angle ϕ and in the case of small strain (which is normally the case for deformation of ceramics) equals the angle in radians. Additional shear forces T' must be applied to the left and right sides of the body in Figure 1.2 in order to maintain rotational stability. They result in a shear stress τ that is equal and opposite to the shear stress on the top and bottom faces. The shear strain γ is the result of both shear stresses.

The example of Figure 1.1 is particularly simple because only one force is applied. Tensile forces could also be applied perpendicular to the length of the bar leading to additional tensile stress and strain components. Additionally, shear forces can be applied to the faces of the bar, leading to shear stresses and strains. For a complete three-dimensional description of stress and strain, each must be represented by second-rank tensors, that is, 3×3 matrices with some special tensor properties.

The example of Figure 1.1 is also simple because the stress and strain are uniform throughout the bar. In more complex problems the stress and strain vary with position inside a body and the definitions need to be modified. For example, if the stress is nonuniform, it is inappropriate to define the strain as the change in overall length divided by the original overall length. This introduces the concept of **stress at a point** and **strain at a point**. However, the definitions of stress and strain at a point are essentially the same except that the definitions involve forces and deformations in an infinitesimally small element instead of the overall body.

1.2 TENSOR NOTATION FOR STRESS

Figure 1.3 shows a small element of material inside a body. Each face of the element is acted upon by forces from the surrounding material. The total vector force $\underline{F}$ on the face of constant x can be resolved into three mutually orthogonal components: a force F_x perpendicular to the face and two surface tractions (shear forces) parallel to the face acting in the y and z directions, T_y and T_z, respectively. Surface area is a vector quantity of magnitude equal to the area and direction normal to the area acting out of the body. For the x face under consideration the vector area is A_x acting in the positive x direction, as shown in the figure. The force components on this face therefore represent three components of stress, a tensile stress and two shear stresses, all acting at mutual right angles.

The components of stress are generally written (Sines, 1969)

$$\sigma_{\text{on } x \text{ plane in } y \text{ direction}} = \sigma_{xy} = \frac{\text{force in } y \text{ direction acting on } x \text{ plane}}{\text{area of plane perpendicular to } x} \quad (1.5)$$

Here "x plane" means "plane perpendicular to the x axis" or "plane of constant x." In terms of indices denoting xyz by x_1, x_2, x_3, the above stress component is written

$$\sigma_{\text{on } x_i \text{ plane in } x_j \text{ direction}} = \sigma_{ij} \quad (1.6)$$

There are thus nine possible stress components in three dimensions. However, it will be shown that $\sigma_{ij} = \sigma_{ji}$ for $i \neq j$, so that there are only six
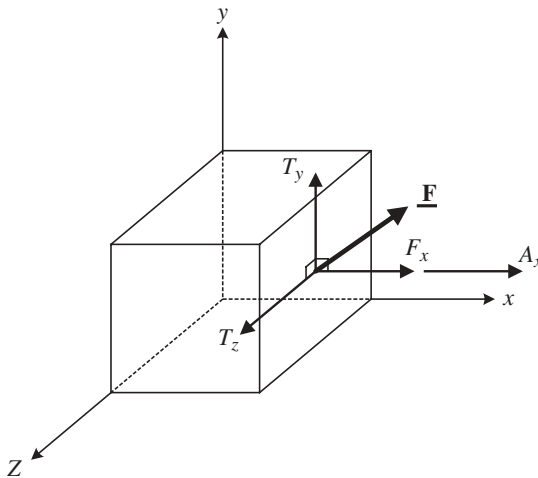
FIGURE 1.3 Forces acting on the face of a small element of material.

independent components. The components with $i = j$ are termed **normal stresses** or **tensile stresses** (with a compressive stress considered a negative tensile stress). For normal stresses the force acts in a direction perpendicular (normal) to the area to which it is applied (parallel to the area vector). The components with $i \neq j$ are termed **shear stresses** for which the force acts in a direction parallel to the area over which it is applied (perpendicular to the area vector). The shear stresses are sometimes written τ_{ij} instead of σ_{ij} to emphasize their nature as shear stresses.

Written as a matrix the components of stress in three dimensions are

$$\underline{\underline{\sigma}} = \begin{pmatrix} \sigma_{11} & \sigma_{12} & \sigma_{13} \\ \sigma_{21} & \sigma_{22} & \sigma_{23} \\ \sigma_{31} & \sigma_{32} & \sigma_{33} \end{pmatrix} \quad \text{or} \quad \underline{\underline{\sigma}} = \begin{pmatrix} \sigma_{xx} & \sigma_{xy} & \sigma_{xz} \\ \sigma_{yx} & \sigma_{yy} & \sigma_{yz} \\ \sigma_{zx} & \sigma_{zy} & \sigma_{zz} \end{pmatrix} \quad (1.7)$$

with

$$\sigma_{12} = \sigma_{21} \qquad \sigma_{23} = \sigma_{32} \qquad \sigma_{31} = \sigma_{13} \qquad (1.8)$$

The double underlines for $\underline{\underline{\sigma}}$ signify that it is a second-rank tensor. It is easier to visualize matters in two dimensions and attention will be restricted accordingly in the next few pages. For two dimensions there are a total of four stress components of which only three are independent. Written as the matrix, the stresses in two dimensions are

$$\underline{\underline{\sigma}} = \begin{pmatrix} \sigma_{11} & \sigma_{12} \\ \sigma_{21} & \sigma_{22} \end{pmatrix} \quad \text{or} \quad \underline{\underline{\sigma}} = \begin{pmatrix} \sigma_{xx} & \sigma_{xy} \\ \sigma_{yx} & \sigma_{yy} \end{pmatrix} \quad (1.9)$$

with

$$\sigma_{12} = \sigma_{21} \qquad (1.10)$$

The stress components in two dimensions are shown in Figure 1.4, which shows an infinitesimal square element acted upon by forces both normal and parallel to each surface. The arrows for the stresses show the direction of action of the forces represented by the stresses—the stresses themselves act in both directions simultaneously. The forces normal to the faces produce normal stresses. The force F_x on the right face (the $+x$ face) is balanced by an equal and opposite force $-F_x$ on the left face (the $-x$ face) to maintain stability. Similar results hold for the upper and lower faces. The forces parallel to the faces produce shear stresses; again each force on one face is balanced by an equal and opposite force on the opposite face. For the element to be under no net torque, the shear forces must balance such that $\sigma_{xy} = \sigma_{yx}$.
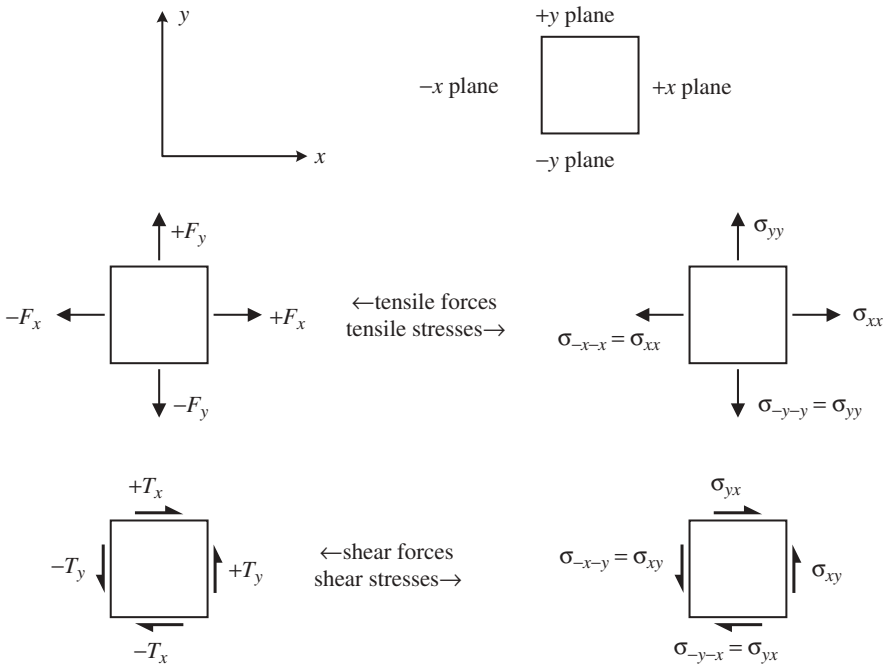
FIGURE 1.4   Components of stress in two dimensions.

The sign convention for stress can be defined in terms of the directions of the force vectors and area vectors. If both the force and area vectors act in the positive direction or in the negative direction, the stress is positive; if the force acts in the negative direction and the area in the positive direction or vice versa, the stress is negative. For example, in Figure 1.4 the component of normal stress on the right-hand side of the element, σ_{xx}, represents a force acting in the positive x direction and the area normal is also in the positive x direction, giving a positive stress. The component on the left, σ_{-x-x}, is a force acting in the negative x direction with an area normal acting in the negative x direction and so is again positive and therefore equals σ_{xx}. This sign convention coincides with that stated earlier, that tensile stresses (i.e., stresses tending to cause extensions) are positive while compressive stresses (tending to cause contractions) are negative. Consider now that the shear stress σ_{xy} as drawn in Figure 1.4 is positive since it is a force acting in the positive y direction is acting on an area whose normal is in the positive x direction. The reader should verify that σ_{yx} as drawn in Figure 1.4 is also acting in the positive sense. Using this sign convention, σ_{xy} and σ_{yx} tend to cause rotations in the opposite sense, but since $\sigma_{xy} = \sigma_{yx}$, there is no net rotational moment.

The dimensions of stress are force divided by area and so the unit is newtons per square meter or the preferred unit the pascal (Pa). Other units that might be

TABLE 1.1   Units of Stress

$1\,\text{N/m}^2 = 1\,\text{Pa}$
$1\,\text{kg/m}^2 = 9.81\,\text{Pa}$
$1\,\text{dyn/cm}^2 = 0.1\,\text{Pa}$
$1\,\text{psi (pound per square inch)} = 6.89476\,\text{kPa}$
$1\,\text{bar} = 0.1\,\text{MPa}$
$1\,\text{atm} = 0.101325\,\text{MPa}$

encountered are listed in Table 1.1 together with their conversion factors to pascals. Stresses encountered while working with ceramics range roughly from 1 to 1000 MPa (1 GPa)—most ceramics survive a normal stress of 10 MPa while few can withstand a stress of a few gigapascals.

1.3   STRESS IN ROTATED COORDINATE SYSTEM

We now examine how a stress tensor is expressed in a rotated coordinate system. Considering the bar of Figure 1.1 and taking the x axis along the long axis of the bar, the stress caused by a load in this direction acting on the cross-sectional area A_x of the bar is

$$\sigma = \frac{F_x}{A_x} = \sigma_{x_1 \text{ plane, } x_1 \text{ direction}} = \sigma_{11} = \sigma_{xx} \tag{1.11}$$

For this bar and this load the other stress components are zero so that the stress tensor anywhere in the bar is given by

$$\underline{\underline{\sigma}} = \begin{pmatrix} \sigma & 0 & 0 \\ 0 & 0 & 0 \\ 0 & 0 & 0 \end{pmatrix} \tag{1.12}$$

For this simple **state of stress**, known as **uniaxial tension**, it is obvious that the frame of reference for the stress tensor should be chosen with one axis parallel to the axis of the bar. However, while this is a convenient choice, the stress could be referred to any other system of axes. The question now arises, if one knows the components of stress referred to some set of axes xyz, what are the components of stress referred to some other set of axes $x'y'z'$ which are rotated with respect to the xyz axes? We will first consider the two-dimensional case in which the stress components to be determined are referenced to axes $x'y'$ which are rotated at an angle θ with respect to the xy axes.

Figure 1.5(a) defines the relationship between the xy and $x'y'$ axes and defines the sense of the rotation angle θ, which is the angle measured
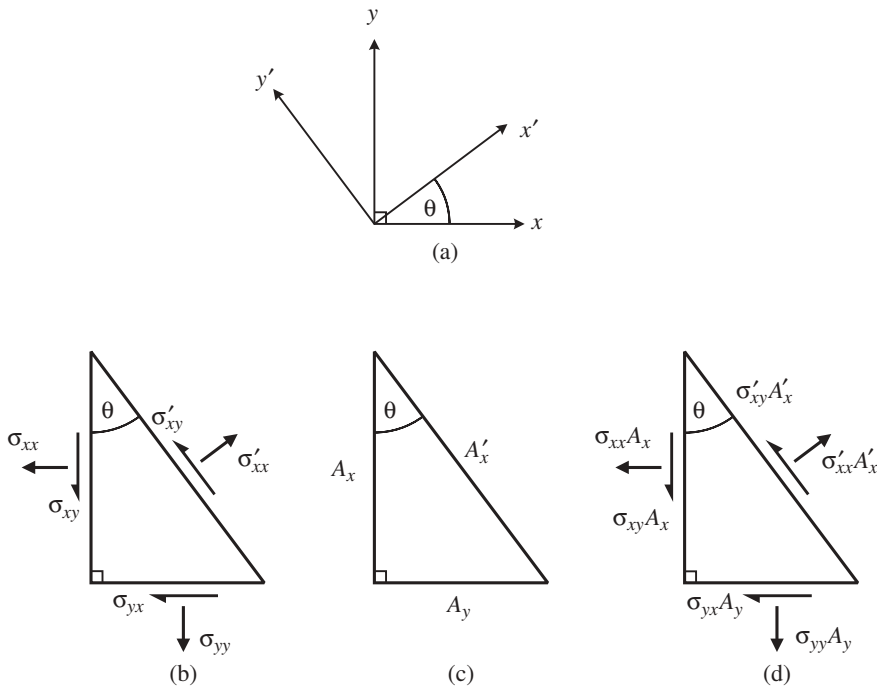
FIGURE 1.5 Stress in a rotated coordinate system: (a) axes; (b) stresses; (c) areas; (d) forces.

counterclockwise from the x axis to the x' axis. We consider the stability of a small element of the solid shown in the lower left portion of Figure 1.5, which has a triangular section whose three faces are perpendicular to the x, y, and x' axes. The stresses experienced by each face of the element do not depend on which set of axes are chosen to describe them and so we may choose any convenient axes provided we use the same set of axes consistently for each face. We therefore refer the two orthogonal faces to the xy axes and the hypotenuse to the $x'y'$ axes. Figure 1.5(b) shows the components of stress acting on each face using this choice of axes. The arrows point in the direction of the forces represented by the stress components. We use the notation here that components of stress referred to the $x'y'$ axes, $\sigma_{i'j'}$, may be rewritten as σ_{ij}' for clarity. The reader should verify that each component of stress points in the positive direction using the sign convention for stresses.

The area of each face is proportional to the length of the side of the triangular section and the three areas are defined in Figure 1.5(c). The forces applied to each face, shown in Figure 1.5(d), are calculated by multiplying each component of stress by the area of the face to which it is applied. The triangular element is stable (i.e., not accelerating) so the net force applied to it must equal

zero. Equating the components of all the forces resolved in the x' direction gives

$$\sigma'_{xx}A'_x = \sigma_{xx}A_x \cos\theta + \sigma_{xy}A_x \sin\theta + \sigma_{yy}A_y \sin\theta + \sigma_{yx}A_y \cos\theta \qquad (1.13)$$

The areas of the sides are related by

$$A_x = A'_x \cos\theta \qquad \text{and} \qquad A_y = A'_x \sin\theta \qquad (1.14)$$

Substitution into Eq. (1.13) and using $\sigma_{xy} = \sigma_{yx}$ give

$$\sigma'_{xx} = \sigma_{xx} \cos^2\theta + \sigma_{yy} \sin^2\theta + 2\sigma_{xy} \sin\theta \cos\theta \qquad (1.15)$$

The shear stress in the $x'y'$ coordinate system is found by resolving components of force in the y' direction:

$$\sigma'_{xy}A'_x = -\sigma_{xx}A_x \sin\theta + \sigma_{xy}A_x \cos\theta + \sigma_{yy}A_y \cos\theta - \sigma_{yx}A_y \sin\theta \qquad (1.16)$$

which gives

$$\sigma'_{xy} = (\sigma_{yy} - \sigma_{xx}) \sin\theta \cos\theta + \sigma_{xy}(\cos^2\theta - \sin^2\theta) \qquad (1.17)$$

It may be shown that Eqs. (1.15) and (1.16) also ensure rotational stability, namely that there is no net torque acting on the element. Similar considerations applied to a triangular element whose hypotenuse is perpendicular to the y' direction provides the final stress component σ'_{yy}:

$$\sigma'_{yy} = \sigma_{xx} \sin^2\theta + \sigma_{yy} \cos^2\theta - 2\sigma_{xy} \sin\theta \cos\theta \qquad (1.18)$$

Using the well-known trigonometric identities

$$\cos 2\theta = \cos^2\theta - \sin^2\theta \qquad \text{and} \qquad \sin 2\theta = 2 \sin\theta \cos\theta \qquad (1.19)$$

the three components of stress can be expressed in terms of 2θ:

$$\sigma'_{xx} = \tfrac{1}{2}(\sigma_{xx} + \sigma_{yy}) + \tfrac{1}{2}(\sigma_{xx} - \sigma_{yy}) \cos 2\theta + \sigma_{xy} \sin 2\theta$$
$$\sigma'_{yy} = \tfrac{1}{2}(\sigma_{xx} + \sigma_{yy}) - \tfrac{1}{2}(\sigma_{xx} - \sigma_{yy}) \cos 2\theta - \sigma_{xy} \sin 2\theta \qquad (1.20)$$
$$\sigma'_{xy} = \tfrac{1}{2}(\sigma_{yy} - \sigma_{xx}) \sin 2\theta + \sigma_{xy} \cos 2\theta$$

Turning now to the three-dimensional case, a general expression for the stresses on a plane of any orientation in three dimensions can be written in
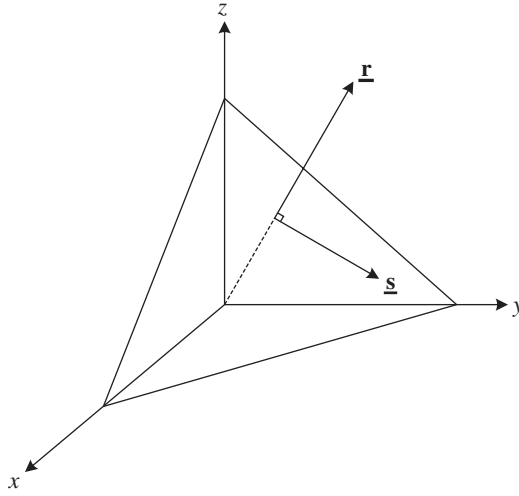
FIGURE 1.6   Plane with normal **r** and direction **s** in the plane.

terms of the direction cosines of the normal to the plane and the direction of action of the stress (Sines, 1969). Consider the plane in Figure 1.6 having a normal **r** with direction cosines a_{ir} to the axes $xyz = x_1x_2x_3$. The stress normal to this plane is

$$\sigma'_{rr} = \sum_i \sum_j a_{ir} a_{jr} \sigma_{ij} \tag{1.21}$$

The shear stress acting on this plane in the **s** direction with direction cosines a_{js} is

$$\sigma'_{rs} = \sum_i \sum_j a_{ir} a_{js} \sigma_{ij} \tag{1.22}$$

1.4   PRINCIPAL STRESS

Examination of Eqs. (1.20) shows that at a particular value of θ defined by

$$\tan 2\theta = \frac{2\sigma_{xy}}{\sigma_{xx} - \sigma_{yy}} \tag{1.23}$$

σ'_{xy} is zero. This means that for any general stress tensor in two dimensions a set of axes can be found for which the shear stresses vanish. These axes are called

the **principal axes** and the directions of the principal axes are **principal directions**. Planes containing pairs of principal axes are **principal planes**. The normal stresses referred to the principal axes are the **principal stresses**. Referred to the principal axes, Eqs. (1.20) become

$$\sigma'_{xx} = \tfrac{1}{2}(\sigma_{xx} + \sigma_{yy}) + R$$
$$\sigma'_{yy} = \tfrac{1}{2}(\sigma_{xx} + \sigma_{yy}) - R \tag{1.24}$$
$$\sigma'_{xy} = 0$$

where

$$R = \sqrt{\left[\tfrac{1}{2}(\sigma_{xx} - \sigma_{yy})\right]^2 + \sigma_{xy}^2} \tag{1.25}$$

The principal stresses σ'_{xx} and σ'_{yy} may be renamed σ_1 and σ_2 where, by convention, $\sigma_1 \geq \sigma_2$.

Inverting Eqs. (1.24) using (1.23) permits calculation of the components of stress referenced to axes inclined at an angle θ to the principal axes in terms of the principal stresses:

$$\sigma_{xx} = \tfrac{1}{2}(\sigma'_{xx} + \sigma'_{yy}) + \tfrac{1}{2}(\sigma'_{xx} - \sigma'_{yy})\cos 2\theta = \sigma'_{xx}\cos^2\theta + \sigma'_{yy}\sin^2\theta$$
$$\sigma_{yy} = \tfrac{1}{2}(\sigma'_{xx} + \sigma'_{yy}) - \tfrac{1}{2}(\sigma'_{xx} - \sigma'_{yy})\cos 2\theta = \sigma'_{xx}\sin^2\theta + \sigma'_{yy}\cos^2\theta \tag{1.26}$$
$$\sigma_{xy} = \sigma_{yx} = \tfrac{1}{2}(\sigma'_{xx} - \sigma'_{yy})\sin 2\theta = (\sigma'_{xx} - \sigma'_{yy})\sin\theta\cos\theta$$

The Mohr circle construction (Sines, 1969; Courtney, 1990) is a graphical method for obtaining the principal stresses that gives useful insight into the properties of the stress tensor. In this construction the abscissa is normal stress σ and the ordinate is shear stress, usually written as τ for the Mohr circle. A different sign convention applies to shear stresses in the Mohr circle construction: Shear stresses causing a clockwise rotation are taken as positive and those causing a counterclockwise rotation are taken as negative (Sines, 1969). In our case with the z axis out of the paper in Figure 1.5, σ_{xy} is a positive rotation so $\tau_{xy} = \sigma_{xy}$ and σ_{yx} is a negative rotation giving $\tau_{yx} = -\sigma_{yx}$. For a given pair of principal stresses σ_1 and σ_2 the locus of Eqs. (1.26) as θ varies is a circle on a shear stress/normal stress plot, as shown in Figure 1.7. One can consider this circle in two ways: (1) for a situation in which the principal stresses and directions are known and (2) when the stress tensor is known and the principal stresses and directions are to be determined.
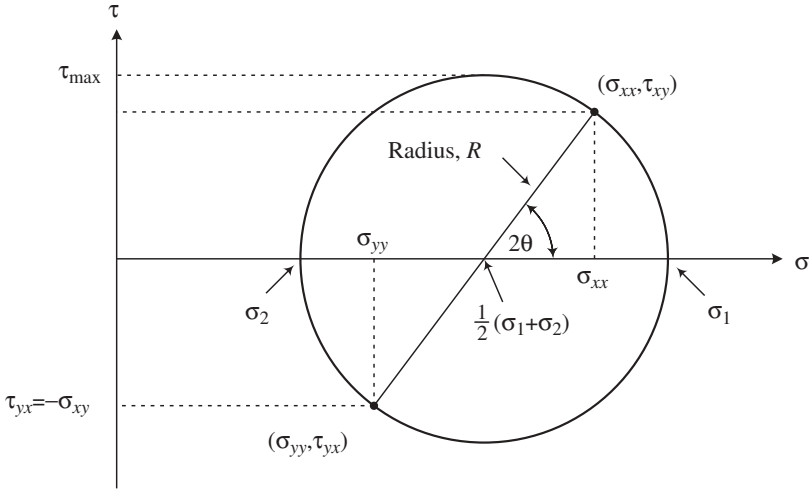
FIGURE 1.7   Mohr circle for biaxial tension.

In the first situation the initial axes are principal axes, $\sigma'_{xx} = \sigma_1$, $\sigma'_{yy} = \sigma_2$, and $\sigma'_{xy} = \sigma'_{yx} = 0$. The center of the circle is on the σ axis at $\frac{1}{2}(\sigma_1 + \sigma_2)$. The radius of the circle is $\frac{1}{2}(\sigma_1 - \sigma_2)$. The circle intersects the σ axis at σ_1 and σ_2. To obtain the stress in a system of coordinates rotated by an angle θ, a diameter of the circle is drawn rotated through an angle 2θ to the σ axis. This diameter intersects the circle at two points. The intersection point adjacent to the 2θ angle has abscissa σ_{xx} and ordinate $\tau_{xy} = \sigma_{xy}$. The intersection of the circle with the opposite end of the diameter has abscissa σ_{yy} and ordinate $\tau_{yx} = -\sigma_{yx} = -\sigma_{xy}$.

In the second situation the initial axes are not principal since the shear stress is not zero. Two points on the Mohr circle are constructed with coordinates $(\sigma_{xx}, \sigma_{xy})$ and $(\sigma_{yy}, -\sigma_{xy})$. Alternatively and equivalently, the Mohr convention for the sign of shear stress (clockwise rotation corresponds to positive shear) may be used and the two points are (σ_{xx}, τ_{xy}) and (σ_{yy}, τ_{yx}). The center of the Mohr circle is on the σ axis at $\frac{1}{2}(\sigma_{xx} + \sigma_{yy})$ and the radius is given by

$$\text{Radius} = R = \left[\left(\frac{\sigma_{xx} - \sigma_{yy}}{2} \right)^2 + \sigma_{xy}^2 \right]^{1/2} \tag{1.27}$$

The principal stresses are the intersection of the circle with the σ axis, and the orientation of the principal axes is given by the angle θ:

$$\theta = \tfrac{1}{2} \tan^{-1} \left(\frac{2\sigma_{xy}}{\sigma_{xx} - \sigma_{yy}} \right) \tag{1.28}$$

Examination of the Mohr circle illustrates two important results. For a given pair of principal stresses σ_1 and σ_2, the maximum normal stress that can be observed in any rotated coordinate system is on the extreme right-hand side of the circle; that is, the maximum normal stress is the bigger principal stress $\sigma_{max} = \sigma_1$. Similarly, the minimum normal stress (most negative stress) is at the extreme left of the circle and equals the smaller principal stress $\sigma_{min} = \sigma_2$. Further, the maximum shear stress occurs at the top and bottom of the Mohr circle, $2\theta = \pm 90°$, $\theta = \pm 45°$, and is given by

$$\tau_{max} = \tfrac{1}{2}(\sigma_1 - \sigma_2) \tag{1.29}$$

These results show the importance of principal stress analysis in understanding the mechanical behavior of ceramics. Most ceramics fail by brittle fracture in tension: Failure is controlled by the biggest tensile stress σ_1. Ceramics at high temperature (as well as most metals and polymers) can deform in shear: This deformation is controlled by the maximum shear stress, which is itself related to the principal stresses. Principal stress analysis is therefore necessary in understanding the response of any material to a complex state of stress.

It is interesting to examine the stresses given by the Mohr circle construction (or equivalently by direct calculation from the above equations) for special situations. Consider the case of a bar under simple uniaxial tension σ such as in Figure 1.1. No other stresses are applied and in particular no shear stresses are applied, so the axis of the bar is principal and an axis perpendicular to the bar is also principal. The principal stresses are therefore $\sigma_1 = \sigma$ and $\sigma_2 = 0$. The Mohr circle for this case is shown in Figure 1.8(a). The center of the circle is at $\tfrac{1}{2}\sigma$ and the radius is also $\tfrac{1}{2}\sigma$. The shear stresses are a maximum at $2\theta = \pm 90°$ with magnitude $\tfrac{1}{2}\sigma$. At this orientation the two normal stresses are both $\tfrac{1}{2}\sigma$. This example illustrates how a ductile material can fail in shear even though only a tensile stress is applied.

As a further example consider the application of two equal stresses $\sigma_1 = \sigma_2 = \sigma$, that is, equi-biaxial tension. The center of the Mohr circle is at σ and the radius is zero. The Mohr circle is just a point, as shown in Figure 1.8(b). As the coordinate system rotates, the values of σ_{xx} and σ_{yy} remain equal to σ and the shear stresses remain equal to zero for all values of θ.

A final example, equi-opposite biaxial tension, is shown in Figure 1.8(c), in which a tensile stress of magnitude σ is applied in one direction and a compressive stress of equal magnitude, $-\sigma$, is applied in a perpendicular direction. Since no other stresses are applied, these stresses are principal so $\sigma_1 = \sigma$ and $\sigma_2 = -\sigma$. The Mohr circle in this case is centered on the origin. At $\theta = \pm 45°$ the normal stresses are zero and the shear stress is the maximum, $\tau_{max} = \sigma$, so in this case axes can be found for which the stress tensor is purely shear.
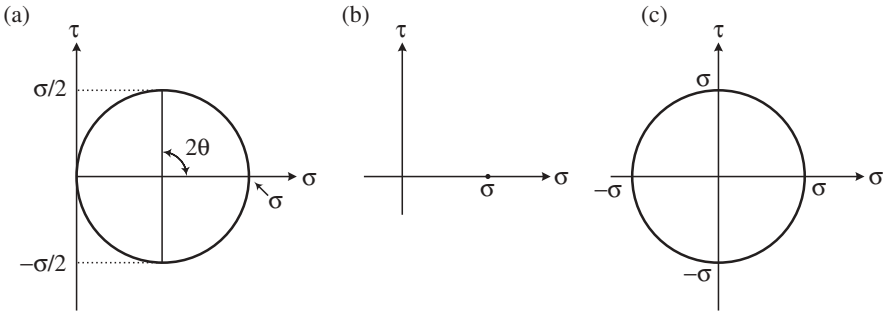
FIGURE 1.8   Mohr circle for (a) uniaxial tension, (b) equibiaxial tension, and (c) equi-opposite biaxial tension.

1.4.1   Principal Stresses in Three Dimensions

The principal stresses in three dimensions are found by solving the eigenequation for the stress tensor:

$$\left|\underline{\underline{\sigma}} - \sigma\,\underline{\underline{I}}\right| = 0 \quad\text{or}\quad \left|\underline{\underline{\sigma}} - \sigma\,\underline{\underline{I}}\right| = \det \begin{vmatrix} \sigma_{11} - \sigma & \sigma_{12} & \sigma_{13} \\ \sigma_{21} & \sigma_{22} - \sigma & \sigma_{23} \\ \sigma_{31} & \sigma_{32} & \sigma_{33} - \sigma \end{vmatrix} = 0 \quad (1.30)$$

where $\underline{I}$ is the identity matrix and σ is a scalar. The eigenequation represents a cubic equation in σ (Courtney, 1990):

$$\sigma^3 - J_1\sigma^2 - J_2\sigma - J_3 = 0 \quad (1.31)$$

where the coefficients J_1, J_2, and J_3 are the **stress invariants** (see below). This equation is solved to find the three eigenvalues σ_1, σ_2, and σ_3. The eigenvectors point in the principal directions and so coincide with the principal axes. Unlike the two-dimensional case, there are no conveniently simple equations for the principal stresses in three dimensions, nor is there a simple geometric solution equivalent to the Mohr circle. However, eigenanalysis is readily performed using a wide variety of computational tools. By convention the eigenvalues are chosen so that $\sigma_1 \geq \sigma_2 \geq \sigma_3$; σ_1 is therefore the largest normal stress in any direction and σ_3 is the smallest (most negative). Analogous to the two-dimensional case, the shear stress has maximum values on planes inclined at $\pm 45°$ to the principal planes. The largest shear stress acting on any plane is therefore

$$\tau_{\max} = \tfrac{1}{2}(\sigma_1 - \sigma_3) \quad (1.32)$$

with locally maximum values of $\tfrac{1}{2}(\sigma_1 - \sigma_2)$ and $\tfrac{1}{2}(\sigma_2 - \sigma_3)$.

Since we exist in a three-dimensional world, it is clear in retrospect that the two-dimensional analysis presented earlier contains the implicit assumption that the z plane is principal. In many practical situations one of the principal planes is known and the two-dimensional treatment is appropriate. For example, a traction-free surface is principal. Most mechanical testing techniques (Chapter 6) apply a simple stress tensor to samples and at least one principal plane is readily identifiable.

1.5 STRESS INVARIANTS

When stresses are transformed from one coordinate system to a rotated system, there are three properties of the stress tensor that remain constant. These three stress invariants are

$$
\begin{aligned}
J_1 &= \sigma_{xx} + \sigma_{yy} + \sigma_{zz} = \sigma_1 + \sigma_2 + \sigma_3 \\
J_2 &= -\sigma_{xx}\sigma_{yy} - \sigma_{yy}\sigma_{zz} - \sigma_{zz}\sigma_{xx} + \sigma_{xy}^2 + \sigma_{yz}^2 + \sigma_{zx}^2 \\
&= -\sigma_1\sigma_2 - \sigma_2\sigma_3 - \sigma_3\sigma_1 \\
J_3 &= \sigma_{xx}\sigma_{yy}\sigma_{zz} + 2\sigma_{xy}\sigma_{yz}\sigma_{zx} - \sigma_{xx}\sigma_{yz}^2 - \sigma_{yy}\sigma_{zx}^2 - \sigma_{zz}\sigma_{xy}^2 \\
&= \sigma_1\sigma_2\sigma_3
\end{aligned}
\tag{1.33}
$$

The existence of these quantities that are invariant under rotations means that the stress tensor is indeed a tensor and not simply a matrix. The **hydrostatic stress** is the mean normal stress:

$$
\sigma_h = \tfrac{1}{3}(\sigma_{xx} + \sigma_{yy} + \sigma_{zz}) = \tfrac{1}{3}J_1
\tag{1.34}
$$

and is clearly invariant, as is the **hydrostatic pressure**, which, taking a compressive stress as a positive pressure, is minus the hydrostatic stress:

$$
p = -\sigma_h = -\tfrac{1}{3}J_1
\tag{1.35}
$$

1.6 STRESS DEVIATOR

It is well known that the effect of multiple forces can be combined by vector addition in which corresponding components of forces are added. It is a general property of vectors such as force and area. A similar result holds for the stress tensor since the components of stress represent components of forces and areas. If multiple stresses are applied to a body, the stress tensors for each stress can

be added together element by element to obtain the overall stress tensor. This is known as the **principal of superposition**—different stress tensors are superimposed by simple tensor addition. This result is useful in a wide variety of situations. Conversely, a total stress tensor can be decomposed into two or more tensors.

It is useful to separate the stress into the components causing dilation without change of shape (pressure) and components causing distortion without change in volume. For example, to a first approximation hydrostatic pressure alone causes transformation in transformation-toughened zirconia. Plastic deformation is not caused by hydrostatic pressure so that it is sometimes useful to subtract the hydrostatic stress and consider only the remaining stresses. The **stress deviator $\underline{\underline{\sigma}}^*$** is defined by

$$\sigma_{ij}^* = \sigma_{ij} - \tfrac{1}{3}J_1$$
$$= \sigma_{ij} + p \qquad i = j \tag{1.36}$$
$$\sigma_{ij}^* = \sigma_{ij} \qquad i \neq j$$

or explicitly

$$\underline{\underline{\sigma}} = \underline{\underline{\sigma}}^* - p\underline{\underline{I}} = \begin{pmatrix} \sigma_{11} + p & \sigma_{12} & \sigma_{13} \\ \sigma_{21} & \sigma_{22} + p & \sigma_{23} \\ \sigma_{31} & \sigma_{32} & \sigma_{33} + p \end{pmatrix} + \begin{pmatrix} -p & 0 & 0 \\ 0 & -p & 0 \\ 0 & 0 & -p \end{pmatrix} \tag{1.37}$$

1.7 STRAIN

When forces are applied to a body, it deforms. Every point in the body is displaced from its original position by an amount that can be represented by a vector. This results in the concept of the **vector displacement field**—at every point in the body the deformation is represented by a vector $\underline{v}$. The three components of $\underline{v}$ in the x, y, and z directions are u, v, and w or, equivalently, u_1, u_2, and u_3. The components of $\underline{v}$ are all functions of position:

$$\underline{v} = \begin{cases} (u, v, w) = (u(x, y, z), v(x, y, z), w(x, y, z)) \\ (u_1, u_2, u_3) = (u_1(x_1, x_2, x_3), u_2(x_1, x_2, x_3), u_3(x_1, x_2, x_3)) \end{cases} \tag{1.38}$$

The strains within the body can be expressed in terms of this vector displacement field. Considering first the two-dimensional case for simplicity, Figure 1.9 shows a small rectangular element $ABCD$ with sides dx and dy which is displaced to $A'B'C'D'$ when forces are applied. The element is deformed by the
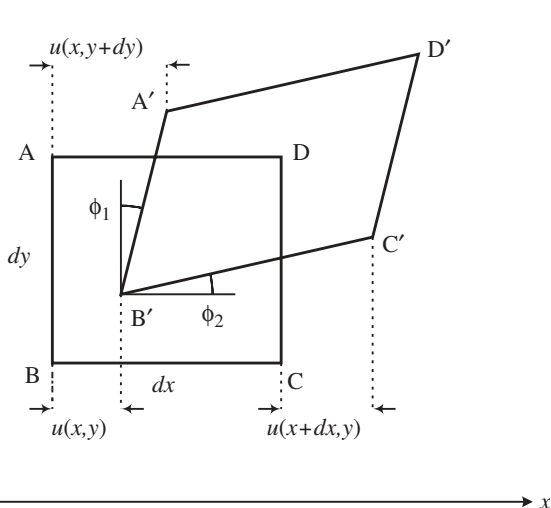
FIGURE 1.9   Definition of strain.

forces so that the sides AB and BC are rotated by angles ϕ_1 and ϕ_2, respectively, from their original orientation. The coordinates of the vertex B are (x, y) so that the displacement BB' in the x direction is $u(x, y)$ and the displacement CC' is $u(x + dx, y)$. The change in length of the side BC measured in the x direction is therefore $u(x + dx, y) - u(x, y)$. The normal strain measured in the x direction in the side BC as it deforms to $B'C'$ [from Eq. (1.2)] is

$$\varepsilon_{xx} = \frac{u(x + dx, y) - u(x, y)}{dx} = \frac{\partial u}{\partial x} \tag{1.39}$$

Similar considerations can be used to obtain the results for the three-dimensional case, giving

$$\varepsilon_{yy} = \frac{\partial v}{\partial y} \qquad \varepsilon_{zz} = \frac{\partial w}{\partial z} \tag{1.40}$$

By changing the coordinate notation to (x_1, x_2, x_3), we find the general form for the three components of normal strain:

$$\varepsilon_{ii} = \frac{\partial u_i}{\partial x_i} \qquad i = 1, 2, 3 \tag{1.41}$$

The vertex AA' is displaced by a distance $u(x, y + dy)$ in the x direction so that the distance $B'A'$ measured in the x direction is $u(x, y + dy) - u(x, y)$. In the

limit of small strain the angle ϕ_1 is given by

$$\phi_1 \simeq \tan \phi_1 = \frac{u(x, y + dy) - u(x, y)}{dy} = \frac{\partial u}{\partial y} \tag{1.42}$$

Similarly the angle ϕ_2 is given by

$$\phi_2 = \frac{\partial v}{\partial x} \tag{1.43}$$

The sides AB and BC are rotated relative to each other by a total angle $\phi = \phi_1 + \phi_2$. Using the definition for engineering shear strain, Eq. (1.4), the shear strain γ_{xy} is

$$\gamma_{xy} = \frac{\partial u}{\partial y} + \frac{\partial v}{\partial x} \tag{1.44}$$

In general, for three dimensions we have

$$\gamma_{ij} = \frac{\partial u_i}{\partial x_j} + \frac{\partial u_j}{\partial x_i} \qquad i, j = 1, 2, 3 \qquad i \neq j \tag{1.45}$$

Examination of (1.45) shows that $\gamma_{ij} = \gamma_{ji}$ so that while there are six components of shear strain there are only three independent components. If i is set equal to j in (1.45), the result differs from the definition for normal strain [Eq. (1.41)] by a factor of 2. Therefore the definitions of normal strain and engineering shear strain are incompatible so that they cannot be grouped together into a tensor and manipulated as a whole. This difficulty is overcome if we define the **simple shear strain** ε_{ij} to be one-half of the engineering shear strain. The general form

$$\varepsilon_{ij} = \frac{1}{2} \left(\frac{\partial u_i}{\partial x_j} + \frac{\partial u_j}{\partial x_i} \right) \qquad i, j = 1, 2, 3 \tag{1.46}$$

is applicable to both normal and shear strains so that they can be grouped together to form the strain tensor:

$$\underline{\underline{\varepsilon}} = \begin{pmatrix} \varepsilon_{11} & \varepsilon_{12} & \varepsilon_{13} \\ \varepsilon_{21} & \varepsilon_{22} & \varepsilon_{23} \\ \varepsilon_{31} & \varepsilon_{32} & \varepsilon_{33} \end{pmatrix} \quad \text{or} \quad \underline{\underline{\varepsilon}} = \begin{pmatrix} \varepsilon_{xx} & \varepsilon_{xy} & \varepsilon_{xz} \\ \varepsilon_{yx} & \varepsilon_{yy} & \varepsilon_{yz} \\ \varepsilon_{zx} & \varepsilon_{zy} & \varepsilon_{zz} \end{pmatrix} \tag{1.47}$$

The stress and strain tensors are both symmetric matrices, which means that many of the properties of the strain tensor are analogous to those of the stress

tensor. In particular, it was noted earlier that for any set of stress compo-
nents there are three orthogonal directions, the principal directions for stress,
for which the shear stresses are all zero. An analogous result holds for strain.
For any set of strain components there are three orthogonal directions, called
the principal directions for strain, for which the shear strains are zero;
the corresponding normal strains are called the principal strains. For an
elastically isotropic body the principal directions for stress and the principal
directions for strain coincide. For an elastically anisotropic body this is not
necessarily so.

The methods described earlier for determining principal stresses can all be
used for determining principal strains; in all equations components of stress are
replaced by the equivalent components of strain. In particular, the Mohr circle
construction can be used for two-dimensional cases (i.e., where the third
direction is known to be principal). Another set of results for stress that can
be adopted for strain is the stress invariants and the definition of deviatoric
stress. The corresponding strain invariants, hydrostatic strain and strain
deviator are given by substituting strain for stress in Eqs. (1.33) and (1.36).
A parameter of interest is the **volumetric strain** ε_V, which is the fractional
change in volume caused by the deformation. It equals the first strain invariant
obtained from Eq. (1.33):

$$J_1 = \varepsilon_{xx} + \varepsilon_{yy} + \varepsilon_{zz} = \varepsilon_1 + \varepsilon_2 + \varepsilon_3 = \varepsilon_V = 3\varepsilon_h \qquad (1.48)$$

1.8   TRUE STRESS AND TRUE STRAIN

The stress defined in Eq. (1.1) and the strain defined in Eq. (1.2) both contain
factors which involve the size of the specimen, namely the cross-sectional area
A and the length L. However, both of these parameters are changing as
deformation takes place. We define now two types of stress and strain:
engineering stress and **engineering strain**, where the cross-sectional area and
length have the original values before the start of the deformation, and **true
stress** and **true strain**, where the instantaneous cross-sectional area and length
are used (Table 1.2). They are equivalent for small stresses and strains.

TABLE 1.2   Engineering and True Stress and Strain

Engineering	True
$\sigma = \dfrac{F}{A_{\text{original}}} = \dfrac{F}{A_0}$	$\sigma^t = \dfrac{F}{A_{\text{instantaneous}}} = \dfrac{F}{A}$
$\varepsilon = \dfrac{\delta L}{L_{\text{original}}} = \dfrac{\delta L}{L_0}$	$\varepsilon^t = \displaystyle\int_{L_0}^{L_0 + \delta L} \dfrac{dL}{L} = \ln\left(\dfrac{L_0 + \delta L}{L_0}\right)$

Engineering stress and strain are convenient to use because in performing a test with uniaxial stress the original length and cross-sectional area are easily measured but it is not as convenient to continually measure their instantaneous values.

1.8.1   True Strain

To consider why we call stresses and strains "true" stresses and strains, we consider strains using the illustration of Figure 1.1. It should be true for a self-consistent definition of strain that, if the rectangular parallelepiped is strained in two steps by extending it first from L_0 to $L_1 = L_0 + \delta L_1$ and then extending again from L_1 to $L_2 = L_1 + \delta L_2$, the two strains should add to the total strain if the deformation were performed all at once, that is, from a length L_0 to a length L_2. That is, the final strain should not depend on how the strain is formed. Consider first the engineering strain:

$$\text{Increment 1}: \qquad \varepsilon_{0-1} = \frac{L_1 - L_0}{L_0} = \frac{\delta L_1}{L_0} \qquad\qquad (1.49)$$

$$\text{Increment 2}: \qquad \varepsilon_{1-2} = \frac{L_2 - L_1}{L_1} = \frac{\delta L_2}{L_0 + \delta L_1} \qquad\qquad (1.50)$$

If the deformation is performed in one step,

$$\text{Total strain}: \qquad \varepsilon_{0-2} = \frac{L_2 - L_0}{L_0} = \frac{\delta L_1 + \delta L_2}{L_0} \neq \varepsilon_{0-1} + \varepsilon_{1-2} \qquad (1.51)$$

Clearly this is not equal to the sum of the partial strains so engineering strain is not additive and does not give a self-consistent measure of strain. However, if we use the instantaneous length to define an infinitesimal increment in true strain,

$$d\varepsilon^t = \frac{dL}{L} \qquad\qquad (1.52)$$

then the total true strain associated with a change in length from L_{initial} to L_{final} is

$$\varepsilon^t = \int_{L_{\text{initial}}}^{L_{\text{final}}} \frac{dL}{L} = \ln\left(\frac{L_{\text{final}}}{L_{\text{initial}}}\right) = \ln\left(1 + \frac{\delta L}{L_{\text{initial}}}\right) \qquad (1.53)$$

Consider now the two-step deformation discussed above. The associated components of true strain are

$$\text{Increment 1}: \quad \varepsilon^t_{0-1} = \ln\left(\frac{L_1}{L_0}\right) \tag{1.54}$$

$$\text{Increment 2}: \quad \varepsilon^t_{1-2} = \ln\left(\frac{L_2}{L_1}\right) \tag{1.55}$$

If the deformation is performed in one step,

$$\text{Total strain}: \quad \varepsilon^t_{0-2} = \ln\left(\frac{L_2}{L_0}\right) = \ln\left(\frac{L_2}{L_1}\frac{L_1}{L_0}\right) = \varepsilon^t_{0-1} + \varepsilon^t_{1-2} \tag{1.56}$$

showing that true strain is additive and so independent of how the deformation is performed. A series expansion of the logarithm in Eq. (1.53) shows that for small strain the engineering and true strains have nearly the same value but at large strains they differ significantly. As an example, if a specimen were strained to twice its length or one-half its length, the engineering strain would be $\varepsilon = 1$ and $\varepsilon = -\frac{1}{2}$ respectively, but the true strains would be $\varepsilon^t = 0.69$ and $\varepsilon^t = -0.69$, respectively.

1.8.2 True Stress

The need for true stress is clear. If a body is subjected to large strains, the cross section can be considerably reduced and the engineering stress badly underestimates the local stress. This is particularly true for some ductile materials which can strain nonuniformly under a tensile load forming local "necks" where the cross section is considerably smaller than the original or the average cross section. In such a case the engineering stress is uniform along the length, but the true stress reaches a high value in the neck region and is a superior representation of stress.

For a uniaxial tension or compression test it is possible to convert engineering strain to true strain and to determine the true stress at a given strain provided the relationship between volume of the sample and the axial strain is known. The analysis is simplified if, as is usually the case, it is assumed that the volume of the sample does not change during plastic deformation. The volume V can be related to the initial (L_0 and A_0) and instantaneous (L_i and A_i) length and cross-sectional area:

$$V = A_0 L_0 = A_i L_i \tag{1.57}$$

Thus

$$\frac{L_i}{L_0} = \frac{A_0}{A_i} \tag{1.58}$$

The engineering strain is given by

$$\varepsilon = \frac{L_i - L_0}{L_0} = \frac{L_i}{L_0} - 1 \qquad \text{or} \qquad \frac{L_i}{L_0} = 1 + \varepsilon \tag{1.59}$$

while the true strain is

$$\varepsilon^t = \ln\left(\frac{L_i}{L_0}\right) = \ln(1 + \varepsilon) \tag{1.60}$$

To determine the true stress at a give strain,

$$\sigma^t = \frac{F}{A_i} = \frac{FL_i}{A_0 L_0} = \sigma(1 + \varepsilon) \tag{1.61}$$

True stress and true strain are only used where relatively large plastic strains are observed since elastic strains are usually so low that engineering and true stresses and strains are the same. For ceramics only elastic deformation is observed except under high temperatures, and so generally engineering stresses and strains are sufficient.

PROBLEMS

1. An elastic ceramic body is placed under a hydrostatic compression of 200 MPa. Additional stresses of $\sigma_{xx} = 400$ MPa, $\sigma_{yy} = 100$ MPa, and $\sigma_{xy} = \sigma_{yx} = 50$ MPa are then superimposed. No other stresses are applied. What is the total stress tensor? What are the principal stresses and what angles do the principal axes make to the x axis? What is the maximum shear stress anywhere in the body and what is its orientation?

2. The stress tensor at a point $P(x,y,z)$ is

$$\sigma = \begin{pmatrix} 300 & 100 & 100 \\ 100 & 0 & 200 \\ 100 & 200 & 0 \end{pmatrix} \quad \text{MPa}$$

Determine the principal stresses and unit vectors in the principal directions. Determine the magnitude and directions of the maximum shear stress at P.

3. A tensile force of 50 N is applied uniformly over the end faces (measuring 10 mm by 100 µm) of a thin ceramic sheet. The sheet contains a small crack whose plane is inclined at 60° to the direction of the force. Find the tensile stress acting normal to the crack and the shear stress acting in the plane of

the crack.
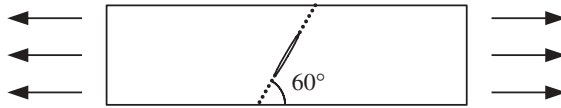
4. Prove by differentiating Eqs. (1.20) with respect to θ that (i) the maximum and minimum normal stresses are the principal stresses and that (ii) the maximum shear stress is one-half of the difference between the principal stresses and acts on planes inclined at $\pm 45°$ to the principal axes.

5. The strains (and hence stresses) in the surface of a solid can be measured using strain gauges. A strain gauge is a thin layer of resistive metal printed in a zigzag pattern on a thin polymer substrate. When the metal pattern is subjected to strain, its resistance changes; the zigzag pattern is chosen so that the resistance change is proportional to the normal strain in only one direction. The substrate is glued to the surface of interest to sense changes in the strain. Strain gauges are not sensitive to shear strains, but the shear strain can be calculated from the three normal strains measured by three gauges arranged in what is called a "strain gauge rosette." The schematic below shows such a rosette with three gauges with their sensitive directions shown by the arrows. Gauges A and C are perpendicular and B lies at 45° between them.

A strain gauge rosette like the one in the sketch is glued to the surface of a specimen while the specimen is under zero stress. When stresses are applied to the specimen, it is determined that the principal strains in the surface are inclined at an angle to the gauges $\theta = 20°$, as shown in the sketch. If the principal strains are $\varepsilon_{xx} = 0.03\%$ and $\varepsilon_{yy} = 0.01\%$, what strains will the three gauges measure?
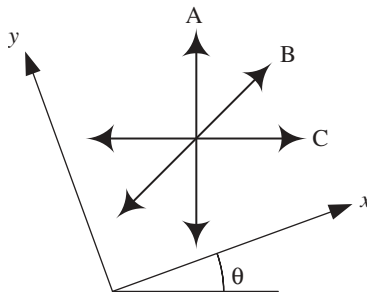
6. Strain gauges attached to the surface of a ceramic body record the following strain components: $\varepsilon_{xx} = 2.00 \times 10^{-4}$, $\varepsilon_{yy} = 1.50 \times 10^{-4}$, and $\varepsilon_{xy} = -1.00 \times 10^{-4}$. Find the principal strains ε_1, ε_2 and their inclination to the

x axis. Also find the maximum shear strain $\varepsilon_{\max}$ and its angles of inclination to the x axis.

7. The components of a displacement field are given by (units are meters)

$$u_x = (x^2 + 20) \times 10^{-3} \qquad u_y = 2yz \times 10^{-3} \qquad u_z = (z^2 - xy) \times 10^{-3}$$

Find the displacements at the point (2,5,7) and the point (3,8,9). Find the change in the distance between these two points. Determine expressions for the total, hydrostatic, and deviatoric strain tensors. Calculate the strain tensor explicitly at the point (2,−1,3). What are the principal strains at this point?

8. Prove that the two-dimensional invariant $\sigma_{xx} + \sigma_{yy}$ is independent of the rotation angle θ. Furthermore, prove that in three-dimensions the invariant $\sigma_{xx} + \sigma_{yy} + \sigma_{zz}$ is independent of the direction cosines. The following relationships may be needed for the proof:

$$a_{xx}^2 + a_{xy}^2 + a_{xz}^2 = 1 \qquad a_{yx}^2 + a_{yy}^2 + a_{yz}^2 = 1 \qquad a_{zx}^2 + a_{zy}^2 + a_{zz}^2 = 1$$

$$a_{xx}a_{yx} + a_{xy}a_{yy} + a_{xz}a_{yz} = 0$$
$$a_{yx}a_{zx} + a_{yy}a_{zy} + a_{yz}a_{zz} = 0$$
$$a_{zx}a_{xx} + a_{zy}a_{xy} + a_{zz}a_{xz} = 0$$

2

TYPES OF MECHANICAL BEHAVIOR

2.1 INTRODUCTION

With the concepts of stress and strain established, one can describe the general types of mechanical behavior of solids. The intention in this chapter is to present the major categories of mechanical behavior in terms of their general characteristics in order to provide an overview and give perspective to the material to follow. The approach here is to follow the historical tradition and discuss types of mechanical behavior in terms of the overall macroscopic response of a solid to stress, considering the solid as a homogeneous body. Real solids are usually inhomogeneous and the overall behavior is the result of detailed processes that take place on an atomic scale. Full and accurate descriptions of various types of mechanical behavior often require further development of concepts and mathematical tools to treat these detailed processes. These concepts and tools will be treated in later chapters for types of mechanical behavior pertinent to ceramics.

The response of a solid to an applied stress is to deform and, if the stress exceeds the strength, to fail. Mechanical behavior categories are generally defined by the modes of deformation and modes of failure. The individual types of mechanical behavior discussed below often closely approximate the real behavior of solids, at least over some range of time and temperature. However, a real solid may have several types of mechanical behavior taking place at once so that the overall behavior is more complex than any one of the somewhat

idealized types discussed below would indicate. Nevertheless, these idealized types of behavior permit quantitative treatments of great usefulness.

2.2 ELASTICITY AND BRITTLE FRACTURE

A relatively simple type of mechanical behavior, and one of great importance for ceramics, is elastic deformation and brittle failure in tension. This type of behavior is illustrated in Figure 2.1, which shows the strain (approximately instantaneous and time independent) as a function of the applied stress. Elastic deformation is defined by full and instantaneous recovery of strain if the stress is removed. Many, but not all, ceramics at room temperature are elastic to a good approximation. Others, such as MgO single crystals, show residual deformation after the load is removed. Even ceramics such as polycrystalline aluminum oxide that are generally considered elastic at room temperature may show small amounts of permanent deformation when strain is measured very accurately. Such effects can be important when accurate dimensional stability, such as in a gyroscope, is required. The precision elastic limit is said to be exceeded when a permanent strain of 10^{-6} is exceeded.

Elastic strain need not be a linear function of stress. Curve A in Figure 2.1 is drawn with distinct nonlinearity to emphasize this fact. When examined closely, all solids show some degree of nonlinearity in their stress–strain curve. However, for many solids, including ceramics, the nonlinearity is quite small so that a linear relation between stress and strain is assumed for most purposes, as is done in this book. The behavior of geological materials under very high pressures is an example requiring consideration of nonlinear elastic effects.

The curves of Figure 2.1 show arrows indicating failure at the highest stress reached. For ceramics under uniform stress at or near room temperature, this failure is usually sudden and complete.
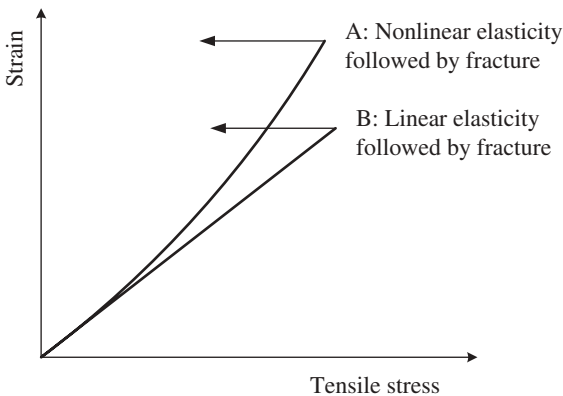
FIGURE 2.1   Elastic behavior.

Much of the design and use of ceramics are based on the conceptually simple model of elastic and brittle behavior described above. In subsequent chapters, linear elasticity (Chapter 3) and linear elastic fracture mechanics (Chapter 5) will be developed extensively to describe the mechanical behavior of ceramics at relatively low temperatures. Despite the apparent simplicity of this concept, its application to materials with defects and complex microstructures is a considerable undertaking. Indeed, there are still unsolved problems. However, the body of successful theory provides very useful guidance.

Another feature is observed if the linear curve of Figure 2.1 is measured on a series of nominally identical ceramic specimens. As shown in Figure 2.2, the elastic deflection repeats quite accurately, but the maximum tensile stress that the sample will sustain varies considerably. This behavior is one of several facts pointing to flaws as the source of failure. Different specimens have flaws with different degrees of effectiveness in reducing strength. The strength of brittle materials is therefore a stochastic variable that is discussed in Chapter 7. This fact is of great importance to the practical use of ceramics, to the practical processing of ceramics, and to the theory of the strength of ceramics. Fracture mechanics concerns the behavior of flaws under stress and is a central subject of this book.

So far in the discussion in this chapter it has tacitly been assumed that any effect of stress is instantaneous. This assumption can be used to provide a good description of behavior for conditions of fairly rapid loading (e.g., tens of seconds to maximum load) and for relatively short time behavior in general (e.g., tens of seconds total time under load) provided the stresses are not too high. At very high strain rates and very high stresses corresponding to ballistic loading, other effects must be considered; we exclude this region of impact behavior from consideration, although ceramics are used as armor. Within the
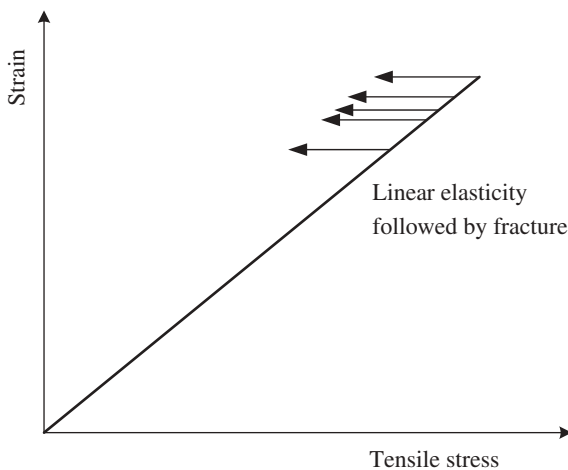
FIGURE 2.2   Fracture of samples under the same loading rates.
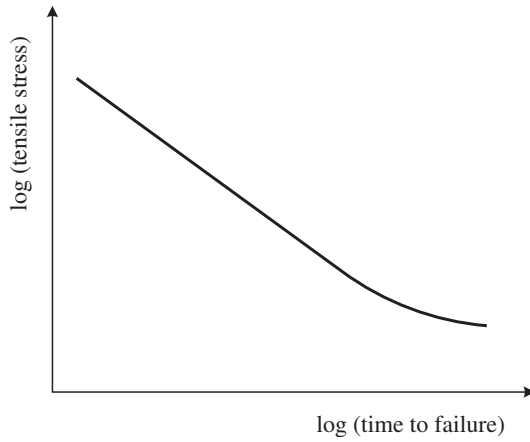
FIGURE 2.3   Stress rupture plot.

range of loading accessible with a normal testing machine, some time-dependent effects must be considered, however. Thus, cracks can have a time-dependent response to stress, namely, slow, subcritical crack growth, which shows itself as an effect on strength.

This time-dependent effect in the mechanical behavior of ceramics becomes apparent if nominally identical samples are tested in certain ranges of temperature and/or corrosive environments by being placed under various constant stress values below the stress required for immediate fracture. As shown in Figure 2.3, each specimen typically breaks after a time. This behavior is termed stress rupture in general. The time to failure increases rapidly as the stress value is decreased so that a log–log plot is commonly used. Sometimes the curve shows an indication of leveling out, indicating a stress level below which
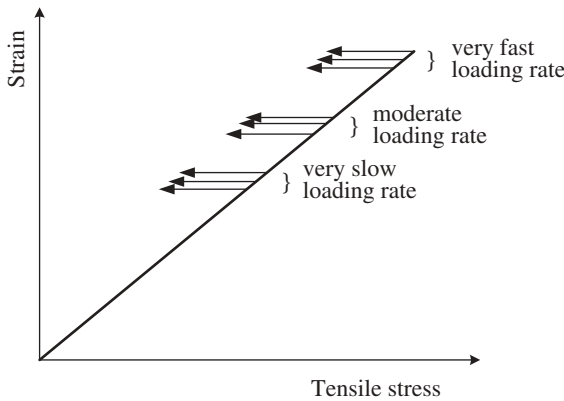
FIGURE 2.4   Fracture of samples under different loading rates.

the specimen life is effectively infinite. Several mechanisms can be at work depending on the material and the temperature. For the case under consideration here of slow crack growth, this behavior is termed static fatigue. Static fatigue is often associated with stress-assisted environmental attack at the tip of cracks. This phenomenon is an important effect that must be taken into account in the use of ceramics in structures intended to carry a load for a long time. A methodology for describing this effect quantitatively and for predicting lifetimes will be described in Chapter 8.

The same static fatigue effect can manifest itself in another way if stress–strain curves are measured out to failure over a wide range of loading rates. As shown in Figure 2.4, the strength is progressively lower as the smaller loading rates are used.

2.3   PERMANENT DEFORMATION

So far we have considered stress–strain curves for solids that undergo only small amounts of elastic deformation followed by fracture. Another class of behavior experienced by some materials involves permanent deformation that is not recovered when the stress is removed. There is always some elastic deformation in addition to the permanent deformation, but for simplicity we omit the elastic component from the following descriptions. An important case of permanent deformation is viscous deformation of a liquid. Glass and fine-grained polycrystalline ceramics at high temperatures behave like highly viscous liquids so that consideration of liquidlike behavior is appropriate. Figure 2.5 shows that for a liquid the response to an applied shear stress is a shear strain rate that depends on the stress value. The simple case where the shear strain rate is proportional to shear stress (Newtonian viscosity) is shown.
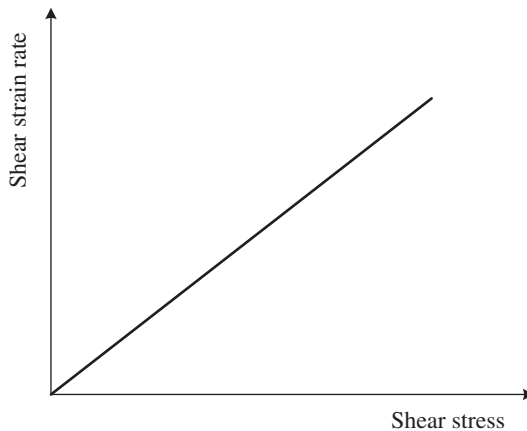
FIGURE 2.5   Viscous deformation.
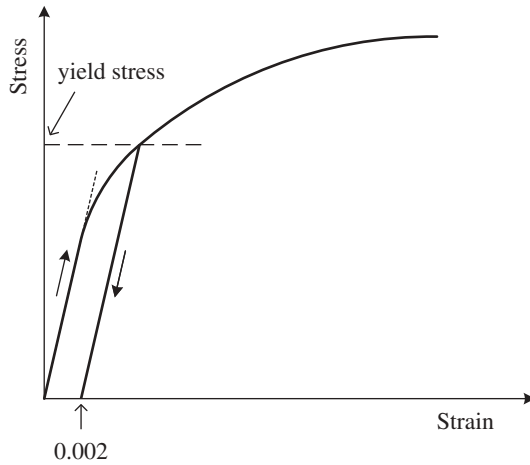
FIGURE 2.6 Plastic deformation.

More complex relationships are possible and are important in many liquids, including ceramic slips, but this topic will not be pursued here.

Another type of permanent deformation is plastic deformation, which will be discussed in Chapters 18 and 19. This deformation can be considered to be time independent even though it is based on dynamic processes whose rates depend on stress. This is because the time elapsing in stress–strain tests is generally long enough for the dynamic processes to reach completion. Figure 2.6 shows a typical stress–strain curve for a plastically deforming
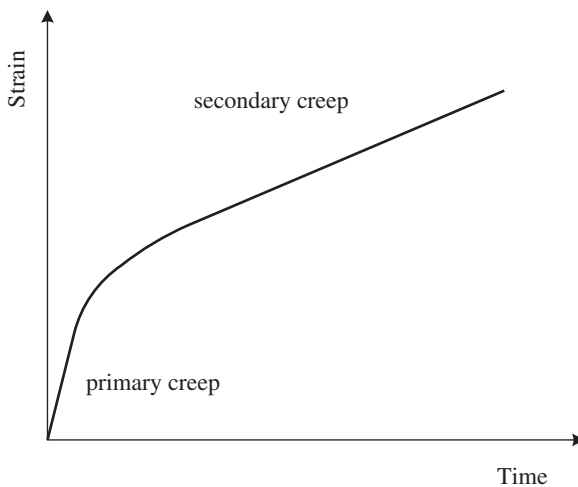
FIGURE 2.7 Creep.

material. If the test is interrupted at some point and the stress is removed, the elastic portion of the strain is recovered but the plastic component is not. The tensile yield strength is generally defined as the stress that upon removal leaves a permanent strain of 0.002, as indicated by the straight line in Figure 2.6. Plastic deformation commonly occurs in metals at room temperature but usually takes place in ceramics only at high temperatures, although localized plastic deformation does occur even in ceramics in special circumstances such as in hardness testing (Chapter 22).

A final type of permanent deformation needing consideration in ceramics is creep. Here permanent deformation begins when stress is applied, slows down in rate, but continues for a long time before ultimate failure. Figure 2.7 shows this type of behavior. These two stages, termed transient and steady-state creep, generally occur in polycrystalline ceramics at low stresses and sufficiently high temperature. In metals there is often a final period of increasing creep rate before failure, termed third-stage or tertiary creep, but in ceramics failure often occurs with little or no third stage. Creep and creep-assisted failure are the primary processes limiting structural use of ceramics at high temperature and are accordingly considered in Chapters 20 and 21.

3

ELASTICITY

3.1   INTRODUCTION

Linear elastic behavior is commonly assumed for ceramics under load at temperatures up to about one-half their absolute melting point. This is usually a good approximation, although there are exceptions, such as single-crystal magnesium oxide for which appreciable bulk plastic deformation occurs at room temperature. Linear elasticity is usually assumed when calculating the stresses caused by loads applied to bodies and so is at the heart of design with brittle ceramics. The basic equations of linear elasticity for elastically isotropic materials are accordingly reviewed.

Anisotropic elasticity can occur in polycrystalline ceramics with preferred orientation and, in fact, does sometimes occur in hot-pressed ceramics, although the anisotropy produced by hot pressing may be small and is sometimes ignored. Two types of ceramics in which a large degree of elastic

anisotropy often occurs are single crystals and composites with oriented reinforcing fibers. Because these are important types of ceramics, the basic equations of anisotropic elasticity are reviewed.

Both the values of the elastic constants and their temperature dependence are related to the interatomic potentials. A few results are described to provide physical insight. Some useful approximate relations for temperature dependence are presented.

3.2 ELASTICITY OF ISOTROPIC BODIES

Consider an elastically isotropic body under a single component of stress σ_{xx}, as shown in Figure 3.1. Hooke's law of elasticity states that the strain is proportional to the stress. For this uniaxial tensile loading, the constant of proportionality defines the **Young's modulus** E:

$$\varepsilon_{xx} = \frac{\sigma_{xx}}{E} \tag{3.1}$$

In addition to the ε_{xx} strain, strains are developed in the transverse directions, ε_{yy} and ε_{zz}, which define **Poisson's ratio**:

$$\nu = -\frac{\varepsilon_{yy}}{\varepsilon_{xx}} \tag{3.2}$$

This elastic constant is also sometimes called the **lateral contraction ratio**. The negative sign is included because most materials contract in directions perpendicular to the tensile stress; ν then has a positive value. The two transverse strains are then given by

$$\varepsilon_{yy} = -\nu\,\varepsilon_{xx} = -\nu\frac{\sigma_{xx}}{E} \qquad \varepsilon_{zz} = -\nu\,\varepsilon_{xx} = -\nu\frac{\sigma_{xx}}{E} \tag{3.3}$$

An idea of the size of elastic deformations in ceramics can be obtained by considering a rod of polycrystalline aluminum oxide having randomly oriented grains with $E = 403\,\text{GPa}$ and $\nu = 0.21$. If a tensile stress $\sigma_{xx} = 500\,\text{MPa}$ is
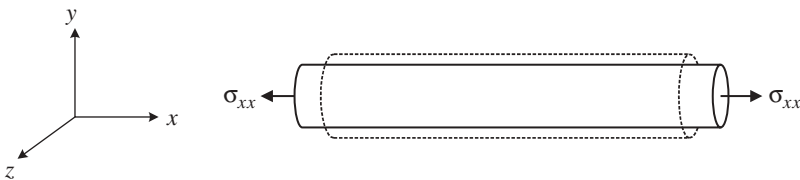
FIGURE 3.1 Rod subjected to uniaxial tension σ_{xx}.

applied, the resulting strains are

$$\varepsilon_{xx} = \frac{500 \times 10^6}{403 \times 10^9} = 0.0012 = 0.12\%$$

$$\varepsilon_{yy} = \varepsilon_{zz} = -0.00026 = -0.026\%$$

(3.4)

The maximum elastic strain that can be achieved in a polycrystalline ceramic prior to failure is typically 0.1% or so. Ceramic fibers and bulk single crystals specially prepared to be nearly flaw free may have elastic tensile strains at fracture as great as 1%.

Consider next the application of a shear stress $\sigma_{xy} = \sigma_{yx}$. Using Hooke's law, the relationship between shear stress and shear strain defines the **shear modulus** or **rigidity modulus** μ:

$$\gamma_{xy} = \gamma_{yx} = \frac{\sigma_{xy}}{\mu}$$

(3.5)

Here μ is used for shear modulus to distinguish from G, which, although used in many books for shear modulus, will be used in this book for the mechanical energy release rate defined in Chapter 5.

There are only two independent moduli of elasticity for an isotropic material. The shear modulus is therefore related to Young's modulus and Poisson's ratio by

$$\mu = \frac{E}{2(1 + \nu)}$$

(3.6)

In the above example with polycrystalline aluminum oxide under 500 MPa tensile stress, the maximum shear stress will occur on planes at $\pm 45°$ to the stress axis and will be half the tensile stress, or 250 MPa [see Figure 1.8(a)]. For $\mu = 160$ GPa, this gives a shear strain of $\gamma_{xy} = 0.0016 = 0.16\%$.

Another important elastic modulus is the **bulk modulus** B defined by

$$B = -V \left(\frac{\partial p}{\partial V} \right)_T \quad \text{or} \quad B = -V \frac{dp}{dV}$$

(3.7)

Elastic constants are always defined under isothermal conditions so the simpler second form in Eq. (3.7) is used throughout this book. The bulk modulus is related to Young's modulus and the shear modulus by

$$B = \frac{E\mu}{3(3\mu - E)}$$

(3.8)

Other elastic moduli have been defined to describe the elastic behavior of isotropic materials. The most frequently encountered moduli include Young's modulus E, the shear modulus μ, Poisson's ratio ν, the bulk modulus B, and λ; λ, μ are called the **Lamé constants**. Interrelationships between these elastic moduli are summarized in Table 3.1.

TABLE 3.1   Relationships between Elastic Moduli for Elastically Isotropic Materials

Moduli	Independent Pairs of Moduli				
	E, ν	E, μ	B, μ	B, ν	λ, μ
E	E	E	$\dfrac{9B\mu}{3B + \mu}$	$3B(1 - 2\nu)$	$\dfrac{\mu(3\lambda + 2\mu)}{\lambda + \mu}$
μ	$\dfrac{E}{2(1 + \nu)}$	μ	μ	$\dfrac{3B(1 - 2\nu)}{2(1 + \nu)}$	μ
B	$\dfrac{E}{3(1 - 2\nu)}$	$\dfrac{E\mu}{3(3\mu - E)}$	B	B	$\lambda + \dfrac{2}{3}\mu$
ν	ν	$\dfrac{E}{2\mu} - 1$	$\dfrac{3B - 2\mu}{2(3B + \mu)}$	ν	$\dfrac{\lambda}{2(\lambda + \mu)}$
λ	$\dfrac{\nu E}{(1 + \nu)(1 - 2\nu)}$	$\dfrac{\mu(E - 2\mu)}{3\mu - E}$	$B - \dfrac{2}{3}\mu$	$\dfrac{3\nu B}{1 + \nu}$	λ

TABLE 3.2   Elastic Moduli of Polycrystalline Ceramics

Substance	Young's Modulus (GPa)	Shear Modulus (GPa)
Al_2O_3	402.8	163.0
Dy_2O_3	170.5	
Er_2O_3	186.3	
MgO	310.9	133.4
ThO_2	261.0	100.6
TiO_2	284.2	111.5
Y_2O_3	138.3	
ZnO	123.5	45.6

Values for Young's modulus and the shear modulus for some pore-free polycrystalline ceramics are given in Table 3.2. These values are in some cases averages of measurements from several authors as given in more detail elsewhere (Wachtman, 1969).

3.3   REDUCED NOTATION FOR STRESSES, STRAINS, AND ELASTIC CONSTANTS

The general form of Hooke's law expresses each elastic strain as a linear combination of each of the stresses (Nye, 1985):

$$\underline{\underline{\varepsilon}} = \underline{\underline{S}} \; \underline{\underline{\sigma}} \qquad \text{or} \qquad \varepsilon_{ij} = \sum_{k=1}^{3} \sum_{l=1}^{3} s_{ijkl} \; \sigma_{kl} \qquad (3.9)$$

where $\underline{\underline{S}}$ is the **elastic compliance tensor**. The stresses can equivalently be expressed as linear combinations of the strains according to:

$$\underline{\sigma} = \underline{\underline{C}}\,\underline{\varepsilon} \qquad \text{or} \qquad \sigma_{ij} = \sum_{k=1}^{3}\sum_{l=1}^{3} c_{ijkl}\,\varepsilon_{kl} \tag{3.10}$$

where $\underline{\underline{C}}$ is the **elastic stiffness tensor**. The quadruple underscores signify that in the general case $\underline{\underline{S}}$ and $\underline{\underline{C}}$ have four dimensions since they are fourth-rank $3 \times 3 \times 3 \times 3$ tensors with 81 components. Note that compliance is commonly represented by $\underline{\underline{S}}$, and stiffness by $\underline{\underline{C}}$, and not the other way as you might expect.

The tensor equations (3.9) and (3.10) represent nine simultaneous equations. However, as already seen in Chapter 1, there are only six independent components of stress and of strain. The situation is significantly simplified if the stress and strain are represented in **reduced notation** or **matrix notation** by 6×1 matrices instead of 3×3 tensors. The relationships between the components of stress in reduced and tensor notation are defined by

$$\underline{\sigma} = \begin{pmatrix} \sigma_1 \\ \sigma_2 \\ \sigma_3 \\ \sigma_4 \\ \sigma_5 \\ \sigma_6 \end{pmatrix} = \begin{pmatrix} \sigma_{11} \\ \sigma_{22} \\ \sigma_{33} \\ \sigma_{23} \\ \sigma_{31} \\ \sigma_{12} \end{pmatrix} \qquad \underline{\underline{\sigma}} = \begin{pmatrix} \sigma_1 & \sigma_6 & \sigma_5 \\ \sigma_6 & \sigma_2 & \sigma_4 \\ \sigma_5 & \sigma_4 & \sigma_3 \end{pmatrix} = \begin{pmatrix} \searrow & \leftarrow \\ & \searrow \\ \uparrow & \leftarrow & \end{pmatrix} \tag{3.11}$$

The last schematic shows the order in which the reduced-notation, single-subscript stress components are placed into a 3×3 matrix to build the equivalent stress tensor.

The strain tensor can be represented in reduced notation in a similar fashion except for one important difference—The shear strain in reduced notation is the engineering shear strain, rather than simple shear strain:

$$\underline{\varepsilon} = \begin{pmatrix} \varepsilon_1 \\ \varepsilon_2 \\ \varepsilon_3 \\ \varepsilon_4 \\ \varepsilon_5 \\ \varepsilon_6 \end{pmatrix} = \begin{pmatrix} \varepsilon_{11} \\ \varepsilon_{22} \\ \varepsilon_{33} \\ 2\varepsilon_{23} \\ 2\varepsilon_{31} \\ 2\varepsilon_{12} \end{pmatrix} = \begin{pmatrix} \varepsilon_{11} \\ \varepsilon_{22} \\ \varepsilon_{33} \\ \gamma_{23} \\ \gamma_{31} \\ \gamma_{12} \end{pmatrix} \qquad \underline{\underline{\varepsilon}} = \begin{pmatrix} \varepsilon_1 & \frac{1}{2}\varepsilon_6 & \frac{1}{2}\varepsilon_5 \\ \frac{1}{2}\varepsilon_6 & \varepsilon_2 & \frac{1}{2}\varepsilon_4 \\ \frac{1}{2}\varepsilon_5 & \frac{1}{2}\varepsilon_4 & \varepsilon_3 \end{pmatrix} = \begin{pmatrix} \searrow & \leftarrow \\ & \searrow \\ \uparrow & \leftarrow & \end{pmatrix} \tag{3.12}$$

In general form Hooke's law in reduced notation becomes

$$\underline{\varepsilon} = \underline{\underline{S}}\,\underline{\sigma} \qquad \varepsilon_i = \sum_{j=1}^{6} s_{ij}\,\sigma_j$$

$$
\begin{pmatrix} \varepsilon_1 \\ \varepsilon_2 \\ \varepsilon_3 \\ \varepsilon_4 \\ \varepsilon_5 \\ \varepsilon_6 \end{pmatrix}
=
\begin{pmatrix}
s_{11} & s_{12} & s_{13} & s_{14} & s_{15} & s_{16} \\
s_{21} & s_{22} & s_{23} & s_{24} & s_{25} & s_{26} \\
s_{31} & s_{32} & s_{33} & s_{34} & s_{35} & s_{36} \\
s_{41} & s_{42} & s_{43} & s_{44} & s_{45} & s_{46} \\
s_{51} & s_{52} & s_{53} & s_{54} & s_{55} & s_{56} \\
s_{61} & s_{62} & s_{63} & s_{64} & s_{65} & s_{66}
\end{pmatrix}
\begin{pmatrix} \sigma_1 \\ \sigma_2 \\ \sigma_3 \\ \sigma_4 \\ \sigma_5 \\ \sigma_6 \end{pmatrix}
\tag{3.13}
$$

The relationships between the stiffness components in reduced (two-subscript) and tensor (four-subscript) notation are (Nye, 1985)

$$
s_{mn} =
\begin{cases}
s_{ijkl} & \text{if both } m \text{ and } n \leq 3 \\
2s_{ijkl} & \text{if either } m \text{ or } n \geq 4 \\
4s_{ijkl} & \text{if both } m \text{ and } n \geq 4
\end{cases}
\quad \text{where} \quad
\begin{aligned}
m &= \begin{cases} i & \text{if } i = j \\ 9 - i - j & \text{if } i \neq j \end{cases} \\
n &= \begin{cases} k & \text{if } k = l \\ 9 - k - l & \text{if } k \neq l \end{cases}
\end{aligned}
\tag{3.14}
$$

The stresses are expressed in terms of the strains in reduced notation by

$$\underline{\sigma} = \underline{\underline{C}}\,\underline{\varepsilon} \qquad \sigma_i = \sum_{j=1}^{6} c_{ij}\,\varepsilon_j$$

$$
\begin{pmatrix} \sigma_1 \\ \sigma_2 \\ \sigma_3 \\ \sigma_4 \\ \sigma_5 \\ \sigma_6 \end{pmatrix}
=
\begin{pmatrix}
c_{11} & c_{12} & c_{13} & c_{14} & c_{15} & c_{16} \\
c_{21} & c_{22} & c_{23} & c_{24} & c_{25} & c_{26} \\
c_{31} & c_{32} & c_{33} & c_{34} & c_{35} & c_{36} \\
c_{41} & c_{42} & c_{43} & c_{44} & c_{45} & c_{46} \\
c_{51} & c_{52} & c_{53} & c_{54} & c_{55} & c_{56} \\
c_{61} & c_{62} & c_{63} & c_{64} & c_{65} & c_{66}
\end{pmatrix}
\begin{pmatrix} \varepsilon_1 \\ \varepsilon_2 \\ \varepsilon_3 \\ \varepsilon_4 \\ \varepsilon_5 \\ \varepsilon_6 \end{pmatrix}
\tag{3.15}
$$

The same rule for conversion from four to two subscripts holds here [Eq. (3.14)], except $c_{ijkl} = c_{mn}$ for all values of m and n.

The compliance and stiffness matrices have 36 components. However, it can be shown that the elastic compliance and elastic stiffness matrices are symmetric; that is, $s_{ij} = s_{ji}$ and $c_{ij} = c_{ji}$ (Nye, 1985; Hearmon, 1961). In the

most general case there are accordingly a total of 21 independent elastic constants whether expressed as compliances or stiffnesses.

One can choose to describe the elastic behavior of single crystals by using the two elastic moduli defined for isotropic materials—Young's modulus and the shear modulus. However, these quantities will vary with orientation for single crystals. The relation between these two elastic moduli and the single-crystal stiffnesses can be seen by considering the meaning of the moduli. The reciprocal of Young's modulus gives the tensile strain in the direction of an applied tensile stress. Taking the x_1 direction as the direction of application of tensile stress then gives

$$E^{-1} = s_{11} \tag{3.16}$$

Similarly, a shear stress in the yz plane produces a shear strain in the yz plane so that the shear modulus for this situation is given by

$$\mu^{-1} = s_{44} \tag{3.17}$$

To obtain either of these elastic moduli for any other crystal direction requires considering a rotated coordinate system and transforming the compliance values. However, the compliance represented in reduced notation is not a tensor quantity and so cannot be subjected to rotational transformations. The procedure is to use the four-index tensor form of the compliances and to work out the transformations of these. The task is straightforward but tedious and the resulting equations are quite lengthy for lower symmetry crystals such as sapphire (Wachtman et al., 1960).

3.4   EFFECT OF SYMMETRY ON ELASTIC CONSTANTS

The existence of crystal symmetry reduces the number of independent elastic constants. The 32 possible crystal point group symmetries fall into 11 categories in terms of the effect of crystal symmetry on elastic properties. The results are given in detail by Nye (1985). Only two cases of special interest will be summarized here: cubic symmetry and elastic isotropy.

Crystals with cubic symmetry have three independent elastic constants and are not elastically isotropic. One might think by analogy with electrical, thermal, and optical properties (for which cubic symmetry ensures isotropic behavior) that cubic crystals would be elastically isotropic. The reason that this is not so is that the tensor compliances and stiffnesses are fourth-rank tensors while the analogous resistivity, dielectric constant, and thermal expansion are second-rank tensors. Application of symmetry operations in any one of the cubic point groups leads to the relations

$$s_{11} = s_{22} = s_{33} \qquad s_{12} = s_{23} = s_{31} \qquad s_{44} = s_{55} = s_{66} \tag{3.18}$$

All the other compliances are required to be zero by cubic symmetry. The same relationships hold with the s_{ij} replaced by c_{ij}.

The compliance and stiffness matrices for cubic symmetry are thus

$$\underline{\underline{S}} = \begin{pmatrix} s_{11} & s_{12} & s_{12} & 0 & 0 & 0 \\ s_{12} & s_{11} & s_{12} & 0 & 0 & 0 \\ s_{12} & s_{12} & s_{11} & 0 & 0 & 0 \\ 0 & 0 & 0 & s_{44} & 0 & 0 \\ 0 & 0 & 0 & 0 & s_{44} & 0 \\ 0 & 0 & 0 & 0 & 0 & s_{44} \end{pmatrix}$$

(3.19)

$$\underline{\underline{C}} = \begin{pmatrix} c_{11} & c_{12} & c_{12} & 0 & 0 & 0 \\ c_{12} & c_{11} & c_{12} & 0 & 0 & 0 \\ c_{12} & c_{12} & c_{11} & 0 & 0 & 0 \\ 0 & 0 & 0 & c_{44} & 0 & 0 \\ 0 & 0 & 0 & 0 & c_{44} & 0 \\ 0 & 0 & 0 & 0 & 0 & c_{44} \end{pmatrix}$$

Note that these forms are only applicable when the xyz axes coincide with the crystallographic axes. The stiffness components are related to the compliances for cubic symmetry by (Nye, 1985)

$$c_{11} = \frac{s_{11} + s_{12}}{(s_{11} - s_{12})(s_{11} + 2s_{12})}$$

$$c_{12} = \frac{-s_{12}}{(s_{11} - s_{12})(s_{11} + 2s_{12})}$$

(3.20)

$$c_{44} = \frac{1}{s_{44}}$$

An elastically isotropic material can be regarded as a cubic material with an additional relation between the elastic constants. Specifically, for elastic isotropy in a cubic crystal

$$s_{12} = s_{11} - \tfrac{1}{2}s_{44} \qquad c_{12} = c_{11} - \tfrac{1}{2}c_{44}$$

(3.21)

TABLE 3.3 Single-Crystal Elastic Stiffnesses (GPa) and Compliances ($10^{-12}\,Pa^{-1}$) for Some Ceramic Crystals with Cubic Symmetry

Substance	c_{11}	s_{11}	c_{44}	s_{44}	c_{12}	S_{12}
C (diamond)	1020	1.12	492	2.07	250	−0.22
MgO	296	3.99	156	6.41	95.1	−0.97
ThO$_2$	367	3.13	79.7	12.5	106	−0.70
UO$_2$	395	2.96	64.1	15.6	121	−0.70

The compliance matrix for an elastically isotropic material written in terms of Young's modulus, Poisson's ratio, and the shear modulus is

$$\underline{\underline{S}} = \begin{pmatrix} 1/E & -v/E & -v/E & 0 & 0 & 0 \\ -v/E & 1/E & -v/E & 0 & 0 & 0 \\ -v/E & -v/E & 1/E & 0 & 0 & 0 \\ 0 & 0 & 0 & 1/\mu & 0 & 0 \\ 0 & 0 & 0 & 0 & 1/\mu & 0 \\ 0 & 0 & 0 & 0 & 0 & 1/\mu \end{pmatrix} \quad (3.22)$$

The stiffness matrix for an elastically isotropic material is most conveniently expressed in terms of the Lamé constants:

$$\underline{\underline{C}} = \begin{pmatrix} \lambda + 2\mu & \lambda & \lambda & 0 & 0 & 0 \\ \lambda & \lambda + 2\mu & \lambda & 0 & 0 & 0 \\ \lambda & \lambda & \lambda + 2\mu & 0 & 0 & 0 \\ 0 & 0 & 0 & \mu & 0 & 0 \\ 0 & 0 & 0 & 0 & \mu & 0 \\ 0 & 0 & 0 & 0 & 0 & \mu \end{pmatrix} \quad (3.23)$$

Elastic constants for some ceramic single crystals with cubic symmetry are given in Table 3.3 (Nye, 1985; Wachtman, 1969). More complete tabulations are given by Hearmon in the Landolt–Bornstein tables (Hearmon, 1966).

3.5 ORIENTATION DEPENDENCE OF ELASTIC MODULI IN SINGLE CRYSTALS AND COMPOSITES

The orientation dependence of Young's modulus in a cubic crystal is given by

$$E^{-1} = s_{11} - 2\left(s_{11} - s_{12} - \tfrac{1}{2}s_{44}\right)\left(\sin^2 \phi \cos^2 \phi + \tfrac{1}{4}\sin^4 \phi \sin^2 2\theta\right) \quad (3.24)$$
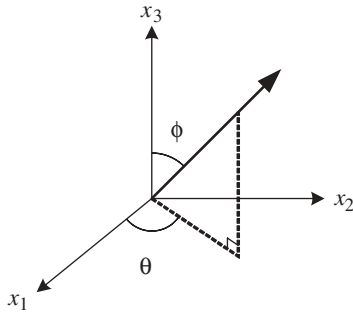
FIGURE 3.2   Polar coordinates for an arbitrary direction.

Here θ and ϕ are the usual polar angles defined in Figure 3.2 where the directions x_1, x_2, and x_3 coincide with the crystallographic axes.

Crystals with orthorhombic symmetry have nine independent compliances: s_{11}, s_{22}, s_{33}, s_{12}, s_{21}, s_{31}, s_{44}, s_{55}, and s_{66}. Such crystals are not often dealt with, but fiber-reinforced composites with continuous, aligned fibers arranged in a square or rectangular array in the plane perpendicular to the fibers have the same elastic symmetry as an orthorhombic crystal and are spoken of as having orthotropic symmetry (Hearmon, 1961; Chawla, 1993). If the arrangement of the aligned fibers in the transverse plane is either random or hexagonal, the elastic symmetry of the composite is the same as that of a hexagonal crystal; that is, five independent elastic constants are required.

Crystals with trigonal symmetry fall into two categories from the point of view of elastic behavior: those with point group symmetry 3 or $\bar{3}$ have seven independent elastic constants while those with symmetry 32, $\bar{3}$, or 3m have six independent elastic constants. The stable form of aluminum oxide, corundum or alpha alumina, falls in the last group. Expressions for the orientation dependence of elastic moduli are available (Wachtman et al., 1960).

3.6   VALUES OF POLYCRYSTALLINE MODULI IN TERMS OF SINGLE–CRYSTAL CONSTANTS

It is of interest to express the elastic moduli of an isotropic polycrystalline body in terms of the single-crystal elastic constants. This is more difficult than it might first appear. Application of a strain to a polycrystalline body causes strains in the individual grains that lead to forces on neighboring grains. Each grain is constrained by its neighbors in a complex way due to the random orientations of the crystallographic axes. There is no exact solution for this problem. Instead, various authors have derived upper and lower bounds for the values of the bulk modulus and the shear modulus of polycrystalline bodies.

For crystals of any symmetry it has been shown that

$$E_v \geq E \geq E_r \tag{3.25}$$

$$\mu_v \geq \mu \geq \mu_r \tag{3.26}$$

where

$$E_v = \frac{(A - B + 3C)(A + 2B)}{2A + 3B + C} \qquad \mu_v = \frac{A - B + 3C}{5} \tag{3.27}$$

$$3A = c_{11} + c_{22} + c_{33} \qquad 3B = c_{12} + c_{23} + c_{31} \qquad 3C = c_{44} + c_{55} + c_{66} \tag{3.28}$$

and where

$$\frac{1}{E_r} = \frac{3A' + 2B' + C'}{5} \qquad \frac{1}{\mu_r} = \frac{4A' - 4B' + 3C'}{5} \tag{3.29}$$

$$3A' = s_{11} + s_{22} + s_{33} \qquad 3B' = s_{12} + s_{23} + s_{31} \qquad 3C' = s_{44} + s_{55} + s_{66} \tag{3.30}$$

The quantities E_v and μ_v are termed the **Voigt moduli** and result from assuming that the strain is uniform in a polycrystalline aggregate and averaging the stress over all possible grain orientations. The quantities E_r and μ_r are termed the **Reuss moduli** and result from assuming that the stress is uniform and averaging the strain (Hearmon, 1961). While the Voigt and Reuss moduli are upper and lower bounds, a reasonable estimate of the moduli of any given polycrystal would be the arithmetic means of the Voigt and Reuss bounds. These are known as the **Hill moduli**:

$$E_h = \tfrac{1}{2}(E_v + E_r) \qquad \mu_h = \tfrac{1}{2}(\mu_v + \mu_r) \tag{3.31}$$

3.7   VARIATION OF ELASTIC CONSTANTS WITH LATTICE PARAMETER

Crystals with the same structure show a systematic variation of elastic constants with lattice parameter. This variation can be understood quite well in terms of the relatively simple Born model for ionic crystals and is instructive in understanding how the macroscopic elastic properties can be related to the

interatomic potentials. In the Born model the lattice energy U of an ionic crystal is assumed to be the sum of two terms according to

$$U = -\frac{Q_1}{r} + \frac{Q_2}{r^n} \tag{3.32}$$

Here the first term arises from the electrostatic attraction and the second from the repulsive force. A simple approach can be used to treat c_{44}, the elastic constant for shear (Gilman, 1963; Davidge, 1979). The force corresponding to a small displacement dr is $-dU/dr$ and the area per atom is approximately r_0^2, where the subscript zero indicates the equilibrium value of r for the unstressed crystal. The stress is then approximately

$$\sigma \simeq \frac{1}{r_0^2} \frac{dU}{dr} \tag{3.33}$$

The elastic constant is

$$c = \frac{d\sigma}{d\varepsilon} = \frac{d\sigma}{(dr/r_0)} = r_0 \frac{d\sigma}{dr} = \frac{1}{r_0} \frac{d^2 U}{dr^2} \tag{3.34}$$

Then the elastic constant is

$$c = \frac{1}{r_0} \frac{d^2 U}{dr^2} \tag{3.35}$$

For shear deformation of ionic crystals the second, repulsive term in Eq. (3.32) can be neglected. This gives

$$c_{44} \approx \frac{\text{const}}{r_0^4} \tag{3.36}$$

The alkali halides obey this relation reasonably well.

A somewhat less approximate yet still simple treatment can be given for the bulk modulus (Born and Huang, 1954; Wachtman, 1969). From thermodynamics the pressure is given by

$$p = -\frac{dU}{dV} \tag{3.37}$$

and the bulk modulus by

$$B = -V\frac{dp}{dV} = V\frac{d^2 U}{dV^2} \tag{3.38}$$

For ionic crystals Eqs. (3.32) and (3.37) give (using $V = \text{const} \times r^3$ so that $dr/dV = r/3V$)

$$p = \frac{1}{3V}\left(-\frac{Q_1}{r} + \frac{nQ_2}{r^n}\right) \tag{3.39}$$

and

$$B = \frac{1}{9V}\left(-\frac{4Q_1}{r} + \frac{n(n+3)Q_2}{r^n}\right) \tag{3.40}$$

Using the condition $p = 0$ at $r = r_0$ in Eq. (3.39) gives

$$\frac{nQ_2}{r_0^n} = \frac{Q_1}{r_0} \tag{3.41}$$

so that for small strain ($r \simeq r_0$, $V \simeq V_0$)

$$B = \frac{(n-1)Q_1}{9r_0V_0} \tag{3.42}$$

The bulk modulus is therefore predicted to vary as $1/r_0V_0 \approx 1/r_0^4$. This is the same dependence on r_0 that was obtained above by a simpler argument for the shear modulus.

Anderson (1966b, 1995) has shown that this predicted $1/r_0^4$ variation is obeyed by the bulk modulus of alkali halides, certain carbides, and the Si family of elements. However, he found that the bulk modulus of oxides instead follows a variation of approximately $1/r_0^9$. He suggested that the bulk modulus of oxides is determined approximately simply by the volume per oxygen atom regardless of whether this volume is the result of a particular chemistry, pressure, or temperature.

3.8 VARIATION OF ELASTIC CONSTANTS WITH TEMPERATURE

Elastic constants of single crystals generally decrease slowly with increasing temperature (Wachtman, 1969). As the temperature is decreased toward absolute zero, the slope of the curve of elastic constant as a function of temperature approaches zero, as required by the third law of thermodynamics. As the temperature increases toward the Debye temperature, the slope approaches a constant for many ceramics. An empirical equation was proposed
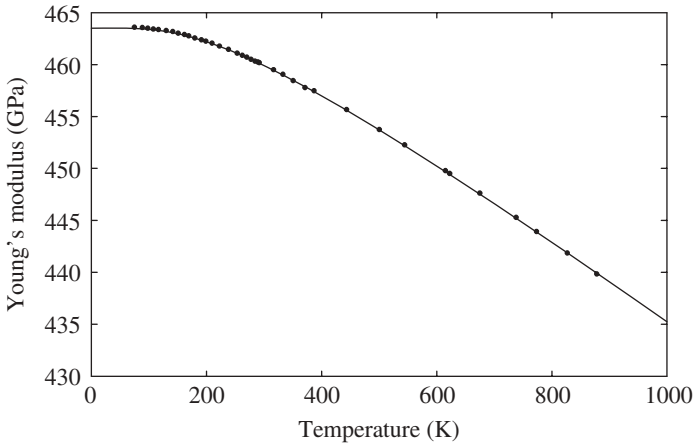
FIGURE 3.3   Temperature dependence of Young's modulus for aluminum oxide single crystal. (Data from Wachtman et al., 1961.)

(Wachtman et al., 1961) that fits the data well for several oxides. This equation written for Young's modulus is

$$E = E_0 - bT \exp\left(\frac{-T_0}{T}\right) \tag{3.43}$$

where E_0 is the value of Young's modulus at absolute zero, b and T_0 are empirical constants, and T_0 was found to be about one-half the Debye temperature. A plot of this equation fitted to data for an aluminum oxide single crystal is shown in Figure 3.3. Anderson (1966b) gave a derivation justifying the form of this equation and providing an interpretation of the parameters. Hillig (1993) has discussed estimating the values of mechanical properties including elastic moduli at high temperature.

For polycrystalline ceramics this variation with temperature also holds, but an additional effect is superimposed (Wachtman and Lam, 1959). At some temperature characteristic of the grain boundary phase the measured elastic moduli decrease rapidly from the linear decrease characteristic of material free of grain boundaries. The additional rapid decrease is attributed to grain boundary softening and sliding and is not really an elastic effect. A useful rule of thumb for common ceramics between room temperature and the onset of grain boundary softening is that the Young's modulus and the shear modulus decrease about 1% per hundred kelvins of temperature increase. More detailed data are given by Wachtman (1969). The extensive and ground-breaking work of Anderson on pressure–volume–temperature relationships for geophysical and ceramic materials is summarized in his book (Anderson, 1995).

3.9   ELASTIC PROPERTIES OF POROUS CERAMICS

Many ceramics have some degree of porosity. In some cases (such as ceramics used as thermal insulators, filters, or catalyst supports) a high degree of porosity is essential for the function that they perform. Mechanical properties such as elastic moduli, strength, and toughness decrease with increasing porosity. Treatments often consider isolated pores in a solid at one extreme and consider a solid, such as a foam, made up of thin-walled cells at the other extreme (Gibson and Ashby, 1988).

It is intuitively evident that porosity will reduce elastic moduli and strength. This effect is usually discussed in terms of the relationship between the volume fraction porosity P and the relative elastic moduli, which are the ratios of the elastic moduli to their values at porosity $P = 0$. Considerable research has been done in fitting empirical curves and developing theoretical models. The problem is difficult because pores differ in shape depending on the processing. It is therefore not to be expected that a simple model based, for example, on spherical pores will accurately represent the behavior of real ceramics. However, the various relationships do provide a useful approximate description. Such relationships have been reviewed by Wachtman (1969) and R. W. Rice (1977). Some of the most widely used relationships are discussed here.

Mackenzie (1950) derived the following expressions for the bulk and shear moduli at small amounts of porosity in terms of their values, B_0 and μ_0, at zero porosity:

$$\frac{1}{B} = \frac{1}{B_0(1-P)} + \frac{3P}{4\mu_0(1-P)} + \text{terms of order } P^3 \qquad (3.44)$$

$$\mu = \mu_0 \left[1 - \frac{5(3B_0 + 4\mu_0)}{9B_0 + 8\mu_0} P \right] + \text{terms of order } P^2 \qquad (3.45)$$

Spriggs (1961) and Spriggs and Brissette (1962) studied the effect of porosity up to fairly large values and proposed the following empirical equations for Young's modulus and the shear modulus:

$$E = E_0 \exp(-bP) \qquad (3.46)$$

$$\mu = \mu_0 \exp(-bP) \qquad (3.47)$$

Here b is a parameter to be fitted empirically; it is usually fitted independently to Young's modulus and shear modulus data and so usually has somewhat different values for the two moduli. The b parameter is typically about 4 for oxides studied in the porosity range 0–40%, as shown in Table 3.4.

TABLE 3.4   Parameters in Spriggs Equations (3.46) and (3.47) for Porosity Dependence of Elastic Moduli

Young's Modulus			
Material	E_0	b	Reference
Aluminum oxide	410.2 GPa	3.95	Knudsen, 1962
Magnesium oxide	317.7 GPa	4.74	Spriggs et al., 1962
Shear Modulus			
Material	μ_0	b	Reference
Magnesium oxide	139.5 GPa	4.90	Spriggs et al., 1962

For the bulk modulus and the shear modulus Hasselman (1962) suggested the equations

$$B = B_0 \left[1 - \frac{AP}{1 - (A+1)P} \right] \tag{3.48}$$

$$\mu = \mu_0 \left[1 - \frac{AP}{1 - (A+1)P} \right] \tag{3.49}$$

where A is a parameter to be fitted empirically.

For small values of P any of these equations reduces to a linear decrease of relative elastic modulus with volume fraction porosity. For example, for Young's modulus, Eq. (3.46) takes the form

$$\frac{E}{E_0} = 1 - bP \tag{3.50}$$

and similarly for the other moduli. The value of b for Young's modulus is typically around 4 (Spriggs, 1961; Knudsen, 1962; Spriggs and Brissette, 1962).

Nielsen (1982, 1984) derived the following equation for the Young's modulus of a solid with pore volume fraction P:

$$E = E_0 \frac{(1-P)^2}{1 + (\rho^{-1} - 1)P} \tag{3.51}$$

Here ρ is the Nielsen shape factor. Nielsen does not give an equation for ρ but states that a value of 0.4 or less is appropriate for materials with porosity that is characteristic of joined particles; a shape factor for porosity that resembles ribbons or dendrites should have a shape factor in the range 0.3–0.7, and a shape factor of 0.6–1.0 is characteristic of pores enveloped by a solid phase.

The slopes of the Spriggs and Nielsen equations for P near zero are

$$\left(\frac{d(E/E_0)}{dP}\right)_{\text{Spriggs for } P\to 0} = -b \tag{3.52}$$

$$\left(\frac{d(E/E_0)}{dP}\right)_{\text{Nielsen for } P\to 0} = -\left(1 + \rho^{-1}\right) \tag{3.53}$$

Plots of the Spriggs and Nielsen equations with b and ρ chosen to give equal initial slopes give very closely the same curve up to about 40% porosity. Either equation can be used within experimental accuracy in this porosity range. A more rigorous test of the equations is how well they represent the data at porosity above 40%. On a linear plot the differences between the two equations may not appear great. However, a better test is to plot experimental data as log (E/E_0) as a function of P. On such a plot the Spriggs equation gives a straight line. Actual data at high porosity typically show that the experimental values fall progressively below this line as the porosity increases above 40%. Work by Ashkin et al. (1990) on silica with porosity ranging from 0.2 to 1 showed that Young's modulus was represented over this entire range fairly well by Nielsen's equation with a single shape factor of $\rho = 0.4$. Closer inspection indicates that the shape factor may be nearer to 0.6 for porosity in the range 0.2–0.5 for some specimens. As noted earlier, it is reasonable that pore shape should depend on the method of preparation. Furthermore, it should change as sintering proceeds from a very porous body to one with low porosity.

Additional theoretical equations for the porosity dependence of elastic moduli have been reviewed by Ramakrishnan and Arunachalam (1993). Rice (1993) has extensively considered the dependence of properties of ceramics, including elastic properties, on porosity and has recently presented a new approach based on mapping the pore and solid shapes.

If one thinks of a porous solid as being analogous to a building, it is plausible that the mechanical behavior of the solid will depend strongly on the details of arrangement of the solid components just as the stiffness and strength of a building or bridge depend on the arrangement of the structural members. Accurate treatment evidently demands detailed knowledge. An important class of porous solids not properly regarded as solids with distributed porosity is the class of cellular solids. Their properties have been reviewed by Gibson and Ashby (1988, p. 1), who give the following definition: ''a cellular solid is one made up of an interconnected network of solid struts or plates which form the edges and faces of cells.'' The reader is referred to their work for further information.

3.10 STORED ELASTIC ENERGY

When a force is applied to an elastic body, the resulting strain causes the point of application of the force to move and so to do work on the body. This energy is stored in the stretched bonds between atoms as a form of potential energy. Since elastic deformation is reversible, the stored energy can in principle be recovered; in particular, the stored elastic energy can be the driving force for crack propagation—linear elastic fracture mechanics will use this concept in Chapter 5. Here we will derive a general relationship for the stored elastic energy in terms of the stress and strain tensors and the elastic properties of the material.

Consider the rod shown in Figure 3.4(a) of length L and cross-sectional area A. When a force F is applied in the x direction, the rod extends by an amount u. Since the material is linear elastic, the force is proportional to the extension, as shown in Figure 3.4(b). The constant of proportionality k, the stiffness, can readily be related to the elastic properties of the material and the dimensions of the bar, but for the current purposes we simply use $F = ku$. At some intermediate force F' the extension will be u' so that $F' = ku'$. If the extension increases by a small amount du', the force does work

$$dW = F' du' = ku' \, du' \tag{3.54}$$

The total work done producing the full extension, u, is therefore

$$W = \int_{u'=0}^{u} ku' \, du' = \tfrac{1}{2}ku^2 = \tfrac{1}{2}Fu \tag{3.55}$$

The work done is therefore the area under the loading curve, the shaded area in Figure 3.4(b). Defining U_e, the **elastic energy density**, as the stored elastic energy
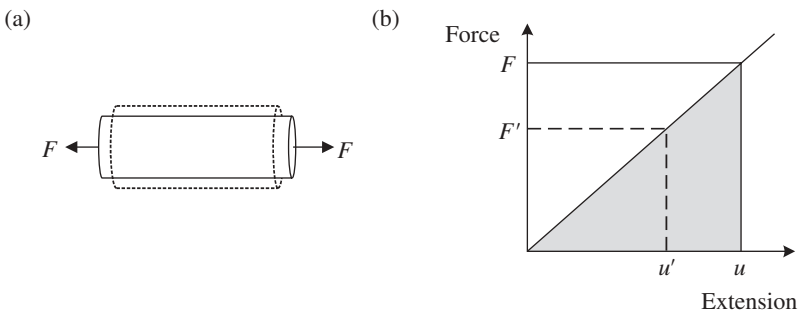
FIGURE 3.4 Force–displacement behavior for a linear elastic body.

per unit volume, we have

$$U_e = \frac{W}{AL} = \frac{1}{2}\frac{F}{A}\frac{u}{L} = \frac{1}{2}\sigma_{xx}\varepsilon_{xx} \tag{3.56}$$

This result may be generalized for more complex states of stress to give the energy density in terms of the stress and strain tensor components and the elastic properties,

$$U_e = \frac{1}{2}\sum_i\sum_j\sigma_{ij}\varepsilon_{ij} = \frac{1}{2}\sum_i\sum_j\sum_k\sum_l S_{ijkl}\sigma_{ij}\sigma_{kl}$$

$$= \frac{1}{2}\sum_i\sum_j\sum_k\sum_l C_{ijkl}\varepsilon_{ij}\varepsilon_{kl} \tag{3.57}$$

PROBLEMS

1. When a metal plastically deforms, to a first approximation, it does not change volume, whereas during elastic deformation the volume of a material changes. Calculate Poisson's ratio v when there is no volume change in an elastic deformation. For polymers $v \sim 0.4$, for metals $v \sim 0.3$, for ionic solids $v \sim 0.25$, and for covalent solids $v \sim 0.2$. In which does the volume change the most during elastic deformation? Can you offer some explanation for the way in which these values of Poisson's ratio are ordered?

2. Use Eqs. (3.20) to check the consistency of the data in Table 3.3.

3. Stresses $\sigma_1 = 100\,\text{MPa}$, $\sigma_3 = 75\,\text{MPa}$, and $\sigma_4 = -50\,\text{MPa}$ (all other components zero) are applied to a diamond single crystal (the directions 1,…, 3 correspond to the crystallographic axes). What strains are generated? Calculate the hydrostatic pressure and volumetric strain.

4. Using the data in Table 3.2, calculate Poisson's ratio and the bulk modulus of polycrystalline alumina.

5. A tensile stress of 50 MPa is applied in the [210] direction to a single crystal of MgO. Calculate the stress tensor referenced to the crystallographic axes. Calculate the strain tensor referenced to the crystallographic axes. Calculate the strain tensor referenced to the principal strain axes. Calculate the angle the direction of the maximum principal strain makes to the direction of the maximum principal stress.

6. The speed of sound in an elastic material is given by $c = \sqrt{M/\rho}$ where ρ is the density and M is the elastic modulus appropriate for the type of sound

wave. For a longitudinal (pressure) wave moving in the x direction, $M = \sigma_{xx}/\varepsilon_{xx}$, while for a transverse (shear) wave moving in the x direction with displacements in the y direction, $M = \sigma_{yx}/\varepsilon_{yx}$. The particular values of the stress–strain ratio depend on the outer boundary conditions for the body. If the wavelength of the sound wave is small compared to a lateral dimension, then there is no normal strain in that direction, while if the wavelength is long, there is no normal stress in that direction.
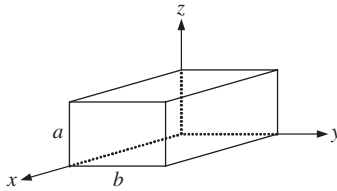
Consider sound waves traveling in the x direction along a long rectangular bar a short length of which is shown above. The section of the bar is $a \times b$ and it is composed of an isotropic material. Find the appropriate modulus for finding the speed of sound for the following sound waves of wavelength λ, expressing all your answers in terms of Young's modulus and Poisson's ratio only:

a. Transverse wave with displacements in the y direction

b. Low-frequency longitudinal wave whose wavelength is much larger than the dimensions of the bar, $\lambda \gg a$ ($\sigma_{zz} = 0$, $\varepsilon_{zz} \neq 0$) and $\lambda \gg b$ ($\sigma_{yy} = 0$, $\varepsilon_{yy} \neq 0$)

c. High-frequency longitudinal wave whose wavelength is much smaller than the dimensions of the bar, $\lambda \ll a$ ($\varepsilon_{zz} = 0$, $\sigma_{zz} \neq 0$) and $\lambda \ll b$ ($\varepsilon_{yy} = 0$, $\sigma_{yy} \neq 0$)

d. Middle-frequency longitudinal wave whose wavelength is much larger than the smaller dimension of the bar, $\lambda \gg a$ ($\sigma_{zz} = 0$, $\varepsilon_{zz} \neq 0$), but much smaller than the larger dimension of the bar, $\lambda \ll b$ ($\varepsilon_{yy} = 0$, $\sigma_{yy} \neq 0$)

4

STRENGTH OF DEFECT-FREE SOLIDS

4.1   INTRODUCTION

Both theory and experiment show that defect-free solids are much stronger than the solids usually encountered. This fact points to the necessity for understanding the behavior of various types of defects in solids under stress in order to understand mechanical behavior and modes of failure. Before turning to the study of defects in relation to mechanical behavior, it is useful to understand the behavior to be expected of ideal solids in which these defects are absent.

The relationship of elastic constants to the lattice energy of a solid was discussed in Chapter 3. The force resulting from a strain was shown to be related to the first derivative of the lattice energy and the elastic constants to the second derivative. This approach can be extended to estimate the strength of a defect-free solid in tension or in shear.

4.2   THEORETICAL STRENGTH IN TENSION

To estimate the strength of a defect-free solid in tension, a treatment due to Orowan (1949) can be used (Davidge, 1979; Kelly and MacMillan, 1986). His

method approximates the stress–strain curve by a sine function. This representation is not exact but has the basic qualitative features needed. To justify the use of a sine function approximation, consider the interatomic potential energy or lattice energy for ions separated by a distance x usually represented by (Kittel, 1968)

$$U = -\frac{A}{x} + B \exp\left(-\frac{x}{C}\right) \tag{4.1}$$

Here the first term is the Coulomb attraction and the second is the repulsion of overlapping electron orbits. This function is plotted in Figure 4.1(a), in which the parameters A, B, and C have been chosen to give values characteristic of sodium chloride, that is, a binding energy per ion pair of 8.14 eV (785 kJ/mol) and an interatomic spacing of 0.28 nm. The interatomic force, given by the derivative of this function, is plotted in Figure 4.1(b) with the sign of the force chosen so that a positive value indicates an attractive force. This figure shows zero force at the equilibrium interatomic spacing and a steeply increasing repulsive force for decreasing atomic separation. As the atomic separation is increased beyond the equilibrium separation, the force becomes attractive. As the separation increases further, the attraction increases to a maximum and then decreases to zero at large separation.

Orowan (1949) assumed a sine function for the stress normal to the planes as a function of the separation between two atomic planes and determined the parameters in his sine function by fitting it to the bond length, the Young's modulus, and the surface energy. He took the equilibrium separation to be
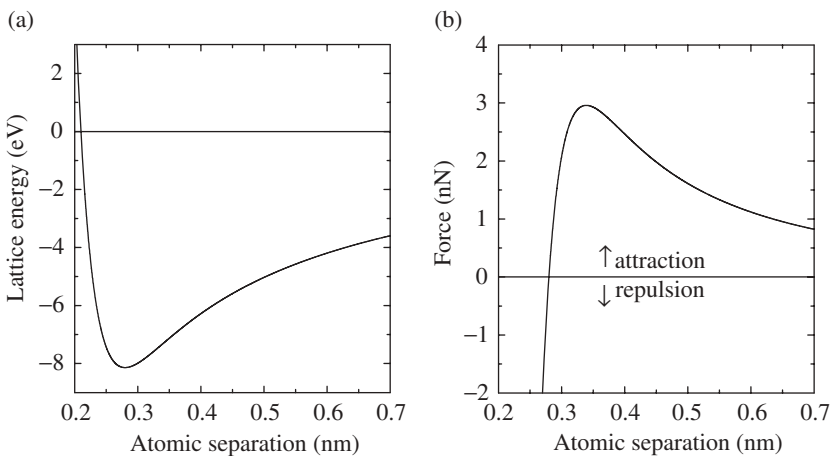
FIGURE 4.1   Potential energy between pair of ions (lattice energy) and interatomic force as function of separation of ions/atoms calculated for sodium chloride.
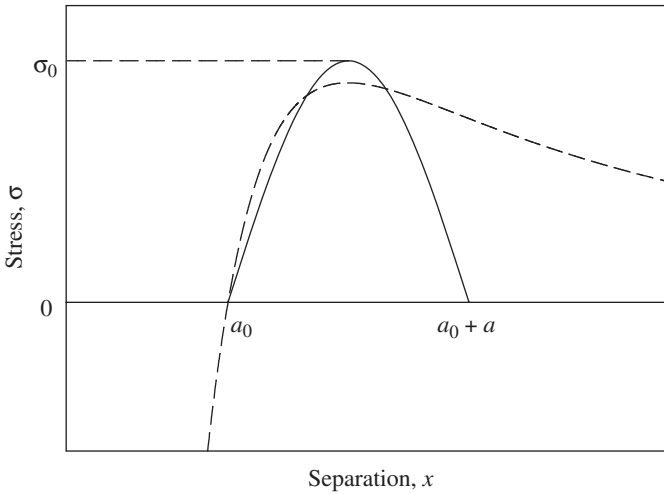
FIGURE 4.2   Sine function approximation to stress between two atomic planes as they are separated.

$x = a_0$ and the separation for maximum restoring force to occur at $x = a_0 + a/2$, as shown in Figure 4.2, and wrote

$$\sigma = \sigma_0 \ \sin\frac{\pi}{a}(x - a_0) \tag{4.2}$$

where a is a measure of the range of interatomic forces and σ_0 is the maximum restoring force. Then Young's modulus E is given by

$$E = \frac{d\sigma}{dx/a_0} = \sigma_0 \pi \ \frac{a_0}{a} \ \cos\frac{\pi}{a}(x - a_0) \tag{4.3}$$

Taking $x = a_0$ gives the value of Young's modulus at zero strain and leads to

$$\sigma_0 = \frac{E}{\pi} \frac{a}{a_0} \tag{4.4}$$

To determine a, Orowan equated the work done in separating the planes to the surface energy of the new surface created. On a per-unit-area basis, this involves equating 2γ, the energy to create two new surfaces, to the work done separating the atomic planes from their equilibrium separation, a_0, to the

position when the force drops to zero at $x = a_0 + a$:

$$2\gamma = \int_{a_0}^{a_0+a} \sigma \, dx = \int_{a_0}^{a_0+a} \sigma_0 \sin \frac{\pi}{a}(x - a_0) \, dx$$

$$= \frac{\sigma_0 a}{\pi} \left[-\cos \frac{\pi}{a}(x - a_0) \right]_{a_0}^{a_0+a} = 2\sigma_0 \frac{a}{\pi} \qquad (4.5)$$

Rearranging gives

$$a = \frac{\pi\gamma}{\sigma_0} \qquad (4.6)$$

Using this to eliminate a from Eq. (4.4) gives

$$\sigma_0^2 = \frac{\gamma E}{a_0} \qquad (4.7)$$

The theoretical breaking stress is the maximum stress encountered as the planes are separated, that is, $\sigma_{\text{theoretical}} = \sigma_0$, giving

$$\sigma_{\text{theoretical}} = \left(\frac{E\gamma}{a_0} \right)^{1/2} \qquad (4.8)$$

Table 4.1 summarizes several values of the theoretical strength in tension for ceramics and other materials.

The Orowan treatment can also be used to give an estimate in terms of the Young's modulus alone. Taking a approximately equal to a_0 in Eq. (4.4) gives

$$\sigma_{\text{theoretical}} \simeq \frac{E}{\pi} \qquad (4.9)$$

Kelly and MacMillan (1966) discuss various attempts to calculate the theoretical strength more accurately and conclude that for ionic crystals

TABLE 4.1   Theoretical Breaking Strengths from Eq. (4.8)

Material	Direction	E (GPa)	γ (J/m^2)	$\sigma_{\text{theoretical}}$ (GPa)
NaCl	$\langle 100 \rangle$	44	0.25	6.3
MgO	$\langle 100 \rangle$	245	1.2	37
Al$_2$O$_3$	$\langle 0001 \rangle$	460	1.0	46
α-Iron	$\langle 100 \rangle$	132	2.0	30
Si	$\langle 111 \rangle$	188	1.2	32
Silica glass	Not applicable	73	0.56	16
Diamond	$\langle 111 \rangle$	1210	5.4	205

Source: From Kelly and MacMillan (1986).

Orowan's estimate is too high by a factor of about 2. Other estimates lead to an often-used rule of thumb that the theoretical strength in tension is about $E/10$ (Davidge, 1979).

Whiskers of sapphire (single-crystal alumina) have exhibited strengths around 15 GPa and carefully polished bulk crystals gave values up to 6.8 GPa (Kelly and MacMillan, 1986). The strength for good polycrystalline alumina in normal use varies but is typically in the range 275–425 MPa. Strengths as high as $E/5$ have been reported in fused quartz (silica glass) fibers with pristine surfaces. Evidently the models for theoretical strength are correct, but in practical bulk ceramics and glasses, flaws lower the strength by a factor of about 100 or more from the theoretical value.

4.3   THEORETICAL STRENGTH IN SHEAR

Another important consideration is the theoretical shear strength of solids. Frenkel (1926; summarized by Kelly and MacMillan, 1986) considered that a plane of atoms in a crystal moves rigidly over an adjacent plane and takes a sine force law analogous to that used in the Orowan analysis. That is, for a displacement x, Frenkel assumed that the restoring shear stress τ is given by

$$\tau = k \sin \frac{2\pi x}{b} \tag{4.10}$$

where b is the distance in the shear direction (i.e., not necessarily along a crystallographic axis) to bring the crystal into registry again (the Burgers vector, Chapter 18). The shear modulus μ is given by

$$\mu = \frac{d\tau}{dx/h} = \frac{2\pi k h}{b} \cos \frac{2\pi x}{b} \tag{4.11}$$

where h is the distance between planes being sheared. For small displacements $\mu = 2\pi k h / b$. The maximum shear stress occurs when the sine is unity so that the theoretical shear stress is

$$\tau_{\max} = k = \frac{\mu b}{2\pi h} \tag{4.12}$$

For a face-centered-cubic (FCC) material such as many metals $b = a/\sqrt{6}$ and $h = a/\sqrt{3}$, where a is the lattice parameter. This gives

$$\tau_{\max} = \frac{\mu}{2\pi\sqrt{2}} \approx \frac{\mu}{9} \tag{4.13}$$

TABLE 4.2   **Theoretical Shear Stress**

Material	μ (GPa)	τ_{max}/μ	τ_{max} (GPa)
Diamond	505	0.24	121
Fe	60	0.11	6.6
Al_2O_3	147	0.115	16.9

Source: From Kelly and MacMillan (1986).

For single crystals the appropriate shear constant must be used as described by Kelly and MacMillan (1986). A more refined calculation by Mackenzie as summarized by Kelly and MacMillan leads to different values of τ/μ for different materials. A summary of their results is given in Table 4.2.

These results for theoretical tensile strength and theoretical shear strength are of great importance to the study of mechanical properties. First, the comparison with values for perfect crystals validates the predicted theoretical tensile strengths within a factor of about 2. The much lower values found in most practical materials direct attention to the study of flaws (in particular microcracks) and offer hope of achieving much higher strengths if flaws can be eliminated or their behavior modified to increase strength. Much of the design and processing of ceramic materials are directed toward these goals.

The high theoretical shear strengths contrast with much lower values that are found for ductile metals. This in turn directs attention to another defect, the dislocation, and its behavior in deformation, including slip and twinning, as will be discussed in Chapter 18. Much of the design and processing of metallic alloys are directed toward controlling the behavior of dislocations. For ceramics, dislocations exist, yet most polycrystalline ceramics typically show brittle behavior at temperatures below about one-half their absolute melting point. The student needs first to understand how dislocations contribute to plasticity in metals through slip and sometimes twinning and then understand what limits their motion and what special effects limit their effectiveness in providing plasticity in ceramics at moderate temperatures even though they have crystal structures in which considerable dislocation mobility is possible.

Consideration of flaws and dislocations and how their interaction with other defects and microstructure affects mechanical behavior is an underlying theme of this book.

PROBLEMS

1. Magnesium oxide has the rock salt structure, its density is $3580 \, kg/m^3$, and $s_{11} = 3.99 \times 10^{-12} \, Pa^{-1}$. The surface energy of the (100) plane is $1.2 \, J/m^2$.

Estimate the bond length of MgO. Estimate the theoretical strength of MgO for cleavage on the (100) plane.

2. Silicon has the diamond structure, atomic weight 28.09, and a density of $2329 \, \text{kg/m}^3$. Young's modulus in the $\langle 111 \rangle$ direction is $188 \, \text{GPa}$ and the surface energy of the (111) plane is $1.2 \, \text{J/m}^2$. Estimate the spacing of the atomic planes in the $\langle 111 \rangle$ direction, a_0. Estimate the theoretical strength of silicon on the (111) plane.

5

LINEAR ELASTIC FRACTURE MECHANICS

5.1 INTRODUCTION

The strength of polycrystalline ceramics is usually much less than that of a corresponding perfect single crystal, as noted in the previous chapter. Understanding the strength of real polycrystalline ceramics requires understanding the behavior of microcracks under stress. A completely successful theory of the behavior of microcracks on an atomic level still does not exist, although progress is being made. Linear elastic fracture mechanics is a very useful theory that treats a crack in a continuous body while avoiding the detail of what happens on an atomic scale. This theory is introduced in stages in this chapter using a minimum amount of mathematical complexity. Basic references include Sneddon and Lowengrub (1969), Kelly and MacMillan (1986), Broek (1987),

Lawn (1993), and the *Fracture Mechanics of Ceramics* series (Bradt et al., 1973a,b, 1978a,b, 1983a,b, 1992).

5.2 STRESS CONCENTRATIONS

Stress concentrations are usually discussed in terms of a thought experiment in which a flaw is introduced into a body that was originally under uniform stress. Consider a sample initially under a uniform tensile stress, σ. If an elliptical flaw whose maximum length is perpendicular to the tensile stress is introduced, the stress will change, especially near the end of the flaw (Inglis, 1913). Figure 5.1 shows a two-dimensional view of a sample with a flaw of length $2c$ in the x direction and a dimension $2b$ in the y direction (i.e., in the direction of the initial tensile stress). The size of the flaw in Figure 5.1 is exaggerated; $2c$ is assumed to be small compared to the sample width.

The equation of the ellipse defining the crack is

$$\frac{x^2}{c^2} + \frac{y^2}{b^2} = 1 \tag{5.1}$$
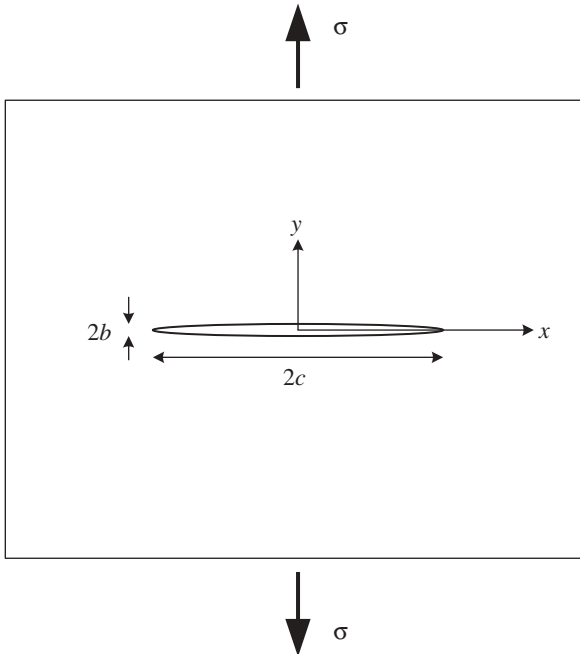
FIGURE 5.1   Elliptical crack in plate subjected to uniaxial tensile stress σ.

The radius of curvature at the end of the major axis of the ellipse is given by

$$\rho = \frac{b^2}{c} \tag{5.2}$$

The stress distribution around the flaw is complex (Timoshenko and Goodier, 1951; Kelly and MacMillan, 1986) but a key result can be stated simply. The maximum normal stress that appears anywhere in the plate is at the "tips" of the crack ($x = \pm c$) and is in the y direction (σ_{yy}); that is, it is in the same direction as the externally applied stress σ. It is given by

$$\sigma_{yy} = \sigma\left(1 + \frac{2c}{b}\right) = \sigma\left[1 + 2\left(\frac{c}{\rho}\right)^{1/2}\right] \tag{5.3}$$

It is interesting to note that the latter form of this equation contains only two characteristics of the elliptical crack: the length c and the radius of curvature at the end of the crack perpendicular to the initial stress, ρ. These two factors give approximately the correct result for cracks of other shapes. To a good first approximation only the length of the crack perpendicular to the applied stress and the radius of curvature at the end of that length determine the maximum stress.

It is evident that for long thin/sharp cracks ($c \gg \rho$) the stress concentration can be great and so accounts for the fact that practical strengths are much less than the theoretical strength.

5.3   GRIFFITH THEORY OF FRACTURE OF A BRITTLE SOLID

The treatment above gives the stress at the tip of a smoothly rounded crack of known geometry. One might attempt to proceed by developing a theory to give the stress at the tip of a very sharp crack and set this equal to the theoretical strength as a criterion for fracture. This presents difficulties because very sharp cracks bring atomic dimensions into play for which it is unreasonable to apply continuum elasticity. Griffith (1920, 1924) avoided this difficulty by developing a theory of brittle fracture based on energy considerations. This type of treatment remains the basis of fracture mechanics. The essential ideas of his treatment are given in the following paragraphs. The discussion here is in modern terms rather than in the original terms. An interesting discussion of the development of knowledge of the strength of glass following Griffith's papers is given by Holloway (1983).

Griffith based his treatment of fracture on energy conservation. The first law of thermodynamics states that

$$dU = dQ - dW \tag{5.4}$$

where U is the internal energy of the specimen (dU is positive for an increase in internal energy), dW is the mechanical work done by the system on its

surroundings (dW is negative when work is done by the external system on the specimen), and dQ is the heat flowing into or out of the specimen (dQ is positive when heat flows into the specimen). We assume rapid crack propagation so that little time is available for heat flow to or from the specimen, $dQ = 0$, and so inquire into the terms dU and dW when a crack propagates from a half length c to $c + dc$ in a specimen under constant applied stress σ corresponding to a constant applied force P.

Griffith assumed that the internal energy was the sum $U_e + U_s$, where U_e is the elastically stored energy in the specimen and U_s is the surface energy of the crack. For a small increase in the crack length, dc, dW and dU_e are potential sources of energy, which is required to make the new crack surface, dU_s. If there is insufficient energy available, the crack cannot grow by dc. However, if the energy made available by external work and changes in the stored elastic energy is greater than or equal to the increase in surface energy, then the crack can grow

$$-dU_e - dW \geq dU_s \qquad \text{or} \qquad \frac{dU_e + dU_s + dW}{dc} \geq 0 \qquad (5.5)$$

Griffith took the critical stress for fracture to be the value for which the energy changes associated with crack growth just balance, giving the criterion for the crack to just start to grow

$$\frac{d(U_e + U_s + W)}{dc} = 0 \qquad (5.6)$$

which is the Griffith energy balance condition. This is a reasonable assumption for a mechanical system, but strictly speaking it is only a necessary condition for the crack to grow. At present, this condition will be taken as both necessary and sufficient and the question of sufficiency will be considered later.

For simplicity a plate of thickness t is assumed to be under uniform tensile stress. A crack through the body and of length $2c$ is then introduced. The problem is to write expressions for the elastically stored energy and the surface energy. The surface energy expression is straightforward and is

$$U_s = 4\gamma ct \qquad (5.7)$$

The total area of surface created by a crack of length $2c$ is $4ct$ and γ is the surface energy per unit area. It is convenient to take the surface energy U_s per unit length of crack in the thickness dimension and so drop the thickness factor t, giving

$$U_s = 4\gamma c \qquad (5.8)$$

Fortunately, there is a general result from the theory of elasticity that for any linearly elastic body undergoing crack extension under constant load the work done by the external loading system as a result of the additional deflection caused by crack growth is equal to minus twice the change in elastically stored

(a)   Displacement
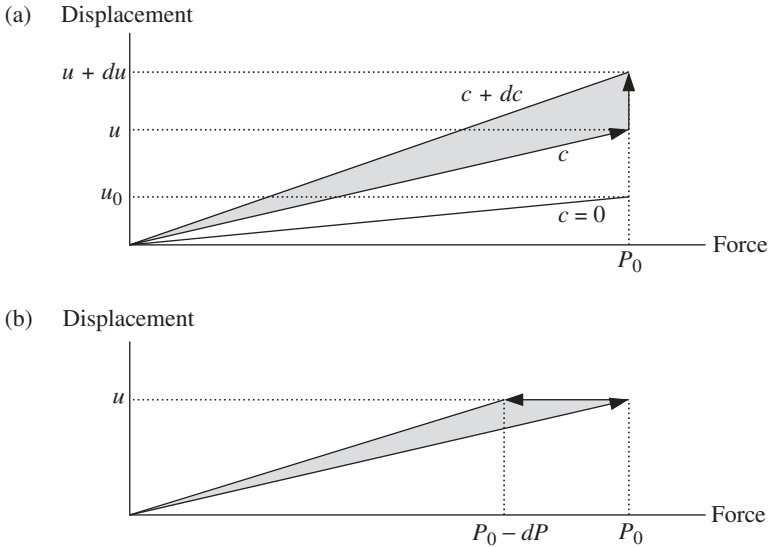
(b)   Displacement

FIGURE 5.2   Force and displacement during crack growth: (a) for constant applied force; (b) for constant displacement.

energy associated with the crack growth deflection; that is,

$$dW = -2\,dU_e \tag{5.9}$$

Before going on to insert this relation into the Griffith energy balance condition and proceeding with the fracture stress derivation, we give a proof for simple constant tensile loading. We consider the work done on a specimen and the elastic energy stored in the specimen under constant force with a small central crack of half length c that extends a distance dc. As a preliminary it is interesting to consider the specimen without a crack. As shown in Figure 5.2(a), the application of a force that increases from zero to P_0 causes a proportional elastic deflection reaching the value u_0. As shown in Chapter 3, the change in stored energy is $\frac{1}{2} \times$ force $\times$ deflection, or simply the area under the displacement–force curve. For this case

$$dU_e(c = 0, P \rightarrow P_0) = \tfrac{1}{2}P_0 u_0 = -dW(c = 0, P \rightarrow P_0) \tag{5.10}$$

Now consider a specimen with crack length c loaded to $P = P_0$ followed by an infinitesimal crack extension dc under constant load and an accompanying infinitesimal specimen deflection du. The external load does work on the specimen during the crack growth so that the energy of the external loading system changes during crack growth by

$$dW(c \rightarrow c + dc, P = P_0) = -P_0\,du \tag{5.11}$$

The change in elastic energy stored in the specimen is

$$dU_e(c \rightarrow c + dc, P = P_0) = U_e(c, P = P_0) - U_e(c + dc, P = P_0)$$
$$= \tfrac{1}{2}P_0(u + du) - \tfrac{1}{2}P_0 u = \tfrac{1}{2}P_0 \, du \tag{5.12}$$

or the shaded area in Figure 5.2(a). Comparing Eqs. (5.11) and (5.12) we see

$$dW = -2 \, dU_e \tag{5.13}$$

which is the relation stated for the general case above. Note that the elastically stored energy increases during crack growth under constant load.

Using the above relation, the Griffith energy balance condition for crack growth, Eq. (5.6), under constant load becomes

$$\frac{dU_e}{dc} = \frac{dU_s}{dc} \tag{5.14}$$

To apply this condition to the crack in a body under stress, an equation for the stored elastic energy is needed. Griffith (1920) based on Inglis (1913) calculated this quantity for a thin plate (corresponding to the condition of plane stress) and obtained

$$U_e = \frac{\pi c^2 \sigma^2}{E} \tag{5.15}$$

For a thick plate (corresponding to plane strain) the result is

$$U_e = \frac{\pi(1 - v^2)c^2 \sigma^2}{E} \tag{5.16}$$

Substituting these expressions into (5.14) and using (5.8) give the Griffith equations for the fracture stress of a brittle solid under plane stress,

$$\sigma_f = \left(\frac{2E\gamma}{\pi c}\right)^{1/2} \tag{5.17}$$

and under plane strain,

$$\sigma_f = \left(\frac{2E\gamma}{\pi(1 - v^2)c}\right)^{1/2} \tag{5.18}$$

The case of infinitesimal crack propagation in a specimen constrained to constant displacement leads to the same Griffith equations. As shown in Figure 5.2(b), the specimen is initially loaded to P_0, causing a deflection u as before. The specimen is then held at constant displacement while the crack propagates an amount dc. The load drops from P_0 to $P_0 - dP$. No work is done on the

specimen; that is,

$$\delta W(c \rightarrow c + dc, u = \text{const}) = 0 \qquad (5.19)$$

Hence Griffith's energy balance condition for crack growth during constant displacement takes the form

$$-\frac{dU_e}{dc} = \frac{dU_s}{dc} \qquad (5.20)$$

In this case of constant displacement the stored elastic energy decreases as the crack extends so that the left-hand side of this equation is positive, allowing the equation to be satisfied. The same Griffith equations for σ_f, Eq. (5.17) and (5.18), follow as before.

5.4   STRESS AT CRACK TIP: AN ESTIMATE

The Griffith equations are based on energy considerations and therefore provide a necessary condition for fracture to occur, as noted above. The question remains whether the stress is actually high enough to break a bond at the crack tip when the Griffith condition is met so that this condition is also a sufficient condition for fracture. The following approximate argument leads to the plausible conclusion that it is. The Inglis condition for stress concentration can be combined with the Orowan estimate of theoretical strength to give an expression for fracture stress and the latter can be compared with the Griffith condition.

The Orowan estimate for the theoretical stress was developed in Chapter 4 and is

$$\sigma_{\text{theoretical}} = \left(\frac{E\gamma}{a_0}\right)^{1/2} \qquad (5.21)$$

For a long sharp crack ($c \gg \rho$) the maximum tensile stress at the tip of the crack is given by the Inglis expression (5.3) as

$$\sigma_{\text{max}} = 2\sigma\left(\frac{c}{\rho}\right)^{1/2} \qquad (5.22)$$

where σ is the uniform tensile stress applied to the specimen. For fracture $\sigma_{\text{max}} = \sigma_{\text{theoretical}}$ and the applied stress is the fracture stress σ_f, giving

$$\sigma_f = \left(\frac{E\gamma}{4c}\frac{\rho}{a_0}\right)^{1/2} \qquad (5.23)$$

The crack tip radius ρ for an atomically sharp crack is about half the interatomic spacing a_0, giving

$$\sigma_f = \left(\frac{E\gamma}{8c}\right)^{1/2} \tag{5.24}$$

This stress is actually lower than the Griffith stress, Eq. (5.17), so that the Griffith condition can be taken to be a sufficient as well as a necessary condition. This is the conclusion adopted in the literature; Lawn (1993) gives an argument in support of this conclusion.

5.5   CRACK SHAPE IN BRITTLE SOLIDS

Accurate calculation of the crack shape in solids remains a challenging problem (Kelly and MacMillan, 1986; Lawn, 1993). It is important, however, to keep in mind the qualitative features that are expected of real cracks in stressed solids as the approximate models of cracks used in fracture mechanics are considered. Figure 5.3 shows a sketch of the shape expected for a real crack under stress. On the left-hand side the uncracked material is bonded and has the normal interatomic spacing slightly expanded by elastic deformation. Far to the right the opposite surfaces of the crack are effectively beyond the range of interatomic forces and are free of force. In the intermediate region atoms on one crack surface experience an attractive force from atoms on the opposite surface. The crack opens smoothly and it is somewhat arbitrary where the crack edge is taken.

This picture of a crack differs from the fracture mechanics model of a crack. The latter assumes a well-defined edge and generally assumes no forces between the opposite faces of a crack behind the edge. The fracture mechanics model has the advantage of allowing a continuum elasticity treatment of stresses in an intermediate region that is near, but not too near, the crack tip. One way of interpreting the success of fracture mechanics is to argue that, whatever the true state of affairs in the region of atomic bonding for the true crack, it will be the
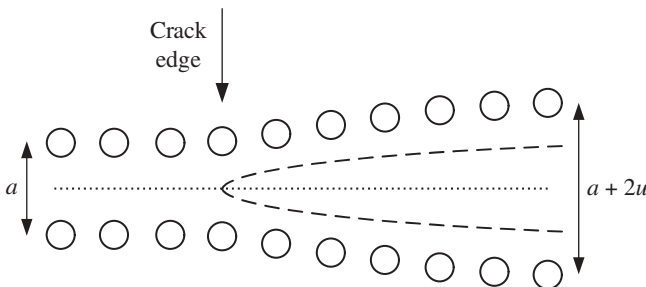
FIGURE 5.3   Atomic planes on either side of a crack.

same in two specimens of the same material provided the stresses in the intermediate region are the same. It can then be assumed that fracture will occur whenever a critical stress state is reached in the intermediate region. Fracture mechanics allows a rigorous connection to be established between the stresses in this intermediate region and the external forces acting on a specimen. Thus fracture mechanics allows any loading geometry to be treated in terms of the assumed critical state of affairs in the intermediate region. Fracture mechanics thus has great practical value as well as providing insight.

5.6   IRWIN FORMULATION OF FRACTURE MECHANICS: STRESS INTENSITY FACTOR

Linear fracture mechanics as developed by Irwin and many others can be introduced in a manner analogous to the way that fracture stress and the Griffith condition were discussed. An important new feature is that, by concentrating attention on stresses in an intermediate region, the stress-based and energy-based treatments can be shown to be equivalent. There are three types of crack opening to be considered, as shown in Figure 5.4. Mode I is crack opening, mode II is in-plane crack shearing or sliding, and mode III is antiplane crack shearing or tearing. The three modes are distinguished by whether the direction of the force components lies parallel or perpendicular to the plane of the crack and to the line of the crack front. Irwin (1957) utilized a solution by Westergaard (1939) for the stresses near the tip of a crack in the xz plane with its edge defined by $x = $ const. For any system of distant loads, the stresses near the crack tip can be expressed in terms of polar coordinates r, θ, z and expanded in a power series in r. The first term of the series expansion of stress as a function of r dominates for small values of r. The stresses σ_{ij} and the displacements u_i have the form

$$\sigma_{ij,m} = \frac{K_m}{(2\pi r)^{1/2}} f_{ij,m}(\theta) \qquad (5.25)$$
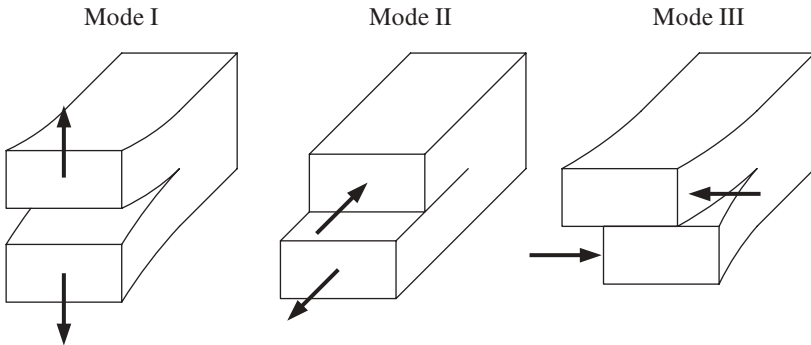
FIGURE 5.4   Fracture in modes I, II, and III.

$$u_{i,m} = \frac{K_m}{2E} \left(\frac{r}{2\pi}\right)^{1/2} f_{i,m}(\theta) \tag{5.26}$$

Here the subscripts i and j take the values 1, 2, 3 and indicate the coordinate directions. The subscript m takes the values I, II, III and indicates the mode of crack opening. The K_m are the **stress intensity factors**. The complete functions $f_{ij,m}(\theta)$ and $f_{i,m}(\theta)$ are given by Lawn (1993). For mode I loading, the tensile stresses parallel to the direction of crack advance, σ_{xx}, perpendicular to the crack plane, σ_{yy}, and parallel to the crack front σ_{zz}, and the shear stress σ_{xy} are given as

$$\sigma_{xx,\mathrm{I}} = \frac{K_\mathrm{I}}{(2\pi r)^{1/2}} \cos\frac{\theta}{2} \left(1 - \sin\frac{\theta}{2} \sin\frac{3\theta}{2}\right)$$

$$\sigma_{yy,\mathrm{I}} = \frac{K_\mathrm{I}}{(2\pi r)^{1/2}} \cos\frac{\theta}{2} \left(1 + \sin\frac{\theta}{2} \sin\frac{3\theta}{2}\right)$$

$$\sigma_{xy,\mathrm{I}} = \frac{K_\mathrm{I}}{(2\pi r)^{1/2}} \sin\frac{\theta}{2} \cos\frac{\theta}{2} \cos\frac{3\theta}{2} \tag{5.27}$$

$$\sigma_{zz} = \begin{cases} 0 & \text{plane stress} \\ \nu(\sigma_{xx} + \sigma_{yy}) & \text{plane strain} \end{cases}$$

where ν is Poisson's ratio. The equations for displacements in the x and y directions are

$$u_{x,\mathrm{I}} = \frac{K_\mathrm{I}}{2E} \left(\frac{r}{2\pi}\right)^{1/2} (1 + \nu)\left[(2\kappa - 1)\cos\frac{\theta}{2} - \cos\frac{3\theta}{2}\right]$$

$$u_{y,\mathrm{I}} = \frac{K_\mathrm{I}}{2E} \left(\frac{r}{2\pi}\right)^{1/2} (1 + \nu)\left[(2\kappa + 1)\sin\frac{\theta}{2} - \sin\frac{3\theta}{2}\right] \tag{5.28}$$

where

$$\kappa = \begin{cases} \dfrac{3 - \nu}{1 + \nu} & \text{plane stress} \\ 3 - 4\nu & \text{plane strain} \end{cases} \tag{5.29}$$

The crack profile in mode I loading is interesting in itself and is used in various theories for toughening. The crack profile is

$$u_{y,\mathrm{I}}(\theta = \pm\pi) = \begin{cases} \pm\dfrac{4K_\mathrm{I}}{E} \left(\dfrac{r}{2\pi}\right)^{1/2} & \text{plane} \\ \pm\dfrac{4K_\mathrm{I}}{E} \left(\dfrac{r}{2\pi}\right)^{1/2} (1 - \nu^2) & \text{plane strain} \end{cases} \tag{5.30}$$

Mode I   Mode II   Mode III
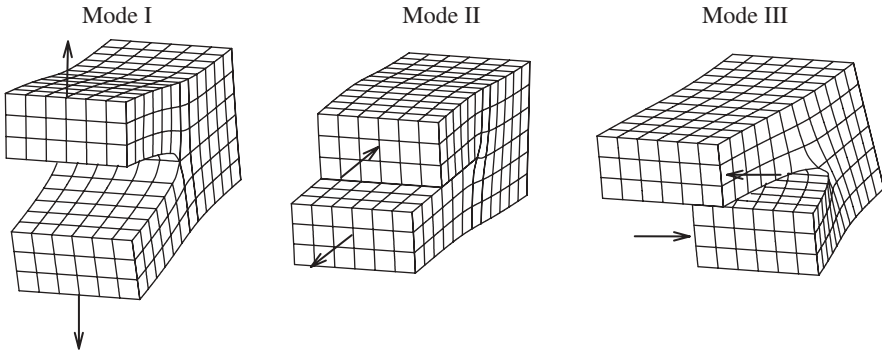
FIGURE 5.5   Crack shape near crack tip for fracture in modes I, II, and III.

Figure 5.5 shows the deformations near the crack tip for the three different modes of fracture calculated in plane strain for the same magnitude of stress intensity in each case.

The factor K_I depends on the applied loading and the specimen geometry and can be determined for any given type of specimen and loading. The radial and angular dependence are separable factors. The reasons for the remarks above about considering stresses in an intermediate region now become apparent. The distance r cannot be taken too small. Continuum elasticity cannot be expected to apply at atomic dimensions and the divergence of the stress equation if r is allowed to approach zero indicates the inadequacy of the treatment for extremely small values of r. If r is allowed to increase too much, higher order terms become appreciable in the power series. However, in the intermediate region three parameters, K_I, K_{II}, and K_{III} (with dimensions stress $\times$ length$^{1/2}$) completely specify the stress for any type of external loading as far as the effect of crack propagation is concerned. For ceramics, it is usually assumed that mode I behavior is overridingly important so that the other K values are ignored. This is perhaps justified for polycrystalline specimens by the argument that flaws of all orientations will occur and that failure will take place from the largest flaw normal to the greatest tensile stress for which K_I is the stress intensity factor driving failure. Fracture control by K_I is assumed here, but the behavior of a flaw under mixed-mode loading leading to simultaneous action of K_I and K_{II} is discussed later. Under this assumption any combination of specimen shape, external loading, and crack configuration leads to a value of K_I acting at the tip of the crack and so a single number characterizes the combined effect of all these factors on the driving force for crack propagation. Calculating this number for a particular combination of specimen shape, loading configuration and intensity, and crack configuration may be a difficult task in practice, but it is just a problem in continuum elasticity that can be solved for each case by numerical methods with computer assistance. For special specimen shapes, loads, and crack configurations there are simple solutions. Some of the most commonly used of these are summarized in Tables 5.1 and 5.2.

TABLE 5.1   Stress Intensity Factors for Small Slot Crack of Total Length $2c$ through Plate under Plane Stress

Uniform tensile stress σ	In-plane shear stress τ	Antiplane shear stress τ
$K_I = \sigma\sqrt{\pi c}; \quad Y = \sqrt{\pi}$	$K_{II} = \tau\sqrt{\pi c}; \quad Y = \sqrt{\pi}$	$K_{III} = \tau\sqrt{\pi c}; \quad Y = \sqrt{\pi}$
Finite-width plate, uniform tensile stress σ	Concentrated line force with force F per unit length	Concentrated double-line force with force $F/2$ per unit length
$K_I = \sigma\left[\dfrac{w}{c}\tan\left(\pi\dfrac{c}{w}\right)\right]^{1/2}\sqrt{c}$	$K_I = \dfrac{F}{\sqrt{\pi c}}$	$K_I = \dfrac{F}{\sqrt{\pi c}}\left(\dfrac{c^2}{c^2 - x^2}\right)^{1/2}$
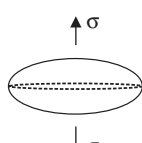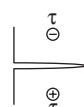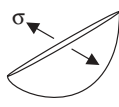
Note: Stress intensities not explicitly given for each case are zero.

The central assumption of linear elastic fracture mechanics is that for a given material there is some critical value of K_I, usually termed K_{IC} (the **critical stress intensity factor** or **toughness**), at which the crack is in equilibrium and above which rapid crack propagation will take place. The fracture condition in this formulation is taken as the equilibrium point so that the fracture condition becomes

$$K_I = K_{IC} \tag{5.31}$$

The quantity on the left is the applied stress intensity factor and that on the right is a property of the particular material under consideration. This equation is the analog of setting the applied stress at the tip of an elliptical crack equal to the theoretical stress. In the present formulation the parameter K_{IC} is usually not calculated in terms of other properties (as was done with the theoretical strength) but is measured. The idea is that K_{IC} can be measured for a particular material using a convenient specimen and loading system, and the resulting value can then be used in design with the same material for more complex shapes and loads. This scheme works well up to a point, and this view will be taken for now. A note of caution is in order concerning the fact that some ceramics show a dependence of K_{IC} on crack length. This is termed *R*-curve behavior and will be discussed in a later chapter. Another important departure from this simple scheme is that some ceramics show slow crack propagation at values of K_I below K_{IC}. Again, this will be taken up later. Setting aside these complications for the time being permits building up the basic treatment, which

TABLE 5.2 Stress Intensity Factors for Different Crack Geometries

Through-plate (scratchlike) surface crack, depth c, uniform tensile stress σ	Circular penny-shaped crack, radius c, uniform tensile stress σ

$$K_I = 1.12\sigma\sqrt{\pi c}; \quad Y = 1.12\sqrt{\pi}$$

$$K_I = \frac{2}{\pi}\sigma\sqrt{\pi c}; \quad Y = \frac{2}{\sqrt{\pi}}$$

Through-plate (scratchlike) surface crack, depth c, antiplane shear stress τ	Semicircular half-penny-shaped surface crack, radius c, uniform tensile stress σ

$$K_{III} = \tau\sqrt{\pi c}; \quad Y = \sqrt{\pi}$$

$$K_I = \frac{2.06}{\pi}\sigma\sqrt{\pi c}; \quad Y = \frac{2.06}{\sqrt{\pi}}$$

Note: Stress intensities not explicitly given for each case are zero.

is very useful and which can subsequently be modified to take into account these complications.

5.7 IRWIN FORMULATION OF FRACTURE MECHANICS: ENERGY RELEASE RATE

The Griffith treatment of fracture was formulated in terms of energy. The Irwin formulation can also be expressed in terms of energy and related to the formulation in terms of stress intensity factor. As in the case of the Griffith treatment, the portion of the energy change that is available to drive any processes associated with creation of new crack surface is considered. In Irwin's formulation the amount of energy available per unit of new crack surface, A, from the mechanical work and change of internal energy is termed G, the **energy release rate** (with dimensions of energy/area, not energy/time), and is

$$G = -\left(\frac{dW}{dA} + \frac{dU_e}{dA}\right) \tag{5.32}$$

This is equivalent to the differentiations in the Griffith energy balance condition as previously stated; there the differentiation was with respect to c

$(dA = tdc)$, where we had taken the specimen thickness $t = 1$. The critical energy release rate can be written in terms of a **crack resistance force** R (again with dimensions of energy/area) as

$$G_c = R \tag{5.33}$$

Note that this definition does not make any assumption as to how the energy required for crack propagation is divided into portions going into new thermodynamic surface energy and into other processes such as local plastic deformation (Evans and Langdon, 1976). When all the energy required is surface energy, the crack resistance force is

$$R = \frac{dU_s}{dA} = 2\gamma \tag{5.34}$$

The energy release rate can be expressed in terms of the internal energy by using the relations derived in Section 5.2 as follows. For crack propagation under constant load, $dW = -2dU_e$, so that

$$G = \frac{dU_e}{dA} \quad \text{(constant load)} \tag{5.35}$$

while for crack propagation under constant displacement, $dW = 0$, so that

$$G = -\frac{dU_e}{dA} \quad \text{(constant displacement)} \tag{5.36}$$

Since the magnitude of G is the derivative of the elastic energy with respect to area in both cases, G is often termed the **strain energy release rate** despite the fact that the strain energy actually increases during crack propagation under constant load.

5.7.1 Relationship between G and K_{I}

The relation between G and K_{I} can be derived by taking the case of a crack in a specimen subjected to pure mode I loading, with fixed displacements at the external loading points so that $dW = 0$ (Irwin, 1957; Jayatilaka, 1979). Consider energy changes as the crack in Figure 5.6 grows from a length c to $c + \delta c$. If the material between the old and new crack tip is fractured, it requires an amount of surface energy

$$\delta U_s = 2\gamma t \, \delta c \tag{5.37}$$

for a plate of thickness t. In terms of the stored elastic energy, the net effect is that the stress σ_{yy} ahead of the original crack relaxes to zero as the new surface relaxes by a distance u_y. Consider an element of the crack extension of width dx a distance x ahead of the original crack tip. Again using the result from Chapter 3
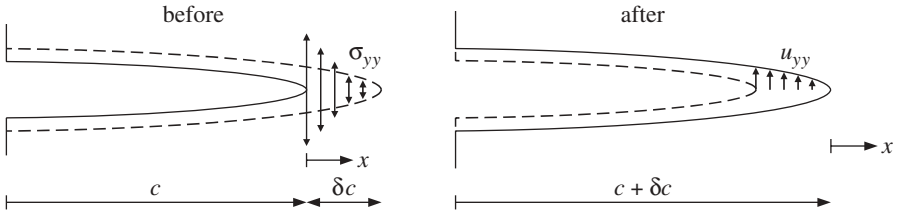
FIGURE 5.6 Geometry of a crack which grows from length c to $c + \delta c$.

that the decrease in elastically stored energy is $1/2 \times$ force $\times$ displacement, we have

$$-\delta U_e = 2 \int_0^{\delta c} \tfrac{1}{2}(\sigma_{yy}\, t\, dx) u_y = \int_0^{\delta c} \sigma_{yy}\, u_y\, t\, dx \tag{5.38}$$

Here the factor 2 in front of the integral arises from the fact that both surfaces of the crack contribute to the energy as they move against the stress. σ_{yy} is the stress a distance x ahead of the original crack, that is, on the $\theta = 0$ plane. Using Eq. (5.27)

$$\sigma_{yy}(r = x, \theta = 0) = \frac{K_\mathrm{I}}{(2\pi x)^{1/2}} \tag{5.39}$$

Here, u_y is the displacement of the crack surface at a corresponding position which is a distance $\delta c - x$ behind the final crack tip, that is, on the $\theta = \pi$ plane. Equation (5.30) gives

$$u_y(r = \delta c - x, \theta = \pi) = \frac{K_\mathrm{I}}{E}\left(\frac{\delta c - x}{2\pi}\right)^{1/2}(1 + v)(\kappa + 1) \tag{5.40}$$

Substituting into (5.38) gives

$$G = -\frac{dU_e}{dA} = \lim_{\delta c \to 0}\frac{-\delta U_e}{\delta A} = \frac{K_\mathrm{I}^2}{2\pi E\, \delta c}(1 + v)(\kappa + 1)\int_0^{\delta c}\left(\frac{\delta c - x}{x}\right)^{1/2} dx \tag{5.41}$$

The integral is readily shown to be $\tfrac{1}{2}\pi\, \delta c$ by using the substitution $x = \delta c \cos^2 \xi$. Using the expressions for κ in Eq. (5.29) gives

$$G = \begin{cases} \dfrac{K_\mathrm{I}^2}{E} & \text{plane stress} \\[2mm] \dfrac{K_\mathrm{I}^2}{E}(1 - v^2) & \text{plane strain} \end{cases} \tag{5.42}$$

The contributions to G by K_{II} and K_{III} are often treated similarly (e.g., Lawn, 1993), leading to the equations

$$
G = \begin{cases}
\dfrac{K_I^2}{E} + \dfrac{K_{II}^2}{E} + \dfrac{(1+\nu)K_{III}^2}{E} & \text{plane stress} \\[2ex]
\dfrac{(1-\nu^2)K_I^2}{E} + \dfrac{(1-\nu^2)K_{II}^2}{E} + \dfrac{(1+\nu)K_{III}^2}{E} & \text{plane strain}
\end{cases}
\tag{5.43}
$$

However, the direction of crack propagation in mode II is not necessarily in the plane of the crack, so that this procedure is questionable and therefore the above equations for G in terms of the K's may not be accurate as far as K_{II} is concerned (Jayatilaka, 1979). This delicate point is generally not pertinent to ceramics because the latter are generally taken to be governed by K_I alone. The idea of additivity of different contributions to G or K_I in ceramics is, however, of great importance, as will be seen in later discussions of toughening.

The energy release rate as developed above can now be used to define an empirical **fracture surface energy** γ_f that can be much larger than the thermodynamic surface energy γ used in the Griffith theory. At the beginning of the chapter, the thermal contribution in the first law of thermodynamics was taken to be zero for crack propagation. There is evidence for radiated energy in the phenomenon of acoustic emission and there may be other means of energy dissipation, as in some degree of plasticity. All these energy contributions are collected into the fracture surface energy so that the crack resistance force R is defined by

$$
R = 2\gamma_f
\tag{5.44}
$$

This gives a modified Griffith equation for fracture:

$$
\sigma_f = \left(\frac{2\,E\,\gamma_f}{\pi c}\right)^{1/2} \quad \text{plane stress}
\tag{5.45}
$$

The measurement of fracture surface energies is discussed in Chapter 6 and the use of fracture mechanics concepts forms a principal theme in the subsequent treatment of the design of microstructures and the design for safe service life. We anticipate a result from that chapter to show the equivalence of the Griffith and Irwin formulations of fracture mechanics. As will be seen in the next section, for uniform tensile stress on a specimen, for the applied stress intensity factor for a thin specimen, elastic theory gives $K_I = Y\sigma c^{1/2}$. For fracture

$$
K_{IC} = Y\sigma_f c^{1/2}
\tag{5.46}
$$

The Irwin fracture condition is

$$
R = 2\gamma_f = G = \frac{K_{IC}^2}{E} = \frac{(Y\sigma_f c^{1/2})^2}{E}
\tag{5.47}
$$

This gives

$$\sigma_f = \left(\frac{2\gamma_f E}{Y^2 c}\right)^{1/2} \tag{5.48}$$

For a through crack under plane stress, $Y = \pi^{1/2}$, giving

$$\sigma_f = \left(\frac{2\gamma_f E}{\pi c}\right)^{1/2} \tag{5.49}$$

which is again the Griffith condition for plane stress but with γ_f substituted for γ.

5.8   SOME USEFUL STRESS INTENSITY FACTORS

As discussed earlier, any combination of specimen shape, external loading, and crack configuration leads to values of the stress intensities K_I, K_{II}, and K_{III} acting at the tip of the crack. Expressions for the stress intensities for a wide range of situations have been found; some of the more important and useful are listed in Tables 5.1 and 5.2. Note that it is customary to define the crack length c as being the distance from where the crack is widest open to its tip, so that a surface crack has length c while an internal crack with two tips has total length $2c$.

Tables 5.1 and 5.2 show that for a uniform applied tensile stress σ the stress intensity is proportional to the stress and the square root of the crack length. This result is typical for relatively simple geometries and the stress intensity is often of the form

$$K_I = Y\sigma c^{1/2} \tag{5.50}$$

where Y, the **crack shape parameter**, is a dimensionless factor that depends on the geometry of the crack, specimen, and loading and has values close to unity. In cases such as this the stress intensity is an increasing function of crack length; if the crack extends, the stress intensity increases. This behavior usually leads to unstable crack growth as soon as the criterion for growth, $K_I = K_{IC}$, is reached. In contrast, in cases such as those in Tables 5.1 where the crack is subjected to concentrated forces, K_I is a decreasing function of crack length, which can lead to stable crack growth; as soon as $K_I = K_{IC}$, the crack will extend, which reduces K_I below K_{IC} and the crack stops. Examples of stable and unstable crack propagation will be considered in Chapter 6.

The simplest situation is a crack of length $2c$ extending through the thickness of a specimen and in the center of the width, similar to Figure 5.1, and several different loading configurations are listed in Table 5.1. The stress intensity factor resulting from a tensile stress $\sigma = \sigma_{yy}$ which is uniform across the

specimen at a large distance from the crack is given by (Jayatilaka, 1979)

$$K_I = \pi^{1/2}\sigma c^{1/2} = 1.772\sigma c^{1/2} \quad \text{(through crack of length } 2c\text{)} \qquad (5.51)$$

when the length of the crack $2c$ is small compared to the width of the specimen. If the length of the crack is an appreciable fraction of the specimen width w, the result is

$$K_I = \sigma\left[w\tan\left(\frac{\pi c}{w}\right)\right]^{1/2} \quad \text{(through crack of length } 2c\text{)} \qquad (5.52)$$

For small values of c/w this becomes

$$K_I = \sigma(\pi c)^{1/2}\left(1 + \frac{\pi^2 c^2}{6w^2}\right) \quad \text{(through crack of length } 2c\text{)} \qquad (5.53)$$

If a through crack is located with one end on the surface, the stress intensity factor will be larger than if the same crack is located within the specimen. This geometry is shown in Table 5.2 and might be used to model the behavior of a long surface scratch or machining damage. For a crack of total length c ending on the surface of a specimen whose width is great compared to the crack length,

$$K_I = 1.12\pi^{1/2}\sigma c^{1/2} = 1.99\sigma c^{1/2} \quad \text{(edge crack of length } c\text{)} \qquad (5.54)$$

However, the centrally located crack discussed above was taken to have a total length $2c$. If this through crack instead ends on the surface, the stress intensity factor would be

$$K_I = 1.12\pi^{1/2}\sigma(2c)^{1/2} = 2.81\sigma c^{1/2} \quad \text{(edge crack of length } 2c\text{)} \qquad (5.55)$$

Thus a through crack perpendicular to the stress and ending at the surface will have a stress intensity factor 1.58 times as great as the same crack distant from the surface. This suggests that a specimen containing many randomly distributed cracks of the same size would usually fail at the surface. Many ceramics and almost all glasses do fail from crack propagation beginning from cracks at the surface. However, surfaces may not be characteristic of the volume of a sample so that failure may begin from flaws within a sample despite the greater stress-concentrating effect of surface flaws. Also, cracks in ceramics are rarely through cracks so that the above simple picture does not apply strictly.

The cracks subjected to concentrated forces have several uses. For example, the double-line force case shown in Table 5.1 can be used as a Green's function

to calculate the stress intensity when the crack is subjected to an arbitrary profile of internal stress.

5.9 THE *J* INTEGRAL

The Irwin strain energy release rate G is defined for linear elastic behavior. It can be generalized to nonlinear elasticity by defining a quantity J that is equal to G for linear elastic behavior (Rice, 1968a,b; Broek, 1987; Lawn, 1993). This quantity also permits the derivation of a relation that is useful in treating toughening by partial bridging of cracks and so it is briefly discussed here. Furthermore, the J integral can be used to formulate a condition for the initiation of cracking in materials that undergo plastic deformation, but care is needed in this case and the reader is referred to texts dealing with this subject (e.g., Broek, 1987).

The fundamental idea underlying the J integral approach to fracture is still that of energy conservation from the first law of thermodynamics applied to the case where only mechanical energy changes are involved, as in the Griffith and Irwin theories. As for the Griffith theory, we consider an edge crack of length c extending through a specimen and take the thickness to be unity. The problem can then be treated in two dimensions as before. We consider any portion of a two-dimensional specimen bounded by a closed contour and consider the changes in mechanical energy as a crack extends infinitesimally. An example of such a contour is *ABCDEFGHIA* shown in Figure 5.7. Changes in the mechanical energy of the portion of the specimen within the contour will depend only on changes in the strain energy per unit volume, U, and the combination of the force vector per unit area acting on the surface, **F** (termed the traction), with the displacement vector of the surface, **u**. In terms of these quantities the mechanical energy within the contour per unit length perpendicular to the plane of the contour is

$$U_M = \int_A U \, dA - \int_S \mathbf{F} \cdot \mathbf{u} \, ds \tag{5.56}$$

where

$$F_i = \sum_i \sigma_{ij} n_j \tag{5.57}$$

and the n_j are the components of the unit vector normal to the contour at the point under consideration. Note that the first integral in Eq. (5.56) is over the area and the second is a line integral taken along the curve bounding the area. Rice showed that the energy release rate could be expressed as a line integral
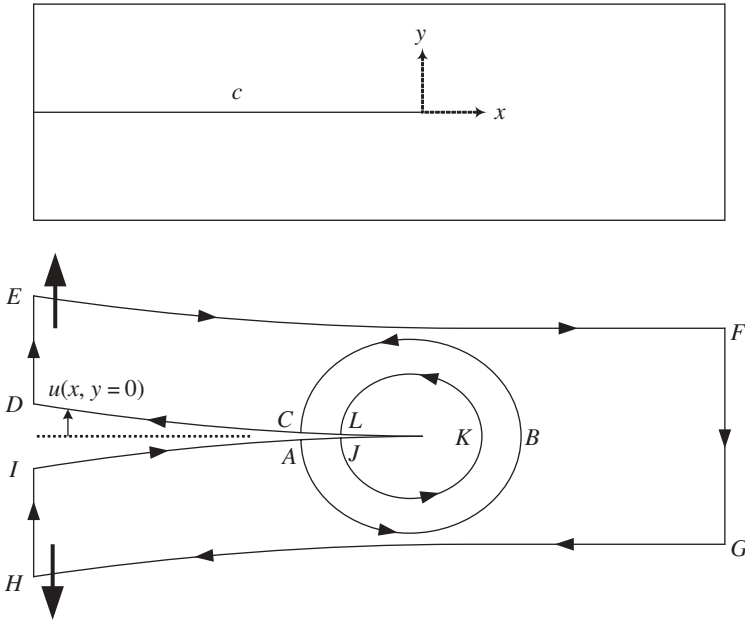
FIGURE 5.7   *J*-Integral contours.

that he defined as J. That is,

$$-\frac{dU_M}{dc} = \int_S \left(U\,dy - \mathbf{F} \cdot \frac{\partial \mathbf{u}}{\partial x}\,ds \right) \equiv J \tag{5.58}$$

This integral can be shown to be zero for any contour, such as *ABCDEFGHIA*, that is taken to enclose a portion of the material free of body and surface forces and that does not enclose a singularity. Here we have been careful to take points *A* and *C* sufficiently far from the crack tip to be outside the crack cohesion zone so that the crack surfaces *CD* and *IA* are free of traction. We can take a second contour *ABCLKJA* still remaining outside the cohesion zone and write *J* as the sum of four contributions from successive parts of the contour:

$$J_{ABCLKJA} = J_{ABC} + J_{CL} + J_{LKJ} + J_{JA} = 0 \tag{5.59}$$

The crack before the opening displacements is shown in the upper portion of Figure 5.7 and is described by $y = 0$ along $x = 0$ to $x = -c$, where c is the crack length so that $dy = 0$ in J_{CL} and J_{JA}. Also, for the portions of the crack surface *CL* and *AJ* the traction is zero so that

$$J_{CL} = J_{JA} = 0 \qquad \text{and} \qquad J_{ABC} = -J_{LKJ} \tag{5.60}$$

If we adopt the convention that the J integral around a crack tip should be taken in a counterclockwise sense, we wish to have J_{JKL}. Reversing the direction of integration along a portion of the contour changes the sign of the integral so that

$$J_{JKL} = -J_{LKJ} \qquad (5.61)$$

and we finally have

$$J_{ABC} = J_{JKL} \qquad (5.62)$$

Thus the contour can be drawn along any path from one face of the crack to the other as long as the end points on the contour are outside the cohesion zone; that is, with this constraint of the end points the J-integral is path independent. The J-integral will be used to obtain an important result for partially bridged cracks in the next section.

5.10   CRACKS WITH INTERNAL LOADING

So far we have considered the crack faces to be free of traction apart from the short cohesion zone near the crack tip. The applied stress intensity factor arises from loads applied to the external surface of the specimen in this case. When traction on the face of a crack exists (as is the case with a crack filled with liquid under pressure, for example), we expect an additional contribution to the applied stress intensity factor. An important type of internally loaded crack results when the crack is partially bridged by fibers or grains that are elastically loaded and so exert a closure stress on the crack faces and lead to toughening of the ceramic. We shall discuss this in more detail in later chapters and here simply summarize some of the fundamental relations that underlie treatment of this form of toughening.

   If a tensile stress $\sigma_{yy} = p(x)$ acts on each face of the crack surface, where x is the distance from the crack tip, it can be shown (Sneddon and Lowengrub, 1969; Lawn, 1993) that the contribution to the stress intensity factor for a straight crack is

$$K_{\mathrm{I}} = 2\left(\frac{c}{\pi}\right)^{1/2} \int_0^c \frac{p(x)}{(c^2 - x^2)^{1/2}}\, dx \qquad (5.63)$$

and for a penny-shaped crack of radius c it is

$$K_{\mathrm{I}} = \frac{2}{(\pi c)^{1/2}} \int_0^c \frac{r\, p(r)}{(c^2 - r^2)^{1/2}}\, dr \qquad (5.64)$$

   For loads that are applied directly to the crack surfaces (as in the case of internal hydraulic loading), these equations can be applied directly. One would

like to apply these formulas to partially bridged cracks and treat the resulting K as a contribution to the critical stress intensity factor. However, for the case of cracks partially bridged by elastic fibers or grains, the closure stress at a point depends on the crack opening $2u$ at that point. This in turn depends on the entire stress distribution over the crack surface. The result is that, before the appropriate one of the two equations above can be used to calculate the K contribution from the closure stress, two equations for this stress must be solved simultaneously by numerical means or simplifying approximations must be made by assuming a crack-opening profile. Both procedures have been used by Marshall and Evans (1986) for the case of a fully bridged crack and their results will be discussed in Chapter 10. To illustrate the problem, we anticipate some of their steps here. For a volume fraction V_f of fibers with Young's modulus E_f and radius r that requires an interfacial sliding stress τ in a matrix with Young's modulus E_m with a crack opening displacement at x of $2u(x)$, the closure stress on the faces of the crack is a function of u given by

$$p(x) = 2\left\{\frac{u(x)\,\tau\,V_f^2 E_f\left[E_m(1 - V_f) + E_f V_f\right]}{rE_m(1 - V_f)}\right\}^{1/2} \tag{5.65}$$

However, the crack-opening displacement for a crack under both a remote uniform stress σ_∞ and a closure stress $p(x)$ is given in general by

$$u(x) = \frac{4(1 - v^2)c}{\pi E_c}\int_{s=x}^1 \frac{1}{(s^2 - x^2)^{1/2}}\int_{t=0}^s \frac{[\sigma_\infty - p(t)]}{(s^2 - t^2)^{1/2}}t\,dt\,ds \tag{5.66}$$

where s and t are normalized position coordinates. These are the equations that must be solved simultaneously for $p(x)$ before the equation for K can be used.

Fortunately, the J integral can be used to derive a relationship for the contribution to the resistance to crack propagation for partially bridged cracks that requires knowledge of the stress as a function of crack-opening displacement and the value of the crack-opening displacement itself at only one point. We consider a crack with a bridged region near the tip giving rise to a stress $p(x)$. Turning again to Figure 5.7, we consider the contour LKJ and shrink it to the surface of the crack itself; that is, the contour then runs from L along the upper surface of the crack to the tip and back to J along the lower surface. Also, the points L and J are taken at the end of the bridging zone. Along the upper and lower crack surfaces, $dy = 0$, so that

$$J = 2\int_0^{u_L} p(x)\frac{du}{dx}dx \tag{5.67}$$

Recognizing that

$$x = x(u) \qquad \text{so} \qquad p(x) = p(u) \tag{5.68}$$

leads to

$$J = 2 \int_0^{u_L} p(u) \ du \tag{5.69}$$

This result allows the toughening due to bridging (the J value from bridging) to be calculated from knowledge of the displacement and the bridging force as a function of displacement at the end of the bridging zone rather than requiring complete knowledge of these quantities over the whole bridged portion of the crack length.

5.11   FAILURE UNDER MULTIAXIAL STRESS

Throughout most of the present book the treatment of brittle fracture is focused on cracks under simple tensile stress perpendicular to the crack plane. This is justified for many situations of interest to ceramic engineers, as in uniaxial tensile or flexural testing of polycrystalline ceramics. Here, even though cracks are presumably found in all orientations with respect to the stress axis, for a random distribution of crack orientations failure should occur from a crack at the maximum end of the crack size distribution that is oriented perpendicular to the uniaxial stress axis. However, situations involving multi-axial loading can arise so that the behavior of cracks under compound loading should be studied. The behavior of a crack under mixed-mode loading is treated by Jayatilaka (1979) and Broek (1987). The treatment of mixed-mode loading is complex and remains somewhat unsatisfactory. We limit ourselves to treatment of two-dimensional mixed-mode loading and content ourselves with showing how the most general two-dimensional case can be reduced to consideration of an inclined crack in a tensile stress and to presenting the results of the simplest mixed-mode fracture criterion.

In the most general case of two-dimensional loading of a central crack in a body, there are three stress components: σ_{xx}, σ_{yy}, and $\sigma_{xy} = \sigma_{yx}$. From the Mohr circle construction one can find an inclined coordinate system in which there are no shear components, as described in Chapter 1. In this principal axis system the crack will be inclined to the principal stress axes. Taking the angle of inclination of the crack to be β relative to the principal stress σ_1, the crack experiences a tensile stress normal to its plane, σ_N, and an in-plane shear stress τ. The stress intensity factors for a through crack of total length $2c$ in plane stress are

$$\begin{aligned}
K_{\mathrm{I}} &= \sigma_N (\pi c)^{1/2} = (\sigma_1 \sin^2 \beta + \sigma_2 \cos^2 \beta)(\pi c)^{1/2} \\
K_{\mathrm{II}} &= \tau (\pi c)^{1/2} = (\sigma_1 - \sigma_2) \sin \beta \cos \beta (\pi c)^{1/2}
\end{aligned} \tag{5.70}$$

Fracture is assumed to occur when the energy release rate exceeds the energy consumption rate. For the combination of mode I and mode II but not mode

III, Eq. (5.43) for the case of plane stress becomes

$$EG = K_{\mathrm{I}}^2 + K_{\mathrm{II}}^2 = \text{const} = K_{IC}^2 \tag{5.71}$$

where it is assumed that the crack propagates only in its initial plane so that the constant can be set equal to K_{IC}^2. The failure criterion then becomes

$$\left(\frac{K_{\mathrm{I}}}{K_{IC}}\right)^2 + \left(\frac{K_{\mathrm{II}}}{K_{IC}}\right)^2 = 1 \tag{5.72}$$

which gives the locus of fracture in the K_{I}, K_{II} plane as a circle. It is more likely that $K_{IC} \neq K_{IIC}$, giving

$$\left(\frac{K_{\mathrm{I}}}{K_{IC}}\right)^2 + \left(\frac{K_{\mathrm{II}}}{K_{IIC}}\right)^2 = 1 \tag{5.73}$$

which gives the locus of fracture in the K_{I}, K_{II} plane as an ellipse.

However, it is commonly observed that cracks placed under mixed-mode loading extend at an angle to their original plane. Two criteria for such propagation under mixed-mode loading have been proposed: the maximum principal stress criterion and the strain energy density criterion (Broek, 1987). The two criteria give very similar results, although neither criterion is free from some objection. Experimental examples given by Broek fit the maximum principal stress criterion reasonably well but also are in fair agreement with the above simple ellipse result despite the experimental fact that cracks under mixed-mode loading are observed to extend at an angle to their original plane and so do not fit the assumption made in deriving the above simple result. The reader is referred to Jayatilaka (1979) and Broek (1987) for further details.

One might suppose that the issue of an appropriate failure criterion for ceramics under multiaxial loading could be settled by experiment and attempts have been made to do so. Thiemeier and Bruckner-Foit (1991) considered several failure criteria: mode I failure, coplanar energy release rate, maximum hoop stress factor, minimum strain-energy density, maximum noncoplanar energy release rate, and an empirical criterion. They developed predictions made with these criteria for the relation of strength in four-point bending to strength measured in a ring-on-ring biaxial flexure test and compared the results to experiments on aluminum nitride. All criteria with the exception of mode I failure, coplanar energy release rate, and minimum strain-energy density for plane strain gave reasonable agreement with experiment. However, the scatter in the data did not permit a unique failure criterion to be determined. The issue of the statistical treatment of fracture under multiaxial stress is discussed in Section 7.11.

Mixed-mode fracture toughness has been studied in polycrystalline alumina by Suresh et al. (1990) using a four-point bending technique with an

asymmetrical notch. They found that the mode II fracture toughness was comparable to the mode I toughness. Combining these results with an earlier study by Suresh and Tschegg (1987), they concluded that the mode III toughness was 2.3 times higher than the mode I value.

PROBLEMS

1. The critical stress intensity factor K_{IC} for a particular material is $1.5\,\mathrm{MPa}\cdot\mathrm{m}^{1/2}$ and its Poisson ratio is 0.3. A thin tensile specimen of the material has an edge crack, as depicted in Figure 6.3. If the specimen fails under a tensile stress of 230 MPa, what is the size of the edge crack? Suppose now that there is some misalignment of the grips such that the specimen experiences some twist about its long axis. This twist results in an antiplane shear stress $\tau = 50\,\mathrm{MPa}$. What tensile stress would cause failure in the presence of the shear? (You may assume for the purposes of this question that the criterion for failure is that the strain energy release rate must reach some critical value G_c such that under mixed-mode loading the crack extends in its own plane and $K_{IIIC} = K_{IC}$.)

2. Why are the plane strain and plane stress forms of several of the fracture mechanics equations different? The fracture surface energy for polycrystalline alumina is $12\,\mathrm{J/m^2}$ and the Young and shear moduli are 404 and 163 GPa, respectively. When a sample of the alumina is broken under conditions of plane strain, its strength is found to be 350 MPa. Assuming that failure occurred at a surface scratch induced by grinding, estimate the depth of the scratch. Estimate K_{IC} for this alumina.

3. Many silicate glasses have a fracture toughness of about $0.7\,\mathrm{MPa}\cdot\mathrm{m}^{1/2}$ and a Young's modulus of about 70 GPa. Estimate the theoretical strength of silicate glass. Estimate the fracture surface energy of silicate glass. If a glass rod subjected to a uniform tension fails at a stress of 7250 psi, estimate the radius of the semicircular surface flaw that caused failure (1 lb = 0.45359 kg, 1 in. = 25.4 mm).

4. The fracture toughness of polycrystalline alumina (Young's modulus 306 GPa) is about $4\,\mathrm{MPa}\cdot\mathrm{m}^{1/2}$ while the toughness of MgO partially stabilized zirconia (PSZ) (Young's modulus 138 GPa) is about $10\,\mathrm{MPa}\cdot\mathrm{m}^{1/2}$.

   a. Estimate the fracture surface energy of (i) alumina and (ii) PSZ assuming these toughness values were obtained under conditions of plane stress.

   b. Polycrystalline ceramics often have intergranular cracks in them due to thermal expansion mismatch. Their strength is therefore limited by these cracks whose size is on the order of the grain size. Calculate the maximum strength you would expect to observe in (i) alumina with a 20-μm-diameter grain size and (ii) PSZ with a 50-μm-diameter grain

size. Model the cracks as internal circular cracks with the same size as the grains.

5. Soda-lime glass has the following properties: Young's modulus 70 GPa, Poisson's ratio 0.22, and fracture surface energy $5 \, \text{J/m}^2$. You may assume conditions of plane stress throughout this question. Calculate the critical stress intensity factor/fracture toughness of soda-lime glass.

One can model the defects in soda-lime glass as semicircular surface cracks whose plane is perpendicular to the glass surface. In a particular application the glass is subjected to a uniaxial tensile stress of 150 MPa. Determine the radius of the biggest semicircular crack that can be tolerated in the surface of the glass for cracks oriented (you may assume that K_{IC} and K_{IIIC} are much larger than K_{IC}):

  i. Perpendicular to tensile stress axis
 ii. At 45° to tensile stress axis
iii. Parallel to tensile stress axis

It is difficult to make glass that does not have cracks bigger than the value you calculated earlier. Glass can be strengthened by "thermal tempering," which involves rapid quenching from a high temperature. This results in a biaxial residual compressive stress in the surface of the glass which must be overcome before fracture can ensue. The effect of tempering can be thought of either as (a) superimposing a compressive stress at the surface on any externally applied tensile stress or (b) applying a negative stress intensity to any crack in the surface.

If the glass to be used in this application is tempered with a resulting 120 MPa compressive stress in its surface, what is the radius of the biggest semicircular crack that can be tolerated in the surface of the glass for cracks oriented perpendicular to the tensile stress axis?

6. Using the information in Table 5.1 for a central through crack of total length $2c$ subjected to a double-line force, determine the stress intensity for such a crack which is filled with fluid at a pressure equal to σ. Comment on the significance of your answer.

6

MEASUREMENTS OF ELASTICITY, STRENGTH, AND FRACTURE TOUGHNESS

6.1 INTRODUCTION

This chapter presents a summary of the commonly used methods for measurement of elastic moduli, strength, and fracture toughness of ceramics. Many tabulations are available (Jayatilaka, 1979; Young, 1989; Lawn, 1993). The reader embarking on a testing program would be well advised to review recent work on developing standards for mechanical and related tests; these are briefly discussed in Chapter 24 and listed in Table 24.2.

The focus is first on elasticity and strength tests for which nominally uncracked specimens are used. That is, no artificial crack is introduced. The sensitivity of ceramics to surface cracks and the possibility of introducing surface cracks in sawing and grinding the specimen to accurate dimensions are special concerns. The surface condition is usually made as close as possible to

that to be used in service when the intention is to produce strength data for design. For research on strength improvement theory, microstructure design, and processing, the surfaces are prepared to be as free as possible of cracks not characteristic of the general microstructure. Although this class of test with nominally uncracked specimens can be used for both elastic moduli and strength determinations, the accuracy of elastic moduli determination is typically a few percent at best. An alternative approach using resonance or ultrasonic methods gives much better accuracy and is summarized in Section 6.8.

The second focus is on fracture toughness test methods in which a crack of known size is deliberately introduced and a critical stress intensity factor is measured, or equivalently a fracture surface energy. Measurement in ductile materials, such as many metals, presents special problems and requires special test procedures. The tests considered here are those appropriate to ceramics characterized by brittle fracture. Three conditions are required for successful fracture toughness testing (Jayatilaka, 1979):

1. The specimen geometry and loading system must allow calculation of the applied stress intensity factor.
2. The crack length and load at the beginning of rapid crack propagation must be accurately determined.
3. The initial crack must be sharp.

An American Society for Testing and Materials (ASTM) standard has been developed for fracture toughness testing; it recommends three methods: the single-edge precracked beam method, the chevron notch method, and the surface crack in flexure method (ASTM standard C 1421-01B, see Chapter 24). All are discussed in the present chapter.

For metals the development of a zone of plastic deformation near the crack tip must be taken into account. For most ceramics at room temperature this complication does not exist. However, ceramics at high temperatures do show plastic effects so plasticity considerations are briefly mentioned here. A characteristic parameter for the size of the plastic zone is $(K_{IC}/\sigma_Y)^2$, where K_{IC} is the critical stress intensity factor and σ_Y is the yield stress. When the yield stress is difficult to measure directly, it is estimated by taking $\sigma_Y = H/3$, where H is the hardness. Typically $(K_{IC}/\sigma_Y)^2$ is about 4 mm for a strong metal but is only about 0.1 mm for a brittle material. Both the crack length and the specimen thickness should exceed $2.5(K_{IC}/\sigma_Y)^2$ (Jayatilaka, 1979).

The second category of test methods (i.e., using specimen with deliberately introduced cracks) is also useful for tests in which a chosen value of stress intensity factor below the critical stress intensity factor is to be applied. Such test methods are useful, for example, in studying slow crack propagation.

The test methods covered in this chapter are appropriate for stiff bars. Test techniques for thin, flexible fibers, such as optical fibers, have been summarized by Matthewson (1994).

6.2   TENSILE TESTS

A straight elastic bar of uniform cross section A is assumed. The loads (tensile or compressive) are applied at the ends uniformly distributed over the cross section. In practice these conditions often apply only to the central portion of a longer specimen with larger ends to which the loads are applied. The y axis is taken along the axis of the bar, as shown in Figure 6.1. Tensile stress is denoted by σ and shear stress by τ as a function of the angle θ between the axis of the bar and the normal to the plane on which the stress acts. Here, P is the applied load, E is Young's modulus, and ν is Poisson's ratio.

The resulting stresses do not depend on the elastic properties and are (Young, 1989)

$$\sigma_{yy} = \sigma(\theta = 0) = \frac{P}{A} \tag{6.1}$$

$$\sigma(\theta) = \frac{P}{A}\cos^2\theta \tag{6.2}$$

The maximum value of $\sigma(\theta)$ occurs when $\theta = 0$ and is P/A. Then

$$\tau(\theta) = \frac{P}{2A}\sin 2\theta \tag{6.3}$$

The maximum value of $\tau(\theta)$ occurs when θ equals $45°$ or $135°$ and is $P/2A$.
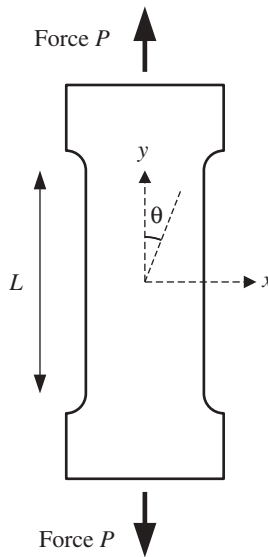
FIGURE 6.1   Schematic of tensile test.

The strains in general depend on the elastic and plastic behavior of the material. For purely elastic behavior the strains are

$$\varepsilon_{yy} = \frac{\sigma}{E} \tag{6.4}$$

$$\varepsilon_{xx} = \varepsilon_{zz} = -v\varepsilon_{yy} \tag{6.5}$$

For linear elastic strain, the strain energy per unit volume is

$$U_e = \frac{1}{2}\frac{\sigma^2}{E} \tag{6.6}$$

The tensile strength as measured in a tensile test is simply the stress P/A at the instant of fracture. The most common experiment is to program a testing machine to increase the displacement (typically for a screw-driven testing machine) or the load (typically for a hydraulic testing machine) at a constant rate. Strength measured in this way at a rapid strain rate is often termed the **instantaneous strength**.

In principle the tensile test has several advantages. It produces a value of stress not dependent on the response of the material provided necking does not occur. It subjects the test section of the specimen to a uniform stress, which facilitates the study of the statistical aspects of failure. However, the tensile test requires very accurate gripping of the ends to eliminate a component of bending. The specimens are complex and expensive. Several special forms of tensile specimens and associated testing equipment have been developed in an attempt to minimize these problems.

The phenomenon of slow crack propagation (treated in Chapter 8) causes the measured strength to decrease with decreasing loading rate. Measurements of strength as a function of loading rate can be analyzed to give information on slow crack propagation.

Another loading pattern used in tensile testing is the **stress rupture test**, in which a constant load corresponding to a tensile stress below the instantaneous strength is applied. The time to failure is determined as a function of the stress. The time to failure increases as the stress is decreased and eventually becomes too large to measure. This type of test can also be used to study slow crack propagation. The resulting behavior is sometimes termed **static fatigue**. At high temperatures other effects associated with creep can also cause stress rupture behavior.

Still another type of loading pattern is used to study **cyclic fatigue** (termed simply as fatigue in the metallurgical literature). The load is typically cycled between a maximum value below the instantaneous strength and some chosen minimum stress. This type of test is important for metallic alloys, which often

display a decrease in strength as the number of fatigue cycles is increased; the effect is related to local plasticity in metals. Cyclic fatigue was once thought unlikely in most ceramics at room temperature because of the lack of plastic deformation, but strong cyclic fatigue effects are now known to occur in many ceramics at room temperature and are treated in Chapter 15.

Tensile tests on specimens containing deliberate flaws can also be used to measure fracture mechanics properties of a ceramic: the critical stress intensity factor or equivalently the fracture surface energy. Some common specimen configurations are summarized in Tables 5.1 and 5.2. A crack geometry of interest is that of a "penny-shaped" crack within a specimen, as shown in Figure 6.2. This crack shape is not used in testing but is encountered in failure analysis using fractography; the latter subject is discussed in Chapter 17. The crack is taken to be oriented perpendicular to the applied stress and to be a circle of radius c located far from any surface. For this geometry (Jayatilaka, 1979; Lawn, 1993)

$$K_I = 2\pi^{-1/2}\sigma c^{1/2} = 1.128\sigma c^{1/2} \tag{6.7}$$

The tensile test can be used to measure the critical stress intensity factor of a ceramic. If a flaw of known size can be introduced and the fracture stress is measured, the stress intensity factor at fracture can be calculated from Eq. (5.45). There are two types of tensile specimens for critical stress intensity factor determination: the edge-cracked tensile specimen and the compact tension specimen (Evans and Langdon, 1976; Tada et al., 1985; Murakami, 1986).
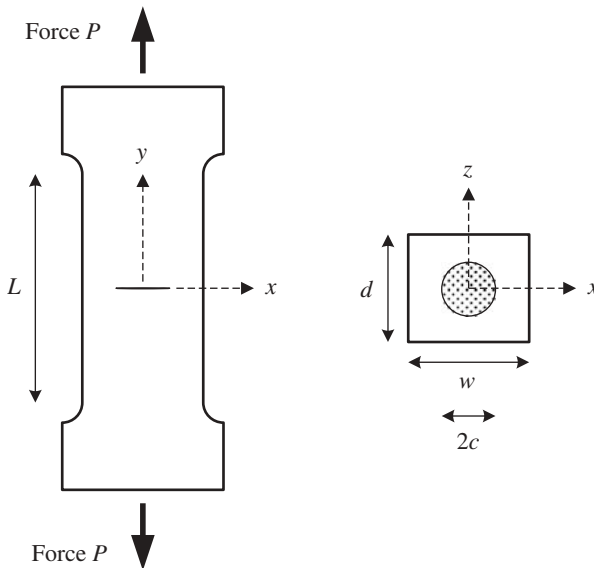
FIGURE 6.2   Tensile test with penny-shaped crack.
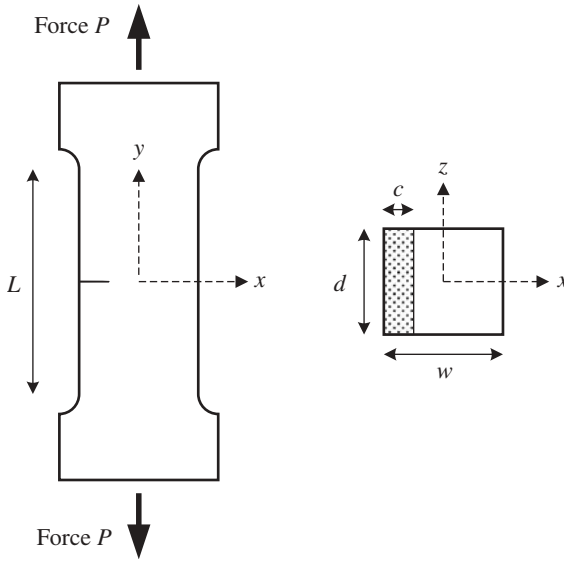
FIGURE 6.3   Tensile test with edge-cracked specimen.

The edge-cracked test uses a tensile specimen, shown in Figure 6.3, under total load P with width w and thickness d containing an edge crack of total length c extending through the thickness. This crack experiences an applied stress intensity factor

$$K_I = \frac{P}{wd} Yc^{1/2} \tag{6.8}$$

where Y, the crack shape parameter, in this case is given by

$$Y = 1.99 + 0.41\left(\frac{c}{w}\right) + 18.70\left(\frac{c}{w}\right)^2 - 38.48\left(\frac{c}{w}\right)^3 + 53.85\left(\frac{c}{w}\right)^4 \tag{6.9}$$

If $c \ll w$, $Y \simeq 1.99$ as given in Table 5.2.

The compact tension specimen shown in Figure 6.4 is again a bar of width w and thickness d with an edge crack of total length c extending through the thickness. However, the load P is not applied over the end of the specimen as in the usual tension test but is instead applied at the edge of the specimen containing the crack. Also, the total length of the specimen, $2h$, is relatively small, $2h/w < 1$. The applied stress intensity factor is given by

$$K_I = \frac{P}{wd} Yc^{1/2} = Y\sigma c^{1/2} \tag{6.10}$$

For this specimen Y depends, for a given h/w, on the value of c/w. For $h/w = 0.4$, $Y = 1.42$ at $c/w = 0.3$ and increases smoothly to $Y = 2.2$ at $c/w = 0.65$.
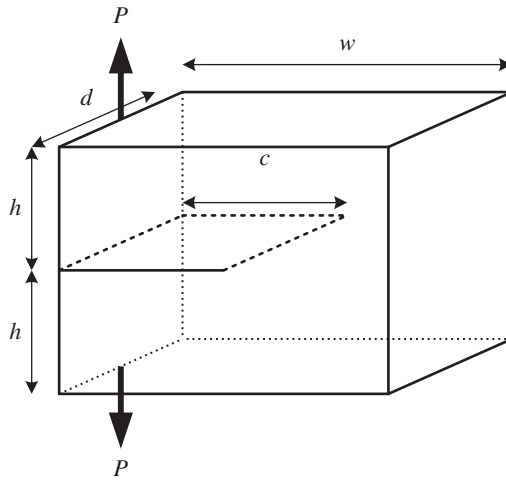
FIGURE 6.4   Tensile test with compact tensile specimen.

Tension tests are often used for measurements of critical stress intensity factors for metals. However, tensile testing of ceramics is difficult as mentioned. Accordingly, bending tests and other specialized tests (some of which are described later) are commonly used to determine critical stress intensity factors of ceramics.

Tensile (and compressive) testing is especially important for studying creep of ceramics at high temperatures. Creep in bending leads to complex behavior because the creep rate in tension is typically greater than in compression at the same stress level, leading to a shift of the neutral axis in bending tests (Jakus and Wiederhorn, 1988). Although a method of analyzing creep tests performed in bending to give creep rate in uniaxial tension has been developed (Hollenberg et al., 1971; Chuang, 1986; Chuang and Wiederhorn, 1988), the procedure is difficult and creep testing in tension when possible, or in compression, is generally considered to be much preferred. A method for creep testing in tension at temperatures up to 1500°C has been developed (Carroll et al., 1989) that uses relatively simple specimens and equipment.

6.3   FLEXURE TESTS

The relative simplicity of flexural (bend) testing and the low cost of the required specimens have made this test very popular for ceramics despite several drawbacks in interpretation of the resulting data. These drawbacks include a stress distribution that is both nonuniform and changes with increasing strain if some plastic deformation takes place. Accordingly, special problems arise in connection with failure probability analyses and with experiments involving
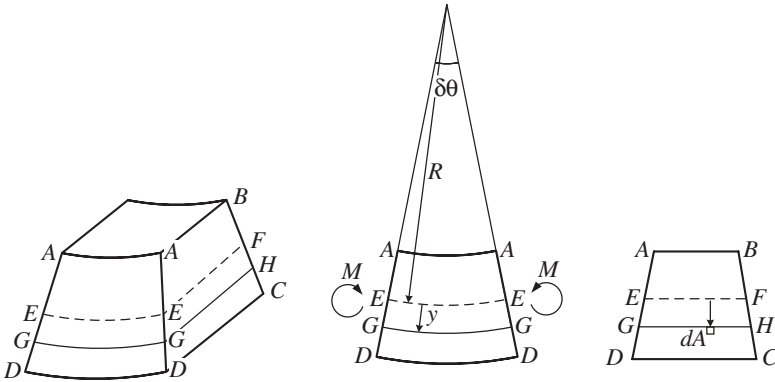
FIGURE 6.5   Flexure of a beam.

creep. These will be discussed in the appropriate chapters. In the present chapter attention is focused on the use of bend tests for linear elastic brittle materials.

Bars of rectangular or circular cross section are generally used for bend tests on ceramics. However, it is useful to recognize that much of the treatment of bending of bars applies to bars of arbitrary cross section. Therefore a general treatment is developed that is then applied to bars of rectangular section. Figure 6.5 shows a short piece of a bent bar with cross section $ABCD$. The element is subjected to bending moments M applied to its ends by the rest of the bar that cause it to bend into an arc which subtends an angle $\delta\theta$ at the center of curvature. The upper surface of the element, AA, is in compression and the lower surface, DD, is in tension. Somewhere between the upper and lower surfaces is a plane EF such that EE is unchanged in length but is bent into the arc of a circle of radius R. Here, EE is termed the **neutral axis** and the plane EF is the **neutral plane**. Consider an element of area dA at a distance y from the neutral axis. The radius of curvature at y is $R+y$. Remembering that the original length of GG before the beam is bent is EE, the strain ε in GG is

$$\varepsilon = \frac{GG - EE}{EE} = \frac{(R+y)\delta\theta - R\delta\theta}{R\delta\theta} = \frac{y}{R} \tag{6.11}$$

That is, the strain is proportional to the distance from the neutral axis. The corresponding stress is calculated by recognizing that the arc GG is subjected to uniaxial tension so that the appropriate elastic modulus for the deformation is Young's modulus E. Hooke's law then gives

$$\sigma = \frac{E}{R} y \tag{6.12}$$

Thus the stress is also proportional to the distance from the neutral axis. The total force acting on the cross section $ABCD$ must be zero because this segment of the bar is only subjected to the bending moment M so that

$$\int \sigma \, dA = 0 \tag{6.13}$$

giving

$$\int y \, dA = 0 \tag{6.14}$$

This condition defines the position of the neutral axis, which thus passes through the centroid of the section. The stress σ acting across the element of area dA corresponds to a force $\sigma \, dA$ which has a moment about the neutral plane, EF. The total bending moment M is therefore

$$M = \int y\sigma \, dA \tag{6.15}$$

so that

$$M = \frac{E}{R} \int y^2 \, dA \tag{6.16}$$

The **second moment of area**, I, is defined by

$$I = \int y^2 \, dA \tag{6.17}$$

This gives the useful equation for bending

$$M = \frac{EI}{R} \quad \text{or} \quad \frac{1}{R} = \frac{M}{EI} \tag{6.18}$$

Integration of Eq. (6.17) over the cross section for a bar of rectangular cross section of width d and height h gives

$$I = \tfrac{1}{12}h^3 d \tag{6.19}$$

while for a rod of radius a

$$I = \tfrac{1}{4}\pi a^4 \tag{6.20}$$

For these symmetrical cross sections, the neutral axis is halfway across the thickness of the bar.

Equation (6.18) can be used to calculate the shape of the bent bar and hence the stress in the bar under various loading conditions. The elastic solutions taken from the literature for three- and four-point bending are given below.

6.3.1 Three-Point Bending

The case of a beam of uniform cross section of thickness h supported at two points and loaded at the center of the span is illustrated in Figure 6.6(a). This configuration is usually termed **three-point bending**. Note that the "points" are
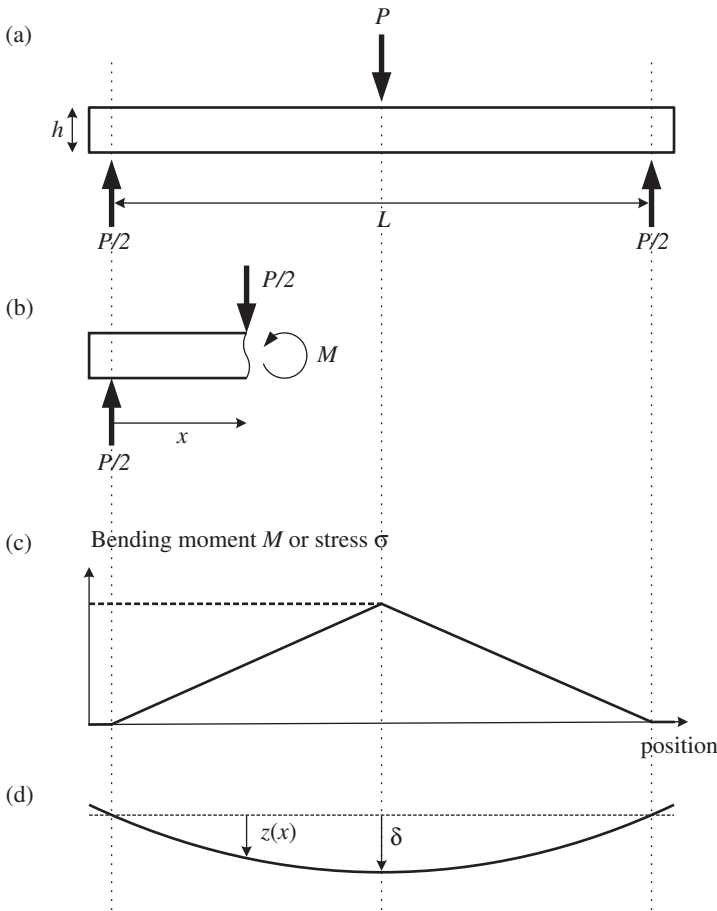
FIGURE 6.6 Three-point bending geometry and distribution of bending moment.

actually line contacts extending across the width of the specimen. Equations (6.12) and (6.18) give

$$\sigma = \frac{M}{I} y \tag{6.21}$$

The bending moment can be found as a function of position along the bar by considering the stability of a section of the bar of length x (measured from the left support), as shown in Figure 6.6(b). The effect of the remainder of the beam is replaced by the vertical force $P/2$ to maintain stability in the vertical direction and the bending moment M. For rotational stability, moments can be taken about the end of the beam to give

$$M = \tfrac{1}{2}Px \qquad 0 \le x \le \tfrac{1}{2}L \tag{6.22}$$

The bending is symmetrical about the center of the bar so the bending moment as a function of position is shown in Figure 6.6(c). The maximum bending moment is at the center of the bar, $x = L/2$, and is given by $M_{max} = PL/4$. Note that there is no bending moment outside the outer support points, $x < 0$ and $x > L$, so that the overhang plays no part. Combining Eqs. (6.21) and (6.22) gives the distribution of stress throughout the bar,

$$\sigma = \frac{P}{2I} xy \qquad 0 \le x \le \tfrac{1}{2}L \tag{6.23}$$

It varies linearly through the thickness and linearly along the length of the bar. This expression is only valid for the left-hand side, but a similar solution can be found for the right-hand side. The stress too is symmetrical about the center of the bar so that the profile of stress along the length is similar to that of the moment, as shown in Figure 6.6(c). The maximum stress occurs on the bottom surface, $y = h/2$, at the center, $x = L/2$, so that

$$\sigma_{max} = \frac{PLh}{8I} = \frac{3PL}{2h^2d} \quad \text{(rectangular bar)} \tag{6.24}$$

A more detailed treatment shows that the concentrated load causes a wedging action, and when this effect is taken into account, the result is

$$\sigma_{max} = \frac{3PL}{2h^2d} \left(1 - \frac{4h}{3\pi L} \right) \quad \text{(rectangular bar)} \tag{6.25}$$

This represents a negligible correction if the length of the span is much greater than the thickness of the bar, $L \gg h$.

The deflection of the bar relative to the support points, $z(x)$, is defined in Figure 6.6(d). It can be found by relating it to the radius of curvature of the neutral axis, R. Equations (6.18) and (6.22) give

$$\frac{1}{R} = \frac{P}{2EI} x \approx -\frac{d^2z}{dx^2} \tag{6.26}$$

The approximation that the curvature is the second derivative of the deflection z is valid provided that the deflection is small, or specifically $dz/dx \ll 1$. The minus sign is introduced to compensate for the definition of M in Figure 6.6(b) being in the negative sense. Equation (6.26) is readily integrated twice. The two constants of integration are found by fitting to the boundary conditions; for the left side of the bar, $z=0$ at $x=0$, and by symmetry, $dz/dx=0$ at $x=L/2$, giving

$$z = \frac{P}{48EI} \left(3L^2x - 4x^3\right) \qquad 0 \le x \le \tfrac{1}{2}L \tag{6.27}$$

A similar solution can be found for the right-hand side. The deflection at the center of the beam, δ, is found by evaluating z at $x=L/2$:

$$\delta = \frac{PL^3}{48EI} = \frac{PL^3}{4Eh^3d} \quad \text{(rectangular bar)} \tag{6.28}$$

6.3.2   Four-Point Bending

As shown in Figure 6.6(c), the stress for three-point bending varies from zero at the support points to a maximum at the center. Thus only a very small portion of the specimen is subjected to a stress at or near the maximum value. For this reason four-point bending rather than three-point bending is often preferred and is commonly used in testing ceramics to obtain design data.

A four-point bend specimen is shown in Figure 6.7. The central portion of the bar (between the two upper loads) is in uniform bending. Similar methods to those given for three-point bending can be used in this case to show that the bending moment in the central portion is constant and is equal to $PD/2$. Note that the total load is taken here as P rather than $2P$, as in some references. The maximum stress (i.e., the stress in the outer tensile surface of the bar) is constant over the central portion and is

$$\sigma_{max} = \frac{PDh}{4I} = \frac{3PD}{h^2d} \quad \text{(rectangular bar)} \tag{6.29}$$

The deflection of the beam is found piecewise by solving for z in the three regions $0 \le x \le D$, $D \le x \le L-D$, and $L-D \le x \le L$, followed by matching
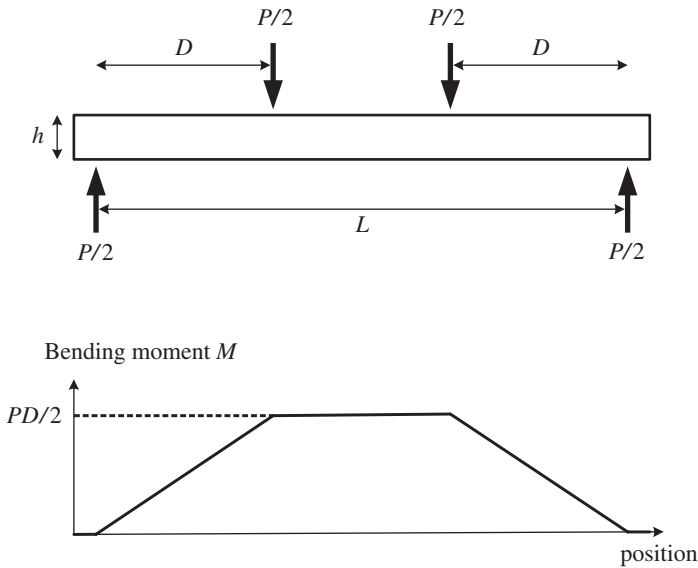
FIGURE 6.7   Four-point bending and moment diagram.

the deflection and gradient of the deflection at the junctures of the regions. The deflection of the center relative to the outer support points is found to be

$$\delta = \frac{PD}{48EI}\left(3L^2 - 4D^2\right) = \frac{PD}{4Eh^3d}\left(3L^2 - 4D^2\right) \quad \text{(rectangular bar)} \qquad (6.30)$$

The three-point bend equations can be recovered by setting $D = L/2$.

Flexure testing in four-point loading is the most widely used technique for strength measurements of ceramics over the temperature range in which creep is not appreciable. Typically quarter-point ($D = L/4$) or third-point ($D = L/3$) loading is used. The use of this test was reviewed by Quinn and Morrell (1991), and a discussion was given by Baratta (1982). Both three- and four-point bending are the subject of the ASTM standard C 1161-02C (see Chapter 24).

6.3.3   Fracture Toughness Measurement by Bending

Flexural tests with precracked specimens are commonly used to determine the fracture toughness of ceramics. One of the simplest is the precracked bend bar in three- or four-point bending. The latter case is shown in Figure 6.8 with an edge crack extending a distance c from the tension surface. The critical stress intensity factor for three-point bending (i.e., $D = L/2$) is given by

$$K_{IC} = Y\frac{3PL}{2h^2d}c^{1/2} \quad \text{(rectangular bar)} \qquad (6.31)$$
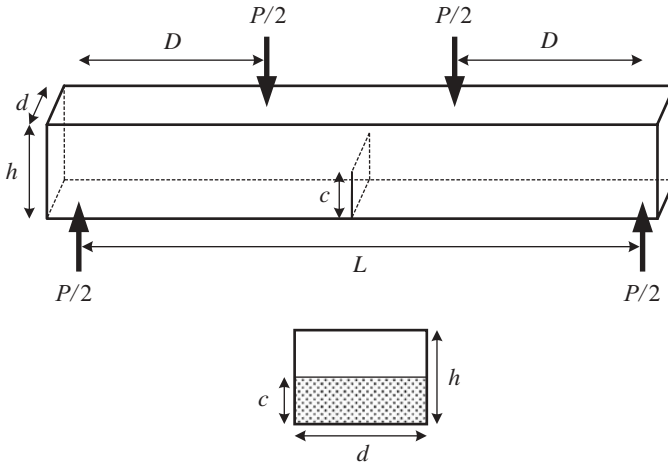
FIGURE 6.8 Bending test with edge-cracked specimen.

where P in the breaking load and the numerical factor for the case $L/h = 4$ is given by (Evans and Langdon, 1976)

$$Y = 1.93 - 3.07\left(\frac{c}{h}\right) + 13.66\left(\frac{c}{h}\right)^2 - 23.98\left(\frac{c}{h}\right)^3 + 25.22\left(\frac{c}{h}\right)^4 \qquad (6.32)$$

For four-point bending of an edge-cracked specimen, Srinivasan and Seshadri (1981) give

$$K_{IC} = Y\frac{3PD}{h^2d}c^{1/2} \quad \text{(rectangular bar)} \qquad (6.33)$$

with

$$Y = 1.99 - 2.47\left(\frac{c}{h}\right) + 12.97\left(\frac{c}{h}\right)^2 - 23.17\left(\frac{c}{h}\right)^3 + 24.8\left(\frac{c}{h}\right)^4 \qquad (6.34)$$

Equations for this type of fracture toughness testing are given in several places (Srawley and Brown, 1965; Brown and Srawley, 1966).

Care is necessary in the use of edge-notched specimens for K_{IC} determination. The value calculated is commonly found to decrease with decreasing slot width. Nishida et al. (1994) found that values of K_{IC} finally level off when the crack tip radius is below 10 μm. They obtained such fine crack tip radii by inserting a razor blade coated with 1-μm-diameter paste into the notch and moving the blade back and forth to machine the tip of the notch. This method has some popularity because it is reliable and easier to perform than the three methods required by ASTM standard C 1421-01B. The test has been designated single-edge V notch beam (SEVNB).

The above test methods generally assume elastic behavior up to the point of failure. When irreversible behavior occurs, such as plastic deformation, phase changes, or some combination of matrix cracking, fiber breaking, and fiber pullout in composites, testing becomes more difficult and complex. A *J*-integral approach is sometimes used in such situations. The technique for plastic metals is summarized, for example, by Broek (1987). A *J*-integral testing approach for ceramic matrix composites has been described by Hashida et al. (1994).

A relatively simple technique for determining fracture toughness in mixed mode I and mode II loading has been presented by Suresh et al. (1990).

Another important form of bend test used to determine the critical stress intensity factor utilizes a specimen with a chevron notch (Munz et al., 1980, 1981; Sakai and Yamasaki, 1983). A beam of original cross section depth *h* and width *w* is notched as shown in Figure 6.9. The load–displacement curves produced by bending chevron-notched brittle specimens differ from the curves produced by bending straight-through-notched brittle specimens. For the latter the load increases linearly with displacement up to the point of failure. For the chevron-notched specimens the load–displacement curve is initially linear but passes through a maximum. Failure occurs at higher displacements and smaller loads than the maximum load. This behavior results from the fact that a crack can propagate some distance from the tip of the solid web of material and come to a stable position. The critical stress intensity factor is given by

$$K_{\mathrm{IC}} = \frac{2DP_{\max}}{wh^{3/2}}\left[3.08 + 5.00\frac{c}{h} + 8.33\left(\frac{c}{h}\right)^2\right]$$

$$\times \left[1 + 0.007\left(\frac{L(L-2D)}{h^2}\right)\right]\left[\frac{b-c}{h-c}\right] \tag{6.35}$$
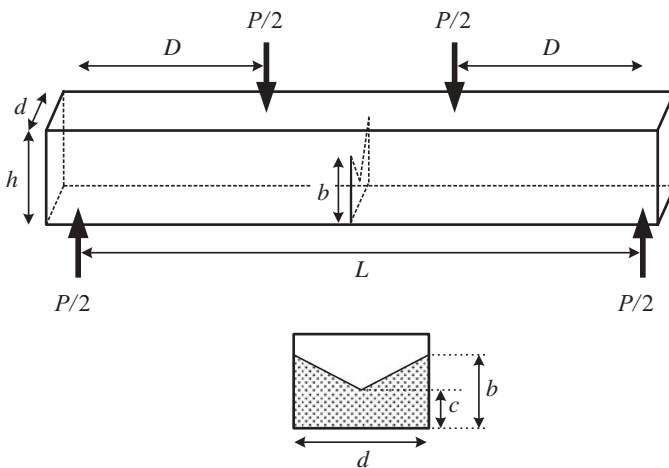
FIGURE 6.9 Bending test with chevron-notched specimen.
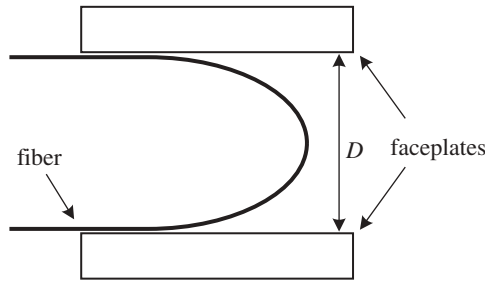
FIGURE 6.10   Two-point bending.

The three- or four-point flexure methods are only useful for specimens which deflect by a small amount at failure (i.e., $\delta \ll L$) and cannot be used for very thin and flexible specimens such as thin fibers and tapes. The two-point bend method, shown in Figure 6.10, has proved useful in this situation and has been used successfully for a variety of specimens, including glass optical fibers and brittle metallic glass tapes. In the two-point bend method a loop of the fiber or tape is bent double and placed between two faceplates which are brought together until the fiber breaks. The faceplate separation at failure, D, is recorded and used to calculate the failure stress. The maximum stress is at the tip of the bend and is given by

$$\sigma_{max} = 1.198E \frac{d}{D - d} \tag{6.36}$$

where d is the diameter of the fiber or thickness of the tape and D is the faceplate separation at failure (Matthewson et al., 1986). For very high strength materials, such as fused silica fibers, the Young's modulus E varies with strain and corrections must be made for this behavior.

Three other types of test for measuring fracture toughness are of considerable importance for ceramics and are reviewed in the following sections: the cantilever beam test, the double-torsion test, and the indentation test.

6.4   DOUBLE-CANTILEVER-BEAM TEST

The double-cantilever beam (DCB) test, shown in Figure 6.11(a), uses a specimen similar to the compact tension test but differs in that the "width" is now the length and is large compared to the height, $2h$. The stress intensity factor is

$$K_I = \frac{\sqrt{3}Pc}{dh^{3/2}} \left(2 + \sqrt{2}\frac{h}{c}\right) \tag{6.37}$$

If a constant load P is used, the applied stress intensity factor increases as the crack length increases so that the crack is unstable once propagation has begun.
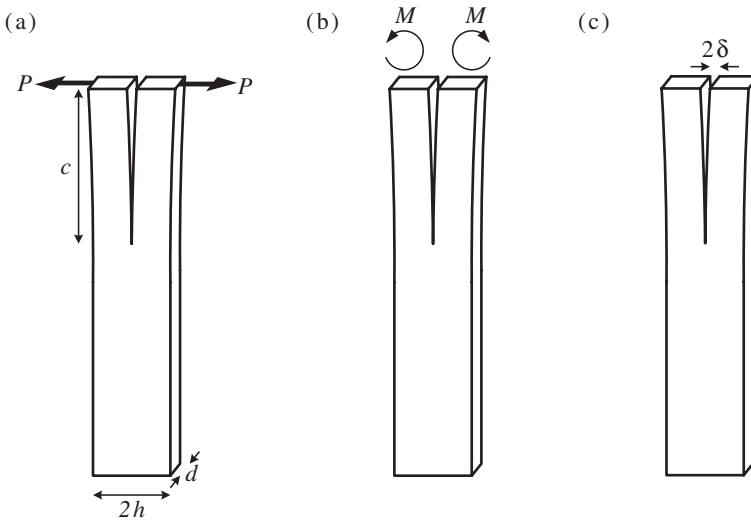
FIGURE 6.11   The DCB test.

A variation on the double cantilever test, the constant-moment double-cantilever beam test, is shown in Figure 6.11(b). Instead of an applied load, this test employs an applied moment M which can be applied using a lever arrangement. The applied stress intensity factor is given by

$$K_{\mathrm{I}} = \frac{M}{(Id)^{1/2}} = \frac{2\sqrt{3}M}{dh^{3/2}} \tag{6.38}$$

where M is the bending moment and I is the second moment of area of a single arm. Taking the total depth of the specimen as $2h$, so that the depth of a single arm is h, gives a second moment of area that is given in Eq. (6.19). An important property of this test is that the applied stress intensity factor is independent of the crack length. This makes the constant-moment double-cantilever beam test particularly appropriate for slow crack growth studies.

Another variation on the double-cantilever test, shown in Figure 6.11(c), wedges open the crack mouth by a distance δ. The applied stress intensity factor in this case is given by

$$K_{\mathrm{I}} = \frac{3E\delta}{c^2}\left(\frac{I}{d}\right)^{1/2} = \frac{\sqrt{3}E\delta h^{3/2}}{2c^2} \tag{6.39}$$

A property of this test is that the applied stress intensity factor is a decreasing function of the crack length. As a result, as δ increases, the crack extends stably. To summarize, the three methods shown in Figure 6.11 illustrate the three possible cases of crack stability: (a) unstable crack growth, (b) neutral crack stability, and (c) stable crack growth.
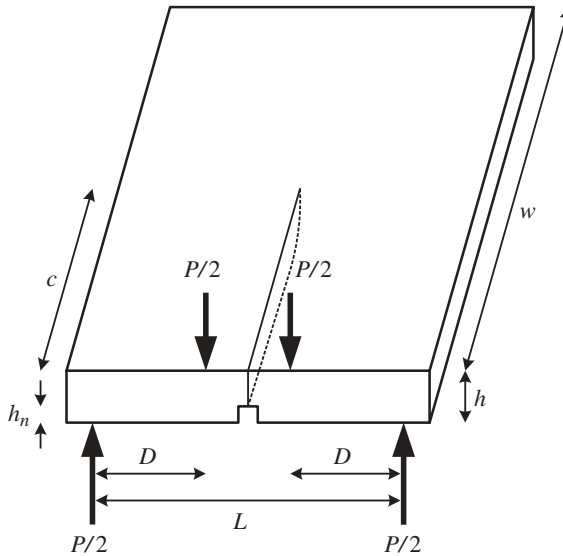
FIGURE 6.12 Schematic of double-torsion test specimen.

6.5 DOUBLE-TORSION TEST

Another test with the property of having a constant applied stress intensity factor independent of the crack length is the double-torsion test shown in Figure 6.12. The double-torsion test can be regarded as a four-point bend test specimen, as in Figure 6.7, but having the loads and supports at the edge of the specimen and having a thickness w that is large compared with the depth h. The specimen is notched on the tension surface, leaving a reduced thickness h_n. The applied stress intensity factor is

$$K_I = PD \left[\frac{3(1 + \nu)}{Lh^3 h_n} \right]^{1/2} \tag{6.40}$$

Here ν is Poisson's ratio and L is the support separation.

Quinn (1987) finds that the notch shown in Figure 6.12 causes the crack to move off center and recommends that a notch not be used. Instead, careful alignment of the specimen should be achieved. In Eq. (6.40), $h^3 h_n$ is then replaced by h^4.

6.6 INDENTATION TEST

When a sharp indenter is loaded onto a ceramic material, a permanent impression is left, indicating that even these materials can deform irreversibly,

that is, plastically. A measure of the resistance to plastic deformation is the **hardness** H, which is the mean contact pressure, that is, the peak load P, divided by the area of residual deformation, A:

$$H = \frac{P}{A} \tag{6.41}$$

Hardness testing is important in itself, but discussion of the topic will be postponed until Chapter 22. However, in addition to plastic deformation, the indentation can also cause crack formation, which is relevant here since the effect can be used to determine the toughness.

Various geometries of indenter can be used, but the most common is the Vickers indenter, which uses a square-based pyramid, usually made of diamond. The Knoop indenter, with greatly unequal diagonals, is also used (see Table 22.1). The definition of hardness in general use in the materials community uses the actual area of the indent for A in Eq. (6.41). For Vickers hardness, this uses the contact area over the four faces of the indenter pyramid, which leads to a definition of $H = 1.8544P/(2a)^2$, where $2a$ is the length of the diagonal of the hardness indent as defined in Figure 6.13. In contrast, many in the ceramics community use the projected area of the indent, leading to a
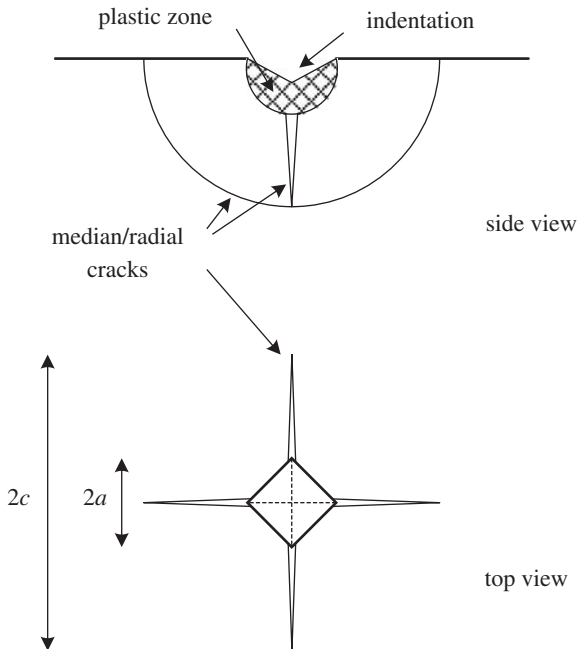
FIGURE 6.13 Cracking around a hardness indentation.

definition of Vickers hardness of $H = 2P/(2a)^2$. This results in a small but significant difference of 7.9% between the two definitions. Here we follow that latter definition, which is widely used in the ceramics community for fracture mechanics measurements, but warn the reader to check the definitions being used before comparing hardness data from the literature.

The indentation test for toughness can be used in several forms to determine the critical stress intensity factor (Lawn and Wilshaw, 1975; Evans and Charles, 1976; Marshall et al., 1979). Only the basic technique for a critical stress intensity factor independent of crack length is summarized here. There are three methods: direct, indirect, and modified.

6.6.1   Direct Method

The direct approach is to use a load P on a pointed indenter to produce a hardness indent with a diagonal length $2a$. The hardness is given by

$$H = \frac{P}{\alpha a^2} \tag{6.42}$$

where α is a numerical factor that depends on the shape of the indenter. For a Vickers indenter $\alpha = 2$.

A detailed discussion of the types of cracks associated with hardness tests and of the sequence of their formation is given by Cook and Pharr (1990). However, the cracks relevant to the current discussion are the radial cracks shown in Figure 6.13. Figure 6.14(a) shows how the compressive indentation load P acts via frictional forces between the indenter and the surface to produce tensile forces F parallel to the surface which are proportional to P. Each radial crack is modeled as a semicircular crack of radius c loaded by central forces F, as shown in Figure 6.14(b). This type of loading produces a stress intensity on the crack which is proportional to $c^{-3/2}$ which decreases for longer cracks. For an initially small crack, K_I is larger than K_{IC} so that a sufficiently small crack will grow. However, with continued growth, K_I decreases until it falls below K_{IC}, at which point the crack stops growing. Therefore the final length of the crack, which can be conveniently measured after removal of the indentation
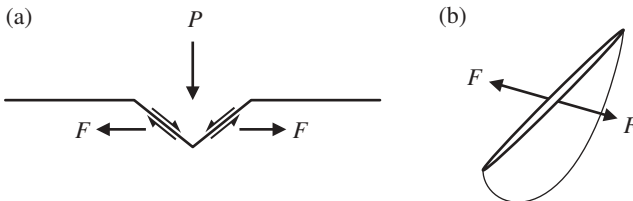
FIGURE 6.14   Forces acting during indentation by a sharp indenter.

load, is a measure of K_{IC}. The result is

$$K_{IC} = \frac{\zeta(E/H)^{1/2}P}{c^{3/2}} \tag{6.43}$$

The term $\zeta(E/H)^{1/2}$ includes the proportionality between P and F as well as the factor α. Studies on many ceramics lead to an average value of 0.016 ± 0.004 for the dimensionless constant ζ (Anstis et al., 1981).

While this method is perhaps not as accurate as the methods to be described next, due to the $\sim 25\%$ uncertainty in the value of η, it makes up for this in convenience. The specimens need only have a single flat surface. Further, several indentations can be performed on a single specimen. This is a distinct advantage in a research environment where a large number of specimens of accurate geometry are either unavailable or would be prohibitively expensive.

6.6.2 Indirect Method

The indirect approach is to measure the strength of the specimen after the introduction of radial cracks by indentation (Chantikul et al., 1981). The behavior of the radial cracks is complicated by the presence of residual stresses that are left after the original indentation load is removed. They arise due to the irreversibility of the plastic deformation; the result is that the plastic zone is under some residual pressure which applies outward forces to the surrounding elastic material, almost as if some of the original indentation load is still applied. The situation is similar to that shown in Figure 6.14(b) except that the proportionality between the original indentation load P and the residual forces F is different.

When subjected to an externally applied stress σ, the crack experiences two components of stress intensity, the first due to the residual stress and the second due to the applied stress. Since both components of stress intensity are mode I, the total stress intensity is found by simple addition:

$$K_I = \frac{\chi P}{c^{3/2}} + Y\sigma c^{1/2} \tag{6.44}$$

where χ characterizes the intensity of the residual stress and Y is the crack shape parameter. The behavior of the crack during loading can be understood with the aid of the K_I-c diagram in Figure 6.15, which shows how K_I varies with crack length for several values of the applied stress. When there is no applied stress, the stress intensity is proportional to $c^{-3/2}$. An initially small crack will experience a stress intensity greater than K_{IC} so it will grow until K_I drops below K_{IC}, at which point $c = c_0$. If some stress is now applied, $\sigma = \sigma_1$, K_I applied to the crack is again greater than K_{IC} so it will again grow until $c = c_1$. In practice, as the stress smoothly increases from zero to σ_1, the length of the crack grows smoothly from c_0 to c_1. Clearly, this stable crack growth does not lead to complete failure; the growth is stable because in this region $dK_I/dc < 0$.
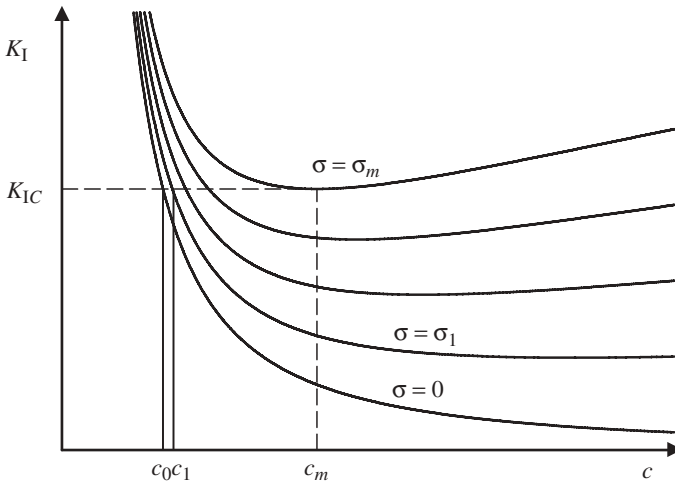
FIGURE 6.15 K_I as function of c for indentation crack subjected to external applied stress σ.

Examination of Figure 6.15 shows that as the stress continues to rise, the crack grows stably until the minimum in the $K_I - c$ behavior corresponds to $K_I = K_{IC}$. Beyond this point $dK_I/dc > 0$ and crack growth is unstable so failure ensues. At this condition $\sigma = \sigma_m$, the measured strength, and $c = c_m$, the maximum stable crack length. Two criteria are therefore needed for complete failure, $K_I = K_{IC}$ and $dK_I/dc = 0$ simultaneously. Applying these criteria to Eq. (6.44) when $\sigma = \sigma_m$ and $c = c_m$ gives

$$K_{IC} = \frac{\chi P}{c_m^{3/2}} + Y\sigma_m c_m^{1/2} \tag{6.45}$$

and

$$\left(\frac{dK_I}{dc}\right)_{c=c_m} = -\frac{3\chi P}{2c_m^{5/2}} + \frac{Y\sigma_m}{2c_m^{1/2}} = 0 \tag{6.46}$$

Equation (6.45) gives

$$\sigma_m = \frac{3\chi P}{Yc_m^2} \tag{6.47}$$

Substitution into (6.45) gives

$$\sigma_m = \frac{3K_{IC}}{4Yc_m^{1/2}} \tag{6.48}$$

Combining Eq. (6.47) and (6.48) gives

$$c_m = \left(\frac{4\chi P}{K_{IC}}\right)^{2/3}$$

(6.49)

Using Eq. (6.49) to eliminate c_m from (6.45) yields

$$K_{IC} = \left(\frac{256\chi Y^3}{27}\right)^{1/4}\left(\sigma_m P^{1/3}\right)^{3/4}$$

(6.50)

This equation can be expressed in the form (Chantikul et al., 1981)

$$K_{IC} = \eta\left(\frac{E}{H}\right)^{1/8}\left(\sigma_m P^{1/3}\right)^{3/4}$$

(6.51)

Experiments on a number of materials led to an average value of

$$\eta = 0.59 \pm 0.12$$

(6.52)

The parameter K_{IC} may be found from the slope of a graph of σ_m versus $P^{-1/3}$.

6.6.3 Modified Method

A modified form of the indentation method developed by Cook and Lawn (1983) combines some aspects of the direct and indirect methods. An indented specimen is broken as in the indirect method. However, in the modified method multiple indents (typically three) are made in the specimen before stressing rather than a single indent. Failure will occur from the crack associated with one of the indents. The indentations that did not cause failure are, however, on the verge of causing failure. The maximum stable crack length just before failure, c_m, can therefore be measured from the surviving indents. From rearrangement of (6.48)

$$K_{IC} = \left(\frac{4Y}{3}\right)\sigma_m c_m^{1/2}$$

(6.53)

The advantage of the modified indentation method is that the parameter χ is not required to calculate K_{IC}. Cook and Lawn (1983) measured critical stress intensity values by the DCB technique and by the modified indentation technique and found a good fit to the equation

$$K_{IC} = A\sigma_m c_m^{1/2} + B$$

(6.54)

with $A = 2.02$ and $B = -0.68\,\text{MPa} \cdot \text{m}^{1/2}$. They suggest the use of this equation in conjunction with the modified indentation method to determine values for the critical stress intensity.

6.6.4   Summary of the Three Methods

Several observations and limitations of the above methods must now be discussed.

The above analyses all assume that the crack only grows for $K_{\text{I}} \geq K_{\text{IC}}$. However, subcritical crack growth, which will be described in detail in Chapter 8, often occurs and the crack can grow significantly for stress intensity below K_{IC}, thus invalidating the above equations. This phenomenon is usually caused by moisture in the test environment. Care should be taken not to allow the crack to elongate by slow crack propagation during the time between indentation and strength measurement. This is usually attempted by placing a drop of oil on the indent to keep reactive species that promote slow crack propagation, such as water, away from the crack. That is, the crack is kept in inert conditions and the strength σ_m under these conditions is measured, typically by bending. This has led to the use of the term "inert strength" to describe this procedure.

The above methods are based on the assumption of half-penny cracks with radial/median geometry. This assumption has been questioned by Cook and Pharr (1990). Smith and Scattergood (1992) made in situ measurements of crack size as a function of stress and showed that the assumption of a half-penny shape causes the toughness to be overestimated and produces an apparent R-curve effect.

Use of the indentation test in the indirect form is common and was the subject of an international round robin (Quinn and Gettings, 1994) using an empirical stress intensity factor equation due to Newman and Raju (1981). Twenty laboratories in Europe and the United States participated. The results on silicon nitride were very good: For Norton NC-132 the toughness was $4.50 \pm 0.37\,\text{MPa} \cdot \text{m}^{1/2}$ while for ESK hot isostatic pressed material the value was $4.95 \pm 0.55\,\text{MPa} \cdot \text{m}^{1/2}$. Fourteen laboratories attempted to measure toughness on zirconia with 3 mol % yttria stabilization, but only eight sent results for analysis. The average toughness was $4.36 \pm 0.44\,\text{MPa} \cdot \text{m}^{1/2}$.

Depending on which indentation method is used, its precision may rely on calibration factors, such as η and χ, as well as the accuracy of the simplified models for the radial cracks and the residual stress field. However, this can be a minor consideration in the face of the distinct advantage of the methods, namely, their convenience.

6.6.5   ASTM Standard C 1421 Method

A method for determining toughness described in ASTM standard C 1421-01B (see Chapter 24) is also an indirect indentation method but eliminates the residual stress contribution to the stress intensity factor by grinding and

polishing away the plastic deformation zone, leaving only the crack. This standard recommends making the indentation using a Knoop indenter, which is not symmetrical with the diagonals having a ratio of 7:1 in length. ASTM C 1421-01B also recommends that the surface be removed to a depth of 4.5–5 times the depth of the indentation to remove any residual stress caused by the indentation. The critical stress intensity factor K_{IC} is determined in three-point bending by Eq. (6.31) and in four-point bending by Eq. (6.33). The values of Y are specified in the ASTM standard. This method is excellent because it uses a small flaw on the order of the size of typical flaws causing failure. The disadvantage of the method is that the flaw size must be determined after the test by looking at the fracture surface, which can be somewhat difficult.

6.7   BIAXIAL FLEXURE TESTING

A relatively simple method to apply biaxial tension to the surface of a sample is to use biaxial bending. Several techniques have been used with ceramics (Wachtman et al., 1972; Marshall, 1980; Shetty et al., 1983; Simpatico et al., 1999) and the subject has been reviewed by de With and Wagemans (1989). The common techniques can be grouped into categories: ball-on-ball, ball-on-ring, ring-on-ring, and pressure-on-ring. The technique of supporting a thin disk on three balls and loading in the center with a fourth ball produces biaxial tension in the center of the lower face and has the advantage that as-fired ceramic specimens can be tested even though they may be slightly warped. This eliminates the expense of machining and, more importantly, allows testing of the surface without any machining damage (Wachtman et al., 1972). Also, edge effects are eliminated provided that the disk is not too thick. The ring-on-ring test is the subject of ASTM standard C 1499-05 (see Chapter 24). The advantage of eliminating edge effects is retained in various other biaxial flexure tests.

6.8   ELASTIC CONSTANT DETERMINATION USING VIBRATIONAL AND ULTRASONIC METHODS

It is difficult to achieve good accuracy in determination of elastic constants by static methods; several percent is typical of the best that can be achieved with care. Dynamic methods can achieve an order-of-magnitude greater accuracy with relative ease. The dynamic methods give adiabatic values and the static methods give isothermal values when sufficient time is allowed for thermal equilibration; the difference is small but should be considered in very accurate work. One interlaboratory study (Dickson and Wachtman, 1971) resulted in an uncertainty of 0.4% for the dynamic Young's modulus and 0.2% for the dynamic shear modulus. These dynamic methods fall into two classes: resonance and ultrasonic wave propagation.

Resonance methods can be used in principle with any shape of solid but are most often used with flexure and torsion of slender bars and cylinders. Resonance methods are described in ASTM standard C 1198-01 and impulse excitation methods in ASTM standard C 1259-01 (see Chapter 24). The following equations are used by both standards. A rectangular bar of length L, thickness t, width w, mass m, and flexural resonance frequency f_f in the thickness direction has a Young's modulus given by

$$E = 0.9465 \frac{mf_f^2}{w} \frac{L^3}{t^3} T_1 \tag{6.55}$$

Here T_1 is a correction factor that approaches unity as the value of t/L approaches zero. For $t/L < 0.05$ one can use

$$T_1 = 1 + 6.585 \left(\frac{t}{L}\right)^2 \tag{6.56}$$

while for larger values an accurate approximating equation for T_1 given in the ASTM standard must be used. For the same bar vibrating with torsional resonance frequency f_t the shear modulus is given by

$$\mu = \frac{4Lmf_t^2}{wt} \frac{B}{1+A} \tag{6.57}$$

where

$$B = \frac{w/t + t/w}{4(t/w) - 2.52(t/w)^2 + 0.21(t/w)^6} \tag{6.58}$$

$$A = \frac{0.5062 - 0.8776(w/t) + 0.3504(w/t)^2 - 0.0078(w/t)^3}{12.03(w/t) + 9.892(w/t)} \tag{6.59}$$

For a circular cylinder of diameter D, Young's modulus is given by

$$E = 1.6067 \frac{L^3}{D^4} mf_f^2 T_1' \tag{6.60}$$

where for $D/L < 0.05$

$$T_1' = 1.000 + 4.939 \left(\frac{D}{L}\right)^2 \tag{6.61}$$

and the shear modulus is given by

$$\mu = 16mf_t^2 \frac{L}{\pi D^2} \qquad (6.62)$$

Another dynamic method requires the measurement of the velocity of ultrasonic waves typically using a piezoelectric transducer and measuring the transit time through the specimen. If υ_L is the velocity of longitudinal waves and υ_T is the velocity of transverse waves, the shear modulus is given by

$$\mu = \rho \upsilon_T^2 \qquad (6.63)$$

and Poisson's ratio is given by

$$\nu = \frac{\frac{1}{2} - (\upsilon_T/\upsilon_L)^2}{1 - (\upsilon_T/\upsilon_L)^2} \qquad (6.64)$$

Young's modulus is obtained from

$$E = 2\mu(1 + \nu) \qquad (6.65)$$

PROBLEMS

1. One end of a light ruler of rectangular section (width d, thickness t in the vertical direction) is firmly clamped in a horizontal plane with a length L (much greater than d and t) projecting from the clamp. A load P is applied downward on the free end of the ruler. Derive an expression for the deflection of the end of the ruler, δ (assume $\delta \ll t$). What is the maximum tensile stress on the ruler, σ_{max}, and how far from the end of the ruler is this maximum stress located, x? In principle, you could measure the strength of the ruler by determining the load at which it breaks. Do you think this is a good strength measurement technique? Why?

2. A four-point bend apparatus has a distance of 12 cm between the outer loading pins and 6 cm between the inner loading pins. A rectangular bar of ceramic 2 cm wide and 3 mm thick has a small edge notch 200 μm deep machined into it. The bar breaks in four-point bending when 2 kg force is applied; what is K_{IC} for this material? If a specimen of the same material but without a notch machined in it breaks from a surface flaw when 17 kg force is applied, estimate the size of the flaw. If the central deflection when the specimen fails in this second experiment is measured to be 0.38 mm, calculate the Young's modulus of this material.

3. An edge-notched bar is loaded in four-point bending with a distance of 80 mm between the outer loading pins and a distance of 20 mm between the inner loading pins. The bar is 2 mm thick and 5 mm wide and the notch is 500 µm deep. It sustains loads up to 2 kg and then fails. What is the critical stress intensity factor for this material?

4. A beam of uniform triangular section is bent with the neutral axis parallel to the base of the triangle (width w), as shown below. The height of the triangle is h. By constraining the total force across the section to be zero $\left(\int y\,dA = 0\right)$ find the height of the neutral axis above the base, y_c. Hence find the second moment of area, $I = \int y^2\,dA$ (where y is the distance from the neutral axis).
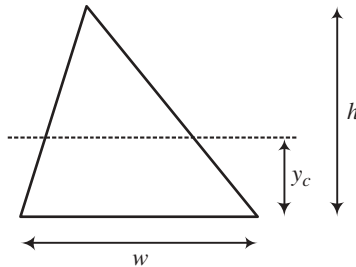
5. A rectangular beam is subjected to both three- and four-point (quarter-point loading with $D = L/4$) flexure. If the outer loading pins have the same separation in each case, calculate the ratio of the applied loads in three- and four-point bending, P_3/P_4, that would give the same maximum stress in the beam in both cases? What is then the ratio of the central deflections, δ_{c3}/δ_{c4}? If the distance between the outer loading pins is L in four-point flexure, what outer pin spacing would be required in three-point flexure, L_3, to obtain the same maximum stress at the same applied load as in four-point flexure?

6. A 1-mm-thick, 12-mm-wide glass plate ($K_{IC} = 0.75\ \mathrm{MPa\cdot m^{1/2}}$) is loaded in three-point flexure with an outer loading pin spacing of 50 mm. The tensile surface of the plate is known to have three large surface flaws (crack shape parameter $Y = 1.16$) of various sizes c and various distances x from the central loading pin, as given in the following table:

Flaw number	1	2	3
c (µm)	1.5	2	8
x (mm)	2	5	16

What is the strength of each flaw, σ_1, σ_2, σ_3 (i.e., in a tensile test at what stress would each break)? Which flaw will cause failure? What will be the maximum stress at failure, σ_{max}? What will be the failure load, P_f?

7. A 20-inch-long 2×4-inch piece of Douglas fir is supported at its ends and is then loaded at its center. Initially the load–deflection behavior is linear; a

load of 800 lb deflects the center of the beam by 0.040 in. The beam breaks when the load reaches 2280 lb.

   a. In which direction does the beam have to be bending to perform this experiment (i.e., is the beam 2 in. thick and 4 in. wide or vice versa)? Explain.

   b. Determine the elastic modulus of the wood.

   c. What is the modulus of rupture of Douglas fir (i.e., the failure stress)? (Provide all answers in SI units; 1 in. = 25.4 mm; 1 kg = 2.20462 lb.)

8. A ceramic with critical stress intensity of $4\,\text{MPa}.\text{m}^{1/2}$ is loaded with a pointed indenter to produce a semicircular radial crack of radius 100 μm. What do you expect the strength of this damaged specimen to be? What is the radius of the crack just before failure? What would the strength be for the same specimen before indentation if it contained a small, penny-shaped central crack of radius 50 μm?

9. An ASTM C1161-02c size B standard specimen is 4 mm wide, 3 mm high and tested in four-point bend with outer span of 40 mm and inner span of 20 mm. The maximum force is 95 N. What was the flexure strength? Failure was actually found to be 12 mm from the center. What was the local fracture stress? The force necessary to fracture a precracked beam specimen of the same dimension and span lengths as above broke at 43 N. The crack depth was measured to be 1.25 mm deep. What K_{IC} was measured?

10. Fracture toughness is measured by the chevron notch method using a specimen of height 6.35 mm and width 6.35 mm. Assume $P_{\max} = 45$ N, $a_0 = 1.25$ mm, and $a_1 = 6.03$ mm. Calculate the toughness.

7

STATISTICAL TREATMENT OF STRENGTH

7.1   INTRODUCTION

Measurement of the strength of a series of nominally identical ceramic specimens typically produces considerable scatter in the results. This behavior is easy to explain qualitatively as resulting from a scatter in the size, position, and orientation of the cracks responsible for failure. The existence of this scatter has important engineering consequences. First, the strength that can safely be used

in design is clearly less than the average measured strength. Second, the probability of failure of a large specimen is greater than that of a small specimen under the same stress because of the larger probability of having a serious flaw in a larger volume. Third, the measured strength of specimens of the same size depends on the measurement technique since different techniques subject different volumes of the specimen to tensile stress. It is desirable to have some means of describing these effects quantitatively and incorporating this description into a method of design for safe use. Weibull analysis provides such a means and is the subject of this chapter. Weibull analysis is a form of extreme-value statistics dealing with a weakest link situation in which the failure of a single element of a specimen causes failure of the whole specimen.

7.2   STATISTICAL DISTRIBUTIONS

For a detailed understanding of the statistical theory of measurements the reader is referred to any one of a number of good texts on this topic. However, it is useful to summarize some well-known concepts in statistics, both as a review and to introduce the notation used in this chapter.

If the strengths of a very large number of specimens are determined, they will be described by probability distribution $p(\sigma)$ where the probability of measuring the strength in the range σ to $\sigma + d\sigma$ is given by $p(\sigma)\,d\sigma$. Whatever the particular form of $p(\sigma)$, it must be normalized to unit probability of failure at any stress:

$$\int_0^\infty p(\sigma)\,d\sigma = 1 \tag{7.1}$$

Here we tacitly assume that strength cannot take negative values so the integration does not include negative values of stress. The **mean** strength is given by

$$\bar{\sigma} = \int_0^\infty \sigma p(\sigma)\,d\sigma \tag{7.2}$$

The **deviation** ε is the amount that a value differs from the mean:

$$\varepsilon = \sigma - \bar{\sigma} \tag{7.3}$$

The **standard deviation** s is the root-mean-square deviation and is defined by

$$s^2 = \int_0^\infty \varepsilon^2\,d\sigma = \int_0^\infty (\sigma - \bar{\sigma})^2\,d\sigma \tag{7.4}$$

where s^2 is also known as the **variance**.

An alternative description to $p(\sigma)$ is the **cumulative probability of failure** $P_f(\sigma)$, which is the probability that failure has occurred by a stress σ. The two distribution functions are related by

$$P_f(\sigma) = \int_0^\sigma p(x)\,dx \tag{7.5}$$

or equivalently by

$$p(\sigma) = \frac{dP_f(\sigma)}{d\sigma} \tag{7.6}$$

The cumulative probability of survival $P_s(\sigma)$ is straightforwardly defined by

$$P_s(\sigma) = 1 - P_f(\sigma) \tag{7.7}$$

The most commonly used distribution for general treatment of experimental data, the Gaussian distribution, is usually described in terms of $p(\sigma)$, but the Weibull distribution, which is generally used for treatment of the statistics of brittle failure, is more readily described in terms of $P_f(\sigma)$.

The probability distribution $p(\sigma)$ is defined for a very large, effectively infinite number of measurements. In practice, the strength is measured a finite number of times. For n repeated measurements of the strength σ, a series of values will be obtained: $\sigma_1, \sigma_2, \ldots, \sigma_i, \ldots, \sigma_n$. The mean strength is

$$\bar{\sigma} = \frac{1}{n} \sum_{i=1}^n \sigma_i \tag{7.8}$$

and the estimate of the variance is

$$s^2 = \frac{1}{n-1} \sum_{i=1}^n \varepsilon_i^2 \tag{7.9}$$

where $n-1$ rather than n is used because one degree of freedom is used in calculating the mean. The parameters $\bar{\sigma}$ and s are only estimates of the true mean and standard deviation of the underlying distribution.

7.3   STRENGTH DISTRIBUTION FUNCTIONS

A variety of distributions could, in principle, be used to describe strength data. The two widely used distributions, the normal, or Gaussian, distribution and

the Weibull distribution, will be described here, although brief mention of the lognormal distribution is also included.

7.3.1 Gaussian, or Normal, Distribution

Probably the distribution most widely used to describe experimental data is the Gaussian, or normal, distribution. Written in terms of the mean $\bar{\sigma}$ and the variance s^2, the normal distribution is

$$p(\sigma) = \frac{1}{s(2\pi)^{1/2}} \exp\left[-\frac{(\sigma - \bar{\sigma})^2}{2s^2}\right] \tag{7.10}$$

Note that $p(\sigma)$ is symmetrical about the mean $\bar{\sigma}$. It can be used to represent the distribution of strength data for values not too far from the mean, but for small values of strength it suffers from the fact that it gives a finite probability of occurrence of negative strengths. That is, it cannot be correct for strengths far below the mean. The Weibull distribution has a more appropriate form for small strengths and is mathematically very much more convenient to use, for example, when incorporating the effect of specimen size.

The lognormal distribution is sometimes used to describe strength data. It is similar to the normal distribution except that the logarithm of σ, rather than σ, follows the normal distribution. It is not symmetrical about the mean strength and so often gives a better fit to experimental data. Another advantage is that the probability of failure at negative stress is zero. However, it is mathematically less convenient to use than the normal or Weibull distribution. Overall, the Weibull distribution is generally a better choice for the description of strength data for ceramics.

7.3.2 Weibull Distribution

Two forms of the Weibull distribution are frequently used to describe strength data: the two- and three-parameter distributions. The two-parameter distribution is

$$P_f(\sigma) = 1 - \exp\left[-\left(\frac{\sigma}{\sigma_0}\right)^m\right] \tag{7.11}$$

where m is the **Weibull shape parameter** or **Weibull modulus**, which is an inverse measure of the distribution width; that is, a high value of m corresponds to a narrow distribution. The **Weibull scale parameter** σ_0 is a measure of centrality, that is, the center of the distribution. In fact, σ_0 is the 63rd percentile; the

probability of failure occurring at or below a stress σ_0 is 0.63, or 63%. The mean $\bar{\sigma}$ and the standard deviation s are given by

$$\bar{\sigma} = \sigma_0 \Gamma\left(1 + \frac{1}{m}\right) \tag{7.12}$$

and

$$s^2 = \sigma_0^2 \left[\Gamma\left(1 + \frac{2}{m}\right) - \Gamma^2\left(1 + \frac{1}{m}\right)\right] \tag{7.13}$$

The **coefficient of variation** C_V is a dimensionless measure of the dispersion of the data and is defined as the ratio of the standard deviation to the mean:

$$C_V = \frac{s}{\bar{\sigma}} = \left[\frac{\Gamma(1 + 2/m)}{\Gamma^2(1 + 1/m)} - 1\right]^{1/2} \approx \frac{1.28}{m} \tag{7.14}$$

The coefficient of variation is a function of m only and the approximate form in Eq. (7.14) is accurate to a few percent for $m \geq 15$. The approximate form clearly demonstrates the inverse relationship between distribution width and m. In Eqs. (7.12)–(7.14) $\Gamma(x)$ is the well-known gamma function, defined by

$$\Gamma(x) = \int_0^\infty y^{x-1} e^{-y} \, dy \tag{7.15}$$

It is a generalization of the factorial function to noninteger arguments; for integer n, $\Gamma(n) = (n-1)!$. Tabulations of $\Gamma(x)$ are readily available (e.g., Abramowitz and Stegun, 1964), but for convenience Table 7.1 provides values of $\Gamma(1 + 1/m)$ for several values of m. The value of $\Gamma(1 + 1/m)$ is approximately unity for commonly encountered values of m.

TABLE 7.1   Values of Gamma Function

m	$\Gamma(1 + 1/m)$	m	$\Gamma(1 + 1/m)$	m	$\Gamma(1 + 1/m)$	m	$\Gamma(1 + 1/m)$
1	1.00000	6	0.92772	11	0.95508	16	0.96758
2	0.88623	7	0.93544	12	0.95829	17	0.96929
3	0.89298	8	0.94174	13	0.96107	18	0.97084
4	0.90640	9	0.94697	14	0.96351	19	0.97223
5	0.91817	10	0.95135	15	0.96566	20	0.97350

The three-parameter Weibull distribution is given by

$$P_f(\sigma) = \begin{cases} 1 - \exp\left\{-\left(\dfrac{\sigma - \sigma_u}{\sigma_0}\right)^m\right\} & \sigma > \sigma_u \\ 0 & \sigma \leq \sigma_u \end{cases} \qquad (7.16)$$

The two- and three-parameter distributions are the same except that for the latter the stress is shifted by σ_u. The three parameters m, σ_u, and σ_0 are generally treated as empirical parameters and determined experimentally. The parameter σ_u is a stress level below which there is zero probability of failure. For ceramics the remote possibility exists of having a very large flaw in a specimen so that the safest assumption is to take $\sigma_u = 0$, which is then the two-parameter distribution, as is usually done. This gives the most conservative estimate of survival probability (i.e., if it errs, it errs on the side of safety). Further discussion is limited to the two-parameter Weibull distribution.

7.3.3 Comparison of the Normal and Weibull Distributions

The normal and Weibull distributions are compared in Figure 7.1. The Weibull distribution is plotted for a mean strength of 300 MPa and a value of $m = 10$. The Gaussian distribution is plotted for the same mean strength and the same standard deviation, 36.1 MPa. The cumulative probability distributions appear similar, but the probability density functions illustrate the lack of symmetry of the Weibull distribution.
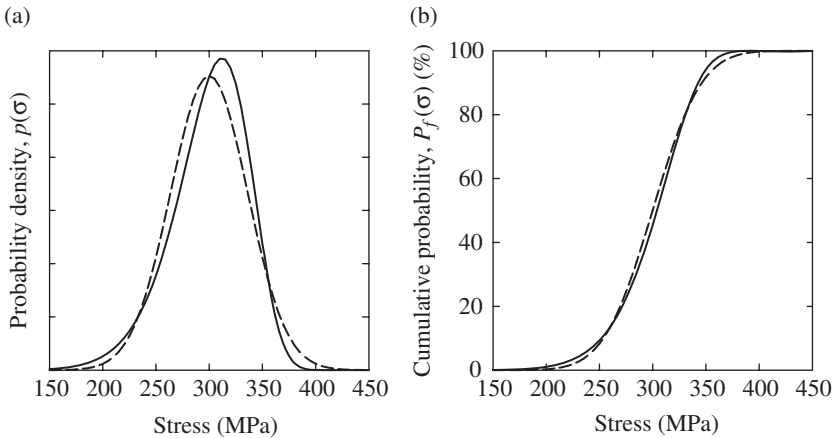
FIGURE 7.1   (a) Probability density function and (b) cumulative probability of failure for Weibull (solid lines) and Gaussian (dashed lines) distributions, both calculated for mean strength of 300 MPa and standard deviation of 36.1 MPa.

7.4   WEAKEST LINK THEORY

The Weibull treatment of failure is in two parts: (1) a weakest link argument leading to a volume dependence for the distribution of strength and (2) the assumption of a particular statistical distribution function. The weakest link argument is based on the idea that failure at any flaw leads to total failure and the material is homogeneous in the sense that the flaws are distributed throughout the volume (Weibull, 1939). Consider a material divided into a very large number of elements n of equal volume δV under stress σ. Take $P_{f,i}(\sigma, \delta V)$ as the probability of failure from the ith volume element by a stress σ. The probability that this element survives σ is therefore $1 - P_{f,i}(\sigma, \delta V)$. Since the stress is taken to be the same for all volume elements and the specimen is assumed to be homogeneous, all $P_{f,i}(\sigma, \delta V)$ can be taken the same, $P_f(\sigma, \delta V)$. For the entire specimen to survive the stress, all the volume elements must survive so that the total probability of survival, $1 - P_f(\sigma, V)$, of a specimen of volume $V = n\,\delta V$ under uniform stress is given by

$$1 - P_f(\sigma, V) = \left[1 - P_f(\sigma, \delta V)\right]^n = \left[1 - \frac{V}{n}\frac{P_f(\sigma, \delta V)}{\delta V}\right]^n$$

$$= \left[1 - \frac{V}{n}\varphi(\sigma)\right]^n \tag{7.17}$$

where we have assumed that as n increases $P_f(\sigma, \delta V)/\delta V$ approaches a limit $\varphi(\sigma)$. As the specimen is subdivided into larger numbers of smaller volumes, n approaches infinity and δV approaches zero. Then

$$\lim_{n \to \infty} \left(1 - \frac{x}{n}\right)^n = \exp(-x) \tag{7.18}$$

so that

$$P_f(\sigma, V) = 1 - \exp[-V\varphi(\sigma)] \tag{7.19}$$

This line of argument shows that the probability of failure of the specimen depends exponentially on the specimen volume times a **risk function** $\varphi(\sigma)$ that characterizes the stress dependence of cumulative failure probability per unit volume at the limit of small volume. This weakest link argument does not give a specific form for $\varphi(\sigma)$, but clearly it must be a monotonically increasing function of σ. Weibull assumed the form

$$\varphi(\sigma) = \left(\frac{\sigma}{\Sigma_0}\right)^m \tag{7.20}$$

This gives the probability of failure of the whole specimen, P_f, as

$$P_f = 1 - \exp\left[-V\left(\frac{\sigma}{\Sigma_0}\right)^m\right] \tag{7.21}$$

Equation (7.21) is the two-parameter Weibull distribution, Eq. (7.11), with scale parameter

$$\sigma_0 = \Sigma_0 \, V^{-1/m} \tag{7.22}$$

Note Σ_0 has the rather odd dimensions of stress $\times$ (volume)$^{1/m}$, which results from the definition of $\varphi(\sigma)$ being the probability per unit volume. Further note that the meaning of the variable "σ_0" has become confused in the literature since it is widely used for both the distribution parameter σ_0 and the Weibull scale parameter that incorporates weakest link theory. Here we define the latter as Σ_0 to clearly distinguish between the two parameters, and as a result we deviate in notation from much of the literature in order to provide a self-consistent general development of the subject. The parameter σ_0 is more straightforward to calculate for any given set of data but it does depend on the size of the specimen; that size must always be reported together with σ_0. The parameter Σ_0 is more fundamental since it does not depend on the size of the specimen; it is the Weibull scale parameter for specimens of unit volume. Note that the value of Σ_0 must be calculated carefully when changing units [say from Imperial to International System (SI)] since the size of the unit volume changes. The mean strength now becomes

$$\bar{\sigma} = \sigma_0 \, \Gamma\left(1 + \frac{1}{m}\right) = \frac{\Sigma_0}{V^{1/m}} \Gamma\left(1 + \frac{1}{m}\right) \tag{7.23}$$

The above analysis assumes the stress is uniform but frequently the applied stress is not uniform and varies with position, that is, $\sigma = \sigma(\mathbf{r})$. An alternative derivation of the weakest link theory shows how to account for this. Consider a body of volume $V + \delta V$ which can be thought of as two pieces, one of volume V and the other of volume δV. The body will only survive if both parts survive, that is,

$$P_s(V + \delta V) = P_s(V) \cdot P_s(\delta V) \tag{7.24}$$

As defined above, $\varphi(\sigma)$ is the probability per unit (small) volume that the material fails by a stress σ so that

$$P_s(\delta V) = 1 - P_f(\delta V) = 1 - \varphi(\sigma) \, \delta V \tag{7.25}$$

Substituting into (7.24) and rearranging give

$$\frac{P_s(V + \delta V) - P_s(V)}{\delta V} = -\varphi(\sigma) \cdot P_s(V) \tag{7.26}$$

As δV becomes small, the left-hand side of this equation approaches the derivative of P_s:

$$\frac{dP_s}{dV} = -\varphi(\sigma) \cdot P_s \tag{7.27}$$

Integrating over the entire specimen volume gives the general result

$$P_f = 1 - P_s = 1 - \exp\left\{ -\int_V \varphi[\sigma(\mathbf{r})] \ dV \right\} \tag{7.28}$$

If φ is assumed to be given by Eq. (7.20),

$$P_f = 1 - \exp\left[-\int_V \left(\frac{\sigma(\mathbf{r})}{\Sigma_0} \right)^m \ dV \right] \tag{7.29}$$

If the applied stress is uniform, σ is a constant inside the integral and the earlier result, Eq. (7.21), is recovered.

We shall use the Weibull distribution in the remainder of this chapter to build up an extensive method of predicting the safe working stress for a chosen level of survival probability. The complexity and power of the method should not obscure the fact that it rests on the assumption of the Weibull form for the distribution of strength and that this distribution is only an assumption that gives a reasonable fit to the data in many cases. Typically, the Weibull distribution is used to fit to a few tens or hundreds of measurements at most (as in the example of Table 7.3 below) and is then used to extrapolate to probability values far outside the range of stresses and probabilities in the experiment (as in Section 7.8). Anticipating later sections, Figure 7.4 fits the Weibull distribution reasonably well for the most part. However, for some measurements it is observed that several points at low stress deviate from the best fit line, suggesting that some other function might sometimes fit the data better. Using some other function in place of the Weibull function can lead to very different estimates of the safe working stress for a chosen value of survival probability.

7.5 DETERMINING WEIBULL PARAMETERS

The process of determining the Weibull parameters m and σ_0 is easiest to describe using the strengths of n specimens determined in a tensile test. The form of the Weibull function for a uniform stress distribution can then be used, Eq. (7.21). Two procedures are possible: (1) least-squares fitting of a linearized form of the distribution or (2) the method of maximum likelihood. The latter procedure is preferred by ASTM standard C 1239-07 (see Chapter 24) (which uses "σ_0" where we use Σ_0) and by some authors but is more complicated, so discussion of this method is deferred until later. The least-squares method is in widespread use and is now discussed. Taking natural logarithms twice of Eq. (7.21) gives

$$\ln\ln\left(\frac{1}{1-P_f}\right) = \ln V + m\ln\sigma - m\ln\Sigma_0 = m\ln\sigma - m\ln\sigma_0 \qquad (7.30)$$

The Weibull parameters can then be determined by fitting a straight line to $\ln\ln[1/(1-P_f)]$ as a function of $\ln\sigma$, as shown schematically in Figure 7.2. The parameter m is simply the slope and σ_0 is related to the intercept on the $\ln\ln[1/(1-P_f)]$ axis at $\ln\sigma = 0$ by

$$\ln V - m\ln\Sigma_0 = -m\ln\sigma_0 = \text{intercept} \qquad (7.31)$$
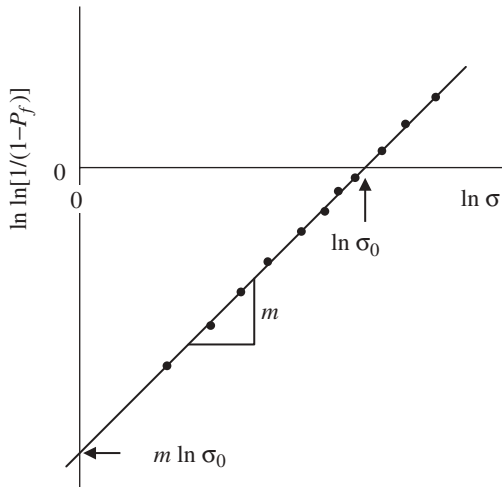
FIGURE 7.2 Schematic of Weibull plot showing relationship between linear regression and Weibull parameters.

Here the point made earlier about distinguishing between σ_0 and Σ_0 is evident again. For a given set of data it is somewhat easier to deal with σ_0 since it is readily calculated using

$$\sigma_0 = [\exp(-\text{intercept})]^{1/m} \tag{7.32}$$

A more straightforward method for determining σ_0 is to note that the intercept on the $\ln \sigma$ axis when $\ln \ln[1/(1-P_f)] = 0$ is $\ln \sigma_0$. In this case $P_f = 0.632$ so that σ_0 is the 63rd percentile failure stress—almost two-thirds of the specimens are weaker than σ_0. The intercept with the probability axis often lies off the plot (depending on the units chosen for stress) while the intercept with the $\ln \sigma$ axis is among the data, meaning it is easier to get an idea of the uncertainty in σ_0.

   Plots can be made on special Weibull graph paper on which the scales are suitably transformed so that values for P_f or P_s as ordinate and σ as abscissa can be directly plotted. A straight line can then be fitted to the data. An easier procedure is to use spreadsheet software to calculate $\ln \ln[1/(1-P_f)]$ and $\ln \sigma$ and then use regression functions to obtain the slope and intercept for the least-squares best fit. The calculation of $\ln \sigma$ is straightforward, but there is some degree of choice in calculating P_f (Davidge, 1979; Brückner-Foit and Munz, 1989), although for large values of n the different choices give very closely the same values. The general procedure is to assign a rank to each strength after sorting into ascending order, assigning 1 to the lowest strength and n to the highest strength. The failure probability usually assigned to the ith strength value (ASTM standard C 1239-07) is

$$P_f = \frac{i - 0.5}{n} \tag{7.33}$$

An example of fitting data measured by bend testing to obtain the Weibull parameters for the two-parameter distribution is given later after the adaptation of the Weibull distribution for bend testing has been discussed.

7.6   EFFECT OF SPECIMEN SIZE

Equation (7.30) may be used to examine the effect of specimen volume. If the strength corresponding to the same failure probability P_f is σ_1 for a specimen of volume V_1 and σ_2 for a specimen of volume V_2, then

$$\ln \ln \left(\frac{1}{1 - P_f} \right) = \left\{ \begin{array}{l} \ln V_1 + m \ln \sigma_1 - m \ln \Sigma_0 \\ \ln V_2 + m \ln \sigma_2 - m \ln \Sigma_0 \end{array} \right\} \tag{7.34}$$

Since Σ_0 is independent of the specimen size, subtracting these two equations gives

$$\frac{\sigma_1}{\sigma_2} = \left(\frac{V_2}{V_1}\right)^{1/m} \tag{7.35}$$

This equation is true for any failure probability so it is also true for the mean strength, giving

$$\frac{\bar{\sigma}_1}{\bar{\sigma}_2} = \left(\frac{V_2}{V_1}\right)^{1/m} \tag{7.36}$$

This proves the expected result that the mean strength is lower for larger specimens and the effect is more pronounced for lower values of m. This result was derived for a uniform tensile stress, but a more general analysis will show it to be correct for a variety of loading schemes.

7.7   ADAPTATION TO BEND TESTING

To adapt the two-parameter Weibull distribution to tests in which the stress varies with position, the general form of the Weibull distribution must be used, Eq. (7.29). For most bend-testing methods, while the stresses increase with increased loading, the shape of the stress field is invariant. Under these conditions the maximum stress anywhere in the specimen, σ_{max}, can be factored out:

$$\sigma(\mathbf{r}) = \sigma_{max}\, g(\mathbf{r}) \tag{7.37}$$

where $g(\mathbf{r})$ is a function of position only. As an example, considering the stress on the outer, tensile surface of a three-point bend specimen, $g(\mathbf{r})$ rises linearly from zero at each outer loading point to unity at the inner loading point (Figure 6.6). Substituting into (7.29) gives

$$P_f = 1 - \exp\left[-\left(\frac{\sigma_{max}}{\Sigma_0}\right)^m \int_V g^m(\mathbf{r})\; dV\right] \tag{7.38}$$

It is convenient to define k, the **loading factor** for the test method, by

$$k = \frac{1}{V}\int_V g^m(\mathbf{r})\, dV \qquad \text{or} \qquad k = \frac{1}{V}\int_V \left(\frac{\sigma(\mathbf{r})}{\sigma_{max}}\right)^m dV \tag{7.39}$$

which simplifies Eq. (7.38) to

$$P_f = 1 - \exp\left[-kV\left(\frac{\sigma_{max}}{\Sigma_0}\right)^m\right] \tag{7.40}$$

where k is a dimensionless function of m characteristic of the test method and specimen geometry. Comparing Eq. (7.21) for uniform tension and Eq. (7.40) and recognizing that $\sigma = \sigma_{max}$ for uniform tension, we can see that for any test method that has a stress field of invariant shape the strength characterized by σ_{max} follows a Weibull distribution with the same shape parameter m as measured in tension but with an effective volume kV. For a given failure probability for any test, a specimen of volume V will have the same strength as a tensile specimen of volume kV, where kV can be interpreted as the effective volume of the specimen under test; that is, it is a measure of how much of the volume of the specimen is under a significant tensile stress. Since the stress everywhere in a specimen is less than or equal to the maximum stress, $g(\mathbf{r}) \leq 1$ and hence $k \leq 1$. Typically, the strength of a specimen, σ, is taken as the value of the maximum stress at failure, σ_{max}. Therefore the mean strength is given by

$$\bar{\sigma} = \frac{\Sigma_0}{(kV)^{1/m}}\Gamma\left(1+\frac{1}{m}\right) \tag{7.41}$$

which clearly shows how the mean strength depends on specimen volume and test technique. To explore this dependence further, consider two test methods; for method 1 with loading factor k_1 and specimen volume V_1, the cumulative probability of failure is P_{f1} when the maximum stress is σ_{max1}; similarly for method 2 the corresponding parameters are k_2, V_2, P_{f2}, and σ_{max2}. Taking logarithms of Eq. (7.40) twice and substituting parameters for the two test methods give

$$\ln\ln\left(\frac{1}{1-P_{f1}}\right) = m\ln\sigma_{max1} - m\ln\Sigma_0 + \ln(k_1V_1)$$

$$\ln\ln\left(\frac{1}{1-P_{f2}}\right) = m\ln\sigma_{max2} - m\ln\Sigma_0 + \ln(k_2V_2) \tag{7.42}$$

(Here we implicitly assume that the material in both tests is the same, that is, has the same distribution of flaws and so m and Σ_0 are the same.) Considering the stresses that give the same probability of failure in the two methods, $P_{f1} = P_{f2}$, gives

$$\ln\sigma_{max1} - \ln\sigma_{max2} = \frac{1}{m}\ln\left(\frac{k_2V_2}{k_1V_1}\right) \tag{7.43}$$

or

$$\frac{\sigma_{max1}}{\sigma_{max2}} = \left(\frac{k_2V_2}{k_1V_1}\right)^{1/m} \tag{7.44}$$

This result is derived for any value of P_f and so gives the ratio of strengths for any failure probability; that is, it is true for the mean strengths, median strengths, quartiles, and so on, and in particular the mean strength

$$\frac{\bar{\sigma}_{max1}}{\bar{\sigma}_{max2}} = \left(\frac{k_2 V_2}{k_1 V_1}\right)^{1/m} \tag{7.45}$$

If the two test techniques are actually the same, then $k_1 = k_2$ and Eq. (7.36) is recovered. Even though that equation was derived for uniform tension, it is generally true for any test method that subjects the specimen to a stress field with an invariant shape.

Equations (7.42) can be used to compare the probabilities of failure in the two test methods when both are subjected to the same maximum stress. Setting $\sigma_{max1} = \sigma_{max2}$ gives

$$\ln \ln \left(\frac{1}{1 - P_{f1}}\right) - \ln \ln \left(\frac{1}{1 - P_{f2}}\right) = \ln \left(\frac{k_1 V_1}{k_2 V_2}\right) \tag{7.46}$$

Equations (7.43) and (7.46) have a useful graphical interpretation: They represent shifts along the $\ln \sigma$ and $\ln \ln[1/(1-P_f)]$ axes, respectively. If the results of one test method are graphed on a Weibull plot, the behavior for the second test method can be simply predicted by shifting the data a distance $[\ln(k_2 V_2/k_1 V_1)]/m$ along the $\ln \sigma$ axis, as shown in Figure 7.3(a), or $\ln(k_1 V_1/k_2 V_2)$ along the $\ln \ln[1/(1-P_f)]$ axis, as shown in Figure 7.3(b). Equation (7.43) involves m and so is based on the assumption that the data follow a Weibull distribution. However, it can be shown that Eq. (7.46) does not depend on the
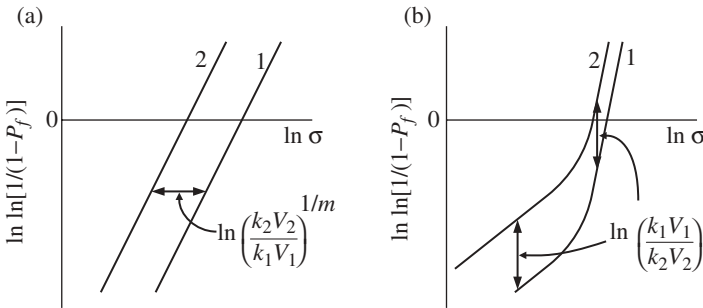
FIGURE 7.3   Weibull plots showing how effect of specimen size and test technique can be interpreted at (a) sideways or (b) vertical shifts of distributions.

assumption of a Weibull distribution and is valid for quite different distributions, such as that shown in Figure 7.3(b).

Once the loading factor k is known, the strength distribution for any test method is given by Eq. (7.40) and the mean strength by (7.41). Now k will be evaluated for two test methods, namely uniaxial tension and three-point bending.

Considering first uniform uniaxial tension, the maximum stress is the applied tensile stress which is uniform throughout the specimen, that is, $g(\mathbf{r}) = 1$, giving the loading factor for uniform tension k_t as

$$k_t = 1 \tag{7.47}$$

The stress on the tensile surface for three- and four-bend tests has been given in Chapter 6. Three-point bending is now considered. Referring to Figure 6.6, it is noted that the stress varies in proportion to the distance y from the neutral axis and in proportion to the distance x from the outer support point. For the left half of the specimen in Figure 6.6, $0 < x < L/2$,

$$\sigma(\mathbf{r}) = \sigma_{3b,\max} \frac{2x}{L} \frac{2y}{h} \qquad g(\mathbf{r}) = \frac{4xy}{Lh} \qquad 0 < x < \tfrac{1}{2}L \tag{7.48}$$

where $\sigma_{3b,\max}$ is the maximum stress in the tensile surface and so corresponds to the measured breaking strength. By symmetry, the contribution to the integral in Eq. (7.39) from each half of the specimen is the same so the loading factor in three-point bending, k_3, can be evaluated by doubling the integration for one-half. Equation (7.39) becomes

$$k_{3b} = \frac{2}{V} \int_0^{L/2} \left(\frac{2x}{L}\right)^m dx \int_0^{h/2} \left(\frac{2y}{h}\right)^m dy \int_0^d dz = \frac{1}{2(m+1)^2} \tag{7.49}$$

where the volume $V = Lhd$, which is the volume of the specimen between the outer loading points, not the total volume of the specimen, which is usually longer than L. Note that the integration over y is only over the tensile half of the thickness of the specimen since only the tensile side ($y > 0$) contributes to the risk of failure.

These results can now be used to give the ratio of the strengths of specimens of equal volume measured in three-point bending and tension:

$$\frac{\bar{\sigma}_{3b,\max}}{\bar{\sigma}_t} = \left(\frac{k_t}{k_{3b}}\right)^{1/m} = [2(m+1)^2]^{1/m} \tag{7.50}$$

Since $m > 0$, the bending strength is expected to be greater than the tensile strength, as is usually observed in practice. For typical commercial ceramics, m values of 10–12 are common, but great efforts are made to improve processing to achieve m values of 20 or higher. Higher values of m are generally desired since then the probability of failure decreases more rapidly as the applied stress is reduced. For m values of 10, 12, and 20, the ratios of strength at constant survival probability in three-point bending to that in tension are predicted by the Weibull theory to be 1.73, 1.62, and 1.40, respectively.

   Table 7.2 lists the loading factors for some common test methods assuming a two-parameter Weibull distribution for flaws distributed uniformly through the specimen volume. Anticipating a later section, loading factors are also provided for flaws uniformly distributed over the surface of the specimen.

   Use of these equations in combination allows data taken with one type of test to be used to predict the behavior of specimens of different volume in a different type of test. An example is given in a later section. At this point we give an example of the least-squares method of determining the Weibull parameters for strength data of silicon nitride determined in bending as part of an international round robin and supplied by the Oak Ridge National Laboratory (Brüchner-Foit and Munz, 1989). The data and analysis methodology are given in Table 7.3 and a Weibull plot with the line determined by a least-squares best fit is shown in Figure 7.4. The strengths in column 1 have been sorted into ascending order in column 2 and assigned a rank in column 4. The probability of failure in column 5 was then calculated from Eq. (7.33). A linear regression analysis of a plot of $\ln \ln[1/(1-P_f)]$, given in column 6, as a

TABLE 7.2 Loading Factors k for Volume- and Area-Distributed Flaws for Two-Parameter Weibull Distribution and Rectangular Specimen of Dimension $L \times w \times h$ with Neutral Plane Perpendicular to Dimension h When Bending

Parameter	Volume-Distributed Flaws	Area-Distributed Flaws
Uniform tension	1	1
Three-point bending	$\dfrac{1}{2(m+1)^2}$	$\dfrac{1}{2(m+1)^2} \dfrac{w(m+1)+h}{w+h}$
Pure bending (constant radius of curvature)	$\dfrac{1}{2(m+1)}$	$\dfrac{1}{2(m+1)} \dfrac{w(m+1)+h}{w+h}$
Four-point bending, quarter-point loading ($D = L/4$)	$\dfrac{m+2}{4(m+1)^2}$	$\dfrac{m+2}{4(m+1)^2} \dfrac{w(m+1)+h}{w+h}$
Four-point bending, third-point loading ($D = L/3$)	$\dfrac{m+3}{6(m+1)^2}$	$\dfrac{m+3}{6(m+1)^2} \dfrac{w(m+1)+h}{w+h}$

Note: The strength distribution and mean strength for volume-distributed flaws may be found by substituting these values of k into Eqs. (7.40) and (7.41) using a specimen volume $V = Lwh$. The strength distribution and mean strength for area-distributed flaws may be found by substituting these values of k into Eqs. (7.73) and (7.74) using a total surface area $A = 2L(w + h)$.

TABLE 7.3   Determination of Weibull Parameters for Silicon Nitride from Strength Measured in Bending

Measurements of σ_f (MPa)

616.6	672.0	656.5	636.3	608.2	561.6
693.2	632.7	708.8	716.8	707.2	669.0
588.1	601.2	618.8	626.2	584.7	674.2
548.6	735.2	552.2	668.0	535.4	699.7
624.8	744.1	619.6	621.0	655.1	663.2
699.4	578.0	616.1	731.4	721.8	712.8
626.3	631.3	607.7	640.7	590.3	657.7
474.0	561.7	580.6	710.0	684.0	595.5
730.3	706.9	718.8	712.7	699.7	667.1
683.5	553.0	583.7	642.2	726.0	589.1

Data Analysis

Raw σ_f (MPa) (1)	Sorted σ_f (MPa) (2)	ln σ_f (3)	Rank, i (4)	$P_f = \frac{(i-0.5)}{60}$ (5)	$\ln\ln[1/(1-P_f)]$ (6)
616.6	474.0	6.1612	1	0.0083	−4.7833
672.0	535.4	6.2830	2	0.0250	−3.6762
656.5	548.6	6.3074	3	0.0417	−3.1568
⋮	⋮	⋮	⋮	⋮	⋮
642.2	731.4	6.5950	58	0.9583	1.1563
726.0	735.2	6.6001	59	0.9750	1.3053
589.1	744.1	6.6122	60	0.9917	1.5660
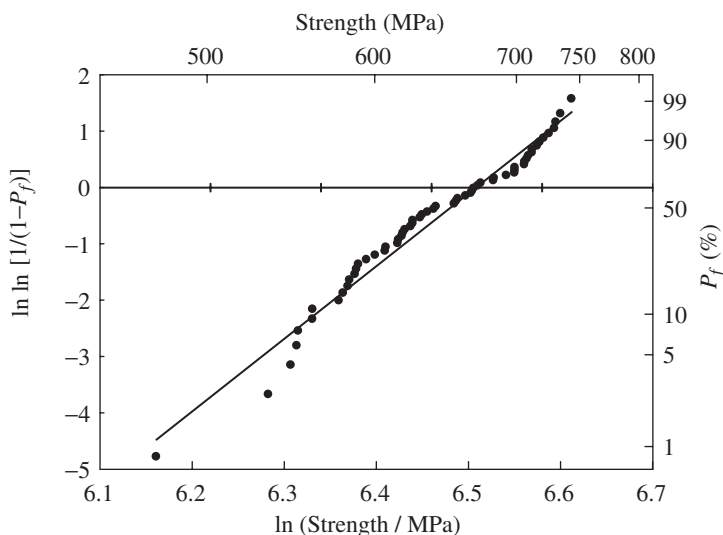
FIGURE 7.4   Weibull plot and fitted Weibull function for silicon nitride strengths determined in bending.

function of ln(strength), given in column 3, yielded $m = 12.89$ and $\sigma_0 = 669.9$ MPa. Confidence intervals are not given here since standard linear regression by least squares does not calculate them properly. A discussion of methods for calculating confidence intervals for the estimates of the Weibull parameters is deferred until Section 7.12.

7.8   SAFETY FACTORS

Another important concept is that of the safety factor, which is the mean strength divided by the value of the maximum allowable design stress that has been chosen. Within the bounds of a statistical treatment of strength, it is not possible to have absolute safety. One can at best choose the working stress as a fraction of the mean stress to provide a calculated low probability of failure. The safety factor treatment can be developed by combining Eqs. (7.40) and (7.41) and representing the stress σ by σ_{max}, giving

$$P_s = \exp - \left[\left(\frac{\sigma}{\bar{\sigma}} \right) \Gamma \left(1 + \frac{1}{m} \right) \right]^m \qquad (7.51)$$

This is a general result that is for any test technique and specimen size since k and V do not appear in the equation. One can now choose some value of P_s considered adequate for safety and solve for the safety factor sf defined as the ratio of the mean strength to the working stress ($\sigma_{allowable}$) necessary to achieve this value of P_s. The result is

$$\text{sf} = \frac{\bar{\sigma}}{\sigma_{allowable}} = \frac{\Gamma(1 + 1/m)}{(-\ln P_s)^{1/m}} \qquad (7.52)$$

Typical allowable failure probabilities range from, say, 10^{-3} for cases where there is no serious consequence of failure to perhaps 10^{-7} or lower where loss of life or other very serious consequences might result from failure. For the former case and m values of 10 and 15, the required safety factors predicted by the Weibull theory are 1.90 and 1.53, respectively. For the latter case the predicted safety factors are 4.77 and 2.83, respectively. A larger value of m permits the use of a working stress much nearer to the mean strength. The reason for striving to achieve high values of m through good processing is evident.

7.9   EXAMPLE OF SAFE STRESS CALCULATION

The usable stress in a particular design depends on the volume and stress distribution as well as the Weibull parameters. A common situation is one in

which the Weibull parameters are determined in a three-point bending test and then applied to a sample of larger volume under some other stress distribution. A simple example that provides for both change of stress distribution and change of volume is given here. It is assumed that the mean strength in three-point bending, $\bar{\sigma}_{3b}$, and the Weibull m parameter of a two-parameter Weibull distribution have been determined from a series of measurements of breaking strength in a given type of test (taken as three-point bending in the present example) of bars of test volume V_{3b}. It is desired to determine the maximum allowable stress $\sigma_{\text{allowable}}$ that can be used to give a survival probability of at least P_s in uniform tension for a piece of the same material of volume V_t. The problem can be solved by any of several equivalent procedures. A three-step procedure is used here to illustrate the ideas involved:

1. Account for the change in the distribution of applied stress. Determine the mean strength in uniform tension, $\bar{\sigma}_t$, of the three-point bending specimens of volume V_{3b} using the loading factors for three-point bending and tension:

$$\bar{\sigma}_t = \bar{\sigma}_{3b}\left(\frac{k_{3b}}{k_t}\right)^{1/m} = \bar{\sigma}_{3b}\left(\frac{1}{2(m+1)^2}\right)^{1/m} \tag{7.53}$$

2. Account for the change in specimen volume. Determine the mean strength in uniform tension, $\bar{\sigma}'_t$, of specimens of volume V_t using the ratio of the volumes:

$$\bar{\sigma}'_t = \bar{\sigma}_t\left(\frac{V_{3b}}{V_t}\right)^{1/m} \tag{7.54}$$

3. Account for the change from mean strength to stress with given survival probability. Determine the maximum allowable stress based on a mean strength of $\bar{\sigma}'_t$ using Eq. (7.52):

$$\sigma_{\text{allowable}} = \bar{\sigma}'_t\frac{(-\ln P_s)^{1/m}}{\Gamma(1+1/m)} \tag{7.55}$$

Combing all three equations gives the required result in terms of the given parameters:

$$\sigma_{\text{allowable}} = \bar{\sigma}_{3b}\frac{1}{\Gamma(1+1/m)}\left(\frac{-\ln P_s}{2(m+1)^2}\frac{V_{3b}}{V_t}\right)^{1/m} \tag{7.56}$$

TABLE 7.4   Calculation of Safety Factors for Strength Data in Table 7.3

	Variable	Results for $m = 12.88$	Results for $m = 20$
Step 1	$\bar{\sigma}_t$	406.0 MPa	459.2 MPa
Step 2	$\bar{\sigma}'_t$	339.5 MPa	409.2 MPa
Step 3	$\sigma_{\text{allowable}}$	101.1 MPa	187.8 MPa
Overall safety factor	$\bar{\sigma}_{3b}/\sigma_{\text{allowable}}$	6.375	3.433

Examination of the equations shows that each change (change is stress distribution, specimen volume, and probability) corresponds to a correction factor so that the order in which the calculation proceeds is unimportant.

Consider the example of the Weibull data discussed earlier for which $m = 12.88$ and the mean strength $\bar{\sigma}_{3b} = 644.5$ MPa. Suppose it is desired to have a probability of failure of less than 10^{-7} (i.e., $P_s = 1 - 10^{-7}$) in uniform tension for a piece of the same material having 10 times the volume of the bend specimen. Table 7.4 shows the results of the calculations which give an overall safety factor of 6.375, suggesting that the mean strength in bending should be over six times higher than the allowable stress in order to reach the required level of reliability. The allowable stress of 101 MPa is over four times weaker than the weakest strength measured, which was 474 MPa. Clearly, such calculations involve making assumptions about parts of the flaw size distribution not explored by the measurements, and the predictions should be treated with some circumspection. Table 7.4 also shows results calculated assuming $m = 20$, which nearly doubles the allowable stress for the same failure probability. Again, this illustrates the desirability of achieving higher values of the Weibull modulus.

7.10   PROOF TESTING

Review of the previous section shows that a very small service stress leads to a very low but nonzero probability of failure during service. Therefore, reliability cannot be completely assured. Worse, the behavior at very low failure probability can only be explored by testing a very large number of specimens, which is usually not possible. Therefore reliability analyses, such as that outlined in the previous section, rely on extrapolating from the measured behavior at higher probability; such extrapolation can usually not be justified and could dangerously overestimate reliability. This gloomy view of reliability can be greatly improved by proof testing.

Proof testing, also known as **screen testing**, involves briefly applying some stress to each component. If a component fails, it is discarded, but if it survives, it can be placed in service but now with a guaranteed minimum strength. This simple idea can be hard to implement in practice if, for example, the

components are subjected to a complex stress distribution in service that cannot be accurately reproduced during proof testing. However, proof testing can still be used to greatly reduce the probability of low strength failure. Proof testing is widely used to good effect; examples include burst testing of glass bottles, spin testing of ceramic turbocharger rotors, and tensile testing of silica glass optical fiber. However, many ceramics, and particularly glasses, are susceptible to slow crack growth during proof testing, which weakens the surviving components. This greatly complicates the effects of proof testing; a more detailed discussion will be presented in the next chapter. The remaining discussion here is only applicable to materials that do not exhibit any weakening during proof testing.

For simplicity, we will assume that the component experiences a uniform tensile stress during proof testing and while in service. The result of this analysis, however, will also be applicable to cases where the shape of the stress distribution during proof testing and during service is the same. Assuming that the strength distribution before proof testing, $P_{f,0}$, follows a two-parameter Weibull distribution

$$P_{f,0}(\sigma) = 1 - \exp\left[-\left(\frac{\sigma}{\sigma_0}\right)^m\right] \tag{7.57}$$

the yield or survival rate after proof testing at a stress σ_p is given by

$$P_{s,p} = \exp\left[-\left(\frac{\sigma_p}{\sigma_0}\right)^m\right] \tag{7.58}$$

The distribution of strength after proof testing, P_f, is given by

$$P_f(\sigma) = \frac{P_{f,0}(\sigma) - P_{f,p}}{P_{s,p}} = 1 - \exp\left[-\left(\frac{\sigma}{\sigma_0}\right)^m + \left(\frac{\sigma_p}{\sigma_0}\right)^m\right] \tag{7.59}$$

The numerator in the first expression is the probability of failing after proof testing, which is what the probability would be before proof testing minus the probability that the specimen is weak enough to have failed during proof testing. The denominator, $P_{s,p}$, renormalizes the strength distribution; it accounts for there being fewer surviving specimens after proof testing. Figure 7.5 compares the strength distribution before and after proof testing. The renormalization means that the distribution after proof testing is not abruptly truncated but smoothly approaches the proof stress asymptotically. It also means that the probability of failure for stresses just above the proof stress is lower than might be expected for an abrupt truncation. The resulting strength distribution no longer follows the two-parameter Weibull distribution; it is a three-parameter Weibull distribution although different from that described in an earlier section.
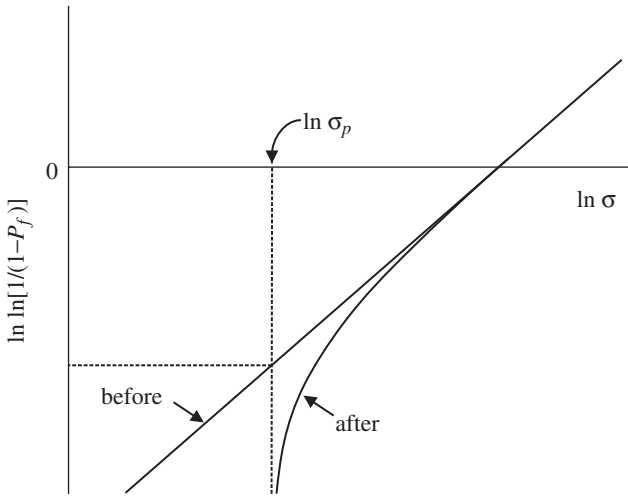
FIGURE 7.5   Schematic Weibull plot showing changes in strength distribution brought about by proof testing to stress σ_p.

7.11   USE OF POOLED FRACTURE DATA IN LINEAR REGRESSION DETERMINATION OF WEIBULL PARAMETERS

The Weibull parameters for a given material are usually determined from a series of strength measurements, all of which are determined using the same test method and specimens of the same size. It is possible to pool data determined from two or more types of strength test with different specimen sizes used in the different test types. Consider two types of tests A and B (perhaps a tensile test and a three-point bend test) for which the specimens have volumes V_A and V_B, respectively, and loading factors k_A and k_B. Substitution into Eq. (7.40) gives

$$\ln P_{sA} = -k_A V_A \left(\frac{\sigma}{\Sigma_0} \right)^m$$
$$\ln P_{sB} = -k_B V_B \left(\frac{\sigma}{\Sigma_0} \right)^m$$

$$(7.60)$$

where P_{sA} and P_{sB} are the survival probabilities for the same stress σ. Dividing gives

$$\frac{\ln P_{sA}}{\ln P_{sB}} = \frac{k_A V_A}{k_B V_B}$$

$$(7.61)$$

One of the specimen sizes and corresponding test methods (say, A) can be chosen as the standard. For each strength in set B, this equation can be used to

calculate the equivalent type A survival probability. This requires assuming a trial value of the Weibull parameter m because the k's depend on m. The entire resulting data set (set A plus the transformed set B) can then be treated as a single set of type A and the linear regression method of determining the Weibull parameters can then be used. The resulting value of m can then be used to again transform the original survival probabilities for set A to those appropriate to set B and the linear regression can be repeated. The process is iterated until the value of m does not change significantly between iterations. The linear regression method thus requires iterative calculations when data from different test methods are pooled. Alternate iterative procedures are discussed by Johnson and Tucker (1993) and Tucker and Johnson (1993), who also treat parameter estimation for the case of surface-distributed rather than volume-distributed flaws.

7.12   METHOD OF MAXIMUM LIKELIHOOD IN WEIBULL PARAMETER ESTIMATION

As noted previously, the Weibull parameters can be estimated not only by the least-squares procedure but also by the method of **maximum likelihood**. Linear regression is straightforward to perform in the relatively simple case in which all the experimental data are taken by one measurement method using specimens of one size, but the maximum-likelihood method requires solving a nonlinear equation by a series of iterations. However, standard least-squares linear regression analysis implemented in software such as Excel makes assumptions about the data which are not valid for fitting to data on a Weibull plot. In particular, it assumes that all the uncertainty is in the vertical coordinate and that each point on the plot is statistically independent of the others. These are clearly violated in the Weibull plot for which the strength data have been sorted and then a rank assigned. As mentioned in the previous section, linear regression loses the advantage of simplicity for more complicated data, such as situations in which data must be pooled from more than one size of specimen and/or more than one measurement technique. In contrast, the maximum-likelihood method is intuitive and is designed specifically for estimating parameters of probability distributions. It is therefore the method recommended by many authors and is required by the ASTM standard C 1239-07. It is a general method that can be applied to any probability distribution, but we limit the treatment to the Weibull distribution.

We consider n strength measurements with results σ_i, $i = 1, \ldots, n$. If the probability of obtaining a given σ_i is p_i, then the total probability of obtaining the complete set of measurements, P, is given by

$$P = \prod_{i=1}^{n} p_i \tag{7.62}$$

The p_i depend on the distribution parameters m and σ_0. The maximum-likelihood method involves finding the values of m and σ_0 that maximize P—these are the **maximum-likelihood estimators** of m and σ_0. It is more convenient to maximize the logarithm of P; $\ln P$ is a monotonically increasing function of P so that, when P takes a maximum value, so does $\ln P$. Equation (7.62) becomes

$$\ln P = \sum_{i=1}^{n} \ln p_i \qquad (7.63)$$

The logarithm of P is maximized by setting its partial derivatives with respect to m and σ_0 equal to zero to obtain a pair of nonlinear simultaneous equations which are solved for the maximum-likelihood estimates of m and σ_0. There now remains the question of how to assign values for the p_i.

In most circumstances the strength data are uncensored; that is, all the σ_i are known to reasonable accuracy. In this case we take the value of p_i to be proportional to the probability density $p(\sigma_i)$, which is found by differentiating the cumulative distribution function with respect to stress:

$$p_i = \left(\frac{dP_f}{d\sigma}\right)_{\sigma=\sigma_i} = m\frac{\sigma_i^{m-1}}{\sigma_0^m}\exp\left[-\left(\frac{\sigma_i}{\sigma_0}\right)^m\right] \qquad (7.64)$$

When substituting into the derivatives of $\ln P$, it is found that σ_0 can be eliminated, yielding a single equation in m only,

$$\frac{n}{m} + \sum_{i=1}^{n}\ln\sigma_i - n\frac{\sum_{i=1}^{n}\sigma_i^m\ln\sigma_i}{\sum_{i=1}^{n}\sigma_i^m} = 0 \qquad (7.65)$$

which is solved iteratively to obtain the maximum-likelihood estimate of m. The maximum-likelihood estimate of σ_0 if then found from

$$\sigma_0^m = \frac{1}{n}\sum_{i=1}^{n}\sigma_i^m \qquad (7.66)$$

The maximum-likelihood estimate of m is statistically biased; if the experiment is repeated many times to generate a distribution of values of m, that distribution is not centered on the true value but is biased high. Thoman et al. (1969) use Monte Carlo methods to characterize the bias and provide tabulated unbiasing factors which depend only on n. They also provide tabulated factors from which the confidence intervals for the estimates of m and σ_0 can be calculated. (ASTM standard C 1239-07 is the recommended source for these

factors since it includes some corrected values.) Applying these methods to the data in Table 7.3 gives the maximum-likelihood estimate of m as 12.65; after unbiasing, $m = 12.38$ with a 95% confidence interval of (10.09,15.13) and $\sigma_0 = 671.5$ MPa with a 95% confidence interval of (656.7,686.3) MPa. Comparing these results to those obtained by linear regression, $m = 12.89$ (12.31,13.47) and $\sigma_0 = 669.9$ (666.8,673.0) MPa, shows that, while linear regression gives similar best estimates of the parameters, it significantly underestimates the confidence intervals for those parameters. The results of standard linear regression analysis should therefore not be used for determining whether different groups of specimens have similar Weibull parameters. Monte Carlo methods similar to those used by Thoman et al. (1969) can be used to obtain more realistic estimates from linear regression analysis, but these methods are usually less efficient than maximum likelihood; that is, linear regression needs more strength measurements than maximum likelihood to obtain the Weibull parameters to any specified precision.

Because the maximum-likelihood method is specifically designed for determining the parameters of a probability distribution, it has some powerful properties. For example, it can be used in a natural way for cases where some of the data are censored. For example, suppose the actual strength is not known for the ith measurement, but it is known to be at least some value σ_i. Then p_i is the probability that the strength exceeds σ_i, which is simply given by the cumulative survival probability $P_s(\sigma_i)$. The overall probability P is again maximized with respect to m and σ_0 to obtain the maximum-likelihood estimators for this case.

Another example where the power of the maximum-likelihood method is useful is when pooling data for measurements using more than one measurement technique and/or using specimens of more than one size. Then σ_0 is different for each measurement technique and each specimen size and the above approach is inappropriate. In this case the more general form of the Weibull distribution is used, Eq. (7.40). If $\sigma_{\max}$ is interpreted at the ith strength, σ_i, then

$$P_f(\sigma_i) = 1 - \exp\left[-k_i V_i \left(\frac{\sigma_i}{\Sigma_0}\right)^m\right] \quad \text{and}$$

$$p(\sigma_i) = mk_i V_i \frac{\sigma_i^{m-1}}{\Sigma_0^m} \exp\left[-k_i V_i \left(\frac{\sigma_i}{\Sigma_0}\right)^m\right] \tag{7.67}$$

where k_i and V_i are the loading factor and specimen volume for the ith measurement. The maximum-likelihood estimate of m is found by solving

$$\frac{n}{m} + \sum_{i=1}^{n} \frac{1}{k_i} \frac{dk_i}{dm} + \sum_{i=1}^{n} \ln \sigma_i - n \frac{\sum_{i=1}^{n} \left[k_i V_i \sigma_i^m \ln \sigma_i + V_i \sigma_i^m (dk_i/dm)\right]}{\sum_{i=1}^{n} V_i k_i \sigma_i^m} = 0 \tag{7.68}$$

and then

$$\Sigma_0^m = \frac{1}{n} \sum_{i=1}^n k_i V_i \sigma_i^m \qquad (7.69)$$

7.13   STATISTICS OF FAILURE UNDER MULTIAXIAL STRESS

The above statistical treatment of failure has tacitly assumed parallel uniaxial tension in each volume element of the specimen, although the magnitude may vary with position as in bending tests. The statistics of failure under multiaxial stress have been treated by a method due to Batdorf (Batdorf and Crose, 1974; Batdorf and Heinisch, 1978; Batdorf and Chang, 1979) and a multiaxial elemental strength model (Evans, 1978a; Lamon, 1988). The Batdorf and Evans theories have been shown to be equivalent (Chao and Shetty, 1990; Andreasen, 1993) provided that the same fracture criterion is used.

Chao and Shetty (1991) used Batdorf's statistical fracture theory to correlate uniaxial strength results (determined in three- and four-point bending) with biaxial strength results (determined with a uniform pressure on the disk method). They considered two failure criteria: the critical normal stress criterion and the noncoplanar strain energy release rate criterion. The former takes the simple form

$$K_I = K_{IC} \qquad (7.70)$$

and thus considers failure to be determined solely by mode I loading of a crack. The latter leads to an approximate equation

$$\left(\frac{K_I}{K_{IC}}\right) + \left(\frac{K_{II}}{CK_{IC}}\right)^2 = 1 \qquad (7.71)$$

originally suggested by Palaniswamy and Knauss (1978) with $C = (2/3)^{1/2} = 0.816$. Measurements were made on two commercial ceramics, an alumina and a silicon nitride, having the properties listed in Table 7.5. The elastic moduli measured by the three flexure methods and by a compression method are listed in Table 7.6 and are seen to be in reasonably good agreement. The Weibull parameters determined in the three flexural tests are given in Table 7.7.

For the alumina specimens the data obtained in four-point bending were fitted to the Weibull distribution using the method of maximum likelihood. The data are shown as a Weibull plot in Figure 7.6 and fit well with a Weibull parameter $m = 23.77$ as shown. The Weibull plots for three-point bending and for biaxial flexure were then predicted from these four-point bending results for

TABLE 7.5   Properties of Two Commercial Ceramics Used in Uniaxial and Biaxial Comparison

Ceramic	E (GPa)	ν	ρ (kg/m^3)	K_{IC} (MPa $\cdot$ m$^{1/2}$)
Alumina (Coors AD-94)	297.2	0.23	3700	3.1
Silicon nitride (GTE SN W-1000)	285.0	0.23	3280	7.2

TABLE 7.6   Elastic Moduli Determined in Different Tests (GPa) for Materials in Table 7.5

Ceramic	Four-Point Bend	Three-Point Bend	Biaxial Flexure	Compression
Alumina	290.1	296.6	301.8	297.2
Silicon nitride	279.9	283.7	291.7	285.0

TABLE 7.7   Measured Weibull Parameters for Materials in Table 7.5

Ceramic	Four-Point Bend		Three-Point Bend		Biaxial Flexure	
	m	σ_0 (MPa)	m	σ_0 (MPa)	m	σ_0 (MPa)
Alumina	23.77	353.4	25.43	385.9	22.25	338.8
Silicon nitride	10.12	768.4	15.67	908.1	12.02	717.1
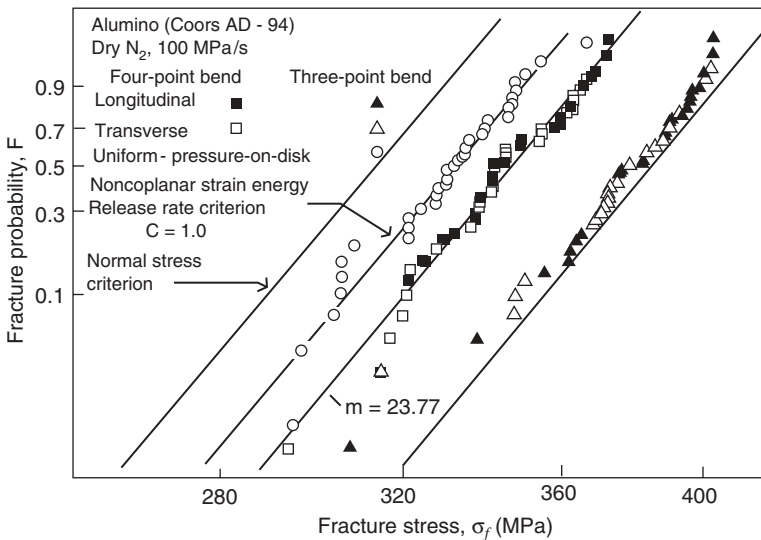
FIGURE 7.6   Weibull plots for alumina. (From Chao and Shetty, 1991. Reprinted by permission of Wiley-Blackwell.)
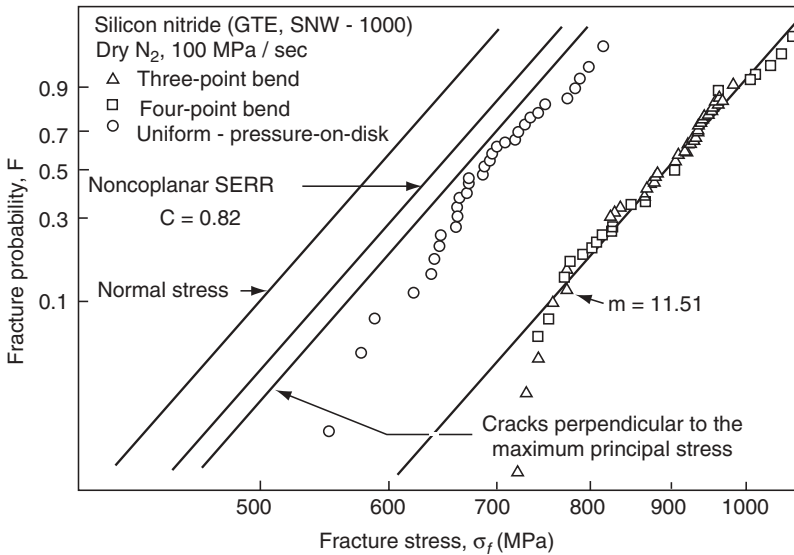
FIGURE 7.7   Weibull plots for silicon nitride. (From Chao and Shetty, 1991. Reprinted by permission of Wiley-Blackwell.)

the normal stress criterion and for the noncoplanar strain energy release rate criterion. The former does not fit but the latter fits the data well using $C = 1$.

For silicon nitride specimens, the method of Batdorf and Sines (1980) was used to obtain $m = 11.51$ and $\sigma_0 = 918.4$ MPa. Figure 7.7 shows a Weibull plot on which the four-point bend strengths have been converted to equivalent three-point bend strengths using loading factors for each. The fracture probabilities for the biaxial flexure test were then predicted. Neither the critical normal stress nor the critical strain energy release rate criteria gave correct predictions; both overestimated the fracture probabilities. Assuming that all flaws are perpendicular to the stress and using the critical normal stress criterion gave predictions closer to the observed biaxial strength data.

7.14   EFFECTS OF SLOW CRACK PROPAGATION AND *R*-CURVE BEHAVIOR ON STATISTICAL DISTRIBUTIONS OF STRENGTH

The above discussion of statistical effects on strength has tacitly assumed that strength is not time dependent and that the critical stress intensity for crack propagation does not depend on crack length. Both assumptions may be incorrect under certain circumstances.

Subcritical crack propagation is treated in Chapter 8 and leads to a dependence of strength on the rate of loading. We show in Section 8.7 that

the Weibull strength distribution can still be used but that the value of the Weibull m parameter, as measured in constant-strain-rate experiments, will be different.

The effect of crack growth resistance that is dependent on crack length (R-curve behavior) is treated in Chapter 9. In Section 9.3 the resulting effect on statistical distributions of strength is briefly discussed, including the possibility that the Weibull distribution may not accurately describe the actual strength distribution.

7.15   SURFACE FLAW DISTRIBUTIONS AND MULTIPLE FLAW DISTRIBUTIONS

Flaws responsible for fracture have so far in this chapter been assumed to be randomly distributed throughout the volume of material. The treatment for predicting failure probabilities for different volumes was based on this assumption. However, as noted in Chapter 6, some types of flaws of the same size should cause failure at a lower stress when they are located on the surface rather than within the volume. It is therefore possible that, for some types of specimens, failure occurs primarily or even entirely from surface flaws as appears to be the case with glass.

For a purely surface distribution of flaws, the risk function $\varphi(\sigma)$ can be redefined as the probability of failure per unit area (instead of per unit volume) and then all analyses presented above can be reworked replacing the specimen volume V by the surface area A. In particular, loading factors can be defined for different test methods:

$$k = \frac{1}{A} \int_A \left(\frac{\sigma(\mathbf{r})}{\sigma_{\max}} \right)^m dA \tag{7.72}$$

and the Weibull distribution becomes

$$P_f = 1 - \exp\left[-kA \left(\frac{\sigma_{\max}}{\Sigma_0} \right)^m \right] = 1 - \exp\left[-\left(\frac{\sigma_{\max}}{\sigma_0} \right)^m \right] \tag{7.73}$$

with mean strength

$$\bar{\sigma} = \frac{\Sigma_0}{(kA)^{1/m}} \Gamma\left(1 + \frac{1}{m} \right) \tag{7.74}$$

Many of the equations appropriate for volume-distributed flaws can be adapted for area-distributed flaws simply by replacing A with V. For example, the

stresses that give the same probability of failure for specimens with different surface areas and test methods are related by

$$\frac{\sigma_1}{\sigma_2} = \left(\frac{k_2 A_2}{k_1 A_1}\right)^{1/m} \tag{7.75}$$

However, the loading factors for different test methods are not the same for surface flaws. Table 7.2 gives the loading factors for several common strength measurement techniques for both volume- and area-distributed flaws. For this particular rectangular geometry of the specimens the two sets of loading factors are closely related; the ratio of the loading factors for two measurement techniques is independent of the type of flaw.

For thin fibers and tapes of uniform cross section the equations can be further modified to consider flaws as if they were distributed along the length. For example, a cylinder of radius r and length L has surface area $A = 2\pi r L$. Substitution into (7.73) gives

$$P_f = 1 - \exp\left[-2\pi r L \left(\frac{\sigma_{max}}{\Sigma_0}\right)^m\right] = 1 - \exp\left[-L\left(\frac{\sigma_{max}}{\Sigma_0'}\right)^m\right] \tag{7.76}$$

Since $2\pi r$ is constant, it can be folded into Σ_0, itself a constant for a given material, to yield a Weibull distribution that effectively describes length-distributed flaws. This approach is widely used, for example, to describe the strength and reliability of kilometer lengths of fused silica optical fiber.

While many materials fail from flaws that are almost exclusively distributed over the surface area or throughout the volume, for many ceramics both surface and volume flaws contribute to failure. Or there might be other types of flaw distributions that are concurrently active. An example that is sometimes observed in bending tests with bars of rectangular cross section is that failure occurs from both surface and edge flaws. In these cases of multiple flaw distributions the failure probability is no longer described by a single Weibull distribution but requires the combination of two or more distributions. Johnson was apparently the first to apply this idea to failure in ceramics in an unpublished report that is the basis for later treatments (Jakus et al., 1981; Johnson, 1983). For the case of volume and surface distributions (denoted by subscripts V and S), the overall survival probability can be written as

$$P_f = 1 - (1 - P_{f,V})(1 - P_{f,S}) \tag{7.77}$$

Taking each of the survival probabilities to be a Weibull distribution gives

$$P_f = 1 - \exp\left[-k_V V \left(\frac{\sigma}{\Sigma_{0,V}}\right)^{m_V} - k_S A \left(\frac{\sigma}{\Sigma_{0,S}}\right)^{m_S}\right] \tag{7.78}$$

When the origin of failure can be assigned for each specimen to either a surface or a volume flaw by subsequent fractographic examination (see Chapter 17), it is possible to analyze the strength data and determine the four Weibull parameters. The analysis, however, is not straightforward. One cannot simply separate the two distributions and analyze each separately. The proper procedure is discussed in Jakus et al. (1981), Service et al. (1985), Sonderman et al. (1985), and ASTM standard C 1239-07.

PROBLEMS

1. The following strength data are determined on a structural ceramic in a three-point bending test (units MPa):

   83.9 87.2   89.6   92.6   93.6   94.7   95.4   96.5   96.9   97.3
   98.7 99.5 100.1 100.3 100.5 102.0 102.6 103.0 104.3 106.4

   Estimate the Weibull modulus σ_0 and Weibull shape parameter m. Determine a 95% confidence interval for your estimates. Provide answers found using both linear regression and the maximum-likelihood technique method as specified in ASTM Standard C 1239-07.

2. You have measured the strength of a large number of specimens with volume of $1\,cm^3$ in three-point bending and found the distribution to be described by a mean strength of 350 MPa and a Weibull modulus of 12. You wish to use the same material in tension with a volume of $15\,cm^3$ and have a failure probability of better than 1 in 10^6. Ignoring subcritical crack growth, what is the highest design value for the tensile stress that you can use to have this failure probability?

3. A ceramic bar of uniform rectangular cross section, width 5 mm, and thickness 3 mm is tested in uniaxial tension with the tensile axis parallel to the axis of the bar. The mean strength is found to be 180 MPa for a 0.5-m test length and 170 MPa for a 1-m test length; these strengths are observed to be independent of the loading rate. Fractographic analysis shows that the failures all originate from interior flaws. Calculate the Weibull modulus for this material. Calculate the maximum allowable service stress that would ensure a better than 99.999% probability of survival of a 10-m specimen similarly loaded in tension. Calculate the mean strength of this material tested in three-point bending when the distance between the outer loading pins is 100 mm.

4. The strength of a ceramic specimen is measured in four-point flexure and the mean strength is found to be 89.1 MPa. Specimens of the same material having 10 times the volume of the flexure specimens are tested in tension and the mean strength is found to be 64.5 MPa. Estimate the Weibull modulus m to the nearest integer.

5. Strength measurements on a certain ceramic are found to follow the Weibull distribution with fit parameters $m = 8.47$ and $\sigma_0 = 346$ MPa. Draw or plot an accurate graph of both the probability density $p(\sigma)$ and the cumulative failure probability distribution $P_f(\sigma)$ on linear/linear axes and for the stress in the range of 0–600 MPa. Calculate the distribution mean, median, mode, variance, standard deviation, and coefficient of variation C_V. Calculate the lower and upper quartiles. Calculate the 95% confidence interval for a single measurement. Calculate the stresses that correspond to failure probabilities of 10^{-3} and 10^{-6}. (You may assume there is not subcritical crack growth in this material.)

6. Tensile strength measurements of glass fibers yield the following results in megapascals:

    3035   3106   3158   3195   3205   3275   3390   3441

    Estimate the Weibull modulus and scale parameter. Estimate the median strength of the distribution. If you measured the strength of a million specimens, what is the weakest strength you expect to encounter?

7. You measure the strength of many specimens (volume V) of an alumina in tension and find the average strength is 400 MPa and the Weibull shape parameter is 12. For the purposes of this question, you may ignore the effects of subcritical crack growth.

    a. What is the largest safe tensile stress to give a failure probability of 1 in 10^4 for a tension specimen of the same volume (V) as the test specimens?

    b. What is the largest safe tensile stress to give a failure probability of 1 in 10^4 for a tension specimen with 10 times the volume of the test specimens, that is, $10V$?

    c. If the test specimens of volume V are proof tested to a stress of 200 MPa, what is the expected failure rate during proof testing?

    d. What would the mean strength of the material be for the volume V tested in three-point bending?

8

SUBCRITICAL CRACK PROPAGATION

8.1 INTRODUCTION

The discussion of crack behavior so far has assumed essentially instantaneous response of cracks to an applied stress. The general assumption has been that a crack does not extend as the applied stress intensity is increased until the critical value is reached, at which point the crack propagates very rapidly. However, in many ceramics cracks grow slowly under values of applied stress intensity well below the critical value for rapid fracture, that is, K_{IC}.

A situation of engineering importance is the behavior of a crack under a service load that causes it to grow slowly so that the applied stress intensity

factor increases until the critical value is reached and failure ensues. This phenomenon is known as **delayed failure**. The basis for safe life design for this situation is presented in this chapter.

The principal subcritical crack propagation mechanism in ceramics at room temperature involves stress-assisted reaction with the environment—especially reaction with water. This mechanism is known as **stress corrosion cracking** or simply **fatigue** (but note that to metallurgists ''fatigue'' usually refers to cyclic fatigue, which will be discussed in Chapter 15). Several other mechanisms have been proposed, including thermal activation of lattice-trapped cracks and mass transport (diffusion). The latter does have practical importance at elevated temperatures and is discussed at the end of this chapter.

8.2   OBSERVED SUBCRITICAL CRACK PROPAGATION

Slow crack propagation occurs in many ceramics and is especially prevalent in ceramics containing a silica phase and in the presence of an appreciable partial pressure of water vapor (Wiederhorn, 1974). For a given material, temperature, and relative humidity, the controlling variable is the applied stress intensity factor. A typical plot of crack velocity as a function of stress intensity factor for soda–lime–silica glass is shown in Figure 8.1 from work by Wiederhorn (1967) (see also Wiederhorn and Bolz, 1970; Wiederhorn, 1974). This figure shows the crack velocity on a logarithmic scale as a function of stress intensity factor. Several important points are illustrated (Wachtman, 1974):

1. The stress intensity factor K_I is the controlling factor; all data from many cracks with various combinations of crack length and applied stress fall on the same master curves when expressed in terms of K_I.

2. At low values of K_I the semilogarithmic plot is linear; such linear behavior is predicted by the theory of Charles and Hillig (1962) (Hillig and Charles, 1965), described later. This range of behavior is termed region I.

3. Within region I the crack velocity for constant K_I is greater for greater values of relative humidity. Crack growth in region I is attributable to a stress-enhanced chemical reaction between water and the glass. The rate of crack growth is reaction rate controlled so that increasing the concentration of the reactant should increase the rate of growth. This prediction is borne out by the results shown in Figure 8.1. Further evidence of chemical control in region I is provided by Figure 8.2 (Wiederhorn and Johnson, 1973), which shows that increasing the pH increases the rate of crack propagation at constant K_I for silica glass in water. The Charles–Hillig theory predicts that the crack velocity depends on temperature; this dependence is observed as shown in Figure 8.3 (Wiederhorn and Bolz, 1970).
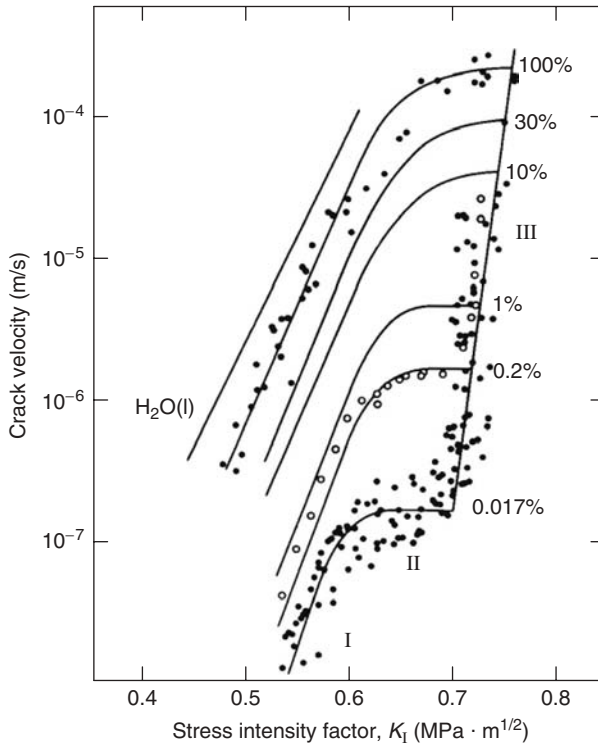
FIGURE 8.1   Crack velocity in soda–lime–silica glass as a function of stress intensity factor in nitrogen at various values of relative humidity. (From Wiederhorn, 1967. Reprinted by permission of Wiley-Blackwell.)

4. Figure 8.1 also shows the existence of region II at higher values of K_I, in which the crack velocity is still dependent on the partial pressure of water but substantially independent of K_I. Here crack growth rate is still controlled by a stress-enhanced chemical reaction between water and glass, but now the rate of growth is determined by the rate of transport of water to the crack tip.

5. At still higher values of K_I, region III occurs, in which crack propagation becomes independent of water in the environment. Here the growth rate at constant K_I depends on the temperature and composition of the glass, as shown in Figure 8.4 (Wiederhorn et al., 1974).

Results similar to those found for glass at room temperature have been found for a variety of ceramic materials, including porcelains, high-alumina ceramics, silicon nitride, vitreous carbon, portland cement, lead zirconate titanate (PZT), and barium titanate. At room temperature both porcelain and polycrystalline aluminum oxide show crack growth rates that depend on the environment; the three regions found for glass are also found in these cases.
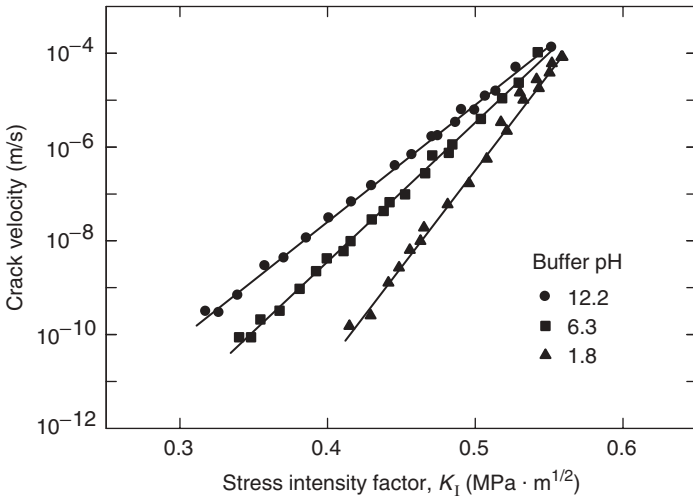
FIGURE 8.2 Effect of pH on crack velocity in silica glass in aqueous environments. (From Wiederhorn and Johnson, 1973. Reprinted by permission of Wiley-Blackwell.)
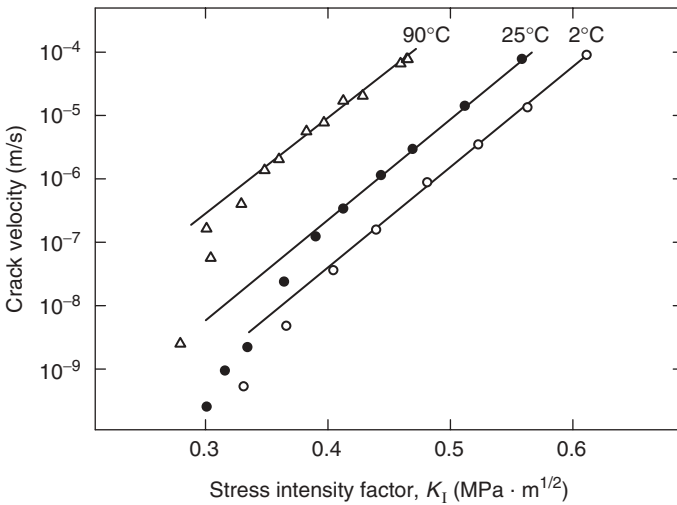
FIGURE 8.3 Effect of temperature on crack velocity in soda–lime–silica glass in water. (From Wiederhorn and Bolz, 1970. Reprinted by permission of Wiley-Blackwell.)

Sometimes a **fatigue threshold** or **fatigue limit** is observed; that is, the crack velocity is zero below some threshold stress intensity K_I^0. This phenomenon is not easy to study since the crack velocity is extremely slow just above the threshold, but the threshold is expected theoretically (Lawn, 1993). The corrosive species adsorbing on the surface of the material reduces the surface
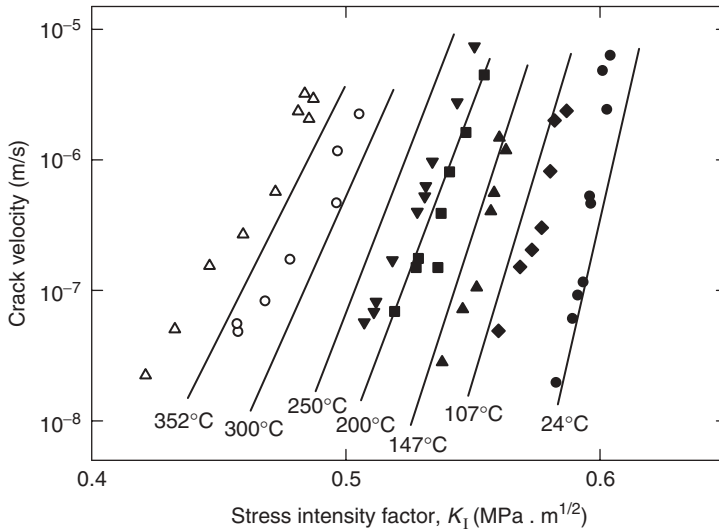
FIGURE 8.4   Effect of temperature on crack velocity of high-lead glass in vacuum. (From Wiederhorn et al. 1974. Reprinted by permission of Wiley-Blackwell.)

energy in the environment, $\gamma_{f,E}$, compared with what it would be in a vacuum, that is, γ_f, as discussed in the previous chapter. Equivalently, the toughness in the environment is less than in a vacuum, $K_{IC,E} < K_{IC}$. If the stress intensity is less than $K_I^0 = K_{IC,E}$, the energy release rate is insufficient to cause facture. If the stress intensity is greater than K_I^0 but less than K_{IC}, the crack does start to grow, but it immediately removes the corrosive species in the region of the crack tip by chemical reaction and can only continue to grow at a rate controlled by how quickly the corrosive species can be transported to and absorbed at the crack tip. While the existence of the threshold has the important practical implication that failure will never occur if the stress intensity never exceeds K_I^0, it is probably unwise to rely on the presence of the threshold when assessing reliability for critical applications.

8.3   CRACK VELOCITY THEORY AND MOLECULAR MECHANISM

According to the Griffith theory, cracks do not propagate below the critical stress required for rapid propagation to complete failure. Charles and Hillig (1962) assumed that the rate of subcritical crack propagation is controlled by a chemical reaction between the glass and the water in the environment. In particular, the water preferentially attacks the strained bonds at the crack tip which are more chemically reactive. Because chemical reactions are thermally activated processes, the crack velocity should depend on an activation energy,

which should in turn depend on stress. The Charles–Hillig theory gives the velocity of chemically assisted crack growth as

$$v = v_0 \exp\left(\frac{-E^+ + V^+\sigma_{\text{tip}} - \gamma V_M/\rho}{RT}\right) \tag{8.1}$$

where E^+ is the activation energy of the chemical reaction for a flat surface in the absence of an applied stress, V^+ is an activation volume, σ_{tip} is the stress at the crack tip, V_M is the molar volume of the material, γ is the interfacial surface energy between the material and the reaction products, and ρ is the radius of the crack tip. The term in γ and ρ arises because the energy associated with a surface depends on its curvature; a concave surface is less reactive than a flat or convex surface. Wiederhorn (1970) expressed the stress in terms of the stress intensity factor using Eq. (5.22) and $K_I = \sigma(\pi c)^{1/2}$ as

$$\sigma_{\text{tip}} = \frac{2K_I}{(\pi\rho)^{1/2}} \tag{8.2}$$

Assuming that ρ does not change as the crack extends, the surface energy term may be included in an effective zero-stress activation energy

$$E^* = E^+ + \frac{\gamma V_M}{\rho} \tag{8.3}$$

leading to

$$v = v_0 \exp\left(-\frac{E^*}{RT} + \frac{2V^+}{(\pi\rho)^{1/2}}\frac{K_I}{RT}\right) \tag{8.4}$$

This provides a basis for the linear dependence of $\ln v$ upon K_I at constant T for environmentally sensitive subcritical crack growth in region I. It is perhaps sufficient to argue qualitatively that the stress intensity factor is the appropriate variable to describe the driving force not only for sudden crack propagation but also for any stress-controlled process at a crack tip, including stress corrosion. The experimental data on crack velocity in samples of a given glass with different crack lengths do fall on a single curve when plotted as a function of the stress intensity factor. As noted below, the functional dependence is as well described by a power of the stress intensity factor as by an exponential; the former is more convenient in lifetime calculations.

The above treatment did not depend on a specific molecular mechanism; a detailed qualitative molecular model has been proposed by Michalske and Freiman (1983) for silicates. For the case of water interacting with stressed silica they suggested a three-step process as follows:

Step 1 A water molecule from the environment attaches to a bridging Si–O–Si bond at the crack tip. The water molecule is aligned by (1) formation of
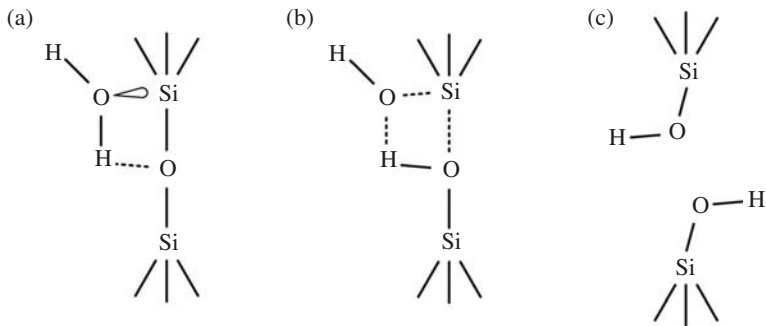
FIGURE 8.5   Molecular mechanism proposed by Michalske and Freiman (1983) for stress corrosion of Si–O–Si bonds by water.

the hydrogen bond with the bridging oxygen atom and (2) interaction of the lone-pair orbitals from O in the water molecule with the Si atom [Figure 8.5(a)]. The lone-pair orbital interaction may involve either van der Waals attraction or some covalent bonding with unoccupied orbitals of Si.

Step 2 A concerted reaction occurs in which proton transfer to the bridging O is accomplished simultaneously with electron transfer from the water O to the Si atom [Figure 8.5(b)]. As a result two new bonds are formed, one between the water O and Si and one between hydrogen and the bridging O; the original bridging bond between O and Si is destroyed.

Step 3 Rupture of the hydrogen bond between the water O and the transferred hydrogen occurs to yield surface Si–O–H groups on each fracture surface [Figure 8.5(c)]. Since the hydrogen bond is weak, this step is expected to occur immediately after proton transfer.

Michalske and Freiman note that there is no need for prior dissociation of the water molecule nor do any reaction products need to be removed from the surface.

Michalske and Freiman studied several nonaqueous environments and found several that enhanced stress corrosion crack growth. Those that enhanced crack growth contained active groups with electron donor sites on one end and proton donor sites at the other, such as ammonia, hydrazine, and formamide. Other nonaqueous environments had no effect provided care was taken to exclude trace amounts of water.

The crack velocity is often found to be sensitive to pH, but the effect is complicated. Wiederhorn and Johnson (1973) found that the velocity depends on the pH at the crack tip; they suggest that at slow velocity it is controlled by the pH of the surrounding electrolyte while at higher velocity it is controlled by the composition of the glass. They also found that at a constant stress intensity the velocity can increase with increasing pH (e.g., fused silica, Figure 8.2) or can decrease with pH (e.g., soda–lime–silicate glass). While details of the specific
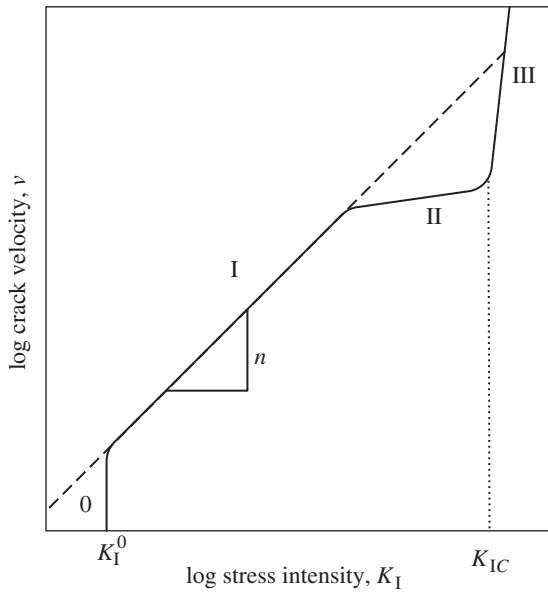
FIGURE 8.6   Idealized v–K_I behavior (solid line) and simplified behavior often used for lifetime calculations (dashed line).

mechanism leading to crack growth may vary for different systems, they are all based upon crack growth due to a stress-assisted, thermally activated chemical reaction between the material and a corrosive environmental species.

Although the data in region I are well described by a semilog plot as shown in Figure 8.1, they can be equally well described by a straight line on a log–log plot of crack velocity v as a function of K_I, as shown schematically in Figure 8.6. This plot leads to the empirical power law for crack velocity,

$$v = AK_I^n \tag{8.5}$$

where n is the **stress corrosion susceptibility parameter**. This law is convenient mathematically and is usually used in lifetime calculations as described in the next section. The effect on lifetime predictions of the type of velocity law that is used has been discussed by Jakus et al. (1981). Tomozawa (1996) argues that crack blunting by water may invalidate such lifetime calculations for glass annealed in water vapor.

8.4   TIME TO FAILURE UNDER CONSTANT STRESS

The effect of subcritical crack propagation on the failure stress under different conditions of loading has been treated by several investigators, including

Davidge et al. (1973), Evans and Wiederhorn (1974), and Ritter (1978). The general fracture mechanics relation for the stress intensity factor K_I for a crack of length c under stress σ is

$$K_I = Y\sigma c^{1/2} \tag{8.6}$$

When the applied stress σ remains constant, the crack grows slowly until $K_I = K_{IC}$, at which point failure occurs at some time after the stress was applied. This phenomenon is termed **delayed failure** and the case where the applied stress is constant is called **static fatigue**; while the applied stress is constant, both the crack length and the stress intensity applied to the crack increase with time. For constant σ the stress intensity factor will increase at a rate given by differentiating Eq. (8.6) with time:

$$\frac{dK_I}{dt} = \frac{\sigma Y}{2c^{1/2}}\frac{dc}{dt} + \sigma c^{1/2}\frac{dY}{dt} \tag{8.7}$$

For cracks that are small compared to the specimen dimensions, the change in Y as the crack grows is small so that the last term may be ignored. Using $v = dc/dt$ and eliminating c using Eq. (8.6) give

$$dt = \frac{2}{\sigma^2 Y^2}\frac{K_I}{v}dK_I \tag{8.8}$$

The crack will grow subcritically from its initial length at which $K_I = K_{Ii}$ until it reaches a length at which $K_I = K_{IC}$, at which time the specimen will fail. The time required for the crack to grow to failure under constant stress σ, t_f, is then given by

$$t_f = \frac{2}{\sigma^2 Y^2}\int_{K_{Ii}}^{K_{IC}}\frac{K_I}{v}dK_I \tag{8.9}$$

As mentioned earlier, the empirical crack growth law commonly used for region I is $v = A K_I^n$, Eq. (8.5). An exact treatment would require using this crack velocity expression only for region I and using an approximately constant value of v for region II in the integration. Because in most circumstances the crack is traveling relatively fast in region II, the time spent in traversing this region is small compared with the time spent in region I if the experiment begins well down in region I. Also it is usual to assume that K_{Ii} is greater than the threshold K_I^0. For simplicity, the crack growth law $v = AK_I^n$ is used for complete integration so the assumed behavior corresponds to the dashed line in Figure 8.6. This procedure slightly underestimates the time to failure; that is, it gives a conservative estimate of the time to failure. Substituting this relation for v into the integral gives

$$t_f = \frac{2}{\sigma^2 A Y^2(n-2)}\left(\frac{1}{K_{Ii}^{n-2}} - \frac{1}{K_{IC}^{n-2}}\right) \tag{8.10}$$

The **inert strength** or **initial strength** σ_i is defined as the strength that would be measured in the absence of stress corrosion cracking. It can be measured either by eliminating the chemical species in the environment that causes the stress corrosion (e.g., water) or by measuring the strength extremely rapidly so that there is insufficient time for significant subcritical crack growth before failure. If the initial crack length before application of stress is c_i, then

$$K_{IC} = Y\sigma_i c_i^{1/2} \tag{8.11}$$

The initial value of K_I, K_{Ii}, is related to the constant applied stress σ by

$$K_{Ii} = Y\sigma c_i^{1/2} \tag{8.12}$$

Equations (8.11) and (8.12) give

$$\frac{K_{Ii}}{K_{IC}} = \frac{\sigma}{\sigma_i} \tag{8.13}$$

If the constant stress σ is well below the inert strength σ_i, then K_{Ii} is well below K_{IC}. If the value of n is large, as it usually is, then $K_{Ii}^{n-2} \ll K_{IC}^{n-2}$ and the term in K_{IC} in Eq. (8.10) can be neglected. For example, for $\sigma = 0.6 \, \sigma_i$ and $n = 12$, dropping the K_{IC} term introduces only 0.6% error in the time to failure. Accordingly,

$$t_f = \frac{2}{\sigma^2 A Y^2(n-2)} \frac{1}{K_{Ii}^{n-2}} \tag{8.14}$$

The approximation $K_{Ii}^{n-2} \ll K_{IC}^{n-2}$ will not be valid when the time to failure is extremely short or for moderate times to failure under nearly inert conditions since in both cases the applied stress σ will be close to the inert strength σ_i.

The term K_{Ii} may be eliminated from Eq. (8.14) using (8.13), which gives the equation commonly used to estimate failure time under constant stress:

$$t_f = \frac{2}{A Y^2(n-2)\sigma^n} \left(\frac{\sigma_i}{K_{IC}}\right)^{n-2} \tag{8.15}$$

This equation can be simplified to highlight the important parametric dependencies by collecting several parameters together into a compound parameter B:

$$t_f = B\frac{\sigma_i^{n-2}}{\sigma^n} \tag{8.16}$$

where

$$B = \frac{2}{A Y^2(n-2)} \frac{1}{K_{IC}^{n-2}} \tag{8.17}$$
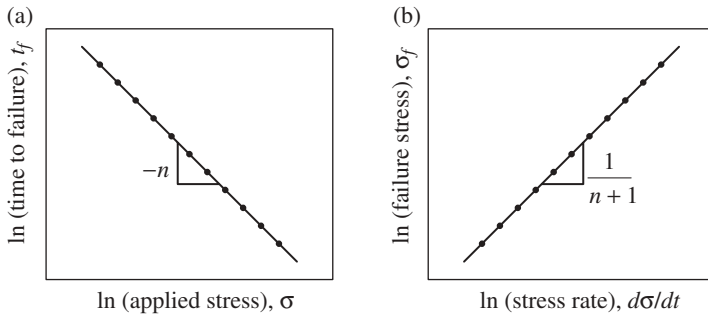
FIGURE 8.7   Plots of (a) static fatigue and (b) dynamic fatigue.

which is a constant for a given test environment. Equation (8.16) illustrates how the time to failure under a constant stress depends on both that stress and the inert strength, that is, the initial strength before degradation by subcritical crack growth.

The parameter n can be evaluated by determining the time to failure in a series of experiments at different values of constant applied stress, all well below the inert strength. The value of n is then obtained from a plot of $\ln t_f$, as a function of $\ln \sigma$, which has a slope of $-n$, as shown schematically in Figure 8.7(a). Values of σ_i and K_{IC} can be obtained from short time or inert atmosphere strength and fracture mechanics experiments, and A can then be calculated from Eq. (8.15).

Equation (8.16) can be used to express the ratio of the times to failure, t_{f1} and t_{f2}, for two specimens with the same inert strength under two corresponding subcritical stresses, σ_1 and σ_2, as

$$\frac{t_{f1}}{t_{f2}} = \left(\frac{\sigma_2}{\sigma_1}\right)^n \tag{8.18}$$

Since this equation is only valid for specimens with the same inert strength, one might wonder about its usefulness considering that strengths of specimens are statistically distributed. We will show later that this equation applies for times to failure with the same cumulative probability of failure. However, in bend tests the existence of a flaw distribution combined with a nonuniform distribution of stress in the specimen introduces more complex behavior. The reader is referred to Hu et al. (1988) for a theory for this case. In the present chapter we shall not introduce this complication and instead continue the conventional treatment.

Typical values of the stress corrosion parameter n range from 15 to 40 or higher and are indeed much larger than unity, as already assumed. Higher values of n are desirable for long-term reliability, which, given Eq. (8.15), perhaps appears counterintuitive. However, if the applied stress exceeds the inert strength, $\sigma \geq \sigma_i$, failure is instantaneous. As the applied stress is reduced below σ_i, the time to failure is finite and increases with reducing stress. It is desirable

that the time to failure should increase more rapidly with reducing stress, which corresponds to higher values of n, where n is effectively infinite for materials that do not exhibit stress corrosion cracking. However, even in such cases there is some slight time dependence to the strength due to thermal fluctuations; for example, Bogatyrjov et al. (1991) estimate $n \simeq 150$ for high-strength fused silica in the absence of moisture. Such high values of n do not lead to significant reliability concerns, although they may be relevant to the effect of proof testing.

ASTM standard C 1576-05 (see Chapter 24) describes a standard test method for measuring the fatigue parameters in flexure using static fatigue; this standard includes methods for calculating the confidence limits of the parameters.

8.5   FAILURE UNDER CONSTANT STRESS RATE

The presence of subcritical crack propagation means that if the strength of a material is determined under noninert conditions, the measured strength is lower than the inert strength due to subcritical crack growth during loading. This further means that the strength depends on the loading rate since for slower loading there is more time for subcritical crack growth and the measured strength will be correspondingly lower. This phenomenon is called **dynamic fatigue**; in contrast to static fatigue, the applied stress is increasing with time. The effect of subcritical crack propagation on failure at constant stress or strain rate was considered by Evans (1973). If a specimen is loaded in a testing machine with a constant rate of crosshead motion, the strain rate $\dot{\varepsilon}$ is approximately constant, as is the stress rate, $\dot{\sigma} = E\dot{\varepsilon}$. The rate of change of stress with crack length can be expressed in terms of the crack velocity by

$$\frac{d\sigma}{dc} = \frac{d\sigma}{dt}\frac{dt}{dc} = \frac{\dot{\sigma}}{v} \tag{8.19}$$

Assuming power law crack growth kinetics, $v = A K_I^n$, and $K_I = Y\sigma c^{1/2}$ gives

$$\frac{d\sigma}{dc} = \frac{\dot{\sigma}}{AK_I^n} = \frac{\dot{\sigma}}{AY^n\sigma^n c^{n/2}} \tag{8.20}$$

Separating variables and integrating from the initial stress $\sigma = 0$ and initial crack length c_i to the fracture stress σ_f and the crack length when $K_I = K_{IC}$, c_f gives

$$\int_0^{\sigma_f} \sigma^n \, d\sigma = \int_{c_i}^{c_f} \frac{\dot{\sigma}}{AY^n} \frac{dc}{c^{n/2}} \tag{8.21}$$

so that

$$\frac{\sigma_f^{n+1}}{n+1} = \frac{2\dot{\sigma}}{(n-2)AY^n} \left(\frac{1}{c_i^{(n-2)/2}} - \frac{1}{c_f^{(n-2)/2}} \right) \tag{8.22}$$

Taking $c_f^{-(n-2)/2} \ll c_i^{-(n-2)/2}$ and neglecting the term in c_f [equivalent to the approximation $K_{Ii}^{n-2} \ll K_{IC}^{n-2}$ used for deriving Eq. (8.14)] and eliminating c_i using Eq. (8.11) give

$$\sigma_f^{n+1} = \frac{2(n+1)\dot{\sigma}}{AY^2(n-2)} \left(\frac{\sigma_i}{K_{IC}} \right)^{n-2} \tag{8.23}$$

As for static fatigue, this equation can be clarified by substituting the parameter B from Eq. (8.17):

$$\sigma_f^{n+1} = (n+1)B\dot{\sigma}\,\sigma_i^{n-2} \tag{8.24}$$

which shows how the measured strength varies with stress rate and initial/inert strength. The value of n can be determined from a plot of $\ln \sigma_f$ as a function of $\ln \dot{\sigma}$, which will have a slope of $1/(n+1)$, as shown schematically in Figure 8.7(b). Another useful result is the comparison of strengths σ_{f1} and σ_{f2} of two specimens with the same inert strength at two stress rates $\dot{\sigma}_1$ and $\dot{\sigma}_2$:

$$\left(\frac{\sigma_{f1}}{\sigma_{f2}} \right)^{n+1} = \frac{\dot{\sigma}_1}{\dot{\sigma}_2} \tag{8.25}$$

Some precautions concerning the use of these equations are appropriate. First, they hold for specimens with the same inert strength, but this cannot be guaranteed for individual specimens. We show in the next section that Eq. (8.25) holds if the strengths of individual specimens are for the same probability of failure or are replaced with the average strengths at two stress rates. Second, Eqs. (8.23)–(8.25) are based on dropping the term in c_f in (8.22) because it is insignificant compared to the term in c_i. As the stress rate is increased, the measured strength will increase according to (8.23) until this approximation fails. With further increase in stress rate the strength will level off and approach the strength in the absence of subcritical crack propagation, that is, the inert strength σ_i. Requiring that the second term in (8.22) be less than 1% of the first term leads to the condition $(c_i/c_f)^{(n-2)/2} < 0.01$. For $n = 20$ the condition is $c_i/c_f < 0.60$. One could check this by measuring the strength without crack propagation, but this requires an additional experiment of a different type. Alternatively, one can measure the strength at several stress rates and check the linearity of the graph of $\ln \sigma_f$ versus. $\ln \dot{\sigma}$. If the relationship is linear, the use of Eq. (8.25) is justified.

Lifetime predictions are very sensitive to the values of the crack growth parameters (A and n). This sensitivity and precautions in determination of crack growth parameters have been discussed by Jakus et al. (1978) and Ritter et al. (1979, 1981). ASTM standard C 1368-06 (see Chapter 24) describes a standard test method for making dynamic fatigue measurements using constant-stress-rate flexure. It gives further information on the use of the above equations and also describes how to make estimates of the uncertainty in the

calculated fatigue parameters. Given the sensitivity of the reliability predictions to these parameters, a careful error analysis is necessary before the significance of any lifetime prediction can be assessed. ASTM standard C 1465-00 (see Chapter 24) describes similar methods for determining the fatigue parameters at elevated temperatures.

8.6 COMPARISON OF TIMES TO FAILURE UNDER CONSTANT STRESS AND CONSTANT STRESS RATE

In a constant-stress-rate, dynamic fatigue experiment, the time to failure $t_{f,\text{dynamic}}$ and the corresponding stress at failure are related by

$$\dot{\sigma} = \frac{\sigma_f}{t_{f,\text{dynamic}}} \tag{8.26}$$

Using this equation to eliminate $\dot{\sigma}$ from the dynamic fatigue equation (8.24) gives the time to failure for a constant-stress-rate experiment:

$$t_{f,\text{dynamic}} = (n+1)B\frac{\sigma_i^{n-2}}{\sigma_f^n} \tag{8.27}$$

If the same specimen had instead been subjected to the constant stress $\sigma = \sigma_f$, the time to failure under static fatigue $t_{f,\text{static}}$ would be observed. These times to failure can be related by comparing Eq. (8.16) and (8.27):

$$t_{f,\text{dynamic}} = (n+1)t_{f,\text{static}} \tag{8.28}$$

Ceramics in service may be subject to stress that varies with time in a more complicated manner than we have discussed so far. Evans and Fuller (1974) have derived lifetime expressions for subcritical crack propagation under cyclic loading while Jakus and Ritter (1981) have treated time to failure for subcritical crack propagation under arbitrary application of stress as a function of time.

8.7 RELATION OF WEIBULL STATISTICAL PARAMETERS WITH AND WITHOUT SUBCRITICAL CRACK GROWTH

So far in this chapter the discussion has tacitly assumed a single specimen or at least a single initial flaw size. In real situations one must consider the combined effect of a statistical distribution of flaws in each specimen (with resulting statistical distribution of strengths in a set of specimens) and of subcritical crack growth. If the two-parameter Weibull distribution is assumed for strengths and the power law crack growth Eq. (8.5) is assumed, then some simple results incorporating the effects of strength statistics on fatigue can be obtained. We caution, however, that neither of these assumptions is necessarily

correct in real materials; the situation has been considered by Singpurwalla et al. (1995), and a detailed example of combining fracture mechanics and moisture-assisted crack growth to develop a statistical treatment of failure of glass has been given by Fuller et al. (1994). Despite this warning, the relatively simple treatment based on these assumptions is a valuable first approximation and so is presented next.

We assume that the inert strengths of specimens are distributed according to a Weibull distribution with Weibull shape parameter m_i and scale parameter σ_{0i}. The cumulative probability of failure by a stress σ_i is

$$P_f(\sigma_i) = 1 - \exp\left[-\left(\frac{\sigma_i}{\sigma_{0i}}\right)^{m_i}\right] \tag{8.29}$$

If instead the same specimens had been subjected to dynamic fatigue at a constant stress rate $\dot{\sigma}$, then the strengths σ_f that would be obtained are given by Eq. (8.24). Using Eq. (8.24) to substitute for σ_i in the above equation gives

$$P_f(\sigma_f) = 1 - \exp\left[-\left(\frac{\sigma_f^{(n+1)/(n-2)}}{\sigma_{0i}[(n+1)B\dot{\sigma}]^{1/(n-2)}}\right)^{m_i}\right]$$

$$= 1 - \exp\left[-\left(\frac{\sigma_f}{\sigma_{0d}}\right)^{m_d}\right] \tag{8.30}$$

Inspection of this equation shows that σ_f also follows a Weibull distribution with slope and scale parameters m_d and σ_{0d} given by

$$m_d = \frac{n+1}{n-2}m_i \tag{8.31}$$

$$\sigma_{0d}^{n+1} = (n+1)B\dot{\sigma}\,\sigma_{0i}^{n-2} \tag{8.32}$$

Since n is usually much larger than unity, this shows that the Weibull modulus for strength measurements in the presence of slow crack growth, m_d, is modestly higher than for measurements in the absence of fatigue, m_i. No comparative data testing the prediction of Eq. (8.31) are known to the authors.

If for a particular value of the failure probability P_f the strength for a stress rate $\dot{\sigma}_1$ is σ_{f1} and for a stress rate $\dot{\sigma}_2$ is σ_{f2}, then substitution of these values into Eq. (8.30) recovers the earlier result, Eq. (8.25). Although earlier derived in the absence of statistical variation in strength, that equation is valid for the measurements made at the same failure probability. Since it is true for any value of P_f, it is certainly true for the mean strengths, giving

$$\left(\frac{\bar{\sigma}_{f1}}{\bar{\sigma}_{f2}}\right)^{n+1} = \frac{\dot{\sigma}_1}{\dot{\sigma}_2} \tag{8.33}$$

This equation provides a useful way to determine the subcritical crack propagation parameter n from

$$n = \frac{\ln(\dot{\sigma}_1/\dot{\sigma}_2)}{\ln(\bar{\sigma}_{f1}/\bar{\sigma}_{f2})} - 1 \tag{8.34}$$

Another relation of interest in predicting lifetime under conditions of subcritical crack growth is the distribution of times to failure under constant load (Paluszny, 1977; Fett and Munz, 1994; Singpurwalla et al., 1995). Substitution of σ_i in Eq. (8.29) using (8.16) gives the distribution of times to failure:

$$P_f(t_f) = 1 - \exp\left[-\left(\frac{t_f\sigma^n}{B\sigma_{0i}^{n-2}}\right)^{m_i/(n-2)}\right] = 1 - \exp\left[-\left(\frac{t_f}{t_{0s}}\right)^{m_s}\right] \tag{8.35}$$

Inspection of this equation shows that t_f follows a Weibull distribution with slope and scale parameters m_s and t_{0s} given by

$$m_s = \frac{m_i}{n-2} \tag{8.36}$$

$$t_{0s} = \frac{B\sigma_{0i}^{n-2}}{\sigma^n} \tag{8.37}$$

Since n is usually much larger than unity, this shows that the Weibull modulus of the time to failure under static fatigue, m_s, is much smaller than the Weibull modulus of inert strength measurements, m_i. This explains the well-known observation that the distribution of times to failure in static fatigue experiments is very much broader than the distribution of strength measured under inert or dynamic fatigue conditions.

Fett and Munz (1994) develop equations for the time to failure under subcritical crack growth conditions when R-curve behavior is present and for cyclic stress as well as constant stress.

8.8   CONSTRUCTION OF STRENGTH–PROBABILITY–TIME DIAGRAMS

Clearly, if a ceramic component is subjected to stress during service, any subcritical crack growth might limit its useful life. In many applications a component experiences a constant stress so that the static fatigue Eq. (8.15) can be used to assess reliability, where the static stress σ is interpreted as the service stress and the time to failure t_f as the service life. Even for applications where the service stress varies over time, a "worst case" reliability analysis might use the peak service stress for σ so that the static fatigue behavior is still usable. A prediction of the in-service lifetime can be made by extrapolating static

fatigue measurements of time to failure for various values of applied stress. However, static fatigue measurements are generally much less convenient to perform than strength measurements, not the least because, as was seen in the previous section, the variability in the time to failure in a static fatigue measurement is very much greater than the variability in strength measured in a dynamic fatigue experiment. An alternative approach is therefore to use dynamic fatigue measurements (strength measurements at several loading rates) to establish the fatigue parameters and so to predict the behavior under a static stress. Davidge et al. (1973) devised a method of constructing strength–probability–time (SPT) diagrams based on strength data. Such diagrams are useful for assessing reliability since they can, for example, be used to graphically display the probability of failure for any applied service stress and design life. The steps involved in constructing SPT diagrams will now be described. It is useful to illustrate the procedures with some data, which are listed in Table 8.1.

1. The first step is to make a set of strength measurements at two or more stress or strain rates. Table 8.1 lists strength measurements (column 1) made at two different strain rates (column 2). These data are simulated based on a

TABLE 8.1   Data Analysis for Construction of SPT Diagram

Strength	Strain Rate	$t_{f,\text{dynamic}}$	$t_{f,\text{static}}$	Stress for $t_f = 1\,\text{s}$	Stress for $t_f = 100\,\text{s}$	Stress for $t_f = 10^4\,\text{s}$
(MPa)	(s^{-1})	(s)	(s)	(MPa)	(MPa)	(MPa)
258.2	10^{-4}	8.61	0.530	247.7	183.1	135.3
292.6	10^{-4}	9.75	0.600	283.0	209.2	154.6
300.1	10^{-4}	10.00	0.616	290.7	214.9	158.9
314.8	10^{-4}	10.49	0.646	305.9	226.1	167.2
317.7	10^{-4}	10.59	0.652	308.9	228.4	168.8
327.3	10^{-4}	10.91	0.672	318.9	235.7	174.3
336.6	10^{-4}	11.22	0.691	328.5	242.9	179.5
345.4	10^{-4}	11.51	0.709	337.7	249.6	184.5
355.2	10^{-4}	11.84	0.729	347.9	257.2	190.1
370.7	10^{-4}	12.36	0.761	364.1	269.2	199.0
196.2	10^{-6}	654.0	40.3	250.0	184.8	136.6
219.7	10^{-6}	732.3	45.1	282.1	208.5	154.1
226.8	10^{-6}	756.0	46.5	291.8	215.7	159.5
238.5	10^{-6}	795.0	48.9	307.9	227.6	168.2
240.0	10^{-6}	800.0	49.3	309.9	229.1	169.4
246.9	10^{-6}	823.0	50.7	319.4	236.1	174.6
255.3	10^{-6}	851.0	52.4	331.0	244.7	180.9
259.6	10^{-6}	865.3	53.3	337.0	249.1	184.1
266.5	10^{-6}	888.3	54.7	346.5	256.2	189.4
273.3	10^{-6}	911.0	56.1	355.9	263.1	194.5
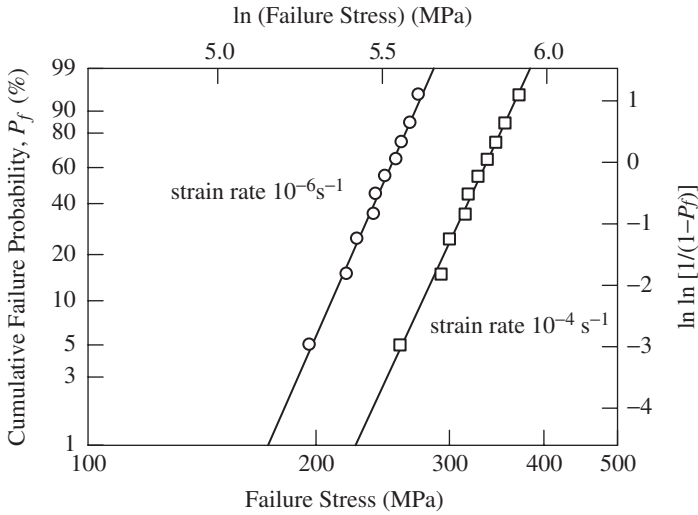
FIGURE 8.8   Weibull plot of simulated dynamic fatigue data at two strain rates.

mean strength of 250 MPa at the slower rate, a Weibull modulus for the strength measurements of $m_d = 12$, and a stress corrosion susceptibility parameter $n = 12$. Figure 8.8 shows a Weibull plot of the data.

2. The strength data are then used to determine the stress corrosion parameter n using Eq. (8.24). Linear regression analysis of the data in Table 8.1 gives $n = 12.24$.

3. The time to failure for each strength measurement is determined from the stress or strain rate using

$$t_{f,\text{dynamic}} = \frac{\sigma_f}{\dot{\sigma}} = \frac{\sigma_f}{E\dot{\varepsilon}} \tag{8.38}$$

Column 3 of Table 8.1 shows the values for the simulated data using Young's modulus $E = 300$ GPa.

4. Equation (8.28) is used to calculate what the time to failure would be under a static applied stress equal to the measured strength σ_f (column 4 of Table 8.1). The result is a distribution of times to failure that would be obtained for a distribution of applied static stresses.

5. For each static failure time $t_{f,\text{static}}$ the constant applied stress σ_{static} is calculated that gives a chosen constant failure time t_{ref} (say, 1 s) by application of Eq. (8.18):

$$\frac{t_{f,\text{static}}}{t_{\text{ref}}} = \left(\frac{\sigma_{\text{static}}}{\sigma_f}\right)^n \tag{8.39}$$
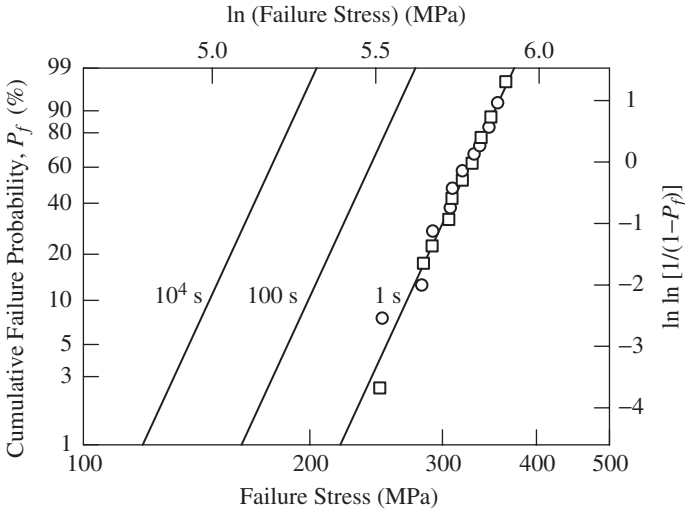
FIGURE 8.9   Weibull plot of data in Table 8.1 for stresses giving times to failure of 1, 100, and 10^4 s.

The results for the simulated data are shown in column 5 of Table 8.1. They represent a distribution of applied stresses that lead to a given time to failure. These data can then be graphed in a Weibull plot as shown in Figure 8.9. If the data follow a Weibull distribution, a straight line can be drawn through them as shown in the figure. An unbiased maximum-likelihood method for calculating the Weibull modulus gives $m = 12.0$.

6. The distribution of applied stresses that lead to any other chosen time to failure can be calculated from the stresses for 1 s using Eq. (8.18). For example, columns 6 and 7 of Table 8.1 show the stresses calculated for failure times of 100 and 10^4 s based on the simulated data. Again, the results can be graphed on a Weibull plot, although for clarity it is useful to show only the lines fitted to the data, as in Figure 8.8. Manipulation of Eq. (8.18) gives

$$\ln \sigma_2 - \ln \sigma_1 = \frac{1}{n} \ln \left(\frac{t_{f1}}{t_{f2}} \right) \tag{8.40}$$

which shows that the lines for different failure times are all parallel since Eq. (8.40) represents a shift along the $\ln \sigma$ axis. Also, the lines for equal factors in time will be equally spaced on the Weibull plot.

The resulting SPT diagram can be used to evaluate reliability for any chosen failure time. The probability of failure can be found for any service stress, or conversely, the maximum permitted service stress can be found that gives a specified survival probability. The SPT diagrams can be shown in other forms. In step 5, instead of calculating the stress for a given time to failure, the time to

failure could be calculated for a given applied stress. The resulting SPT diagram shows a family of lines for different service stresses which can be used, for example, to determine the failure rate during the life of a component. Also, graphs of ln(stress) versus ln(time) can be generated with a family of lines that represent the *loci* of equal failure probability.

The SPT diagrams can also be calculated more directly by eliminating the parameter B from the static and dynamic fatigue Eqs. (8.16) and (8.24) to give

$$\frac{\sigma_f^{n+1}}{(n+1)\dot{\sigma}} = t_f \sigma^n \qquad (8.41)$$

For each measurement of a set of measurements of strength at various stress rates, $\{\sigma_f, \dot{\sigma}\}$, the static stress for a given time to failure can be calculated (or the time to failure for a given static stress). The resulting distribution can be graphed on a Weibull plot. Equation (8.41) shows the interesting result that only the stress corrosion parameter n needs to be known to make reliability estimates based on SPT diagrams, but not the parameter B [or equivalently the factor A in the kinetics equation (8.5)]. This illustrates the central importance of the value of the stress corrosion parameter n in making reliability predictions.

The methods described here for constructing SPT diagrams are a little different from those devised by Davidge et al. (1973). In their work the Weibull modulus m was in effect determined from the distribution of a number of strength measurements made at the same stress rate and the value of m was then used to determine the width of the distribution in the SPT diagrams. Here, m is in effect determined from all the data in the SPT diagram itself. This approach has some advantages:

1. It pools all the strength data to determine the underlying statistical distribution of strength, rather than a subset for one stress rate.
2. It does not require that a large number of measurements be made at one stress rate.
3. It does not rely on the data following a Weibull distribution—the data points in Figure 8.9 show the estimated form of the distribution which could deviate significantly from the Weibull distribution.

Care should be taken in making reliability assessments based on SPT diagrams or indeed based on any method. Such estimates usually involve characterizing the strength and fatigue behavior based on measurements of strength made on a conveniently short timescale. However, reliability is usually needed over much longer timescales so that reliability predictions frequently involve a considerable amount of extrapolation, with all the well-known attendant dangers. Also, the methods described here are based on power law crack growth kinetics, Eq. (8.5). While mathematically convenient, this model is empirical and is not based on any physical model. Physical models, such as the Charles and Hillig (1962) model, are generally based on reaction rate theory and so result in exponential or nearly exponential subcritical crack growth

kinetics. Jakus et al. (1981) show that extrapolations based on exponential models can predict significantly shorter lifetimes than those predicted by the power law. For critical applications, predictions based on the power law should be avoided or at least treated with considerable circumspection. The exponential forms are less convenient to deal with since the fatigue equations require numerical integration. However, with some effort the needed calculations can be made. For example, Matthewson (2006) has demonstrated how to calculate SPT diagrams for exponential forms of the crack growth kinetics.

8.9 PROOF TESTING TO GUARANTEE MINIMUM LIFE

Proof testing, as described in the previous chapter, can be used to ensure a minimum strength by discarding specimens weaker than the proof stress. However, the situation is complicated by the subcritical crack growth that will occur during application of the proof stress. In particular, all surviving specimens are weakened by proof testing, albeit by a small amount in most cases. It is also necessary to examine the meaning of "minimum assured strength" in this case.

If a proof stress σ_p is applied to each specimen for a short time and then unloaded very rapidly, any crack in the component will grow from its initial length c_i to a final value c_p. If the proof stress applied to the final crack length produces a stress intensity K_{Ip}, those that survive will experience a final stress intensity less than the critical value, that is,

$$K_{Ip} = \sigma_p Y c_p^{1/2} < K_{IC} \tag{8.42}$$

For specimens that only just survive, $K_{Ip} = K_{IC}$. Examination of Eq. (8.42) shows that the instantaneous strength of the very weakest specimen that can survive proof testing will be σ_p. Therefore proof testing to a proof stress σ_p assures minimum *inert* strength equal to σ_p; the strength after proof testing determined under ambient conditions can be less than σ_p due to additional subcritical crack growth during loading.

A "worst case" reliability analysis can be performed by considering the behavior of the weakest specimen surviving proof testing. The minimum time to failure under a service stress σ_s can be obtained by setting the applied stress to $\sigma = \sigma_s$ and $\sigma_i = \sigma_p$ in the static fatigue Eq. (8.15), giving

$$t_{\min} = \frac{2}{A\,Y^2(n-2)K_{IC}^{n-2}\,\sigma_s^2}\left(\frac{\sigma_p}{\sigma_s}\right)^{n-2} \tag{8.43}$$

This equation gives a straight line with slope –2 on a plot of ln t as a function of ln σ_s for each value of σ_p/σ_s. By superimposing a series of lines for different values of the σ_p/σ_s ratio, it is possible to read off the needed proof stress that ensures a given lifetime for a given service stress. Further, additional lines can be superimposed for different failure probabilities for the specimens prior to

proof testing, as described in the previous section. Provided there is negligible strength loss during proof testing (very short duration proof test or proof testing in inert environment), the intersection of these lines of constant probability with the lines of constant σ_p/σ_s can be used to estimate the failure rate during proof testing (Davidge, 1979).

An important caution is that the above considerations assume that the proof test does not cause crack growth during unloading so that fast unloading or inert conditions must be used. If there is some crack growth during unloading, the minimum assured inert strength is somewhat lower than σ_p. A further difficulty with proof testing is that the stress state imposed in the proof test should duplicate that in service. This is difficult to do for complex shapes and loadings. For example, a turbocharger rotor can be proof tested by spinning at an angular velocity exceeding that to be used in service. This procedure gives a good simulation of the service stresses caused by centrifugal force, but simple spinning does not duplicate the additional stresses caused by the gas pressure exerted on the rotor blades during service and so is not a fully faithful proof test. Despite this shortcoming, spinning has been used successfully as a proof test for turbocharger rotors (Matsui et al., 1986).

Jakus (1986, p. 202) has reviewed proof testing and given the following summary:

> Proof testing is a widely used, viable tool for increasing product reliability of many glass and ceramic components. It is, however, a technique whose practical benefits can be diminished by fatigue, unfortunately a rather common strength degradation phenomenon in glass and ceramic materials. To realize the greatest benefits from proof testing, good ''proof-test control'' must be maintained: Fatigue during the test must be minimized, either by providing a dry, inert environment or by using fast loading and very fast unloading rates. If fatigue is eliminated, the after-proof distribution becomes truncated; hence, a minimum strength is ensured, and furthermore, the strength distribution also substantially improves. In fatigueless cases, the proof-test theory predicts the experimental results very well. When fatigue becomes significant, one can no longer ensure a minimum strength for the survivors, although the strength of the population as a whole still may be substantially improved by proof testing. When very severe fatigue conditions exist, proof testing may not be beneficial, and proof-test theory is ill-equipped to predict the outcome. Although eliminating fatigue during proof testing may not be a trivial task in many industrial environments, it may nevertheless be necessary in critical applications, since it is perhaps the only way of ensuring ceramic-component reliability.

8.10   SUBCRITICAL CRACK GROWTH AND FAILURE FROM FLAWS ORIGINATING FROM RESIDUAL STRESS CONCENTRATIONS

Fuller et al. (1983) have considered subcritical crack growth under circumstances where local residual stress modifies crack growth. In particular, they

considered failure from flaws caused by hardness indentations. Their treatment is an extension of the earlier work of Lawn and his collaborators on hardness indentations summarized in Section 8.6. They found that if power law crack growth kinetics are assumed, giving the time to failure under constant stress by Eq. (8.15), then the corresponding behavior of the crack in the presence of a residual stress shows approximately the same form as (8.15) for large n but with an apparent stress corrosion susceptibility parameter n' given by

$$n' = \frac{rn + 2}{r + 1} \tag{8.44}$$

where $r = 1$ for "line" flaws and $r = 3$ for "point" flaws; the crack will exhibit power law fatigue whether or not a residual stress is present. A general conclusion from this work is that experiments on delayed failure from subcritical crack growth will show the same characteristics for cracks subject to residual stress and for cracks free of such stress. Thus the tests themselves do not distinguish between the two conditions despite the fact that a different interpretation of the parameters obtained is appropriate for the two cases. These authors discuss the use of tests at constant strain rate to obtain slow crack propagation parameters for use in lifetime prediction. The reader considering the use of data obtained in dynamic tests for the purpose of lifetime prediction should consult their discussion, which is too long to summarize here. Suffice to say, residual stresses are frequently encountered due to handling damage, machining, polishing, thermal stress, and so on, so their potential impact on reliability assessments must be considered.

8.11   SLOW CRACK PROPAGATION AT HIGH TEMPERATURE

Until now, the discussion in this chapter has examined subcritical crack propagation at and near room temperature at which environmentally assisted subcritical crack propagation appears to be the major mechanism. Other mechanisms are possible and a variety of theories have been developed (Evans and Dalgleish, 1987). It appears that some of the other mechanisms do have practical importance in creep rupture at high temperatures. Chuang et al. (1986) have examined kinetic theories of these mechanisms and have compared their predictions to experiments on α-silicon carbide. They classify the mechanisms underlying these theories into three types: bond breaking, chemical corrosion, and matter transport. The Charles–Hillig theory, discussed earlier, is of the second type. Kinetic theories of crack growth typically lead to the possibility of crack healing below a threshold value of the applied stress intensity factor and so predict a threshold value K_{th} below which static fatigue should not take place. Several theories of diffusive crack growth exist; that of Chuang (1982) appears to be in reasonable agreement with experiment. His theory gives a threshold stress intensity factor for diffusive crack growth greater than the stress intensity

TABLE 8.2   Predicted and Experimental Values of K_{th} in MPa $\cdot$ m$^{1/2}$ for SiC at 1200°C

Mechanism	K_{th}/K_G	Hot-Pressed α-SiC	Oxidized Sintered α-SiC	As-Machined Sintered α-SiC
Bond breaking	1.0	0.752	0.711	0.564
Chemical corrosion	0.61	0.459	0.433	0.344
Matter transport	1.69	1.271	1.201	0.954
Experimental results		2.25	1.75	2.25

[a] *Source*: From Chuang et al. (1986).

factor for a crack not modified by this process. Table 8.2 gives the theoretical lower limit values and the experimental values from Chuang et al. (1986). Column 2 gives the predicted values of K_{th}/K_G, where

$$K_G = \left(\frac{E(2\gamma_s - \gamma_{gb})}{1 - \nu^2} \right)^{1/2} \tag{8.45}$$

is the Griffith value for a grain boundary crack. Chemical corrosion, as expected, gives a threshold value below the Griffith value. The observed threshold is well above the Griffith value, leading the authors to the conclusion that matter transport (i.e., diffusive growth of the crack) is the controlling mechanism for the materials and conditions studied. The fact that the experimental values are considerably greater than the predicted values is rationalized by the authors as being due to effects of crack deflection and shielding.

It should be noted that at values below K_{th} an infinite life is not to be expected. Instead, the process of cavity formation (not considered in the above kinetic theories) would presumably come into play at long times and lead eventually to failure for values of K above a cavitation threshold.

Yavuz and Tressler (1993) used static fatigue tests to determine K_{th} for a fully dense α-SiC hot isostatically pressed (HIPed) without additives and for a pressureless sintered α-SiC, which contained aluminum as a sintering aid. Chemical vapor deposition (CVD) SiC also exhibited delayed failure at 1300 and 1400°C but a reliable K_{th} could not be determined for this material because of scatter in the data. Table 8.3 shows the comparison of observed values with predictions of Chuang's theory. The agreement is good at 1300 and 1400°C for the sintered material. There was evidence of a damage process concurrent with slow crack growth at 1400°C. For the HIPed material, static loading below the threshold stress intensity strengthened the material at 1300 and 1400°C probably by a stress relaxation mechanism at the crack tip in the viscous silica phase present along the grain boundaries and some of the triple-grain junctions.

TABLE 8.3   Comparison of Observed K_{th} in MPa · m$^{1/2}$ with Values Predicted by Chuang's Model

Temperature (°C)	Sintered		HIPed	
	Predicted	Observed	Predicted	Observed
1200	2.00	3.3	2.13	3.1
1300	1.97	2.2	2.10	2.7
1400	1.94	1.7	2.03	2.2

[a] *Source*: From Yavuz and Tressler (1993).

PROBLEMS

1. The time to failure of an alumina specimen at room temperature in air at 40% relative humidity under 290 MPa tensile stress is 42 min and at 250 MPa the time to failure is 200 h.

   a. What is the subcritical crack propagation parameter n?

   b. What is the time to failure under 200 MPa and the same conditions?

   c. What is the maximum stress level to give 100 years life under constant stress under these conditions?

2. The measured failure stresses of an alumina with Young's modulus 410 GPa at various constant strain rates at room temperature in air at 40% relative humidity are as follows:

Strain rate, s^{-1}	0.003162	0.0001	0.000316	0.001	0.01	0.031623	0.1
Failure stress, MPa	343	301	313	330	356	377	390

   a. Calculate the stress corrosion susceptibility parameter n.

   b. If a stress of 301 MPa were instantly applied and held constant, what failure time would you expect?

3. Silicate glass specimens are subjected to a series of static applied stresses. The following table shows the median failure times for each stress level:

Stress, GPa	2.78	2.74	2.70	2.66	2.63	2.57
Median time to failure, min	1.58	8.5	114	1,090	3,740	93,700

   a. Calculate the stress corrosion susceptibility parameter n. Include an estimate of the uncertainty in your value.

   b. Calculate the stress that gives 25 years median lifetime. Include an error analysis.

    c. If the times to failure exhibit a Weibull distribution with modulus $m = 2.3$, calculate:
       i. Maximum allowed service stress that gives a failure rate of less than 1% in 25 years
      ii. Maximum allowed service stress that gives a failure rate of less than 0.01% in 25 years

4. a. The mean strength of a glass component is found to be 544 MPa when the loading rate is 2.76 MPa/s and 724 MPa when the loading rate is 2.179 GPa/s. What is the stress corrosion parameter n?

    b. For the same component, what constant service stress would give a mean time to failure of 25 years?

    c. While making the strength measurements it was noticed that the specimens exhibited a large amount of scatter in their strength. The components are to be used in a critical application requiring 25 years design life. In order to completely ensure survival of the components, they are proof tested by applying a short pulse of stress of magnitude 700 MPa followed by rapid unloading. Failing components are discarded. The mean strength of the components before proof testing is 2.1 GPa when testing rapidly in a dry environment (i.e., under inert conditions). What is the maximum allowable service stress that would ensure survival of all components for 25 years?

5. In static fatigue experiments in a humid environment, the time to failure is 1 h when measured under a constant stress of 800 MPa and 100 h for a stress of 600 MPa.What is the stress corrosion parameter n? What is the maximum stress σ_1 that this material could withstand for 100 years under the same conditions of environment and temperature? In the application, the humidity could be higher than in the laboratory measurements. Calculate the maximum permitted stress σ_2 for 100 years survival in an environment in which the humidity is doubled (you may assume that the preexponent A is proportional to humidity).

6. The fatigue parameter for fused silica optical fiber is $n = 20$. In static fatigue experiments in bending, the mean time to failure is 251 s for an applied stress of 3.244 GPa. The intrinsic or inert strength measured in bending under completely dry conditions is 12.0 GPa.

    a. What is the maximum applied stress that ensures survival for 40 years?

    b. Unfortunately, the answer to (a) is very optimistic—optical fiber has occasional very weak defects which are unlikely to be encountered in the bending experiments. It is therefore decided to proof test the fiber at 0.7 GPa to remove the worst defects. What is the maximum applied stress that would ensure survival for 40 years even for the weakest defects surviving proof testing?

9

STABLE CRACK PROPAGATION AND *R*-CURVE BEHAVIOR

9.1   Introduction
9.2   *R*-Curve (*T*-Curve) Concept
9.3   *R*-Curve Effects of Strength Distributions
9.4   Effect of *R* Curve on Subcritical Crack Growth
      Problems

9.1   INTRODUCTION

As discussed in previous chapters, the Griffith theory and its extension by Irwin and others lead to the conclusion that a crack in a body under uniform stress far from the crack will propagate catastrophically for values of this stress slightly exceeding a critical value given by

$$\sigma_f = \frac{K_{IC}}{Yc^{1/2}} \tag{9.1}$$

where K_C is the critical stress intensity factor, c is the appropriate crack size, and Y is a geometric factor. In the Griffith theory the crack will be stable under σ_f and will heal for smaller stress values. The predicted healing effect is usually ignored on the grounds that various effects such as crack surface contamination prevent it in practice although a freshly extended crack can show some degree of healing when the stress is removed. The point of interest here is that the Griffith theory as discussed to this point does not allow stable crack propagation; once the critical stress is exceeded, the crack extends indefinitely. There is, of course, the phenomenon of subcritical crack propagation behavior, as

discussed in Chapter 8. This subcritical crack propagation is associated with transport effects such as diffusion of water and stress-assisted chemical attack. This category of subcritical crack growth introduces concepts outside the basic Griffith theory and is not the subject of the present chapter. Without introducing such effects it is still possible to have stable crack propagation within the conceptual framework of the Griffith theory under appropriate circumstances. There are two fundamentally different sets of such circumstances: (1) combinations of specimen geometry and details of load application that lead to a decreasing applied stress intensity factor as the crack elongates and (2) in materials that exhibit a critical stress intensity factor that is not constant but increases faster than the applied stress intensity factor increases as the crack elongates (i.e., in materials that show *R*-curve behavior). In practice, both effects can act together, but it is convenient to separate them for discussion.

The first category of changing stress in a material of constant critical stress intensity factor is certainly important and is the basis for methods of creating a controlled crack such as forcing a wedge into a slot. It is, however, the second category that has become of great importance in designing microstructures to produce high toughness in ceramics and that is the subject of this chapter. Discussion of the microstructural effects producing *R*-curve behavior is left primarily to subsequent chapters. The present chapter concentrates on formulating the concept of *R*-curve behavior and reviewing some of the evidence for the existence of the effect.

The *R*-curve concept arose from studies of fracture in metals and alloys in the 1960s as described by Broek (1986) and was later applied to ceramics (Huebner and Jillek, 1977; Knehans and Steinbrech, 1982; Marshall, 1986). Particularly striking effects occur in transformation-toughened ceramics (Swain and Hannink, 1983; Heuer, 1987; Lutz et al., 1991a) and in fiber-reinforced ceramic–ceramic matrix composites and will be discussed in later chapters. There is some difference in the notation used by various authors. In particular, Lawn (1993) has advocated the use of the term *T* curve (i.e., toughness curve) to emphasize the distinction between applied stress intensity factor and the critical stress intensity factor of the material. Butler and Fuller (1993) summarize what is apparently becoming standard usage in speaking of *R*- or *T*-curve behavior: to use the *R* curve when the effect is discussed in terms of strain energy release rate and the *T* curve when the discussion is in terms of stress intensity factor. The distinctions are summarized in Table 9.1. The

TABLE 9.1   Summary of Terms Used for Describing *R* Curves

General Description	Applied Critical Driving Force for Crack	Materials Resistance
Stress intensity factor	K_{IC}	T
Energy release rate	G_{IC}	R

R-curve notation is used here for the general effect and the *R*-versus-*T* distinction is used for the corresponding specific descriptions. It should be noted, however, that the *R*-versus-*T* distinction has not yet become universal in the literature on ceramics; the term *R* curve is still used for the description of crack-length-dependent toughening behavior by some authors.

9.2   *R*-CURVE (*T*-CURVE) CONCEPT

We begin the discussion in terms of the crack extension force G, the crack resistance R, the stored elastic energy U_e, the energy associated with the crack U_s, and the crack length c (Broek, 1986; Butler and Fuller, 1993). As discussed in Section 5.6, these are defined by

$$G = -\left(\frac{dW}{dc} + \frac{dU_s}{dc}\right) \quad \text{and} \quad R = \frac{dU_s}{dc} \tag{9.2}$$

Here we have taken the crack area as $A = ct$ and taken the thickness t as unity. The energy condition for crack propagation is

$$G \geq R \tag{9.3}$$

where the equality is a condition of balance and slight excess causes catastrophic propagation. To guarantee that an excess of driving force persists as the crack extends, the additional condition

$$\frac{dG}{dc} \geq \frac{dR}{dc} \tag{9.4}$$

is required. We examine the meaning of these conditions in graphical form beginning with the case of a constant crack resistance, as shown in Figure 9.1. The upper portion of this figure shows G and R plotted as a function of crack length, where G is given by

$$G = \frac{Y^2 \sigma^2 c}{E} \tag{9.5}$$

for plane stress σ. Thus G increases linearly with crack length for a particular applied stress. The G line has been drawn for a stress value just large enough to give $G = R$ at the initial crack length c_i. The crack will be unstable and will propagate under the slightest increase in crack length or stress because the other condition, $dG/dc > dR/dc$, is satisfied. It is convenient to draw this diagram with the origin taken at the initial crack tip, as in the lower portion of Figure 9.1. In this case G curves for two different initial crack lengths, c_{i1} and c_{i2} are shown. Different values of stress have been taken so that either crack is just in balance and would propagate catastrophically for any slight disturbance.
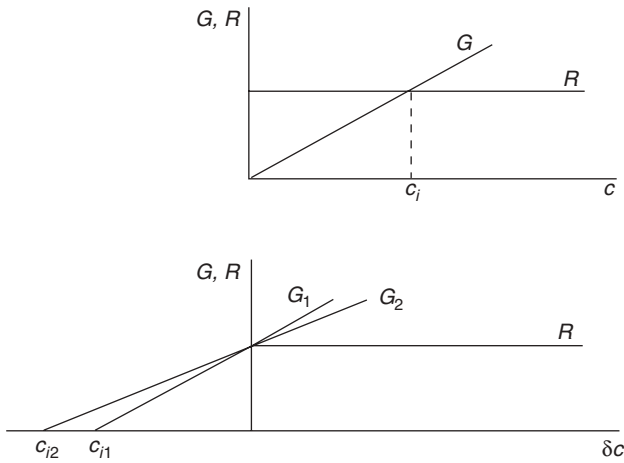
FIGURE 9.1   Representation of energy balance with constant resistance.

We can use a second drawing to illustrate behavior for the case in which the resistance increases as a crack grows from its initial length. This is a common and very important case in polycrystalline ceramics and ceramic–ceramic composites and can arise from crack shielding and crack bridging, as discussed in Chapter 10. For the moment we omit discussion of the causes of R-curve behavior and focus on the effects on crack propagation. Figure 9.2 shows a rising R curve. The G_1 curve is drawn for a stress such that $G_1(c_i) = R(c_i)$. However, as is evident from the drawing, $dG_1/dc < dR/dc$, and so the crack will not extend. For a somewhat higher value of stress the curve G_2 exceeds the

FIGURE 9.2   Representations of energy balance with increasing resistance.

initial crack resistance so that the crack will extend an amount δc such that $G_2(c_i + \delta c_2) = R(c_i + \delta c_2)$. The crack will not extend further because $dG_2/dc < dR/dc$ at this point. Thus the existence of a rising R curve can lead to a region of stable crack propagation under stress.
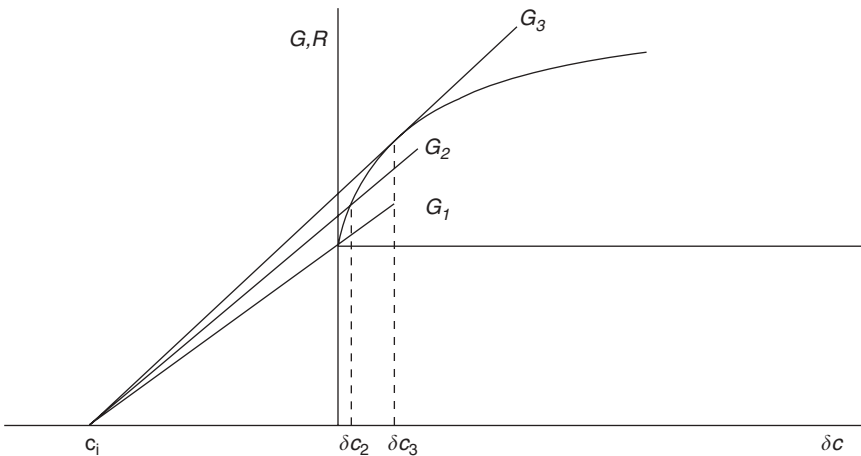
Further increase in stress leads eventually to the G_3 curve, which is tangent to the R curve. The crack will extend from its initial length to $G_2(c_i + \delta c_3) = R(c_i + \delta c_3)$ but will continue extending catastrophically because at the point of tangency $dG/dc = dR/dc$.

There is thus a region of stable crack propagation for stresses between the lines and G_1 and G_3.

We now turn to a description of the same behavior in terms of the applied stress intensity factor K, that is, to T-curve behavior. In a material without microstructural features (such as an ideal glass) the value of the stress intensity factor required for crack propagation is a constant independent of crack length and can be written as

$$T = K_{IC} = K_0 \tag{9.6}$$

In ceramics with microstructural features an advancing crack interacts with the microstructure. It is the interaction in the wake of the crack that causes the rising R curve. The crack resistance rises as the crack lengthens and increases the number of bridges behind the crack tip. Steinbrech et al. (1990) experimentally showed that the length of this interaction zone in the wake of the crack determines the crack resistance. By cutting away the interaction zone with a diamond saw, the crack resistance was reduced (see Chapter 10). Figure 9.3 illustrates that the rate of growth of the R curve decreases as the crack gets longer. The crack-opening displacement increases with increasing distance from
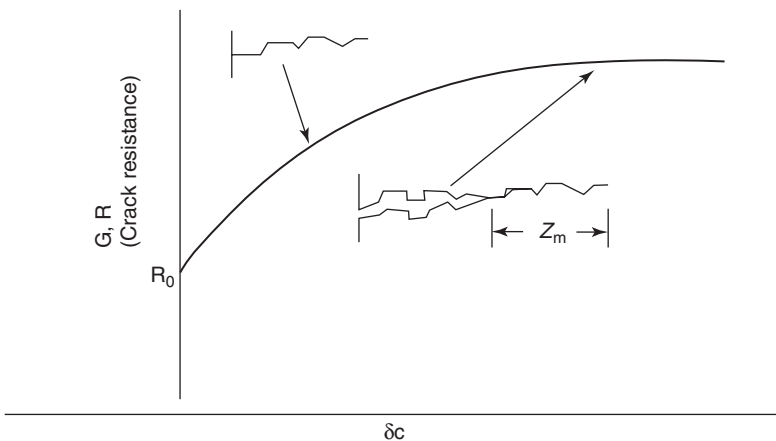

FIGURE 9.3   Crack resistance plateaus as interaction zone is broken.

the crack tip. At some distance from the crack tip bridging ligaments break, and then with further crack growth the length of the interaction zone, z_m, does not change. A variation of this process may occur with different types of crack wake zones and will be discussed in future chapters.

One can take two views as to how to describe why crack resistance rises. In the first view, the stress intensity factor required to propagate a planar crack remains the same but the local stress intensity acting at the crack tip is no longer that calculated from a simple equation of the type

$$K = Y\sigma c^{1/2} \tag{9.7}$$

where σ is the uniform tensile stress at a long distance from the crack caused by external forces on the ceramic specimen. Instead, the applied stress intensity factor at the crack tip is also affected by internal stresses caused by the interaction of the crack with the microstructure as the crack advances. The crack tip is said to be shielded by the interaction processes and the resulting internal stresses. In other words, the toughness is regarded as unchanged in this first view and the effect of microstructural interaction is taken as a change in the local applied stress intensity factor.

It is found to be useful to consider the same effects in terms of a different description. In this second view, the applied stress intensity factor due to the external loads alone is considered to be the effective driving force for crack propagation and the internal stresses arising from the interaction of the advancing crack with microstructure are regarded as changing the toughness of the material by an amount K_μ. The stress intensity factor required for crack propagation changes as the crack length increases and can be written as

$$T = K_0 + K_\mu = T(c) \tag{9.8}$$

The conditions for fracture are analogous to those involving G and R and are

$$K \geq T \qquad \text{and} \qquad \frac{dK_a}{dc} = \frac{dT}{dc} \tag{9.9}$$

A plot analogous to Figure 9.2 but in terms of K and T is shown in Figure 9.4. Following a suggestion by Evans, the arc tangent function has been used to represent the T curve. Although experimental data sometimes indicate a flatter T curve, the arc tangent provides a useful qualitative illustration (Heuer, 1987). The T curves of Figures 9.4–9.6 are given by

$$T = 6 + 6\tan^{-1}\left(\frac{\delta c}{10}\right) \tag{9.10}$$

where T is in $\mathrm{MPa \cdot m}^{1/2}$ and δc is crack extension in micrometers.

Two K curves in Figure 9.4 (*A* and *C*) for stress values (390 and 552 MPa, respectively) chosen so that K passes through the initial T value are given for
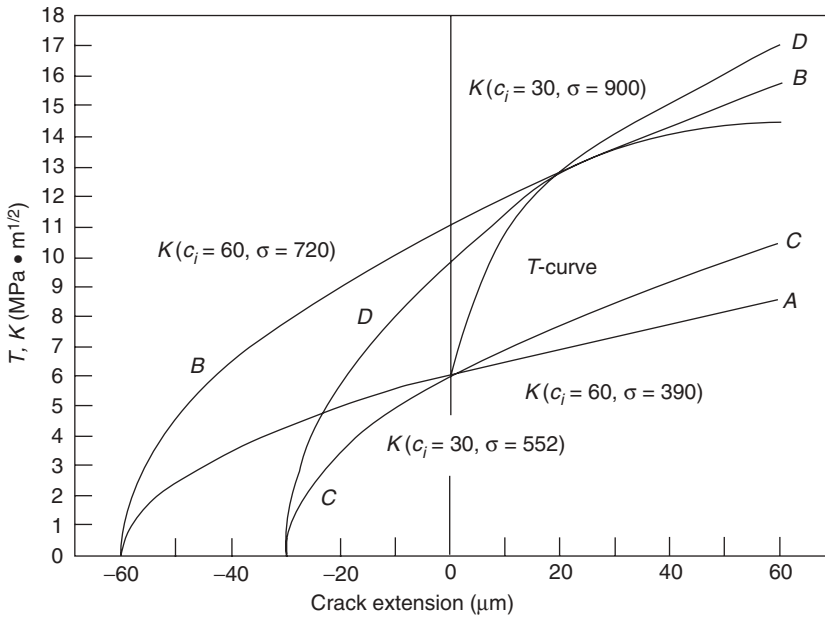
FIGURE 9.4   *T*-curve in *K* linear format with linear crack length scale.
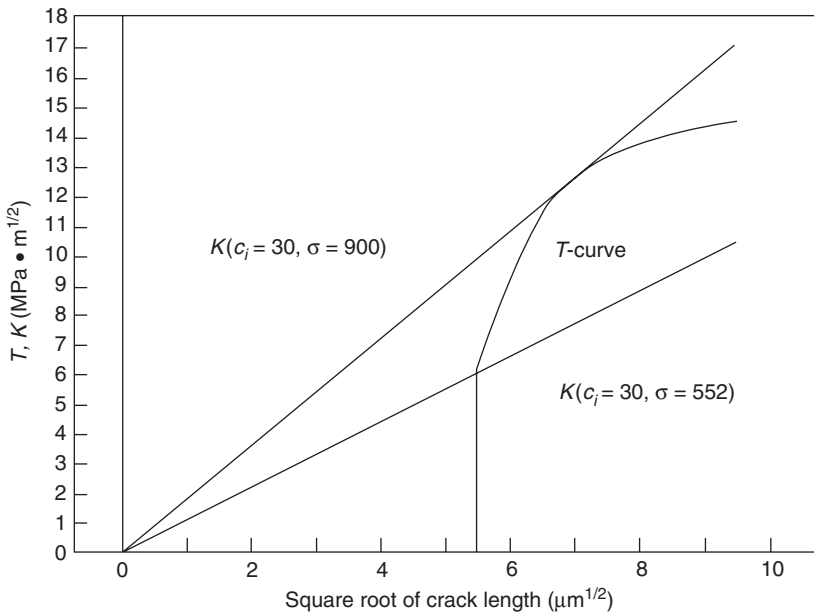

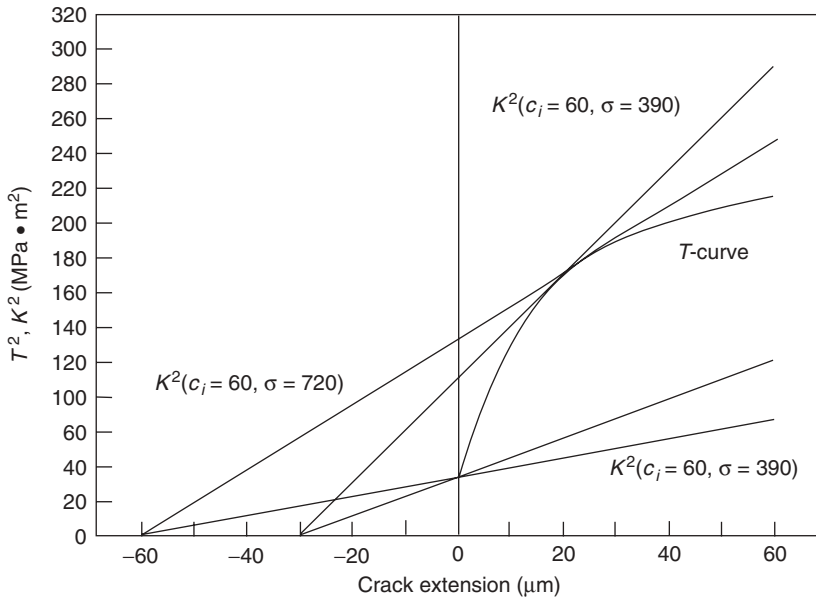**FIGURE 9.5**   *T*-curve in *K* linear format with square-root crack length scale.

FIGURE 9.6   *T*-curve in K^2 format with linear crack length scale.

two values of initial crack length (60 and 30 μm, respectively). Under these conditions the crack will not propagate because $dK/dc < dT/dc$. Two other K curves (*B* and *D*) for the same initial crack lengths but for higher stress values (720 and 900 MPa, respectively) such that the K curves are tangent to the T curve are also shown. For the latter conditions the crack will propagate catastrophically. For intermediate stress values (390–720 MPa for the 60 μm initial crack length and 552–900 MPa for the 30 μm initial crack length), some stable crack propagation would occur.

The plot of Figure 9.4 is not the best format because the K curves are not linear. Two ways to linearize the K curves are shown in Figures 9.5 and 9.6. In Figure 9.5 the abscissa is taken as the square root of the crack length and the resulting linear K curve is shown for the values of stress bounding the range of stable crack propagation. In Figure 9.6 the ordinate is taken as T^2 and K^2 and the abscissa as crack length so that the curve of K^2 is linear. The representation of Figure 9.6 is perhaps most useful because the origin can be taken at the initial crack tip so that curves for two initial crack lengths can be placed on the same plot as shown. Again the K^2 curves are drawn for the values of stress bounding the region of stable crack propagation.

It should be noted that more complex R and T curves may exist leading to more complex behavior. In particular, cracks below a certain initial length may be unstable under the action of internal stresses arising from thermal expansion differences between grains in a polycrystalline ceramic but then become stable again. In this case the crack is believed to "pop in" to a certain length

corresponding to a short initial portion of decreasing R and T curves before the subsequent increase. Butler and Fuller (1993) give examples of such curves.

9.3   *R*-CURVE EFFECTS OF STRENGTH DISTRIBUTIONS

We learn from Figure 9.2 and the subsequent discussion that the size of the flaw that ultimately results in unstable crack growth and failure is altered by the R curve. Since the Weibull distribution in ceramics is a measure of the critical flaw size distribution, the shape of the R curve as well as the initial flaw size distribution will determine the Wiebull parameter m. Kendall et al. (1987) considered the effect of the R-curve behavior on the Weibull parameter m; their work was extended by Cook and Clarke (1988) and Shetty and Wang (1989). Kendall et al. (1987) concluded that increasing the toughness of a material to a higher value, which was still not dependent on crack length, did not change the m value. Only when there was R-curve behavior did the Weibull modulus increase, as in the cases of transformation toughening or toughening by reinforcement with ceramic fibers. They developed a model for the effect of R-curve behavior on the Weibull modulus by representing the variation in toughness with crack length over a measured range of crack lengths as

$$K_{\mathrm{IC}} = A_K \, (\delta c)^n \tag{9.11}$$

where we have introduced subscript K to distinguish from the parameters in the empirical crack velocity law (8.1). According to their model the Weibull modulus m_R for material with R-curve behavior in terms of that for the same material without R-curve behavior m is given by

$$m_R = m \frac{0.5}{0.5 - n_K} \tag{9.12}$$

Li and Yamanis (1989) reported on a silicon nitride with R-curve behavior $m_R = 18.5$ and $n_K = 0.221$, with the latter determined by indented-strength measurements. They compared this to another silicon nitride without significant R-curve behavior and $m \approx 10$. The model of Kendall et al. (1987) gives a predicted ratio of $m_R/m = 1.79$, in good agreement with the directly measured ratio of 1.8.

   A caution in regard to attempting to improve reliability through an R-curve effect is provided by the work of Kovar and Readey (1994). Grain bridging has been identified as a mechanism for toughening polycrystalline alumina. These authors studied aluminas with grain sizes of 5, 16, and 27 μm. Increasing the grain size was found to give enhanced flaw tolerance caused by a rising R curve. However, no reduction in strength variability was found with increasing grain size.

9.4   EFFECT OF *R* CURVE ON SUBCRITICAL CRACK GROWTH

Fett and Munz (1992) have studied subcritical crack growth in polycrystalline alumina using an edge-notched beam with constant load and have provided a summary of references to earlier work showing *R*-curve effects on subcritical crack growth. They found that despite a monotonically increasing value of the externally applied stress intensity factor with time due to crack growth, the crack velocity actually decreased with time during a portion of the experiment. They attribute this behavior to crack shielding in these materials that exhibit strong *R* curves (see Problem 7). Evidently the life prediction techniques given in Chapter 8 for subcritical crack growth cannot be applied without modification to materials with strong *R*-curve behavior.

PROBLEMS

1. Stable crack growth:
   a. What differentiates subcritical crack growth from stable *R*-curve crack growth?
   b. For a rising *R* curve the value of the critical stress intensity factor acting at the crack tip does not change with crack length. Explain this on an atomistic level.

2. In the double-cantilever beam specimen a wedge is driven into the end of a several-centimeter-long crack. (See Chapter 6.) This type of loading is constant displacement rather than constant stress. Using an *R*-versus-*c* curve explain why the crack grows by stable crack growth even if *R* (or *T*) is almost constant?

3. The area under the stress–strain curve of a tensile specimen could be used to determine the fracture energy per unit volume (ε times σ has units of energy over volume) but only when crack growth and fracture are entirely by stable crack growth. Why only then?

4. The *R* curve for a ceramic follows the equation $R = 60 + 1000\delta c^{0.3}$ (δc is in meters). Solve both graphically and analytically for the strength if $c_i = 60\,\mu\text{m}$. Assume a central through crack, plane stress, and $E = 400\,\text{GPa}$.

5. Two different specimens with entirely different microstructures and different *R* curves yield the same toughness of $\sim 80\,\text{J/m}^2$. In the strength test the initial largest flaw is $c = 40\,\mu\text{m}$ (central through cracks) in both specimens. Yet their strength is different since the shape of the *R* curve is different. The shapes of the *R* curves for specimens A and B are described by the following two equations:

$$R = 30 + 60[1 - \exp(-8 \times 10^4 \delta c)] \quad \text{(material A)}$$

$$= 20 + 60 \tan^{-1}\left(\frac{\delta c}{6 \times 10^{-5}}\right) \qquad \text{(material B)}$$

where G and R are in joules per meters squared and δc, the crack extension, is in meters and plane stress is assumed. Calculate the fracture strength of specimens A and B graphically. The crack is a central through crack and $E = 400\,\text{GPa}$.

6. In Problem 5, estimate graphically the original and final crack length for the specimens whose strengths are (A) $\sigma_f = 645\,\text{MPa}$ and (B) $\sigma_f = 301\,\text{MPa}$.

7. This question combines two areas of study: stable crack growth and subcritical crack propagation? Consider a rising R curve that follows $R = 30 + 60[1-\exp(-8 \times 10^4 \delta c)]$ where δc is in meters. If the crack starts at $c = 40\,\mu\text{m}$ and the stress was applied so that $G = 30\,\text{J/m}^2$ and then maintained constant, would the crack grow by stable R-curve growth? Suppose subcritical crack growth occurs. Could the crack eventually become unstable? if subcritical crack growth occurs, why might the driving force for crack growth vary with time? (Use the R curve as a basis for discussion.)

8. A method has been proposed for determining the shape of the R curve. Five indents were placed on the surface of a bent bar near the center with a diamond indenter, each at a different indenter load, but all produced cracks extending from the corners underneath the intent. Then the indentation itself was polished away, leaving just the five cracks, each of a different length, but all perpendicular to the direction of stress in the bent bar. The length of each crack was measured: Their lengths were $c_1 = 10\,\mu\text{m}$, $c_2 = 20\,\mu\text{m}$, $c_3 = 30\,\mu\text{m}$, $c_4 = 40\,\mu\text{m}$, and $c_5 = 50\,\mu\text{m}$. The specimen was then fractured in four-point bending so that all five cracks were subject to the same stress. Dry oil was placed over all five cracks during the test. After the test, the length of the cracks were measured exactly again.

   a. The fracture origin was at which crack (easy question)?
   b. Why did the other four cracks grow during the fracture test? For example, their final lengths may be $c_1 = 13\,\mu\text{m}$, $c_2 = 25\,\mu\text{m}$, $c_3 = 38\,\mu\text{m}$, and $c_4 = 52\,\mu\text{m}$.
   c. Sketch an R curve. Indicate the length of the initial five cracks to the left of the R curve. Show how, by knowing the crack length before and after of the four cracks and the stress at failure, one could determine the shape of the R curve.
   d. Why were the cracks covered with dry oil?

10

OVERVIEW OF TOUGHENING MECHANISMS IN CERAMICS

10.1   INTRODUCTION

An issue of the greatest importance to the load-bearing use of ceramics is that of increasing toughness. From the fundamental fracture mechanics equation

$$\sigma_f = \frac{K_{IC}}{Yc^{1/2}} \tag{10.1}$$

one can see that increasing strength σ_f requires some combination of increasing the toughness K_{IC} and reducing the size c of the largest crack. Becher (1991) summarizes the fracture toughness of glasses and single-crystal ceramics as lying in the range $0.5–2 \, \mathrm{MPa \cdot m^{1/2}}$ and states that in polycrystalline ceramics not employing special microstructural design toughening techniques the toughness is higher but usually does not exceed $5 \, \mathrm{MPa \cdot m^{1/2}}$. With this toughness, achieving a strength of 800 MPa for a penny-shaped crack far from an external surface ($Y = 1.128$) requires a maximum crack radius of about $30 \, \mu m$. Extreme efforts in control of processing from the synthesis of raw materials through forming and sintering to the final finishing are constantly made to reduce the maximum crack size, and the continuing development of very fine powders and improved processing techniques offers promise of further progress (Lange, 1989). However, there are limits to how small cracks can be made in practical ceramics. Also,

TABLE 10.1   A Classification of Toughening Mechanisms in Ceramics

General Mechanism	Detailed Mechanisms
Crack tip shielding by crack bridging	Second-phase brittle fibers with partial debonding
	Frictional and ligamentary grain bridges
	Second-phase ductile ligament bridging
Crack tip shielding by process zone activity	Microcracking
	Transformation toughening
	Ductile yielding in process zone
Crack deflection	Tilt and twist out of crack plane around grains and second-phase additions
Crack bowing	Bowing in crack plane between second-phase crack-pinning points

a ceramic with a small crack size used near its fracture strength is in danger of sudden failure from a larger crack introduced by contact with a hard material. Designing and producing microstructures to increase toughness, and thus better flaw tolerance, have thus perhaps become the main goals of research on structural ceramics. Evidently a theory of how microstructure can influence toughness is crucial to guide development of tougher ceramics. A general classification of toughening mechanisms in ceramics is given in Table 10.1. These mechanisms will be taken up in later sections of this chapter.

The practical achievements in toughening ceramics are illustrated in Table 10.2.

The behavior of real cracks in ceramics with complex microstructures is difficult to model quantitatively but has been discussed extensively by Rice (1981, 1984, 1985). There are many theories of the effects of microstructure on crack propagation in ceramics, including toughening. These have been discussed in several review papers (Evans, 1990; Becher, 1991; Rodel, 1992; Steinbrech, 1992). There does not appear to be a single master theory that includes all toughening effects. This is because each effect becomes very complex when treated mathematically in full generality. Indeed, in treating a single toughening effect it is generally necessary to introduce simplifying assumptions with the goal of making the treatment mathematically practicable while attempting to preserve the essential physics of the toughening behavior. The situation is thus that many theories of individual toughening effects exist. It is recognized that several toughening effects can take place together and that the combined effect is not necessarily a simple linear combination of the individual effects. Furthermore, some of the effects considered in early work, although significant in some special ceramic microstructures, now appear to be less important in most high-strength, high-toughness ceramics than other effects treated later. Thus at the time of this writing attention to toughening polycrystalline ceramics centers on crack tip shielding processes often acting in conjunction with crack deflection. Other toughening mechanisms discussed in earlier literature, such as crack bowing, now appear to be of more specialized

TABLE 10.2   Fracture Toughness Values for Various Ceramic Materials

Material	Grain Size (μm)	Fracture Toughness (MPa·m$^{1/2}$)
Alumina	1–2, 10–12	2.5–3, 4.5
Alumina + 20 vol. % SiC whiskers	1–2	8–10
Alumina + 20 vol. % TZP (1 mol % yttria)[a]	2	8
Alumina + 40 vol. % TZP (12 mol % ceria)[a]	2	13
Polycrystalline cubic zirconia	50	3
TZP (12 mol % ceria)[a]	4–6	15–18
TZP (2 mol % yttria)[a]	1.5	12
TZP (2 mol % yttria)[a]	0.5	7
PSZ (9 mol % magnesia) with increasing precipitate size[a]	50	8–16
Silicon nitride, equiaxed grains	2–3	4
Silicon nitride, elongated grains	~4[b]	10
Silicon carbide, densification additive—alumina	2	3.5–4
Silicon carbide, densification additive—boron and carbon	5–7	2.5–3
Silicon carbide + 25 vol. % titanium carbide	2.5	6

Note: Values determined at room temperature using precracked (3–5 mm precrack length) applied moment double-cantilever beam specimen. TZP is polycrystalline tetragonal zirconia; PSZ is partially stabilized zirconia. Grain size of equiaxed polycrystalline matrix phase.

Source: From Becher (1991).

[a] Toughness values are quite sensitive to test temperature.

[b] Diameter of grain.

interest. The present chapter presents a brief summary of the main categories of Table 10.1. Subsequent chapters treat transformation toughening and toughening with fibers in more detail because of their importance and complexity. There appears to be general consensus in the literature concerning the qualitative aspects of the major toughening mechanisms in polycrystalline ceramics, but the detailed descriptions vary somewhat, as does the way in which the mechanisms are grouped for discussion. For example, Lutz et al. (1991a) state that "the toughening mechanisms can be subdivided into (1) crack deflection, (2) contact shielding processes (wedging caused by broken-out grains or rough crack surfaces, and crack bridging), and (3) stress-induced zone-shielding processes (transformation and microcracking, and residual stress fields)."

10.2   TOUGHENING BY CRACK DEFLECTION

Crack deflection can take place when there are local areas in a ceramic that have lower resistance to crack propagation than an average plane cutting through at right angles to the tensile stress (Wiederhorn, 1984). An important

case is that of grain boundaries, which typically require about half the fracture surface energy of a single crystal. A crack advancing through a polycrystalline ceramic should thus attempt to follow along the grain boundaries. However, as shown in Chapter 5, the stresses acting in inclined planes near a crack tip depend on the angles involved. For a straight crack that tilts about a direction perpendicular to the crack advance through an angle θ, the stress intensity factor required for crack propagation is given by

$$K(\theta) = K(\theta = 0) \ \sec^2(\tfrac{1}{2}\theta) \tag{10.2}$$

A crack that twists about the direction of crack advance through an angle ϕ will experience a stress intensity factor given by

$$K(\phi) = K(\phi = 0) \ \sec^2(\phi) \tag{10.3}$$

Thus a given twist angle is more effective than the same angle of tilt in increasing the stress intensity factor in the original crack plane necessary to drive the crack out of the plane.

A crack advancing in a polycrystalline body and following grain boundaries will be made up of many sections at various angles. Wiederhorn (1984) states that K_{IC} for a polycrystalline body should be approximately twice that for a corresponding single crystal based on the geometric effect of deflection alone. Faber and Evans (1983a, b) considered cracks deflected by spheres, rods, and disks in an otherwise uniform body. They reached several important conclusions:

1. The increase in toughness due to crack deflection depends on the particle shape and volume fraction of particles but not on the particle size.
2. The most effective morphology for increased toughening is the rod shape, followed in turn by the disk and sphere. For rods the toughening effect increases with increasing aspect ratio up to a ratio of about 12.
3. The toughness increases with increasing volume fraction of deflecting particles up to a volume fraction of about 20% and increases very little with further increases in volume fraction.
4. The maximum toughness caused by rods (i.e., with aspect ratio 12 and volume fraction 20%) is about four times the toughness without deflecting particles when expressed in terms of R (i.e., in terms of fracture surface energy) or about two times when expressed in terms of T (i.e., in terms of the critical stress intensity factor).

The above remarks about polycrystalline materials and deflecting particles relate only to the geometric effects of deflection. Crack deflection can also cause partial bridging by grains or second-phase particles since the crack may deflect around a grain/whisker in its path, leaving the grain/whisker bridging the crack. This important toughening effect will be treated later. Rodel (1992) has reviewed the interaction between crack deflection and crack bridging in

whisker-toughened alumina and in silicon nitride containing rod-shaped grains. He concludes that crack bridging is probably the most important mechanism of toughening in these materials (rather than the direct effect of crack deflection) but that crack deflection is required for the development of crack bridging.

Crack deflection appears to be the dominant toughening mechanism in platelet-reinforced alumina, as discussed in Section 14.5.

10.3   TOUGHENING BY CRACK BOWING

It has long been recognized (Hasselman and Fulrath, 1966) that the introduction of second-phase inhomogeneities into a brittle material (such as the introduction of small nickel spheres into glass) can lead to an increase in strength. It is now also recognized that the toughness can also be increased and theories of crack bowing have been introduced in an attempt to explain these effects. Crack bowing is the development of a nonlinear crack front for a planar crack and must be distinguished from crack deflection, which is the development of out-of-plane portions of the crack. The concept of crack bowing was introduced by Lange (1970, 1971) and studied further by Evans (1972) and by Green et al. (1979).

Lange (1970) proposed that strong second-phase particles could act as barriers to crack advance. He visualized a crack advancing in a plane but pinned by barriers with an average spacing d and bowing out between the pinning points under the action of a stress. He assumed that the crack acts as if it had a line tension T and concluded that the critical value of the strain energy release rate required to propagate the crack is

$$G_C = 2\left(\gamma_0 + \frac{T}{d}\right) \tag{10.4}$$

where γ_0 is the fracture surface energy for the glass without the inclusions. He noted that the strength S is given from the Griffith condition by

$$\sigma_f \propto (G_C)^{1/2} \tag{10.5}$$

Lange related the obstacle spacing d to the volume fraction of particulates V_f and the particle diameter D by taking the spacing to be equal to the mean free path as calculated by Fullman (1953):

$$\ell = 2D\left(\frac{1 - V_f}{3V_f}\right) \tag{10.6}$$

Lange noted that his theory was consistent with the strength data of Hasselman and Fulrath (1966) and went on (Lange, 1971) to obtain both strength and fracture energy data on borosilicate glass containing dispersed alumina particles. His results showed increases in both strength and toughness with increasing volume fraction of alumina and supported his theory.

10.4   GENERAL REMARKS ON CRACK TIP SHIELDING

A simplified view of toughening by crack tip shielding that illustrates the basic physical processes is useful (Marshall et al., 1983; summarized by Steinbrech, 1992). Crack tip shielding is divided, as in Table 10.1, into two basic categories: process zone effects and bridging zone effects.

Process zone effects depend on volume elements of the material near the crack undergoing a nonlinear stress–strain effect such as to produce a local compressive stress around the crack which acts as a closure force on the crack. This is idealized as elastic behavior up to σ_c followed by a permanent tensile strain ε^T upon a small increase in stress. Further increases in stress are assumed to produce elastic behavior, perhaps with a different elastic constant. If this permanent strain occurs in a volume fraction V_f over a distance h on either side of an advancing crack, the increase in the critical strain energy release rate is

$$\Delta G_C = 2 V_f \sigma_c \varepsilon^T h \tag{10.7}$$

as discussed in more detail in Chapter 12. Alternatively, a stress intensity factor approach can be taken, leading to an increase in toughness due to transformation toughening of

$$\Delta K_C^T = 0.30 \, V_f \varepsilon^T E h^{1/2} \tag{10.8}$$

The equivalence of these two approaches is shown in Chapter 12. We discuss the relationship between the energy approach and the stress intensity factor approach in general later in the present section after discussing bridging zone effects.

Bridging zone effects depend on a closure stress $p(u)$ acting on the crack opening, where u is the crack-opening displacement. This stress acts up to a maximum value of crack-opening displacement, u^*, at which the bridging element fails. If a bridging zone exists for a distance from the crack tip and attention is focused on the end of the bridging zone away from the crack tip, as shown in Section 5.7 by the J-integral method (Rice, 1968b; Evans and McMeeking, 1986; Lawn, 1993), the corresponding increase in the critical strain energy release rate is

$$\Delta G_C = 2 \int_0^{u^*} p(u) \, du \tag{10.9}$$

If $\sigma(u)$ is the stress in a bridging element (fiber, particulate, grain, etc.) and a volume fraction V_b are bridging, $p(u) = V_b \sigma(u)$, so that

$$\Delta G_C = 2 V_b \int_0^{u^*} \sigma(u) \, du \tag{10.10}$$

As in the case of process zone effects, bridging zone effects can also be treated by a stress intensity factor approach. This treatment leads to a set of coupled

equations which are discussed in Chapter 12 but are not given here because of their complexity.

As discussed in the following sections, permanent deformation in a process zone can arise from several different effects, as can the bridging forces. However, all the effects fit into the general form given in the preceding equations for ΔG and the equivalent ΔK formulation. If the permanent deformation process also leads to a reduction in the local elastic modulus, a contribution to ΔK due to shielding by reduction of the elastic modulus in the crack process zone must also be taken into account.

We next consider how these effects appear to a person performing a fracture mechanics test to measure a critical stress intensity factor. Typically, a crack of length c is created and a stress σ that is uniform tension at a distance from the crack is applied. An applied stress intensity factor K_a is calculated from

$$K_a = Y\sigma c^{1/2} \tag{10.11}$$

The value of K_a at the instant of fracture is taken to be the observed critical stress intensity factor K_C:

$$K_{IC} = K_{\text{tip at fracture}} \tag{10.12}$$

When no toughening process is operating, this measured critical stress intensity factor is equal to the critical stress intensity factor required at the crack tip, which we here designate $K_0 = K_{\text{tip at fracture}}$. That is, for no toughening mechanism operating

$$K_{IC} = K_0 \tag{10.13}$$

However, when some toughening mechanism such as transformation toughening or fiber bridging is operating, the stress intensity factor characterizing the stress near the crack tip is

$$K_{\text{tip}} = K_a - \Delta K \tag{10.14}$$

where ΔK is the reduction in the stress intensity at the crack tip as a result of some toughening process such as transformation toughening or crack bridging. We have taken ΔK as a positive number and recognized that the action of fiber bridging or transformation is to produce a force tending to close the crack. The crack tip is said to be shielded from the full effect of the applied stress. The applied stress intensity factor is now

$$K_a = K_{\text{tip}} + \Delta K \tag{10.15}$$

At the instant of fracture the applied stress intensity factor is again taken to be the measured critical stress intensity factor and the value of K at the tip must again be K_0, so that

$$K_C = K_0 + \Delta K \tag{10.16}$$

From the point of view of the observer determining the measured critical stress intensity factor, the material has been toughened by ΔK despite the fact that the required local stress intensity factor $K_{tip(critical)}$ for fracture is unchanged. In other words, the effect of the toughening process in partially shielding the crack tip is to cause a larger applied stress to be required for crack propagation and so a larger macroscopic toughness is observed.

The same effect can be described in terms of required mechanical energy release rate. The observer performing the fracture mechanics test will determine the critical mechanical energy release rate G_C required of the applied stress at the instant of fracture, which is

$$G_C = G_{a \text{ at fracture}} = G_{tip \text{ at fracture}} + \Delta G = G_0 + \Delta G \qquad (10.17)$$

where G_0 is the critical mechanical energy release rate in the absence of any toughening mechanism.

An important question is the relationship between the critical stress intensity factor and the critical mechanical energy release rate. In Section 5.7 the Irwin relation between G and K was established in the absence of toughening by carrying out the integration in Eq. (5.39). This integration was performed along a length Δx from the crack tip and the limit was taken as $\Delta x \to 0$. If the same calculation is now performed when a toughening mechanism is operating over a process zone near the crack, the result is that the stresses and strains entering the integral are those characterized by a stress intensity factor K_0 and the corresponding energy release rate is G_0. The result of the integration in the notation of the present section is

$$G_0 = \begin{cases} \dfrac{K_0^2}{E} & \text{for plane stress} & (10.18) \\[2mm] \dfrac{K_0^2}{E}(1 - v^2) & \text{for plane strain} & (10.19) \end{cases}$$

The same integration can be done from the point of view of the external observer, leading to

$$G_C = \begin{cases} \dfrac{K_C^2}{E} & \text{for plane stress} & (10.20) \\[2mm] \dfrac{K_C^2}{E}(1 - v^2) & \text{for plane strain} & (10.21) \end{cases}$$

Combining these equations with (10.16) and (10.17) gives, for plane stress,

$$E(G_0 + \Delta G) = (K_0 + \Delta K)^2 \qquad (10.22)$$

or

$$\Delta K = (K_0^2 + E\,\Delta G)^{1/2} - K_0 \tag{10.23}$$

Note especially that $\Delta K \neq (E\,\Delta G)^{1/2}$. Similarly, for plane strain,

$$\frac{E}{(1-\nu^2)}(G_0 + \Delta G) = (K_0 + \Delta K)^2 \tag{10.24}$$

or

$$\Delta K = \left(K_0^2 + \frac{E}{1-\nu^2}\Delta G\right)^{1/2} - K_0 \tag{10.25}$$

The same results were obtained by Lawn (1993) using a *J*-integral argument. Our discussion of the crack tip and the external observer corresponds, respectively, to his enclave observer and global observer.

   The conclusion of this discussion is that, in considering toughening caused by either process zone or bridging zone effects, one may use either a mechanical energy release rate approach (in which the total critical mechanical energy release rate when toughening is present is the sum of that for the untoughened material plus the total resistance effect due to all shielding mechanisms that are operating, with care taken to include energy dissipation effects such as frictional sliding of fibers against the matrix) or a stress intensity factor approach (in which the total critical stress intensity factor when toughening is present is the sum of that for the untoughened material plus the total toughening due to all shielding effects that are operating). We emphasize two points. First, the preceding statement applies to the contributions to energy release rate or stress intensity factor due to the simultaneous effect of all the shielding processes that are operating. Second, there is a nonlinear relationship between ΔK and ΔG as shown in the immediately preceding equation. Examples of the use of Eq. (10.25) in calculating toughening ΔK from ΔG determined by energy considerations and comparing the results to a direct calculation of ΔK from stress considerations are given in Chapter 11 for transformation toughening and in Chapter 14 for whisker bridging.

11

EFFECT OF MICROSTRUCTURE ON TOUGHNESS AND STRENGTH

11.1   INTRODUCTION

To this point in the text little has been said about how the microstructure can be designed to affect the toughness and strength of ceramics. In the previous chapter several mechanisms leading to higher toughness were described, but if materials are to be designed to achieve outstanding mechanical properties, the materials scientist must understand how elements of the microstructure can be varied to take advantage of these toughening mechanisms. This chapter describes how variations in the microstructure affect toughness and strength. In addition, it has been observed that fracture strength is not always linearly related to toughness as would be expected from Eq. (10.1), and so the effect of microstructure on fracture strength must be discussed separately from fracture toughness. This chapter will describe how fracture strength varies with fracture toughness and why.

There is considerable literature on the subject of microstructure–mechanical properties relationships. Much of the literature on grain size and second-phase particle size effects on mechanical properties has been summarized in a recent book by Rice (2000). Another recent book by Rice (1998) summarizes the literature on the effect of porosity on mechanical properties.

A major difficulty in describing how fracture properties depend on microstructure is deciding how the microstructure is defined. Grain size is usually taken to be the average diameter of equiaxed grains without considering grain size distribution or grain shape. Many investigators have, for instance, proposed that the largest grain controls fracture strength since the largest grain may control the size of the largest flaw. An alternative is to measure the grain size at the fracture origin. A second difficulty is that an insufficiently wide range of microstructures are often considered by a single investigator and correlating results of several investigators who use different techniques for testing leads to uncertainty. Another difficulty is that most toughness tests measure toughness of flaws on the order of 1 mm, whereas fracture initiates most often from flaws of 20–50 μm.

Since there is such a large body of data on the subject, we cannot review all the literature in this chapter. Rice (2000) is an excellent review of much of the data. Here we will try only to choose the best correlations and draw some conclusions about trends and mechanisms that explain the data. This chapter covers the normal features of a microstructure, such as grain size, particles size, and porosity. Chapters 12–14 discuss special toughening mechanisms to achieve high-toughness/strength composite ceramics.

11.2   FRACTURE MODES IN POLYCRYSTALLINE CERAMICS

The fracture toughness of pure polycrystalline ceramics is generally a factor of 2 higher, on an energy basis, than that for easy cleavage planes of a single crystal of the same material and can be as high as a factor of 10 higher. There are two features of a polycrystalline ceramic that lead to higher toughness: the fracture path and internal stresses. The presence of pores or grain boundary phases in polycrystals also has an effect but generally it is to lower fracture toughness.

Crack propagation may be either intergranular (along the grain boundary) or transgranular (through the grain). The transgranular fracture surface is nearly flat independent of grain orientation while the intergranular fracture surface is rougher since it follows the topology of the grain boundaries. In the discussion in Chapter 10 it was pointed out that a change in direction of the crack path to follow a grain boundary may occur because the crack path has a lower fracture energy. Whether the crack will follow this path or not is determined by how much the crack must tilt or twist. Likewise, whether the fracture continues through the grain instead of deviating along a grain boundary is determined by whether the grain is in a favorable orientation for cleavage. The cleavage energy

TABLE 11.1   Energy and Stress Intensity Factors for Cleavage of Sapphire

| Plane	γ (J/m^2)[a]	K_{IC} (MPa·m$^{1/2}$)[b]
(0001)	>40	4.54 ± 0.32
(10$\bar{1}$0)	7.3	3.14 ± 0.30
(10$\bar{1}$2)	6.0	2.38 ± 0.14
(11$\bar{2}$0)		2.43 ± 0.26

[a] From Iwasa and Bradt (1984).
[b] From Wiederhorn (1969).

of fracture through a grain depends on the crystallographic orientation. As an illustration, Table 11.1 contains fracture energies and toughness values in different crystallographic directions for sapphire. Though usually close-packed planes have the lowest cleavage energy, it is interesting to note that the (0001) plane does not have the lowest cleavage energy. According to Wiederhorn (1969) and Cannon (1982) this may be due to the nonequilibrium termination of the surface ions and, furthermore, there may be a lack of charge neutrality as the (0001) plane cleaves. Besides favorable cleavage energies, tensile residual stresses and pores may make intergranular fracture easier. Fracture is generally intergranular at very fine grain sizes but transgranular as the grain size increases. Then in anisotropic materials fracture may revert again to intergranular at even larger grain sizes due to internal stresses. The effect of internal stresses due to anisotropy will be discussed in the next section.

The presence of intergranular fracture is a necessary condition for significant bridging in the wake of a crack or deflection of a crack propagating through a polycrystalline ceramic. As mentioned in Chapter 10, the current consensus is that crack bridging is more frequently the source of toughening than crack deflection. This is certainly true for long cracks. A series of experiments by Knehans and Steinbrech (1982) and Reichl and Steinbrech (1988) proves, at least for large grain and long cracks in alumina, that crack bridging accounts for most of the toughening. Figure 11.1 illustrates the results of a study by Knehans and Steinbrech (1982). They found that fracture energy rises as the crack lengthens (rising R-curve behavior), but if the specimen is removed from the fixture and the wake of the crack removed with a diamond saw and then measured again, toughness reverts back to the low initial value. Thus the rise in the R curve originated from the crack wake.

Figure 11.2 (Swanson et al., 1987) shows micrographs of cracks bridged by uncracked grains in the crack wake and shows the progression in the deterioration of those bridges as the crack extends. Dashed lines enclose the three bridging grains which are being followed during crack extension. When viewing such a micrograph, it is important to realize that the crack extends below the surface and is continuous around the isolated bridging grain. It is apparent in Figure 11.2 that the crack-opening displacement increases at increasing distance from the crack tip. As the crack propagates the crack-opening displacement at a
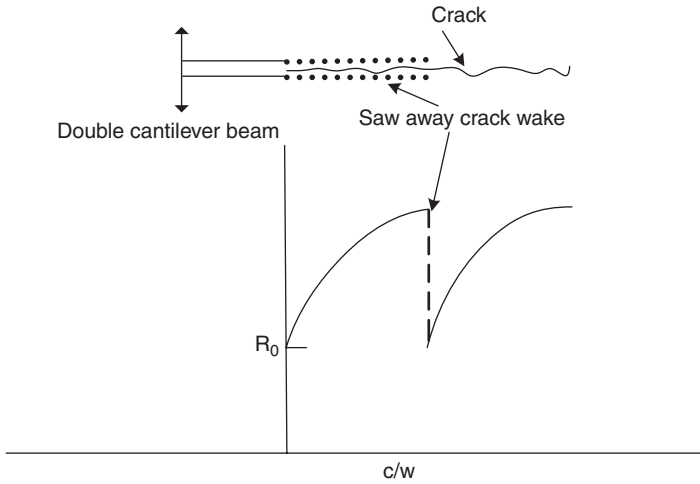
FIGURE 11.1   Notch beam test toughness test. Rising R curve is eliminated by cutting away the wake of the crack; c/w is crack length divided by specimen width. Schematic illustrating Knehans and Steinbrech (1982) results.

given bridge increases and at some point the opening exceeds the critical strain for that bridge, causing it to fracture. It is also clear from Figure 11.2 that the initial crack path around a bridge may not be the favorable one for breaking the bridging grain. For the leftmost bridge, the crack begins to propagate under the grain, but as the crack opening increases, the crack finds an easier path above the grain. Crack bridges remain intact for hundreds of micrometers behind the crack tip, which is consistent with the R curve rising for hundreds of micrometers.

The crack bridges shown in Figure 11.2 are all unbroken grains, which later fracture. In many cases cracks eventually encircle the grain bridges, but then frictional forces between the matrix and the isolated grain may still provide a closure force on the crack surface. A classical example of grain separation at the top and frictional forces on the side of the grain is shown in Figure 11.3. If grains are very elongated, frictional bridging is exceptionally effective in raising the toughness. Such intergranular fracture is necessary to achieve the highest toughnesses. A good example of this is in situ reinforced Si_3N_4, which has very elongated β-Si_3N_4 grains. If an intergranular glassy phase is not present in Si_3N_4, transgranular fracture through the elongated β-Si_3N_4 will occur and toughness falls from a value of about 10 to $4\,MPa \cdot m^{1/2}$.

In contrast to crack bridging, which is a wake-toughening mechanism, crack deflection is a crack-tip-toughening mechanism and should not be affected by elimination of material surrounding the crack wake. This is the strongest evidence favoring crack bridging. Two comments should be made at this point. First, experiments such as by Knehans and Steinbech (1982) leave little doubt
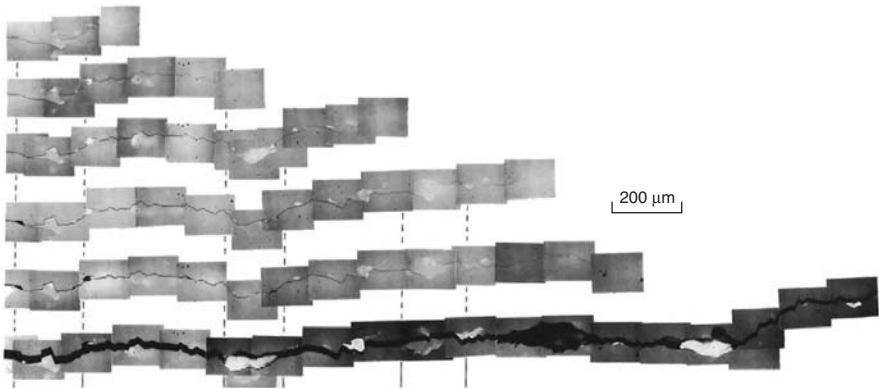
FIGURE 11.2   Progressive composite micrographs of crack propagation in alumina. (From Swanson et al., 1987. Courtesy of Brian Lawn. Reprinted with permission of Wiley-Blackwell.)
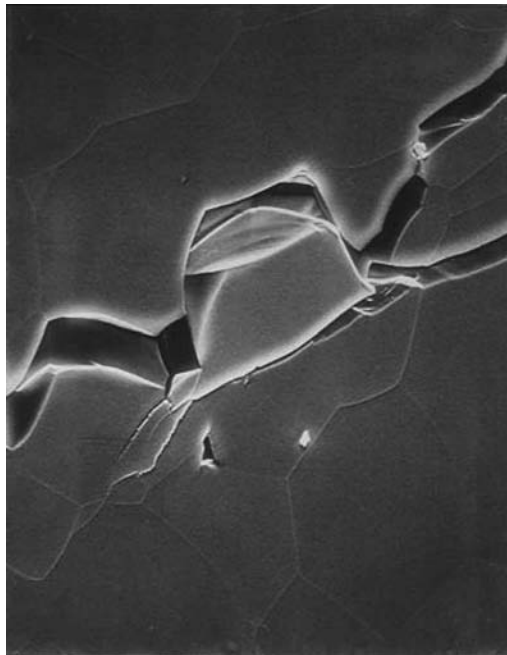
FIGURE 11.3   Micrograph showing pullout of bridge in wake of crack. (From Swanson et al., 1987. Courtesy of Brian Lawn. Reprinted with permission of Wiley-Blackwell.)

that crack wake bridging is the dominant mechanism when cracks are on the order of a millimeter in length. This may not be the case for short cracks. It is sufficiently difficult to perform *R*-curve measurements on short cracks, the size of natural flaws, to draw a firm conclusion that bridging is the dominant mechanism in all cases. Second, we have only discussed polycrystals so far. Glass has none of the features described above and consequently has a rather low value of toughness, less than $1.0\,\mathrm{MPa} \cdot \mathrm{m}^{1/2}$.

11.3   CRYSTALLINE ANISOTROPY IN POLYCRYSTALLINE CERAMICS

A polycrystalline material having anisotropic thermal expansion (different thermal expansion coefficients in different crystallographic directions) or a two-phases ceramic with different values of thermal expansion for each phase will develop internal stresses when cooled from the sintering temperature. In some volume elements in a given direction the internal stresses will be tensile and, if sufficiently large and in the presence of a potential flaw, may lead to localized microcracking. The origin of the microcrack is often a very small pore, much smaller than the length of the grain boundary, preferentially located at the grain boundary triple point. The internal stress usually extends the length of the grain boundary and the typical microcrack extends the length of the grain. Even if the local stress intensity factor from anisotropic thermal expansion stresses is subcritical for a particular flaw, the microcrack may develop after a stress is applied, in which case the fracture strength will be lower than otherwise.

Materials having anisotropic thermal expansion coefficients also have anisotropic elastic constants that can produce local stress concentrations leading to lower failure stresses. These topics are relevant to both toughening behavior and strength. Elastic anisotropy only produces internal stresses when the material is under an external load. It is simply due to the difference in stiffness of neighboring grains or particles. If one grain is stiffer than the neighbor, then it carries the greater load. The stresses may be concentrated over small volume elements in the crystal and so enhance stress intensity factors on the local crack initiation site.

Microcracking from thermal expansion anisotropy will occur spontaneously above a particular grain size, d_c, characteristic of each material (Matsuo and Sasaki, 1966; Kuszyk and Bradt, 1973). A full theory requires treatment of complex stress distributions and statistical effects. There is a long history of attempts to provide judiciously simplified theoretical models to deal with the essential physics (Clarke, 1964, 1980; Davidge and Tappin, 1968; Kuszyk and Bradt, 1973; Evans, 1978b; Sridhar et al., 1994).

Evans (1978b) considered a two-dimensional grain having an anisotropic thermal expansion cooled from the sintering temperature in a matrix with a mean thermal expansion coefficient for all three directions of $\langle \alpha \rangle$ (Figure 11.4).
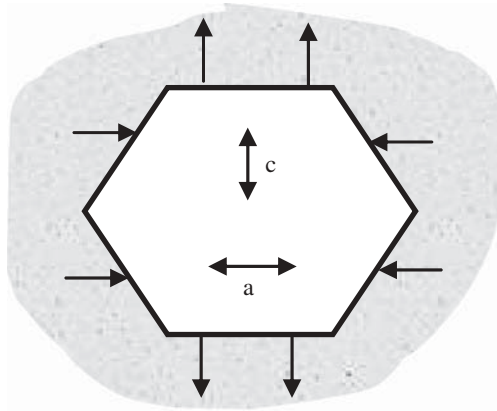
FIGURE 11.4 Two-dimensional grain having anisotropic thermal expansion immersed in media of thermal expansion $\langle\alpha\rangle$.

This simple model is only used for illustration purposes and is not exact since the individual stresses across the grain boundary depend on the orientation of the neighboring grain. The "c" crystallographic axis has a higher thermal expansion, α_c, than the "a" crystallographic axis, α_a. Here, $\Delta\alpha_a = \langle\alpha\rangle - \alpha_a$, $\Delta\alpha_c = \langle\alpha\rangle - \alpha_c$, and ΔT is the difference between room temperature and the temperature at which the polycrystal became rigid, T_{sr}, that is, where creep could no longer relax the stresses. The stress is approximated by

$$\sigma_a = -\frac{\langle E\rangle\Delta T(\Delta\alpha_a - \nu\Delta\alpha_c)}{1 - \nu^2} \tag{11.1}$$

$$\sigma_c = -\frac{\langle E\rangle\Delta T(\Delta\alpha_c - \nu\Delta\alpha_a)}{1 - \nu^2} \tag{11.2}$$

In polycrystalline Al_2O_3: $\alpha_a = 8.6 \times 10^{-6}$, $\alpha_c = 9.5 \times 10^{-6}$ C^{-1}, $\langle E\rangle = 380$ GPa, $\nu = 0.22$, $\Delta T = 1200°C$. Then $\sigma_a = -207$ MPa and $\sigma_c = 319$ MPa. A much higher stress is observed for the very anisotropic polycrystalline Al_2TiO_5: $\alpha_a = -3.0 \times 10^{-6}$, $\alpha_b = 11.8 \times 10^{-6}$ C^{-1}, $\alpha_c = 21.8 \times 10^{-6}$ C^{-1}, $\langle E\rangle \approx 100$ GPa, $\nu \cong 0.22$. Then $\sigma_a = -1975$ MPa and $\sigma_c = 1827$ MPa. (Values were taken from Table 11.2.) From these calculations it is easy to see why Al_2TiO_5 is more prone to microcracking than Al_2O_3.

Note that Eq. (11.1) contains no grain size term. Yet spontaneous microcracking of polycrystalline ceramics is experimentally found to be grain size dependent, occurring only above a specific grain size d_c. Furthermore, d_c decreases as anisotropy increases. The early explanation presented in the literature is that, although stress is grain size independent, strain energy released is grain size dependent. Kuszyk and Bradt (1973) proposed a model

TABLE 11.2   Thermal Expansion and Estimated Strains of Materials from Figure 11.6, $\Delta T = 1200°C$

Material	α_a (10^{-6})	α_b (10^{-6})	α_c (10^{-6})	α_{poly} (10^{-6})	$\Delta\varepsilon_{rms}$ (10^{-3})	E (GPa)
Al_2O_3	8.6	8.6	9.5	8.9	0.5	400
BeO	9.6	9.6	8.5	9.2	0.6	380
TiO_2	8.3	8.3	10.2	8.9	1.1	270
Nb_2O_3	5.2	0.0	5.9	3.7	3.2	150
$MgTi_2O_5$	2.3	10.8	15.9	9.7	6.6	250
Fe_2TiO_5	0.6	10.1	16.3	9.0	7.8	180
Al_2TiO_5	−3.0	11.8	21.8	10.2	12.2	100

Source: From Rice et al. (1981).

that considers the conversion of the strain energy into surface energy. They assume an average strain energy ΔU_e per unit volume associated with a constrained grain of size d and therefore an initial total strain energy $\Delta U_e\, d^3$. They assume that a crack of area d^2 having a surface energy per unit area, γ_f, develops and completely relieves the strain energy. The change in energy upon cracking is

$$\Delta U = -\Delta U_e\, d^3 + \gamma_f d^2 \tag{11.3}$$

They assume that ΔU_e is not a function of d. Considering progressively larger grain sizes, it is evident that a point is reached at which the energetically favorable situation is to have a crack develop and that the critical size is given by

$$d_c \propto \frac{\gamma_f}{\Delta U_e} \tag{11.4}$$

This model gives some rationale for the existence of a minimum grain size for microcracking but avoids discussion of the details of the process.

   Clarke (1964) presented the first detailed theory, which was subsequently discussed by Davidge and Tappin (1968). He assumed a grain diameter of d and a boundary of length $\frac{1}{2}d$ with a pore of diameter $2c_0$ at each end (Figure 11.4). He proposed that strain energy associated with the residual tensile stress along a boundary reduces the resistance to crack growth. The strain energy release as the crack grows the length of the grain boundary $(d/2 - 2c_0)$ was determined to be

$$\Delta U_e = \frac{E\varepsilon_{gb}^2 (d/2 - 2c_0)}{12(1 - \nu)} \tag{11.5}$$

Where ε_{gb} is simply given by $\Delta T(\alpha_c - \alpha_a)$. The Griffith equation then becomes

$$\sigma = \left\{ \frac{E\left[2\gamma_{gb} - E\varepsilon_{gb}^2(d/2 - 2c_0)/12(1 - \nu^2) \right]}{\pi c_0} \right\}^{1/2} \tag{11.6}$$

For spontaneous cracking, that is, σ goes to zero and $d/2 \gg 2c_0$, $\nu = 0.25$:

$$d_c \approx \frac{45\gamma_{gb}}{E\varepsilon_{gb}^2} \tag{11.7}$$

Rice (1980) showed that a plot of d_c versus ε_{gb}^{-2} for many oxides having different anisotropies follows a linear relationship consistent with Eq. (11.7) but suggested a numerical factor of 9 instead of 45.

Evans (1978b, p. 1846) has noted that a proper theory should use as the critical condition for microcrack development "the energy transfer that occurs during the *crack increment* at which the strain energy *release* just exceeds the energy *dissipation*." Tvergaard and Hutchinson (1988) and Ghahremani et al. (1990) performed two- and three-dimesnsional finite element analysis, respectively, considering both thermal expansion anisotropy and elastic anisotropy and found that at three grain triple points and, especially, four grain vertices the strain energy release rate of cracks of a given size increases as the grain size increases. These locations in the microstructure are the likely sites for microcrack initiation. Of course, these also are the likely sites for the location of a pore that has not been eliminated during sintering. Thus it is understandable that as the grain size increases the likelihood of spontaneous microcracking increases. At a certain grain size the strain energy release rate of typical pores or other flaws becomes critical and spontaneous microcracking occurs. Of even greater importance under an applied stress both elastic anisotropy and thermal expansion anisotropy stresses contribute to the strain energy release rate of preexisting flaws near triple points or four grain vertices and so finer grained ceramics will form microcracks . Also it must be remembered that there is a distribution of grain sizes and flaws sizes and that some microcracking occurs over a range of average grain sizes.

11.4   EFFECT OF GRAIN SIZE ON TOUGHNESS

Elastic and thermal expansion anisotropies affect both fracture toughness and strength and so the discussion of the effects of grain size on these two properties is divided into ceramics having cubic crystal symmetry and those having noncubic symmetry. Rice (2000) surveyed fracture toughness values of cubic polycrystals and concluded that fracture toughness is almost independent of grain size. Figure 11.5 shows results for Y_2O_3 and $Fe_{0.94}O$. Monroe and Smyth (1978) and Rice (2000) noted that there are some indications of a maximum toughness in the mid-grain-size range of some cubic polycrystals. In contrast, polycrystals with noncubic crystal structures consistently exhibited a pronounced K_{IC} maximum in the mid-grain-size range (Figure 11.6). The grain size at which the maximum occurs is related primarily to thermal expansion mismatch stresses. Table 11.2 shows that the grain size of the peaks falls
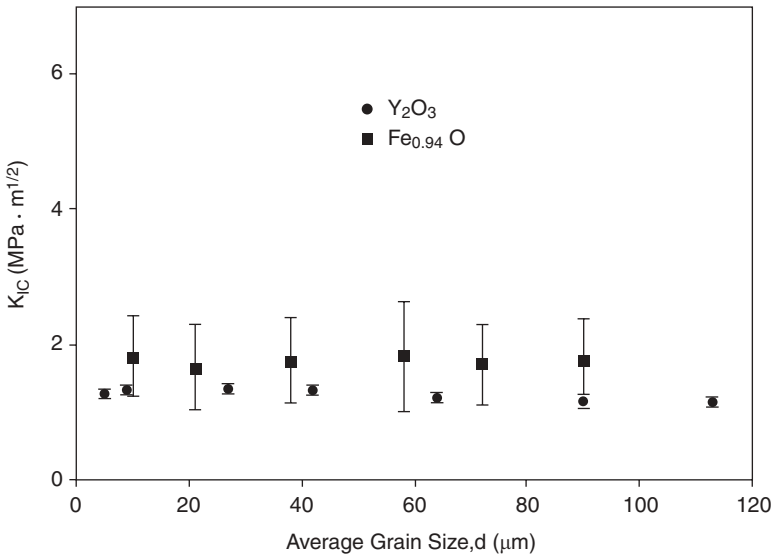
FIGURE 11.5 K_{IC} versus average grain size for polycrystalline Y_2O_3 and $Fe_{0.94}O$ with cubic crystal structure. K_{IC} values were determined by the double-cantilever beam method and converted from fracture energies by the equation $K_{IC} = (2E\gamma)^{1/2}$ $E_{Y_2O_3} = 172\,MPa$, $E_{FeO} \approx 200\,MPa$. (From Rice et al., 1981. Reprinted with permission of Wiley-Blackwell.)
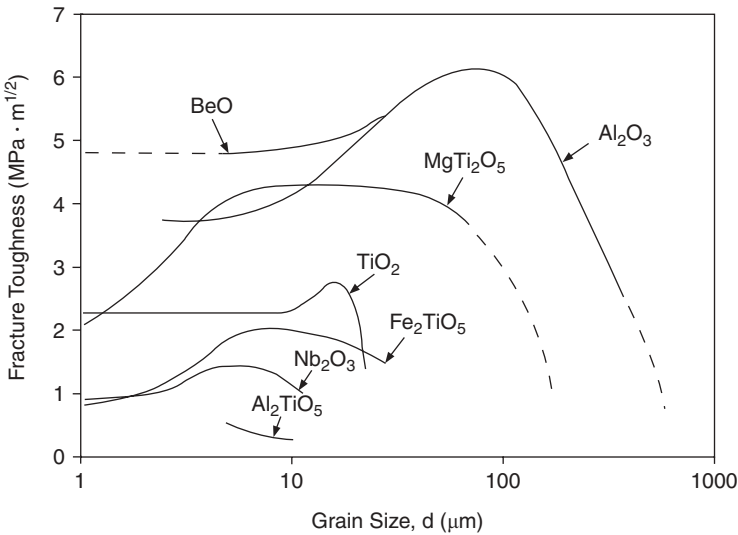
FIGURE 11.6 K_{IC} versus average grain size for noncubic polycrystals. Fracture energies were converted to K_{IC} using $K_{IC} = (2E\gamma)^{1/2}$. E values are shown in Table 11.2. [From Rice (2000) and Rice et al. (1981). Reprinted with permission of Wiley–Blackwell.]

approximately in the same order as the root-mean-square strains $\Delta\varepsilon_{rms}$ due to thermal expansion anisotropy where $\Delta\varepsilon_{rms} = \langle(\alpha_i - \alpha_{polycrystal})\Delta T\rangle_{rms}$ for i in the a, b, and c crystallographic directions ($\Delta T = 1200°C$).

From the foregoing it would appear that an explanation of Figure 11.6 must include the effect of thermal expansion in first increasing, then decreasing toughness. The explanation for decreasing fracture toughness to the right of the maximum is quite straightforward. The maximum is approximately the critical grain d_c beyond which microcracking is spontaneous, so crack propagation of the main crack merely connects the microcracks and toughness decreases with larger grain size. On the fine-grained side the toughness mechanism is of most interest. As mentioned above the current view is that crack bridging is the primary source of the increased toughness. Swanson et al. (1987) (Figure 11.2), Bennison and Lawn (1989), Rödel et al. (1990), Venkinis et al. (1990), and Chantikul et al. (1990) present micrographs of bridging grains in the wake of the crack and offer models for explaining the increased toughness with increased grain size. The general explanation is that toughness increases with increasing grain size since larger grains offer a stronger closure force on the crack surfaces and can withstand a higher crack-opening displacement before they fracture. The maxima in the curves are less pronounced when fracture toughness measurements are made on shorter cracks, as would be expected.

Bennison and Lawn (1989) proposed that the significant rising toughness with grain size is present only in noncubic ceramics because the frictional clamping force on bridging grains is enhanced by compressive stresses from thermal expansion anisotropy. Figure 11.3 shows an example of a clamped bridging grain being pulled out in the crack tip wake. As the bridging grain is pulled further out at longer distances behind the crack tip, there is less frictional surface area and the closure stress $p(x)$ decreases. For large grains the frictional area is larger leading to higher $p(x)$ and accordingly a higher toughness. An additional explanation might be proposed. Larger grains are not so severely strained ($\varepsilon = u/d$) at a comparable crack-opening displacement u provided the strain extends over the entire grain and so bridges are less likely to fracture leading to longer bridging zones. In fine-grained alumina ($d = 11\,\mu m$) Rödel et al. (1990) estimated that $p(x)$ became negligible at about $1.5\,\mu m$ where the crack-opening displacement was about $1.3\,\mu m$. If the grains were nanosized, one certainly would not expect a long bridging zone and consequently bridging would not as likely be the effective toughening mechanism.

In the fine-to-medium grain size range where toughness is increasing, toughness exhibits a rising R-curve behavior. According to Eq. (9.8) fracture occurs when

$$T = K_0 + K_\mu \equiv T(c) \tag{11.8}$$

where K_0 is the materials toughness when there is no bridging, that is, at the true base of the R curve. (Whether experimental R curves start at K_0 or not depends on whether the initial crack is bridged or not.) Here, K_μ is the increased

toughness above K_0 due to bridging. It is probably true that in both cubic (Figure 11.5) and noncubic (Figure 11.6) polycrystals the toughness approaches T_0 at the smallest grain sizes.

Elongated, high-aspect-ratio grains are particularly effective in toughening ceramics. They have similar toughening effects to whiskers described in Chapter 14. In fact, in situ toughened Si_3N_4 is so named because long prismatic rod-shaped β-Si_3N_4 grains are similar to whiskers. More discussion of the operating mechanism of whisker toughening will be given in Chapter 14, but it is important to note here that the in situ whiskerlike β-Si_3N_4 grains have a 1–1.5-nm-thick intergranular glass film which allows them to debond. This is an important ingredient of fiber or whisker-reinforced toughening. Recent efforts have been made to understand the important qualities of this intergranular film by Peterson and Tien (1995) and Becher et al. (2000). The intergranular film has about twice as high a thermal expansion coefficient as Si_3N_4, which helps initiate microcracks within the film. The cracking of the film is also enhanced by certain ionic additives in the glass that lead to cracklike defects under stress and to epitaxial growth of SiAlON on the edges of the β-Si_3N_4 grain if Al_2O_3 is in the glass phase. Toughness values as high as 10 MPa $\cdot$ m$^{1/2}$ are achieved with the proper grain boundary phase heat treatment to grow the elongated grains and control of texture.

11.5   NATURAL FLAWS IN POLYCRYSTALLINE CERAMICS

Before discussing how microstructures affect fracture strength, it is useful to review briefly the nature of common flaws causing fracture. Up to now flaws have been presented as elliptical or sharp tipped and planar. Figure 11.7 shows a few natural flaws of different origin. These flaws originate during processing. Examples chosen show quite different flaw shapes. The pore in Figure 11.7(a) is narrow and sharp and probably originates from a piece of organic matter in the green ceramic, whereas the pore in Figure 11.7(c) is nearly spherical and so the actual failure origin may be a flaw on the surface of the pore. The fracture origin in Figure 11.7(b) is not a crack but a second-phase impurity at which microcracks may initiate from the stress field caused by the difference in its thermal expansion coefficient from that of the matrix, as discussed in Section 11.7. Figure 11.7(d) is also not a crack but a patch of larger grains around which microcracks may develop.

Fractography has revealed that the most common "origin of failure" flaws are machining flaws introduced from surface finishing flexure specimens. The most convincing evidence that machine flaws dominate strength is that in some studies the fracture strengths of specimens machined parallel to the long axis of the flexure specimen are on the order of twice the strengths of specimens machined perpendicular to the specimen axis. Figure 11.8(a) and 11.8(b) show two sets of flaws that result from machining. Those flaws parallel to the abrasive track are longer though not much deeper than those perpendicular to

(a)   (b)

(c)   (d)
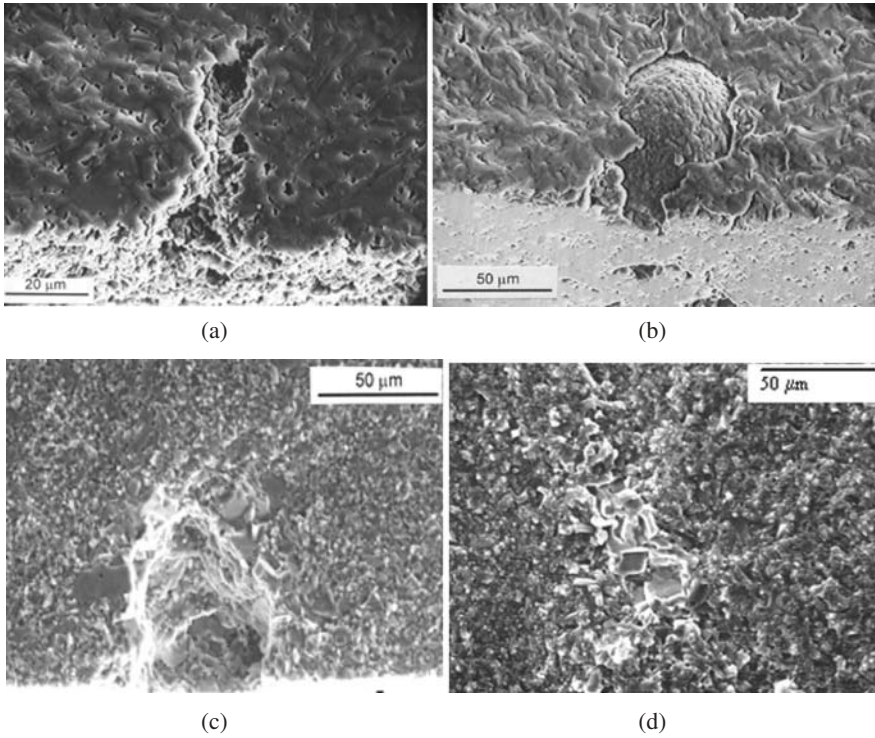
FIGURE 11.7   Micrographs of (a) elongated pore in α-SiC, perhaps from organic impurity; (b) Fe inclusion in Si_3N_4; (c) large pore in sintered Al_2O_3; and (d) agglomerate in α-SiC. Micrographs courtesy of George Quinn.

the machining direction. As a result, in specimens machined perpendicular to the specimen axis, the longer surface cracks are perpendicular to the stress direction and so are weaker. ASTM C 1161, which is a U.S. standard for flexure testing, specifies that grinding must be parallel to the specimen's long axis. Four alternate surface finishes are specified: (1) natural as-sintered surfaces (this

(a)   (b)
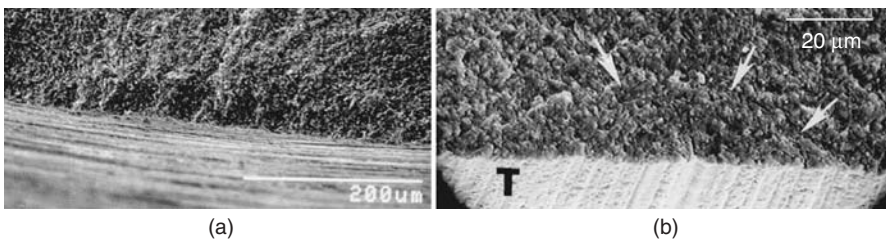
FIGURE 11.8   Machine flaws (a) parallel and (b) perpendicular to grinding direction. Arrows point to the edge of the flaw. (Micrographs courtesy of George Quinn.)

option is less often used because specimens distort during sintering, making it difficult to test in bending because of parasitic stresses); (2) application-matched machining; (3) customary machining procedures used for that material; and (4) a standard procedure described within ASTM C1161.

Two observations might be made about the particular flaws in Figures 11.7 and 11.8. One is that all of these flaws are much larger than the grain size. The second observation is that some flaws clearly have no bridges across the crack surfaces. This is particularly true of the flaws in Figures 11.7(a) and (c). The toughness at initial crack length in this case is then K_0.

Though less commonly tested, as-sintered specimens without machining can be tested, particularly in biaxial-ball-on-ring testing. Results may not be too different from machined specimens in that failure may originate from surface flaws due to grain boundary grooving sites on the surface. These are cusp-shaped grooves formed by more rapid vaporization of grain boundary ions than grain surface ions. Coble (1971) has shown that grain boundary grooves on as-sintered surfaces can be origins of failure and may be $\frac{1}{15}d$ to d deep.

11.6   EFFECT OF GRAIN SIZE ON FRACTURE STRENGTH

Historically it has long been observed that finer grain size ceramics have higher fracture strengths than coarse-grained ceramics. Typically fracture strength/grain size results are plotted as σ_f versus $d^{-1/2}$. Such a plot is shown in Figure 11.9. There are two possible reasons for plotting fracture data this way. First is because of the Hall–Petch equation, discussed in Chapter 18. It gives the dependence of grain size on microplastic crack initiation, which in materials where this is important determines the fracture stress.

The Hall–Petch equation is

$$\sigma_f = \sigma_y + k_y d^{-1/2} \tag{11.9}$$

where σ_Y is the yield stress for the easiest slip system of a single crystal and k_y is a constant. The second reason is that the critical crack length to failure may be directly proportional to the grain size as discussed below. Since the Griffith equation predicts σ_f versus $c^{-1/2}$, the relationship σ_f versus $d^{-1/2}$ results.

Carniglia (1972) originally proposed for alumina microplastic strain-in-itiated cracks in the fine-grain branch to the right side of Figure 11.9 and at lower stresses in the coarse-grained branch to the left side of Figure 11.9 fracture was initiated from preexisting flaws. However, the magnitude of the stress in the fine-grain branch is much lower than σ_Y for fine-grained alumina [Eq. (11.9)]. In fact, it has been recognized since that time that there are only a few polycrystalline ceramics whose yield stress is sufficiently low that micro-plasticity influences fracture, for example, CsI, KCl, PbTe, CdTe, BaTiO$_3$, MgO, and CaO. These are reviewed in Rice (2000). Contrary to Carniglia's suggestion that the fine-grain branch has its origin in microplastic crack
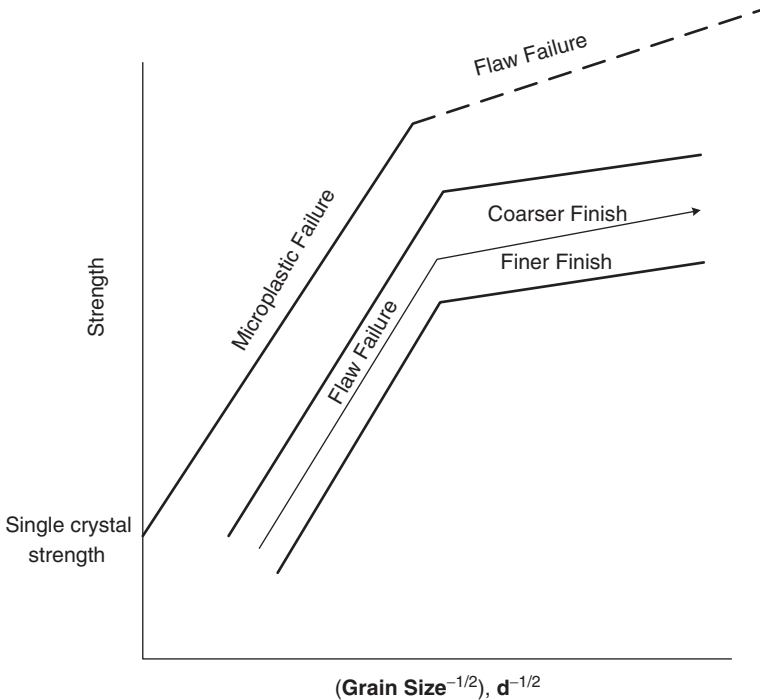
FIGURE 11.9   Schematic of σ_f versus $d^{-1/2}$ typical for polycrystalline ceramics.

initiation, it is the coarse-grain branch of the compounds listed above which can have their origin in microplastic crack initiation. In the fine-grain branch the stress for crack initiation by microplasticity is much higher than fracture initiated by preexisting flaws and so fracture in the fine-grain branch is from preexisting flaws. It should be noted that the extrapolation of the coarse-grain branch to $d \rightarrow 0$ should be the stress for plastic deformation in the easiest slip systems of single crystals. For many of the more common ceramics microscopic examination near crack surfaces has failed to find evidence of dislocation activity and so fracture generally has its origin in preexisting cracks, not microplasticity.

It has been observed (Rice, 2000) that most critical flaws in machined flexure specimens are observed to be in the range of 20–50 μm and do not vary too greatly with grain size and that the intersection of the two branches of Figure 11.9 occurs at $d/2 \leq c \leq 3d$. To a first approximation the intersection is approximately $d \approx c$. So in the fine-grain branch the flaw size is much larger than the grain size and in the coarse-grain branch it is smaller than the grain size. If the flaw is in the interior of the grain and smaller than the grain, the grain is a single crystal to the flaw. During a fracture test it may grow to the length of the grain or perhaps a few grains beyond where it experiences the higher toughness of a polycrystalline ceramic. If the flaw is in a grain boundary, it experiences the toughness of a grain

boundary until it extends the length of that grain boundary and impinges on the next grain. Since the toughness of a single crystal is below that of a polycrystal, the crack propagation sees a low toughness for the distance of one crack length and then toughness begins increasing toward the toughness of a polycrystal. In noncubic polycrystal, the characteristic length of residual stresses is approximately one grain length, adding to the ease of propagation if the stress happens to be tensile. As the crack enters the next grain, the residual stress may be compressive. Both effects contribute to a "pop-in" (Swanson et al., 1987; Chantikul et al., 1990) of a crack to approximately one grain length during the early part of a fracture test. Since the stress must be raised further for unstable crack propagation, it is the flaw length after pop-in that determines strength. Substituting, therefore, d for c into the Griffith equation (10.1) gives

$$\sigma_f = \frac{K_{IC}}{Y} d^{-1/2} \tag{11.10}$$

where the slope is K_{IC}/Y. This holds for the coarse-grain branch.

In the fine-grain branch the crack is much larger than the grain diameter and so the fracture strength should be independent of grain size. It is, however, strongly dependent on surface finish, which determines the flaw size.

Alumina has been the most widely studied polycrystalline ceramic. Figure 11.10 summarizes fracture strength data of several different investigators taken from Rice's (1997) compilation combined with Zimmermann et al.'s (1998) results. There has been some controversy as to whether the average grain size or the maximum grain size should be used in such a graph (Rice, 2006), as stated in the chapter introduction. Rice (1996) contends that fractography seldom finds the critical flaw lying on the largest grain, d_{max}, and therefore, it is more appropriate to use the average grain size or some size in between. Alternatively, the grain size at the origin of failure may be used. Rice (1997) noted that data points could move from the fine-grain branch to the coarse-grain branch if d_{max} was used instead of d_{avg}. The large scatter observed in the fine-grain branch arises because data compiled from several investigators with a variety of different sources and sizes of flaws, that is, surface finish, pores, and large grains, and in the use of d_{max} in some cases rather than d_{avg}. The choice for grain size is noted in the caption of Figure 11.10. In spite of the variability in the data, there is a definite trend toward increasing strength with decreasing grain size. Results from single investigators with well-defined sources of flaws exhibit much less scatter. The results of Zimmermann et al. (1998) in Figure 11.10 show the same trend.

Since in the coarse grain branch it is assumed that the critical flaw length is d, in Figure 11.10 two lines are drawn through the coarse-grained branch, one through the origin having slope K_{IC}/Y yielding $K_{IC} = 3.5\,\text{MPa} \cdot \text{m}^{1/2}$ and the other with a least-square fit to the data yielding $K_{IC} = 2.6\,\text{MPa} \cdot \text{m}^{1/2}$. The former value is slightly lower than values shown in Figure 11.6 for coarse-grained polycrystalline Al_2O_3. Low values are expected for several reasons.
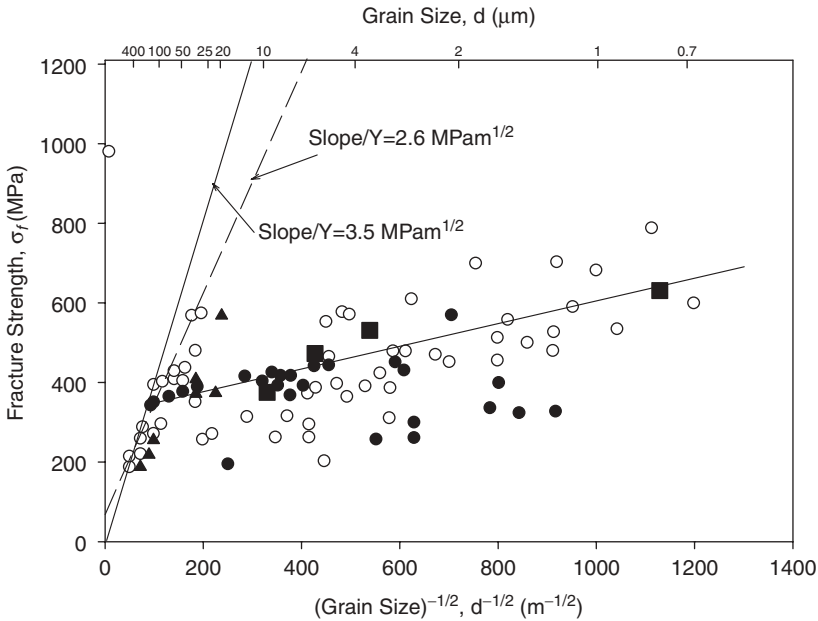
**FIGURE 11.10**   Summary of data for σ_f versus $d^{-1/2}$. Compilation of various investigators' results from Rice (1996): ($\bigcirc$) from fractography of isolated or clusters of large grains at origin; ($\blacktriangle$) from fractography of individual grains or cluster size, ($\bullet$) d_{max} from fractography at origin. (From Zimmermann et al. (1998): ($\blacksquare$) d_{avg}.)

Most importantly, d cannot generally be substituted directly into Eq. (11.10) since the critical crack is usually longer than a grain length. A crack size larger than the grain size would lead to a slope lower than K_{IC}.

Since in the coarse-grain branch the toughness starts at the single-crystalline value and rises to the polycrystalline value after it has traversed at least one grain, toughness can be described as R-curve behavior. Rice (2000) presented a graph of increasing fracture energy with increased c/d ratio, reproduced in Figure 11.11. Values of fracture energy were estimated primarily from fractographic analysis. This figure suggests that polycrystalline fracture energies may not be achieved until as much as $c/d = 5$.

It is possible to derive σ_f-versus-$d^{-1/2}$ curves based solely on R-curve behavior. Chantikul et al. (1990) determined R curves from indentation fracture measurements as a function of grain size and successfully predicted a σ_f-versus-$d^{-1/2}$ curve for the coarse-grain branch.

From compilations of single- and multi-investigator data such as shown in Figure 11.10 there is increasing consensus that a positive slope to the fine-grained branch exists. This could be significant if the trend holds into the nanocrystalline range. If the solid line in the fine-grained branch of Figure 11.11 is extrapolated to 50 nm, the fracture strength would be 2200 MPa. There are several arguments
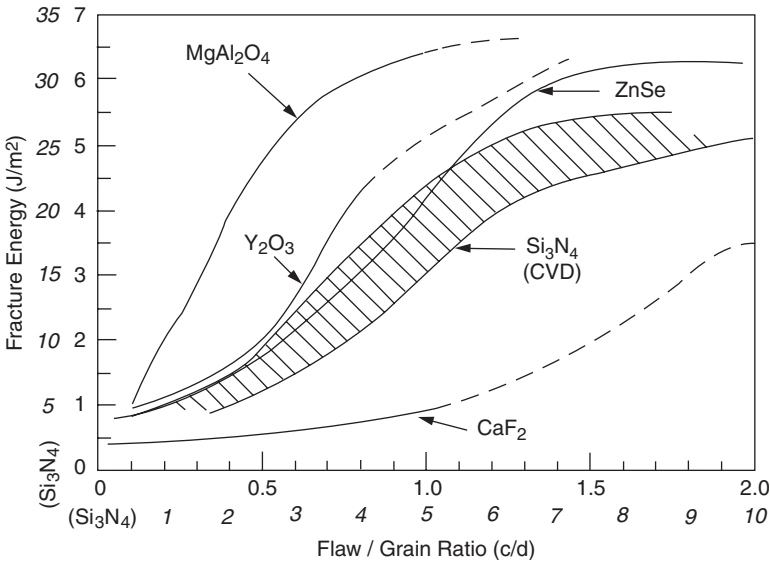
FIGURE 11.11   *R* curves for initial cracks smaller than one-grain diameter. Toughness grows from single-crystalline to polycrystalline value. (From Rice, 2000. Reprinted with permission of Marcel Dekker.)

for why the slope should be positive, though it is still uncertain that it should continue into the nanocrystalline grain size range. Several arguments follow:

1. Even though flaw sizes from specimen machining are relatively independent of grain size in the fine-grain branch, there is some decrease in flaw size with decreasing grain size. Evans and Charles (1976) found empirically that the length of a crack emanating from a microhardness indent fits

$$c \propto \left(\frac{P}{K_{IC}}\right)^{2/3} \left(\frac{E}{H}\right)^{1/3} \tag{11.11}$$

where *P* is the applied load to the indenter. Hardness *H* follows a similar Hall–Petch relationship as Eq. (11.9) and can be rewritten as (see Chapter 18)

$$H = H_0 + k_h d^{-1/2} \tag{11.12}$$

Combining Eq. (11.11) with Eq. (11.12) yields

$$c \propto \left(\frac{P}{K_{IC}}\right)^{2/3} \left(\frac{E}{H_0 + k_y d^{1/2}}\right)^{1/3} \tag{11.13}$$

Considering that indents are very much like abrasive grit used in machining, there should be a rather weak dependence of crack length on grain size. Even if

the surface is not machined, grain boundary grooving tends to be deeper for specimens annealed for longer times/higher temperatures, which are most often used to achieve larger grains.

2. In noncubic polycrystals thermal expansion anisotropy and elastic anisotropy lead to higher strain energy release rates on incipient cracks and consequently to microcracking. Even though these internal stresses lead to higher toughnesses, they may lead to lower strength with increasing grain size.

3. Even though flaws are much larger than the grain diameter, grains in the stress field of the large flaw may control the critical flaw size. To illustrate this, Zimmermann et al. (1998) introduced artificial spherical pores 85–88 μm in diameter into various fine-grained alumina with average grain sizes 0.8–9.2 μm in diameter. Because the pores were spherical, they did not act as the critical flaws even though they were much larger than any other flaw. [see Figure 11.7(c)] Instead the critical flaw was found to be around the edge of the pore and estimated to be about two grain diameters in size, that is, much smaller than the pore diameter. The large pore acted as a stress riser. The strength was lower in specimens containing the large pore as compared to specimens with natural flaws but still had the same grain size dependence (data shown in Figure 11.10), giving support to the proposal that the stress concentration near the pore contributes to failure.

4. Finer grains have lower concentrations of impurities along the grain boundaries and, therefore, may be stronger.

11.7   EFFECT OF SECOND-PHASE PARTICLES ON FRACTURE STRENGTH

Internal stresses and the resultant microcracking also develop around second-phase particles whose thermal expansion and elastic stiffness do not match the matrix. In addition stresses might arise from phase transformations in the second phase. The internal stresses that develop around isolated spherical particles in an isotropic matrix due to thermal expansion mismatch are estimated from the equations

$$\sigma_{rr} = -\frac{pR^3}{r^3} \qquad \text{and} \qquad \sigma_{\theta\theta} = \frac{pR^3}{2r^3} \qquad (11.14)$$

where the sign of pressure, p, follows the convention that compressive pressure is positive, which is opposite to the stress convention. The pressure p is given by

$$p = \frac{\Delta\alpha\,\Delta T}{(1 + v_m)/2E_m + (1 - 2v_p)/E_p} \qquad (11.15)$$

where the subscript m refers to the matrix and the subscript p to the second-phase particle: $\Delta\alpha = \alpha_m - \alpha_p$. The stress distribution is illustrated in
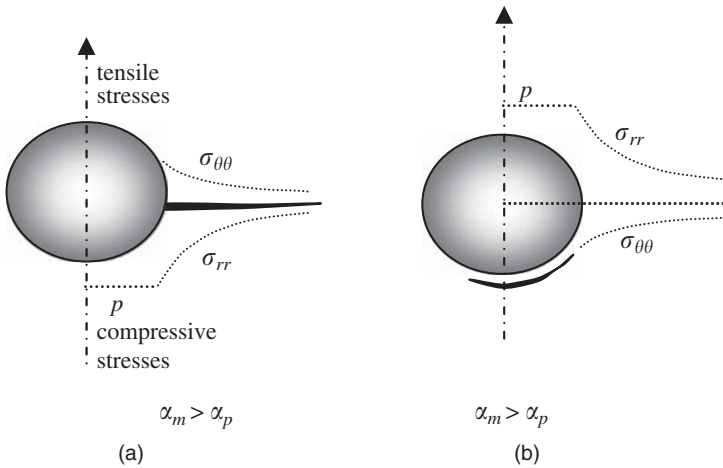
FIGURE 11.12   Microcrack formation around particles when (a) $\alpha_m > \alpha_p$ and (b) $\alpha_m < \alpha_p$. Dotted lines represent the stress distribution along the centerline of the particles. Cracks are shown to indicate the type of crack that forms under the stress state.

Figure 11.12. The stress inside the entire particle is a constant equitriaxially compressive or tensile depending on the sign of $\Delta\alpha$. The radial stress σ_{rr} outside the particle drops off as the cube of the distance from the center of the particle and the tangential stress, $\sigma_{\theta\theta}$, changes sign abruptly at the interface, and then drops off as the cube of the distance from the center of the particle at half that of σ_{rr}. The consequence of this stress distribution is that, if $\alpha_m > \alpha_p$, microcracks extend out radially from the edge of the particle, but when $\alpha_m < \alpha_p$, microcracks are in concentric arcs, as shown in Figure 11.12. Radial cracks are less desirable since the radial crack may propagate to neighboring particles and connect several particles, resulting in a large critical crack. The ring cracks are preferable since they remain localized and may not reach the critical size. In the latter case advantage may be taken of ring cracks to toughen the ceramic. This mechanism was briefly discussed in the previous chapter under crack shielding by microcracks. The mechanism would only be effective if $\alpha_m < \alpha_p$ and the internal stress from the thermal expansion mismatch is insufficient alone to cause microcracking so that ring cracks only form in the stress field of the advancing crack.

In glass matrix studies it has been shown that the highest strength particulate composites are those whose thermal expansion matches the matrix and, therefore, no cracks extend from or around the particle. The lowest strength composites are when $\alpha_m > \alpha_p$ and strengths become increasingly lower as $\alpha_m \gg \alpha_p$.

The effect of second-phase particle size on fracture strength is quite similar to the grain size effect on fracture strength. The strain energy release rate is higher for flaws near larger particles, all else being equal, and consequently

cracks grow more readily around larger particles. Rice (2000) compared ceramic particles (Al_2O_2, ThO_2, $ZrSiO_4$) in glass matrix studies from the literature similar to Figure 11.9, plotting fracture strength σ_f versus $D_p^{-1/2}$, where D_p is the particle diameter. The result was much the same as for grain size. There was both a coarse-particle branch with a steep slope and a fine-particle branch with little or no slope similar to Figure 11.9. Rice (2000) contended that the explanation was also the same. At the intersection of the two branches the flaw length and particle size are approximately equivalent. At finer particle sizes, flaws are much larger than the particles and in machined specimens vary only slightly with decreasing particle size. In the coarse branch the flaw size was essentially the particle size.

The effect of the volume fraction of ceramic particles in glass has also been studied. The fracture toughness of glass is low, and so increasing the volume fraction of ceramic particles increases the toughness. Strength most often does not follow the same trend and may, in fact, follow an opposite trend with toughness. As will be discussed in the next section, increasing strength does not always follow from increasing toughness. Strength and toughness relationships to particle size, volume fraction, and thermal expansion mismatch when particles are embedded in a polycrystalline matrix instead of glass follow the above principles for particle composites superimposed upon polycrystalline ceramics with grain size and anisotropic effects.

11.8   RELATIONSHIP BETWEEN STRENGTH AND TOUGHNESS

The Griffith equation, written in terms of toughness, dictates that σ_f is directly proportional to the toughness, K_{IC} [Eq. 10.1], as long as the flaw size is constant. However, we have shown in the previous section that increased grain size and second-phase particle size, while increasing the toughness, also increase the flaw size. It is useful to compare Figures 11.6 and 11.10 for Al_2O_3. In Figure 11.6, fracture toughness increases with increasing grain size between 10 and 100 μm, but in Figure 11.10, σ_f decreases sharply in the same grain size range. This is often the case that toughness and strength vary in the opposite directions, particularly when increased toughness is associated with increased grain or particle size.

By proper design of the microstructure both high strength and high toughness can be achieved. In situ reinforced Si_3N_4 is a good example of a successful attempt to combine high strength and high toughness. Two elements of the design are key. The length of the β-Si_3N_4 grain must be small compared to the flaw size, but within this constraint, the larger the β-Si_3N_4 grains, the more effective. The intergranular film must be designed to optimize intergranular fracture. A successfully designed microstructure should lead to a steep R curve. Figure 11.13 illustrates why a steep rather than a shallow R curve leads to higher strength. In spite of curve B having a higher plateau toughness, curve A leads to the higher strength because of the steeper slope.
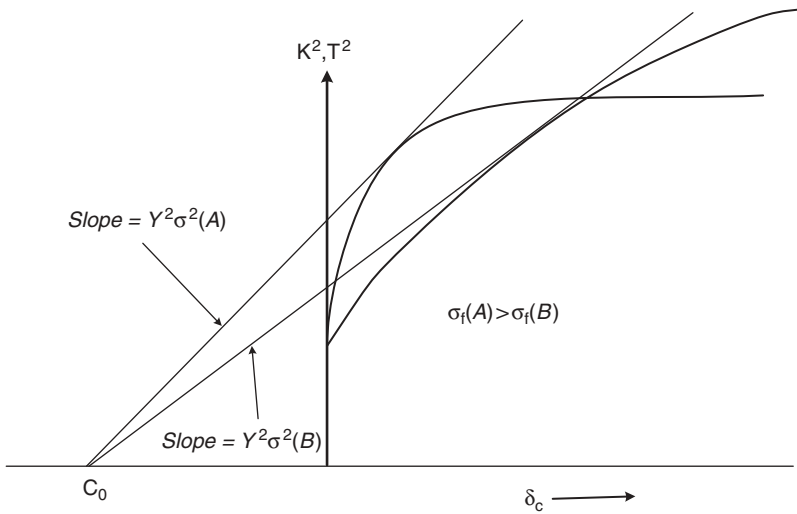
FIGURE 11.13   Schematic showing how steeper slope of R curve leads to higher strength even though plateau toughness is lower.

Figures 11.14 and 11.15 illustrate how varying the microstructures results in widely different R curves and fracture strengths. Larger in situ β-Si_3N_4 grains are derived by adding larger β-Si_3N_4 seeds mixed in with finer powder before hot pressing. The microstructure of Figure 11.14(a) resulted in the highest plateau and steepest R curve and the highest measured strength (Figure 11.15, curve a). Though complete understanding of the relationship between microstructure and properties cannot be demonstrated by these figures, several observations might be made. In the highest toughness Si_3N_4 debonding of interfaces occurred readily. R curves were measured from 50 μm on up, which is slightly higher than the critical flaw size. Generally, increasing the slope of the R curve led to higher strength with the exception of specimen (c), which had a higher strength than specimen (b). Presumably the critical flaw size was smaller in specimen (c). As the density of large β-Si_3N_4 increases, there is an increased likelihood of forming clusters of large β-Si_3N_4 grains that can act as critical flaw sites. Steeper R curves result from increased area of bridging grains. β-Si_3N_4 grains may be aligned to increase the number of bridges across the crack by applying large shear rates during the forming operation. Tape casting is often used to align the seeds, which leads to alignment of β-Si_3N_4 grains. This, however, only increases the toughness in a direction normal to the alignment direction.

## 11.9   EFFECT OF POROSITY ON TOUGHNESS AND STRENGTH

Section 3.9 discussed how Young's modulus falls off with increased porosity. The same relationships are used to empirically describe the decrease in
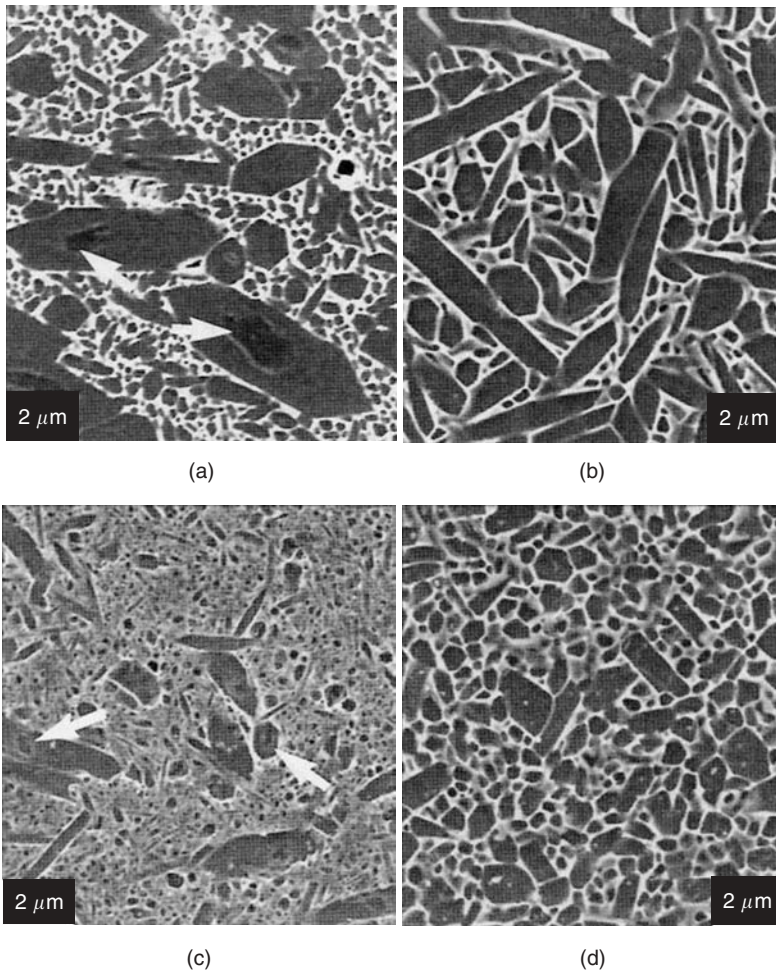
FIGURE 11.14 Micrographs of Si_3N_4 illustrating various types of R-curve behavior based on nature of large elongated grains and finer matrix: (a) 2 wt. % elongated seed particles added to the α-Si_3N_4 powder prior to gas pressure sintering at 1850°C for 6 h; (b) no elongated seeds added to α-powder, hot pressed, 1750°C for 2 h; (c) no elongated seeds added, hot pressed, 1750°C for 0.33 h; (d) no elongated seeds added to β-powder, hot pressed, at 1750°C for 2 h. (After Becher et al., 1998. Reprinted with permission of Wiley-Blackwell.)

toughness and strength with increasing porosity. Rice (1996), for instance, uses an equation of the same form as Eq. (3.46) to describe the relationship between toughness K_C and porosity P:

$$K_C(P) = K_0 \exp(-bP) \tag{11.16}$$
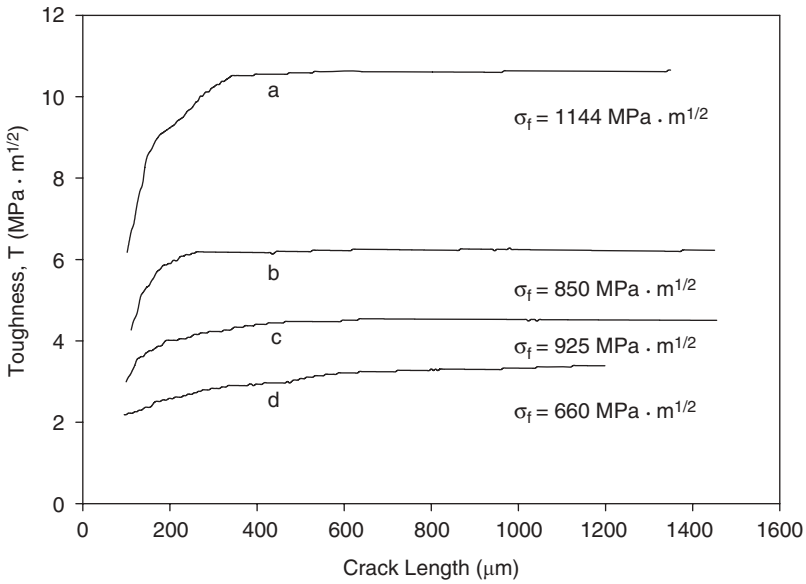
FIGURE 11.15 *R* curves of Si_3N_4 corresponding to microstructures in Figure 11.15(a), (b), (c), and (d), respectively. (From Becher et al., 1998. Redrawn with permission of Wiley-Blackwell.)

Where K_0 is the fully dense toughness. Ostrowski and Rödel (1999) use a relationship similar to Phani and Niyogi (1987):

$$K_C(P) = K_0' \left(1 - \frac{P}{P_0} \right)^n$$

where K_0' is the crack tip toughness extrapolated to 100% density. Unlike the grain size the porosity dependence of toughness, K_C, and fracture energy, G, are different since they are related through $E(P)$ according to Eq. (5.42). According to Rice (1996), G has a more gradual decrease with P than does K_C. The fracture strength generally has a strong P dependence similar to $E(P)$. Measurements by Ostowski and Rödel indicate a similar dependency of fracture strength on porosity as $K_C(P)$ in a fine-grain alumina, leading one to believe that $K(P)$ is the most important term in the Griffith equation (10.1). Other terms $Y(P)$ and $c(P)$ are also dependent on P but are likely not so strongly porosity dependent.

11.10 FRACTURE OF TRADITIONAL CERAMICS

Traditional ceramics are fabricated from natural minerals, mostly clay, and when fired contain 20–30% glass in addition to crystalline particles. The

measured toughness of these ceramics lies somewhere between glass, $K_{IC} < 1$ MPa $\cdot$ m$^{1/2}$, and polycrystalline ceramics, $K_{IC} = 2.5$–5 MPa $\cdot$ m$^{1/2}$ depending on the amount of glass in the microstructure. Fracture strengths of porous steatite, cordierite, and forsterite are usually < 50 MPa. The fracture strengths of quartz and cristobalite porcelains, alumina porcelain, normal steatite, and vitreous forsterite are usually 50–100 MPa. The fracture strengths of porcelain with high alumina and low-loss steatites may range from 100 to 200 MPa. See Morrell (1985). As compared to fine-grained alumina (see Figure 11.10) these strengths are not particularly high.

   Electrical porcelain, as an example, is fabricated from approximately 45–55% clay (ball clay and china clay), 25–35% feldspar, and 20% silica. Figure 11.16 shows a polished surface of electrical porcelain after being fired at 1350°C. By the time the porcelain reaches 1350°C the feldspar has reacted with some of the clay, forming a large amount of glass. Above 1000°C mullite needles begin to form and are readily apparent in the micrograph of porcelain fired at 1350°C. Around 1200°C clay and feldspar begin dissolving quartz particles, forming a solution rim around each particle. During cooling ring cracks develop because of a transformation of quartz particles from high quartz to low quartz at 573°C due to a 2% decrease in volume. For high-strength porcelain alumina is sometimes used because alumina does not undergo a deleterious phase transformation and the thermal expansion coefficient is higher than the matrix. However, it is a more expensive filler than quartz. The strength and toughness of these traditional ceramics would be much lower if it were not for the mullite needles that grow among the glass.
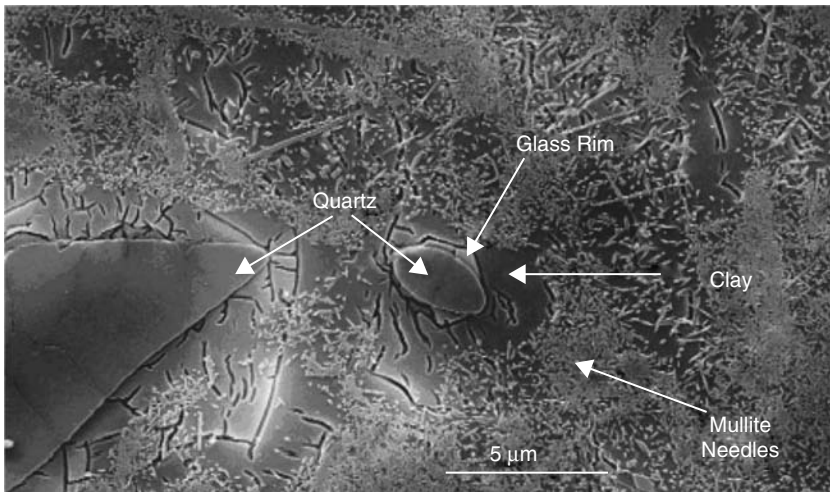
FIGURE 11.16   Microstructure of electrical porcelain fired at 1350°C. (From Islam et al., 2004. Reprinted with permission of Elsevier Press.)

PROBLEMS

1. Compare the two columns in Table 11.1 to determine whether they agree with each other by converting fracture energy γ into K_{IC} under plane stress conditions using equations for the isotropic elastic properties for polycrystalline Al_2O_3, that is, $E = 380\,GPa$. Determine γ for the highest toughness for Al_2O_3 in Figure 11.6. Explain why the value is higher than those shown in Table 11.1 for single crystals. The average surface energy γ_s for various crystallographic planes in Al_2O_3 is $1.2\,J/m^2$. Speculate why the value is lower than values shown in Table 11.1.

2. Toughening mechanisms might be divided into crack tip mechanisms and crack wake mechanisms. Knehans and Steinbrech's experiment (Figure 11.2) really only proved that toughening of their specimens was due to a crack wake mechanism. From Chapter 10, Table 10.1, which mechanisms are crack wake and which are crack tip mechanisms?

3. Consider a small edge crack ($c = 25\,\mu m$) whose crack tip is in a grain of Al_2O_3 and the crack plane is the prismatic plane (0001) and so the direction in which the crack opens is the "c" direction.
   a. What is the total local tensile stress at $1\,nm$, $100\,nm$, and $1\,\mu m$ directly ahead of the crack tip of the crack when the applied stress is $300\,MPa$ including thermal stresses? Assume that Eq. (5.27) for isotropic elastic properties holds for the stresses in front of the crack tip.
   b. If the thermal and applied stresses both act across the entire crack surface and $K_{IC} = 4\,MPa \cdot m^{1/2}$, will the crack grow?
   c. From parts a and b, what conclusion might you draw about how the thermal expansion stresses affect the crack?

4. It is suggested in Chapter 12 that internal stresses σ_i due to thermal expansion are higher at the corners of the grain according to the equation $\sigma_i = \sigma_{TEA}(d/r)$ where σ_{TEA} is the thermal stress, d the grain diameter, and r the distance from the corner of the grain. This equation cannot be used at exactly the corner since it leads to an infinite stress. Assume that σ_c is the value at $d/r = 2$. What is the average stress over a $c = 1\,\mu m$ crack perpendicular to the c axis and lying in line between the middle of the grain and the corner for $d = 20\,\mu m$ and $d = 100\,\mu m$ according to the above equation? What is the strain energy release rate on each of the cracks. Assume $\alpha_a = \alpha_b = 8.3 \times 10^{-6}C^{-1}$; $\alpha_c = 10.2 \times 10^{-6}$ $v = 0.22$, $\Delta T = 1200°C$, and $E = 240\,GPa$. Could this lead to a grain size dependence on strength? Why or why not?

5. Consider Al_2O_3 spheres in a glass matrix cooled from $1000°$ to $25°C$. If cracks form around the spheres, what direction will the cracks propagate relative to the spheres? What will the stress be at the surface of the particle on each side of the interface? What might stop the crack from propagating further?

Assume $E_{glass} = 70\,GPa$, $\nu_{glass} = 0.25$, $\alpha_{glass} = 9 \times 10^{-6}$, $E_{Al_2O_3} = 380\,GPa$, $\nu_{Al_2O_3} = 0.23$, and $\alpha_{Al_2O_3} = 8.3 \times 10^{-6}$.

6. Consider a spherical particle whose thermal expansion coefficient is $8 \times 10^{-6}/°C$ in a matrix whose thermal expansion coefficient is $4 \times 10^{-6}/°C$. During cooling from the sintering temperature, $\Delta T = 1100°C$, thermal expansion stresses develop around the particle ($E_m = E_p = 380\,GPa$, $\nu_m = \nu_p = 0.2$). A flaw approaches the particle along a path in line with the center of the particle. The applied stress on the crack produces $K_I = 4$ $MPa \cdot m^{1/2}$. Using the principle of superposition (stresses are additive), determine the following.

a. Write an equation for the local stress σ_{yy} between the crack tip and particle as a function of distance from the crack tip to the particle along $\theta = 0$ where the crack tip is $6\,\mu m$ away from the edge of the particle. [See Eq. (5.27)]. Assume the origin at the crack tip. The particle diameter is $15\,\mu m$. What is the local stress at $4\,\mu m$ from the particle edge?

b. Will the crack in part a be deflected by the particle or will it be attracted to the particle?

12

TOUGHENING BY TRANSFORMATION

12.1   INTRODUCTION

Transformation-toughened ceramics constitute a major family of tough and flaw-tolerant ceramics. These desirable qualities can be combined with high strength. These good properties are usually optimized at room temperature and decrease with increase in temperature. Thus far, only zirconia (including some typical hafnia content) has been used as the transforming phase in practical transformation toughening, although other possible transforming ceramics have been considered by Kriven (1988). The effect of transformation of some zirconia grains on the thermal expansion of a zirconia ceramic was studied long ago by Geller and Yavorsky (1945), and it was realized that there were advantages to using partially stabilized zirconia rather than fully stabilized zirconia, although the mechanisms were not initially understood. King and Yavorsky (1968) spoke of "a rather remarkable ceramic material which displays a great tolerance to stress concentration" and considered stress relief by plastic deformation as a possible contributing mechanism. Recognition that stress-induced martensitic transformation from the tetragonal to the

monoclinic phase can occur in the high-stress field near a crack tip and cause significant toughening initiated development of a variety of toughened zirconias and other ceramics (such as alumina) toughened by the addition of zirconia grains (Garvie et al., 1975; Evans and Heuer, 1980; Claussen, 1983; Heuer et al., 1986; Evans and Cannon, 1986; Heuer, 1987; Cannon, 1989; Green et al., 1989; Hannink and Swain, 1994). At least three mechanisms of toughening can operate in zirconia and in dual-phase oxides containing zirconia (Stevens, 1991): (1) stress-induced transformation toughening, (2) the development of compressive surface layers as a result of transformation caused by surface stresses, and (3) toughening by microcracking, as discussed in Chapter 11. Hannink and Swain (1994, p. 360) discuss transformation toughening in terms of three crack tip shielding mechanisms: "1. direct crack-tip shielding: deflection and meandering as a result of precipitates and grain size; 2. crack wake-zone shielding: which for zirconia-bearing ceramics includes transformation toughening and microcrack toughening; 3. contact shielding: which includes tetragonal grain wedging, sliding of grain facets and elongated precipitates, and particle bridging." The present chapter focuses on the phenomenology and theory of stress-induced transformation toughening. Successful use of this theory is presented at the end of this chapter.

12.2 BASIC FACTS OF TRANSFORMATION TOUGHENING

A notation used to designate various types of transformation-toughened ceramics has been developed and is summarized in Table 12.1 (Claussen, 1983; Heuer, 1987). The basic crystallographic facts about zirconia pertinent to transformation toughening will now be summarized following Heuer (1987). Pure zirconia exhibits a stable, cubic form (fluorite structure) from the melting point (about 2850°C) to about 2350°C. With further decrease in temperature pure zirconia transforms to a tetragonal form that remains stable to about 1240°C with transformation strains $c \rightarrow t$ of $\varepsilon_1 = \varepsilon_2 = -0.00878$, $\varepsilon_3 = 0.01209$.

TABLE 12.1 Types and Acronyms for Zirconia-Toughened Ceramics (ZTCs)

Mg–PSZ, Ca–PSZ, etc. (precipitation-toughened ceramics; PS = partially stabilized)	Mg–partially stabilized zirconia, Ca–partially stabilized zirconia
Y–TZP (nearly single-phase ceramics based on tetragonal ZrO_2 solid solutions; $T–ZrO_2$)	Yttria-containing tetragonal solid solutions
ZTA, ZTM, etc. (dispersion-toughened ceramics; ZDC or DZC = dispersed zirconia ceramics)	ZrO_2–toughened Al_2O_3, ZrO_2–toughened $3Al_2O_3 \bullet 2SiO_2$ (mullite), etc.

Sources: Claussen (1983) and Heuer (1987).
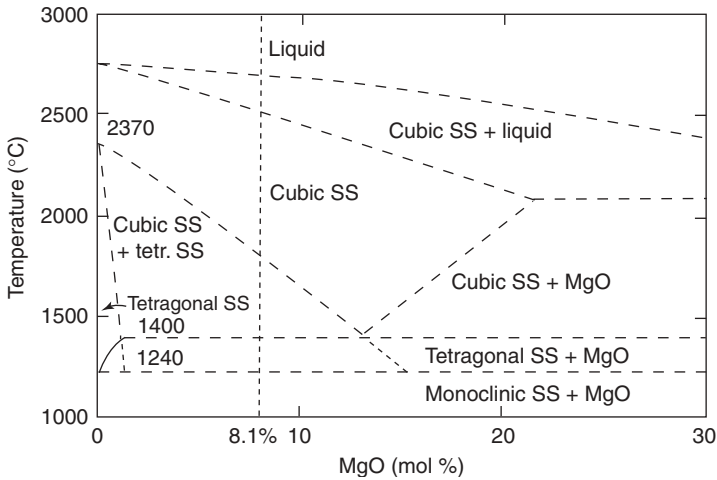
FIGURE 12.1 Zirconia-rich end of the zirconia–magnesia phase diagram. (From Grain, 1967. Reprinted by permission of the American Ceramic Society.)

Further decrease in temperature causes a transformation from tetragonal to monoclinic that is stable at lower temperatures and undergoes a $t \rightarrow m$ transformation strain of $\varepsilon_{11} = -0.00149$, $\varepsilon_{22} = 0.02442$, $\varepsilon_{33} = 0.02386$, $\varepsilon_{13} = \varepsilon_{31} = 0.08188$. That is, the $t \rightarrow m$ transformation of an isolated crystal is accompanied by both a volume change $\varepsilon_{ii}^{T} = \varepsilon_{11} + \varepsilon_{22} + \varepsilon_{33} = 0.04759$ and a shape change. The phase diagram for zirconia–magnesia as determined by Grain (1967) and redrawn by Porter and Heuer (1979) is shown in Figure 12.1. The transformation temperatures can be considerably modified by solid solution and the term *stabilization of zirconia* is used to designate the lowering of the cubic to tetragonal transformation temperature. The $c \rightarrow t$ transformation has not been studied in pure zirconia but is displacive and nonmartensitic in cubic solid solutions in the $Y-ZrO_2$ system. The tetragonal-to-monoclinic transformation is martensitic. A model of the mechanics of the stress-induced phase transformation in zirconia has been given by Budiansky and Truskinovsky (1993).

The strains associated with the tetragonal-to-martensitic transformation cause microcracking in pure zirconia when sintered materials are cooled through the transformation temperature. Zirconia fully stabilized with an additive such as MgO can be sintered in the cubic phase at moderate temperatures and subsequently cooled to room temperature without cracking because of the sluggish transformation. However, these materials have low thermal conductivity and high thermal expansion, giving poor thermal shock resistance. An early empirical development was that of partially stabilized zirconias containing enough MgO to produce a mixture of cubic and tetragonal precipitates. These materials have lower thermal expansion due to the volume expansion associated with the transformation upon cooling.

Subsequently, it was recognized that the tetragonal-to-monoclinic transformation temperature of a precipitate constrained by a matrix depends on the precipitate size. The temperature at which some precipitates begin to transform from tetragonal to monoclinc as the temperature is being lowered is termed the martensitic start temperature M_s. A controlled distribution of tetragonal precipitate sizes is usually achieved by sintering in the single-phase cubic field and then aging in the field in which a mixture of cubic and tetragonal phases is stable. This process produces precipitates of a tetragonal solution that are coherent with the cubic phase from which they precipitate. The size of these tetragonal precipitates and hence their martensitic start temperatures are sensitive to the thermal history.

12.3   THEORY OF TRANSFORMATION TOUGHENING

Transformation toughing of ceramics by crack tip shielding require a phase transformation of zirconia in the high-stress field near the crack tip. As noted above, the $t \rightarrow m$ transformation of zirconia causes both a volume and shape change so that one might expect the stresses driving the transformation to include both dilatational and shear terms. However, a constrained zirconia grain usually undergoes extensive twining as the $t \rightarrow m$ transformation occurs so that the shape change is minimized. Accordingly, it is generally assumed in a first-order theory that only the dilatational component of stress drives the $t \rightarrow m$ transformation. A basic theoretical treatment of this type was given by McMeeking and Evans (1982) followed by Budiansky et al. (1983). The latter investigators introduced the term supercritical transformation to refer to conditions where the tetragonal particles fully transform to monoclinic when a critical dilatational tensile stress is exceeded as opposed to subcritical transformation when the transformation is not complete even though the critical stress to begin transformation is exceeded. It is fully recognized that shear stresses also play some part, as discussed, for example, by Chen (1991) and Stump (1991). We shall here consider only the effect of the dilatational strain and its coupling with the dilatational component of stress because this is sufficient to account for the main effects. As discussed in Section 1.7, the dilatational component of the stress field (minus the pressure) is given by

$$\sigma = -p = \tfrac{1}{3}(\sigma_{xx} + \sigma_{yy} + \sigma_{zz}) \tag{12.1}$$

Following Marshall et al. (1983) and Evans and Cannon (1986), $-p$ is written as σ in this section. It is assumed that tetragonal grains constrained in the matrix will transform to monoclinic at any point at which the dilatational stress exceeds a critical value (dependent on grain size) at a given temperature. If σ_c is the critical value of dilatational stress needed to cause transformation, one can solve for the radius from the crack tip at which the dilatational stress becomes equal to this critical value. That is, given the value of the applied stress intensity

factor K_I one can solve for r_c for which $\sigma > \sigma_c$ as long as $r < r_c$. Recalling the equations for the stresses for plane strain near a crack tip (I refers to mode I opening),

$$\sigma_{xx,I} = \frac{K_I}{(2\pi r)^{1/2}} \cos\frac{\theta}{2}\left(1 - \sin\frac{\theta}{2}\sin\frac{3\theta}{2}\right) \tag{12.2}$$

$$\sigma_{yy,I} = \frac{K_I}{(2\pi r)^{1/2}} \cos\frac{\theta}{2}\left(1 + \sin\frac{\theta}{2}\sin\frac{3\theta}{2}\right) \tag{12.3}$$

$$\sigma_{zz,I} = \nu(\sigma_{xx} + \sigma_{yy}) \tag{12.4}$$

leads to

$$r_c = \frac{2(1+\nu)^2}{9\pi}\left(\frac{K_I}{\sigma_c}\right)^2 \cos^2\frac{\theta}{2} \tag{12.5}$$

A plot of this stress contour is shown in Figure 12.2. The ordinate is

$$y = r_c \sin\theta \tag{12.6}$$

A crack under no applied stress in a ceramic containing a volume fraction V_f of tetragonal zirconia grains is assumed to cause no transformation. When a stress is applied to produce a stress intensity factor K, it is assumed that all tetragonal grains within the zone having $\sigma > \sigma_c$ transform to the monoclinic phase. If the crack propagates as shown in Figure 12.2, the grains are assumed to remain in the monoclinic phase, producing a "wake" of width $w = y_{max}$ on either side of the crack as shown. The ordinate y has its maximum value at $\cos\theta = \frac{1}{2}$
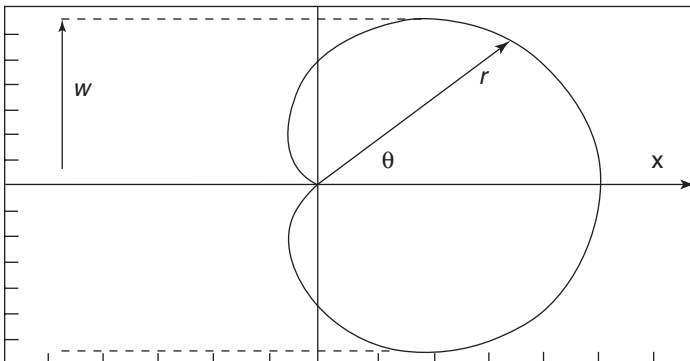

FIGURE 12.2   Stress contour for transformation and wake.

so that

$$w = \frac{3^{1/2}(1+\nu)^2}{12\pi}\left(\frac{K_I}{\sigma_c}\right)^2 = 0.046(1+\nu)^2\left(\frac{K_I}{\sigma_c}\right)^2 \qquad (12.7)$$

or

$$K_I = \frac{(4 \times 3^{1/2}\pi)^{1/2}\sigma_c w^{1/2}}{1+\nu} \approx \frac{\sigma_c w^{1/2}}{0.21(1+\nu)} \qquad (12.8)$$

It can be shown that there is no increment of toughening, that is, $\Delta K = 0$, for only the frontal zone (Figure 12.2). Toughening comes as the crack propagates and develops a wake. This is understood by noting that transforming particles directly ahead of the crack are expanding. From the previous chapter, expanding particles constrained by the matrix create a tensile circumferential stress in the matrix. Such stress would aid in crack propagation. On the other hand, particles more to the side of the crack tip place the crack in compression due to radial compressive stresses around the particle, which applies a closure force to the crack. The incremental toughness due to an element dA at (r, θ) ahead of the crack tip is given by

$$dK(r, \theta)_{dA} = \frac{2EV_f\varepsilon^T(1+\nu)\cos(3\theta/2)\,dA}{3(1-\nu^2)(8\pi r^3)^{1/2}} \qquad (12.9)$$

where V_f is the volume fraction of tetragonal particles transformed within the zone. For $\theta \leq 60°$, $\Delta K < 0$. (Positive ΔK means toughening. The opposite-sign convention has often been used in describing transformation toughening.) For

TABLE 12.2   Steady-State Toughness Values

Net Strain Coupling	Zone Shape	Toughness	Comment
Dilation	Hydrostatic contour	$\dfrac{0.22EV_T\varepsilon_{ii}^T w^{1/2}}{1-\nu}$	No reversal
		$\dfrac{0.21EV_t\varepsilon_{ii}^T w^{1/2}}{1-\nu}$	Reverses with maximum hysteresis
	Shear-band profile	$\dfrac{0.38EV_T\varepsilon_{ii}^T w^{1/2}}{1-\nu}$	No reversal
Uniaxial dilation	Maximum principal stress contour	$0.55EV_T\varepsilon_u^T w^{1/2}$	No reversal
Dilation and relaxed shear strain	Relaxed shear front	$\dfrac{0.22E\,V_T\varepsilon_{ii}^T w^{1/2}}{1-\nu}$	

Source: After Evans and Cannon (1986).

higher angles $\Delta K > 0$. If Eq. (12.9) is integrated over the entire frontal zone, $\Delta K = 0$. Integrating, however, over the wake for a fully developed and long crack wake gives a $\Delta K > 0$ (toughening),

$$\Delta K^T = \frac{0.2143 E V_f \varepsilon^T w^{1/2}}{1 - \nu} \tag{12.10}$$

In a later, more complete treatment, Evans and Cannon (1986) considered not only the possibility of a purely dilatational effect but several other possibilities, as summarized in Table 12.2.

12.4 SHEAR-DILATANT TRANSFORMATION THEORY

As noted earlier, shear stresses should play a role in causing the tetragonal-to-monoclinic transformation as well as dilatational stress. Chen (1991) has summarized theoretical work by others taking shear stress into account and presented an extension of the theory whose results we briefly summarize here. For a dilatational stress criterion alone Chen obtains

$$\Delta K^T = \frac{0.2143 \varepsilon^T E \, w^{1/2}}{1 - \nu} \tag{12.11}$$

which is the McMeeking–Evans result. When a shear-dilatational criterion is used, he obtains

$$\Delta K^T = \frac{0.4783 \varepsilon^T E w^{1/2}}{1 - \nu} \tag{12.12}$$

The stronger toughening effect appears to be in better agreement with experimental data.

12.5 GRAIN-SIZE-DEPENDENT TRANSFORMATION BEHAVIOR

As noted above, the transformation temperature of a tetragonal zirconia particle constrained in a matrix will be altered from that of a free particle. The temperature at which a constrained particle will spontaneously transform is termed the martensitic start temperature M_s. It is commonly observed that the martensitic start temperature depends on the size of the transforming grains. We now summarize a theory of this effect due to Becher and Swain (1992). The change in free energy of a tetragonal particle embedded in a matrix undergoing the phase transformation to monoclinic is

$$\Delta F_0 = \Delta F_{\text{chem}} + \Delta U_e + \Delta U_s - \Delta U_I \tag{12.13}$$
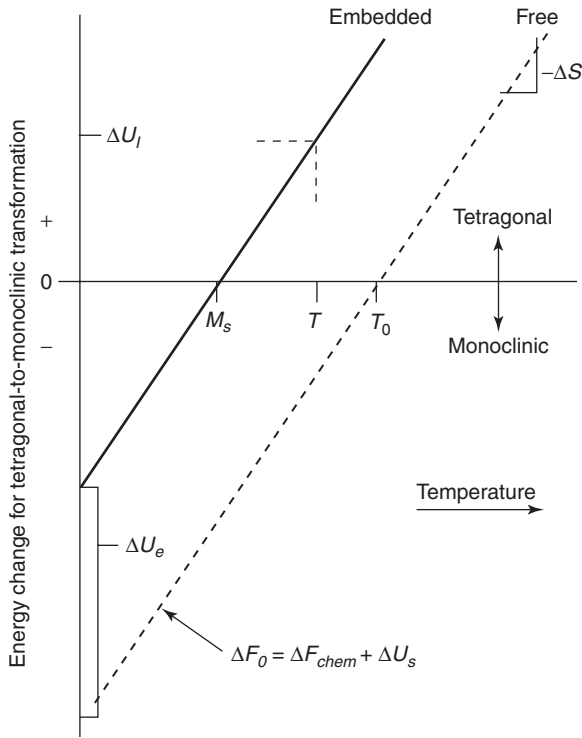
FIGURE 12.3   Free energy of tetragonal to monoclinic transformation of zirconia. (From Becher and Swain, 1992. Reprinted by permission of the American Ceramic Society.)

where ΔF_{chem} is the chemical free-energy change. The free-energy change associated with the interfacial energy (or for a free particle the change in surface energy) is ΔU_s, and the strain energy change is ΔU_e. The term ΔU_I is the interaction term caused by the applied stress on the transforming particle. Figure 12.3 shows the free-energy change with temperature for a free particle and the curve for an embedded particle shifted vertically by ΔU_e. The difference between the chemical free energy of transformation at a temperature T and that at T_0 is

$$\Delta F_{\text{chem}} = \Delta S^{t \to m}(T_0 - T) \tag{12.14}$$

where $\Delta S^{t \to m}$ is the transformational entropy change and has the value $-3.2 \, \text{J/mol} \cdot \text{K}$ below $100°\text{C}$. The transformation temperature T_0 of a free particle is reduced to M_s for an embedded particle. Cooling to M_s initiates the transformation without application of stress. Cooling to T intermediate between T_0 and M_s does not initiate transformation; a stress sufficient to produce an

interaction term ΔU_I to bring ΔF_0 to zero or less is necessary to initiate transformation according to

$$\Delta F_0 = \Delta S^{t \to m}(M_s - T) - \Delta U_I \tag{12.15}$$

The interaction energy is

$$\Delta U_I = \sigma \varepsilon^T \tag{12.16}$$

where σ is the applied stress and ε^T is the dilatant strain. Requiring ΔF_0 to be zero and solving for the stress give the critical stress for transformation as

$$\sigma_c = \frac{\Delta S^{t \to m}(M_s - T)}{\varepsilon^T} \tag{12.17}$$

The change in critical strain energy release rate due to transformation for the zone on two sides of the crack is (Marshall et al., 1983)

$$\Delta G_C^T = 2V_f \sigma_c \varepsilon^T w \tag{12.18}$$

Substituting Eqs. (12.7) and (12.17) into Eq. (12.18) yields the equation

$$\Delta G^T = \frac{2V_T B}{\Delta S^{t \to m}(M_s - T)}(K_I \varepsilon^T)^2 \tag{12.19}$$

where

$$B = 0.046(1 + \nu)^2$$

From Eq. (10.24) the critical stress intensity factor is

$$K_C^2 = (K_0 + \Delta K^T)^2 = \frac{E}{1 - \nu^2}(G_0 + \Delta G^T) \tag{12.20}$$

where K_0 and G_0 refer to crack extension in the matrix in the absence of transformation and E is Young's modulus. Solving for ΔK^T and noting that, from Eq. (10.21), $K_0^2 = [E/(1 - \nu^2)]G_0$ give

$$\Delta K^T = \left(\frac{E\Delta G^T/(1 - \nu^2)}{1 + 2\,K_0/(\Delta K^T)}\right)^{1/2} \tag{12.21}$$

Substituting an average experimental value of 1.25 for $(1 + 2K_0/\Delta K^T)^{1/2}$ gives

$$\Delta K^T \approx 0.8\left[\left(\frac{E}{1 - \nu^2}\right)\Delta G^T\right]^{1/2} \tag{12.22}$$

Substituting for ΔG^T from (12.19) gives

$$\Delta K^T = 1.1 \left[\frac{EV_T B}{(1 - v^2)\Delta S^{T \to m}(M_s - T)} \right]^{1/2} (K_{\mathrm{I}}\varepsilon^T) \qquad (12.23)$$

This gives a value of ΔK^T that is dependent on the applied stress intensity factor K_{I}. It is useful to eliminate the K_{I} dependence. Substituting $K_{\mathrm{I}} = K_0 + \Delta K^T$ into (12.23) and rearranging give

$$\frac{K_0}{\Delta K^T} = 0.9 \left[\frac{(1 - v^2)\Delta S^{t \to m}(M_s - T)}{BEV_T(\varepsilon^T)^2} \right]^{1/2} - 1 \qquad (12.24)$$

Thus the value of ΔK^T depends on the difference between the martensitic start temperature and the test temperature. The half-width of the transformation zone in terms of K_0 is (Becher and Swain, 1992)

$$w^{-1/2} = \left[\frac{\sigma_c(1 - v^2)}{K_0 B^{1/2}} \right] - \left[\frac{(0.8\sigma_c EV_T \varepsilon^T)^{1/2}}{K_0} \right] \qquad (12.25)$$

Substituting for σ_c gives the dependence of w on the temperature and the martensitic start temperature as

$$w^{-1/2} = \frac{(1 - v^2)[\Delta S^{t \to m}(M_s - T)]^{1/2}}{B^{1/2}K_0 \varepsilon^T}$$

$$\times \left[[\Delta S^{t \to m}(M_s - T)]^{1/2} - 0.9\varepsilon^T \left(\frac{BEV_T}{(1 - v^2)^2} \right)^{1/2} \right] \qquad (12.26)$$

These results show that parameters affecting the martensitic start temperature should have a strong influence on both the toughness achieved at a given temperature and the temperature range over which the transformation makes a contribution to the toughness. The factors influencing the martensitic start temperature include the type and amount of solutes (as these affect the phase diagram) and the size of the tetragonal grains. For example, adding ceria to tetragonal zirconia decreases the M_s temperature. The effect of grain size on the transformation temperature is shown in Figure 12.4 from Becher and Swain (1992) for 12 mol % ceria–tetragonal zirconia ceramics. The temperature at which the expansion percent suddenly increases is M_s. This figure shows a systematic increase in M_s as the grain size is increased from 1.3 to 8 μm. The original argument that was made for the grain size effect was a thermodynamic one. In Eq. (12.13) the free energy ΔF_0 must be negative for the transformation
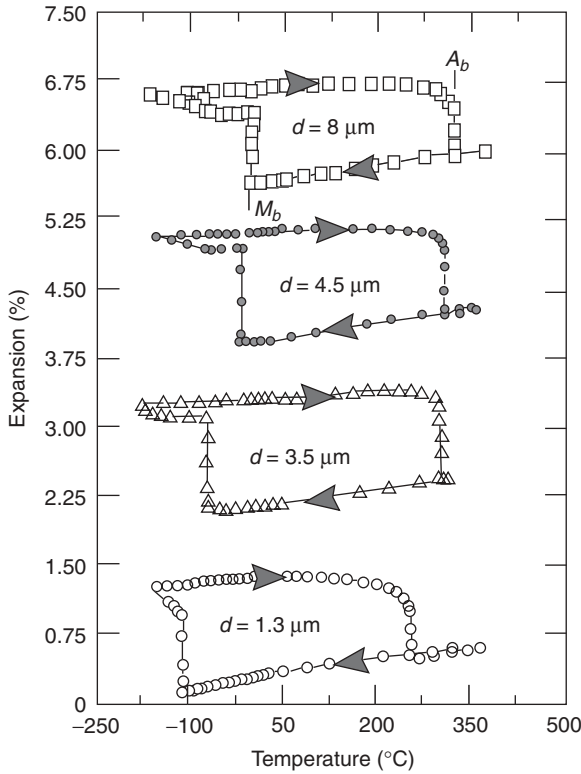
FIGURE 12.4 Thermal expansion hysteresis in 12 mol % ceria tetragonal zirconia ceramics. (From Becher and Swain, 1992. Reprinted by permission of the American Ceramic Society.)

to monoclinic to occur. Here, ΔF_{chem} is always negative at room temperature, ΔU_e is positive, ΔU_s is thought to be positive, and $-\Delta U_I$ is always negative near the crack tip. Since ΔF_{chem} and ΔU_e vary with the particle volume $\sim d^3$ whereas ΔU_s varies with $\sim d^2$, at larger d the positive value of ΔU_s becomes less important and the grain becomes less stable in the tetragonal phase and thus M_s increases. It has since been argued that transformations are not easily reversible and must depend on an activated process for nucleation. Thus the energy for nucleation controls the transformation rate and is not just a function of the beginning and final free energies. Several investigators have discussed the nucleation of monoclinic grains (Heuer et al., 1982; Chen and Chiao, 1983) and local tensile stress has been shown by Hannink (1983) and Hannink and Swain (1983) to promote the transformation. Thus in the following we will discuss toughness as being nucleation controlled.

Becher and Swain introduce the effect of local tensile stress from thermal expansion anisotropy by assuming that the internal stress at a distance r from
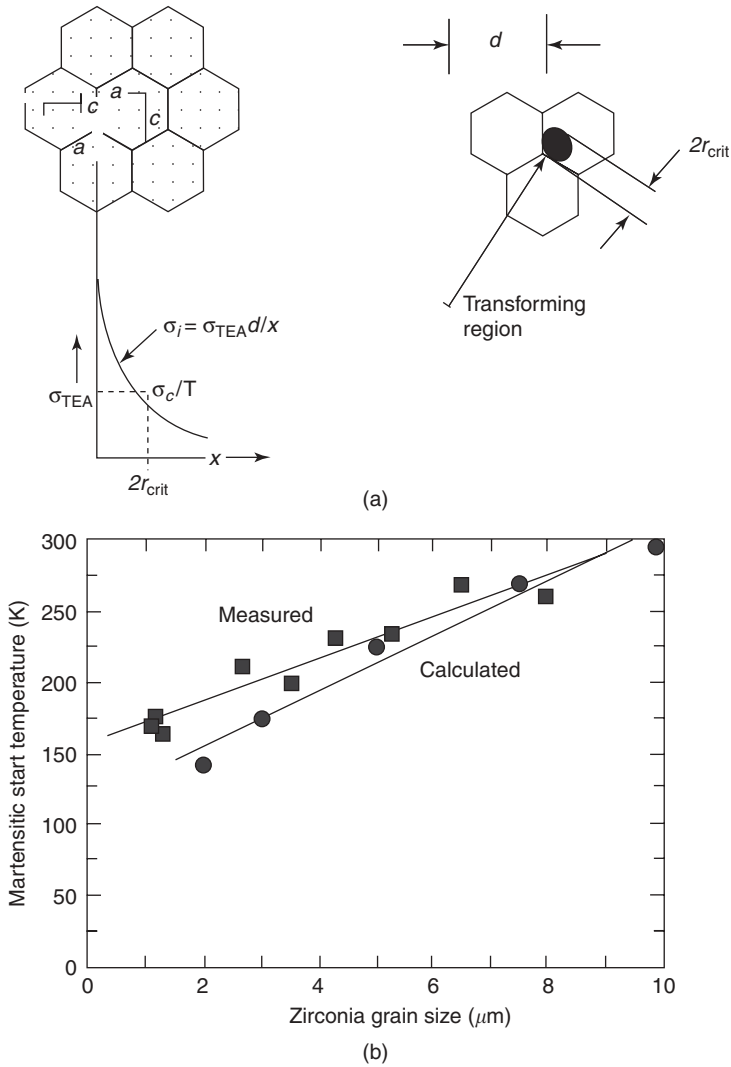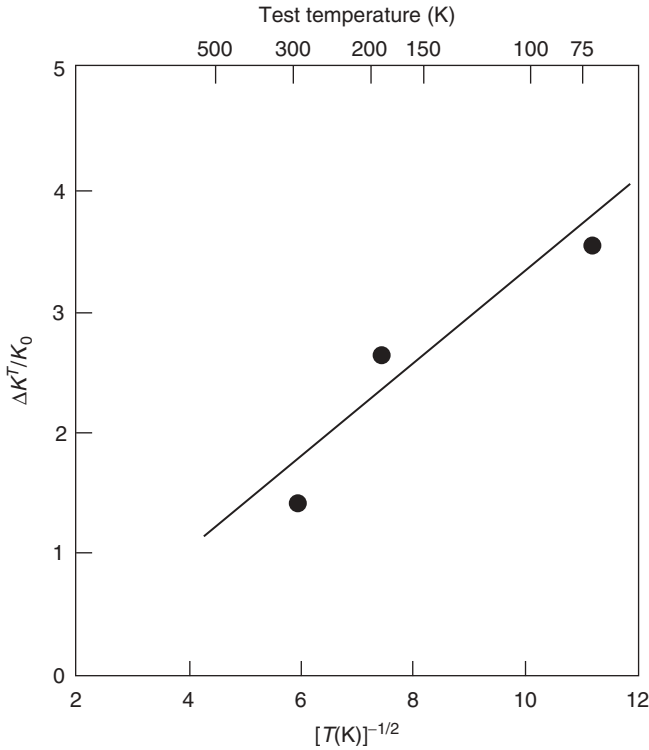
FIGURE 12.5 (a) Local stress concentrations at grain corners due to thermal expansion anisotropy. (b) The effect of these stresses on the martensite start temperature. (From Becher and Swain, 1992. Reprinted by permission of the American Ceramic Society.)

the corner of a grain of diameter d will be given by

$$\sigma_{TEA}\frac{d}{r} \tag{12.27}$$

FIGURE 12.6 Dependence of transformation toughening on test temperature. (From Becher and Swain, 1992. Reprinted by permission of the American Ceramic Society.)

where σ_{TEA} is the thermal expansion stress discussed in Section 11.3. Qualitatively similar stress behavior was obtained in a detailed analysis by Rao et al. (1992) for ZrO_2. Equation (12.24) for the critical applied stress for transformation then becomes

$$\sigma = \sigma_c^* - \sigma_{TEA}\frac{d}{r} = \frac{\Delta S^{t\rightarrow m}(M_s - T)}{\varepsilon^T} \tag{12.28}$$

where

$$\sigma_c^* = \frac{\Delta S^{t\rightarrow m}(M_s^0 - T)}{\varepsilon^T} \tag{12.29}$$

where σ_c^* is the critical transformation stress when no internal stress is present and M_S^0 is the martensitic start temperature in the absence of stress but still on
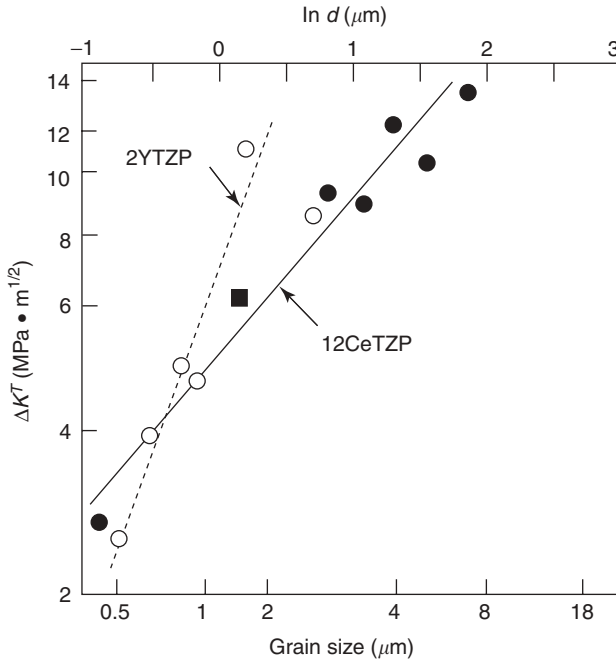
FIGURE 12.7 Dependence of transformation toughening on grain size. (From Becher and Swain, 1992. Reprinted by permission of the American Ceramic Society.)

an embedded particle. The martensitic start temperature is then

$$M_s = M_s^0 - \sigma_{\text{TEA}} \frac{\varepsilon^T}{r\,\Delta S^{t\to m}} d \tag{12.30}$$

using $\sigma_{\text{TEA}} = E\,\Delta\alpha\,\Delta T$ with $\Delta T = T_{\text{sr}} - M_s$, where T_{sr} is the temperature below which thermal stresses cannot relax, and defining

$$a = E\,\Delta\alpha \frac{\varepsilon^T}{r_{\text{crit}}\,\Delta S^{t\to m}} \tag{12.31}$$

where r_{crit} is the radius over which nucleation of the tetragonal phase occurs (see Figure 11.5). From Eq. (12.30)

$$M_s = \frac{M_s^0 - aT_{\text{sr}}d}{1 - ad} \tag{12.32}$$

For 12 mol % CeO_2 in T–ZrO_2 the result is a nearly linear dependence of M_s on d, as shown in Figure 12.5. Equation (12.32) predicts such a relationship if $ad \ll 1$ and a is negative.
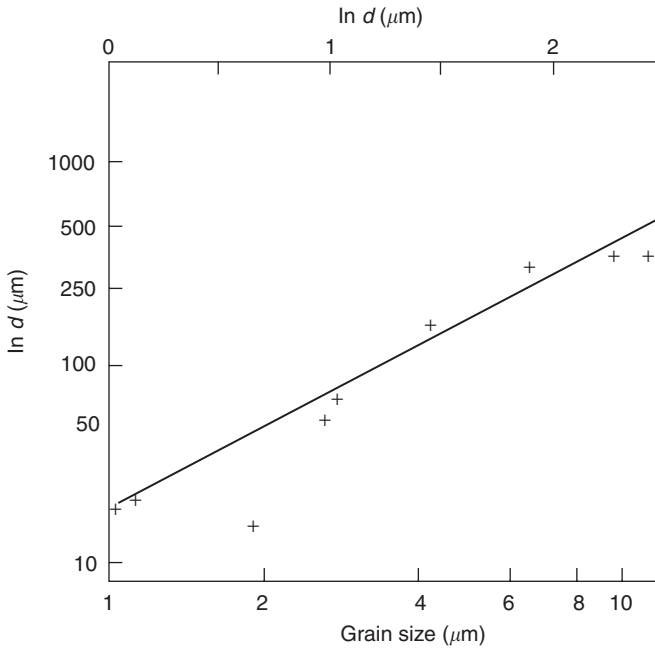
FIGURE 12.8 Dependence of transformation zone width on grain size. (From Becher and Swain, 1992. Reprinted by permission of the American Ceramic Society.)

The effect of grain size on ΔK^T can be treated similarly by substituting for M_s in terms of d. The result is

$$\frac{K_0}{\Delta K^T} = 0.9$$

$$\times \left(\frac{\Delta S^{t \to m} \{ M_s^0 - \sigma_{\text{TEA}}[\varepsilon^T/(r\,\Delta S^{t \to m})]\,d - T \}(1-v^2)^2}{1.6 BE V_T (\varepsilon^T)^2} \right)^{1/2} - 1$$

(12.33)

[Equation (12.33) differs from Eq. (13) in Becher and Swain (1992) by a minus sign after M_2^0 rather than a plus sign.] Equation (12.33) predicts that as the temperature approaches the M_s temperature or as grain size increases, toughening due to transformation should increase. These predicted effects are confirmed by the data of Becher and Swain (1992) shown in Figures 12.6 and 12.7.

Still another effect predicted by the treatment of Becher and Swain is that the width of the transformed zone should increase as the temperature is decreased. This prediction is confirmed by their data, as shown in Figure 12.8.
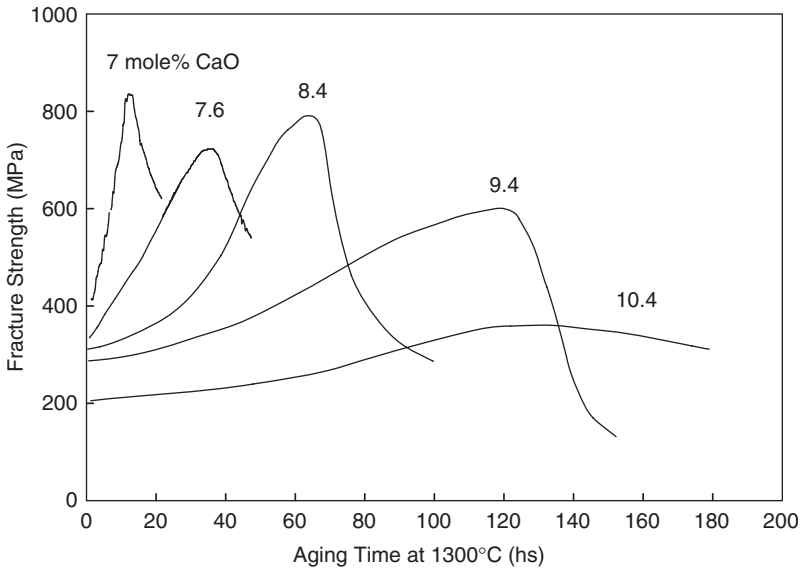
FIGURE 12.9   Flexural strength of Ca–PSZ as function of aging time. (From Garvie et al., 1978.)

12.6   APPLICATION OF THEORY TO CA-STABILIZED ZIRCONIA

A few additional examples will illustrate how the stability of tetragonal zirconia particles or precipitates can be manipulated to achieve the optimum toughness and strength. Calcium-stabilized zirconia will be used as an illustration because its microstructure–mechanical properties relationships are simple. The Ca-stabilized zirconia phase diagram is similar to the Mg-stabilized phase diagram shown in Figure 12.1. In these studies Ca-stabilized zirconia was sintered just into the cubic phase field and well above the eutectoid temperature (1140°C), resulting in large-grained ($\sim$50-μm) cubic zirconia. Heat treatment at 1300°C, which is in the cubic + tetragonal phase field, causes fine tetragonal particles to nucleate and grow. Figure 12.9 illustrates how with increased annealing time there is an increased size and number of tetragonal particles causing the room temperature strength to go up (M_s increases towards room temperature). The strength peaks because at an annealing time sufficiently large some of the particles grow to a size where they become so unstable that they convert to monoclinic during cooling and strength begins to drop.

A more fundamental study of (8.4 mol % or 3.8 wt. %) materials shows how K_{IC} is related to the particle size (Figure 12.10). At the optimum size of $\sim$225 nm the toughness peaks. When the tetragonal particles are larger, they convert to monoclinic on cooling and, therefore, do not contribute to
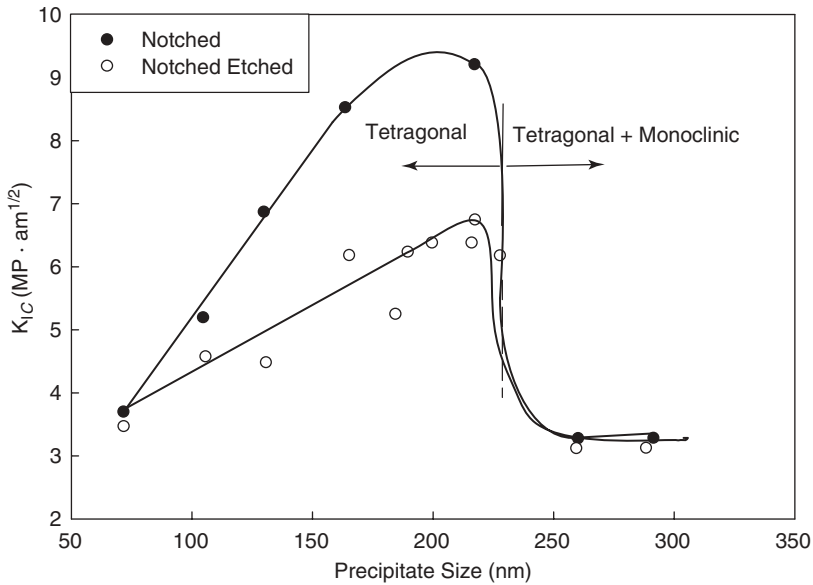
FIGURE 12.10   Critical stress intensity factor of 8.4 mol % Ca–PSZ as function of aging time. (From Swain et al., 1983.)

transformation toughening and toughness falls off rapidly. When machining a notch in the specimen, tetragonal particles near the surface convert to monoclinic, placing the surface in compression, resulting in a higher toughness. Etching the surface removes $\sim 50\,\mu m$ of material, effectively relieving the surface stress.

Figures 12.11(a), (b), and (c) illustrate the effect of the temperature at which the specimens are tested. In Figure 12.11(a) the toughness decreases with decreasing particle size and increasing test temperatures, both of which cause tetragonal particles to be more stable. In Figure 12.11(b) increased test temperature and decreased particle size result in a smaller percentage of the particles found on the fracture surface to have converted to monoclinic. Finally, in Figure 12.11(c) increased temperature and decreased particle size resulted in smaller process zone radii.

Similar trends are observed for transformation-toughened alumina (Figure 12.12). Claussen and Jahn (1980) found that both fracture strength and toughness peak with increasing milling time of powders prior to sintering. At short milling times the zirconia particles in the sintered specimens are large and so convert more easily to monoclinic on cooling. At longer milling times particles are small and stable to transformation toughening. Figure 12.12, however, shows that the effect is mostly due to transformation near the surface of the notch, putting it in compression, and so when specimens are annealed to transform zirconia near the ground surface back to tetragonal, there is very
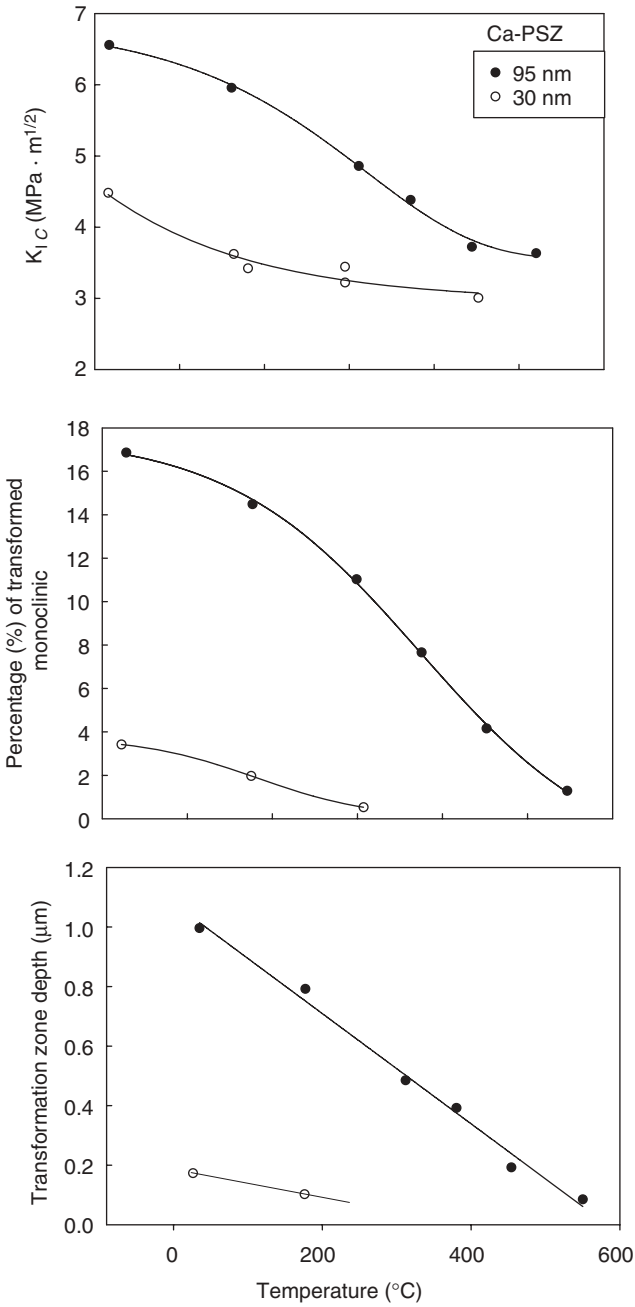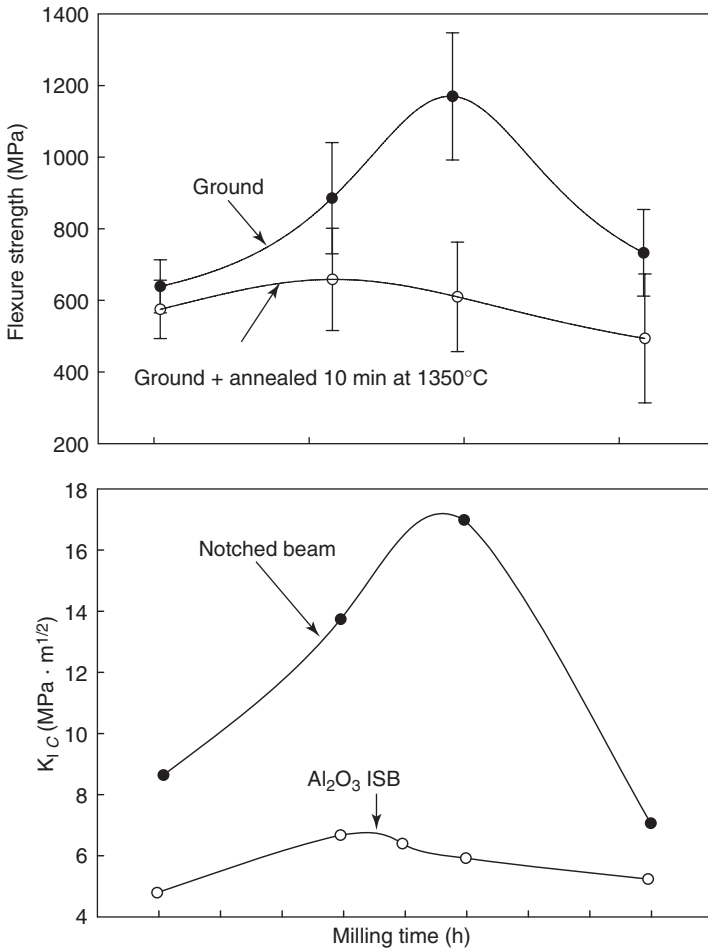
FIGURE 12.11   Temperature dependence for 8.4 mol % Ca–PSZ. (From Swain et al., 1983.)

FIGURE 12.12 Flexure strength and critical stress intensity factor as function of milling time of batch prior to sintering: 15 vol. % ZrO_2–Al_2O_3.

little toughening. Thus surface grinding is important to increasing the toughness.

PROBLEMS

1. Estimate the width of the process zone for Mg–PSZ, Ca–PSZ, and Y–PSZ from the following table. Assume $E = 230\,GPa$ and $\nu = 0.23$ for all compositions. Assume all precipitates transform and that transformation is due only to dilatational stress.

Single Crystal	Composition % Additive to ZrO_2	Precipitate (vol. %)	Fracture Toughness $(MPa \cdot m^{1/2})$
Mg–PSZ	2.8	48	4.82
Ca–PSZ	4.0	38	3.97
Ca–CSZ	9	0	2.54
Y–PSZ	5	52	6.92
Y–CSZ	20	0	1.91

Source: From Ingel et al. (1983).

2. Zirconia is quite unusual in that the lower temperature monoclinic phase has a lower density than the higher temperature tetragonal phase. Can you make a thermodynamic argument for this? What would the effect be on transformation toughening if the low-temperature phase were denser than the high-temperature phase?

3. The density of zirconia is $5.7\,g/cm^3$ and $\nu = 0.23$.
   a. If σ_c measured at $-60°C$ is 300 MPa, determine M_s and then estimate σ_c at $-10°C$ and at $10°C$? Will the toughness be higher measured at room temperature or at $-50°C$?
   b. Calculate the width of the process zone for the three temperatures of part a when $K_I = 2\,MPa \cdot m^{1/2}$.
   c. Calculate ΔG_c and K_{IC} for the three temperatures in part a if $E = 230\,GPa$ and $K_0 = 2.5\,MPa \cdot m^{1/2}$. Assume $V_f = 0.5$.

4. If $K_{IC} = 5.5\,MPa \cdot m^{1/2}$ measured at $25°C$, determine M_s if the width of the process zone is $5\,\mu m$ measured by Transmission electron microscopy (TEM) after fracture. The density of zirconia is $5.7\,g/cm^3$, the molecular weight is $123.2\,g/mol$, and $\nu = 0.23$.

5. Explain the order of the following room temperature toughness values for Mg–PSZ after being annealed:

Annealing time, h	1	2	4	7
Fracture surface energy, $J/m^{1/2}$	220	320	260	150

6. Explain the following toughness values for Mg–PSZ measured at temperatures above room temperature:

Temperature, °C	200	400	600	800
Toughness, $MPa \cdot m^{1/2}$	8.5	6.5	5.5	5

7. Transformation-toughening Al_2O_3 has a higher toughness and strength than pure polycrystalline Al_2O_3: $E_{Al_2O_3} = 380\,GPa$ and $E_{ZrO_2} = 230\,GPa$, $\nu_{Al_2O_3} = 0.23$, and $\nu_{ZrO_2} = 0.31$.

a. Offer a thermodynamic explanation why the toughness of 15% pure ZrO_2 in Al_2O_3 is greater than that of 15% (ZrO_2/3% Y_2O_3) in Al_2O_3.

b. Suppose that grinding the surface of ZrO_2–Al_2O_3 converts tetragonal ZrO_2 to monoclinic. Calculate the stresses surrounding the particle. Assume an isolated particle and no cracking occurs. Is the latter a good assumption?

c. The net stress from all the particles at the surface (part b) is compression. Will this stress increase the fracture strength?

d. Transformation toughening is a low-temperature toughening mechanism; that is, at 500–1000°C it is not too effective. Why?

e. Why might the compressive surface layer (part c) be effective to a higher temperature? To what temperature?

13

MECHANICAL PROPERTIES OF CONTINUOUS-FIBER-REINFORCED CERAMIC MATRIX COMPOSITES

13.1   INTRODUCTION

The mechanical behavior of composites is an essential aspect of the study of the mechanical behavior of ceramics for several reasons. First, polycrystalline ceramics usually involve a grain boundary phase and are thus a two-phase composite. The properties of the ceramic, both fracture and creep, can strongly be influenced by the composite nature of the material. Second, efforts to toughen ceramics have led to the class of ceramic matrix composites in which a reinforcing phase, usually fibrous but sometimes plate shaped, is added. Third,

ceramic fibers are combined with other materials to make metal matrix composites or polymer matrix composites. The basic behavior of fiber-reinforced composites is accordingly treated in this chapter. The term *composites* will be used to refer to fiber-reinforced materials here.

The potential benefits of reinforcing glass with strong fibers have been recognized for a long time (Sambell et al., 1972), and extensive development has been stimulated by the work of the United Technologies group (Prewo and Brennan, 1980; Prewo, 1989). The development of fibers made predominantly of silicon carbide (Yajima et al., 1976) has greatly stimulated work on fiber-reinforced ceramic matrix composites. A good historical review is given by Lewis (1996) and an overall general treatment by Chawla (1993). Lewis's paper is especially valuable for its discussion of the need to consider all failure modes and to achieve more cost-effective ceramic matrix composites.

The conceptual mechanisms of toughening of ceramic matrix composites have been discussed by Rice (1981, 1985). Brennan and Prewo (1982) demonstrated silicon carbide–reinforced glass–ceramic matrix composites with high strength and toughness. Extensive experimental and theoretical developments followed. Basic references to theory include Kelly and MacMillan (1986), Aveston et al. (1971), Marshall et al. (1985), Budiansky et al. (1986), Evans and Marshall (1989), Thouless et al. (1989), Cao et al. (1990), and Campbell et al. (1990). Useful reviews of toughening, including toughening in composites, can be found in Evans (1990), Shah and Ouyang (1991), and Steinbrech (1992).

13.2   ELASTIC BEHAVIOR OF COMPOSITES

Consider first a composite made up of a matrix containing continuous fibers aligned in the direction of applied stress, as shown in Figure 13.1. We shall deal later with the question of the stress necessary to propagate the crack; at present we assume the crack is not present and examine the elastic behavior under tensile stress parallel to the fibers. A load P_c is applied. Of this load P_f is carried by the reinforcing fibers and P_m by the matrix, giving
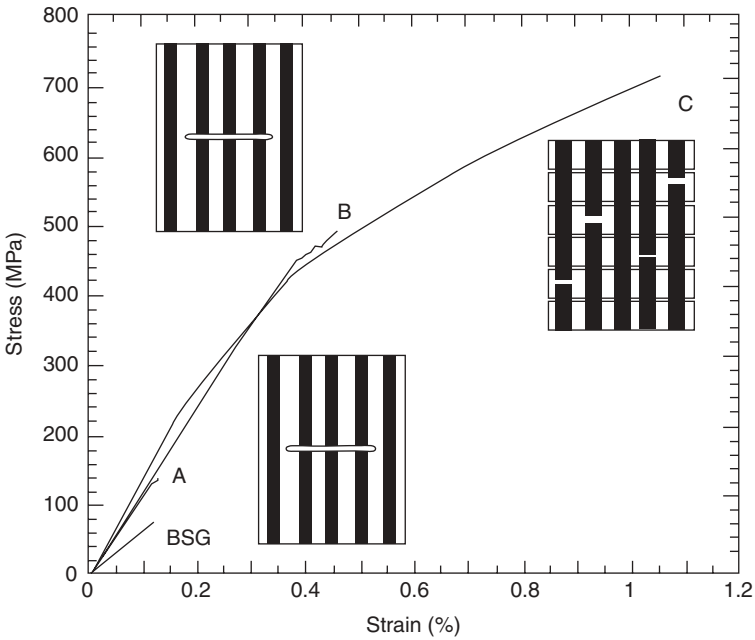
$$P_c = P_f + P_m \tag{13.1}$$

Using σ and A to represent stress and area and using subscripts c, f, and m to indicate the composite, fibers, and matrix, respectively, this load equation becomes

$$\sigma_c A_c = \sigma_f A_f + \sigma_m A_m \tag{13.2}$$

or

$$\sigma_c = \sigma_f \frac{A_f}{A_c} + \sigma_m \frac{A_m}{A_c} \tag{13.3}$$

FIGURE 13.1   Stress–strain curves for composites. The curve labeled BSG is for unreinforced borosilicate glass; A is for a composite with a strong bond to the fibers; and B and C are for composites with weaker bonds. (From Karandikar et al., 1996. Reprinted by permission of the American Ceramic Society.)

Letting V denote volume fraction and Vol denote volume and noting that the area fractions are equal to the volume fractions for either a composite made up of aligned continuous fibers or a composite made up of randomly dispersed short fibers, that is,

$$\frac{A_f}{A_c} = \frac{\text{Vol}_f}{\text{Vol}_c} = V_f \tag{13.4}$$

and

$$\frac{A_m}{A_c} = \frac{\text{Vol}_m}{\text{Vol}_c} = V_m \tag{13.5}$$

gives

$$\sigma_c = \sigma_f \, V_f + \sigma_m \, V_m \tag{13.6}$$

The Young's modulus of the composite is obtained by writing Eq. (13.6) as

$$E_c \varepsilon_c = E_f \, \varepsilon_f \, V_f + E_m \, \varepsilon_m \, V_m \tag{13.7}$$

and using the equality of strains to get

$$E_c = E_f V_f + E_m V_m \tag{13.8}$$

Thus the elastic modulus of the composite is given simply by the rule of mixtures.

It is interesting to see how the average stress in the composite compares to the stress in the matrix. This can be done by equating the strains in the composite, fibers, and matrix,

$$\varepsilon_c = \frac{\sigma_c}{E_c} = \varepsilon_f = \frac{\sigma_f}{E_f} = \varepsilon_m = \frac{\sigma_m}{E_m} \tag{13.9}$$

and so $\sigma_f = (E_f/E_m)\sigma_m$ and noting that $V_f + V_m = 1$ give

$$\sigma_c = \sigma_f V_f + \sigma_m (1 - V_f) = \sigma_m \left[1 + V_f \left(\frac{E_f}{E_m} - 1 \right) \right] \tag{13.10}$$

Thus, if V_f is high and $E_f > E_m$, then the average stress in the composite is higher than the stress in the matrix and so the load must have been shifted more to the fibers.

The ratio of the total load carried by the composite to the load carried by the fibers can be expressed as

$$\frac{P_c}{P_f} = \frac{\sigma_c A_c}{\sigma_f A_f} = \frac{E_c}{E_f} \frac{1}{V_f} \tag{13.11}$$

The equations of this section allow one to make predictions about the behavior of uniaxial composites, but they should be used with the understanding that they are approximate because no account has been taken of the variation of stress and strain locally around the ends of fibers. Also, the above treatment assumes an uncracked matrix. We take up the question of matrix cracking in the next section.

The above discussion of elastic deflection of composites with aligned, continuous reinforcements is adequate for our present purpose. However, we note that a more complete discussion of elastic behavior of such composites requires five independent elastic constants characteristic of transversely isotropic solids. These constants can be chosen in various ways. A useful choice (Christensen and Waal, 1972) is E_{11}, Young's modulus in the direction of fiber alignment; ν_{12}, Poisson's ratio for stress in the aligned direction; K_{23}, the plane strain bulk modulus in the plane containing the transverse axes; μ_{12}, the shear modulus for a plane including the aligned direction; and μ_{23}, the shear modulus for distortion in the transverse direction. The relation of the elastic moduli of the composite to the elastic properties of the fibers and matrix has been treated by Hashin and Rosen (1964).

13.3   FRACTURE BEHAVIOR OF COMPOSITES WITH CONTINUOUS, ALIGNED FIBERS

Composites of continuous ceramic fibers in a ceramic matrix differ from the more common ceramic fibers in a polymer matrix (e.g., fiber glass) or in a metal matrix in that in the ceramic–ceramic composite's failure of the more brittle matrix comes before failure of the fibers and the reverse is true for ceramic fiber polymer or metal composites. Two reasons may be given why the ceramic fiber is stronger than the ceramic matrix. First, the most popular ceramic fibers such as borosilicate glass, alumina, or SiC fibers have a diameter on the order of 12 μm. The largest flaw, naturally, must be much less than 12 μm; otherwise the fibers could not be manufactured in large lengths. Even a flaw penetration 10% of the diameter according to the Griffith equation would lead to strengths on the order of 2 GPa. Second, we might refer back to Chapter 7 where it was shown that $\sigma_f \sim V^{-1/m}$ [Eq. (7.41)], which resulted from the likelihood of finding a small flaw as the volume diminishes (or surface area). Since the volume (or surface area) per unit length of a single fiber is very small, the likelihood of finding a large flaw is also very small. Thus fiber strengths are high. It is then not too serious if some of the load shifts from the matrix to the fiber.

With the advent of these very strong commercial fibers, composites with the improved fracture behavior have been developed. The fracture behavior is illustrated in Figure 13.1 from Karandikar et al. (1994). Experiments show very different behavior depending on whether the brittle matrix is reinforced or not and on whether the reinforcing fibers are coated with a nonreactive material. The stress–strain curve labeled BSG is for unreinforced borosilicate glass. The behavior is elastic up to sudden and complete failure at a strain of about 0.1%. The stress–strain curve labeled A is for borosilicate glass reinforced with uncoated Nicalon SiC parallel and continuous fibers. Again the behavior is elastic until complete brittle failure occurs at about the same 0.1% strain but at appreciably higher stress. The higher fracture stress is reasonable from Eq. (13.10), which predicts that the stress in the composite just before failure is greater than the stress in the matrix as long as $E_f > E_m$ and $V_f > 0$. Brittle failure of the composite occurs when the stress in the matrix reaches the fracture stress for the matrix provided that the sharp crack propagates through the fiber, as shown in the lower drawing in Figure 13.1. If, however, the crack passes around the fiber rather than through it, a bridged crack results, as shown in the upper left-hand drawing in Figure 13.1. This is the case for the stress–strain curve labeled B, which is for the same composite except that the fibers have been coated with a weak, nonreactive coating. Much higher stress and strain values at failure are evident. Finally, the curve labeled C is for the case of multiple cracks and some fiber failure accompanied by energy dissipation as the fibers are drawn out of the matrix. Nearly 10 times as much strain and 6 times as much stress at failure occur than for the unreinforced glass. It is clear that a weak, nonreacting coating is critical for higher strength of ceramic–ceramic

composites. Coatings on silicon carbide fibers are most often made of carbon, but these coatings cannot withstand temperatures greater than about 800°C where carbon burns out rapidly. Boron nitride coatings allow about 200°C increased higher temperature and are also a weak, nonreacting coating. More recently oxide matrix–oxide fiber composites, for instance, aluminum oxide or mixed mullite and aluminum oxide fibers in an aluminum oxide matrix, have been developed. At the time of writing the most popular oxide–oxide composites do not use a coating at all but have a weak porous aluminum oxide matrix so that crack will deflect through the matrix rather than through the fiber. Weak oxide coatings have also been developed. Two examples of weak oxide coatings are Monazite (LaPO$_4$) and Sheelite (CaWO$_4$).

For cases B and C, where the fibers continue to carry the load after partial or complete matrix failure, the fibers must have sufficient strength. The requirement is that

$$V_f \sigma_{fu} \geq V_f \sigma_{fi} + V_m \sigma_{mu} \tag{13.12}$$

or

$$V_f \geq \frac{1}{1 + (\sigma_{fu}/\sigma_{mu}) - (\sigma_{fi}/\sigma_{mu})} \tag{13.13}$$

where the second subscript u indicates ultimate strength and σ_{fi} is the stress in the fiber just before failure of the matrix. Assuming equality of strain in the matrix and fiber just before matrix failure gives [from Eq. (13.9)]

$$\sigma_{fi} = \frac{E_f}{E_m} \sigma_{mu} = \varepsilon_{mu} E_f \tag{13.14}$$

The minimum volume fraction for the fibers to carry the load for a fully cracked matrix is then

$$V_f \geq \frac{1}{1 + (\sigma_{fu}/\sigma_{mu}) - (E_f/E_m)} \tag{13.15}$$

As an example, lithium aluminosilicate glass with $E_m = 88$ GPa and $\sigma_{mu} = 0.17$ GPa reinforced with SiC with $E_f = 180$ GPa and $\sigma_{fu} = 2.5$ GPa requires $V_f \geq 7.5\%$.

Matrix cracking without fiber failure in the plane of the crack can occur only if the concentrated stress at the head of the crack does not propagate the crack through the fiber. The alternative process is crack propagation along the interface between the fiber and the matrix at right angles to the primary crack plane. This may only occur when the coating is weak or when the matrix lacks sufficient toughness that the crack is deflected along the fiber. That is, partial debonding of the fiber from the matrix is required for the fiber to remain unbroken as the matrix crack passes around it. He and Hutchinson (1989) have shown that this requires $\gamma_i/\gamma_f \leq 0.25$, where γ_i is the fracture surface energy for

TABLE 13.1   Constituent Properties of Ceramic Matrix Composites (1996)

Property	Typical Values
Matrix fracture energy, γ_m	5–50 J/m^2
Matrix Young's modulus, E_m	50–200 mPa
Matrix Poisson's ratio, ν	0.25–0.30
Fiber Young's modulus, E_f	180–415 mPa
Fiber Poisson's ratio, ν_f	0.25–30
Fiber strength, σ_{fu}	1.2–3 GPa
Fiber Weibull parameter, m	5–20
Fiber-matrix debond energy, γ_i	0–5 J/m^2
Fiber-matrix sliding stress, τ	1–200 mPa
Fiber-matrix misfit strain, $\delta\varepsilon$	0–2 × 10^{-3}

Source: Zok et al. (1996).

the fiber–matrix interface and γ_f is the fracture surface energy for crack propagation through the fiber. Once the crack is deflected along the fiber, the stress at the tip of the main crack no longer is concentrated on the fiber and so the fiber does not crack. Now the fiber becomes a short tensile specimen of approximate length of the width of the crack with somewhat lower stress along the debonded portion of the fiber. Over this small length the fiber does not fail easily because of the very large tensile strength of such a small tensile specimen.

The above treatment assumed a single value for the ultimate strength of the fibers, although in reality a distribution of values is observed. Evidently the process of fracture in a composite involves many more factors than in a monolithic material, and it is to be expected that a complete theory of fracture of composites will be complex. A minimal list of factors that should enter into such a theory has been given by Zok et al. (1996), and is repeated in Table 13.1.

13.4   COMPLETE MATRIX CRACKING OF COMPOSITES WITH CONTINUOUS, ALIGNED FIBERS

It is easiest to consider a composite made up of a matrix reinforced with parallel, continuous fibers of uniform radius. As stated above the usual case is that of fibers which are stronger than the matrix. Under an increasing tensile stress parallel to the fibers, the matrix will eventually crack. Aveston et al. (1971) treated the matrix-cracking stress as a property of the composite and derived an expression for it. Their treatment was subsequently extended to a full fracture mechanics treatment to deal with the stress necessary to propagate a crack of variable length (Marshall et al., 1985; McCartney, 1987). The earlier Aveston–Cooper–Kelly result for matrix-cracking stress was shown to be the limiting case for the stress necessary to propagate a long matrix crack and so is of considerable interest.

The fiber stress just before matrix cracking, σ_{fi}, can be related to the matrix stress just before cracking, σ_{mu}. Combining Eq. (13.12) with Eq. (13.14) yields

$$\sigma_{fc} = \sigma_{fi} + \sigma_{mu}\frac{V_m}{V_f} = \sigma_{fi}\left(1 + \frac{E_m V_m}{E_f V_f}\right) = \sigma_{fi}(1 + \eta) \qquad (13.16)$$

where σ_{fc} is the stress on the unbroken fiber at the point where it intersects the crack and

$$\eta = \frac{E_m V_m}{E_f V_f} \qquad (13.17)$$

If the fiber debonds from the matrix along the coating, then the stress in the fiber is distributed along the debond length ℓ. The fiber–matrix interface shown in Figure 13.2 is assumed to have a frictional shear stress τ. Near the matrix crack the fiber will slip along the length ℓ such that the total interface force on the fiber of radius r along this distance causes a fiber stress equal to the increase of the fiber stress calculated above. Thus

$$2\pi r \ell \tau = (\sigma_{fc} - \sigma_{fi})\pi r^2 \qquad (13.18)$$

and combining with Eq. (13.16) gives

$$\frac{2\pi r \tau \ell}{\pi r^2} = (\sigma_{fc} - \sigma_{fi}) = \eta \sigma_{fi} = \eta \sigma_{mu}\frac{E_f}{E_m} = \eta \varepsilon_{mu} E_f \qquad (13.19)$$
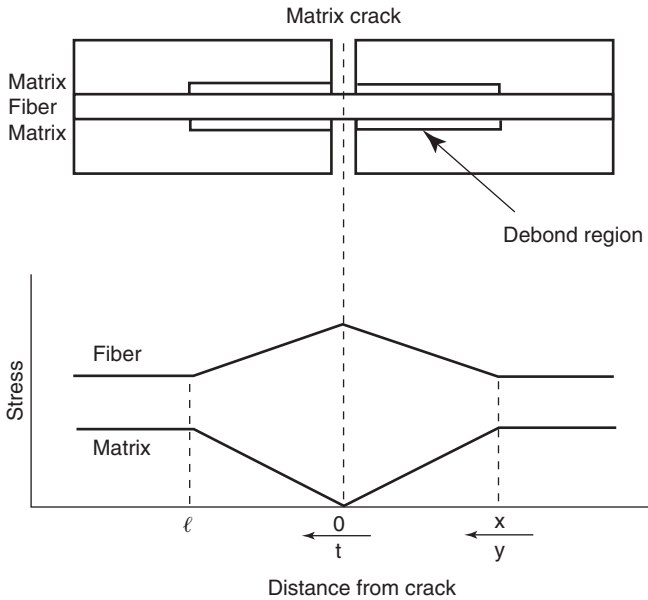

FIGURE 13.2 Debonding and stress distribution in composite.

where ε_{mu} is the strain in the matrix just prior to cracking. Thus the fiber slips along a distance

$$\ell = \frac{\eta \varepsilon_{mu} E_f \, r}{2\tau} = \left(\frac{E_m V_m}{V_f}\right) \frac{\varepsilon_{mu}}{2\tau} r = \left(\frac{V_m}{V_f}\right) \frac{\sigma_{mu} r}{2\tau} \tag{13.20}$$

The matrix stress is thus zero at the crack and rises linearly with distance from the matrix crack to reach its original value σ_m at a distance ℓ, as shown in Figure 13.2. Correspondingly, the fiber stress has the value σ_{fc} at the crack and drops linearly with distance from the matrix crack to reach its original value σ_{fi} at a distance ℓ.

One can now consider the behavior of the composite under constant load, evaluate the work done and energy conversions that take place, and take an energy balance as in the Griffith theory to obtain the matrix-cracking strain and stress. Five changes in energy must be considered: (1) the work ΔW done by the external force as the composite expands as the crack runs; (2) the decrease ΔU_m in elastically stored energy in the matrix due to stress reduction within the distance ℓ; (3) the increase ΔU_f in elastically stored energy in the fiber due to stress increase within the distance ℓ; (4) the dissipation ΔU_s of energy associated with sliding against the friction force; and (5) the energy $2\gamma_m V_m$ required for creation of the crack surface. We consider each of these energies as energy per unit area perpendicular to the fibers.

The work done by the external force can be obtained from considering the motion of the composite against the force per unit area of composite, $A_f \sigma_f / A_c = V_f \sigma_f$, as the strain in the fibers changes from the initial to the final value. At the crack the change in strain will be

$$\Delta \varepsilon = \frac{\sigma_{fc} - \sigma_{fi}}{E_f} = \frac{\eta \sigma_{fi}}{E_f} = \eta \varepsilon_{mu} \tag{13.21}$$

The average change in strain over the distance ℓ is half this value. The motion is equal to the average change in strain times ℓ, or

$$\text{Motion} = \frac{\ell \eta \varepsilon_m}{2} \tag{13.22}$$

The work done per unit area is the force per unit area times distance times 2 to take into account both sides of the crack, and using (13.14), (13.16), and (13.20),

$$\Delta W = 2\left(\frac{\ell \eta \varepsilon_{mu}}{2}\right) V_f \sigma_{fc} = \ell \eta \varepsilon_{mu} V_f (1 + \eta) \varepsilon_{mu} E_f = E_f V_f \varepsilon_{mu}^2 \ell \, \eta (1 + \eta)$$

$$= \frac{E_f E_m V_m \varepsilon_{mu}^3}{2\tau} r \eta (1 + \eta) \tag{13.23}$$

Here the work done is taken as positive since it provides additional energy that could contribute to crack opening.

The matrix undergoes a relaxation leading to a loss in elastically stored energy. This energy change is taken as positive in terms of being energy available to go into crack creation. After the crack passes through, the matrix stress at the crack surface is zero and rises linearly to a value σ_m at a distance ℓ so that the stress at a distance t from the crack will be

$$\sigma_m(t) = \sigma_{mu} \frac{t}{\ell} \quad \text{for } 0 \leq t \leq \ell \tag{13.24}$$

The elastically stored energy at any point t is

$$\frac{\sigma(t)\, \varepsilon(t)}{2} = \frac{[\sigma(t)]^2}{2E_m} \tag{13.25}$$

The original energy stored per unit area in the two regions of thickness ℓ under uniform stress σ_{mu} is

$$\frac{\ell V_m}{E_m} (\sigma_{mu})^2 \tag{13.26}$$

The energy after relaxation stored in the two regions of thickness ℓ is

$$\frac{\ell V_m}{E_m} (\sigma^2)_{\text{ave}} \tag{13.27}$$

where the average or the square of the stress is taken over the length ℓ and is

$$(\sigma^2)_{\text{ave}} = \frac{1}{\ell} \int_0^\ell \left(\sigma_{mu} \frac{t}{\ell} \right)^2 dt = \frac{(\sigma_{mu})^2}{3} \tag{13.28}$$

The resulting value of the decrease in elastic energy stored in the matrix using Eq. (13.20) is

$$\Delta U_m = \tfrac{2}{3} E_m V_m (\varepsilon_{mu})^2 \ell = \frac{E_f E_m V_m}{3\tau} \varepsilon_{mu}^3 r \eta \tag{13.29}$$

where the decrease is taken as positive because it is energy available to create a new crack surface.

After matrix cracking the fiber experiences a stress given by, using Eq. (13.16),

$$\sigma_{ff} = \sigma_{fi} + \frac{y(\sigma_{fc} - \sigma_{fi})}{\ell} = \sigma_{fi} + \eta \sigma_{fi} \frac{y}{\ell} \quad \text{for } 0 \leq y \leq \ell \tag{13.30}$$

Where $y = t - \ell$ runs from 0 to ℓ, as shown in Figure 13.2. The change in elastically stored energy in the fibers in the two regions of thickness ℓ adjacent to the crack that is available to propagate the crack is

$$\Delta U_f = \frac{2V_f \ell}{2E_f} \left[\left(\sigma_{fi}^2 \right) - \left(\sigma_{ff}^2 \right)_{\text{ave}} \right] \tag{13.31}$$

The average of the stress squared is taken in the same manner as was done above for the matrix,

$$\left(\sigma_{ff}^2 \right)_{\text{ave}} = \frac{1}{\ell} \int_0^\ell \left(\sigma_{fi} + \eta \sigma_{fi} \frac{y}{\ell} \right)^2 \, dy \tag{13.32}$$

giving

$$\left(\sigma_{ff}^2 \right)_{\text{ave}} = \left(\sigma_{fi} \right)^2 \left(1 + \eta + \tfrac{1}{3} \eta^2 \right) \tag{13.33}$$

The result for the change in elastic energy in the fibers is, using Eq. (13.14) and (13.20),

$$\Delta U_f = -E_f V_f (\varepsilon_{mu})^2 \ell \, \eta \left(1 + \tfrac{1}{3} \eta \right) = -\frac{E_f E_m V_m}{2\tau} \varepsilon_{mu}^3 \, r \, \eta \left(1 + \tfrac{1}{3} \eta \right) \tag{13.34}$$

where the minus sign is appropriate because the increase in energy stored in the fibers reduces the energy available for a new crack surface.

As the matrix relaxes within the distance ℓ from the crack after cracking and the fiber picks up the load, the matrix surface layer slides back while the fiber slides forward against the frictional force τ so that energy is dissipated. The relative displacement of the fiber and matrix at a point y can be calculated by noting that $\Delta \varepsilon_f - \Delta \varepsilon_m = du/dy$, where u is displacement. The change in strain resulting from the relaxation of stress in the matrix is, using (13.14) and (13.30),

$$\Delta \varepsilon_f - \Delta \varepsilon_m = \frac{\Delta \sigma_f}{E_f} - \frac{\Delta \sigma_m}{E_m} = \frac{\sigma_{ff} - \sigma_{fi}}{E_f} - \frac{\Delta \sigma_m}{E_m} = \frac{\eta \sigma_{fi}}{E_f} \frac{y}{\ell} - \left(\frac{-\sigma_{mu}}{E_m} \frac{y}{\ell} \right)$$

$$= \varepsilon_{mu} (1 + \eta) \frac{y}{\ell} \tag{13.35}$$

The displacement as a function of y then is

$$u(y) = \int_0^y \left(\Delta \varepsilon_f - \Delta \varepsilon_m \right) dy = \varepsilon_{mu} (1 + \eta) \int_0^y \frac{y \, dy}{\ell} = \frac{\varepsilon_{mu} (1 + \eta)}{2\ell} y^2$$

A segment dy experiences a force $2\pi r \tau \, dy$ and dissipates energy $2\pi r \tau \, u(y) \, dy$. The energy dissipated per area πr^2 at the interface is then

$$\Delta U_s = \frac{2V_f}{\pi r^2} \int_0^\ell 2\pi r \tau \left(\frac{\varepsilon_{mu} (1 + \eta)}{2\ell} \right) y^2 \, dy \tag{13.36}$$

The result is, using Eq. (13.17) and (13.20),

$$\Delta U_s = \frac{2\,V_f \tau \, \varepsilon_{mu} \ell^2 (1+\eta)}{3r} = \frac{E_f E_m V_m}{6\tau}\, \varepsilon_{mu}^3 r\, \eta\, (1+\eta) \tag{13.37}$$

The Griffith energy balance condition then is

$$2\gamma_m V_m + \Delta U_s \le \Delta W + \Delta U_m + \Delta U_f \tag{13.38}$$

which reduces to

$$2\gamma_m V_m + \Delta U_s \le \tfrac{2}{3} E_c \varepsilon_m^2 \ell\, \eta \tag{13.39}$$

This in turn becomes

$$\varepsilon_{mu} \le \left[12\tau\, \gamma_m \left(\frac{V_f^2}{rV_m} \right) \left(\frac{E_f}{E_c E_m^2} \right) \right]^{1/3} \tag{13.40}$$

This is equivalent to the composite matrix–cracking stress σ_{cmc} required for matrix cracking of

$$\sigma_{\mathrm{cmc}} = E_c\, \varepsilon_{mu} = \left(\frac{12\tau\, \gamma_m V_f^2 E_f E_c^2}{rV_m E_m^2} \right)^{1/3} \tag{13.41}$$

13.5 PROPAGATION OF SHORT, FULLY BRIDGED CRACKS

The above treatment of Aveston et al. (1971) leads to a strength for matrix cracking that is not explicitly dependent on the size of flaws. Their treatment does not start with an initial flaw size nor does it consider the condition to propagate it as a function of size. Instead, their treatment assumes a single value of matrix strength and corresponding maximum matrix strain. Marshall et al. (1985) and McCartney (1987) considered the propagation of a crack of given initial size in the matrix. We summarize the treatment of Marshall, Cox, and Evans (MCE).

A long, fully bridged crack is shown in Figure 13.3. The length is c and the crack-opening displacement far from the tip is $2u_0$. This limiting separation is approached at a distance c_0 from the tip. At this distance the stress in the fiber reaches the value of Eq. (13.16) and just exactly balances the applied stress. For cracks with $c > c_0$ the matrix-cracking stress should be that calculated by Aveston et al. For $c < c_0$ the stress for crack propagation should depend on the crack length as for monolithic materials. The crack in the composite can be considered to be formed as a crack in a monolithic material (i.e., cutting through the fibers as well as the matrix) followed by tractions $T(x)$ for each fiber to pull fiber ends back to their original positions. One can approximate the effect of these tractions on the crack surface by replacing them with a
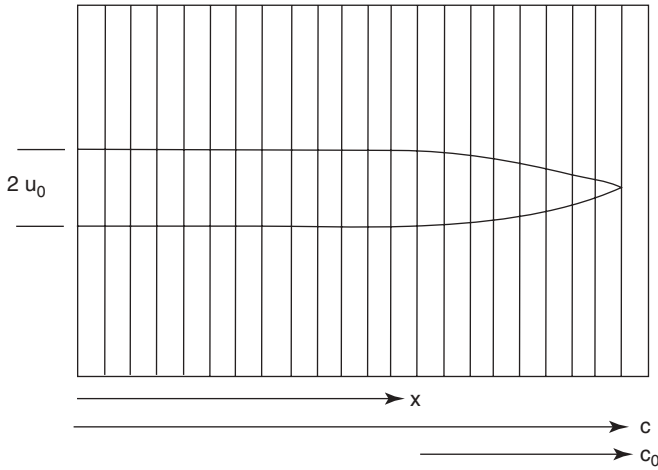
FIGURE 13.3   Fully bridged matrix crack in composite.

continuous stress $p(x) = T(x)V_f$. The crack surfaces then experience a total stress of $\sigma_\infty - p(x)$, where σ_∞ is the distant applied stress. The effective composite stress intensity factor, which is just the crack tip stress intensity factor, is correspondingly reduced from its value if the fibers were not present. The crack tip stress intensity factor in the composite, assuming a homogeneous material at the crack tip, is then given by Eq. (5.57) as

$$K(\text{tip}) = 2\left(\frac{c}{\pi}\right)^{1/2} \int_0^c \frac{[\sigma_\infty - p(x)]\,dx}{(c^2 - x^2)^{1/2}} \tag{13.42}$$

For a penny-shaped crack from Eq. (5.58) the crack tip stress intensity factor is

$$K(\text{tip}) = \frac{2}{(\pi c)^{1/2}} \int_0^1 \frac{[\sigma_\infty - p(r)]r\,dr}{(c^2 - r^2)^{1/2}} \tag{13.43}$$

The stresses in the fiber and matrix at the tip of the crack scale with their Young's moduli and so the stress intensity factors do likewise. The composite crack tip stress intensity factor can be written as

$$K(\text{tip}) = K^M(\text{tip}) \frac{E_c}{E_m} \tag{13.44}$$

The condition for crack growth in the matrix is that $K^M(\text{tip})$ attain a critical value $K_c^M(\text{tip})$ so that the condition for matrix crack growth can be expressed as

$$K(\text{tip}) = K_C(\text{tip}) = K_C^M(\text{tip}) \frac{E_c}{E_m} \tag{13.45}$$

An analysis similar to that of the Aveston–Cooper–Kelly treatment gives the value of the stress p as a function of the crack half opening u as

$$p = 2 \left[\frac{u\tau V_f^2 E_f (1 + \eta)}{r} \right]^{1/2} \tag{13.46}$$

The crack half opening is given by Sneddon and Lowengrub (1969) for a straight crack as

$$u(x) = \frac{4(1 - v^2)c}{\pi E_c} \int_X^1 \frac{1}{(s^2 - X^2)^{1/2}} \int_0^1 \frac{[\sigma_\infty - p(t)]t\, dt}{(s^2 - t^2)^{1/2}} \, ds \tag{13.47}$$

and for a penny-shaped crack as

$$u(x) = \frac{4(1 - v^2)c}{\pi E_c} \int_X^1 \frac{1}{(s^2 - X^2)^{1/2}} \int_0^1 \frac{[\sigma_\infty - p(t)]t\, dt}{(s^2 - t^2)^{1/2}} \, ds \tag{13.48}$$

where $X = x/c$ and s and t are normalized position coordinates. Solving for the stress to propagate short cracks thus requires solving the equations for p and u followed by solving for σ_∞ from the K(tip) equation with K(tip) set equal to K_c(tip). Marshall et al. (1985) performed a numerical solution and also obtained an approximate analytical solution. The latter gives a good approximation and also provides physical insight. The approximate analytic solution is obtained by assuming that the crack profile for $x > c - c_0$ is that of a simple, unbridged crack with the value of $K = K$(tip) of the composite. That is, the crack-opening displacement for a half-penny crack is assumed to be

$$u(x) = \frac{2(1 - v^2)K(\text{tip})c^{1/2}(1 - x^2/c^2)^{1/2}}{E_c \pi^{1/2}} \tag{13.49}$$

The stress is then

$$p(x) = [\alpha K(\text{tip})c^{1/2}(1 - x^2/c^2)^{1/2}]^{1/2} \tag{13.50}$$

where

$$\alpha = \frac{8(1 - v^2)\tau\, V_f^2 E_f (1 + \eta)}{E_c r\, \pi^{1/2}} \tag{13.51}$$

This solution for $u(x)$ is exact for x near c but is not correct for small x because the crack opening approaches a constant value for a bridged crack. This constant value is obtained by putting $p = \sigma_\infty$ in (13.47) to obtain

$$u_0 = \frac{\sigma_\infty^2\, r}{4\tau V_f^2 E_f (1 + \eta)} \tag{13.52}$$

The transition crack length c_0 is obtained by taking $u = u_0$ and $x = 0$ in the approximate equation for u, (13.49), and is

$$c_0 = \frac{\sigma_\infty^4}{\alpha^2 [K(\text{tip})]^2} \tag{13.53}$$

For fully bridged cracks longer than c_0 the approximate crack opening is constant for $x < c - c_0$ and is given by the above approximate near crack tip solution for $x > c - c_0$. Using this approximate crack-opening displacement in (13.42) and (13.43), the crack tip stress intensity factor becomes

$$K(\text{tip}) = Y\sigma_\infty c^{1/2} - I\left(\frac{4\alpha}{\pi}\right)^{1/2} [K(\text{tip})]^{1/2} c^{3/4} \tag{13.54}$$

where Y and I are dimensionless constants. For a straight crack $Y = \pi^{1/2}$ and $I = 1.20$, while for a penny-shaped crack $Y = 2/\pi^{1/2}$ and $I = \frac{2}{3}$. Substituting $K(\text{tip}) = K_c(\text{tip})$ gives the stress necessary to propagate a crack with $c \leq c_0$ as

$$\sigma_\infty = \frac{K_C(\text{tip})}{Yc^{1/2}} + \left(\frac{4\alpha K_C(\text{tip}) I^2}{\pi Y^2}\right)^{1/2} c^{1/4} \tag{13.55}$$

This can be put in normalized form as

$$\frac{\sigma}{\sigma_{\text{norm}}} = \left(\frac{1}{3}\right)\left(\frac{c}{c_{\text{norm}}}\right)^{-1/2} + \left(\frac{2}{3}\right)\left(\frac{c}{c_{\text{norm}}}\right)^{1/4} \tag{13.56}$$

where

$$c_{\text{norm}} = \left(\frac{\pi K_C(\text{tip})}{I^2 \alpha}\right)^{2/3} \tag{13.57}$$

and

$$\sigma_{\text{norm}} = \left(\frac{6 I^{2/3}}{\pi^{1/2} Y}\right)\left(\frac{(1 - v^2)\left(K_C^M\right)^2 \tau E_f v_f^2 V_m (1 + \eta)^2}{E_m r}\right)^{1/3} \tag{13.58}$$

For $c > c_0$ the stress σ_∞ to propagate a matrix crack is independent of crack length. Marshall et al. show that for straight cracks $\sigma_\infty = 1.02\sigma_{\text{norm}}$ and $c_0 = 1.88c_{\text{norm}}$, while for penny-shaped cracks $\sigma_\infty = \sigma_{\text{norm}}$ and $c_0 = c_{\text{norm}}$.

The stress to propagate a fully bridged matrix crack in a composite with continuous, aligned fibers according to this approximate solution is shown in Figure 13.4 as the curve labeled "fully bridged." The stress to propagate a crack in the unreinforced matrix is shown in comparison. The stress for the unreinforced matrix decreases without limit as the crack length increases according to the usual fracture mechanics result for material with a resistance to fracture that is independent of crack length. The stress required for matrix
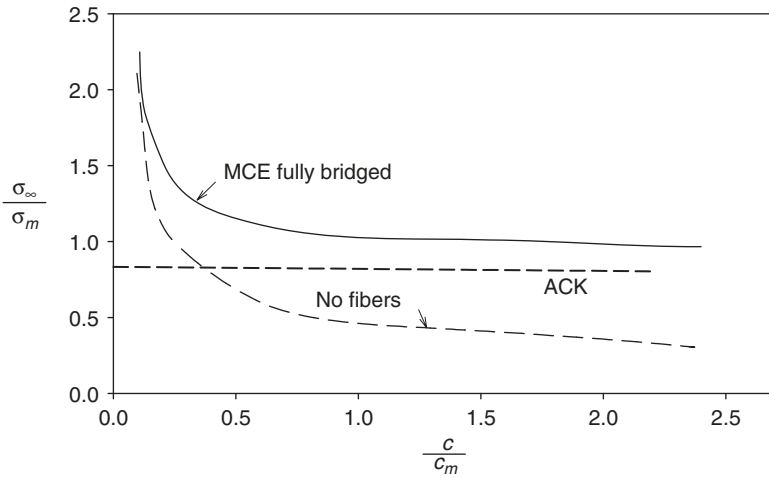
FIGURE 13.4   Stress to propagate a fully bridged matrix.

crack propagation in the composite initially decreases with crack length but levels off at the Aveston–Cooper–Kelly (ACK) stress for long cracks. This provides a degree of insensitivity to flaws for the composite. That is, if stresses on the composite are kept below the ACK stress, the composite will not fail from any size of matrix crack.

The above results can also be expressed in terms of a toughening due to bridging (Marshall and Evans, 1986). That is, the stress intensity factor at the crack tip can be written as

$$K(\text{tip}) = K_\infty - K_p \tag{13.59}$$

where K_p is the contribution due to the fibers and the sign has been chosen to make it a positive quantity. At matrix fracture $K(\text{tip}) = K_C(\text{tip})$ and for a penny-shaped crack

$$K_\infty = Y\sigma_\infty c^{1/2} \tag{13.60}$$

and [see Eq. (13.54)]

$$K_p = \frac{2}{3}\left(\frac{4\alpha}{\pi}\right)^{1/2} K_C^{1/2}(\text{tip})\, c^{3/4} \tag{13.61}$$

13.6   PROPAGATION OF PARTIALLY BRIDGED CRACKS

The treatment of the previous section assumes fully bridged cracks. In practice, the fibers may not be strong enough to remain unbroken over the full length of the crack and so may remain unbroken only some distance back from the crack
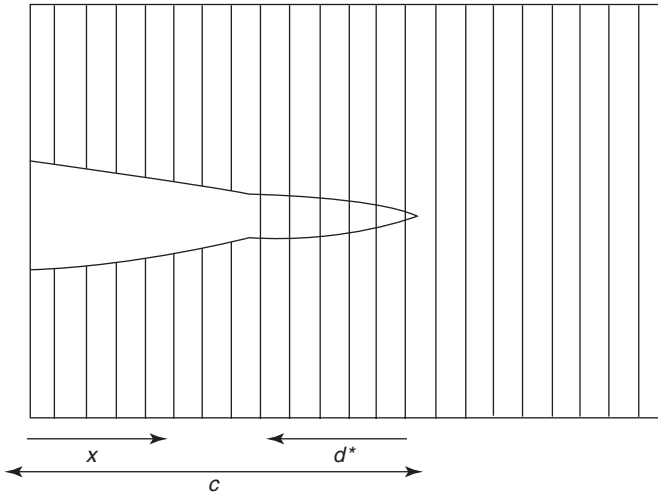
FIGURE 13.5   Partially bridged crack.

front. Variation in fiber strength introduces a further complication, which we will consider later. In the present section the treatment of Marshall and Evans (1986) is followed in which a uniform strength is assumed leading to a region of crack bridging extending back from the crack tip a distance d until a critical length d^* is reached beyond which, independent of the crack length, there will be a completely unbridged portion further from the crack tip, as shown in Figure 13.5. For this case at fracture

$$K_p = \left(\frac{16\alpha}{9\pi}\right)^{1/2} K_C^{1/2}(\text{tip})\left[d^*\left(2-\frac{d^*}{c}\right)\right]^{3/4} \tag{13.62}$$

The value of d is obtained by requiring $p(x) = \sigma_{fu}V_f$ at $x = c-d^*$, which gives, from Eq. (13.50),

$$d^*\left(2-\frac{d^*}{c}\right) = \frac{(\sigma_{fu}V_f)^4}{[\alpha K_C(\text{tip})]^2} \tag{13.63}$$

This gives a toughening contribution from the partial bridging of

$$K_p = \left(\frac{4}{3\pi^{1/2}}\right)\frac{(\sigma_{fu}V_f)^3}{\alpha K_C} \tag{13.64}$$

and a dimensionless stress for matrix crack propagation of a partially bridged crack of

$$\frac{\sigma}{\sigma_{\text{norm}}} = \frac{1 + 2(\sigma_{fu}V_f/\sigma_{\text{norm}})^3}{3(c/c_{\text{norm}})} \tag{13.65}$$

Note that in this case "partial bridging" means that the length of the bridged portion of the crack has been determined by the applied stress. A crack that was initially completely unbridged (such as a sawn notch) would propagate some distance before the bridged length built up to the extent that the fibers at the rear would fail. The normalized stress for such a partially bridged crack is shown in Figure 13.6 (Marshall, Cox, and Evans (MCE) plot). A short matrix crack that was initially fully bridged would extend under the stress given by the MCE plot. As progressively longer, fully bridged cracks are considered, the MCE plot continues to apply as long as $\sigma/\sigma_{norm} < \sigma_{fu}V_f/\sigma_{norm}$ and would continue to be fully bridged so that the horizontal portion of the MCE plot would be reached. If, however, $\sigma_{fu}V_f/\sigma_{norm} < 1$ a point on the MCE plot will be reached where $c/c_{norm} = (\sigma_{fu}V_f/\sigma_{norm})^4$, where the fibers most distant from the crack tip can no longer sustain the load and a partially bridged crack develops. Then the plot labeled Marshall and Evans (ME) would apply. Over the range of application of the MCE plot, the stress required for crack propagation drops with the reciprocal square root of crack length in the ME approximation, but the stress for crack propagation in the composite would be higher than for the same crack length in the unreinforced matrix, as shown in Figure 13.6. For large cracks that approach a constant crack-opening displacement the approximate treatment no longer applies and the entire composite will fail at $\sigma = \sigma_{fu}V_f$ so that the ME curve no longer applies below this stress, as indicated by the horizontal line in Figure 13.6.

Another case of interest is that of an initially unbridged crack of length c_0 that is stressed and develops a bridged portion of length d so that $c = c_0 + d$. The stress for further propagation is given by Marshall and Evans (1986) as

$$\frac{\sigma}{\sigma_{norm}} = \frac{1}{3}\left(\frac{c_{norm}}{c}\right)\left[1 + 2\left(\frac{d}{c_{norm}}\right)^{3/4}\left(2 - \frac{d/c_{norm}}{c/c_{norm}}\right)^{3/4}\right] \tag{13.66}$$
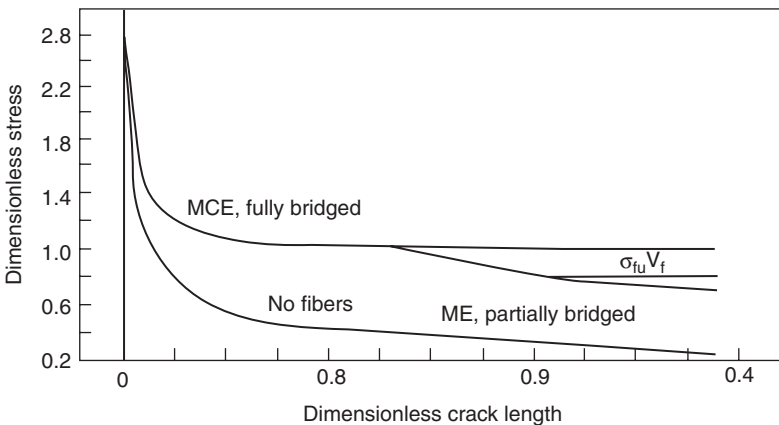

FIGURE 13.6   Stress to propagate a partially bridged matrix crack.

This result can be expressed equivalently as a *T*-curve behavior with a crack resistance K_R that varies with crack length according to

$$\frac{K_R}{K_C} = 1 + 2\left(\frac{d}{c_{\text{norm}}}\right)^{3/4}\left(2 - \frac{d/c_{\text{norm}}}{c/c_{\text{norm}}}\right)^{3/4} \tag{13.67}$$

The result is that crack growth will be stable for $c_0/c_{\text{norm}} \geq 0.15$ and $d < d^*$. As the stress is increased, stable crack growth occurs until $d = d^*$ when fiber failure occurs and catastrophic failure happens. Further detailed discussion of fracture behavior is given by Marshall and Evans (1986).

13.7   ADDITIONAL TREATMENT OF CRACK-BRIDGING EFFECTS

An extensive literature has subsequently developed on various aspects of bridging and its effects on fracture of continuous, aligned, brittle-matrix composites. The subject is too large and complex for full treatment here. We mention some of the important papers and the effects treated and then give a brief summary of two important effects not treated so far here: the effects of residual stress and the effect of statistical distribution of strength of fibers, including the breaking of some fibers at a distance from the crack plane and subsequent toughening due to fiber pullout.

Both Budiansky (1993) and Butler and Fuller (1993) have provided excellent general reviews of the theory of toughness in ceramic matrix composites. A review of progress in continuous-fiber ceramic composites is available (Lehman et al., 1996) in which two chapters are particularly pertinent (Karandikar et al., 1996; Zok et al., 1996). Further treatments of matrix fracture and related effects have been given by Budiansky et al. (1986) and McCartney (1987). Marshall and Evans (1988) have considered the effect of residual stress on the toughness of composites and Sigl and Evans (1989) have considered the effect of residual stress and frictional sliding. Budiansky and Amazigo (1989) treated toughening by frictionally constrained fibers. Debonding properties of residually stressed composites were treated by Charalambides and Evans (1989). Cox (1991) and Cox and Lo (1992) have considered the effect of external factors such as load ratio, notch, and scale effects on the propagation of cracks in composites. The effect of a statistical distribution of fiber strengths on behavior of composites has been treated by Cox et al. (1989), Knowles and Yang (1991), and Cao et al. (1990). The interaction of fiber and transformation toughening has been treated by Cui (1992) and Cui and Budiansky (1993).

The results from various theories, including effects of residual stress, fiber sliding properties, and statistical distribution of strength, have been summarized concisely by Cao et al. (1990). These authors state that long cracks will propagate at the stress given by the ACK formula modified by a term for the initial stress:

$$\sigma_{\text{cmc}} = \left[\frac{12\tau\gamma_m V_f^2 E_f E_c^2}{r V_m E_m^2}\right]^{1/3} - q\frac{E_c}{E_m} \tag{13.68}$$

Here allowance has been made for an axial residual stress in the matrix, q, resulting from fiber–matrix misfit, with $q > 0$ indicating tensile stress. Steady-state matrix cracking should occur when

$$\sigma_{\text{cmc}} < \frac{S_b}{V_f} \tag{13.69}$$

where S_b is the fiber bundle strength. The condition for the matrix-cracking stress equation to hold is that the crack length c obey

$$c > c_c = \left[\frac{\pi}{4(2/3)^{4/3}} \right] \left[\frac{\gamma_m^{1/2} E_m^{3/2} V_m^2 r (1 + \eta^{-1})}{\tau V_f^2 E_f (1 - v^2)} \right]^{2/3} \tag{13.70}$$

When c is smaller than the critical crack length c_c, a higher stress is needed to propagate the crack. As the crack length increases, the stress required for propagation drops until the length reaches c_c.

If the stress is increased above σ_{mu}, a set of parallel cracks develops. The crack spacing reaches a saturation value d_s when the stress within the uncracked blocks is smaller than the matrix blocks can support. This saturation spacing is related to the sliding stress between the fiber and matrix, τ, by

$$\tau = \lambda \left(\frac{V_m^2 \gamma_m E_f E_m r^2}{V_f E_c d_s^3} \right)^{1/2}$$

where $\lambda = 1.337 \left(\frac{3}{4} \right)^{1/2} = 1.34$. The matrix-cracking stress can be expressed in terms of the saturation crack spacing through

$$\sigma_{\text{cmc}} = (6\lambda)^{1/3} \left(\frac{V_v \gamma_m E_f E_c}{E_m d} \right)^{1/2} - q \frac{E_c}{E_m} \tag{13.71}$$

The ultimate strength σ_u is the stress required to cause fiber bundle failure and is given by (Evans and Marshall, 1989; Cao et al., 1990)

$$\sigma_u = V_f \hat{S}_b \exp \left(\frac{1 - (1 - \tau d_s / r \hat{S}_b)^{m+1}}{(m+1)[1 - (1 - \tau d / r \hat{S}_b)^m]} \right) \tag{13.72}$$

with

$$\left(\frac{r \hat{S}_b}{\tau d_s} \right)^{m+1} = \frac{(A_0 / 2\pi r L)(r S_0 / \tau d_s)^m}{1 - (1 - \tau d_s / r \hat{S}_b)^m} \tag{13.73}$$

where S_0 and m are the Weibull parameters for fiber bundles, A_0 is another scale parameter (usually set equal to $1\,\text{m}^2$), and L is the specimen gage length.

The effect of the sliding stress τ on σ_u appears directly and also through its effect on the crack spacing d_s, while the effect of residual stress is present indirectly through its effect on τ.

13.8   ADDITIONAL STATISTICAL TREATMENTS

Cho et al. (1992) have carried out a theoretical analysis that shows that the matrix strength statistics have a notable effect on the distribution of matrix cracks in continuous fiber-reinforced composites. A significant size effect is predicted.

Yang and Knowles (1992) have reviewed the generally accepted ACK theory that cracking of the matrix of a composite will continue until the matrix is separated into blocks each of a length between the debond length ℓ and 2ℓ, where [Eq. (13.20)]

$$\ell = \frac{V_m \sigma_{mu} r}{2 V_f \tau} = \frac{\sigma_{\text{cmc}}\, r}{2 V_f \tau} \left(\frac{1}{1 + [(E_f V_f)/(E_m V_m)]} \right) \tag{13.74}$$

They consider that the matrix has a Weibull distribution of strength as a function of the length L in the direction of the reinforcing fibers,

$$P_s(\sigma, L) = \exp\left[\frac{L}{L_0} \left(\frac{\sigma}{\sigma_0} \right)^m \right] \tag{13.75}$$

and find a distribution of crack spacings beginning at ℓ and extending to values as high as 8ℓ for $m = 4$ and as high as 4ℓ for $m = 20$.

Thouless and Evans (1988) allowed for fiber strength variation by using the Weibull distribution. The result is that fibers generally fail some distance from the crack plane and some do not break at all. They obtain an increase in toughness as measured by the required strain energy release rate given by

$$\Delta G = \Delta G_b + \Delta G_p \tag{13.76}$$

where the subscripts b and p refer, respectively, to the unbroken bridging fibers and the broken fibers that contribute to toughness through frictional resistance to pullout. Their theory gives

$$\Delta G_b \propto \left[\frac{r^{m-5}}{\tau^{m-2}} \right]^{1/(m+1)} \tag{13.77}$$

and

$$\Delta G_p \propto \left[\frac{r^{m-3}}{\tau^{m-2}} \right]^{1/(m+1)} \tag{13.78}$$

For the range of m values generally found ($m > 5$), it is thus desirable to have large radius and small friction for high toughness.

13.9   SUMMARY OF FIBER-TOUGHENING MECHANISMS

Campbell et al. (1990) classified the toughening mechanisms associated with fibers in ceramic matrices into four categories and gave an equation with a term for each. Their expression is presented in the context of a discussion of whisker toughening but is more general and provides insight into fiber or whisker toughening. The contribution to the strain energy release rate G_c imparted by fibers or whiskers is

$$\frac{\Delta G_c}{V_f \ell} \approx \frac{\sigma_{fu}^2}{E_f} - E\varepsilon_{\text{mf}}^2 + \frac{4\gamma_i}{rV^m} + \frac{\tau}{\ell} \sum_i \frac{h_i^2}{r} \qquad (13.79)$$

Here γ_i is the interface fracture energy, ε_{mf} is the misfit strain between fiber and matrix, and h_i is the pullout length of the ith fiber.

The first term, σ_{fu}^2/E_f, is the strain energy stored in the fiber over the debonded length on both sides of the matrix crack before the fiber fails. This energy contributes positively to the toughening because it is dissipated as acoustic waves.

The second term is the residual strain energy within the debond length of the composite caused by the misfit strain ε_{mf}. This strain energy is lost when the fiber fails and so is taken by Campbell et al. as contributing to the energy needed for crack propagation and thus reduces the toughness.

The third term is the energy needed to create the debond fracture surface and the fourth term is the pullout contribution.

13.10   OTHER FAILURE MECHANISMS IN CONTINUOUS, ALIGNED-FIBER COMPOSITES

Marshall and Evans (1985) have investigated the failure mechanisms in unidirectional ceramic fiber–ceramic matrix composites. For tensile loading parallel to the fibers, failure occurs in several stages as the above theory predicts: multiple matrix cracking followed by fiber fracture and pullout. In flexural loading a complex failure process occurs. The matrix cracks begin at the tension face and propagate only about halfway through the bar and the crack openings on the tensile surface do not become large enough to cause complete fiber pullout before compressive failure occurs on the compressive surface. Evidently care is necessary in using flexure testing to assess mechanical behavior of composites or in applying theories developed for uniform tension to members in bending.

Aligned-fiber composites are usually made in successive layers (lamina). Interlaminar strengths are an inherent weakness. For this reason three-dimensional arrangements of fibers made by textile machine techniques and then impregnated with the matrix material have been tried.

A serious limitation on the high-temperature use of ceramic matrix composites made with nonoxide reinforcing fibers is the oxidation of the fibers that typically occurs at temperatures above about 1000°C.

13.11   TENSILE STRESS–STRAIN CURVE OF CONTINUOUS, ALIGNED-FIBER COMPOSITES

A model describing the tensile stress–strain curve of ceramic fiber composites has been developed by Cao and Thouless (1990). They used a composite of SiC fibers in a lithium aluminum silicate glass ceramic matrix with the properties given in Table 13.2. The general type of stress–strain curve expected for a brittle-matrix composite reinforced with aligned, continuous fibers is shown is Figure 13.7 and has the features of matrix cracking followed by rising stress to the ultimate strength, in turn followed not by sudden failure but by a period of decreasing stress with further strain as the weaker fibers break before ultimate failure of the composite. Their theoretical model gives the results shown in Figure 13.8, which also displays the experimental results. The model describes the behavior quite well up to the stage of fiber pullout. Their model did not take into account the load supported by the broken fibers during pullout. Despite this limitation, the comparison suggests that the behavior of this class of composites is now well understood and well described by quantitative theory.

A subsequent treatment of tensile constitutive behavior of ceramic matrix composites that relates this behavior to constituent properties has been given by Evans et al. (1994). These authors point out that linear elastic fracture mechanics as developed for metals cannot be applied directly because the failure mechanism is not that of propagation of a dominant mode I crack. An improved approach is that of large-scale bridging mechanics in which

TABLE 13.2   Material Properties for SiC–Glass Ceramic Composite

Property	Value
Fiber Young's modulus, E_f	200 MPa
Fiber radius, r	8 μm
Fiber volume fraction, V_f	0.5
Matrix Young's modulus, E_m	85 GPa
Statistical property, S_0	2.988 MPa
Statistical property, m	2.1
Interface sliding stress, τ	2 mPa
Matrix crack spacing, l	400 μm
Matrix cracking stress, σ_m	290 MPa
Matching compliance, C	0.093 m/MN
Cross-sectional area of composite, A_c	2.18 mm by 2.48 mm
Gage length, L	15 mm
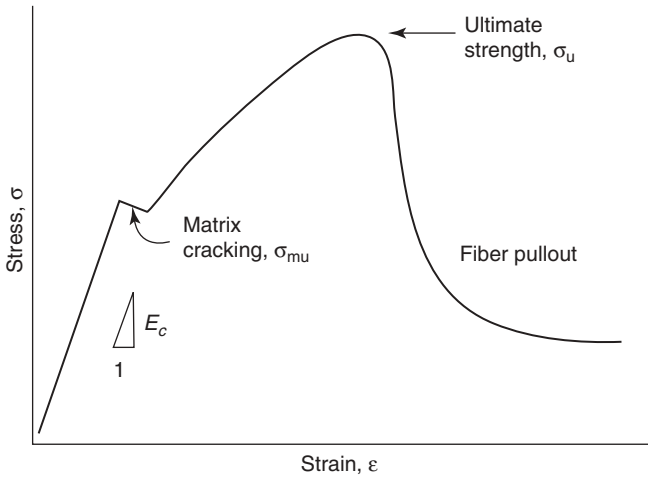
FIGURE 13.7 Schematic tensile stress–strain curve for a "tough" fiber composite. (From Cao and Thouless, 1990. Reprinted by permission of the American Ceramic Society.)
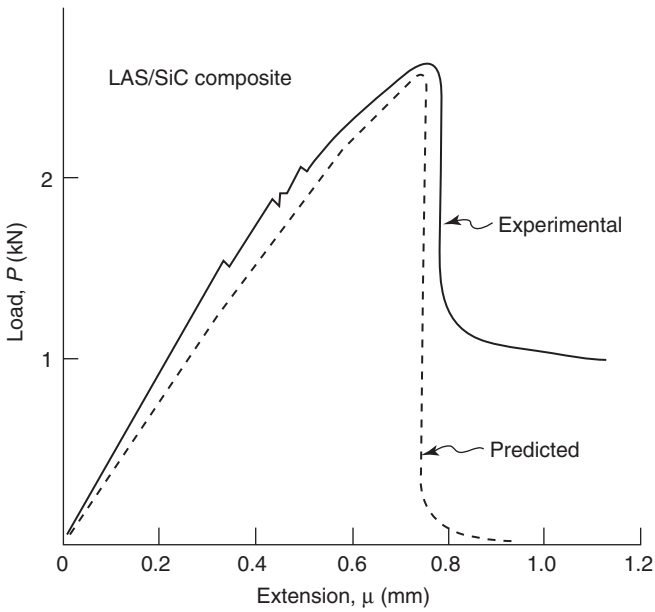
FIGURE 13.8 Comparison of predicted and experimental load–displacement curves. (From Cao and Thouless, 1990. Reprinted by permission of the American Ceramic Society.)

large-scale bridging of matrix cracks by fibers is treated. It needs, however, to be augmented by continuum damage mechanics (Hayhurst et al., 1991). These authors classify fracture behavior from a notch in a ceramic matrix composite into three categories. Class I is the model considered earlier in the present chapter in which fibers break some distance from the plane of a single dominant crack and then undergo pullout as the crack advances. Class II involves matrix cracking with crack branching without fiber failure. Class III involves shear damage by multiple matrix cracking at an angle to the notch plane. The results are too complex to present here. A model for delamination cracking in laminated ceramic matrix composites has been developed by Charalambides (1991).

13.12   LAMINATED COMPOSITES

The fracture behavior discussed in this chapter focused on propagation of cracks perpendicular to the direction of parallel, continuous reinforcing fibers. It is evident that cracks propagating parallel to the fibers would not experience the toughening and strengthening imparted to cracks perpendicular to the fibers. That is, the benefits of reinforcement of parallel fibers apply primarily to cracks in one set of parallel planes. Attempts to extend these benefits to fracture on other inclined planes involve making a three-dimensional woven structure of reinforcing fibers or making a laminated structure from layers of continuous, parallel fiber composites with the fiber directions oriented differently in successive layers. The latter family of laminated composites is discussed briefly in the present chapter. As would be expected, models for mechanical behavior in terms of the properties and arrangement of the constituents become quite complex mathematically. No attempt is made here to present such models, partly because they appear usually to have only partial success in describing behavior as local fractures develop. Only brief mention of some selected work is given to indicate qualitatively the directions being pursued.

The elastic behavior of composites with continuous, parallel fibers was treated in Section 13.2 in a manner sufficient for the purpose of discussing basic models of fracture behavior. Such composites are actually characterized elastically by nine independent elastic constants referred to a set of axes, with one axis along the direction of the continuous fibers (Hearmon, 1961; Chawla, 1993). For tilted axes these constants transform into a full set of constants. The relation of elastic constants of a composite to the elastic constants of the components is an extensive subject and is not treated here. The elastic deflection of composites of general orientation is also complex and is beyond our scope.

Study of laminated ceramic–ceramic composites with regard to damage mechanism and the effect of internal damage on elastic behavior, toughness, and strength is in a relatively early stage. Some individual results are briefly described here to give an idea of the approaches being investigated.

Sbaizero and Evans (1986) made symmetric (0°/90°) composites composed of SiC fibers in a lithium aluminosilicate glass matrix and tested them in both tension and flexure. Several types of local failure taking place before overall failure were identified: matrix cracking, delamination cracks, and fiber bundle failure. Beyerle et al. (1992) made further studies of the same composite system. Basic matrix-cracking models gave a good description of the incidence of cracking. However, attempts to model the effects of internal cracking on elastic properties were less successful.

Russo et al. (1992) have made a three-layer laminated composite with the intention of improving both strength and toughness. All three layers were made of alumina with 20 vol. % aluminum titanate, termed AST20. Both external surface layers were processed to have fine and homogeneous microstructures having high strength but relatively low toughness and little R-curve behavior. The interior layer was fabricated to have inhomogeneous microstructure with lower strength but having pronounced R-curve behavior. They succeeded in producing composites having high toughness and flaw tolerance without sacrificing strength in the small-flaw regime. The design is intended for situations in which tensile stress is a maximum at the surface.

A somewhat similar concept to that of Russo et al. (1992) of a hard surface combined with a tough interior was used by Chen and Mecholsky (1993), who made laminated composites with five layers of alumina and four layers of nickel. They found that the strength and toughness of the composites were greatly improved in comparison to that of monolithic alumina. The indentation strength values of the laminates were approximately constant for indentation loads between 10 and 100 N. The results suggest that such a composite would have good damage tolerance.

PROBLEMS

1. The properties of one high-quality SiC fiber are $r = 6\,\mu m$, $\sigma_{fu} = 2.6\,GPa$, and $K_{IC} = 4\,MPa \cdot m^{1/2}$.

   a. Calculate the ratio of fiber diameter to critical flaw size (semicircular surface flaw) according to the Griffith equation?

   b. Calculate the ratio of the tensile strength of a monolithic ceramic bar $r = 1\,cm$ to a fiber $r = 6\,\mu m$ both made from the same material if they have a Weibull modulus of 10. Assume σ_0 is the same in both and the flaw is a surface flaw. Make the same calculation for an interior flaw.

2. Consider the fracture of a parallel fiber composite along the direction of the fibers. Assume $E_f = 420\,GPa$, $E_m = 100\,GPa$, $\sigma_{mu} = 250\,MPa$, $V_f = 0.4$, $r = 6\,\mu m$, $\tau = 20\,MPa$, and $\gamma_m = 5\,J/m^2$.

   a. Calculate σ_c in the above composite considering only elastic load shifting.

   b. Assume the fibers remain intact as the crack propagates. Calculate the strength according to the ACK theory.

c. Calculate the necessary strength of the fiber to avoid complete failure as the matrix crack extends across the specimen.

d. What is the crack-opening displacement (distance)?

3. Calculate the debond length for the fiber composite in Problem 2. If one of the fibers fails below the crack at 10% greater than σ_{fi} in Problem 2, what will be the pullout length? (You must solve Problem 2 first.)

4. Consider a fiber composite having the following properties: $E_f = 320\,\text{GPa}$, $E_m = 75\,\text{GPa}$, $\sigma_{mu} = 150\,\text{MPa}$, $V_f = 0.4$, $r = 0.6\,\mu\text{m}$, $\tau = 25\,\text{MPa}$, $\gamma_m = 2\,\text{J/m}^2$, $\nu = 0.22$, and $K_C^M = 3\,\text{MPa}\cdot\text{m}^{1/2}$.

a. Would a straight-through crack ($c = 100\,\mu\text{m}$) be a partially or fully bridged crack at the ACK stress if $\sigma_{fu} = 1.2\,\text{GPa}$?

b. Parallel aligned fiber ceramic composites tend to develop periodic cracks in the matrix along the length of the specimen normal to the fibers prior to complete failure. Suppose that cracks were spaced the "debond length" apart and each crack was open the maximum crack opening, u_0 at $\sigma_\infty = \sigma_c$. Calculate the engineering strain in the composite resulting just from all the cracks along the sample length. Compare this strain with the total purely elastic strain of the composite just before σ_c.

5. A fiber composite has the following properties: $E_f = 400\,\text{GPa}$, $E_m = 250\,\text{GPa}$, $V_f = 0.35$, $r = 6\,\mu\text{m}$, $\tau = 25\,\text{MPa}$, and $\gamma = 5\,\text{J/m}^2$. Determine the stress in a bridging fiber midway in a long crack just before and just after the matrix crack extends across the specimen.

14

MECHANICAL PROPERTIES OF WHISKER-, LIGAMENT-, AND PLATELET-REINFORCED CERAMIC MATRIX COMPOSITES

14.1 INTRODUCTION

We have discussed aligned-fiber ceramic matrix composites in Chapter 13 and the technique of improving properties in two directions through lamination. An approach to imparting good mechanical properties in all directions is to use relatively short fibers distributed in random or near-random orientations. In this way good mechanical properties have been achieved in aluminum oxide reinforced with silicon carbide whiskers for which isotropic toughness values as high as $9\,\mathrm{MPa}\cdot\mathrm{m}^{1/2}$ have been reached (Becher et al., 1988). Toughening in this class of materials was briefly summarized in Chapter 10. We present more detail in the present chapter. The processes causing toughening in whisker-reinforced ceramics are thought to be fundamentally the same as those in ceramic matrix composites reinforced with aligned, continuous fibers but modified in detail by the short length and random orientation of the whiskers and by differences

in the whisker–matrix interfaces as compared to typical fiber–matrix interfaces. In random whisker-reinforced ceramics, toughening is thought to be caused by a combination of crack deflection, whisker bridging, and whisker pullout. Whisker pullout apparently is less important because of the short whisker lengths (usually $<50\,\mu m$). A model developed by Becher and his associates fits many experimental observations and is described in the next section.

Good lists of basic references are given in Becher et al. (1988, 1989), Becher (1991), and Evans (1990).

14.2   MODEL FOR WHISKER TOUGHENING

In this discussion we follow the treatment of Becher, Hsueh, Angelini, and Tiegs (1988), denoted BHAT. Parameters describing the formation of a crack
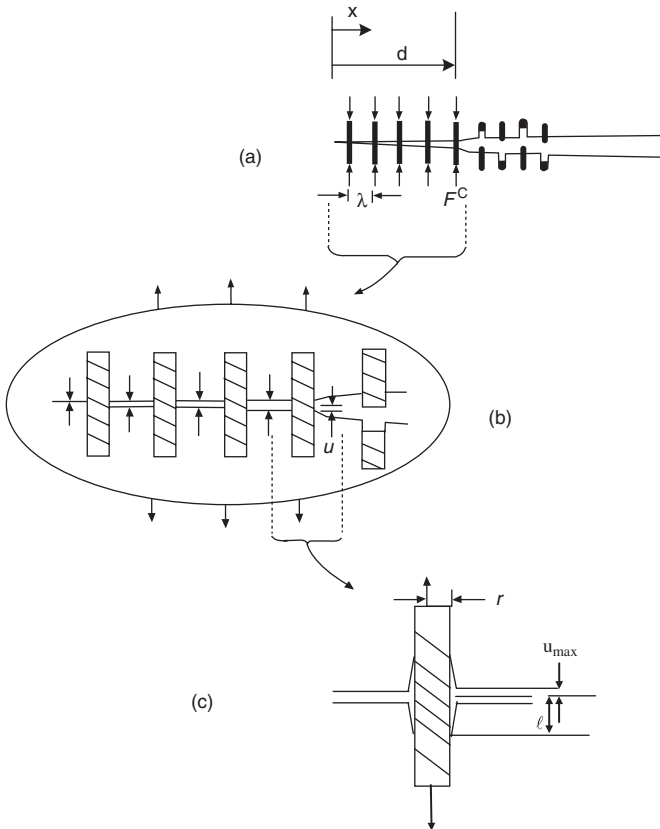
FIGURE 14.1   Crack with whisker-bridging zone. (From Becher et al., 1988. Reprinted by permission of the American Ceramic Society.)
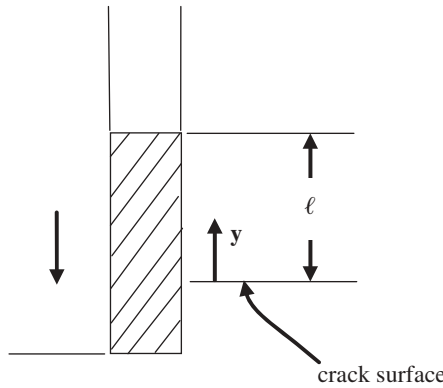
FIGURE 14.2 Debonding at end of bridging zone. (From Becher et al., 1988. Reprinted by permission of the American Ceramic Society.)

with a bridged zone of length d are shown in Figures 14.1 and 14.2 from BHAT. The fibers have radius r, are spaced a center-to-center distance λ apart, and debond a distance ℓ on either side of the crack. The crack-opening displacement is $2u$. The forces imposed by the bridging fibers are on average equivalent to a stress $p(x)$, where x is the distance along the crack from the tip. At the end of the bridging zone $x = d$ and $u = u_{max}$. The toughening due to bridging is

$$dK = 2\left(\frac{c}{\pi}\right)^{1/2} \int_0^d \frac{p(x)}{[c^2 - (c-x)^2]^{1/2}} dx \qquad (14.1)$$

for a through crack of total length $2c$ in an infinite medium. When $c \gg x$ ($c \gg d$) this becomes

$$dK = \left(\frac{2}{\pi}\right)^{1/2} \int_0^d \frac{p(x)}{x^{1/2}} dx \qquad (14.2)$$

If the closure stress is taken as constant, $p(x) = p^c$, analogous to the Dugdale–Barrenblat zone treatments, the result is

$$dK = 2p^c \left(\frac{2d}{\pi}\right)^{1/2} \qquad (14.3)$$

This constant closure stress approximation is used by BHAT, who point out that assuming that the closure stress varies linearly from zero at the crack tip to p^c at the end of the bridging zone would cause $2p^c$ to be replaced by $2p^c/3$.

To proceed it is necessary to determine p^c and d in terms of the properties of the composite. The closure stress is given by the whisker strength σ_{wu} times the volume fraction of whiskers V_w:

$$p^c = \sigma_{wu} V_w \tag{14.4}$$

The crack-opening displacement from linear elastic fracture mechanics for plane stress conditions is

$$u = \left(\frac{8}{\pi}\right)^{1/2} \frac{K(1 - v^2)x^{1/2}}{E_c} \tag{14.5}$$

where E_c is the composite Young's modulus and v is Poisson's ratio. Substituting Eq. (14.3) and $K = K_0 + dK$ in Eq. (14.5) gives the crack-opening displacement at the end of the bridging section:

$$u = \frac{4(1 - v^2)K_0 d^{1/2}}{E_c (2\pi)^{1/2}} + \frac{8(1 - v^2)p^c d}{\pi E_c} \tag{14.6}$$

The maximum displacement supported by the whisker is

$$u_{\max}^w = \frac{\sigma_{wu} \ell^*}{E_w} \tag{14.7}$$

where ℓ^* is the unbonded length over which the displacement occurs. The debond length from Budiansky et al. (1986) is given by

$$\ell = r\left(\frac{G^M}{6G^I}\right) \tag{14.8}$$

where G^M and G^I are the required mechanical energy release rates for the matrix and the interface, respectively. Approximating $\ell^* = \ell$ and setting $u_{\max}^w$ equal to the crack-opening displacement at the end of the debonding zone gives

$$d^{1/2} = \frac{[(K_0)^2 + 2E_c V_w (\sigma_{wu})^2 r G^M / (3G^I (1 - v^2) E_w)]^{1/2} - K_0}{4(2)^{1/2} V_w \sigma_{wu} / \pi^{1/2}} \tag{14.9}$$

Substituting (14.9) and (14.4) into (14.3) gives

$$dK^{wr} = \frac{[(K_0)^2 + 2(\sigma_{wu})^2 V_w r E_c G^M / (3(1 - v^2) E_w G^I)]^{1/2} - K^0}{2} \tag{14.10}$$

It is noteworthy that the critical stress intensity for the unreinforced matrix, K_0, appears in the toughening expression. For small toughening from whiskers

[i.e., when $(K_0)^2$ is large compared to the other term in the square root], the toughening can be approximated as

$$dK^{wr} \approx \frac{(\sigma_{wu})^2 V_w r E_c G^M}{6(1 - v^2) E_w G^I K_0} \qquad (14.11)$$

For large toughening from whiskers [i.e., when $(K_0)^2$ is small compared to the other term in the square root], one can approximate this result as

$$dK^{wr} \approx \sigma_{wu} \left(\frac{V_w r}{6(1 - v^2)} \frac{E_c}{E_w} \frac{G^M}{G^I} \right)^{1/2} \qquad (14.12)$$

which clearly shows the influence of the various parameters on the toughening.

An analysis of toughening from the mechanical energy release point of view was also presented by BHAT. It produces the same dependence on composite parameters as (14.10) but gives a different numerical constant, presumably because of the approximate nature of the treatments. Their energy analysis is given here to emphasize the equivalence of the treatments when the Irwin equation is properly used, as discussed in Section 10.4. This treatment proceeds by calculating the sum of the changes in the elastic energy stored in the unbonded portion of the whisker, ΔU_e, and the energy required for frictional sliding of the unbonded portion of the whisker, ΔU_s. Assuming constant interfacial shear stress to slide the whisker, the force to slide the whisker at a distance y from the crack plane is $2\pi r(\ell - y)\tau$ and the force exerted by the whisker is $\pi r^2 \sigma(y)$, giving

$$\sigma(y) = \frac{2(\ell - y)\tau}{r} \qquad (14.13)$$

The elastic energy stored in the whisker is

$$dU_e = \frac{\pi r^2 \sigma^2(y)\, dy}{2 E_w} = \frac{2\pi(\ell - y)^2 \tau^2 dy}{E_w} \qquad (14.14)$$

The work done by an element dy in sliding against τ is

$$dU_s = 2\pi r \tau u\, dy \qquad (14.15)$$

where the displacement of the fiber relative to the matrix is

$$u = \int_y^\ell \varepsilon(y)\, dy = \int_y^\ell \frac{\sigma(y)}{E_w} dy \qquad (14.16)$$

giving

$$u = \frac{(\ell - y)^2 \tau}{E_w r} \tag{14.17}$$

Substituting (14.17) into (14.15) gives

$$dU_s = \frac{2\pi(\ell - y)^2 \tau^2 \, dy}{E_w} = dU_e \tag{14.18}$$

The energy required per unit area of crack surface to stretch and slide the whiskers is

$$\Delta G = 2N \int_0^\ell (dU_e + dU_s) = 4N \int_0^\ell dU_e = \frac{4N\pi\tau^2\ell^3}{3E_w} \tag{14.19}$$

where N is the number of whiskers per unit area. The stress in the whisker is greatest at $y = 0$ and the toughness is greatest when this stress is equal to the fiber strength σ_{wu} so that

$$\sigma_{wu} = \frac{2\ell\tau}{r} \tag{14.20}$$

and

$$\Delta G = \frac{(\sigma_{wu})^2 V_w \, r \, G^M}{18 \, E_w \, G^I} \tag{14.21}$$

The equivalent toughening dK is obtained by using (10.25) and is

$$dK^{wr} = \left(K_0^2 + \frac{(\sigma_{wu})^2 V_w r E_c G^M}{18(1 - v^2) E_w \, G^I} \right)^{1/2} - K_0 \tag{14.22}$$

The numerical constant is different but the same dependence on the composite parameters is obtained as for the direct stress intensity calculation, Eq. (14.10). As before, this expression can be approximated for small toughening from whiskers as

$$dK^{wr} \approx \frac{(\sigma_{wu})^2 V_w r E_c G^M}{18(1 - v^2) E_w G^I K_0} \tag{14.23}$$

and for large toughening from whiskers as

$$dK^{wr} \approx \sigma_{wu}\left(\frac{(V_w)6r}{18(1-v^2)}\frac{E_c}{E_w}\frac{G^M}{G^I}\right)^{1/2} \tag{14.24}$$

Comparing Eqs. (14.23) and (14.24) with (14.11) and (14.12), one sees that the factor 6 obtained in the direct stress intensity calculation has been replaced by the factor 18 in the result obtained from the energy calculation. BHAT discuss some of the approximations made in the treatments that may be responsible for the difference. However, the important point is that the same functional dependence is obtained. The approximate nature of the calculation is not likely to give an accurate numerical coefficient in either case.

The main predictions of this model have been confirmed experimentally by BHAT, as we illustrate with Figures 14.3–14.7 from their work. Figure 14.3 shows alumina and mullite matrices reinforced with 0.4-μm-radius SiC whiskers with low surface oxygen content. The model's prediction of linearity in $V_w^{1/2}$ is confirmed for alumina. Curvature in the plot for mullite is attributed to the effect on E_c for the mullite case of $E_w \gg E_m$. The model also predicts a linear dependence on $(E_c/E_w)^{1/2}$, and this is borne out by the results shown in
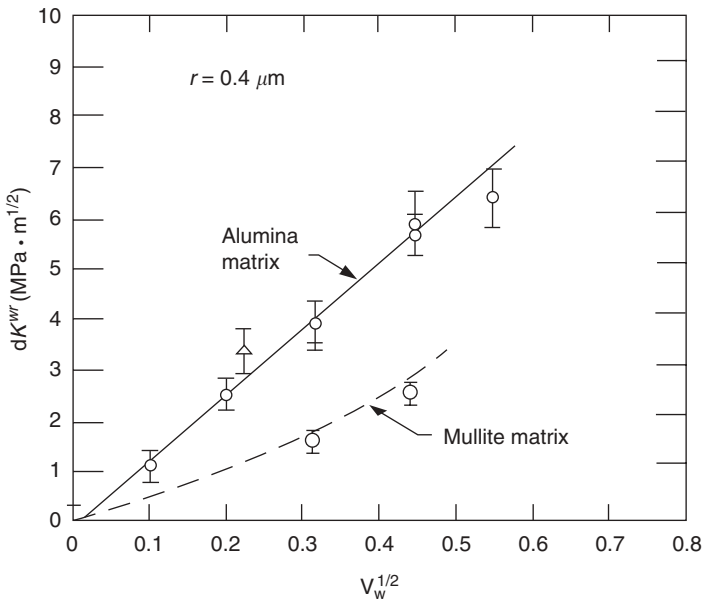
FIGURE 14.3   Toughening as function of square root of volume fraction of whiskers. (From Becher et al., 1988. Reprinted by permission of the American Ceramic Society.)
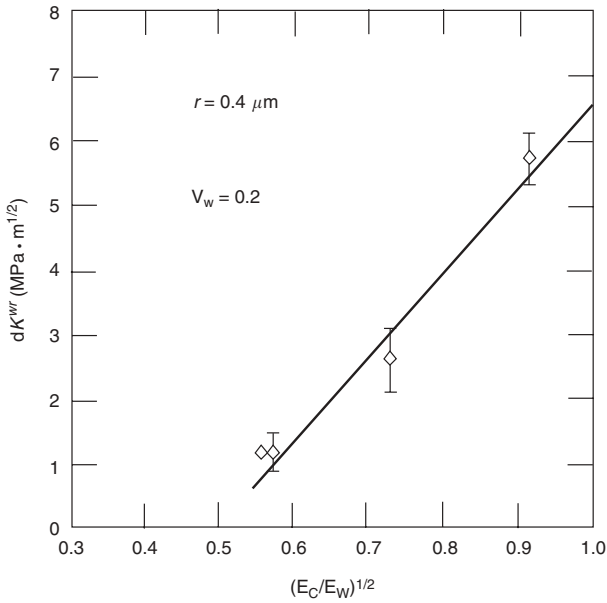
FIGURE 14.4   Toughening as function of square root of Young's modulus ratio. (From Becher et al., 1988. Reprinted by permission of the American Ceramic Society.)
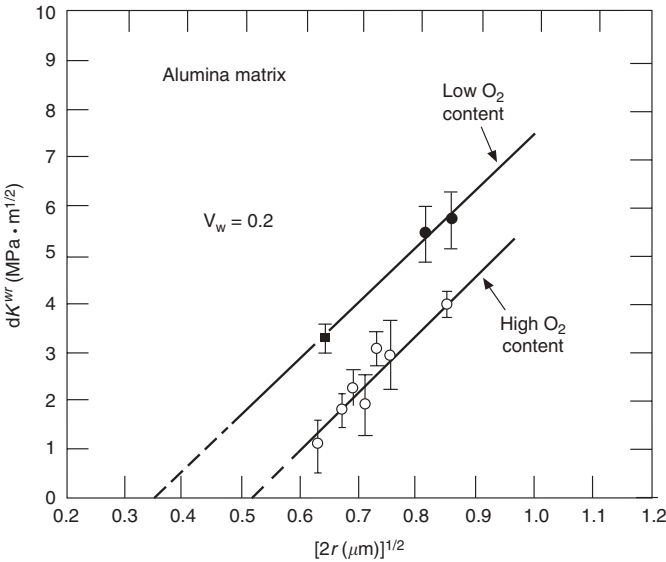
FIGURE 14.5   Toughening as function of the square root of whisker radius. (From Becher et al., 1988. Reprinted by permission of the American Ceramic Society.)
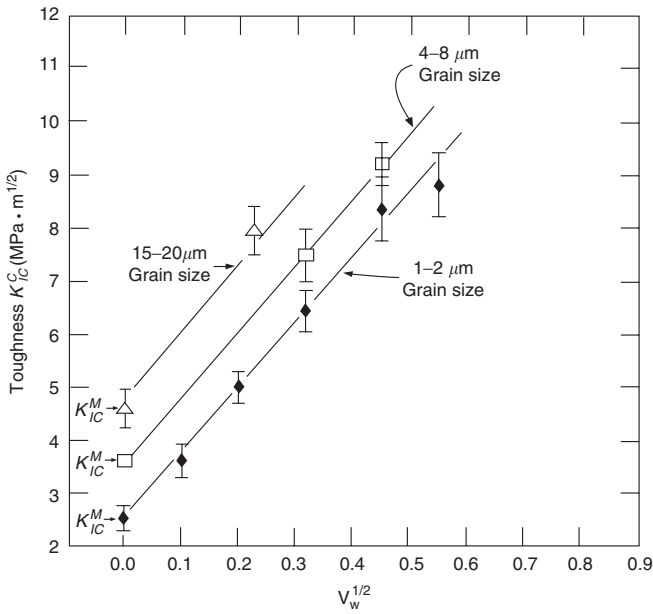
FIGURE 14.6   Toughness as function of square root of volume fraction of whiskers. (From Becher et al., 1988. Reprinted by permission of the American Ceramic Society.)
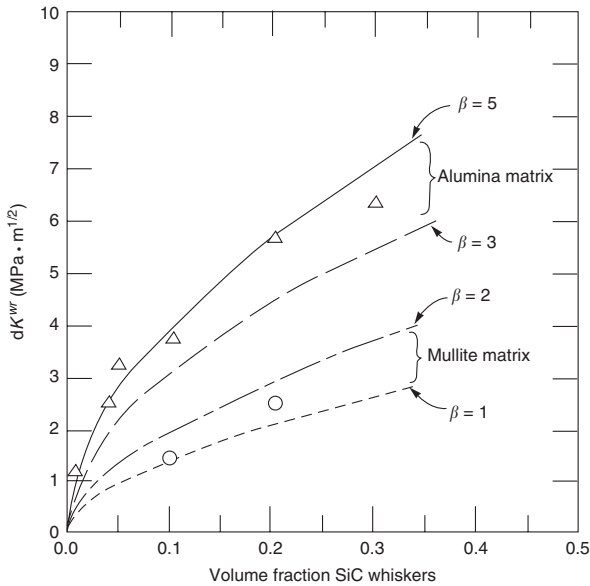
FIGURE 14.7   Toughness values calculated with selected β values. (From Becher et al., 1988. Reprinted by permission of the American Ceramic Society.)

Figure 14.4, which are for 20 vol. % of 0.4-μm whiskers with low surface oxygen content in matrices of glass, mullite, and alumina that have progressively increasing values of E_m. The model predicts that the toughness should increase with $r^{1/2}$ for a constant volume fraction of whiskers, and this is shown to be obeyed for 20 vol. % SiC whiskers in alumina in Figure 14.5. The toughness data for two sets of whiskers having, respectively, low and high surface oxygen content fall on parallel lines. The data can be rationalized by assuming a lower τ value for the high surface oxygen content as is reasonable. Another interesting experimental result is shown in Figure 14.6, which shows the effect of varying the grain size in an alumina matrix on the overall toughness of composites with varying volume fractions of 0.4-μm SiC whiskers. A series of parallel straight lines were obtained as a function of $V_w^{1/2}$. The toughness of the unreinforced alumina increases with increasing grain size and provides the base upon which the toughness due to fiber reinforcement is added.

The authors were able to determine the pullout length ℓ_{PO} experimentally and took this to be equal to the debond length ℓ. They obtained values of β = $\ell/r = \ell_{PO}/r$ for low-surface-oxygen-content 0.4-μm SiC whiskers of 5 in alumina matrices, 1–2 in mullite matrices, and 0.5–1 in glass matrices. Using their model they estimated the fracture strength of the whiskers in the composites to be in the range 7–11 GPa. This is consistent with strength values of 8–9 MPa measured directly on free, longer (≫5-mm) whiskers with a larger diameter (≈4 μm). They accordingly took a value of 10 MPa for whiskers in their calculations. Figure 14.7 was calculated from Eq. (14.10) using the β values indicated; the calculated curves fit the data well. The authors used their theory to predict the combinations of r and V_w that would be required for β values of 5 or 10 to give toughness values of 10 or 20 MPa. The results are shown in Figure 14.8.

Despite its success, the above model has some limitations. The model takes the number of whiskers per unit area involved in bridging equal to V_w, which is a reasonable assumption for parallel fibers but not for randomly oriented whiskers. An empirical constant A_{fb} equal to the area fraction of the whiskers effectively bridging the crack can be introduced into the theory. Another limitation of the above model is that the equations take no account of the possibility of whiskers breaking at some distance from the crack plane and pulling out against the sliding stress and thus dissipating additional energy. Fibers having a distribution of strengths would be expected to fail at various points near the crack plane and so undergo pullout. This is, in fact, observed. In Chapter 13 we mentioned a treatment by Thouless and Evans (1988) for composites with aligned, continuous fibers that considers the statistics of this process. Becher (1991) treats the effect of breaking and pullout by assuming that an area fraction A_{PO} break at an average distance ℓ_{PO} from the crack and undergo pullout. Becher's treatment for this case gives the increase in the critical mechanical energy release rate ΔG^{PO} (discussed by him in terms of J)
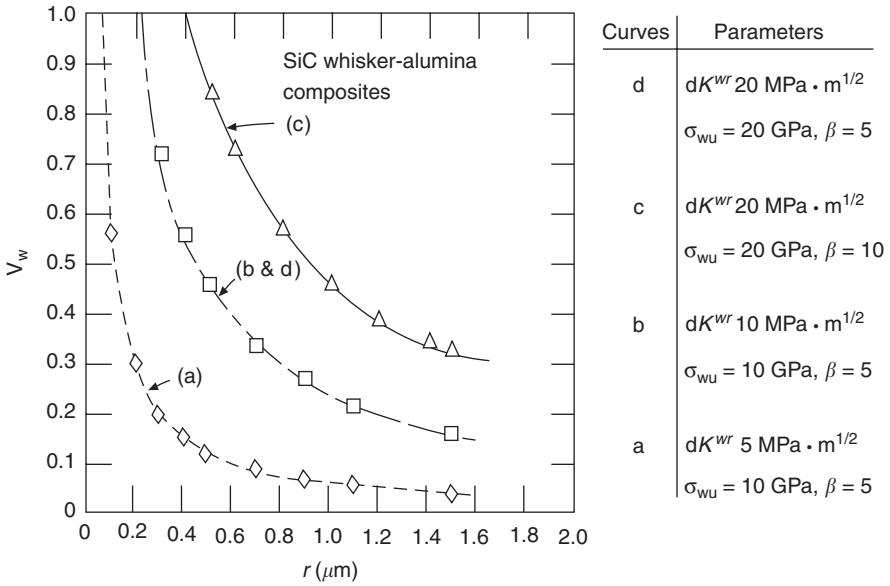
FIGURE 14.8 Combinations of fiber radius and volume fraction needed for detected toughness values. (From Becher et al., 1988. Reprinted by permission of the American Ceramic Society.)

caused by pullout as

$$\Delta G_{PO} = A_{PO}\, \tau \left(\frac{\ell_{PO}}{r}\right) \ell_{PO} \tag{14.25}$$

and the corresponding increase in the critical stress intensity factor as

$$dK_{PO} = \frac{(E_c A_{PO} \tau r)^{1/2} \ell_{PO}}{r} \tag{14.26}$$

From these equations the ratio of contribution to the critical energy release rate from pullout to that from frictional bridging is

$$\frac{\Delta G_{PO}}{\Delta G_{FB}} = 3\frac{\ell_{PO}}{r} \frac{\tau E_f}{(\sigma_{wu})^2} \frac{A_{PO}}{A_{FB}} \frac{\ell_{PO}}{\ell_{DB}} \tag{14.27}$$

It is evident that the relative effects of bridging without breakage and breakage with pullout depend strongly on ℓ_{PO}/r, ℓ_{PO}/ℓ, and A_{PO}/A_{FB}. Becher has estimated that for SiC whisker-reinforced alumina $\Delta G_{PO} \approx 1.5\Delta G_{FB}$, while for SiC whiskers in mullite $\Delta G_{PO} \approx 0.1\Delta G_{FB}$ and for SiC in soda–lime glass ΔG_{PO} is negligible.

14.3   COMBINED TOUGHENING MECHANISMS IN WHISKER-REINFORCED COMPOSITES

The simultaneous action of microcracking, load transfer, bridging, and crack deflection mechanisms of toughening in whisker-reinforced ceramic matrix composites has been considered by Giannakopoulos and Breder (1991). They assume that the load transfer between the matrix and the whiskers is due to Coulomb friction, models the whiskers as bridging springs, carries out a J-integral calculation, and uses the Irwin relation to obtain the stress intensity factor of the toughened composite. Without reviewing their model in detail, we present their final result. In their treatment K_{tip} is the untoughened crack tip stress intensity factor and K_∞ the applied stress intensity value (i.e., the measured toughness). They consider a hot-pressed composite where the axis of the whiskers are all normal to the hot-pressing direction but isotropically oriented in the two-dimensional (2D) plane. They obtain

$$\frac{1 - \nu_{2D}^2}{E_{2D}} K_\infty^2 = (1 - V_w) \frac{1 - \nu_m^2}{E_m} \left[1 + \frac{15\pi + 56}{30\pi} \left(\frac{E_m}{E_s} - 1 \right) \right] D K_{tip}^2 + V \quad (14.28)$$

where ν_w and ν_m are the Poisson ratios for the whisker and matrix, respectively, D is the strain energy release rate divided by the surface energy gained by deflection of the crack around the whisker, and V is the energy dissipated at the moment the bridging whisker fails. Using this equation they calculate the fracture resistance for an alumina reinforced with 25 vol. % whiskers. The results are shown in Figure 14.9 from their paper.

The relative effects of contributing mechanisms in combined toughening can change with temperature according to White and Guazzone (1991), who studied crack growth resistance in SiC-whisker-reinforced alumina at 20, 1200, and 1400°C. They found that a frontal zone mechanism, probably microcracking, dominates at room temperature. At 1200°C a following wake zone mechanism of crack face whisker bridging is dominant.

14.4   LIGAMENT-REINFORCED CERAMIC MATRIX COMPOSITES

Interest in ceramics toughened by metal inclusions has been stimulated by the high toughness values achieved, although their use is limited by the temperature and oxidation limits of the reinforcing metal ligaments. Flinn et al. (1993) presented a literature survey and developed a model that gave good fits to experimental data on alumina containing aluminum ligaments. These specimens had 28 vol. % aluminum in the form of fibers about 19 μm in diameter. Initial toughness values were about $3\,\mathrm{MPa} \cdot \mathrm{m}^{1/2}$ but increase to about $35\,\mathrm{MP} \cdot \mathrm{am}^{1/2}$ after crack extensions of 1.5–2.5 mm.
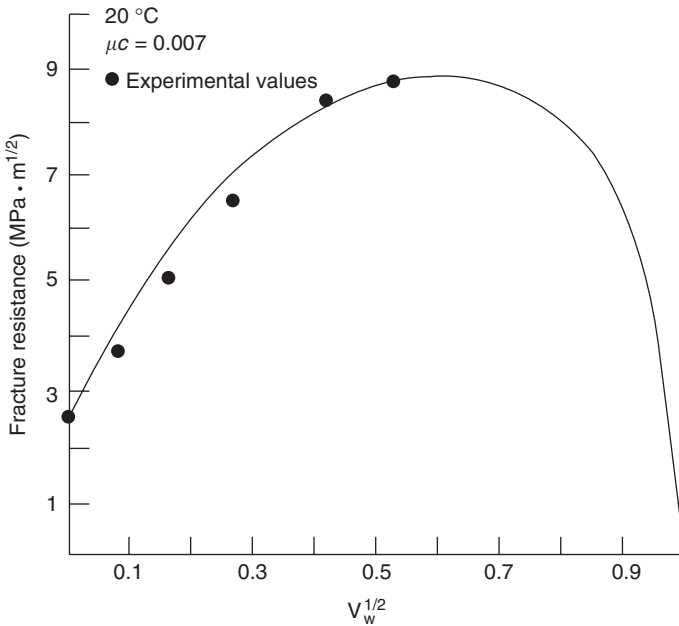
FIGURE 14.9 Toughness of SiC–alumina composites as function of volume fraction of whiskers. (From Giannakopoulos and Breder, 1991. Reprinted by permission of the American Ceramic Society.)

14.5 PLATELET-REINFORCED CERAMIC MATRIX COMPOSITES

Ceramic matrix composites toughened with platelets are generally not as tough as those toughened with whiskers. Chou and Green (1993) studied hot-pressed alumina and found that the average fracture toughness could be increased from $4.3\,MPa\cdot m^{1/2}$ for unreinforced alumina to $7.1\,MP\cdot am^{1/2}$ for alumina reinforced with 30 vol. % SiC platelets. They concluded that crack deflection is the dominant toughening mechanism.

PROBLEMS

1. Equation (14.12) was derived assuming all the whiskers were perpendicular to the crack as it propagates. In reality whiskers are at a random angle to the crack.

   a. Sketch a crack whose plane is at an angle of approximately $80°$ to the axis of the whisker and show why the whisker must bend in the gap of the crack opening.

   b. Assume all whiskers are at the same angle to the crack and all are bent through the same radius of curvature. How does the dependence of dK on r change in Eq. (14.12)? *Hint:* Consider the fiber as a bending beam.

2. From Eq. (14.12), the table below and Figure 14.3 estimate the ultimate fracture strength of the whiskers, σ_{wu}, in the alumina matrix whisker composite. Assume $G_M/G_I = 4$.

	E	ν
Al_2O_3	380	0.23
SiC w	581	0.17
Units	GPa	

15

CYCLIC FATIGUE OF CERAMICS

15.1 INTRODUCTION

Cyclic fatigue is the loss of strength of material under cyclic loading. It can lead to failure at stresses well below the short-time failure stress. It has long been known to be a very important cause of failure in metals and so has been studied extensively in metals. More recently, cyclic fatigue has been recognized to occur in ceramics, including ceramics with microstructures designed for enhanced toughness under noncyclic stress. Cyclic fatigue work on metals is very briefly reviewed in this chapter before turning to fatigue in ceramics. In the metallurgical literature the term *fatigue* is used rather than cyclic fatigue (Suresh, 1991).

The term *cyclic fatigue* is used here to distinguish strength deterioration essentially dependent on the cyclic nature of loading from the type of subcritical crack propagation treated in Chapter 8. The latter takes place under constant stress. This constant-stress effect is sometimes termed "static fatigue." If the stress is cyclically varied from some value to a lower value, subcritical crack propagation of this static fatigue type can still take place at a rate that varies during the cycle but is still dependent only on the tensile stress acting instantaneously. A treatment of the effect of static-fatigue-type slow crack

propagation under alternating stress was presented by Evans and Fuller (1974) and under arbitrary stress–time history by Jakus and Ritter (1981). Cyclic-fatigue-type strength loss is a different phenomenon than static-fatigue-type slow crack propagation and can be a very strong effect. The mechanisms of cyclic fatigue in ceramics are still under investigation. For ceramics toughened by crack bridging it is thought that the periodic reduction of stress causes partial crack closure and damages the crack-bridging elements, leading to a higher critical stress intensity at the crack tip under the next maximum stress during the stress cycle and so to a loss of strength.

15.2   CYCLIC FATIGUE OF METALS

The most common type of failure of structural metallic alloys is fatigue failure so that a large body of work on metallic fatigue exists (Hertzberg, 1989; Courtney, 1990). Some of the basic features of metallic fatigue are briefly summarized here because phenomenologically similar behavior is observed in ceramics, so that the existing framework used to describe metallic fatigue is also used to describe fatigue in ceramics. It should be borne in mind that the underlying processes are not necessarily the same in ceramics, however.

Fatigue tests are usually conducted under periodically varying stress or strain. A simple and common situation is sinusoidally varying stress, as shown in Figure 15.1. The minimum stress may be less than zero (i.e., compression) as shown or may simply be a smaller value of tensile stress. Both the maximum stress σ_{max} and the difference in stress $\Delta\sigma = \sigma_{max} - \sigma_{min}$ are important parameters determining the fatigue behavior. A typical measurement is to
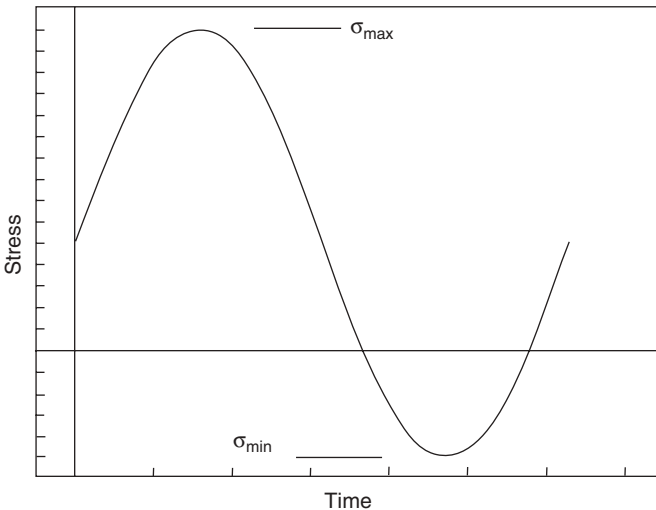
FIGURE 15.1   Cyclic stress for fatigue testing.

determine the number of cycles required for failure as a function of one of the stress parameters such as the maximum stress. The results when plotted are termed *S–N* curves. These curves typically show a large increase in number of cycles required for failure as the stress is decreased. For stresses below a critical value, no failure may occur over any practically observable number of cycles, suggesting the existence of a fatigue limit. Another important observation is that the presence of a notch generally drastically reduces the number of cycles required for failure.

Fatigue in metals is generally considered to be a three-stage process: Figure 15.2 shows (I) fatigue crack initiation, (II) fatigue crack propagation, and (III) final failure. Microscopic examination of a fatigue fracture surface typically shows a region of parallel markings (termed clam shell markings) corresponding to the slow and intermittent crack propagation characteristic of the second stage of fatigue. The subsequent portion of the fracture surface is typically rough and fibrous and is associated with the final fracture stage.

The initial stage of fatigue crack nucleation in metals is not fully understood in terms of detailed mechanisms but is believed to be associated with localized plastic deformation. It generally begins at an external surface or at some internal surface such as the interface with an inclusion. The direction of the development of the initial fatigue crack is determined by the direction of slip rather than the direction of maximum tensile stress. Fatigue crack initiation requires that at least a part of the stress cycle consist of tensile stress. Fatigue failure in metals apparently does not take place under stress cycles that are entirely compressive.
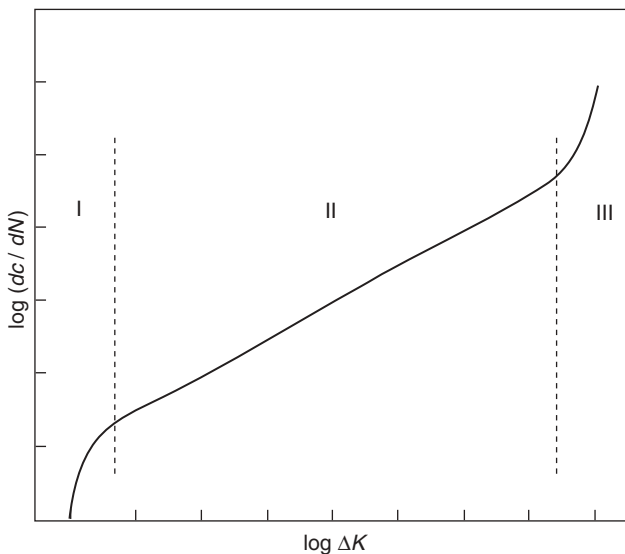
FIGURE 15.2   Schematic of crack growth rate during cyclic fatigue.

Stage II of fatigue crack propagation is characterized by crack growth perpendicular to the direction of maximum tensile stress. The growth rate is controlled primarily by the difference between the maximum and minimum tensile stress rather than by the average stress.

Stage III of fatigue failure is an overload failure that occurs when the remaining cross section can no longer sustain the maximum tensile stress.

Because stage II is a crack propagation process, it is plausible that the stress intensity factor should be the appropriate controlling variable rather than the stress. Careful studies have shown that this is so. The rate of crack growth in stage II is usually found to obey the Paris law:

$$\frac{dc}{dN} = A\,(\Delta K)^{m_f} \tag{15.1}$$

where c is the crack length, N is the number of cycles of stress, $\Delta K = Y(\sigma_{max}-\sigma_{min})c1/2$, and A and m_f are empirical parameters that generally depend on the material, the environment, the frequency, the temperature, and the ratio $\sigma_{min}/\sigma_{max}$. Here m_f is not the Weibull m. The fatigue parameter m_f typically has values in the range 2–4 for metals but can be much greater for ceramics.

A schematic plot of log dc/dN as a function of log ΔK is shown in Figure 15.2. The Paris law (straight-line portion of the figure) is a good approximation of the observed behavior over most of the range of ΔK, but for small values the crack growth rate typically drops off sharply and suggests the existence of a threshold value ΔK_{th} below which fatigue crack growth does not occur. This threshold value depends, however, on $\sigma_{min}/\sigma_{max}$. The Paris law can be used to predict the number of cycles required for failure for a constant σ_{max} and constant $\sigma_{min}/\sigma_{max}$ by using the relation

$$\Delta K = Y(\Delta\sigma)c^{1/2} \tag{15.2}$$

and following the crack length until the stress intensity value under maximum stress is sufficient to cause fast fracture. In general, Y varies with crack length so that numerical integration of the crack length is required. When Y is independent of crack length (as in the case of a circular flaw far from the surface of the specimen), the integration can be carried out in closed form and the result (Hertzberg, 1989) for the number of cycles to failure, N_f, is

$$N_f = \frac{2}{(m_f-2)A\,Y^{m_f}(\Delta\sigma)^{m_f}}\left[\frac{1}{c_i^{(m_f-2)/2}} - \frac{1}{c_f^{(m_f-2)/2}}\right] \quad \text{for } m \neq 2 \tag{15.3}$$

where c_i is the initial fatigue crack length, c_f is the crack length at failure (i.e., the length at which the stress intensity factor under maximum stress is sufficient to cause fast failure), and $\Delta\sigma = \sigma_{max}-\sigma_{min}$.

15.3   CYCLIC FATIGUE OF CERAMICS

Until recently ceramics were thought not to undergo fatigue at or near room temperature (apart from the effects of subcritical crack propagation of the type discussed in Chapter 8). This belief was apparently based on the fact that fatigue in metals is associated with plastic deformation and the assumption that sufficient plastic deformation to cause fatigue does not occur in most ceramics at room temperature. Fatigue at room temperature has now been found in many ceramics, although the mechanisms appear to involve degradation of the toughening elements of microstructure rather than plastic deformation. A comprehensive review of fatigue in ceramics was presented by Ritchie and Dauskardt (1991) and extensive references to work on fatigue on ceramics were also given by Dauskardt et al. (1992) and by Hu and Mai (1992).

Fatigue in many ceramics (including zirconia, graphite, alumina, silicon nitride, silica glass ceramics, LAS–SiC$_f$, Al$_2$O$_3$–SiC, and laminated graphite– pyrolytic carbon composites) has been demonstrated by comparing static fatigue curves with S–N curves on the same material. The time to failure under constant stress was determined as a function of stress in the static fatigue experiment. From these results the predicted time to failure from the static fatigue process alone was obtained by integrating. The predicted time is longer for a particular maximum stress under the assumption of alternating stress than under a constant stress equal to the maximum alternating stress. The time to failure under alternating stress was measured and plotted as a function of the maximum stress in the S–N experiments. Techniques used were zero-tension and tension–tension cantilever bending and three- and four-point bending. Tension–compression testing was done in rotary bending, uniaxial push–pull, or tension–torsion testing. The failure times in the alternating stress experiments were found to be shorter than in the static fatigue experiments, indicating the occurrence of a true cyclic fatigue effect.

The indicated fatigue limit determined from S–N curves was generally much less than the strength in simple loading to failure. For medium-strength-grade (midtoughness) zirconia, the fatigue limit as determined with 10^8 cycles and $\sigma_{min}/\sigma_{max} = -1$ was about 50% of the single-cycle strength. An alumina was found to fail at 10^8 cycles at a stress of 25–40% of the single-cycle strength.

Fatigue crack propagation studies on ceramics have been done in two modes: long-crack and short-crack studies. The long-crack studies (typically with crack length about 3 mm) were done with through cracks in precracked specimens, such as single-edge-notched specimens in three- and four-point bending or tapered double-cantilever beam specimens, or compact tension specimens. Crack lengths were monitored optically or by measuring the resistance of a conducting coating. Short-crack experiments (typically with cracks less than 250 μm in length) were done by bending beams using surface cracks introduced from a notch or by indentation. The long-crack propagation studies gave results that could be described by the Paris law, but the exponent m varied between 12 and 40, which is much larger than the values of 2–4 typical of

metals. The short-crack studies gave much greater crack growth rates than the long-crack studies at equivalent applied stress intensity values. Also, the crack growth takes place in the short-crack studies at stress intensities below the threshold value required in long-crack studies (Ritchie and Dauskardt, 1991).

Typical results of long-crack cyclic fatigue studies on zirconia are shown in Figures 15.3–15.5 from Dauskardt et al. (1990). Toughness curves (T curves) for several grades of zirconia are shown in Figure 15.3. The corresponding crack growth rate curves showing Paris law behavior are shown in Figure 15.4. Transformation toughening greatly increases the ΔK value required to produce a given rate of crack growth per cycle. Proof that the effect is truly cyclic fatigue is shown in Figure 15.5, which contrasts the crack velocity in cyclic tests with that measured under constant stress. The growth rates in cyclic fatigue are up to seven orders of magnitude greater than those under the corresponding constant stress.

Lui and Chen (1991) examined short-crack fatigue growth in 3Y–TZP and noted that when the results were analyzed using the Paris law there was a strong effect on the $\sigma_{min}/\sigma_{max}$ ratio but not such a strong effect if dc/dN were plotted against K_{max} rather than ΔK. They proposed the equation

$$\frac{dc}{dN} = A' K_{max}^{m-2} \, \Delta K^2 \qquad (15.4)$$
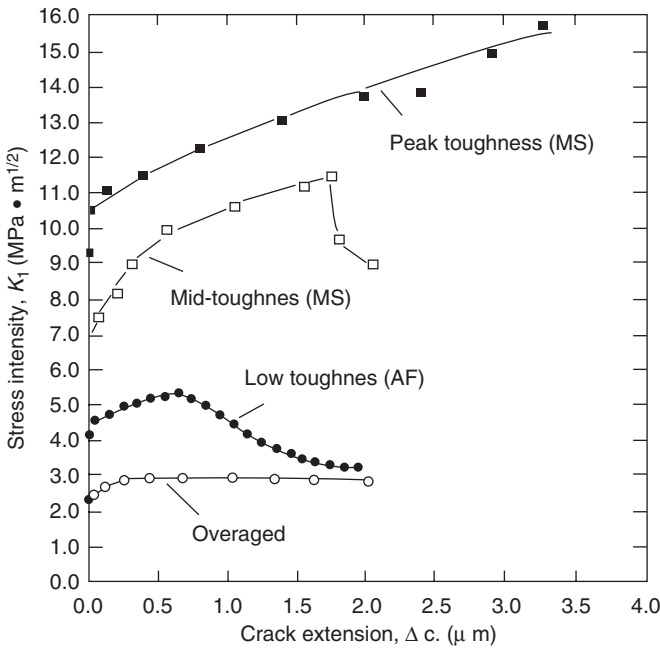
FIGURE 15.3 Fracture toughness behavior of Mg–PSZ subeutectoid aged to a range of toughness values. (From Dauskardt et al., 1990. Reprinted by permission of the American Ceramic Society.)
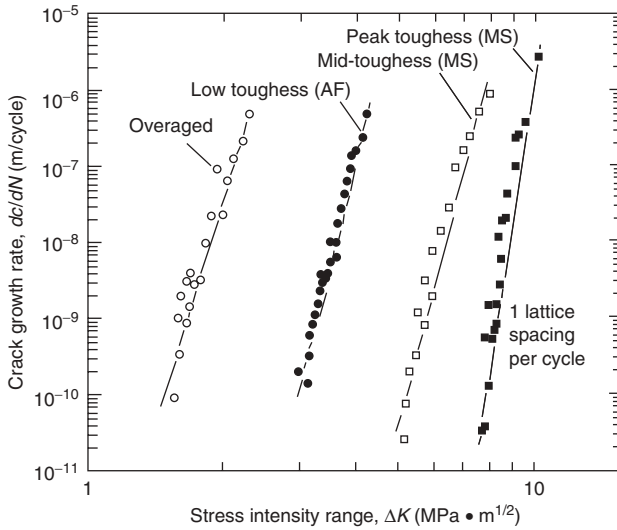
FIGURE 15.4   Cyclic fatigue crack growth behavior for Mg–PSZ subeutectoid aged to a range of toughness values. (From Dauskardt et al., 1990. Reprinted by permission of the American Ceramic Society.)
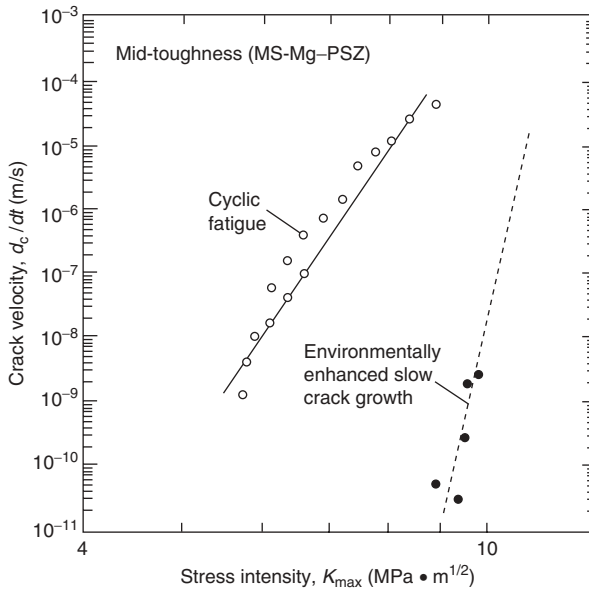
FIGURE 15.5   Subcritical crack growth behavior in midtoughness Mg–PSZ, showing comparison of cyclic and static conditions. (From Dauskardt et al., 1990. Reprinted by permission of the American Ceramic Society.)

15.4   MECHANISMS OF CYCLIC FATIGUE OF CERAMICS

Mechanisms of cyclic fatigue in ceramics have not yet been definitely established. The possible mechanisms have been classified into two categories (Ritchie and Dauskardt, 1991): intrinsic and extrinsic. The intrinsic mechanism would involve the creation of a fatigue-damaged microstructure ahead of the crack tip that would produce a crack advance mechanism operating uniquely in cyclic fatigue. Possible mechanisms are alternating crack tip blunting and resharpening or, for whisker-reinforced composites, whisker breakage.

Extrinsic mechanisms may not involve a change in the crack propagation mechanism under cyclic fatigue conditions. Instead, the unloading may change the value of the crack tip stress intensity factor under the next maximum stress by reducing the crack tip shielding. Thus cyclic fatigue might reduce the crack tip shielding effect of transformation toughening or crack tip bridging.

More than one mechanism of fatigue may be active simultaneously. For example, Jacobs and Chen (1994) have found evidence in silicon nitride for both environmentally sensitive fatigue combined with an environmentally insensitive component apparently associated with damage to the crack wake shielding zone.

15.5   CYCLIC FATIGUE BY DEGRADATION OF CRACK BRIDGES

Definite evidence for cyclic fatigue by degradation of bridging grains in alumina has been presented by Lathabai et al. (1991). Tension–tension cyclic loading tests were conducted on a coarse-grained (23–35-μm average grain size) alumina that shows T-curve behavior by grain-interlock bridging. Fatigue effects were observed with both small cracks introduced with an indenter and large cracks using compact tension specimens. Bridge degradation was identified using a special device for in situ observation of crack propagation in the electron microscope.

Hu and Mai (1992) have developed a compliance method of determining the bridging stress and applied this method to a study of alumina ceramics under monotonic and cyclic loading. They found that the bridging stress after 4.3×10^5 cycles of stress with $\sigma_{min}/\sigma_{max} = -1$ was much smaller than that obtained with monotonic loading. They conclude that the frictional grain bridges are damaged by the compressive part of the cycle. They thus conclude that the use of an R curve (T curve) determined in monotonic loading is not appropriate for cyclic fatigue conditions.

15.6   SHORT-CRACK FATIGUE OF CERAMICS

Studies of cyclic fatigue in ceramics using long-crack techniques are clearly important in understanding basic fatigue phenomena in ceramics, and data

obtained in such experiments may apply to design considerations in some circumstances. However, the same problem arises as with other uses of long-crack data. Namely, ceramics having only the naturally occurring short cracks are generally used for load-bearing applications so that fatigue data with short cracks is needed. Two approaches are being explored: cyclic loading studies under Hertzian loading conditions and under pointed indenters.

Reece and Guiu (1991) studied indentation fatigue of a high-purity alumina bioceramic in various alcohols, toluene, and simulated physiological environments with high water content. They applied a load P to a pointed indenter, removed the load, and then repeatedly applied a load $P' \leq P$ and determined the number of repeated loadings necessary to cause chipping. They constructed plots of the number of cycles to failure as a function of P' analogous to the usual S–N fatigue curves. The resulting curves showed that the presence of water considerably decreased the number of cycles to failure. However, the length of crack produced by the preload was independent of environment. The results suggest that relative humidity and chemical activity of water alone cannot fully account for the observed behavior. Gui et al. (1992) studied cyclic fatigue in alumina and concluded that cyclic loads cause degradation of the strength of bridging ligaments.

Lawn and his collaborators have done extensive work on short-crack fatigue of ceramics using Hertzian loading (Guibertau et al., 1993, 1994; Lawn et al., 1994a, b; Cai et al., 1994). A spherical ball of radius R, Young's modulus E', and Poisson's ratio v' is pressed with a force P against a flat specimen with Young's modulus E and Poisson's ratio v. The deflection of the ball and substrate causes a circular contact of radius a. The mean compressive stress immediately under the ball is

$$\sigma = \frac{P}{\pi a^2} \tag{15.5}$$

If the deflection is purely elastic, the Hertz theory of contact stresses can be used to obtain

$$a = \left(\frac{4\kappa P R}{3E} \right)^{1/3} \tag{15.6}$$

where

$$\kappa = \frac{9}{16} \left[(1 - v^2) + (1 - v')^2 \left(\frac{E}{E'} \right) \right] \tag{15.7}$$

Under these conditions the compressive stress in the center just under the ball is $\frac{3}{2}$ of σ. Substituting P from (15.6) into (15.5) gives

$$\sigma = \frac{3E}{4\pi\kappa} \left(\frac{a}{R} \right) \tag{15.8}$$

Lawn and his collaborators treat σ as indentation stress and a/r as indentation strain. The Hertz theory predicts a linear elastic curve of indentation strain as a function of indentation stress as shown by (15.8). Experimental results on several polycrystalline aluminas are given in Figure 15.6, which shows an initially linear portion as predicted. At higher stresses greater strain occurs corresponding to multiple subsurface cracking. The stress field below the surface is complex but is the sum of an isostatic compression and a shear stress in a roughly spherical volume below the contact circle. The isostatic pressure allows the shear stress to reach a value sufficient to cause inelastic shear deformation to take place in alumina at room temperature (see Chapter 23) predominantly by twinning and possibly also by slip under high shear stress. The resulting grain boundary stress concentrations, acting in concert with thermal anisotropy stresses, cause grain boundary microcracking. Some amount of this type of damage occurs upon a single loading and unloading. Lawn and his collaborators have used repeated cycles of loading to study localized cyclic fatigue from Hertzian loading. Figure 15.7 shows that a single loading on the ball causes a decrease in the biaxial strength (average of four measurements) and that repeated cycles of loading and unloading on the ball cause further decrease in the subsequently measured biaxial strength. Damage from Hertzian loading is greatest for large-grain-size materials. Such damage is relatively insensitive to preexisting flaws because the shear deformation process generates flaws.

Lawn and co-workers conclude that the strategy for microstructural design to reduce damage from contact with blunt objects is to use small grain size and reduce the grain size distribution to eliminate the occasional large grains. This
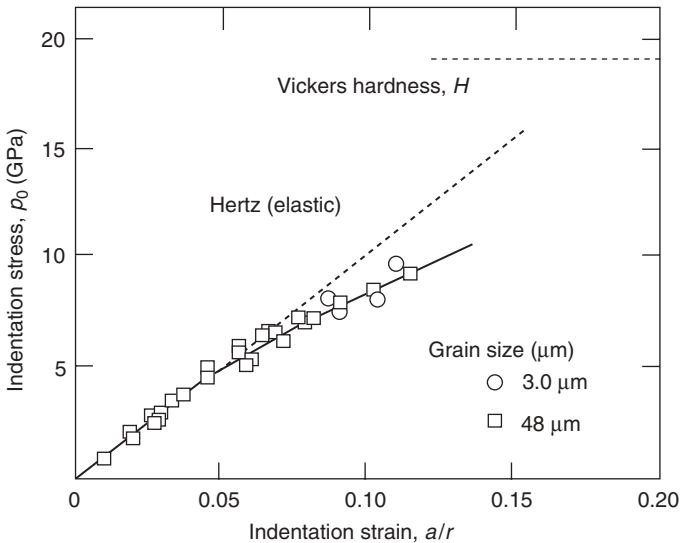
FIGURE 15.6   Indentation stress–strain curve on alumina. (From Guiberteau et al., 1994. Reprinted with permission of the American Ceramic Society.)
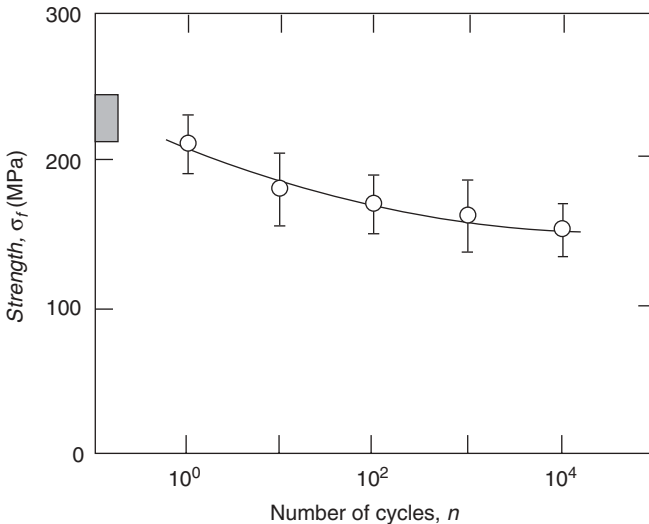
FIGURE 15.7   Biaxial strength of 23-µm-grain-size polycrystalline alumina as function of number of cycles of loading with sphere of radius 3.18 mm and load of 1000 N. (From Guiberteau et al., 1993. Reprinted by permission of the American Ceramic Society.)

is in contrast to the strategy for increasing long-crack toughness in materials that exhibit toughening by grain-interlock toughening. For the latter situation large grain size is favored for high toughness.

15.7   IMPLICATIONS OF CYCLIC FATIGUE IN DESIGN OF CERAMICS

Earlier chapters, including Chapter 8 on the static fatigue type of slow crack propagation, have presented the basis for a flaw-tolerant method of design with ceramics under load. In this approach the existence of cracks with an initial maximum length is assumed. Minimal safe life under a chosen stress can then be predicted based on the fracture mechanics approach to the static fatigue type of slow crack propagation. Recent results on cyclic fatigue of ceramics indicate that this procedure may drastically overestimate the safe life under stress when a significant component of time-varying stress is present. Prediction of safe life of ceramics under cyclic fatigue conditions appears to be a problem that has not yet been fully addressed.

PROBLEMS

1. The exponent in the Paris law for a certain ceramic is 10. A specimen is found to fail in four days when the stress is varied between 100 and 120 MPa

at a frequency of 500 Hz. The specimen does not fail under a static stress of 120 MPa. Assume that the constant A in the Paris law is independent of $\sigma_{max}/\sigma_{min}$.

a. What is the significance of the last statement?

b. Calculate the time to failure when the stress varies from 100 to 120 MPa at a frequency of 2 kHz.

c. Calculate the time to failure when the stress varies from 120 to 140 MPa at a frequency of 2 kHz.

d. Calculate the time to failure when the stress varies from 90 to 130 MPa at a frequency of 500 Hz.

e. Under service conditions, the material is expected to experience vibrations at a frequency of 5 kHz. If the design life of the component under these conditions is five years, what is the maximum amplitude of the stress oscillations that can be tolerated without failure?

16

THERMAL STRESS AND THERMAL SHOCK IN CERAMICS

16.1   INTRODUCTION

Temperature gradients in ceramics cause stresses to develop because of the constraining effect of adjacent elements of the body. The theory of heat flow and temperature distribution resulting from given external conditions applied to a sample is well developed (Carslaw and Jaeger, 1959). The theory of thermal stress resulting from heat flow is also well developed (Boley and Weiner, 1960). If the thermal stress is large enough, it can cause crack propagation, which may be either stable or unstable depending on the temperature distribution. If the crack propagation is stable, the result is a body with longer cracks and the strength is progressively lowered as the severity of the shock is increased. If the crack propagation is initially unstable but stops as the strain is relieved, the body experiences a discontinuous change in strength, as discussed later. Some cases have been worked out for specific cracks and temperature distributions, but the general problem is complex. Experimental results of single and multiple thermal shock experiments for a variety of ceramics have been presented by Lewis and Rice (1981). In this chapter we present some theoretical treatments based on the extensive work of Hasselman (1969, 1985). Before giving these

results we give an example illustrating the magnitude that thermal stress can reach.

16.2   MAGNITUDE OF THERMAL STRESSES

A simple example is that of a bar or cylinder constrained at the ends and heated in the center. This will approximate a furnace tube clamped at both ends in a water-cooled metal housing and heated in the middle. The resulting stress value indicates why some flexibility allowing movement of the tube ends is required in practice. If the heated length is L and the temperature is T while the temperature at which the ends were rigidly clamped is T_0, the change in length is $\Delta L = \alpha(T-T_0)L$, where α is the average thermal expansion coefficient for the temperature range involved. This is a strain of $\varepsilon = \alpha(T-T_0)$ and produces a stress of $E\alpha(T-T_0)$. For $\alpha = 7 \times 10^{-6}$, $E = 400\,\text{GPa}$, and $T-T_0 = 1000\,\text{K}$, the resulting thermal stress is 2800 MPa, which is well above the strength of most ceramics. The example is crude but indicates that thermal stresses can be large and destructive. Allowing for thermal stresses in design with ceramics is thus crucial in devices that experience thermal gradients.

Such gradients can be constant in time, as in cases of steady-state heat flow, or can change rapidly with time, as when a furnace or heat engine is shut off. Failure resulting from the latter situation is termed failure from thermal shock.

16.3   FIGURE OF MERIT FOR VARIOUS THERMAL STRESS CONDITIONS

Hasselman (1985) has considered various situations in which thermal stresses arise and can cause harmful effects if too large. Such harmful effects include not only crack failure (local or general) but also elastic instability. That is, there are various failure criteria such as fracture or elastic instability. For each combination of geometry and failure criterion, a particular combination of properties of the material appears in the expression for the maximum allowable temperature difference for the conditions assumed. This combination is termed a figure of merit for the material. Examples given by Hasselman are summarized below.

1. Flat plate externally constrained to prevent in-plane thermal expansion and of sufficient thickness to prevent thermoelastic instability (buckling) and subject to a uniform temperature change ΔT. This is the same problem discussed above. The maximum allowable temperature difference is

$$\Delta T_{\max} = \frac{\sigma_f(1 - \nu)}{\alpha E} \tag{16.1}$$

where σ_f is the strength in tension σ_{ft} for $\Delta T < 0$ and is the strength in compression σ_{fc} for $\Delta T > 0$. Thus for the maximum allowable temperature

difference one needs maximum strength, minimum thermal expansion, and minimum elastic modulus.

2. Thin rod constrained in the axial direction as above but subject to thermoelastic instability. The maximum allowable temperature difference without thermoelastic instability is

$$\Delta T_{\max} = \frac{C\pi^2 I}{\alpha A L^2} \tag{16.2}$$

where C is a constant that depends on the rotational constraints at the end of the rod, L is the length, I is the cross-sectional moment of inertia, and A is the cross-sectional area. As far as material properties go, maximizing ΔT simply means minimizing the thermal expansion.

3. Infinitely long hollow concentric cylinder undergoing radially outward heat flow:

$$\Delta T_{\max} = \frac{\sigma_f(1-\nu)}{\alpha E}\left[2\ln\left(\frac{b}{a}\right)\right] \times \left[1 - \frac{2a^2}{b^2 - a^2}\ln\left(\frac{b}{a}\right)\right]^{-1} \tag{16.3}$$

where a and b are the inner and outer radii of the tube. The figure of merit of the material for maximum temperature difference is $\sigma_f(1-\nu)/\alpha E$. If the tube is used as a heat exchanger, the maximum amount of heat flux per unit length without thermal shock failure is

$$Q = \frac{4\pi(1-\nu)K}{\alpha E}\left[1 - \frac{2a^2}{b^2 - a^2}\ln\left(\frac{b}{a}\right)\right]^{-1} \tag{16.4}$$

where K is the thermal conductivity. The figure of merit of the material for maximum heat flux in a heat exchanger is $\sigma_f(1-\nu)K/\alpha E$.

4. Solid circular cylinder of radius b initially at uniform temperature subject to an instantaneous decrease in temperature. The heat transfer is assumed to be linearly convective with a heat transfer coefficient of h:

$$\Delta T_{\max} = \frac{1.45\sigma_{ft}(1-\nu)}{\alpha E}\left(1 + \frac{3.41K}{bh}\right) \tag{16.5}$$

For a large convective heat transfer rate compared to conduction (i.e., $3.41K/bh \ll 1$)

$$\Delta T_{\max} \approx \frac{1.45\sigma_{ft}(1-\nu)}{\alpha E} \tag{16.6}$$

so that high strength together with small thermal expansion and small Young's modulus is desirable for this condition. For larger conduction compared to

convection (i.e., $3.41K/bh \gg 1$)

$$\Delta T_{max} \approx \frac{4.94\sigma_{ft}(1-\nu)K}{\alpha Ebh} \tag{16.7}$$

so that high strength and thermal conduction combined with low values of thermal expansion and Young's modulus are desirable.

5. Solid circular cylinder initially at a uniform temperature subjected to an instantaneous decrease in the temperature of the surrounding medium with infinite boundary conductance:

$$\Delta T_{max} = \frac{\sigma_{ft}(1-\nu)}{\alpha E}\left[\left(\frac{K_1\rho_1 c_1}{K_2\rho_2 c_2}\right)^{1/2}+1\right] \tag{16.8}$$

where the subscripts 1 and 2, respectively, designate the cylinder and the surrounding medium, K is thermal conductivity, ρ is density, and c is specific heat. For large thermal conductivity [i.e., $(K_1\rho_1 c_1/K_2\rho_2 c_2)^{1/2} \gg 1$], the material figure of merit is $\sigma_{ft}(1-\nu)(K\rho c)^{1/2}/\alpha E$. For small thermal conductivity [i.e., $(K_1\rho_1 c_1/K_2\rho_2 c_2)^{1/2} \ll 1$], the material figure of merit is $\sigma_{ft}(1-\nu)/\alpha E$.

6. Solid opaque circular cylinder with emissivity ε at a low initial temperature suddenly heated by black-body radiation with no convective cooling. The maximum radiant heat flux to avoid tensile fracture at the center is

$$q_{max} = \frac{4\sigma_{ft}(1-\nu)K}{\alpha E \varepsilon b} \tag{16.9}$$

The figure of merit for the material under these conditions is $\sigma_{ft}(1-\nu)K/\alpha E\varepsilon$.

Hasselman discusses these and other examples and points out that the same figures of merit for the material apply to other shapes with the same thermal boundary conditions. In all cases a low thermal expansion is desirable. In most cases a low value of Young's modulus is desirable.

16.4 CRACK PROPAGATION UNDER THERMAL STRESS

The above examples describe conditions to avoid failure. In some circumstances, such as thermal shock, failure may not be complete. That is, cracks may propagate some distance and then stop as they outrun the thermal stress field. In a classic paper, Hasselman (1969) presented an analysis that is quite useful in understanding the effect of thermal shock in lowering the strength of ceramics when it does not lead to complete failure. He assumed randomly

distributed, circular cracks of radius c with a crack density of N per cubic meter. He assumed a solid body constrained in all directions and uniformly cooled through a temperature difference ΔT. This produces a triaxial tensile stress given by

$$\sigma = \frac{\alpha \Delta T\, E}{1 - 2\nu} \tag{16.10}$$

or equivalently a triaxial tensile strain given by

$$\varepsilon = \alpha\, \Delta T \tag{16.11}$$

The elastically stored energy per unit volume is

$$U_e = \frac{\sigma^2}{2B} = \frac{(\alpha \Delta T)^2 E^2}{2B(1 - 2\nu)^2} = \frac{3}{2}\left(\frac{(\alpha \Delta T)^2 E}{1 - 2\nu}\right) \tag{16.12}$$

where B is the bulk modulus and the latter equality follows from $B = E/3(1-2\nu)$. Using the Walsh (1965) expression for the bulk modulus of a body with cracks gives

$$E = E_0\left(1 + \frac{16(1 - \nu^2)Nc^3}{9(1 - 2\nu)}\right)^{-1} \tag{16.13}$$

or

$$U_e = \frac{3(\alpha \Delta T)^2 E_0}{2(1 - 2\nu)}\left(1 + \frac{16(1 - \nu^2)Nc^3}{9(1 - 2\nu)}\right)^{-1} \tag{16.14}$$

The surface energy is

$$U_s = 2\pi Nc^2\gamma \tag{16.15}$$

Using the Griffith condition for this system [i.e., $d(Ue + Us)/dc = 0$] gives

$$\Delta T_C = \left(\frac{\pi\gamma(1 - 2\nu)^2}{2E_0\alpha^2(1 - \nu^2)}\right)^{1/2}\left(1 + \frac{16(1 - \nu^2)Nc^3}{9(1 - 2\nu)}\right)c^{-1/2} \tag{16.16}$$

This expression can be simplified for the two cases of short and long cracks. For short cracks the second term in parentheses is small compared to 1 so that

$$\Delta T_C = \left(\frac{\pi\gamma(1 - 2\nu)^2}{2E_0\alpha^2(1 - \nu^2)}\right)^{1/2}c^{-1/2} \tag{16.17}$$

while for long cracks the expression becomes

$$\Delta T_C = \left(\frac{128\pi\gamma(1-v^2)N^2c^5}{81\alpha^2E_0}\right)^{1/2} \qquad (16.18)$$

The expression (16.16) for critical temperature difference can be converted into an expression for critical thermal strain by dividing the equation by the first parentheses (assume $v = 0.25$). The result is plotted in Figure 16.1 to give the critical thermal strain to initiate crack propagation as a function of crack half length.

After the crack reaches the region of instability, it will propagate rapidly while the temperature changes very little. An expression for the crack length after propagation can be derived by assuming that cracks extend until all the energy released is converted into crack surface energy. This is done by setting the difference of (16.14) written for initial and final crack lengths equal to the difference of (16.15) written for initial and final crack lengths:

$$\frac{3(\alpha\,\Delta T_C)^2E_0}{2(1-2v)}\left\{\left[1+\frac{16(1-v)Nc_0^3}{9(1-2v)}\right]^{-1}-\left[1+\frac{16(1-v)Nc_f^3}{9(1-2v)}\right]^{-1}\right\}=2\pi N\gamma\left(c_f^2-c_0^2\right)$$

$$(16.19)$$
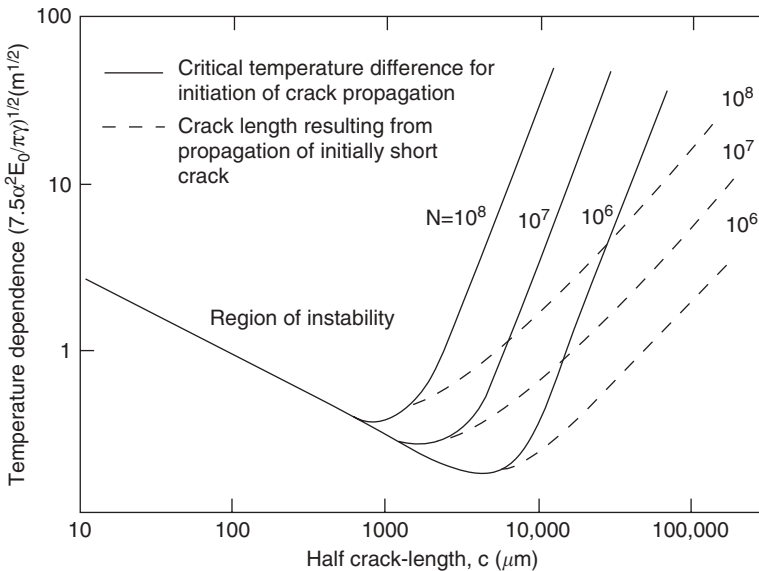
FIGURE 16.1 Minimum thermal strain ($\alpha\,\Delta T$ normalized to give units of square root of length) required to initiate crack propagation as function of crack length and crack density N for Poisson's ratio = 0.25. (From Hasselman, 1969. Reprinted with permission of the American Ceramic Society.)

For initial crack lengths that are small compared to the final crack length, the cubic term in c_0 in Eq. (16.19) can be dropped and Eq. (16.16) can be used to eliminate ΔT_C to give the final crack length as

$$c_f = \left(\frac{3(1-2v)}{8(1-v^2)c_0 N} \right)^{1/2} \tag{16.20}$$
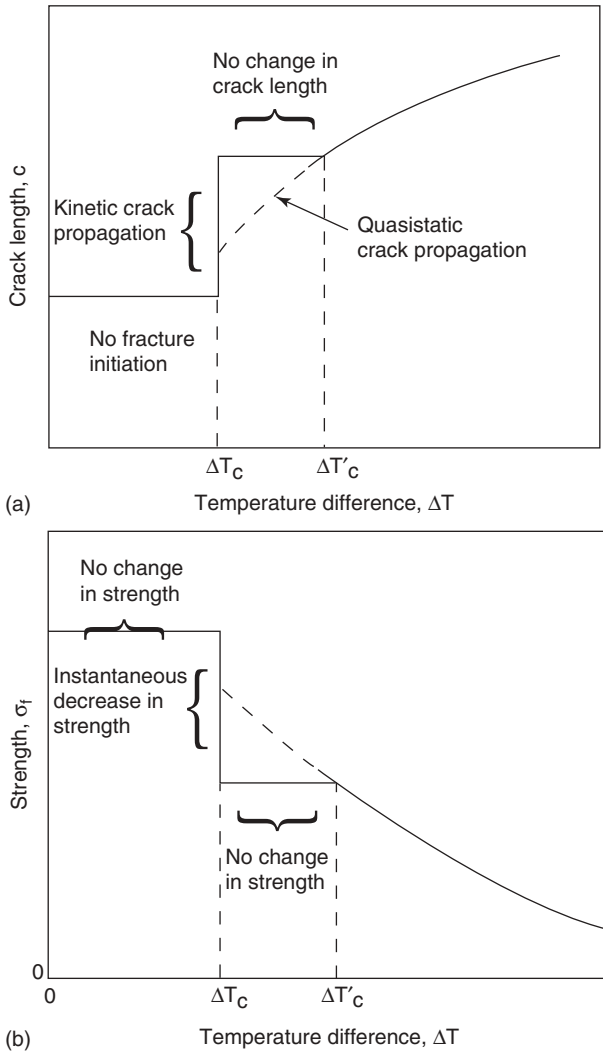
FIGURE 16.2 Crack length and specimen strength as function of thermal history. (From Hasselman, 1969. Reprinted with permission of the American Ceramic Society.)

The final crack lengths for initially short cracks after the critical temperature difference is exceeded are shown by the dashed lines in Figure 16.1. Note that after propagating in the region of instability the crack does not stop but continues to propagate in the region of stability until the length reaches the dashed line. The overshoot of crack propagation beyond the solid-line limit of crack instability is due to the kinetic energy accumulated while propagating in the region of instability. The consequence is that as the temperature difference continues to increase the crack will not grow until it once again reaches the border of the region of instability. This prediction is shown in Figure 16.2. As the size of the initial temperature difference is increased there is no crack propagation and no reduction in specimen strength until a critical value ΔT_C is exceeded, upon which the cracks extend kinetically to a new length, giving the specimen a lower strength. Exposing the specimen to a subsequent, slightly greater temperature difference causes no further crack propagation or further decrease in strength. If the weakened specimen is thermally shocked through a set of progressively larger
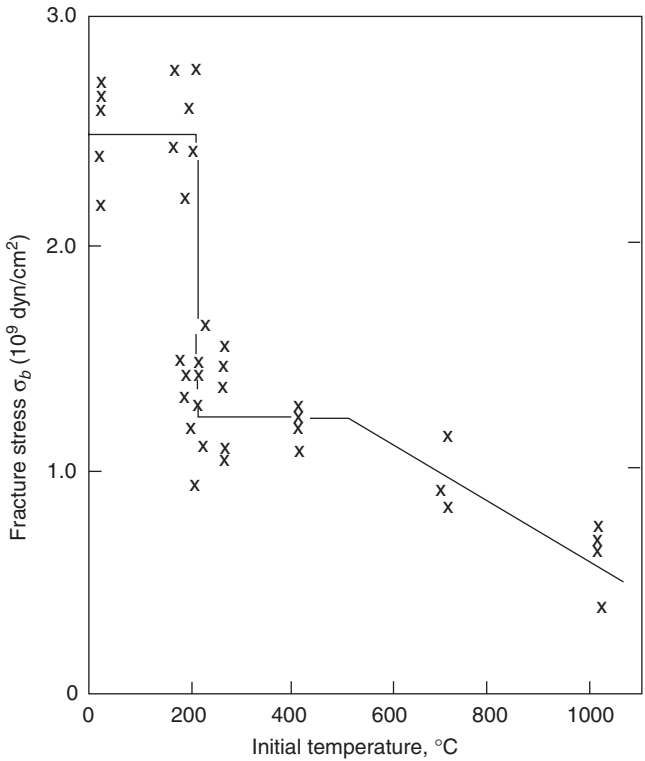
FIGURE 16.3 Strength at room temperature of 5-mm-diameter alumina rods after quenching into water. (From Hasselman, 1969. Reprinted with permission of the American Ceramic Society.)

temperature differences, eventually a critical value $\Delta T_C'$ is reached, at which point further crack propagation and strength decrease do take place. Experimental data from Davidge and Tappin (1967) replotted by Hasselman (1969) is shown in Figure 16.3. The data fit Hasselman's general theoretical predictions quite well.

Specimens with initial crack lengths longer than the length corresponding to the minimum in the plot of Figure 16.1 should propagate stably. The predicted behavior of crack length and strength under increasing temperature difference is shown in Figure 16.4 (Larson et al., 1974). The left portion of this figure repeats the behavior shown in Figure 16.3 expected from the unstable propagation of initially short cracks. The right portion of Figure 16.4 shows the behavior expected for specimens with cracks longer than the length at the minimum of Figure 16.1. Figure 16.5 shows the expected behavior for a high-alumina refractory.

Analysis of these data was based on a treatment of thermal shock of the type given above that was modified to deal with the propagation of surface cracks (Hasselman, 1971). This treatment uses an effective Young's modulus given by

$$E_{\text{eff}} = E(1 - 2\pi N c^2)^{-1} \qquad (16.21)$$
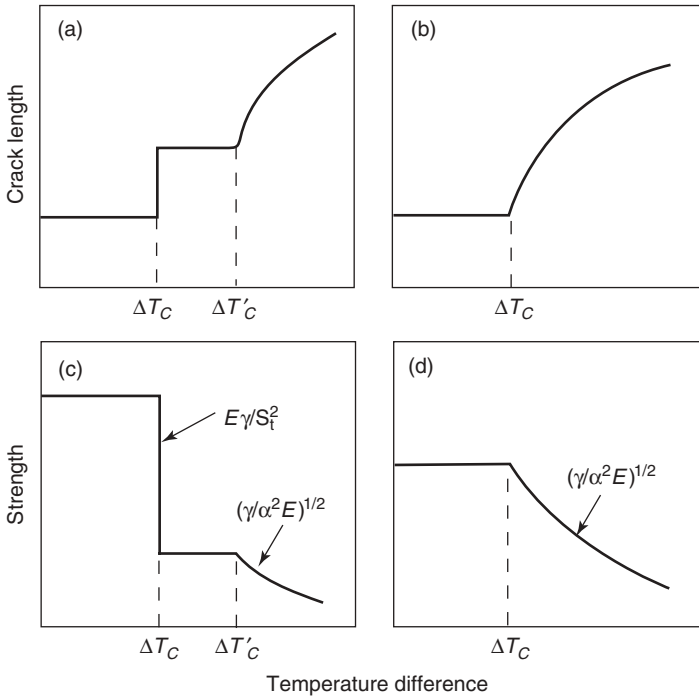
FIGURE 16.4   Crack propagation and strength for (a, c) unstable and (b, d) stable crack propagation conditions. (From Larson et al., 1974. Reprinted by permission of the American Ceramic Society.)
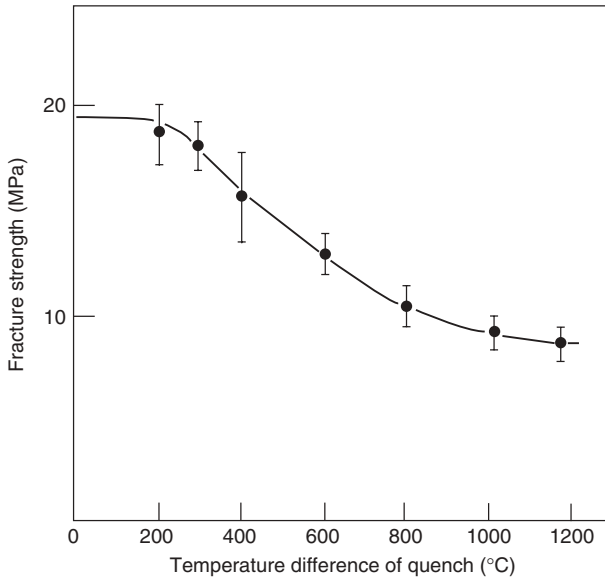
FIGURE 16.5   Strength of 90% alumina refractory quenched in water. (From Larson et al., 1974. Reprinted by permission of the American Ceramic Society.)
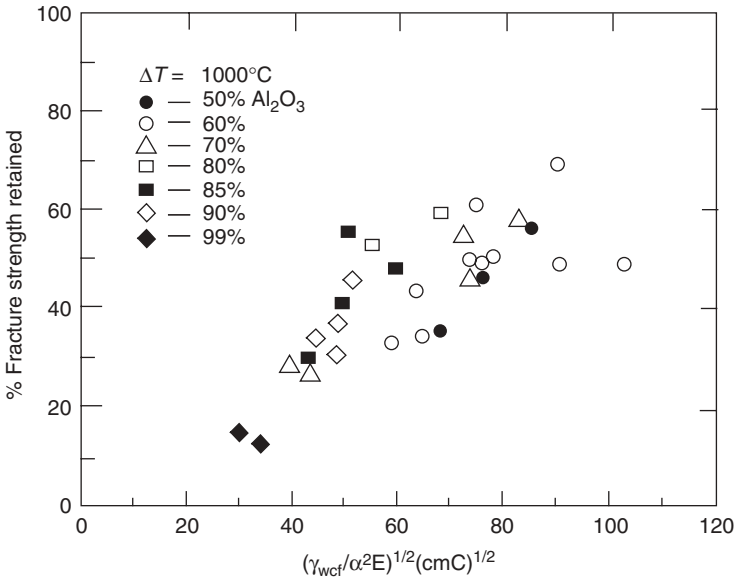
FIGURE 16.6   Retained strength of high-alumina refractories quenched into water as function of thermal stress–resistance parameter. (From Larson et al., 1974. Reprinted by permission of the American Ceramic Society.)

The treatment leads to a curve of the same shape as that in Figure 16.1 with the critical temperature difference given by

$$\Delta T_C = \left(\frac{2\gamma}{\pi\alpha^2 E_0 c_0}\right)^{1/2} (1 + 2\pi N c_0^2) \qquad (16.22)$$

having a minimum at a crack length of

$$c_m = (6\pi N)^{-1/2} \qquad (16.23)$$

and a final crack length for initially short cracks of

$$c_f = \frac{\sigma_f^2}{8N\gamma E} = \frac{1}{8\pi N c_0} \qquad (16.24)$$

For short cracks the relation between temperature difference and crack length is the same as in the previous model, but for long cracks the result is

$$\Delta T_C = \left(\frac{8\pi\gamma^2 c^3}{\alpha^3 E}\right)^{1/2} \qquad (16.25)$$

The strength retained after thermal shock was found to correlate with the fracture surface energy determined in a work of fracture measurement, as shown in Figure 16.6. Lutz et al., 1991b have shown that critical temperature for thermal shock is not very much different in "duplex ceramics" (dispersions of monoclinic zirconia particles in a matrix) but that the retained strength after exceeding the critical shock temperature is significantly improved compared with the matrix material.

PROBLEMS

1. The necessary information for calculating the thermal shock figures of merit are given in the following table:

Material	Flexure Strength (MPa)	Young's Modulus (GPa)	Poisson's Ratio	Thermal Expansion Coefficient (K^{-1})	Thermal Conductivity $(Wm^{-1}K^{-1})$
Hot pressed Si_3N_4	906	311	0.27	3.0×10^{-6}	17
Sintered α-SiC	552	400	0.24	4.4×10^{-6}	110
Al_2O_3	552	386	0.22	8.4×10^{-6}	39
Al_2TiO_5	25	5.5	0.25	0.7×10^{-6}	1

Rank the four material thermal shock resistances of a solid circular cylinder where $bh = 100\,\mathrm{Wm^{-1}\,K^{-1}}$.

2. Equations (16.1)–(16.9) predict thermal shock resistance for, for example, a flat-plate, solid cylinder. In addition to materials properties found in a handbook, what microstructural features might also be considered in choosing a thermal shock resistant material?

3. What is the slope on a log–log scale of the curve to the left of the minimum in Figure 16.1? What is the slope of the three solid-line curves to the right? What is the approximate transition point from the curves to the left and those to the right?

4. Using Figure 16.1 determine the final length of $c = 100$-μm cracks quenched through $\Delta T(7.5\alpha^2 E_0\pi\gamma)^{1/2} = 50\,\mathrm{m}^{1/2}$, $N = 10^7$?

5. Sketch a graph of fracture strength versus ΔT, where ΔT is the quench temperature interval. Start with $c = 1000\,\mu\mathrm{m}$ and sketch σ_f versus ΔT curves for $N = 10^6$, 10^7, 10^8.

6. From the figure below estimate the size of the critical flaw before thermal shock for both pure Al_2O_3 and Al_2O_3–9 vol. % ZrO_2. Can you offer an explanation for the more gradual decrease in strength above ΔT_c than predicted in Figure 16.2? Assume $E_{Al_2O_3} = 380\,\mathrm{GPa}$, $\alpha_{Al_2O_3} = 8.3\times 10^{-6}\,\mathrm{C^{-1}}$, and $\nu_{Al_2O_3} = 0.23$, and $E_{ZrO_2} = 230\,\mathrm{GPa}$ (use rule of mixture).
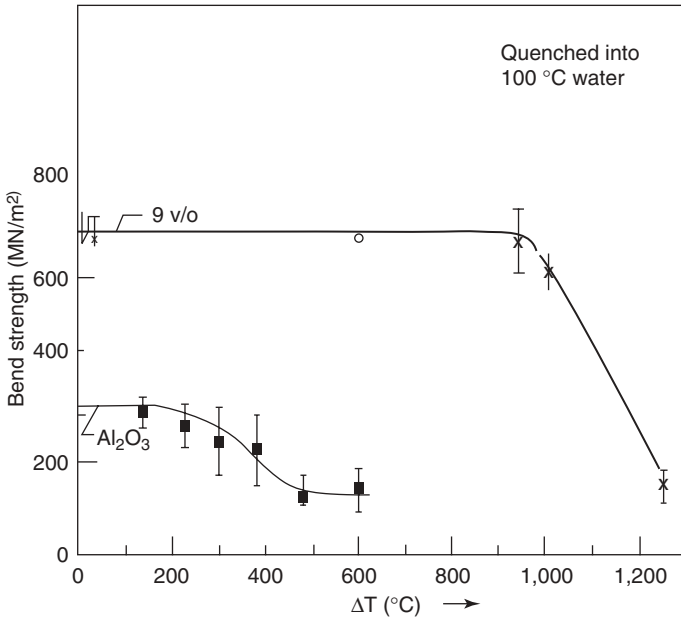
7. a. A thin square sheet of material lies in the x–y plane. It is subjected to in-plane normal strains $\varepsilon_{xx} = \varepsilon_{yy} = \varepsilon$. No stresses are applied to the top or bottom surfaces of the sheet. Derive an expression for stress in the sheet, $\sigma = \sigma_{xx} = \sigma_{yy}$, in terms of ε and the Young's modulus E and Poisson's ratio v of the material of which the sheet is composed.

b. The result of part a may be used to determine the residual thermal stresses that develop in a thin film applied to a thick substrate upon changing the temperature. If the combination of film and substrate is stress free at a temperature T_1 and the linear thermal expansion coefficients of the film and substrate are α_f and α_s, respectively, derive an expression for the stress developed in the film when the system is cooled to temperature T_2, that is, cooled by an amount $\Delta T = T_1 - T_2$. You may assume that the substrate is very thick compared to the film and so does not itself have any significant mechanical strain.

c. Calculate the stress in a glaze film ($\alpha = 6\,\text{ppm/K}$, $E = 75\,\text{GPa}$, $v = 0.3$) on a thick substrate ($\alpha = 9\,\text{ppm/K}$) when the system is cooled from the stress-free state at 650°C to room temperature, 25°C.

d. Is the stress calculated in part c tensile or compressive?

17

FRACTOGRAPHY

17.1 INTRODUCTION

Fractography is the study of fracture surfaces and their interpretation in terms of fracture origin, failure stress, and time under stress before failure. Under favorable circumstances information on each of these aspects of fracture can be obtained. The results are often useful in design of materials, control of processing, assessment of service conditions, and failure analysis. Fractography is sometimes important in legal cases involving responsibility for failure. In practice, failure analysis is a mixture of art and science in which fractography is a critical component, but the experience and judgment of the analyst are important. Scientific principles based on fracture mechanics are involved. The present chapter presents a summary of such principles, but it is important to keep in mind the need for practical experience in the interpretation of fracture surfaces.

Fractography is the subject of three ASTM standards: C1322-05B, C1678-07, and C1256-93R03 (see Chapter 24), which define standard practices for fractography in advanced ceramics and glasses. Quinn (2007) provides practical details on how to perform a fractographic analysis; Quinn also describes several informative case studies. Other useful reviews include Hull (1999), Bradt and Tressler (1994), Mecholsky (1991), Michalske (1991), Varner (1991),

Fréchette (1990), Richerson (1986), and Mecholsky and Powell (1984). Important basic papers include Kirchner and Conway (1987a,b), Kirchner and Kirchner (1979), and Mecholsky et al. (1974, 1977, 1979).

17.2   QUALITATIVE FEATURES OF FRACTURE SURFACES

A brief overview of fractography will be given here to give a sense of its power and to illustrate how the theoretical ideas developed in earlier chapters can be used to understand this topic of practical importance. The discussion will initially consider only homogenous solids, which principally means amorphous materials such as the inorganic glasses, but the behavior of single crystals and polycrystalline materials will be briefly mentioned later. The discussion will outline the steps taken in analyzing an in-service failure for which the state of the system at failure might be unknown. Much of the discussion will also be relevant to understanding the failure of specimens under known laboratory conditions of environment, stress, and so on.

One of the key aims of fractography is to locate the fracture origin so that, if failure results in many fragments, those fragments need to be reassembled to examine the fracture patterns. This can be aided when testing specimens in flexure under laboratory conditions by applying adhesive tape to the compression side. Mating surfaces on the fragments should only be placed in direct contact with extreme care since this could damage the surfaces and mask or remove key evidence about the original failure. After reassembly the resulting fracture pattern contains significant information.

Examination of Figures 5.4 and 5.5 shows that the stresses leading to mode II and III fracture apply a turning moment to the crack front. This causes the crack to extend out of its plane and rotate until it grows perpendicular to the maximum tensile stress. Therefore the crack tends to follow a path perpendicular to the direction of the maximum principal stress. The crack path near the origin therefore provides information on the disposition of stresses at the moment of failure. When the crack is long, it perturbs the overall stress distribution in the body so its path might not indicate the orientation of the principal stresses before it started to grow, but even so, useful information can still be obtained.

Brittle failure frequently results in many fragments so that there must be a mechanism for crack multiplication since the failure usually starts with a single crack. The primary mechanism is by **crack branching** or **bifurcation**. One criterion for crack extension developed in Chapter 5 is that the crack will grow when the energy release rate G exceeds the crack growth resistance R; that is, crack extension initiates when $G = R$. In most cases G increases with crack length so that once the crack starts to grow it will accelerate until $G = 2R$, at which point it is energetically possible for the single crack to branch into two cracks. The maximum crack velocity is a significant fraction of the speed of sound in the material—approximately one-third of the shear wave velocity.

The growth of the crack causes the distribution of stress throughout the body to change which is brought about by stress waves which travel at the speed of sound. When the crack is running at an appreciable fraction of the speed of sound, there is insufficient time to establish a quasi-static stress field around the crack tip similar to the stress distribution discussed in Chapter 5 for static conditions. The result is that the stress field ahead of the running crack is distorted in such a way that there are two planes in the region of the crack tip across which local maxima in the tensile stress lie, instead of the single plane in the static case, thus providing a mechanism for the formation of two cracks from the original single crack. The branch will form for some value of G around $2R$. The branched cracks will accelerate and can themselves later branch into further cracks, producing a fracture pattern near the fracture origin, as shown in Figure 17.1. The number of crack branches in the specimen correlates with its strength because stronger specimens have more stored elastic energy at failure. The extent of fragmentation is therefore a measure of strength. As will be discussed, the distance from the origin to the first branch, r_{cb}, gives a quantitative measure of the failure stress. The branching angle θ shown in Figure 17.1 depends on the stress biaxiality, that is, the relative magnitudes of the maximum principal stress, σ_1, and the second principal stress acting in the direction of propagation of the crack, σ_2, as shown in Figure 17.2. Referring to Figure 1.8, we see that simple axial tension and three- and four-point bending corresponds to uniaxial tension with $\sigma_2 = 0$, giving a bifurcation angle of $\sim 45°$. The center of the specimen in biaxial flexure tests, such as ball-on-ring, correspond to equi-biaxial stress with $\sigma_2 = \sigma_1$, giving a bifurcation angle of $120°$–$160°$. Torsion of a rod applies pure shear to a surface crack and corresponds to $\sigma_2 = -\sigma_1$; the maximum principal stress lies at $45°$ to the torsion axis of the rod so any crack will extend also at $45°$, leading to a spiraling crack leaving a characteristic roughly conical end, such as that shown in Figure 17.12(d). Bifurcations in this case have an angle of $\sim 15°$.
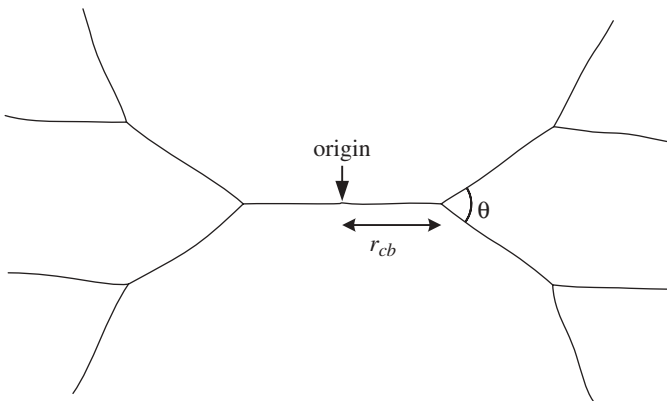

FIGURE 17.1   Typical crack-branching pattern.
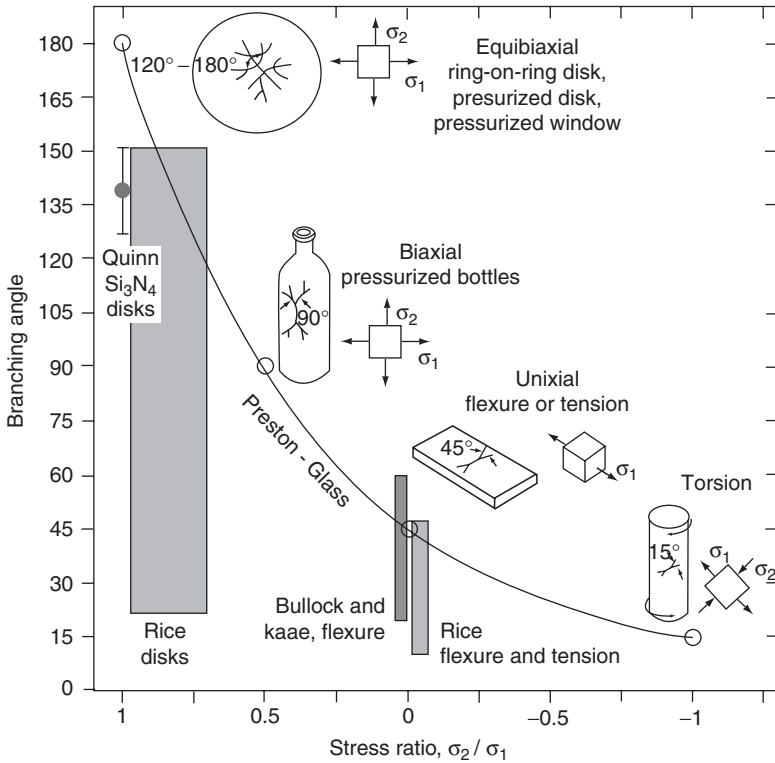
FIGURE 17.2   Relationship between branching angle and stress biaxiality, σ_2/σ_1. (From Quinn, 2007. Courtesy of G. D. Quinn, NIST.)

The crack branching also provides information on the direction of crack growth; in particular, the branches point back toward the fracture origin. Note that the segment of crack containing the fracture origin is the only segment with the crack propagating in both directions. **Wallner lines** can be used to provide more detailed information on the crack growth direction. Wallner lines are small ripples or ridges on the fracture surface caused by the interaction between a stress pulse (a short-duration sound wave) with the crack front. When the stress pulse intersects part of the crack front, the orientation of the principal stresses is slightly perturbed, leading to a slight deviation in the crack path. Once the pulse has passed, the crack returns to its original propagation direction, leaving behind the ripple in the plane of the crack which, even though it is small, is relatively easy to see using optical microscopy for fracture in glasses. The stress pulses that lead to Wallner lines come from a variety of sources which may or may not be directly related to the crack propagation. As an example, Figure 17.3 shows how a "primary" Wallner line is formed for the case where a thin plate is broken in flexure. The origin of the fracture is on the

top surface off to the left. The crack propagates both down and laterally away from the defect so that at some distance the growth is primarily lateral. Since the top surface is in tension, crack growth along the top surface leads growth along the lower surface, giving the curved crack front as indicated in the figure. If there is a preexisting defect in the surface at position "0," a stress pulse is emitted when the crack jumps to the defect. The stress pulse spreads as a spherical wave. Figure 17.3 shows the positions of the crack front (solid lines) and stress pulse (dashed lines) at several subsequent time intervals. The crack front is perturbed where the stress pulse intersects the crack front; the Wallner line formed (bold solid line) is the locus of the intersection point. The curvature of the Wallner line gives an indication of the direction of crack growth. Also, the shape of the line provides information on the distribution of stress through the thickness. If there is significant bending stress, the crack front at the tensile surface leads, while if the stress is uniform, the crack front is symmetrical through the specimen thickness. The different shape of the crack front obviously leads to a different shape of the Wallner line. Figure 17.4 shows the fracture surface of a glass plate broken in bending. The particularly prominent line formed when the crack interacted with a scratch in the upper surface of the plate.

Failure due to a uniform tensile stress or a bending stress can frequently be distinguished by how the crack emerges from the side of the specimen opposite the failure origin, as shown in Figure 17.5, which shows a specimen that failed from a defect in the upper surface. In Figure 17.5(a) the specimen is loaded in uniform tension and the crack propagates straight across the specimen. In Figure 17.5(b) the specimen is loaded in bending by a moment M which puts the upper surface in tension and the lower surface in compression. As the crack approaches the rear surface, the stress in the thin ligament of uncracked material just ahead of the crack is rapidly changing from compression to tension. These rapid changes are communicated throughout the region by stress waves. However, the crack is moving at a significant fraction of the speed of the stress waves so that there is insufficient time for the expected quasi-static stress
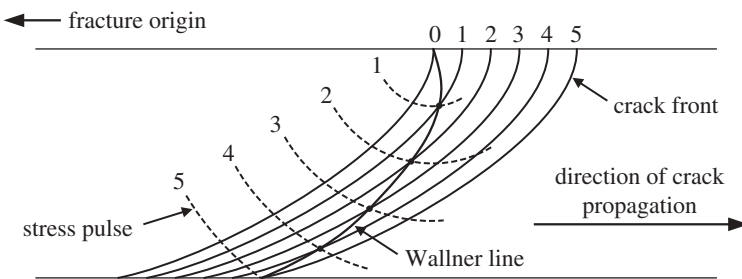

FIGURE 17.3 Formation of primary Wallner line due to interaction between crack front and surface defect for thin specimen broken in flexure. The tensile surface is at the top and the fracture origin is off the figure to the left. (After Fréchette, 1990.)
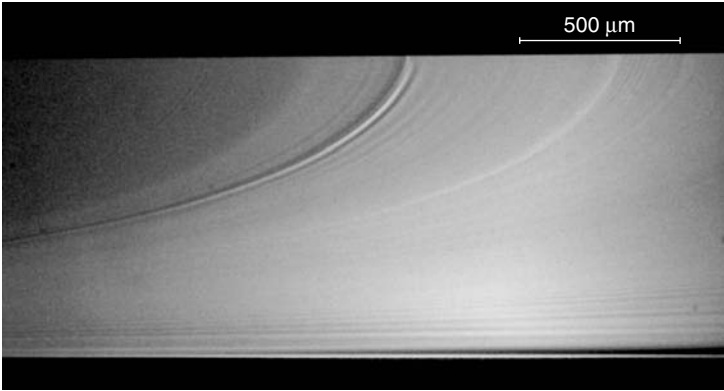
FIGURE 17.4 Wallner lines in glass plate broken in bending. The most prominent line was caused by a scratch on the top surface. (From Quinn, 2007. Courtesy of G. D. Quinn, NIST.)

field to be established. As a result the orientation of the principal stresses changes in an unpredictable way as stress waves pass and any asymmetry in the loading is amplified, causing the crack to wander out of its original plane. The result is a characteristic lip on the surface opposite the original flaw known as **cantilever curl**, as shown in Figure 17.6.

It will now be assumed that a careful study has located the fracture origin using the overall fracture pattern and the Wallner lines. Characteristic
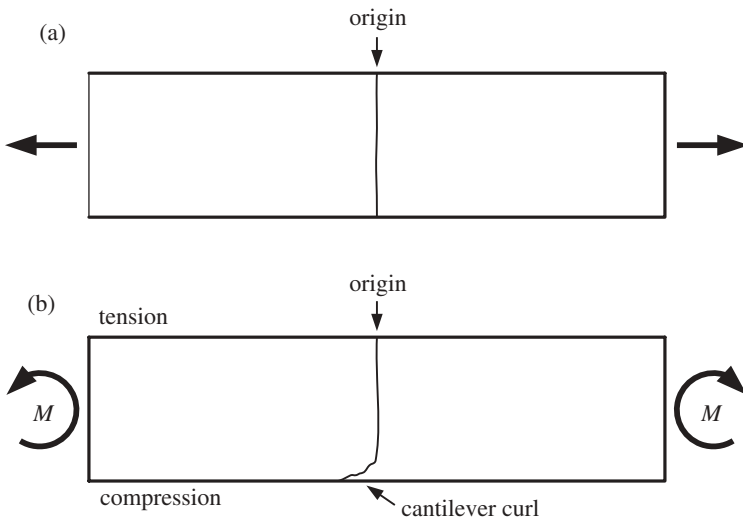
FIGURE 17.5 Formation of cantilever curl in specimens broken in bending: behavior for (a) uniform tensile stress and (b) bending stress.
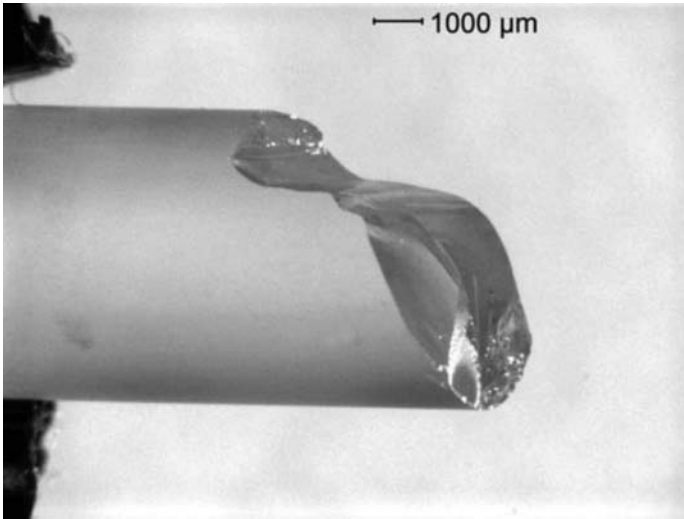
FIGURE 17.6   Optical micrograph of fused silica rod that broke in bending at stress of 88.5 MPa. (From Quinn, 2007. Courtesy of G. D. Quinn, NIST.)

mirror–mist–hackle features are observed around the origin, as shown schematically in Figure 17.7 for a surface flaw (Mecholsky et al., 1974). These features approximate semicircles for fracture originating from a half-penny-shaped surface crack in a specimen under uniform tension. The central region is the source of failure and is often approximately semicircular; it is represented in the
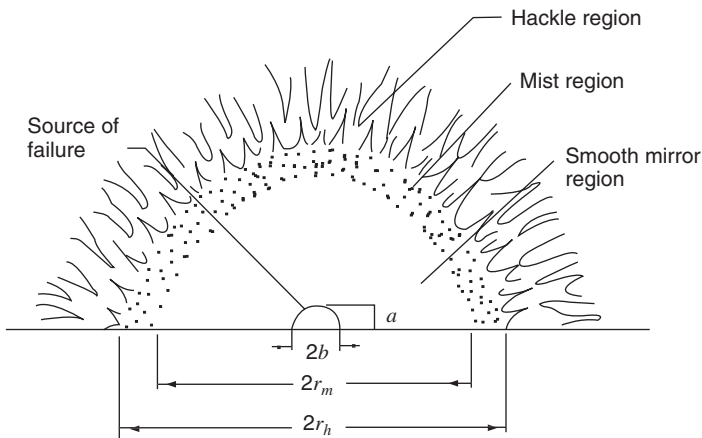
FIGURE 17.7   Schematic of glass fracture surface showing fracture mirror, mist region, and hackle region. (From Mecholsky et al., 1974. Reprinted by permission of Wiley-Blackwell.)

figure by a half ellipse with semiaxes *a* and *b*. This is surrounded by a smooth, flat region termed the **fracture mirror**, which is reflective under optical illumination. Beyond the mirror region is a ring of small radial ridges termed the **mist region** since it gives diffuse reflection under optical illumination. The mist region terminates in a region of bigger radial ridges called **velocity hackle**. These features are thought to result from changes in the crack velocity as it grows under stress. The radii of the boundaries between the mirror and mist regions and the mist and hackle regions are denoted by r_m and r_h, respectively.

These regions are usually quite obvious in fracture surfaces of glass and they can generally be used to find the fracture source at the center of the mirror region. This source can be studied in higher magnification and then various characterization techniques (including chemical analysis when the fracture source appears to be a region of different composition) can be used to determine the nature of the source.

Figure 17.8 shows optical micrographs at low and high magnifications of the fracture surface of a silica glass rod broken in bending, showing the prominent mirror–mist–hackle regions. The neutral axis is from left to right with the peak tension at the bottom of the photograph. Cantilever curl is apparent at the top of the photograph in Figure 17.8(a) where the fracture surface deviates out of the focal plane, resulting in blurring. Figure 17.8(b) shows the mirror–mist–hackle regions in detail. In this case the features are distorted from a semicircular shape because the flaw was not at the position of peak stress—the stress gradient is not perpendicular to the surface in the region of the flaw leading to a loss of symmetry of the mirror–mist–hackle region.

To summarize, careful examination of the features on the fracture surface yield considerable detail about the circumstances of failure, including the magnitude and three-dimensional distribution of stress and the nature and size of the strength-limiting flaw. This brief overview of the subject has not addressed, for example, the effects of residual stress, thermal stress, grinding

(a)   (b)
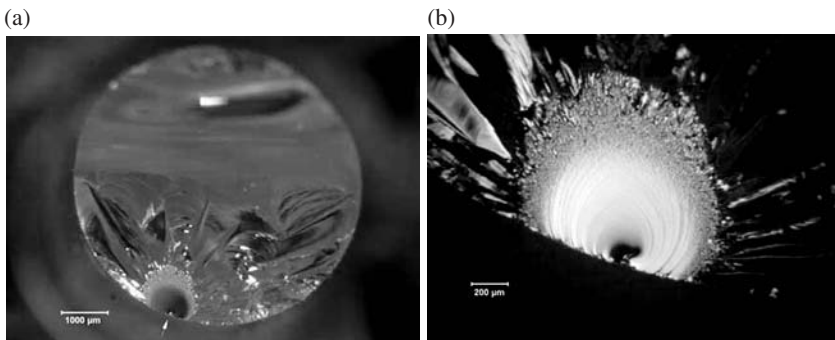
FIGURE 17.8 Optical micrographs of fused silica rod that broke in bending at stress of 96.2 MPa. (From Quinn, 2007. Courtesy of G. D. Quinn, NIST.)

and impact damage, external environment, and internal flaws. The reader is referred to excellent texts, such as Quinn (2007), for in-depth treatments of the subject.

17.3 QUANTITATIVE FRACTOGRAPHY

The size of the features in the mirror–mist–hackle region has been found to be closely correlated with the specimen strength. For a given material, fractography data generally obey the relation

$$\sigma r_j^{1/2} = M_j \tag{17.1}$$

where σ is the fracture stress, r_j ($j = m, h$, cb) is the radius of the mirror–mist (r_m), mist–hackle (r_h), or crack-branching (r_{cb}) boundary and M_j ($j = m, h$, cb) is the set of corresponding **mirror constants** (specifically the **mirror constant**, **hackle constant**, and **crack-branching constant**) associated with these boundaries for the given material. Note that r_j should be measured in a constant-stress field, that is, for a flexure bar, along the tensile surface. A more general expression was developed by Kirchner and Kirchner (1979) and Kirchner and Conway (1987a,b) and can be expressed succinctly as

$$\sigma Y_j r_j^{1/2} = K_j \qquad j = 0, \dots, 3 \tag{17.2}$$

where r_j is now either the crack size c [$j = 0$; often taken as $c = (ab)^{1/2}$ for $a \neq b$] or the mirror–mist ($j = 1$), mist–hackle ($j = 2$), or crack-branching ($j = 3$) boundaries; K_j are the corresponding critical stress intensity constants for the formation of the features; and Y_j are the geometric constants corresponding either to the crack or mirror boundaries. Note that $j = 0$ corresponds to Eq. (5.46).

Examples of plots of fracture stress as a function of the mirror and hackle radii for various glasses are shown in Figure 17.9 (Mecholsky et al., 1974). Krohn and Hasselman (1971) used experiments on strength and critical stress intensity factors in soda–lime–silica glass to obtain $c = 0.10 r_m$. Mecholsky et al. (1974) studied a range of materials listed in Table 17.1 for which they also determined the strength in bending and measured c, r_m, and r_h. The ratios of mirror to flaw size generally are about 10; the two exceptions have over 20% porosity. The ratio of hackle radius to flaw size is generally about 13. Table 17.2 shows the mirror constants for the same glasses calculated from the data of Figure 17.9.

If the mirror constants are known, then the failure stress can be estimated from r_m, r_h, and/or r_{cb} using Eq. (17.1). If the toughness of the material is known, the size of the flaw causing failure, which might be hard to distinguish, can then be calculated using Eq. (5.46). Alternatively, if the size of the flaw can
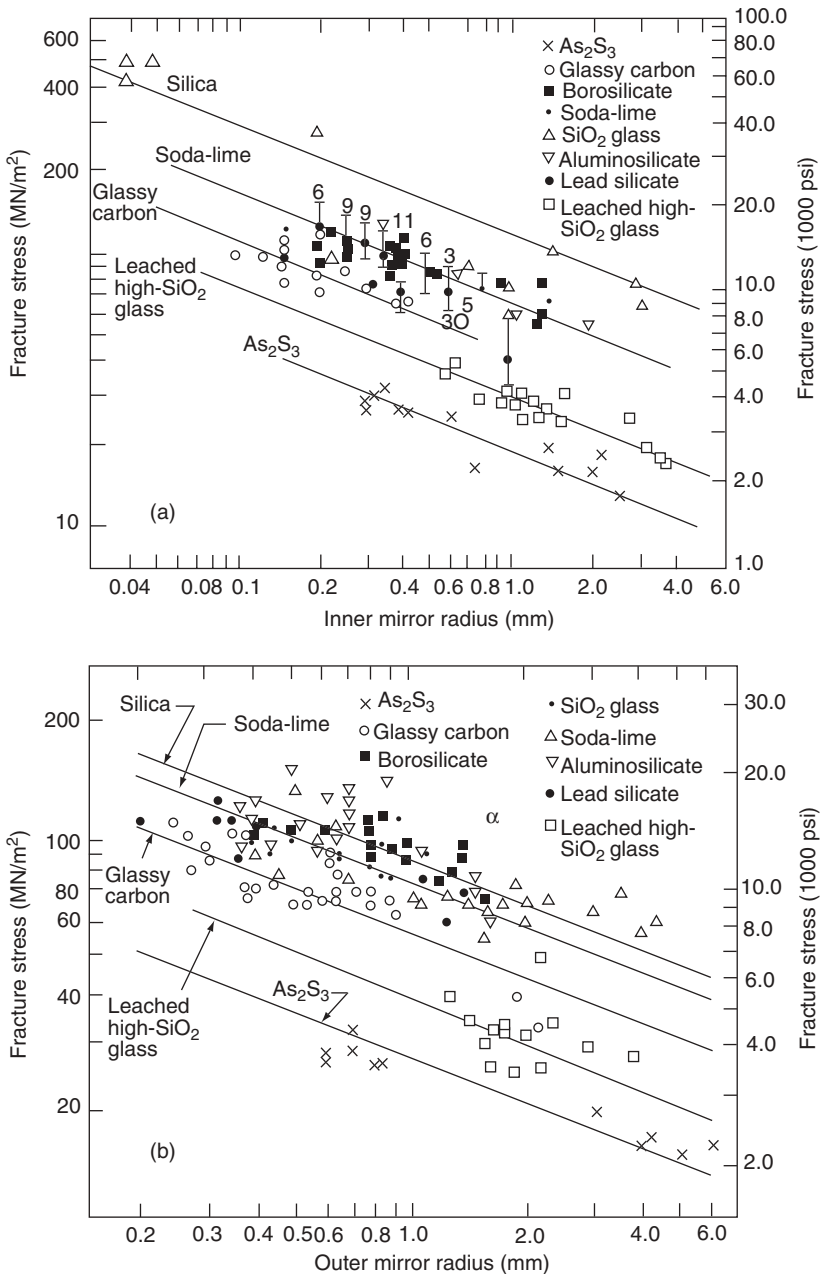
FIGURE 17.9 Strength as function of (a) inner mirror (mirror–mist) radius and (b) outer mirror (mist–hackle) radius. (From Mecholsky et al., 1974. Reprinted by permission of Wiley-Blackwell.)

TABLE 17.1   Flaw-to-Mirror Size Ratios

Glass	Mirror Radii (mm)		Flaw Size, c (mm)	Ratio	
	r_m	r_h		r_m/c	r_h/c
SiO_2	1.02	1.31	0.08	12.5	16.7
Aluminosilicate	0.71	0.86	0.06	12.5	14.3
Borosilicate	0.78	1.04	0.08	10.0	12.5
Soda–lime	0.59	0.85	0.05	12.5	16.7
Lead silicate	0.61	0.77	0.06	10.0	12.5
Leached high SiO_2	0.75	1.40	0.04	14.3	25.0
Glassy C	0.18	0.32	0.04	4.6	7.7
As_2S_3	0.95	1.25	0.11	8.3	12.5
$0.3PbSe-0.7Ge_{1.5}As_{0.5}Se_3$	0.28	0.37	0.05	7.1	9.1
$Ge_{33}As_{12}Se_{35}$	0.75	1.10	0.07	10.7	15.7

be measured from the fracture surface, the fracture toughness can be estimated using the same equation. Mecholsky et al. (1974) found good agreement between the fracture surface energy determined from fractographic measurements and using a constant-moment, double-cantilever-beam technique.

The above treatment does not consider the effect of slow crack growth on fractography, but this was studied by Mecholsky et al. (1979). In dead-weight loading experiments at 50% relative humidity, the flaw size grew slowly from its initial value to a critical value and fracture then occurred. The ratio of fracture mirror radius to initial flaw size is a function of time, but the ratio of mirror size to critical flaw size is a constant. The mirror constants were found to be the same in delayed and rapid fracture.

TABLE 17.2   Mirror Constants

Glass	Mirror Constants (MPa $\cdot$ m$^{1/2}$)	
	M_m	M_h
SiO_2	2.23	2.42
Aluminosilicate	2.14	2.40
Borosilicate	1.87	2.10
Soda–lime	1.92	2.21
Lead silicate	1.61	1.78
Leached high SiO_2	0.91	1.19
Glassy C	1.17	1.67
As_2S_3	0.56	0.65
$0.3PbSe-0.7Ge_{1.5}As_{0.5}Se_3$	0.48	0.55
$Ge_{33}As_{12}Se_{35}$	0.55	0.65

17.4   FRACTAL CONCEPTS IN FRACTOGRAPHY

The concept of fractals was introduced by Mandelbrot (1982) and has been applied to the description of various irregular outlines and surfaces including fracture surfaces (Mecholsky and Freiman, 1991). The fracture surface is rough so that the actual surface area is greater than the projected surface area. However, the roughness is **fractal**, which means that the surface is rough over a range of length scales. As a result the measured surface area depends on the resolution of the measurement technique—higher resolution means that more structure is resolved in the surface and the measured surface area is higher. This behavior can be characterized by D, the fractal dimension. A perfectly flat surface has $D = 2$, while a fractally rough surface has a fractal dimension $D = 2 + D^*$, where D^* is the fractional part of the fractal dimension. A relatively flat surface might have $D^* \simeq 0.1$, while a very rough surface almost filling three-dimensional space might have $D^* \simeq 0.9$. It has been shown that there is a relationship between the fractal dimension and the toughness of the form

$$K_{IC} = E a_0^{1/2} D^{*1/2} \tag{17.3}$$

where E is Young's modulus and a_0 is a parameter with units of length. This result is understandable—a more tortuous surface (higher value of D^*) will require more energy for fracture than a smoother surface. Mecholsky and Freiman (1991) use this result to predict that the ratio of the mirror or mist or hackle radii to the crack size is related to D^*, and in particular for the mirror radius

$$\frac{r_m}{c} \propto \frac{1}{D^*} \tag{17.4}$$

Measurements on a broad range of materials confirm this relationship and suggest that the constant of proportionality is close to unity, giving

$$\frac{r_m}{c} \simeq \frac{1}{D^*} \tag{17.5}$$

17.5   FRACTOGRAPHY OF SINGLE CRYSTALS AND POLYCRYSTALS

The ideas described above for homogeneous materials are still relevant to inhomogeneous materials such as single crystals and polycrystals. However, while single crystals and polycrystals might show similar fracture surface features to those found in glasses, the situation can be greatly complicated by the lack of homogeneity. For example, single crystals do not have isotropic fracture surface energy and fracture tends to occur on crystal planes with low fracture energy, known as **cleavage planes**. If the cleavage plane is oriented nearly perpendicular
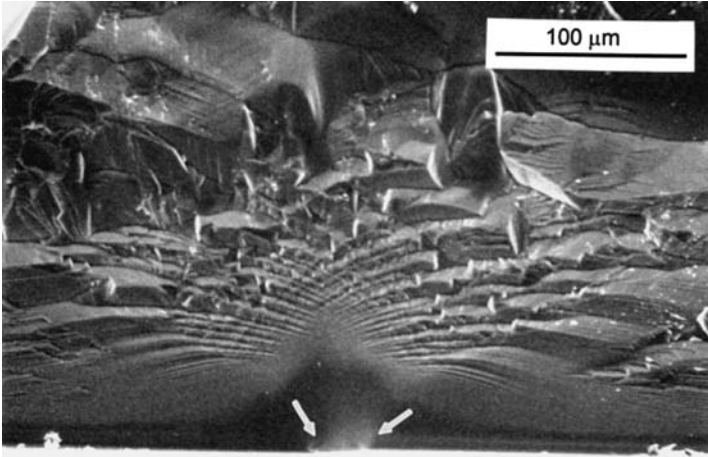
FIGURE 17.10 Fracture surface in silicon single crystal broken in biaxial flexure. (From Quinn, 2007. Courtesy of G. D. Quinn, NIST.)

to the maximum principal stress, a relatively flat fracture surface can result. However, if the cleavage plane is inclined to the maximum principal stress, fracture will still start to grow along that cleavage plane but another cleavage plane might become more favorable and the crack will abruptly change direction. Further on the situation might reverse and the crack will rejoin a
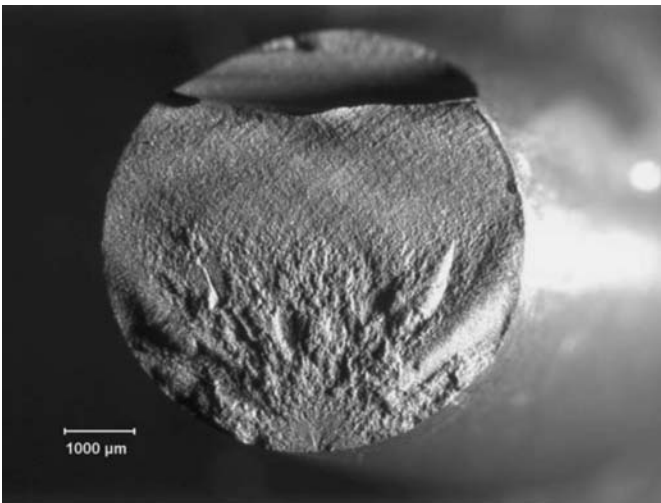
FIGURE 17.11 Optical micrograph of ceramic rod broken in bending. Note the cantilever curl at the top of the picture. (From Quinn, 2007. Courtesy of G. D. Quinn, NIST.)
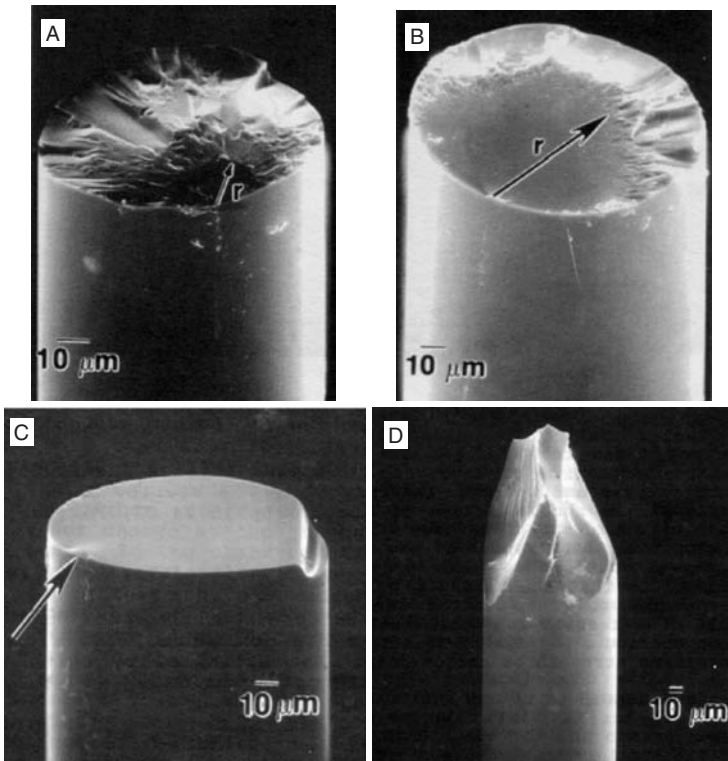
FIGURE 17.12 SEM images of fracture surfaces on 125-μm-diameter fused silica optical fibers. (From Wagner (1993), reprinted with permission SPIE.)

plane parallel to the original cleavage plane. This effect can occur repeatedly, leaving many steps on the fracture surface, such as shown in Figure 17.10.

The situation is further complicated for polycrystals as the fracture is now influenced by the microstructure, including the effect of intergranular stresses, transgranular versus intergranular fracture, and so on. Roughness on the length scale of the grains tends to obscure the fracture surface features. Such an example is the ceramic bar broken in tension shown in Figure 17.11. However, it is obvious that the fracture origin is in or very near the surface of the rod at the bottom of the image and there is clear suggestion of the mirror and hackle regions.

PROBLEMS

1. Estimate the mirror constant for the ceramic in Figure 17.11. The mirror constant of this material is actually $8.5\,\mathrm{MPa}\cdot\mathrm{m}^{1/2}$; use this value to check your estimate of the position of the mirror.

2. A fractographic analysis should include a photograph of the mirror–mist–hackle zone viewed from a perpendicular direction to avoid the length scale in the photograph varying with direction. However, such photographs are not always available. The mirror constant for fused silica is $2.1 \, \text{MPa} \cdot \text{m}^{1/2}$. Use the photographs in Figure 17.12 to determine the following:

   a. Estimate the failure stress for the fiber in photographs A and B.

   b. Estimate an upper limit for the failure stress of the fiber in photograph C.

   c. What was the state of stress (e,g., tension, bending) for the fibers in photographs B, C, and D? Explain.

18

DISLOCATIONS AND PLASTIC DEFORMATION IN DUCTILE CRYSTALS

18.1   INTRODUCTION

Dislocations are the crystal defect primarily responsible for plastic deformation in crystals. They have a fundamental importance to studies of plasticity analogous to the fundamental importance of microcracks to brittle fracture. The study of dislocations forms a large part of the study of mechanical properties

of metals. For ceramics dislocations are certainly important but do not occupy the same central place because of two facts. First, dislocations in many ceramics require for movement a stress higher than the fracture stress at moderate temperatures, typically below half the absolute melting point. Second, although dislocations do move at achievable stresses in some ceramics, in particular, the oxides with rock-salt structures such as MgO, the resulting plasticity is much more limited than in ductile metals and alloys. Dislocations in MgO interact with each other and with other microstructural features to cause failure at small plastic deformations in polycrystalline ceramics. On the whole, then, in the study of mechanical properties of ceramics, dislocations take second place to fracture mechanics and the study of plastic effects associated with point defects, grain boundaries, and glassy phases. Dislocations, however, do occur in ceramics and are important in hardness indents and in wear, in some cases, and do come into play at high temperatures in ceramics. Accordingly, they are treated here. The basic aspects of dislocations are covered in a series of texts from the classical period of dislocation theory development (Cottrell, 1953; Read, 1953; Weertman and Weertman, 1992; Hull, 1965) and in later books (Nabarro, 1979–1989; Hirth and Lothe, 1982; Hull and Bacon, 1982).

18.2   DEFINITION OF DISLOCATIONS

A dislocation is a line imperfection in a crystal with an associated misfit in the crystal. A dislocation is thus characterized by a description of the line (which need not be straight) and by the associated misfit vector, called the Burgers vector. This definition is best understood from examples.

The simplest example is a straight dislocation running through a crystal. Figure 18.1(a) shows an edge dislocation consisting of an extra half plane of
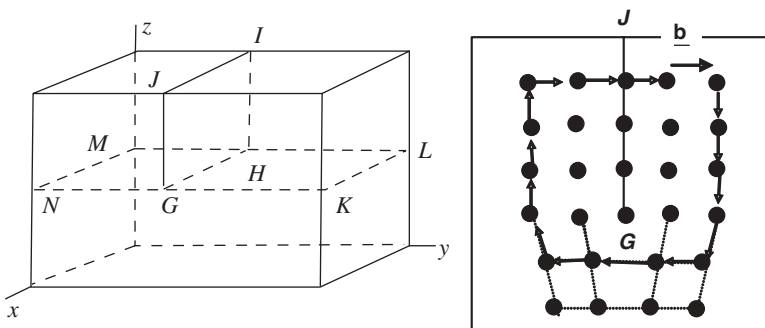
FIGURE 18.1   Edge dislocation: (a) extra half plane *GHIJ* inserted between planes of perfect crystal; (b) schematic of edge dislocation Burgers circuit. In a perfect crystal the path (4 down, 4 left, 4 up, and 4 right) would close. The gap in the crystal containing an edge dislocation is the Burgers vector.
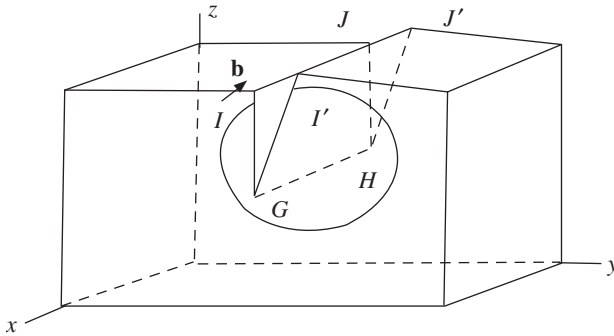
FIGURE 18.2   Schematic of screw dislocation.

atoms *GHIJ*. The dislocation can be considered to have been produced by making a cut *GHIJ*, inserting a half plane of atoms, and rejoining the crystal. The dislocation line *GH* is the edge of the extra half plane.

Another example of a simple straight dislocation is the screw dislocation shown in Figure 18.2. Here the dislocation can be produced by making a cut *GHIJ* as before but, instead of inserting an extra plane of atoms, one face of the cut is displaced parallel to *GH* through one atomic distance and rejoined. That is, *I* goes to *I'* and *J* to *J'*. This is termed a screw dislocation. The dislocation line is again *GH*.

Dislocations are conveniently discussed using the concept of the Burgers circuit. Such a circuit is any path enclosing the dislocation line that would close in a perfect crystal. Figure 18.1(b) can be used to visualize the definition of a Burgers vector by using the Burgers circuit. F. C. Frank (1951) considers a reference crystal of the material under consideration which is perfect (i.e., free of imperfections) and draws a closed path in it. A path is then drawn in the real (imperfect) crystal with one-to-one correspondence between the atoms in the reference and the real crystal. The Burgers vector is the vector needed to close the Burgers circuit around the dislocation line from the point that the circuit would close if the crystal were perfect. The convention concerning Burgers vectors requires choosing a positive direction along a dislocation line such as *GH* (the opposite direction, *HG*, could equally well be chosen). A circuit is then drawn in a clockwise direction while looking along the positive direction of the dislocation line, as shown in Figure 18.1. An equivalent way to express this rule is to use the right-hand rule with thumb along the positive-dislocation direction and fingers curled in the circuit direction. Unit cells are counted along the line *AB* until enough have been traversed to close the line in a perfect crystal. The distance required to close the line in the actual crystal is the Burgers vector. In Figure 18.1 the Burgers vector **b** for the edge dislocation *GH* is perpendicular to the plane *GHIJ*. In Figure 18.2 the Burgers vector for the screw dislocation *GH* is parallel to the dislocation *GH*.
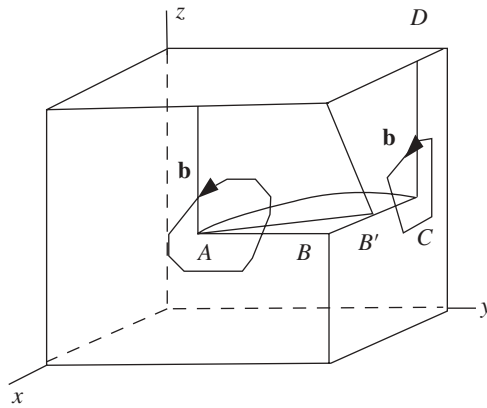
FIGURE 18.3   Burgers circuit for curved dislocation showing continuous change from screw to edge character.

A dislocation can change character from edge to screw, as shown in Figure 18.3. Here a cut has been made on ABC, the point B is displaced to B', and the crystal is rejoined. An extra row of atoms can be identified above point C. A Burgers circuit drawn in the plane about C gives a Burgers vector parallel to BC and hence perpendicular to the segment of the dislocation line AC nearest to C. That is, the dislocation AC is an edge dislocation at C. A Burgers circuit drawn about A also gives a Burgers vector parallel to BC. However, the segment of the dislocation line nearest A is parallel to **b**. That is, the dislocation AC is a screw dislocation at A. The character of the dislocation changes continuously from screw to edge in going from A to C. At any point the dislocation can be described as having a given amount of edge and screw character in terms of the
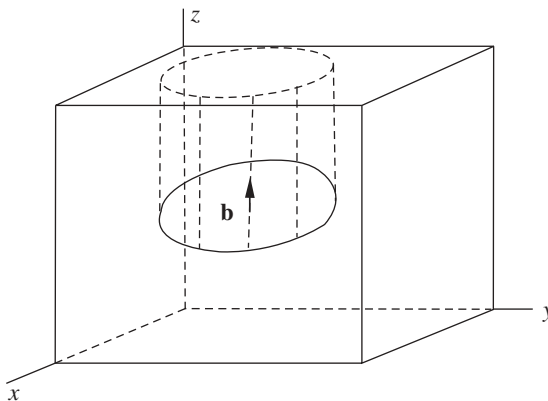
FIGURE 18.4   Closed dislocation loop in crystal.

components of the Burgers vector perpendicular and parallel to the dislocation at that point.

If a Burgers circuit does not close in the real crystal, it encloses a dislocation. The vector from the end of the path to the beginning is the Burgers vector of the dislocation. Such a Burgers circuit can be moved along the dislocation and the Burgers vector will remain constant unless the circuit cuts through a dislocation as the circuit moves. Evidently dislocations cannot terminate within a crystal but terminate only on the surface of the crystal. A dislocation line can close within a crystal by forming a loop, as shown in Figure 18.4. Here the dislocation can be considered as having been made by cutting the crystal in half, adding a disk of material one atomic layer thick, and rejoining the crystal. The Burgers vector is normal to the plane.

18.3   GLIDE AND CLIMB OF DISLOCATIONS

A dislocation can move by glide (also called slip) without needing the removal or addition of material. The slip surface (slip plane) is the plane that contains the dislocation line as it glides. The slip plane must contain the dislocation line and the Burgers vector. The slip direction is the crystallographic direction in which the dislocation moves. In Figure 18.1 the slip plane for the edge dislocation GH is the plane $KLMN$ containing both GH and **b**. A screw dislocation has greater freedom of glide movement. In Figure 18.2 any plane through the screw dislocation GH will contain the Burgers vector so that the screw dislocation can glide on any plane through itself. In Figure 18.3 the plane ABC is the slip plane. In Figure 18.4 the slip surface is a cylinder, the glide cylinder, consisting of all the straight lines parallel to **b** and passing through the dislocation loop.

Glide (slip) is a motion that conserves material, in contrast to climb, which requires the addition or removal of material. Suppose that in Figure 18.1 atoms diffuse to the line GH and add an extra row, thus moving the dislocation line one atomic spacing perpendicular to the plane $KLMN$. This is an example of climb. A general theorem is that if a closed loop of dislocation moves so as to change its projected area on a plane normal to the Burgers vector, then mass transport is required.

18.4   FORCE ON A DISLOCATION

A dislocation in a general stress field will experience a force component tending to cause glide and a force component tending to cause climb (Read, 1953; Weertman and Weertman, 1992).

To obtain the force causing glide, consider the effect of a shear stress $\tau = \sigma_{yz}$ on the edge dislocation shown in Figure 18.1. If the dislocation glides in the y direction, the crystal will undergo a shear strain ε_{yz} and work will be done. This

work is τb per unit area because the upper surface of the crystal is offset by b and the force on it is τ per unit area. The force per unit length of the dislocation is defined as the work done per unit length of dislocation and per unit of motion. The force per unit length on the dislocation caused by the stress τ is thus τb. The force is in the y direction; it tends to cause glide. It is noteworthy that the magnitude of this force does not depend on the direction of the dislocation line.

To obtain the force tending to cause climb, consider the effect of a tensile stress $\sigma = \sigma_{yy}$ on the edge dislocation of Figure 18.1. If enough atoms diffuse to the dislocation line GH to move the dislocation down one atomic spacing, the crystal will expand and work will be done by the tensile stress. The work is σb per unit area. The force per unit length on the dislocation caused by σ is σb. This force is in the z direction; it tends to cause climb. An equation for the force per unit length on a dislocation segment of arbitrary character in an arbitrary direction in a general stress field can be written (Weertman and Weertman, 1992). The dislocation segment is defined by a unit vector $\hat{t} = t_x\hat{x} + t_y\hat{y} + t_z\hat{z}$ along the segment and the Burgers vector $\underline{b} = b_x\hat{x} + b_y\hat{y} + b_z\hat{z}$ which can be at any angle to $\hat{t}$. The most general stress has components σ_{ij}. It is convenient to define a vector $\underline{G} = G_x\hat{x} + G_y\hat{y} + G_z\hat{z}$ in terms of the stress and the dislocation direction by

$$G_x = \sigma_{xx}\, b_x + \sigma_{xy}\, b_y + \sigma_{xz}\, b_z$$
$$G_y = \sigma_{yx}\, b_x + \sigma_{yy}\, b_y + \sigma_{yz}\, b_z \qquad (18.1)$$
$$G_z = \sigma_{zx}\, b_x + \sigma_{zy}\, b_y + \sigma_{zz}\, b_z$$

The vector $\underline{F}$ giving the force per unit length on the dislocation is given by the Peach–Koehler equation:

$$\underline{F} = \hat{t} \times \underline{G} \qquad (18.2)$$

The total force on the dislocation line is always perpendicular to the line because of the vector cross product.

It is instructive to examine the force acting on the curved dislocation of Figure 18.3 under the stress $\sigma_{xz} = \sigma_{zx} = -\tau$. The dislocation is shown in the xy plane with the z axis into the page in Figure 18.5. Consider the forces acting on the dislocation at the three points A (where the dislocation is pure screw), C (where the dislocation is pure edge), and E (where the dislocation is mixed with half-edge and half-screw character). Assume t_z is zero everywhere so that only t_x and t_y need be considered. The positive direction of $\hat{t}$ is from C to A. The components of the Burgers vector are $b_x = b$, $b_y = b_z = 0$. Since both σ_{ij} and b_i are constant along the dislocation, G_{ij} will be constant along the dislocation. Accordingly, $G_x = 0$, $G_y = 0$, and $G_z = b\, \sigma_{zx}$.

At point A, the unit vector tangent to the dislocation is $t_x = -1$ and $t_y = 0$. The force components are $F_x = 0$, $F_y = -\tau b$, and $F_z = 0$. At point C, the unit
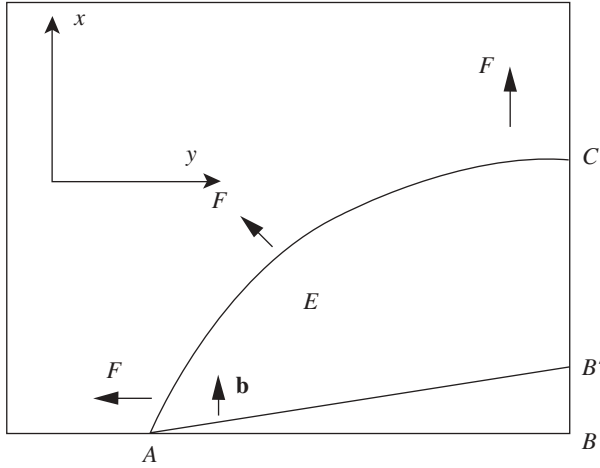
FIGURE 18.5   Force on curved dislocation.

vector tangent to the dislocation is $t_x = 0$ and $t_y = -1$. The force components are $F_x = \tau b$ and $F_y = 0$. At point E, the unit vector tangent to the dislocation is $t_x = -\sqrt{2}/2$ and $t_y = -\sqrt{2}/2$. The force components are $F_x = (\sqrt{2}/2)\tau b$ and $F_y = (-\sqrt{2}/2)\tau b$. The magnitude of the total force at point E is τb and the direction is perpendicular to the dislocation at that point.

The result for the dislocation segment AEC is that the shear stress $\tau = -\sigma_{xz} = -\sigma_{zx}$ applies a constant force everywhere perpendicular to the curved dislocation line, tending to expand the area that has undergone slip.

18.5   STRESS FIELD AND ENERGY OF A DISLOCATION

The stresses associated with a dislocation in an otherwise perfect crystal free of stress from any external forces are of interest in determining the energy of the dislocation and its ability to interact through stress with other dislocations. The calculations are too lengthy to give here. The results for an edge dislocation lying along the z direction with the Burgers vector $\underline{\mathbf{b}}$ in the x direction are

$$\sigma_{xx} = -\frac{\mu b}{2\pi(1-v)}\frac{y(3x^2+y^2)}{(x^2+y^2)^2} \tag{18.3}$$

$$\sigma_{yy} = \frac{\mu b}{2\pi(1-v)}\frac{y(x^2-y^2)}{(x^2+y^2)^2} \tag{18.4}$$

$$\sigma_{zz} = v(\sigma_{xx}+\sigma_{yy}) = -\frac{\mu b v}{\pi(1-v)}\frac{y}{(x^2+y^2)} \tag{18.5}$$

$$\sigma_{xy} = \frac{\mu b}{2\pi(1-\nu)} \frac{x(x^2 - y^2)}{(x^2 + y^2)^2} \tag{18.6}$$

$$\sigma_{xz} = \sigma_{yz} = 0 \tag{18.7}$$

The self-energy of a dislocation can be obtained by integrating the energy density expressed in terms of the stresses associated with the dislocation. The stresses are written in polar coordinates and integrated over the distance r from the dislocation. The integral diverges both at the origin and at infinity. Accordingly, the lower limit of integration is taken to be $5b$ and the energy from the material within this core is evaluated separately. The upper limit of integration is left as $\mathscr{R}$, corresponding to the size of the crystal. The result for the energy per unit length of an edge dislocation is

$$U = \frac{\mu b^2}{4\pi(1-\nu)} \ln \frac{\mathscr{R}}{5b} \tag{18.8}$$

An important feature of this result is the dependence on b^2. Evidently dislocations with the smallest Burgers vector possible are favored from the point of view of minimizing energy.

Weertman and Weertman (1992) estimate the core energy as being about $\mu b^2/10$ and conclude that the core energy is typically only 10–20% of the energy from the logarithmic formula above. They estimate the self-energy of a dislocation in aluminum to be about 3.3 eV per atomic length and contrast this with the energy of about 1 eV needed to produce a lattice vacancy in aluminum.

18.6   FORCE REQUIRED TO MOVE A DISLOCATION

The concept of dislocations was originally introduced to explain how crystals could undergo slip at shear stress values far below the theoretical shear stress of a perfect crystal. It is evident from qualitative arguments that a dislocation should be able to move at far lower stresses. For an edge dislocation, the atoms above the slip plane are displaced in one direction on one side of the dislocation and in the other direction on the other side. The component of the interatomic forces parallel to the slip plane will be in opposite directions for atoms an equal distance from the dislocation on either side. The force to slightly displace the dislocation appears to be zero from this qualitative argument. A more detailed treatment leads to the Peierls–Nabarro equation for the resistance, τ_p, to motion by a screw dislocation:

$$\tau_p = \alpha \frac{\mu b}{2a} \exp\left(-\frac{2\pi w}{a}\right) \tag{18.9}$$

Here α is a constant which depends on whether the dislocation is edge or screw, a is the atomic spacing in the direction of motion of the dislocation, and

w is the width of the dislocation, where τ_p is most often called the Peierls stress. This equation is interesting in showing that the resistance to dislocation motion depends strongly on the width of the dislocation. In ceramics dislocations generally have small widths and high resistance to motion. More detailed calculations show that the resistance to motion depends very strongly on the interatomic forces. Accurate calculations of the resistance appear to await improved knowledge of interatomic force laws.

18.7   LINE TENSION OF A DISLOCATION

The self-energy per unit length of a dislocation loop of radius R replaces Eq. (18.18) when $R < \mathscr{R}$:

$$U \approx \frac{\mu b^2}{4\pi} \ln \frac{R}{5b} \tag{18.10}$$

This self-energy per unit length is equivalent to a line tension T of the same value:

$$T \approx \frac{\mu b^2}{4\pi} \ln \frac{R}{5b} \tag{18.11}$$

It is customary to take

$$\frac{1}{4\pi} \ln \frac{R}{5b} \approx 1 \tag{18.12}$$

giving

$$T \approx \mu b^2 \tag{18.13}$$

A curved dislocation line at a point r under tension T is subject to a force F per unit length perpendicular to the line given by (Weertman and Weertman, 1992)

$$\mathbf{F} = T \frac{d^2 \mathbf{r}}{dr^2} \quad \text{and} \quad \left| \frac{d^2 \mathbf{r}}{dr^2} \right| \approx \frac{1}{R} \tag{18.14}$$

This gives a force per unit length perpendicular to the dislocation due to line tension of

$$|F| \approx \frac{\mu b^2}{R} \tag{18.15}$$

18.8   DISLOCATION MULTIPLICATION

As noted above, a shear stress on a dislocation segment in a slip plane will tend to cause slip. The dislocation should move over the entire plane and be annihilated by forming a step at the surface of the crystal. Thus plastic deformation of a crystal would be expected on this simple picture to remove dislocations from crystals. Experiments showed the opposite. Plastic dislocation greatly increases the dislocation density. This puzzling discrepancy was solved by the discovery of mechanisms for dislocation multiplication. The Frank–Read source is shown in Figure 18.6. Here a segment of a line dislocation pinned between A and B is shown in five successive stages of movement. The initially straight dislocation (labeled 1 in Figure 18.6) bows out under a shear stress until a position (labeled 2) is reached at which the restoring force (force due to line tension plus the Peierls force) equals the driving force caused by the applied stress. If the stress is increased, the loop expands until position 3 is reached. Any further increase in stress causes the radius of curvature to decrease and the loop becomes unstable, sweeping around as shown in position 4. At C the dislocation is a left-handed screw dislocation and at D a right-handed screw dislocation. (For a right-handed screw dislocation **b** is in the opposite direction as $\hat{t}$ and the opposite is true for a left-handed dislocation.) When these lobes meet, the right- and left-handed screw dislocations annihilate each other, producing two separate dislocations, dislocation 1′ and 5. The segment labeled 1′ can now repeat the multiplication process.

An extension of the Frank–Read source by Koehler (Weertman and Weertman, 1992) is shown in Figure 18.7. A portion *JK* of a curved dislocation in the slip plane *ABCD* is parallel to the Burgers vector and so has screw
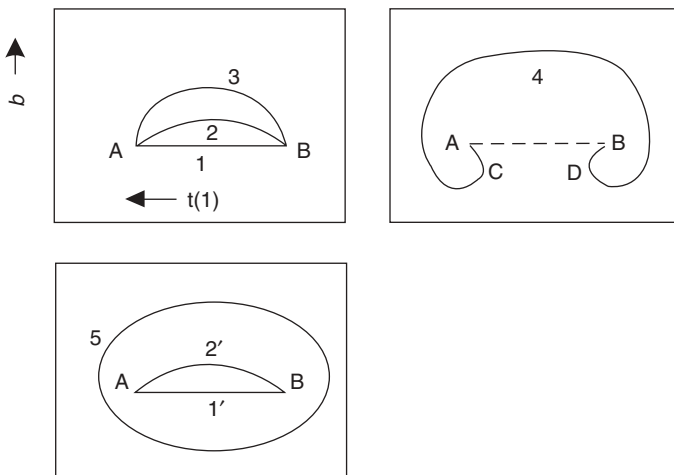
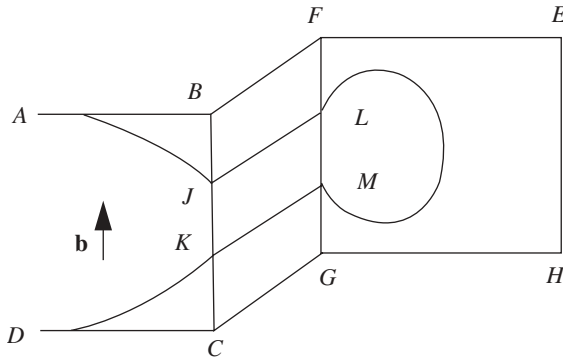FIGURE 18.6   Frank–Read dislocation source.

FIGURE 18.7   Cross slip leading to Frank–Read source.

character. This portion can slip on any slip plane containing the Burgers vector such as the plane *FBCG*. After *JK* slips to the position *LM*, it then forms a Frank–Read source on the slip plane *EFGH*. The stress needed to cause a Frank–Read source to spin off dislocations can now be calculated. If the pinning points of a Frank–Read source are a distance *L* apart in a slip plane and if a shear stress τ is applied, the dislocation will bow out and the radius of curvature will decrease until $R = L/2$. Since the force on a dislocation is τb, the critical stress needed to bow the Frank–Read source into a semicircle is

$$\tau = \frac{\mu b}{R} = \frac{2\mu b}{L} \tag{18.16}$$

A slight increase in stress will push the dislocation further out, the radius of curvature will decrease, and the dislocation loop becomes unstable, causing the source to produce free dislocation loops.

18.9   FORCES BETWEEN DISLOCATIONS

Two dislocations will in general cause forces on each other because one produces a stress field that causes a force on the other. Two parallel screw dislocations having Burgers vectors of magnitude b_1 and b_2 produce a force along the line joining the dislocation center of magnitude:

$$F = \frac{\mu b_1 b_2}{2\pi r} \tag{18.17}$$

The force is repulsive if the Burgers vectors are in the same direction and attractive if the two Burgers vectors are oppositely directed.

Two edge dislocations of the same sign (the half plane extends up on both of them) with parallel Burgers vectors are shown in Figure 18.8. If they have
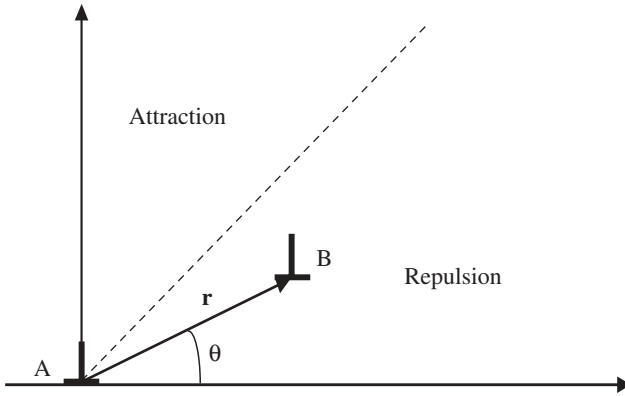
FIGURE 18.8   Force between parallel edge dislocations.

Burgers vectors of magnitude b_1 and b_2, they create force components given by

$$F_x = \frac{\mu b_1 b_2}{2\pi r} \cos \theta \, (\cos^2 \theta - \sin^2 \theta) \qquad (18.18)$$

$$F_y = \frac{\mu b_1 b_2}{2\pi r} \sin \theta \, (1 + 2 \cos^2 \theta) \qquad (18.19)$$

If the angle θ from the slip plane to the line joining the dislocations is equal to $45°$, the component of force between the dislocations parallel to the slip
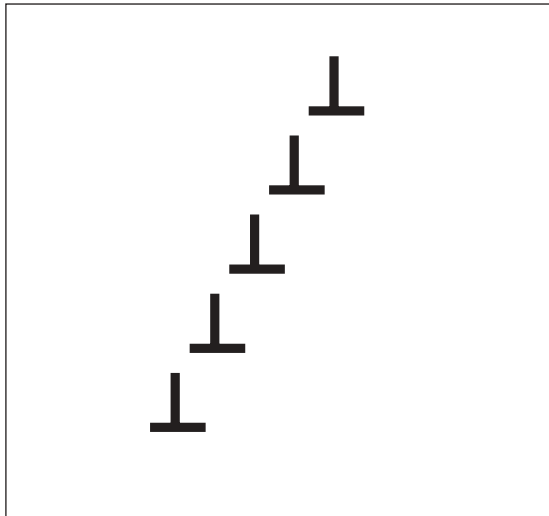

FIGURE 18.9   Dislocations for small angle boundary.

plane is zero. For $0<\theta<45°$ or $135°<\theta<180°$ the force parallel to the slip plane is repulsive so that the dislocations will be driven apart. For $45°<\theta<135°$ the force is attractive. In the latter range of θ the dislocations will be attracted to a position directly above one another. For a whole series of parallel edge dislocations the result is the formation of a small-angle grain boundary as shown in Figure 18.9. Dislocations are represented by $\perp$.

18.10   DISLOCATION PILEUPS

If a dislocation source operates under a shear stress in a plane containing an obstacle to dislocation motion, such as a grain boundary, dislocations pile up against the boundary and exert a back stress on subsequent dislocations emerging from the source. The result affects either the yield behavior or the fracture behavior depending on whether the boundary permits a dislocation to pass through or causes a crack to nucleate. The penetration of a dislocation allows dislocations in the neighboring grain to multiply, leading to general yielding of all grains. The resulting equation for the yield stress or the fracture stress is called the Hall–Petch relation (Hall, 1951; Petch, 1953, 1968). We consider the case of fracture and follow the treatment given by Davidge (1979). Figure 18.10 shows a dislocation pileup against a boundary with the edge dislocations. A set of N dislocations under a shear stress τ produces a tensile stress $\sigma = N\tau$ at the head of the pileup. Each dislocation has to overcome the slip resistance τ_p (the Peierls stress) so that the fracture (or yield) condition is

$$N(\tau - \tau_p) = \sigma_{th} \tag{18.20}$$

where σ_{th} is the theoretical strength if we are talking about fracture or the stress to allow a dislocation to pass through if we are talking about yield. The number
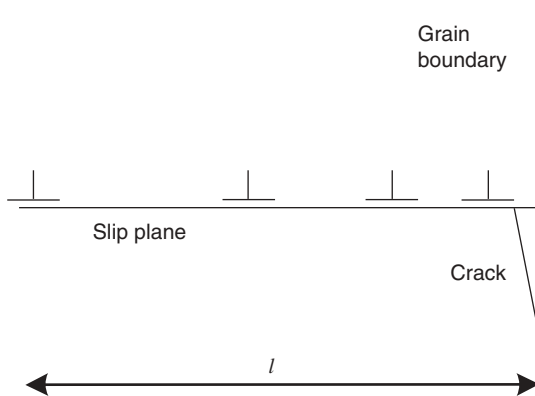
FIGURE 18.10   Dislocation pileup causing crack at grain boundary.

of dislocations in the pileup can be expressed in terms of the length of the pileup l by setting the elastic shear displacement written in terms of the dislocation parameters equal to its value written in terms of stress and shear modulus μ to give

$$\frac{Nb}{l} = \frac{\tau - \tau_p}{\mu} \tag{18.21}$$

Eliminating N leads to

$$(\tau - \tau_p)^2 = \frac{\mu b}{l} \sigma_{\text{th}} \tag{18.22}$$

Recalling that $\mu = E/[2(1 + \nu)]$ and that for the most favorable orientation for slip $\sigma = 2\tau$ gives the tensile stress to open a crack at the grain boundary as

$$\sigma_f = \sigma_0 + \left(\frac{2Eb\sigma_{\text{th}}}{1 + \nu}\right)^{1/2} l^{-1/2} = \sigma_0 + k_f l^{-1/2} \tag{18.23}$$

The quantity k_f has the dimensions of a critical stress intensity factor but is associated with the length of the dislocation pileup rather than a crack length. Since the longest pileup possible is the length of the grain, d, this equation gives a dependence of strength upon the reciprocal square root of grain size. As discussed in Chapter 11, there are a few ionic polycrystals where fracture initiates from dislocation pileups, but for those the fracture strength follows the $d^{-1/2}$ dependence because of crack nucleation. Dislocation mobility appears to be too low to justify use of this fracture model at or near room temperature in most other ceramics, however. Hardness in ceramics, on the other hand, often follows the Petch relationship (see Rice et al., 1994).

For materials with appreciable dislocation-based ductility, the Petch–Hall relationship is used to describe the grain size dependence of the yield stress σ_y by writing

$$\sigma_y = \sigma_0 + k_y d^{-1/2} \tag{18.24}$$

18.11   OROWAN'S EQUATION FOR STRAIN RATE

Orowan's equation gives the strain rate produced by glide or climb of a dislocation. The treatment of Poirier (1985) is followed here for the case of glide of an edge dislocation but the resulting equation is general for climb or glide of an arbitrary dislocation. Consider a block of crystal with dimensions L, l, and h, respectively, in the x, y, and z directions. An edge dislocation running through the crystal in the y direction glides in the x direction, causing a

displacement of the upper surface with respect to the lower by the Burgers vector **b**. The shear strain [Eq. (18.39)] is

$$\varepsilon_{xy} = \frac{b}{2h} \tag{18.25}$$

If the dislocation moves only a distance ΔL, the shear strain is

$$\varepsilon_{xy} = \frac{b}{2h}\frac{\Delta L}{L} \tag{18.26}$$

If N parallel dislocations each move through ΔL, the strain is

$$\varepsilon_{xy} = \frac{1}{2}\frac{N}{hL}\,b\,\Delta L = \frac{1}{2}\rho b\,\Delta L \tag{18.27}$$

where $\rho = N/hL$ is the dislocation density. Taking ρ and ΔL as average values and differentiating with respect to time give

$$\dot{\varepsilon}_{xy} = \frac{1}{2}b\left[\Delta L\frac{d\rho}{dt} + \rho\frac{d(\Delta L)}{dt}\right] \tag{18.28}$$

In some cases, such as steady-state creep, it is reasonable to assume that the dislocation density changes only slowly with time and that its time derivative can be taken as zero compared with the other term, giving Orowan's equation

$$\dot{\varepsilon}_{xy} = \tfrac{1}{2}\rho bv \tag{18.29}$$

where v is the average dislocation velocity.

18.12   DISLOCATION VELOCITY

The velocity of dislocations gliding on a slip plane under shear stress is the result of a balance of the driving force caused by the stress (discussed earlier) and the resistance force. The latter is the sum of the resistance of the otherwise perfect crystal (termed the Peierls force) and the resistance caused by other dislocations and other imperfections. Several studies of isolated dislocations (Johnston and Gilman, 1959; Gilman and Johnston, 1960; Stein and Low, 1960) indicate that the velocity of a dislocation at a given temperature in the absence of other imperfections is a strong function of the shear stress. For LiF, edge dislocations were found to move somewhat faster than screw dislocations,

but over a range of about 6–20 MPa both ranged over about six orders of magnitude and followed the empirical equation

$$v = v_0 \left(\frac{\tau}{\tau_0} \right)^P \tag{18.30}$$

where v_0, τ_0, and P are experimentally determined constants. For LiF, $P \approx 16.5$. This equation cannot hold to very high stress levels because the limiting velocity of a dislocation is thought to be that of sound shear waves. The experimental data on LiF indicate a bending over of the velocity curve at high stresses consistent with this theoretical limit.

Dislocation velocity is usually limited by obstacles such as discrete particles and other dislocations so that the above equation for dislocation velocity is not generally used in the description of plasticity or creep. The process of dislocation motion is instead viewed as the overcoming of obstacles with the assistance of thermal activation. The mean velocity is written as

$$v_{\mathrm{mean}} = \beta b v e^{-(\Delta E^*(\tau)/kT)} \tag{18.31}$$

where β is a numerical constant, b is the magnitude of the Burgers vector, v is a frequency, and ΔE^* is the activation energy that depends on the shear stress τ (Frost and Ashby, 1982). The form of the stress dependence of the activation energy depends on the type and geometric arrangement of the obstacles. For a example, for a regular array of box-shaped obstacles the result is

$$\Delta E^*(\tau) = \Delta F \left(1 - \frac{\tau}{\hat{\tau}} \right) \tag{18.32}$$

where ΔF is the activation energy without applied stress and $\hat{\tau}$ is the shear strength in the absence of thermal energy and includes the effects of the obstacles. This method of treating dislocation velocity is the basis for constructing portions of the deformation maps developed by Frost and Ashby. We consider primarily plastic effects in the present chapter, take up creep and related dynamic effects in Chapter 20, briefly discuss the representation of plasticity and creep in deformation maps in Chapter 20, and consider fracture maps in Chapter 21.

18.13   HARDENING BY SOLID SOLUTION AND PRECIPITATION

Impurities and solid-solution atoms can interact with dislocations through elastic, electrical, and chemical effects. Elastic interactions are particularly important and easy to visualize quantitatively. An edge dislocation has a region of compression on the side of the slip plane with the extra half plane of atoms and a region of expansion on the other side of the slip plane. Evidently impurity

atoms larger than the normal atoms of the crystal can minimize their elastic misfit energy by locating in the expanded region. Given time to diffuse to the dislocation they will tend to do so. Similarly, impurity atoms smaller than the normal atoms of the material will tend to diffuse to the compression side of the slip plane near an edge dislocation. The increased concentration of impurities that develops near a dislocation is termed a dislocation atmosphere. It requires energy to separate a dislocation from its atmosphere. If the dislocation is forced by stress to move faster than the atmosphere can diffuse to keep up with its motion, an extra resistance must thus be overcome. Once the dislocation has moved some distance away from its atmosphere, the force to continue motion is less. This is one effect that leads to a yield point in a constant-strain-rate experiment.

An alloy with a solid solution in equilibrium at a high temperature may no longer be in equilibrium if the temperature is lowered. Typically, the new equilibrium state is a mixture of precipitates of one composition in a more dilute solid solution. A dislocation moving on a slip plane containing a precipitate may be able to glide through the precipitate particle but more typically finds it difficult to do so. Instead, the dislocation can bend around the particle (much in the manner of a Frank–Read source), rejoin on the other side, and leave behind a loop of dislocation surrounding the precipitate. Both dislocation atmospheres and precipitate particles are important sources of hardening in metals and alloys. Ceramics at temperatures and stresses that permit dislocation motion show similar effects.

For strong obstacles every obstacle will pin the dislocation so that the mean distance between pinning points will be the same as the mean spacing of obstacles, L. Then the shear stress necessary to break free a semicircular loop of dislocation is given by

$$\tau_{\mathrm{max}} = \frac{\mu b}{L} \qquad (18.33)$$

If the obstacles are not too strong the dislocation will pull free at a less than semicircular shape and the average spacing between pinning points will be larger. Both effects lower the hardening effect of obstacles (Courtney, 1990).

18.14   SLIP SYSTEMS

Dislocations require a higher shear stress to glide on some crystallographic planes than on others. The direction of slip is also important since that determines the Burgers vector and the self-energy of a dislocation which according to Eq. (18.8) is proportional to b^2. The combination of the crystallographic slip plane and slip direction is called the slip system. In metals closed-packed planes are preferred because of the larger spacing between planes and closed-packed directions because of the small Burgers vector. In ceramics

additional considerations come to bear, as will be discussed in Chapter 19. The criterion for favorable slip in metals is to minimize the b/h ratio, where h is the distance between planes. Since b/h represents the shear strain for dislocation movement of a distance b, shear strain is minimized. Figure 18.11 compares the b/h ratio for the FCC slip systems $(1\,1\,1)[0\,\bar{1}\,1]$ and $(1\,0\,0)[0\,\bar{1}\,1]$. In the FCC lattice the distance between $(hk.\ell)$ planes whose lattice parameter is a is

$$h = \frac{a}{\sqrt{h^2 + k^2 + \ell^2}} \tag{18.34}$$

Thus the $\{1\,1\,1\}\langle 0\,\bar{1}\,1\rangle$ is the preferred slip system in FCC metals.

The resolved shear stress on a given plane and in a given direction is described by the equation

$$\tau = \sigma \cos \theta \cos \psi \tag{18.35}$$

where θ is the angle between the direction of dislocation glide and the stress axis and ψ is the angle between the slip plane normal and the stress axis. The example below illustrates how the equation determines which slip system would

(111) [0$\bar{1}$1]

$$b = \frac{\sqrt{2} \cdot a}{2} = \frac{a}{\sqrt{2}}$$

$$h = \frac{a}{\sqrt{3}}$$

$$\frac{b}{h} = \frac{3}{\sqrt{6}} = 1.22$$

(100) [0$\bar{1}$1]

$$b = \frac{a}{\sqrt{2}}$$

$$h = \frac{a}{2} \text{ (planes are ½ lattice spacing apart)}$$

$$\frac{b}{h} = \frac{2}{\sqrt{2}} = 1.41$$
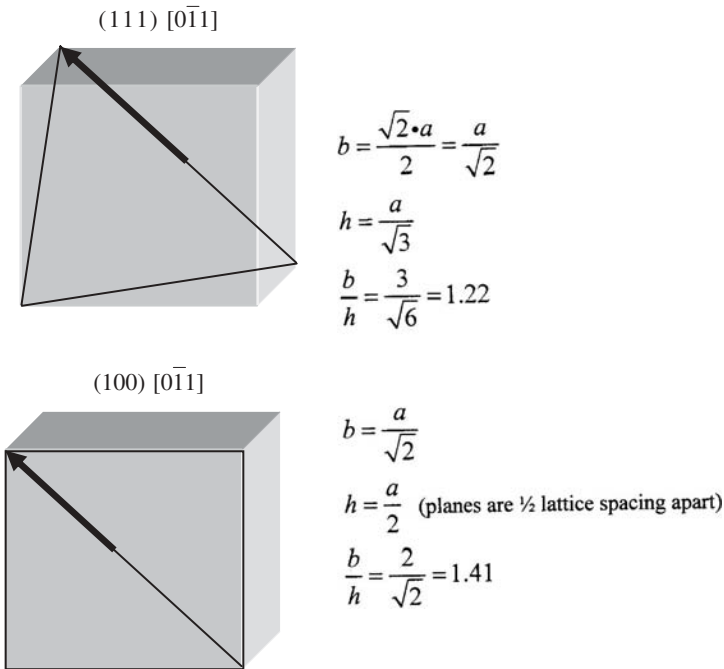
FIGURE 18.11   Comparison of two FCC slip systems. The higher h/b ratio is the preferable slip system.

have the largest resolved shear stress for a crystal of a given orientation with respect to the stress axis. Consider the easiest slip system for FCC $(1\,1\,1)\big[0\,\bar{1}\,1\big]$ and determine whether the resolved shear stress on the slip system would be higher if the stress were applied along the $[0\,0\,1]$ or the $\big[1\,1\,\bar{1}\big]$ directions. To determine the cosine of the angle between two planes $[h_1, k_1, \ell_1]$ and $[h_2, k_2, \ell_2]$,

$$\cos\theta \ \text{or} \cos\ \psi = \frac{h_1 h_2 + k_1 k_2 + \ell_1 \ell_2}{\sqrt{h_1^2 + k_1^2 + \ell_1^2}\sqrt{h_2^2 + k_2^2 + \ell_2^2}} \qquad (18.36)$$

and so

$$\tau_{[0\,0\,1]} = \sigma\cos\theta\cos\psi = \sigma\left(\frac{1}{\sqrt{2}}\frac{1}{\sqrt{3}}\right) = 0.41\sigma \qquad [0\,0\,1]$$

$$\tau_{[1\,1\,\bar{1}]} = \sigma\cos\theta\cos\psi = \sigma\left(-\frac{2}{\sqrt{6}}\frac{1}{3}\right) = 0.27\sigma \qquad [1\,1\,\bar{1}]$$

Thus the $[0\,0\,1]$ stress results in the highest resolved shear stress on the $(1\,1\,1)\big[0\,\bar{1}\,1\big]$ slip system. There are 12 slip systems $\{1\,1\,1\}\langle 1\,\bar{1}\,0\rangle$ in FCC. Since this is the easiest slip system, substituting the yield stress of an FCC single crystal into Eq. (18.35) could determine the critical resolved shear stress τ_{CRSS}, that is, the shear stress sufficient for dislocation motion in that slip system.

18.15   PARTIAL DISLOCATIONS

Up to this point we have considered dislocations whose Burgers vectors are a repeat distance in the crystal. Such a dislocation is termed a perfect dislocation and is a line defect. That is, large distortions of the crystal structure occur only in a small core region surrounding the mathematical line describing the position of the dislocation. Outside the core the crystal structure is perfect apart from some degree of elastic deformation. In some crystal structures a perfect dislocation can break up (dissociate) into two partial dislocations connected by a strip of material (a stacking fault) across which the normal interatomic distances and angles are not those of the perfect crystal. This process can be visualized for a an FCC crystal having one atom per lattice point for which the atomic positions are shown in Figure 18.12. If the atoms are considered to be spheres, the $(1\,1\,1)$ plane is a hexagonal array as shown in Figure 18.13. The initial $(1\,1\,1)$ plane is labeled A. The next plane of atoms above the A plane is located above the site labeled B and the plane above that is located above the site labeled C. The stacking sequence of $(1\,1\,1)$ planes in this FCC structure is thus $ABCABC\ldots$. A hexagonal close-packed (HCP) structure with a single atom per lattice point has (0001) plane with the same atomic arrangement as
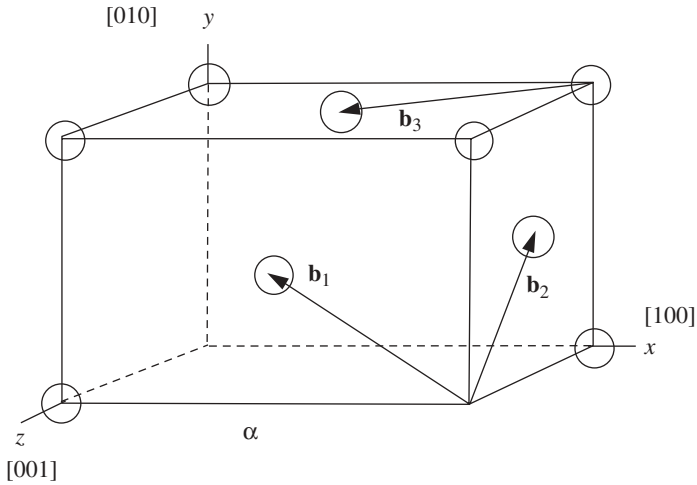
FIGURE 18.12 FCC structure $\mathbf{b}_1 = (a/2)\left[\bar{1}\,1\,0\right]$, $\mathbf{b}_2 = (a/2)\left[0\,1\,\bar{1}\right]$, and $\mathbf{b}_3 = (a/2)\left[\bar{1}\,0\,1\right]$.

layer A of Figure 18.13. The next (0001) plane is located above the site labeled B, but the plane above that is located above A. The stacking sequence of (0001) planes is thus $ABABAB\ldots$. The nearest-neighbor relationships are the same in the FCC and HCP structures so that the energy difference results from differences in the relationships of the next-nearest and more distant neighbors.

A total dislocation (td) with Burgers vector $\underline{\mathbf{b}}_1$ can dissociate into two partial dislocations (pd) and a stacking fault (sf) as indicated symbolically using
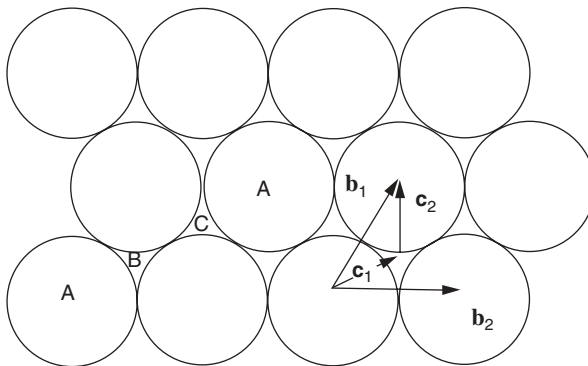
FIGURE 18.13 Atomic arrangement in (1 1 1) plane. Successive (1 1 1) planes are stacked in the sequence $ABCA\ldots$.

boldface to indicate vectors by

$$\text{td } (\mathbf{b}_1) \rightarrow \text{pd } (\mathbf{c}_1) + \text{pd } (\mathbf{c}_2) + \text{sf}$$

with

$$\mathbf{b}_1 = \mathbf{c}_1 + \mathbf{c}_2 \tag{18.37}$$

so that the Burgers vector is conserved. From Figure 18.13, $\mathbf{c}_1$ is given by the vector sum

$$\mathbf{c}_1 = \tfrac{1}{3}(\mathbf{b}_1 + \mathbf{b}_2) = \tfrac{1}{6}a\left[\bar{1}\,2\,\bar{1}\right] \tag{18.38}$$

and

$$\mathbf{c}_2 = \mathbf{b}_1 - \mathbf{c}_1 = \tfrac{1}{6}a\left[\bar{2}\,1\,1\right] \tag{18.39}$$

Approximating the energy of a dislocation as μb^2 as discussed in Sections 18.5 and 18.7 it follows that the energy of the two partial dislocations is less than that of the total dislocation because

$$b_1^2 = \tfrac{1}{2}a^2 \tag{18.40}$$

and

$$c_1^2 = c_2^2 = \tfrac{1}{6}a^2 \tag{18.41}$$

so that the energy difference

$$\mu\left\{(b_1)^2 - [(c_1)^2 + (c_2)^2]\right\} = \tfrac{1}{6}\mu\,a^2 \tag{18.42}$$

is available to form a strip of stacking fault between the two partial dislocations. Another important feature of partial dislocations is that they can act to form a deformation twin, which is an important mechanism of deformation in some ceramic crystals, including aluminum oxide and zirconium oxide.

18.16 DEFORMATION TWINNING

Deformation twinning is a process by which a portion of a crystal translates into a different position forming a mirror image across a plane called the twin plane. The shifted (twinned) portion of the crystal cannot be brought into registry with the rest of the crystal by translation but can be made to coincide

by a mirror plane symmetry operation. The history of attempts to understand and correctly describe twinning is extensive (Cahn, 1954); we shall give only a brief summary of the deformation produced and the geometric elements used to describe this deformation.

Twinning is produced by a uniform shear of a portion of a crystal as shown in Figure 18.14. Below $y = 0$ the crystal is undisturbed while the portion above undergoes a uniform shear s. The twin is described by two undistorted planes (K_1, K_2), two special directions (η_1, η_2), and s. The displacements u, v, w of a point initially at x, y, z are $u = ys, v = w = 0$, where y is in units of the lattice spacing. The plane $y = 0$ is undistorted by the shear in the x direction; this plane and direction x are termed K_1 and η_1, respectively. There is a second plane within which distances are unchanged by the shear; a point P is carried into a point P' such that $OP = OP'$(Figure 18.15). In contrast, the point Q is carried into Q' but $OQ \neq OQ'$. Distances in the plane through OP and the z axis are unchanged; this plane is termed K_2 and OP is termed η_2. The result of the motions is that K_1 is a mirror plane. Twins may be related by other symmetry elements such as a glide plane.

The above summary of the geometry of twinning describes the motion of lattice points; for a crystal with a single atom per lattice point, as in an FCC metal, the atomic motions in deformation twinning correspond to the lattice point motions. For a crystal with more than one atom per lattice point the atomic motions must correspond to the symmetry element, often a mirror plane, linking the twinned and untwinned portions of the crystal.

The formation of a deformation twin can be described by the motion of a partial dislocation on each plane above the K_1 plane. Following Weertman and Weertman (1992), Figure 18.16 shows schematically the formation of a deformation twin in an FCC structure with $K_1 = (1\,1\,1)$. On each plane above K_1 a partial dislocation with $\mathbf{c}_1 = \frac{1}{6}a[\bar{1}\,2\,\bar{1}]$ has entered the crystal from the left and moved halfway across. The first plane above K_1 is shifted $A \rightarrow B$. The
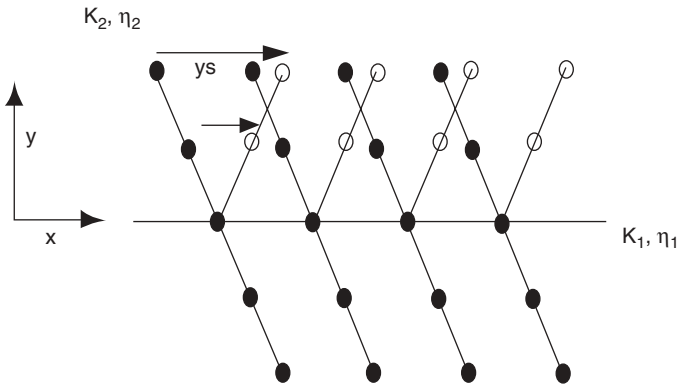
FIGURE 18.14   Twinning showing motion of lattice points.
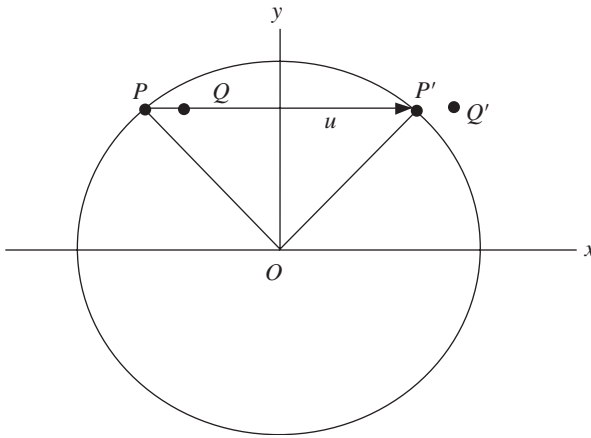
FIGURE 18.15   Twinning showing uniform shear.

second plane above experiences the shifting effect of two partials and so is shifted $B \to C \to A$. Successive planes are shifted in this pattern, resulting in the stacking sequence shown on the left. Plane K_1 is thus a mirror plane relating the twinned portion of the crystal to the untwinned portion. A stacking fault (incorrect next-nearest-neighbor stacking sequence between the planes immediately on either side of K_1) extends from the left edge of the crystal to the stack of partial dislocations.
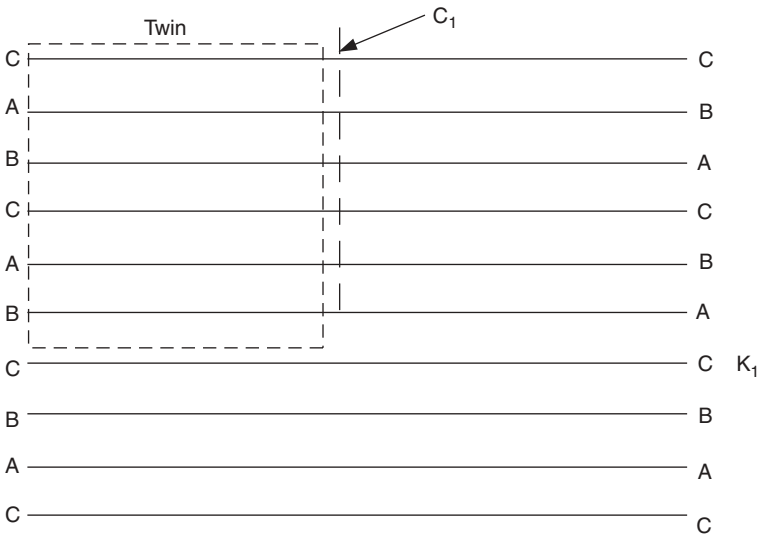
FIGURE 18.16   Deformation twin formed by motion of partial dislocations in FCC crystal.

PROBLEMS

1. Consider two edge dislocations of the same sign. The number one dislocation is pinned and cannot move. Number two is approaching it from the right on a parallel slip plane 2 nm in the "y" direction above the slip plane of number one (see Figure 18.8). What stress will allow the dislocation at the right to overcome the stress barrier in the x direction?

$$\mu = 42\,\text{GPa} \qquad b_1 = b_2 = 1 \times 10^{-10}$$

2. Equations for dislocation generation, bowing, and pileup break down for nanocrystalline materials. At $\mu/6$ shear can take place without dislocations and probably even at lower stresses along a grain boundary so this the maximum shear stress available. Determine the grain size where [*make whatever assumptions you wish*].

   a. Dislocation pileups can no longer be sustained using the number of dislocation is a pileup, $N = \tau\ell/(\pi\mu b)$.

   b. Elastic stresses between dislocations are too large; $x = b\mu/[2\pi(1 - v)\tau]$, where x is the distance between dislocations.

   c. Where dislocations cannot bow to multiply in Frank–Reed sources.

3. Consider dislocation movement and interaction in a metal with $b = 0.2\,\text{nm}$, $\mu = 100\,\text{GPa}$, and $v = 0.33$.

   a. A dislocation is pinned at two points 1 μm apart in the center of a grain. What stress is necessary to operate a Frank–Reed source?

   b. Sketch a dislocation loop (circle). Draw a Burgers vector in some arbitrary direction perpendicular to the loop at a point. Label the parts of the loop that are edge dislocations and those that are screw. What equation decides whether the loop expands or contracts?

   c. If the first dislocation operates as a Frank–Reed source and forms a loop 5 μm in diameter and is then stopped at a barrier, what stress is necessary for the second dislocation to be forced within 10 nm of the first dislocation?

4. Use the Peach–Kohler equations to show that a dislocation loop formed from a Frank–Reed source under an applied shear stress will continue to grow.

5. Consider dislocation movement and interaction in Cu with $b = 0.2\,\text{nm}$, $\mu = 124\,\text{GPa}$, and $v = 0.33$. If the slope of a curve σ_y versus $d^{1/2}$ is $4.7 \times 10^5\,\text{MPa} \cdot \text{m}^{-1/2}$, estimate τ_{th} for dislocation nucleation in the neighboring grain. Assume the most favorable angle between the dislocation plane and the stress axis.

19

DISLOCATIONS AND PLASTIC DEFORMATION IN CERAMICS

19.1   INTRODUCTION

Polycrystalline ceramics are usually considered to be completely brittle at room temperature and to exhibit permanent deformation before failure only at elevated temperatures. This view is correct in an engineering sense for practical purposes, although considerable plastic deformation is possible in individual ceramic single crystals depending on the ceramic involved and the stress system. The lack of significant plasticity in polycrystalline ceramics is the result of limitations on the number of slip systems leading to a yield strength much higher than the fracture strength. The next section describes some of the reasons why there are usually no slip systems with a low critical resolved shear stress. In this chapter we sketch the basic behavior of two ceramics that may serve as prototypes of the plastic behavior of ceramics: alumina and magnesia.

19.2   SLIP SYSTEMS IN CERAMICS

Ionic charges in ceramics increase the Peierls stress for dislocation glide and most often determine the slip systems for easy glide. To illustrate the latter point, we compare two slip systems in the rock salt structure (NaCl, MgO, etc.) in Figure 19.1. The extra half plane of edge dislocations must contain both anions and cations; otherwise charge neutrality would be violated. Thus two rows of ions must be removed rather than just one row of atoms, which is the case for metals. Furthermore, glide in the $\{001\}\langle010\rangle$ slip system would bring like charges into juxtaposition during slip whereas glide in the $\{011\}\langle0\bar{1}1\rangle$ slip system would not. Therefore, the $\{011\}\langle0\bar{1}1\rangle$ slip system is preferred even though the b/h ratio is lower in the $\{001\}\langle010\rangle$ slip system. A further requirement for slip is that the second, third, and so on, nearest-neighbor ions must also be considered. For instance, the $\{001\}\langle0\bar{1}1\rangle$ slip system has a smaller b/h than the $\{011\}\langle0\bar{1}1\rangle$ slip system. In both systems like charges of first nearest neighbors do not come into direct juxtaposition but considering, for example, second nearest neighbors there is a higher electrostatic force at the intermediate position of glide in the $\{001\}\langle0\bar{1}1\rangle$ slip system since the ions come into a position equidistant from positive and negative ions and so the $\{011\}\langle0\bar{1}1\rangle$ is the preferred slip system for NaCl and MgO. Polarizability also affects glide, and so in PbTe, for example, which has the rock salt structure, glide on the $\{001\}$ $\langle010\rangle$ is preferred. A relaxed form of the $\{011\}\langle0\bar{1}1\rangle$ dislocation which would have a lower self-energy is also shown in Figure 19.1(c) .

A generalization may be made that a major reason why the Peierls stress for glide is higher in ionic solids than in metallic solids is due to electrostatic forces. A more detailed discussion of the electrostatic forces of the dislocation at the intermediate positions, as well electrostatic forces from charged jogs and kinks that develop as dislocations intersect each other, is given by Hirth and Lothe
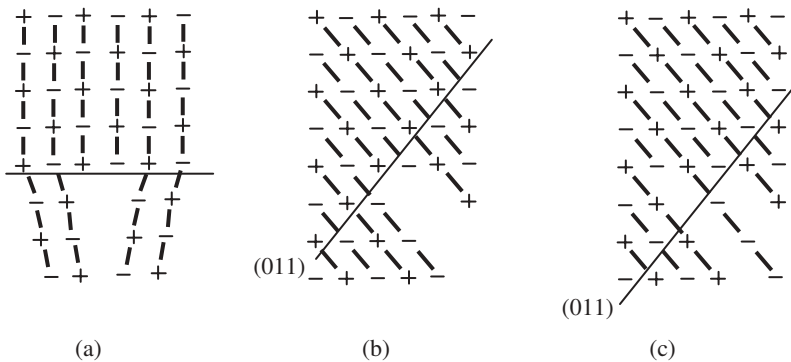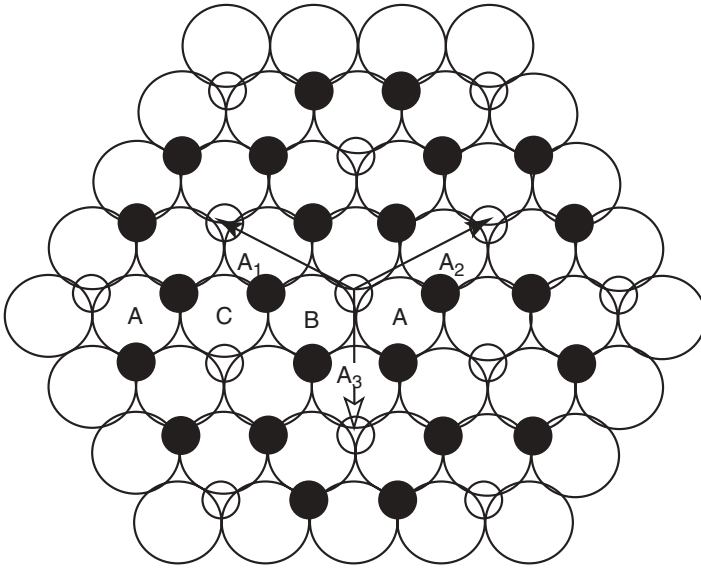

FIGURE 19.1   Dislocation glide on (a) $(001)[010]$ slip system of rock salt structure versus (b) glide in $(0\bar{1}1)[011]$ slip system; (c) relaxed form of $(0\bar{1}1)[011]$ slip system.

FIGURE 19.2   Oxygen ions (large open circles), aluminum ions (small solid circles), and unoccupied octahedral interstitial sites = holes (small open circles).

1968. In addition to the electrostatic forces the Burgers vector of a ceramic dislocation is always longer. For instance, in the dislocations of Figure 19.1, because the extra half plane contains both an anion plane and a cation plane, the Burgers vector is longer. In addition ceramic crystal structures are often more complex. Cations often do not fill all the interstices, as for instance α-Al_2O_3 in Figure 19.2, which will be discussed in the next section. The shortest shear distance to bring the crystal structure back into registry is shown by the vector A_1 and is 1.732 times the distance between oxygen ion centers. Extremely high Peierls forces are observed in $Y_3Al_5O_{12}$ because $\underline{\mathbf{b}} = 12\,\text{Å}$ for $\frac{1}{2}[1\,1\,1]$.

In addition to the above considerations, dislocation glide in covalent ceramics is even more difficult since covalent bonds are directional. In the intermediate position, at propagation distances less than a Burgers vector, bond angles are greatly distorted. The Peierls stress, therefore, is very high and so at moderate stresses in strongly covalent solids dislocations are seldom seen, but the high stresses generated under a Vickers indentation dislocations have been observed.

19.3   INDEPENDENT SLIP SYSTEMS

In most cubic metals the crystallographically equivalent slip systems are sufficiently numerous to permit complete flexibility in the sense that glide of dislocations on slip planes can produce all the strain components and thus produce any change of shape. If the number of operative slip systems is limited,

only certain components of strain can be produced. This has pertinence not only for allowing arbitrary deformation of single crystals but also for allowing the grains of a polycrystalline aggregate to conform as the sample as a whole is deformed. A minimum of five independent slip systems is needed to permit an arbitrary change of shape. A procedure for determining the number of independent slip systems was developed by Groves and Kelly (1963), and the systems have been tabulated for many crystals by Kelly and MacMillan (1986). The result is that, for sapphire, basal slip alone gives only two independent slip systems so that arbitrary deformation of a single crystal or any uniform plastic deformation of a polycrystalline body cannot be produced by basal slip alone.

For MgO below 650 K, slip on all the equivalent $\{110\}$ planes in $\langle 1\bar{1}0 \rangle$ directions gives only two independent slip systems. Above 650 K slip is also possible on (001) planes in $\langle 1\bar{1}0 \rangle$ directions, giving a total of five independent slip systems so that arbitrary deformation on a single crystal or uniform deformation of a polycrystalline material is possible in principle. However, stresses arising as a result of the operation of these slip systems unfortunately lead to fracture before significant bulk plasticity occurs in MgO (Kelly and MacMillan, 1986).

For zirconia stabilized in the cubic form the slip system is $\{001\} \langle 110 \rangle$ (Heuer et al., 1989).

19.4   PLASTIC DEFORMATION IN SINGLE-CRYSTAL ALUMINA

The crystal structure of sapphire (single-crystal aluminum oxide) is more complex than that of the FCC and HCP metals used for the initial development of dislocation theory. More complex dislocations and dislocation behavior are to be expected. We present a portion of the treatment of the structure and dislocations in sapphire given by Kronberg (1957). The crystal structure of sapphire corresponds closely (with small deviations in atomic positions) to oxygen ions in hexagonal close packing with aluminum ions in two out of three of the octahedral interstitial positions between the oxygen ions. Kronberg refers to the stacking sequence of the oxygen ions as 1, 3, 1, 3 (rather than *ABAB* as in Section 18.15) and reserves 2 to refer to the sheet of octahedral interstitial sites between the sheets of oxygen ions. The basic stacking sequence is thus 1, 2, 3, 1, 2, 3 before the differences in position of the holes (interstitial octahedral sites unoccupied by aluminum ions) is taken into account. He uses the notation *ABCABC* to refer to the stacking sequence of the holes and aluminum ions as shown in Figure 19.2. Thus the complete description of the stacking sequence in Kronberg's notation is 1, 2*A*, 3, 2*B*, 1, 2*C*, 3, 2*A*, 1, 2*B*, 3, 2*C*, 1,…. Accordingly, six sheets of oxygens must be stacked above the first one to return the sequence of oxygen and aluminum ions to coincidence with the starting ones; that is, the translation vector perpendicular to the sheets of oxygen atoms is $c = 1.297$ nm. The symmetry of the crystal structure is trigonal

rather than hexagonal, but it is convenient and conventional to use a hexagonal rather than a rhombohedral unit cell. Moreover, a morphological hexagonal cell with $c = 0.6485$ and $c/a = 1.365$ is generally used rather than a structural cell with $c/a = 2.730$. The hexagonal base plane axes are shown in Figure 19.2 as A_1, A_2, and A_3, which are, respectively, the $[2\,\bar{1}\,\bar{1}\,0]$, $[\bar{1}\,2\,\bar{1}\,0]$, and $[\bar{1}\,\bar{1}\,2\,0]$ directions. The directions of the rows of oxygen atoms in the morphological hexagonal cell are $[\bar{1}\,0\,\bar{1}\,0]$ and equivalent directions.

Moderately high temperatures are required for significant macroscopic plastic deformation of nominally pure alumina single crystals (synthetic sapphire rods) by slip in tension at atmospheric pressure and the stress required for deformation increases with the deformation rate imposed. In static tests this effect is manifested as an incubation time required for measurable creep in a fixed time of observation. Wachtman and Maxwell (1954) investigated the plastic deformation of sapphire in the temperature range 900–1300°C and found that slip took place on the $(0\,0\,0\,1)$ plane in the $[1\,1\,\bar{2}\,0]$ direction. They used a 100-h period and considered that creep (time-dependent deformation) occurred if more than 0.01% strain was measured over this time after the initial elastic deformation. In practice, either less than 0.01% deformation took place before a given stress, termed the creep yield stress for 100 h, or much more deformation occurred if the stress was higher. The controlling stress was found to be the shear stress acting on the slip plane in the slip direction (i.e., the critical resolved shear stress) given by Eq. (18.34). Typical creep curves for a sapphire rod in tension at 1100°C are shown in Figure 19.3 from Wachtman
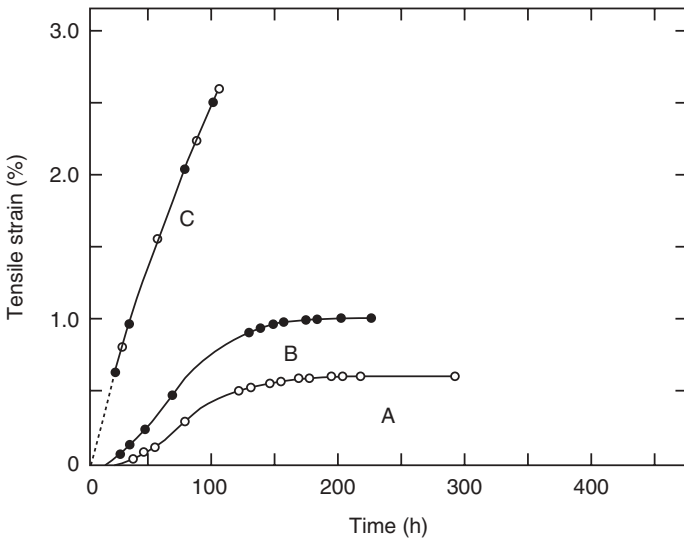
FIGURE 19.3 Creep of sapphire at 1100°C under resolved shear stress of (*A*) 67 MPa, (*B*) 91 MPa, and (*C*) 120 MPa. (From Wachtman and Maxwell, 1954. Reprinted by permission of the American Ceramic Society.)

and Maxwell (1954). Under 67 MPa resolved shear stress, the creep rate is at first immeasurably slow, then rises to a maximum, and decreases again to an immeasurably slow rate. Subsequent application of a somewhat higher stress causes a second, similar curve. Further application of a still higher stress causes a much faster initial creep rate. Two explanations (or a combination of both) appear possible for the initial period of slowly increasing creep rate: a yield point due to dislocation breakaway from impurities or slow multiplication of dislocations to give a great enough number to support a measurable creep rate. Experiments on sapphire containing chromium (ruby) indicate an increase in creep yield point. However, dynamic yield points measured in constant-strain-rate experiments by Kronberg are consistent with the dislocation multiplication hypothesis. An indication that some type of yielding has taken place is provided by Figure 19.4 from Wachtman and Maxwell (1957), showing that the stage of relatively rapid creep is reached under 44 MPa at 1000°C and that it will continue if the stress is reduced to 34 MPa, which is below the creep yield stress for a previously untested crystal at this temperature.

The 100-h creep yield stress was determined as a function of temperature by Wachtman and Maxwell (1957) with the result shown in Figure 19.5. The creep yield stress rises rapidly as the temperature is decreased and becomes immeasurably high below 900°C for the experimental conditions used. One sees in this a reason for the brittleness of aluminum oxide at lower temperatures. Even in the temperature range for which observable creep is found in alumina single
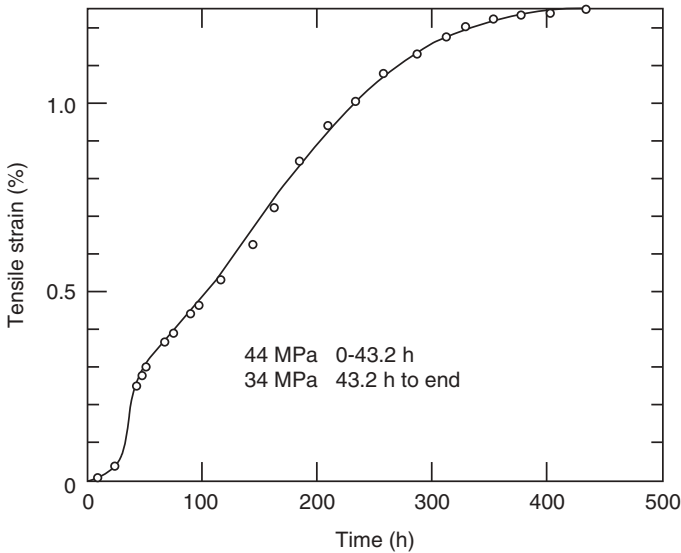
FIGURE 19.4 Creep curve of sapphire at 1000°C showing creep continuing below creep yield stress after being started under higher stress. (From Wachtman and Maxwell, 1957. Reprinted by permission of the American Ceramic Society.)
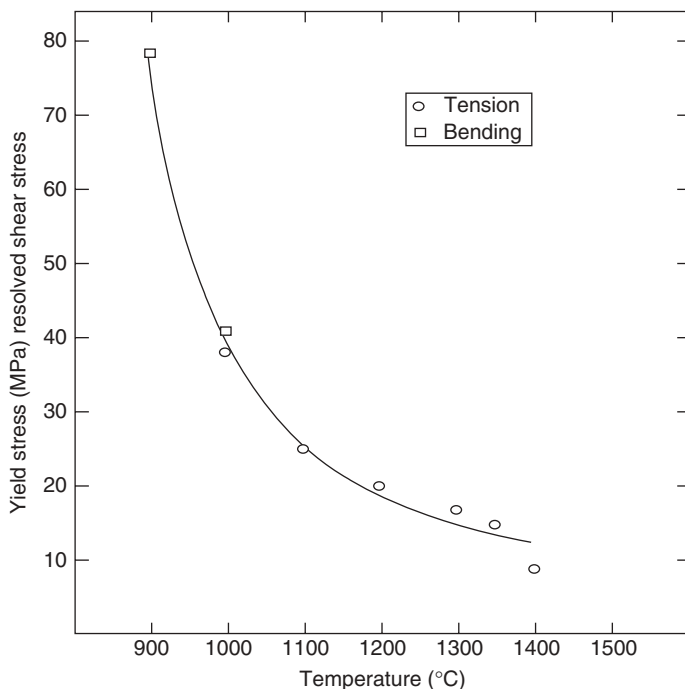
FIGURE 19.5 Creep yield stress as function of temperature for 100-h tests. (From Wachtman and Maxwell, 1957. Reprinted by permission of the American Ceramic Society).

crystals, there is still reason for brittle behavior of polycrystalline alumina in the fact that the $(0\,0\,0\,1)\,[1\,1\,\bar{2}\,0]$ slip system does not provide the five degrees independent slip systems needed for the most general change of shape. This slip system alone can accommodate shear in any direction only on the hexagonal (strictly the trigonal) base plane. Attempts to deform sapphire in tension with the base plane parallel or perpendicular to the tensile axis gave no measurable plastic deformation until a temperature of about 1600°C was used.

Kronberg (1962) used constant-strain-rate testing to show that a dynamic yield point that is the analog of the creep yield point occurred in sapphire oriented for basal slip. He developed (Kronberg, 1957) detailed models for dislocations in the corundum structure and discussed their role in slip and deformation twinning. Firestone and Heuer (1976) studied the yield point in constant-strain-rate experiments and concluded that the yield point was caused by a dislocation multiplication mechanism rather than an impurity atmosphere.

Creep of sapphire single crystals with the tensile axis parallel to the c axis has been studied at temperatures above 1600°C by Tressler and Barber (1974) and Firestone and Heuer (1976). The latter concluded that slip on rhombohedral planes was involved. The crystallography of slip systems in sapphire, including

their description in alternative unit cells, was reviewed by Snow and Heuer (1973).

Extensive subsequent work by many authors has elucidated the dislocation mechanisms of slip and twinning in alumina. A sketch of the basic results is given here based on a general summary presented by Lagerlof et al. (1994a). Single crystals of alumina in the stable corundum structure show no macroscopic deformation below about 900°C under 1 atm pressure in macroscopic tensile tests. Hockey (1971) has shown that the complex stress system existing under a hardness indentation does produce local deformation (microplasticity) and that dislocations are generated. At higher temperatures three slip systems are known to operate in simple tension under 1 atm as listed in Table 19.1.

Lagerlof et al. (1992a, b) conducted a series of experiments by superimposing uniaxial compressive stress on silver-sheathed sapphire single crystals under isostatic pressure of 1.5 GPa applied by NaCl. One set of specimens, termed type I, was favorably oriented for prismatic slip and the other, termed type II, was favorably oriented for basal slip. Their experiments were carried out at a constant strain rate of $2 \times 10^{-5}\,\mathrm{s}^{-1}$. Under these conditions it was found that type I specimens could be plastically deformed at temperatures as low as 200°C while 400°C was required for type I specimens. Typical stress–strain curves are shown in Figure 19.6. An interesting point is that the initial portion of the stress–strain curve had a slope less than that for elastic deformation so that some type of plastic deformation was occurring even in this initial portion of the curve, perhaps twinning. The accuracy of measurement was not sufficient for detailed analysis of this slope (A. H. Heuer, personal communication, 1994).

However, the authors took the point of view that a pronounced change in slope indicated yielding for slip under these experimental conditions. Type I specimens showed no work hardening after yield, but type II specimens showed appreciable work hardening after yielding. Plots of the yield stress as a function of temperature are shown in Figure 19.7. Under these experimental conditions prismatic slip predominates below about 700°C while basal slip predominates at higher temperatures. The critical resolved yield stress τ_{crs} was found to vary

TABLE 19.1   Slip Systems in α-Alumina (Corundum = Sapphire)

| System Name	Slip System	Remarks
Basal	$(0\,0\,0\,1)\frac{1}{3}\langle 2\,\bar{1}\,\bar{1}\,0\rangle$	Dominant system under shear superimposed on 1 atm pressure
Prismatic	$\{\bar{1}\,2\,\bar{1}\,0\}\langle 1\,0\,\bar{1}\,0\rangle$	Occurs above 1600°C under shear superimposed on 1 atm pressure
Pyramidal	$\{1\,0\,\bar{1}\,1\}\frac{1}{3}\langle \bar{1}\,1\,0\,1\rangle$ or possibly $\{\bar{1}\,0\,1\,2\}\frac{1}{3}\langle \bar{1}\,1\,0\,1\rangle$ or possibly $\{2\,\bar{1}\,\bar{1}\,3\}\frac{1}{3}\langle \bar{1}\,1\,0\,1\rangle$	Occurs above 1600°C under shear superimposed on 1 atm pressure
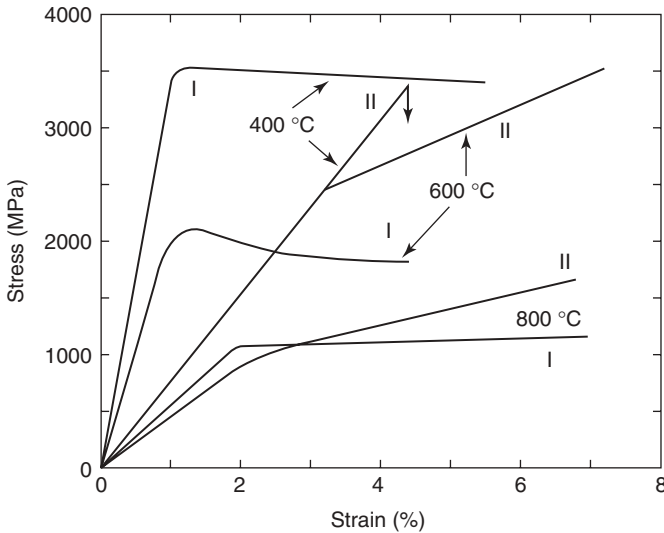
FIGURE 19.6 Stress–strain curves for samples oriented for prism plane slip (type I) and basal slip (type II). (From Lagerlof et al., 1994a). Reprinted with permission of the American Ceramic Society).

with temperature according to

$$\ln \tau_{crs} = \ln \tau_0 - BT \tag{19.1}$$

where τ_0 and B are constants. This form of temperature dependence cannot be explained on the basis of the usual picture of thermally activated slip with a constant activation energy. Lagerlof et al. propose a model of stress-dependent activation energy involving dissociation of dislocations into partial dislocations that leads to the observed form of temperature dependence.

An earlier summary of the available data on the temperature dependence of the tensile stress required for flow (the creep yield stress) on sapphire single crystals oriented for slip on the basal, prismatic, and pyramidal systems is shown in Figure 19.8 (Heuer et al., 1980). For plastic flow in polycrystalline alumina to occur, five independent slip systems must operate. Two independent slip systems come from basal slip, two from prismatic slip, and two from pyramidal slip, and so all three slip, systems must operate to achieve plastic flow in polycrystal alumina. According to Figure 19.8, at a strain rate of $4 \times 10^{-5} \, \mathrm{s^{-1}}$ and 1800°C, all three slip systems would operate only at a stress exceeding 230 MPa. Provided the fracture stress exceeds 230 MPa, the polycrystal would be ductile. The ductile-to-brittle transformation temperature at 230 MPa might, according to Figure 18.9, be 1800°C. Ductility due to dislocations has not been achieved for two reasons. The stress is above the
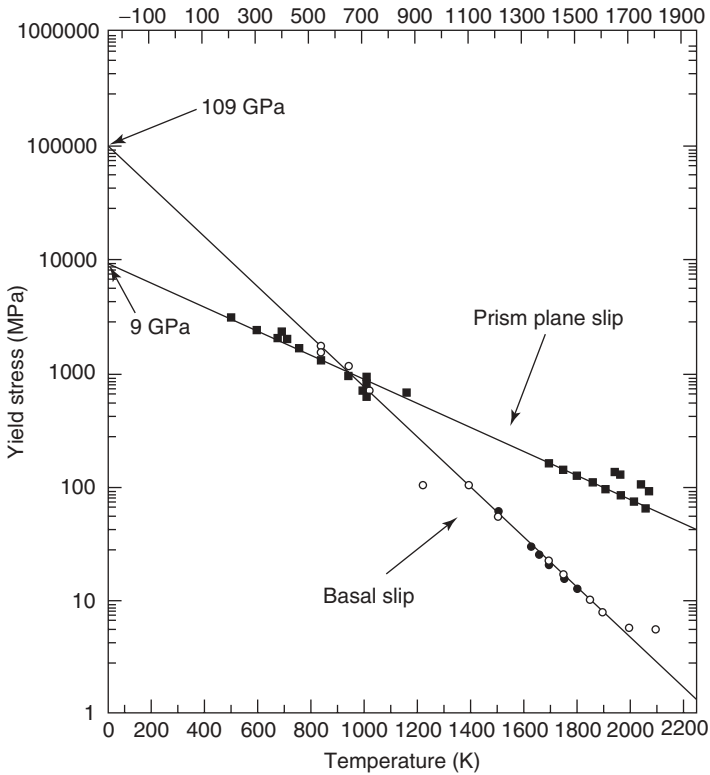
FIGURE 19.7   Yield stress as function of temperature for prism plane slip and basal plane slip. (From Lagerlof et al., 1994a. Reprinted with permission of the American Ceramic Society).

high-temperature fracture stress, and second diffusional creep, discussed in Chapter 20, usually occurs at a lower stress.

The atomic mechanisms of slip and twinning in sapphire have recently been reviewed in detail, including consideration of the real structure rather than the slightly idealized structure used by Kronberg (Bilde-Srensen et al., 1995; Geipel et al., 1996).

19.5   TWINNING IN ALUMINUM OXIDE

Deformation twinning has long been known to occur in alumina under atmospheric pressure at temperatures as low as 77 K (Heuer, 1966; Scott and Orr, 1983). Both basal and rhombohedral twins occur.

The elements of basal twinning are $K_1 = (0\,0\,0\,1)$, $\eta_1 = \langle 1\,0\,\bar{1}\,0 \rangle$, $K_2 = \{1\,0\,\bar{1}\,1\}$, and $\eta_2 = \langle \bar{1}\,0\,1\,2 \rangle$ using structural indices with $c/a = 2.73$ and
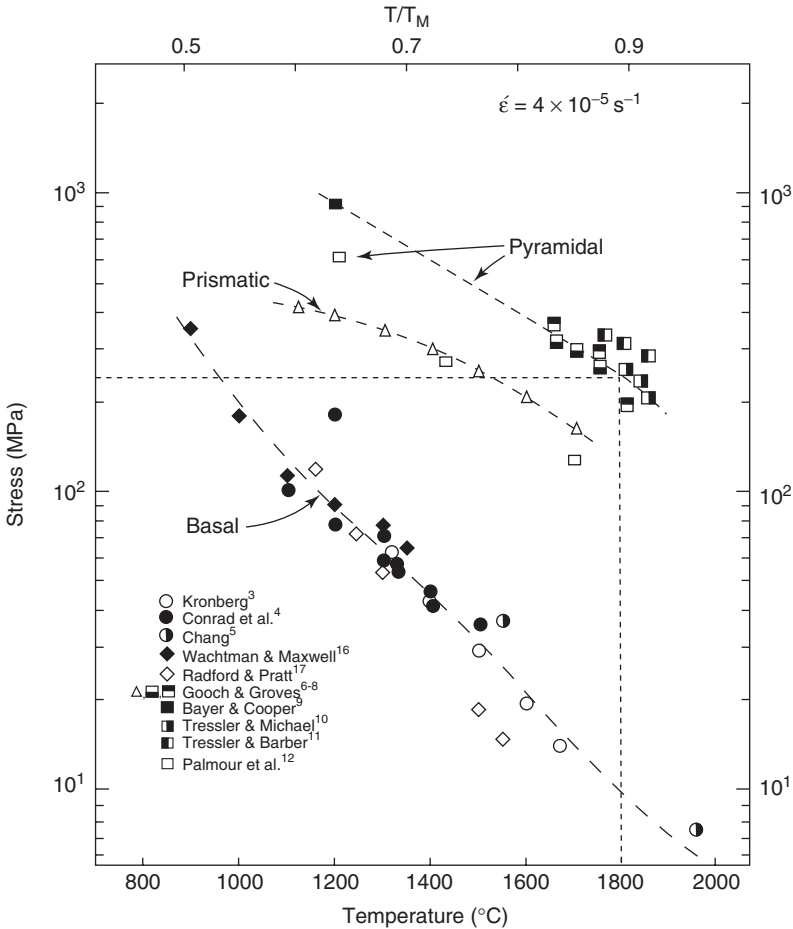
FIGURE 19.8 Tensile flow stress in single-crystal and polycrystalline alumina. (From Heuer et al., 1980. Modified by permission of the American Ceramic Society).

$s = 0.635$ (Lagerlof et al., 1994b). The authors propose a model for basal twinning based on an expanding partial dislocation loop similar to a Frank–Read source on the basal plane with a Burgers vector of $\frac{1}{3}\langle 10\bar{1}0\rangle$. The loop is assumed to expand once and to be blocked from a second expansion because the stacking fault energy formed on the second expansion is of a different type and has higher energy. Instead, the loop is assumed to cross slip and to expand again on a new plane. Repetition of this process forms the basal twin.

The elements of rhombohedral twinning are $K_1 = \{01\bar{1}2\}$, $\eta_1 = \langle 0\bar{1}11\rangle$, $K_2 = \{0\bar{1}14\}$, $\eta_2 = \langle 022\bar{2}1\rangle$, and $s = 0.202$, where again structural indices are used (Heuer, 1966). The symmetry element relating the twinned portion to the untwinned portion of the crystal is a screw axis consisting of a twofold rotation

about η_1 accompanied by a translation along the rotation axis of $\frac{1}{6}[0\,\bar{1}\,1\,1]$. A zonal dislocation mechanism has been proposed by Geipel et al. (1994).

19.6   PLASTIC DEFORMATION OF SINGLE-CRYSTAL MAGNESIUM OXIDE

As discussed in Section 19.2, magnesium oxide has the rock salt structure and its mechanical properties parallel those of softer materials with the rock salt structure (such as NaCl) to some degree, but the behavior of dislocations in MgO is sufficiently different in detail to make it a unique material. Magnesium oxide single crystals were extensively studied in the late 1950s and in the 1960s with the hope that the degree of dislocation mobility they possessed could be manipulated to produce ductile polycrystalline MgO materials. This was not achieved and MgO is today considered to be a semibrittle material rather than a ductile material. Many people contributed to the understanding of the mechanical properties of MgO, especially R. J. Stokes and his collaborators (Stokes, 1962, 1965, 1966a,b 1968, 1972; Stokes et al., 1960; Stokes and Li, 1962, 1963, 1964). The following discussion is based primarily on an informal, unpublished summary by R. J. Stokes (personal communication, 1994).

Stokes considers the mechanical properties of MgO and related materials in two categories: (1) dislocation behavior and the mechanical yield strength of materials and (2) slip band characteristics and the fracture behavior of semibrittle materials.

From the Orowan Eq. (18.29) for strain rate

$$\dot{\varepsilon} = \tfrac{1}{2}\rho bv \tag{19.2}$$

It is evident that the strain rate depends on the density of mobile dislocations and their velocity. The distinction of the density of mobile dislocations rather than total density of dislocations is crucial in MgO. A striking fact about MgO is that the dislocations produced by crystal growth do not move under stresses up to values approaching the theoretical shear strength. They are very effectively pinned. However, fresh dislocations can very easily be introduced by the slightest contact due to the concentrated Hertzian stresses upon contact. The fresh dislocations do move under relatively low stresses. The problem in studying "grown-in" dislocations is to avoid introducing fresh dislocations during the preparation of the sample. Careful chemical polishing combined with annealing to pin the remaining fresh dislocations can produce samples with no fresh dislocations. Such samples are completely elastic up to very high stresses.

The velocity is very sensitive to stress, typically varying as stress to a power such as 10. The velocity is also affected by any feature of the crystal that retards the slip of the dislocation. These include interactions between the stress field of the mobile dislocation and the internal stress fields due to impurity particles

(solid-solution strengthening and vacancy cluster hardening), dislocation entanglement with precipitate particles (precipitation hardening), and dislocation entanglement with other dislocations (strain hardening). Thus hardening can be considered in two categories: static hardening (stationary dislocations are pinned by heat treatment) and dynamic hardening (moving dislocations are impeded by interaction with other defects) (Sprackling, 1976; R. J. Stokes, personal communication, 1994).

The density of mobile dislocations in MgO grows rapidly as slip proceeds due to the double-cross-slip multiplication mechanism. Extensive slip takes place in a narrow band from a single fresh, mobile dislocation as it moves, cross slips, and multiplies under stress. This produces a highly deformed region (the slip band) adjacent to a region of crystal that is purely elastically deformed. Evidently large stresses can develop at the junction of these two regions as the elastic strain increases so that the two regions remain compatible.

Cracks in MgO initiate (nucleate) because of the inability of the crystal to respond to the demands of anisotropic shear such as that at the junction of a slip band with a region with no plastic deformation. The theoretical stress can be exceeded locally and a small crack suddenly forms. This occurs in MgO at room temperature and has been seen in LiF at liquid nitrogen temperature. These small cracks can then undergo subcritical crack growth as the crystal undergoes further plastic strain and eventually a length is reached for catastrophic crack growth.

The strength of MgO containing mobile dislocations is thus at or near the yield stress since the process of yielding leads to crack nucleation and growth. The MgO single crystals with no mobile dislocations can have much higher strength.

19.7 PLASTIC DEFORMATION OF SINGLE-CRYSTAL CUBIC ZIRCONIA

Cubic yttria-stabilized zirconia single crystals containing tetragonal zirconia precipitates were studied by Heuer et al. (1989) and Martinez-Fernandez et al. (1993, 1995). Stress–strain curves were measured at 1400°C after various annealing times at 1600°C. The annealing causes precipitation of lamellae whose spacing increases with time due to Ostwald ripening. The initial yield stress for 0.2% strain offset was about 400 MPa but increased in proportion to lamella spacing and was about 500 MPa after 150 h. Annealing increased the spacing from the initial value of 20 to 60 nm.

PROBLEMS

1. From the sketch of the (0001) crystallographic plane of Al_2O_3 in Figure 19.2 determine the length of the Burgers vector in the A_1 direction if the ionic

radius of O^{-2} is 1.32 Å? Compare this with the closed-packed direction for the oxygen ion.

2. Speculate how the number of independent slip systems affect the following: (a) fracture initiation by Hall–Petch, (b) hardness, and (c) increased toughness due to plastic deformation around a crack tip.

3. According to Figure 19.8, how high does the fracture stress need to be to achieve ductility in polycrystalline Al_2O_3 at 1600°C?

20

CREEP IN CERAMICS

20.1 INTRODUCTION

Creep can most simply be described as the phenomenon of continuing plastic deformation under constant stress. Creep effects may be studied with other loading schedules, but the same basic processes are involved. Typically, creep in ceramics takes place at high temperatures under modest stress levels and with low strain rates. Creep is sometimes discussed as if it were a different phenomenon than plastic deformation and the latter is treated as if it occurred instantaneously when stress is applied.

Fundamentally, however, plastic deformation is not qualitatively different from creep. In this chapter the phenomenological description of creep in terms of stages is first given and then several important mechanisms of creep in ceramics are discussed. An excellent general reference on creep is Poirier (1985).

Creep in ceramics has been reviewed thoroughly by Cannon and Langdon (1983, 1988). These authors classify creep in ceramics into two categories

depending on the way in which the creep rate depends on the stress. In the first category the creep rate depends on the stress to a power close to 1. In the second category the creep rate depends on stress to a higher power, typically approximately 3 or 5. Creep with a stress exponent of 5 is believed to take place as in metals by a dislocation motion with five independent slip systems operating. Diffusion plays a role associated with the freeing of tangled or pinned dislocations rather than with the primary transport process. Creep with a stress exponent of about 3 is taken to result from dislocation climb under conditions such that five independent slip systems cannot interpenetrate or when there are fewer than five independent slip systems operating.

Creep is most often measured under a constant stress. Figure 20.1 shows a typical creep curve. The creep strain ε resulting from application of constant stress is often written as

$$\varepsilon = \varepsilon_0 + \beta t^{1/3} + kt \tag{20.1}$$

Here ε_0 is the elastic strain and β and k are constants for a given material with a given microstructure (including defect structure) at a particular temperature. The second and third terms describe what is called, respectively, primary and steady-state creep. The justification for this equation is empirical; it fits much of the experimental creep data. If a dislocation mechanism controls creep, primary creep results from hardening as dislocations tangle with each other and eventually develop a steady-state substructure. If the Nabarro–Herring mechanism, described below, controls creep, the primary stage may be caused by grain growth. If creep is continued long enough, a tertiary stage is encountered, especially in metals. In tension this tertiary stage is an accelerating creep rate leading to failure.
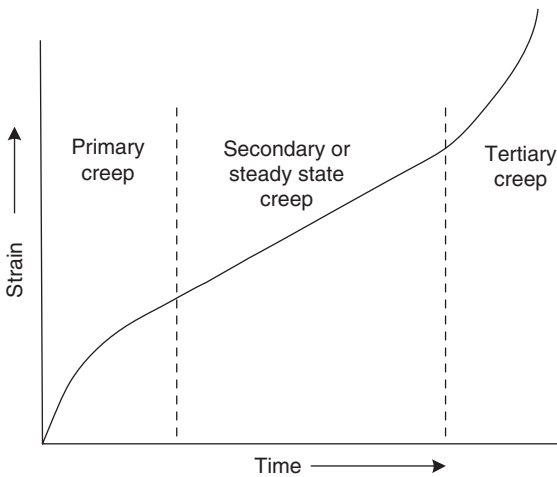
FIGURE 20.1   Typical creep curve measured under constant stress.

Most of the attention in creep studies is focused on steady-state creep or at least what is taken as steady-state creep. The assumption is made here that a sufficient period of time giving nearly constant creep rate is studied experimentally to justify the fitting of models for steady-state creep and these models are presented.

20.2 NABARRO–HERRING CREEP

Nabarro (1948) considered a small cube of material under a pure shear stress resulting from tension in one direction (say, the z direction) and sufficient compression in the x and y directions to give zero pressure. He showed that vacancies would flow from the face under tension to the faces under compression, causing a shear of the material so as to elongate it in the z direction and cause it to shrink in the x and y directions. The equilibrium atomic fraction of vacancies at temperature T is given by

$$N_v = \exp\left(-\frac{\Delta G_f}{kT}\right) \tag{20.2}$$

where ΔG_f is the Gibbs free energy of formation of one vacancy and k is Boltzmann's constant. The equilibrium concentration is then

$$C_0 = \frac{N_v}{\Omega} \tag{20.3}$$

where Ω is the atomic volume. Creation of a vacancy at the face under tension σ is assisted by a contribution $\sigma\Omega$ to the free energy, while extra free energy of the same amount is needed to create a vacancy at the face under compression.

The local equilibrium concentrations at the tension and compression faces, respectively, are then

$$C^+ = C_0 \exp\left(\frac{\sigma\Omega}{kT}\right) \tag{20.4}$$

$$C^- = C_0 \exp\left(\frac{-\sigma\Omega}{kT}\right) \tag{20.5}$$

There will be a flux of vacancies from the higher concentration face to the lower concentration face given by Fick's equation for diffusion,

$$J = -D_v \nabla C \approx \alpha D_v \frac{C^+ - C^-}{d} \tag{20.6}$$

where α is a numerical constant and d is the edge of the cube. The number of vacancies passing through an area d^2 per second, φ, is

$$\varphi = Jd^2 \tag{20.7}$$

The volume arriving per second is $\varphi\Omega$. Dividing by the area of a face, d^2, gives the elongation per second, and dividing this in turn by the length d gives the strain rate $\dot{\varepsilon}$:

$$\frac{d\varepsilon}{dt} \equiv \dot{\varepsilon} = \varphi\frac{\Omega}{d^3} \tag{20.8}$$

$$\dot{\varepsilon} = \frac{\Omega}{d^3}Jd^2 = \frac{\Omega}{d}\alpha D_v\frac{C^+ - C^-}{d} = \frac{\alpha\Omega D_v C_0}{d^2}\left(\exp\frac{\sigma\Omega}{kT} - \exp\frac{\sigma\Omega}{kT}\right) \tag{20.9}$$

For $\sigma\Omega/kT < 1$

$$\dot{\varepsilon} = 2\alpha\frac{D_v\Omega^2\sigma C_0}{kTd^2} \tag{20.10}$$

Recognizing that the self-diffusion constant D_l is given by

$$D_l = D_v\Omega C_0 \tag{20.11}$$

leads to

$$\dot{\varepsilon} = 2\alpha\frac{D_l\Omega\sigma}{d^2kT} \tag{20.12}$$

Herring (1950) gave a thermodynamic treatment and considered the case of grains in a solid and found $\alpha = 16$ when there is no grain boundary sliding or $\alpha = 40$ when there is sufficient grain boundary sliding to completely relax shear stresses on the boundary. The usual creep experiment is done in simple tension. When Herring's result and the relationship of simple tensile stress to the stress system used above to give simple shear are taken into account, the result for complete grain boundary sliding is (Poirier, 1985; Cannon and Langdon, 1988)

$$\dot{\varepsilon} = 13.3\frac{D_l\Omega\sigma}{d^2kT} \tag{20.13}$$

where σ is now the tensile stress in a simple tensile test. The important characteristics of Eq. (20.13) is that $\dot{\varepsilon}$ is directly proportional to the stress and inversely proportional to grain diameter squared.

20.3   COMBINED DIFFUSIONAL CREEP MECHANISMS

The above derivation of Nabarro–Herring creep assumed only one diffusion path (through the solid grains) and only one diffusing species. In ceramics there are often two possible diffusion paths (through the grains or in the grain boundaries), as illustrated in Figure 20.2, and two diffusing species
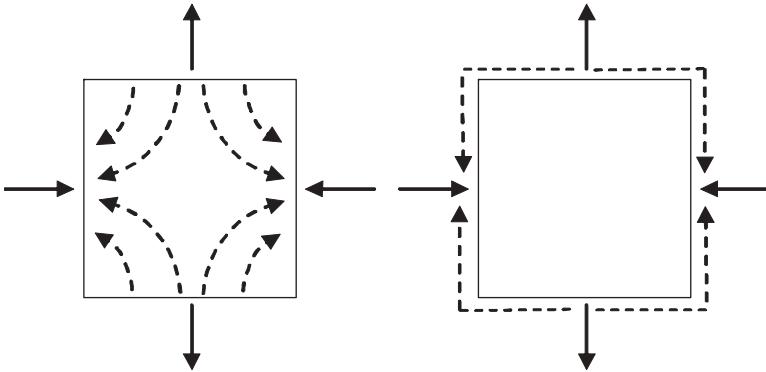
FIGURE 20.2 (a) Nabarro–Herring creep by lattice diffusion. (b) Coble creep by grain boundary diffusion.

(e.g., oxygen and aluminum in aluminum oxide). Cannon and Langdon (1988) have summarized the equations for these situations as presented in the following.

First we will write the Nabarro–Herring equation in a different format, which allows comparing diffusional creep equations with dislocation creep equations. Taking the atomic volume Ω as $0.7b^3$, where b is the magnitude of the Burgers vector, Eq. (20.13) may be written as

$$\dot{\varepsilon} = 9.3 \frac{D_l \mu b}{kT} \left(\frac{b}{d}\right)^2 \left(\frac{\sigma}{\mu}\right) \tag{20.14}$$

where μ is the shear modulus and d is the grain diameter. Equation (20.14) is written in such a way that terms in parentheses are dimensionless.

If the transport of matter is through the grain boundaries, the process is termed Coble creep (Coble, 1963). The diffusional creep equation then is

$$\dot{\varepsilon} = \frac{150 \Omega \delta D_{gb} \sigma}{\pi d^3 kT} \tag{20.15}$$

where D_{gb} is the diffusion constant for transport in the grain boundaries and δ is the grain boundary width. Again writing Eq. (20.15) in universal format with $\Omega = 0.7b^3$, the creep rate is

$$\dot{\varepsilon} = 33.4 \frac{D_{gb} \mu b}{kT} \left(\frac{\delta}{b}\right) \left(\frac{b}{d}\right)^3 \left(\frac{\sigma}{\mu}\right) \tag{20.16}$$

Because the activation energy for grain boundary diffusion is less than that for diffusion through the grains, Coble creep is favored over Nabarro–Herring creep at lower temperatures. Because of the inverse cubic dependence on grain

size, Coble creep is favored over Nabarro–Herring creep at very small grain sizes.

Actually, Nabarro–Herring creep and Coble creep take place in parallel so that the total diffusional creep rate is given by

$$\dot{\varepsilon} = 9.3 \frac{D_l \mu b}{kT} \left(\frac{b}{d}\right)^2 \left(\frac{\sigma}{\mu}\right) \left[1 + 3.6 \frac{D_{gb}}{D_l} \left(\frac{\delta}{d}\right)\right] \tag{20.17}$$

In a ceramic $M_a X_\beta$ both anions and cations can diffuse, leading to (Gordon, 1973, 1975)

$$\dot{\varepsilon} = 9.3 \frac{D_{a,\text{eff}} \cdot D_{c,\text{eff}}}{\alpha D_{c,\text{eff}} + \beta D_{a,\text{eff}}} \frac{\mu b}{kT} \left(\frac{b}{d}\right)^2 \frac{\sigma}{\mu} \tag{20.18}$$

where

$$D_{i,\text{eff}} = D_{i,l} + 3.6 D_{i,gb} \left(\frac{\delta_i}{d}\right) \tag{20.19}$$

and where i is a or c for the anion and cation, respectively.

Evans and Langdon (1976) considered the possibilities for the usual cases in which there are large differences in the diffusion rates. Their general conclusion is that the creep rate is controlled by the slower diffusing species along the faster diffusion path.

Li et al. (1999) presented evidence that grain boundary diffusion strongly affects the creep rate of polycrystalline Al_2O_3. When Al_2O_3 was doped with as little as 100 ppm rare earth additives (Y^{3+}, Nb^{3+}, La^{3+}), creep rates fell by two orders of magnitude. Even lower creep rates were achieved by codoping with Nb^{3+} and Zr^{4+}. Secondary ion mass spectrometry revealed that the dopants segregated to the grain boundaries. Wang et al. (2000) suggest the much larger rare earth ions substituted for the very small Al^{3+} ions in the grain boundary and relieved the stress in normally stretched bonds. Less free volume was now available for grain boundary diffusion. Since the dopants were expected to have affected only grain boundary diffusion, two possibilities exist: (1) $D_{Al,gb}$ or $D_{O,gb}$ were rate controlling and the rare earth additive decreased their grain boundary diffusion rate or (2) lattice diffusion controlled by one ion changed to the other ion. Originally, for instance, $D_{Al,l}$ controlled the creep rate because O^{2-} ions traveled rapidly through the grain boundary, that is, $(\delta/d)D_{O,gb}$ was higher than $D_{O,l}$ while $(\delta/d)D_{Al,gb}$ was lower than $D_{Al,l}$. With the addition of rare earth ions $D_{O,gb}$ decreased sufficiently so that O^{2-} ions must travel through the bulk and $D_{O,l}$ now controlled the creep rate.

20.4   POWER LAW CREEP

In this section the concept of creep by dislocation slip with the rate-controlling process being the thermally activated freeing of dislocations is summarized.

The succession of ideas is that of long- and short-range stress, thermal activation of dislocations over barriers, the balancing of hardening and recovery and the resulting Bailey–Orowan equation, and the Weertman model of creep by slip with rate control by climb.

Metals often creep with a steady-state creep rate varying with approximately the fifth power of the stress. Weertman (1957) developed a theory for glide of piled-up dislocations from an operating source with climb being the rate-controlling process. He obtained

$$\dot\varepsilon = \frac{B_2 \Omega D_l \sigma^{4.5}}{\mu^{3.5} M^{0.5} b^{3.5} kT} \tag{20.20}$$

where B_2 is a constant and M is the concentration of the active dislocation sources. Taking $B_2 = 0.2$ (Hazzledine, 1967; Cannon and Langdon, 1988) gives

$$\dot\varepsilon = \frac{0.14}{b^{1.5} M^{.5}} \left(\frac{D_l \mu b}{kt}\right) \left(\frac{\sigma}{\mu}\right)^{4.5} \tag{20.21}$$

Some ceramics exhibit stress dependence with a power near 5 and are assumed to creep by a dislocation mechanism of the Weertman type.

Metals or ceramics undergoing power law creep form a substructure within grains with the subgrains bounded by small-angle grain boundaries with an average size λ. The dislocation density within the grains is ρ. Cannon and Langdon (1988) conclude that ceramics deforming by dislocation creep show the same behavior as metals in that the average subgrain size is inversely related to the stress,

$$\frac{\lambda}{b} = \text{const} \times \frac{\mu}{\sigma} \tag{20.22}$$

The constant is in the range of 20–30 for ceramics and is typically 20 for metals. The normalized dislocation density within subgrains for ceramics was found to be given by

$$b\rho^{1/2} = \text{const} \times \frac{\sigma}{\mu} \tag{20.23}$$

Here the constant ranges from 1 to 2 for ceramics and is around 1 for metals.

Other ceramics exhibit a stress dependence with a power near 3. Cannon and Langdon (1988) examined theories giving this type of stress dependence and concluded that the most likely was a mechanism of creep through climb of dislocations from Bardeen–Herring sources. The theory predicts

$$\dot\varepsilon = 0.22 \frac{D_l \mu b}{kt} \left(\frac{\sigma}{\mu}\right)^3 \tag{20.24}$$

Chokshi and Langdon (1991) examined the power law creep of ceramics and concluded that there are two broad categories of behavior: A stress exponent

close to 5 represents control by dislocation climb and fully ductile behavior whereas a stress exponent close to 3 arises from control by climb from Bardeen–Herring sources under conditions where there are less than five interpenetrating independent slip systems.

20.5   COMBINED DIFFUSIONAL AND POWER LAW CREEP

Cannon and Langdon (1988) compared the creep rates of ceramics with the creep rates of metals using the universal form of the creep equation. Equations (20.14), (20.16), (20.20), and (20.23) may all be written in the form

$$\dot{\varepsilon} = B\frac{D\mu b}{kT}\left(\frac{b}{d}\right)^{p}\left(\frac{\sigma}{\mu}\right)^{n} \tag{20.25}$$

where $p = 0$ for dislocation mechanisms, $p = 2$ for Nabarro–Herring creep, and $p = 3$ for Coble creep. The parameter D does not specify whether it is a lattice or a grain boundary diffusion coefficient and B incorporates other constants and grain boundary widths. Rearranging yields

$$\frac{\dot{\varepsilon}kT}{D\mu b} = B\left(\frac{b}{d}\right)^{p}\left(\frac{\sigma}{\mu}\right)^{n} \tag{20.26}$$

Thus a universal curve for dislocation mechanisms plots $\dot{\varepsilon}kT/(D\mu b)$ versus (σ/μ) on a log–log scale. Diffusional creep results may be included on the same plot as long as the grain size is specified. Such a plot is shown in Figure 20.3. A summary of the creep data of ceramics is reviewed in Cannon and Langdon (1988), and it is shown that most results where $n \simeq 1$ fit the Nabarro–Herring equation provided D_{cation} is used as the diffusion coefficient. On the other hand for power law creep D_{anion} is used. Under these assumptions and noting that in most cases $D_{cation}/D_{anion} = 100$, Figure 20.3 summarizes the creep data from the literature for both coarse-grained ceramics which exhibit power law creep and fine-grained ceramics which exhibit diffusional creep. Literature power law creep data in metals superimpose reasonably well on the ceramic power law creep data. Diffusional creep is not often observed in metallic systems. Because the diffusion coefficient is the most strongly varying factor, it is concluded that creep rates depend primarily on the diffusion rates independent of whether they are metals or ceramics. The large difference in the mobility of dislocations in metals and ceramics is not important since freeing of dislocations by dislocation climb controls the creep rate. It may further be observed in Figure 20.3 that the stress range over which diffusional creep occurs widens as the grain size is decreased. It is because the typical grain size for advanced ceramics is much smaller than in typical polycrystalline metals that diffusional creep is most often observed in ceramics.
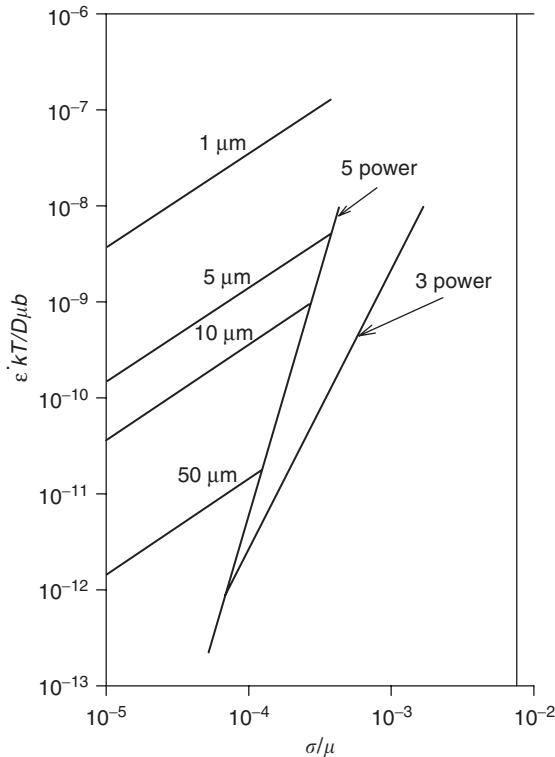
FIGURE 20.3   Universal curve for diffusional and dislocation creep mechanisms. It is assumed that $D_{cation}/D_{anion} = 100$ and that diffusional creep is controlled by the anion and dislocation creep by the cation. (From Cannon and Langdon, 1988. Reprinted with permission from Springer Verlag).

20.6   ROLE OF GRAIN BOUNDARIES IN HIGH-TEMPERATURE DEFORMATION AND FAILURE

Grain boundaries often play a crucial role in deformation and fracture of ceramics. We follow Langdon (1982, 1991a, b, 1993a, b, 1994a, b) in presenting a summary considering behavior of metals and ceramics. Grain boundaries play two important but conflicting roles in deformation: contributing to the deformation and promoting local cracking and ultimate failure. The grain size determines the degree of grain boundary contribution to deformation and failure. Langdon defines four grain sizes in this regard—macroscopic, mesoscopic, microscopic, and nanoscopic:

- Macroscopic grains are large enough, typically with grain diameter $d > 1000 \, \mu m$, so that grain boundaries play no significant role in deformation.

- Mesoscopic grains are smaller but still large enough that the grain boundaries make a relatively minor contribution to deformation (such as in grain boundary sliding as a secondary process) but the boundaries may be dominant in controlling fracture. In metals typical mesoscopic grains range from 10 to 1000 µm in diameter. For materials deforming by dislocation slip, a substructure forms within mesoscopic grains consisting of subgrains of average diameter λ with small misorientations between adjacent subgrains.
- Microscopic grains are still smaller (typically 10–0.01 µm) and grain boundaries play a dominant role in flow and often also in fracture.
- Nanoscopic grains are still smaller and are only beginning to be investigated as processing methods for making polycrystalline materials with grains in this range are still being developed. It is anticipated that grain boundaries will contribute most of the deformation in these materials.

Grain boundaries are important for ultimate failure in tension because they provide sites at which cavities can be nucleated and paths for the growth of cavities into intergranular cracks. For ceramics these processes are significant in damage-assisted creep and subsequent failure. However, under suitable conditions, both metals and ceramics with microscopic grain size can undergo large tensile deformations before failure, as discussed in a later section on superplasticity.

20.7   DAMAGE-ENHANCED CREEP

An additional feature of creep in ceramics that has not been considered so far is damage-enhanced creep. It is often observed, especially at higher stresses in ceramics with a viscous phase in the grain boundaries, that voids form at the grain boundaries as creep continues. Results of Wiederhorn et al. (1988) on siliconized silicon carbide are reviewed here to illustrate the phenomenon. Damage-enhanced creep has also been reported by other investigators in various materials, including lithium zinc silicate glass ceramics (Morrell and Ashbee, 1973), reaction-bounded silicon nitride (Birch et al., 1978), siliconized silicon carbide (Carroll and Tressler, 1988), and SiAlON–YAG ceramics (Chen et al., 1991).

The experiments of Wiederhorn et al. (1988) were done with a siliconized silicon carbide, KX01, made by SOHIO Corp. This material is approximately 33% silicon by volume and contains grains of silicon carbide ranging from 2 to 5 µm in diameter. These authors measured creep at 1300°C in tension and compression and found that the creep rate in tension was 30 times or greater than the creep rate in compression at the same stress. Furthermore, the dependence of creep rate on stress was bimodal in both cases. Their results are summarized in Figure 20.4, a log–log plot of creep rate as a function of
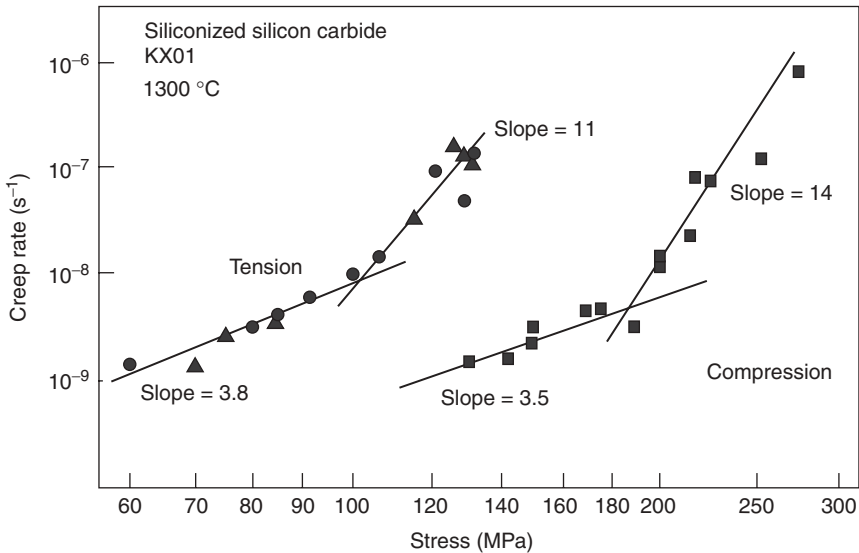
FIGURE 20.4 Stress dependence of creep rate. (From Wiederhorn et al., 1988. Reprinted by permission of the American Ceramic Society.)

stress. The results can be described by a power law equation of the form

$$\dot{\varepsilon} = k\sigma^n \tag{20.27}$$

where k and n are constants. For creep in tension $n = 3.5$ at stresses below 100 MPa and $n = 11$ for higher stresses. For creep in compression $n = 3.5$ for stress below 200 MPa and $n = 14$ for higher stresses. The authors attribute the creep in the range of stresses corresponding to the lower n values to power law deformation in the silicon phase. They find some formation of voids (cavitation) at tensile stresses as low as 75 MPa, but very much more cavitation in experiments at 100 MPa for 100 h. They attribute the higher creep rates above 100 MPa in tension to the effects of cavitation. For creep in compression in the stress range corresponding to the lower n values, power law creep is also assumed. The authors suggest that friction between silicon carbide grains affects the stress on the silicon phase and hence the creep rate. It is plausible that these frictional forces would be greater in compressive creep and so increase the stress required to achieve the same creep rate. The authors searched for cavitation in the compressive creep specimens but did not find evidence of it. The cause for the change to $n = 14$ at higher stresses in compression was not determined.

A study showing the combined effect of a basic creep mechanism and damage-assisted creep in siliconized silicon carbide was reported by Carroll and Tressler (1989). They found a threshold for creep damage of 132 MPa at

1100°C. Below this stress the stress exponent was about 4. At stresses above the creep damage threshold the stress exponent increased with increasing stress to around 10 at 172 MPa. The activation energy for creep also increased with increasing stress above the threshold. Creep below the stress threshold was attributed to dislocation activity in the silicon phase. Above the stress threshold for damage, cavities formed and contributed to the creep strain. Models developed by Raj (1982) and Hasselman and Venkateswaran (1984) were used to separate the damage component, leading to the conclusion that the remaining component of the creep strain is still well described by a stress exponent of 4 to the highest stresses used.

20.8   SUPERPLASTICITY

Many polycrystalline materials, including some ceramics, can sustain very large creep deformations (several hundred percent) in uniaxial tension at high temperature (typically above one-half the absolute melting temperature) before failing (Nieh and Wadsworth, 1990b). Fine grain size (a few micrometers or less) and an equiaxed structure are required. A striking feature of superplastic behavior is that grain shape does not change appreciably during deformation, in contrast to normal plastic deformation in ductile polycrystalline materials. In the latter, the grains typically elongate to the same extent as the specimen as a whole.

Of the ceramic materials exhibiting superplastic deformation, Y–TZP (Y_2O_3–ZrO_2) is by far the most widely studied. It fills the necessary requirements of a fine grain size, typically 0.4-μm-diameter and equiaxed grains. According to Chen and Xue (1990), an additional feature of Y–TZP necessary for high elongations is a low grain boundary energy, which reduces the tendency toward cavity formation along the grain boundaries.

It is generally agreed that superplastic deformation takes place by grain boundary sliding, but at the time of writing there is still much discussion about exactly how this can occur. To illustrate superplastic deformation by grain boundary sliding, Figure 20.5 shows grains on a polished surface of a Y–TZP specimen strained in compression to 0, 14, 28, 42, and 56%. Usually superplastic deformation is defined by tensile deformation, but compression tests can still be used to study the mechanism. It is observed in Figure 20.5 that grains do not significantly change size or shape but they change position relative to one another. Grain 1 comes together with grains 6 and 7, grains 3 and 5 move apart, and grain 4 disappears into the surface. The specimen becomes shorter because grains switch positions, leading to a smaller number of grains along the length of the specimen rather than grains themselves changing shape. According to Duclos (2004), 80% of the deformation can be accounted for from these grain-switching events. If the specimen were deformed instead, in tension the number of grains along the length of the specimen would increase and new grains would appear on the surface.
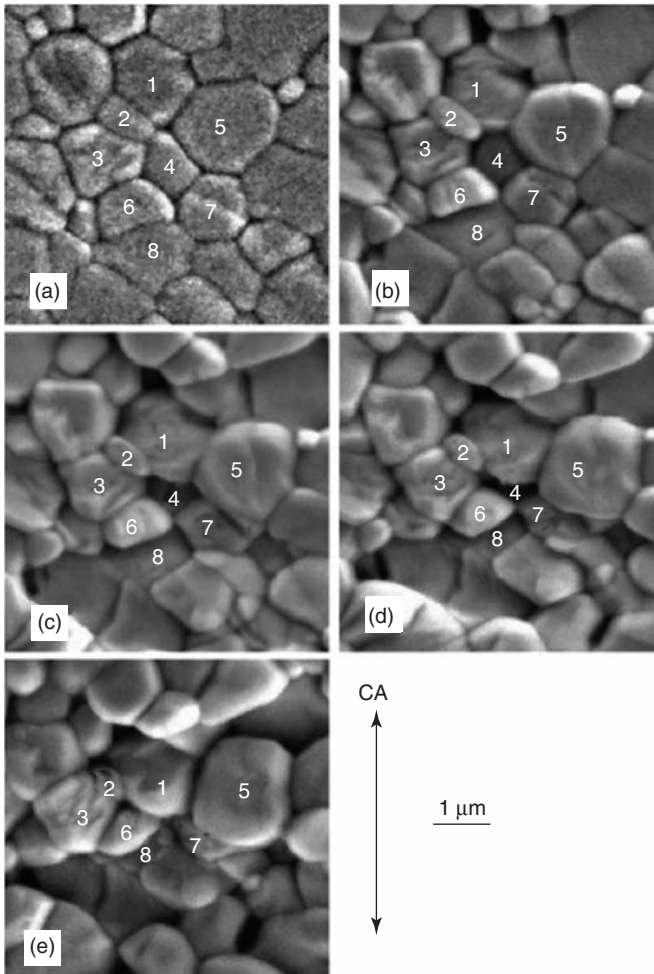
FIGURE 20.5 Polished surface of Y–TZP after (a) 0%, (b) 14%, (c) 28%, (d) 42%, and (e) 56% deformation in compression: CA = compression axis. Grain 4 disappears into the surface and grain 1 comes together with grains 6 and 7. (After Duclos, 2004. Reprinted with Permission of Elsevier Press.)

Grain-switching events may be local or may extend across the specimen. If shear occurs in straight lines across the entire specimen, it is called cooperative grain boundary sliding. Figure 20.6 depicts cooperative grain boundary sliding in a schematic depiction using circular grains. Each row of grains along the dark lines shifts one grain distance in the direction of the arrows. The picture illustrates how under compressive strain grain 2 can disappear from the surface while grains 1 and 3 above and below grain 2 come together. One
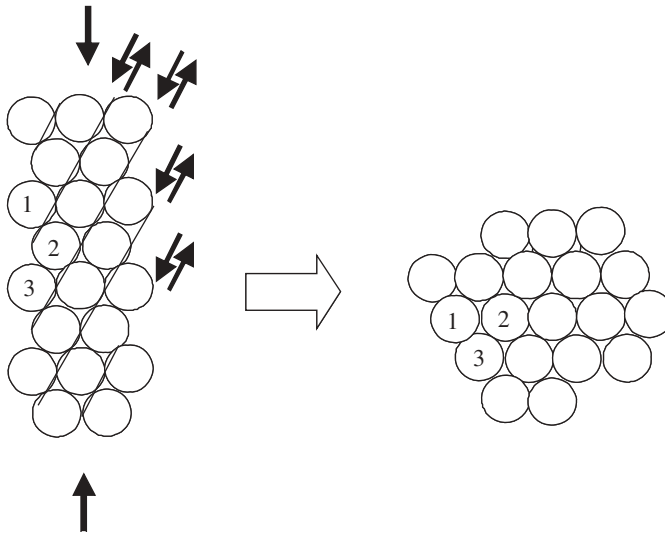
FIGURE 20.6 Grains represented as circles illustrate cooperative grain boundary sliding. Grain slide one grain length downward to left. Grain 2 disappears from the surface and grains 1 and 3 come together.

can visualize tensile strain by going from the figure on the right to one on the left rather than from the left one to the right one. Then grain 2 appears on the surface.

It is somewhat more difficult to depict a local grain-switching event. Nevertheless the literature contains many attempts at modeling these local switching events that are reviewed by Zelin and Mukherjee (1996). Most of these models, however, require temporary creation of voids or intermediate steps of greatly altered grain shape. There is some evidence from micrographs such as Figure 20.5 that bands of grain boundaries shear across the entire specimen, but this was not seen by Duclos (2004). Thus it is uncertain whether cooperative grain boundary sliding can account for most of the strain. Regardless of the manner in which grain-switching events occur, grain boundary sliding cannot take place without some sort of accommodation at grain boundary triple points because grain boundary are not aligned along a flat plane. Some possibilities that have been suggested are diffusional accommodation, dislocation accommodation, and grain boundary migration to straighten out the plane of the grain boundary. Ashby and Verrall (1973) proposed grain-switching events which require a combination of diffusional creep and grain boundary migration. There is certainly abundant evidence that superplastic deformation enhances grain boundary migration and so grain boundary migration could easily play an important role in superplastic deformation.

One accommodation mechanism which has been popular in explaining how grains move past each other is Gifkin's 1976 core-and-mantle mechanism,
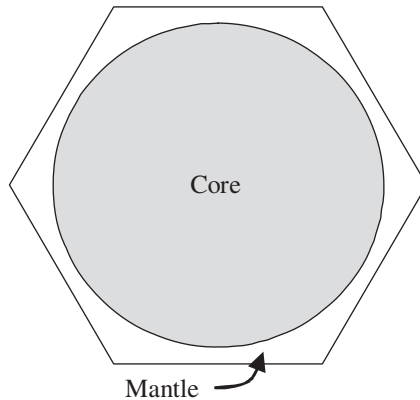
FIGURE 20.7   Core-and-mantle model.

illustrated in Figure 20.7. The core is rigid and the mantle is fluid, deforming by grain-boundary-enhanced processes such as grain boundary diffusion and solution precipitation. One can imagine how grains might slide past each other if the corner and edges are fluid.

The question of what mechanism controls the creep rate will again be illustrated by the results for Y–TZP. Superplasticity in Y–TZP, as with superplastic metals, shows several regions of different stress dependence on creep rate in which Eq. (20.27) holds. In region II, $n = 2$ in both ceramics and metals. In region I at low stresses (low strain rates), $n > 2$. [Region I is not observed in Y–SZP containing >0.1 wt. % total impurity content, according to Jimenez-Melendo et al. (1998).] There is good evidence that in high-purity Y–TZP there exists a threshold stress below which the grain boundary sliding mechanism no longer operates and creep is very slow. In the transition between the threshold stress and the stress of region II the stress exponent n is high. Jimenez-Melendo et al. (1998) reviewed the large amount of literature on Y–TZP creep and concluded that the creep rate behavior in region II is controlled by Zr^{4+} ion diffusion through the lattice and that $\dot{\varepsilon}/D_{Zr^{4+}}$ agrees very well for a given σ/E with $\dot{\varepsilon}/D_{\ell}$ for superplastic metals whose creep rate is controlled by lattice diffusion. In accordance with Nabarro–Herring creep, the creep rate is proportional to $1/d^2$.

Superplasticity in ceramics has been considered as a forming mechanism. A potential problem is the development of internal voids. Ma and Langdon (1993) have studied superplastic deformation at 1723 K of dense TZP (3 mol % yttria) with a grain size of 0.5 μm. For strain rates of 0.0028, 0.00028, and $0.000028\,s^{-1}$, the engineering strains at failure were 85, 195, and 355%, respectively. Cavitation took place in each case, but the amount at failure increased with increasing strain rate. They concluded that cavitation is likely to be a problem in materials with very small grain sizes because of the large number of grain boundaries providing fast diffusion paths to feed cavity

growth. In superplastic metallic alloys the superplastic strain is limited by necking. It can be shown that the stress exponent n in Eq. (20.27) determines the sensitivity to necking of a particular material.

Assuming constant volume for plastic deformation and substituting in Eq. (20.27) yield

$$\dot{\varepsilon} = \frac{1}{L}\frac{dL}{dt} = -\frac{1}{A}\frac{dA}{dt} = k\sigma^n \tag{20.28}$$

so, since $\sigma = F/A$,

$$\frac{dA}{dt} = -kF^n A^{(1-n)} \tag{20.29}$$

One can now consider what would happen under constant-force creep conditions to a portion of the specimen in which the cross-sectional area A_2 is slightly smaller than the rest of the specimen, A_1, so that $A_2/A_1 < 1$. If $n = 1$ and, therefore, $1-n = 0$, the rate of decrease of the cross-sectional area is constant everywhere. If $n > 1$ so that $1-n = -\delta$ with δ positive, then

$$\frac{d(A_2/A_1)}{dt} = \left(\frac{A_1}{A_2}\right)^{\delta} \tag{20.30}$$

The right-hand side of Eq. (20.30) is a positive number greater than 1 so that the smaller cross-sectional area decreases faster than the larger cross-sectional area. Thus as n approaches 1 the tendency to necking decreases. Langdon (1982) has shown that the total creep strain before failure correlates well with n for many metals and metal alloys. The lower n values and highest total strain in metals and metal alloys is in region II where $n \cong 2$.

Chen and Xue (1990) have shown that percent elongation to failure of superplastic ceramics does not correlate well with n but does correlate well with the applied tensile stress. That is, elongation to failure is approximately inversely related to the tensile stress. It is not unexpected that elongation to failure is inversely related to stress and not to n, which is a necking sensitivity parameter since necking in ceramics is not generally observed and would not be expected because n usually approximates 1. On the other hand, failure of ceramics is very sensitive to formation of cavities along grain boundaries, as discussed in Chapter 21, and cavity formation is very sensitive to tensile stress. Thus, to achieve a high tensile strain, a ceramic must have very low creep resistance so that a large amount of strain can be achieved at a low stress and it must be very resistant to cavitation along grain boundaries. The most outstanding result at the time of writing is the result of Kim et al. (2001), who reported superplastic tensile deformation of 1050% in 26 s in a triphasic Al_2O_3–$MgAl_2O_4$–ZrO_2 ceramic at 1650°C. The average grain size was 0.21 μm.

Other unique features of superplastic ceramics as compared to superplastic metals and alloys from Langdon (1991b) are as follows. In superplastic metals
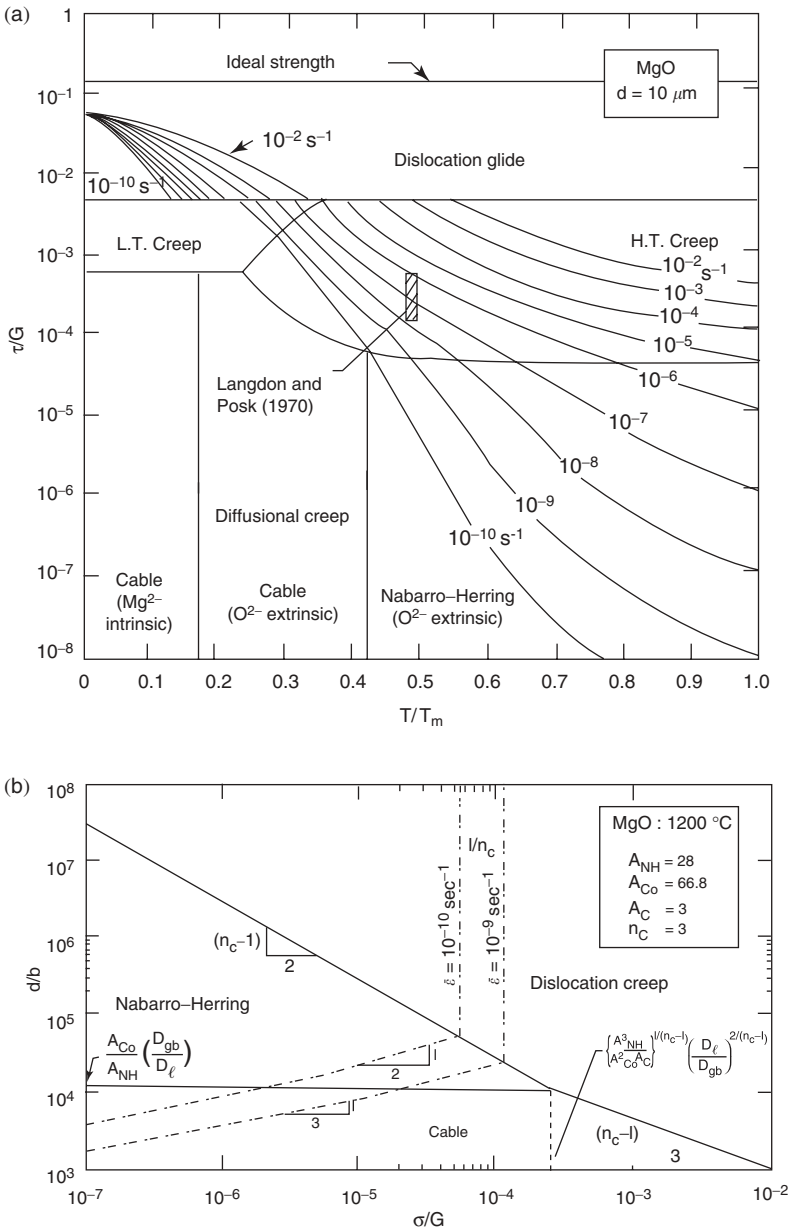
FIGURE 20.8 Deformation mechanism maps for MgO with (a) 10-μm grain size, and (b) at 1200°C. (Langdon and Mohamed, 1976. Reprinted with permission of Springer Verlag.)

and metallic alloys grain size does not affect the value of n, whereas in superplastic ceramics n increases as d decreases. Maximum cavitation occurs at the slowest strain rates in superplastic metals and metallic alloys whereas maximum cavitation occurs at the fastest strain rate in superplastic ceramics.

20.9 DEFORMATION MECHANISM MAPS

A very useful way of summarizing the dominant deformation mechanisms in a single drawing was apparently first suggested by Weertman and Weertman (1983) and has been developed by Ashby and his collaborators (Ashby, 1972; Frost and Ashby, 1982). The basic concept of these authors was to show, for a given grain size, the regions of stress and temperature in which each deformation mechanism dominates. Langdon and Mohamed (1976) have also presented diagrams of this type but for a constant temperature where stress and grain size are the variables. The border between two regions is the line along which the neighboring mechanisms have equal strain rates. Several types of plots are possible, but the most useful is a plot of log normalized stress (stress divided by the shear modulus), homologous temperature (absolute temperature divided by the melting temperature), or log normalized grain size (grain diameter divided by the Burgers vector). Two such plots for MgO are shown in Figure 20.8(a) and (b). In Figure 20.8(a), for MgO of 10 μm grain size, Langdon and Mohamed (1976) indicate a region where the dominant diffusional flow mechanism is controlled by magnesium diffusion in the boundary, another at higher temperatures controlled by oxygen in the boundary, and still another at a still higher temperatures where oxygen diffusion in the lattice is controlling. In these plots *intrinsic* and *extrinsic* refer to creep controlled by intrinsic or extrinsic diffusion.

A second type of deformation map shown in Figure 20.8(b) is at constant temperature (Langdon and Mohamed, 1976, 1978; Langdon, 1980). The axes are homologous grain size (grain size divided by the magnitude of the Burgers vector) and homologous stress (stress divided by the shear modulus). This type of deformation map shows the regions in which the predominant deformation mechanism is Nabarro–Herring creep, Coble creep, or dislocation creep. Lines of constant strain rate are overlaid on both of these maps.

PROBLEMS

1. Under 100 MPa stress a certain polycrystalline alumina underwent 5% strain in 25 h at 1500°C. The steady-state strain rate was measured to be $5 \times 10^{-7}\,\text{s}^{-1}$. Estimate the strain after only 1 h? Assume $E_{\text{Al}_2\text{O}_3}(1500°\text{C}) = 380\,\text{GPa}$. Also assume there was a primary creep stage.

2. The creep rate of polycrystalline alumina of grain diameter $d = 18.4\,\mu\text{m}$ exhibited a stress exponent $n = 1.2$, an activation energy $Q_c = Q_{\text{diffusion}} =$

595 kJ/mol K, and a grain size dependence $p = 2.3$. The measured steady-state creep rate at 1650°C and 110 MPa was $4.8 \times 10^{-6}\,\mathrm{s}^{-1}$. Estimate the creep rate of a similar specimen whose grain size $d = 2\,\mu\mathrm{m}$ at 1400°C at 25 MPa and

$$D = D_0 \exp\left(\frac{-Q_{\text{diffusion}}}{RT}\right)$$

3. Assume that the activation energies for diffusion of ions during creep follow in the order $Q_{c,\text{gb}} < Q_{a,\text{gb}} < Q_{c,l} < Q_{a,l}$. Sketch a graph of combined diffusional creep rate versus $1/T$. Draw four straight lines representing the creep rate versus $1/T$ for each of the diffusion paths with none of the lines intersecting at the same point and label each line as $D_{a,l}$, $D_{c,l}$, $\delta D_{a,\text{gb}}$, or $\delta D_{c,\text{gb}}$. Show by a dark or colored line which is the rate-controlling diffusion path across the entire temperature span. Assume that d and σ are constant across the entire temperature range and that the factors 13.3 and 150 in Eqs. (20.13) and (20.15) are not significant to the creep rate differences.

4. An effort is being made to achieve the very high creep resistance (low creep rates) of single-crystalline YAG with polycrystalline YAG. If the grain size is large enough at a moderate stress, then the creep of polycrystalline ceramics becomes controlled by a dislocation mechanism as illustrated in Figure 20.2. The steady-state creep rate of single-crystalline YAG at 1300°C is given by

$$\dot{\varepsilon} = 1.4 \times 10^{-12}\sigma^3 \exp\left(-\frac{720kJ}{RT}\right)\mathrm{s}^{-1}$$

Assuming that the creep rate of the coarse-grained polycrystal is that of the single crystal, calculate how large one must grow the grain size for dislocation creep. The creep rate of a YAG specimen having a grain size $d = 10\,\mu\mathrm{m}$ at a stress of 20 MPa and at 1300°C was found to be $3.4 \times 10^{-9}\,\mathrm{s}^{-1}$. The service stress is expected to be 100 MPa. Assume Nabarro–Herring creep at finer grain sizes.

5. Consider Figure 20.5. In the two-dimensional schematic of circular grains how much strain accumulates from sliding the grains along the bold lines one full grain length.

21

CREEP RUPTURE AT HIGH TEMPERATURES AND SAFE LIFE DESIGN

21.1 INTRODUCTION

All ceramic materials undergo some degree of creep at sufficiently high temperatures. Polycrystalline ceramics in tension at high temperatures typically develop small internal flaws that eventually lead to fracture. Design for safe use of ceramics under load at high temperature seeks to avoid both excessive deflection (e.g., avoidance of sufficient creep of turbine blades to cause contact between the blade tips and the shroud) and fracture. It is thus important to know the creep strain as a function of stress, temperature, and time and to have a failure criterion to predict the time to failure at a given stress and temperature.

21.2 GENERAL PROCESS OF CREEP DAMAGE AND FAILURE IN CERAMICS

We follow Wilkinson (1992) in summarizing creep damage mechanisms in ceramics. He classifies the microstructures of ceramic materials for

high-temperature use into three categories. The first category is single-phase materials processed to give clean grain boundaries such as pure alumina. This class of materials constitutes a good system for model studies, but such materials are not generally regarded as useful as high-temperature structural materials. The second category is materials with a bonding phase such as sintered silicon nitride. This boundary phase is typically liquid at the sintering temperature and facilitates sintering to full density. In older silicon nitrides the grain boundary phase usually became a glass at lower temperatures, leading to a microstructure of crystalline grains embedded in a continuous glass matrix distributed as a thin layer between grains and larger pockets. In modern silicon nitrides intended for load bearing at high temperatures, combinations of composition and heat treatment are used to form a crystalline grain boundary phase. The third category is multiphase crystalline ceramics, often containing discontinuous reinforcements such as particles, platelets, or whiskers. All these types of ceramic materials exhibit cavity formation under appropriate circumstances. Ultimate failure at high temperatures typically involves cavity growth at grain boundary triple junctions and linking along grain boundaries to form a crack that ultimately propagates catastrophically. The nucleation of these cavities is apparently not fully understood but often seems to occur at inhomogeneities caused by processing. In particular, some small pores can generally be found even in material nominally pore free such as hot-pressed alumina. Other stress-concentrating inhomogeneities may also be involved in cavity nucleation. Cavities often nucleate at three-grain junctions. Thus microstructure always plays a key role in failure, but the flaws responsible for high-temperature failure may be quite different from those responsible for failure at low temperatures. The process leading to failure can be complicated by additional, parallel processes such as grain growth or devitrification of an initially glassy grain boundary phase.

The status of knowledge of creep damage development in structural ceramics was reviewed by Chan and Page (1993), who also presented new data on cavity development in alumina and silicon nitride. They distinguish two extremes of cavity damage accumulation and ultimate failure. In one extreme, cavities nucleate and grow throughout the specimen. Failure occurs when enough cavities coalesce to form a microcrack that can propagate by fast fracture. In the other extreme, cavities nucleate and grow in the concentrated stress field associated with some microstructural inhomogeneity. These cavities coalesce to form a microcrack that then grows subcritically by means of cavitation ahead of the crack tip. Actual failure may involve a combination of these two extremes. Bulk damage is thought to be favored at low stresses and long times while high stresses and short failure times favor localized damage.

They obtained data on cavity number and size by the technique of small-angle neutron scattering (SANS). This technique presents average data and so does not give a direct picture of coalescence. For polycrystalline alumina without a glassy phase (Lucalox), their results are shown in Figure 21.1. The density of cavities increases with increasing creep strain, but the size does not
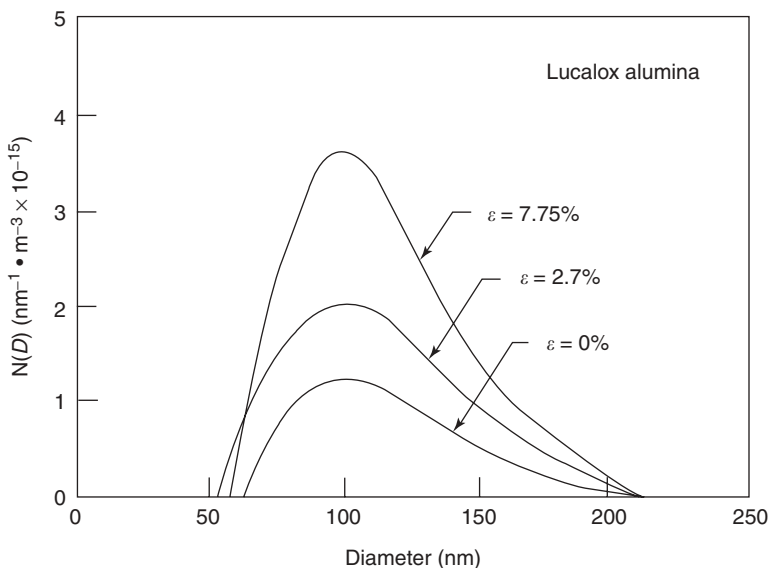
FIGURE 21.1 Cavity size distribution as function of creep strain in alumina without glassy phase. (From Chan and Page, 1993. Reprinted by permission of the American Ceramic Society.)

increase, indicating nucleation-dominated behavior. For polycrystalline alumina with a glassy silica phase (Coors AD99), their results are shown in Figure 21.2. Here the density of cavities and their size both increase, indicating concurrent nucleation and growth. For polycrystalline SiC (Norton NC203), the peak density of cavities changes little, as shown in Figure 21.3, but the size at the peak increases with increasing creep strain, indicating growth-dominated behavior.

Direct observations of creep–crack growth in many ceramics suggest the schematic crack growth curve shown in Figure 21.4. The first region to the left is the near-threshold region although thresholds are not always found. Second is a power law growth region in which the crack velocity is characterized empirically by

$$V = A_c K_I^{N_c} \tag{21.1}$$

To differentiate this equation from Eq. (8.1) for subcritical crack propagation due to, for example, humidity, A_c and N_c are used instead of A and n. Third is the fast-fracture region. Chan and Page have compiled the available data on the crack growth exponent N_c and find values ranging from 1.88 to 270 for silicon nitride. Values in the range 1.88–13 appear to be characteristic of region II and the mechanism of creep–crack growth is thought to be viscous or diffusive flow in this region. (Blumenthal and Evans, 1984; Johnson et al., 1984).
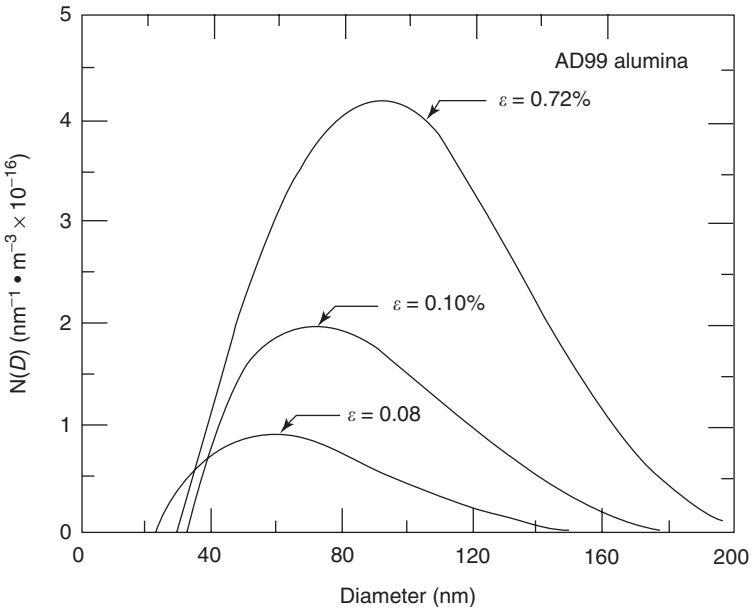
FIGURE 21.2   Cavity size distribution as function of creep strain in alumina with glassy phase. (From Chan and Page, 1993. Reprinted by permission of the American Ceramic Society.)
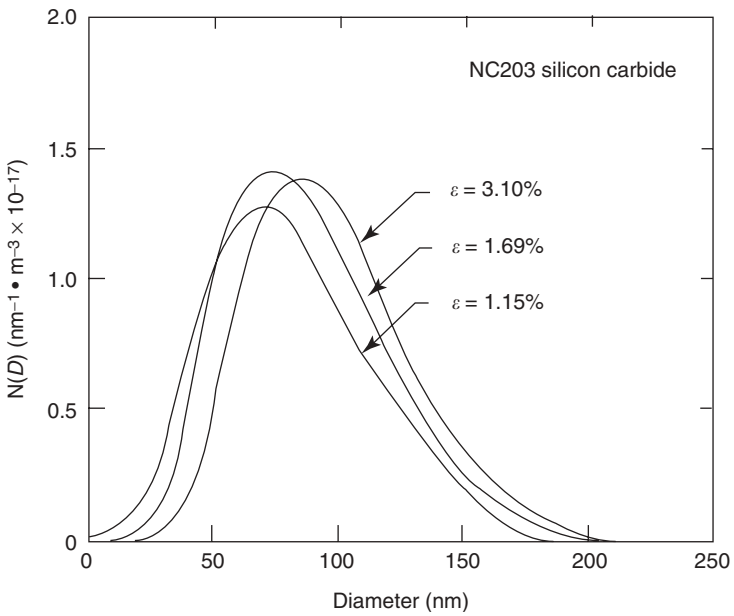
FIGURE 21.3   Cavity size distribution as function of creep strain for polycrystalline SiC. (From Chan and Page, 1993. Reprinted by permission of the American Ceramic Society.)
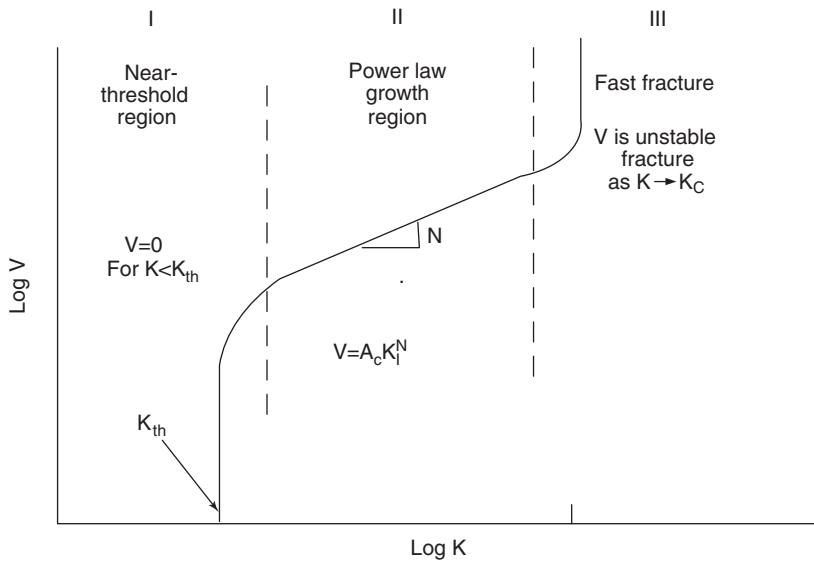
FIGURE 21.4 Schematic of creep–crack growth curve for ceramics showing three characteristic regions. (From Chan and Page, 1993. Reprinted by permission of the American Ceramic Society.)

21.3   MONKMAN–GRANT TECHNIQUE OF LIFE PREDICTION

Most ceramic materials at high temperature follow the Monkman–Grant type of empirical creep–rupture relationship, so that use of this relationship provides a good way to summarize data and also leads to one means of lifetime prediction under creep conditions. An empirical correlation of steady-state creep rate with time to failure was suggested by Monkman and Grant (1956). For many materials a plot of the logarithm of the steady-state creep rate $\dot{\varepsilon}_s$ and the logarithm of the time to failure t_f can be well represented by a straight line leading to the empirical relationship

$$t_f = C\dot{\varepsilon}_s^{-M} \tag{21.2}$$

where M is a dimensionless constant close to 1. The important point for the use of this relationship for prediction of lifetime under stress is that this single curve holds for data for a given material over a wide range of stresses and temperatures. Monkman and Grant found that $M = 1$ fit the data on their materials well. This led to the use of a constant total strain as a criterion for failure caused by creep. More recent work on ceramics creeping in tension shows that M cannot be taken as 1; values of 1.45 and 2.39 were found for two different types of siliconized carbide and a value of 1.69 was found for silicon nitride reinforced with silicon carbide whiskers (Wiederhorn and Hockey, 1991; Wiederhorn et al., 1991). The total strain for failure thus decreases

with increasing strain rate for materials with $M > 1$. The Monkman–Grant relation can still be used as a failure criterion with the proper M value for the material. In developing lifetime prediction equations, Wiederhorn et al. (1991) presented derivations of the Monkman–Grant equation for either of two extreme types of failure from cavity formation: (1) creep–crack nucleation and propagation and (2) cavity coalescence to form a critical size crack.

For the first type of failure they assumed that the time to nucleate cracks was short compared to the time for crack growth. They assumed a power law crack velocity equation like (8.1) with a thermally activated factor:

$$V = A'_c K_I^{N_c} \exp\left(-\frac{Q}{RT}\right) \tag{21.3}$$

The time to failure from crack propagation under constant stress can be determined in the same manner as (8.15) and is

$$t_{f,\sigma} = \frac{B' \sigma_{f,t=0}^{N_c-2} \exp(Q/RT)}{\sigma^{N_c}} \tag{21.4}$$

$$B' = \frac{2}{A_c Y^2 (N_c - 2)} \frac{1}{K_{IC}^{N_c-2}} \tag{21.5}$$

Here B is a material constant of the same form as Eq. (8.17) and $\sigma_{f,t=0}$ is the strength at temperature set by the initial flaw size. They then assumed that the steady-state creep rate was given by the power law Eq. (20.27), modified by adding a thermal activation factor

$$\dot{\varepsilon} = k' \sigma^n \exp\left(-\frac{H}{RT}\right) \tag{21.6}$$

Solving this for stress and substituting into (21.4) gives the failure time from crack growth in terms of the steady-state strain rate as

$$t_{f,\sigma} = \dot{\varepsilon}^{-N_c/n} B' \left\{ \exp\left(\frac{(-N_c/n)H + Q}{RT}\right) \right\} (\sigma_{f,t=0})^{N_c-2} k^{N_c/n} \tag{21.7}$$

From this equation the Monkman–Grant parameter is $M = N_c/n$. The Monkman–Grant equation will be temperature independent only if $Q - N_c H/n = 0$. Otherwise a series of parallel lines for different temperatures will be obtained on a Monkman–Grant plot. For the case of cavity coalescence they eventually obtain from a combination of empirical data and theoretical relationships

$$t_{f,\sigma,cc} = \left[\left(\frac{\pi}{2b}\right)^{1/2} (K_{th} k'^{(1/n)}) \right]^{5.3} \dot{\varepsilon}^{-(1+5.3/n)} \tag{21.8}$$

where $b = 1 \times 10^{-4}\,\mu\mathrm{m}$ and K_{th} is the threshold stress intensity factor for propagation of a crack formed by cavity coalescence. For a siliconized silicon carbide the value required to fit the data on lifetime was $K_{\mathrm{th}} \approx 0.4\,\mathrm{MPa}\cdot\mathrm{m}^{1/2}$, in contrast to the value of critical stress intensity factor measured in a chevron notch experiment at high temperature of about $15\,\mathrm{MPa}\cdot\mathrm{m}^{1/2}$. This high critical stress intensity value is thought to be due to the development of a substantial cavitation zone that develops around a deliberately introduced crack. In contrast, cracks that are nucleated by creep do not develop large cavitated zones. Thus self-nucleated cracks apparently propagate differently from those introduced by indentation or other external means.

They note that if Monkman–Grant data and data on stress dependence of creep rate are collected separately, only a relatively small number of experiments are needed as a basis for creep time to failure. They suggest that only a small number, such as six, creep rupture tests can be used to determine the Monkman–Grant parameters and that as few as two specimens (with multiple creep experiments on each) can be used to determine the stress and temperature dependence of the creep rate, although the use of more specimens is desirable. Wilkinson (1992) discusses models for the power law stress dependence of creep life and concludes that an exponent of 2.4 is predicted and that this is in good agreement with experiments.

21.4   TWO-STAGE STRAIN PROJECTION TECHNIQUE

As discussed previously, the traditional convention for metals and the continuing convention of most workers on ceramics is to regard the curve of strain as a function of time under creep conditions as divided into three stages: primary, steady state, and tertiary. A competing viewpoint developed more recently by some workers on metals is that creep curves in metals and alloys can generally be accurately described mathematically in terms of just two stages: primary and tertiary. The intervening portion previously termed "steady-state creep" is regarded as just a transition between the primary and tertiary stages. The transition can require a long time and produce a creep curve that gives a long interval of nearly constant creep rate. A good discussion of this two-stage representation, including some theoretical justification in terms of creep mechanisms and practical examples of creep prediction for several metals, is given by Evans and Wilshire (1993). We present a summary of this two-stage representation and refer the reader to Evans and Wilshire for fuller treatment.

The creep strain is written as the sum of a part due to the primary stage, ε_p, and a part, ε_t, due to the tertiary stage:

$$\varepsilon = \varepsilon_p + \varepsilon_t \tag{21.9}$$

The contributions from the two stages are written in terms of four experimental parameters θ_1, θ_2, θ_3, and θ_4 as

$$\varepsilon_p = \theta_1[1 - \exp(-\theta_2 t)] \tag{21.10}$$

$$\varepsilon_t = \theta_3[\exp(\theta_4 t) - 1] \tag{21.11}$$

giving strain rates

$$\dot{\varepsilon}_p = \theta_1\theta_2 \exp(-\theta_2 t) \tag{21.12}$$

$$\dot{\varepsilon}_t = \theta_3\theta_4 \exp(\theta_4 t) \tag{21.13}$$

The first equation describes a primary creep rate that decreases exponentially with time and approaches zero (i.e., the primary creep strain approaches a constant value) at long times. The second equation describes an accelerating process producing a tertiary strain and tertiary strain rate that both increase indefinitely with time. In practice the second process is terminated by failure of the specimen if creep continues for sufficient time. The transition from predominantly primary to predominantly tertiary creep leads to a minimum creep rate at time

$$t_{\min} = \frac{1}{\theta_2 + \theta_4}\ln\frac{\theta_1\theta_2^2}{\theta_3\theta_4^2} \tag{21.14}$$

with value

$$\dot{\varepsilon}_{\min} = \theta_1\theta_2\left(\frac{\theta_1\theta_2^2}{\theta_3\theta_4^2}\right)^{\theta_2/(\theta_1+\theta_2)} + \theta_3\theta_4\left(\frac{\theta_1 + \theta_2^2}{\theta_3\theta_4^2}\right)^{\theta_4/(\theta_2+\theta_4)} \tag{21.15}$$

From an engineering point of view these equations have proved very useful for metals and alloys in accurately describing creep curves. The four parameters are functions of temperature and stress and must be determined experimentally over a range of both variables and their dependence on these variables must be described by empirical equations. Once this information is available, the strain rate equations can be used to predict behavior at intermediate temperatures and stresses or even used to forecast behavior outside the range of measurement, although the latter is, of course, risky.

Two practical applications are to calculate the combination of stress and time that will lead to failure either through the occurrence of strain larger than the maximum tolerable or through the occurrence of stress rupture. The former condition simply requires integration of the strain rate equations to give strain as a function of time followed by determination of the time required to reach the maximum strain permitted by the limits of deflection of the part in question. The latter condition requires a fracture criterion. The fracture

criterion commonly assumed for stress rupture under constant stress is that the total strain reaches a value ε_f termed creep ductility. For a Cr–Mo ferritic steel, ε_f typically increases slightly with increasing stress at constant temperature and increases with temperature at constant stress (Evans and Wilshire, 1993). Values of ε_f for this steel range from 0.13 to 0.23 over a stress range of 150–350 MPa and a temperature range of 808–868 K. The failure time, however, ranges over orders of magnitude over the same range of stress and temperature. Use of the creep strain equation, including the stress and temperature dependence of the θ parameters combined with a value of the creep ductility, allows the time to failure in stress rupture to be estimated.

21.5   FRACTURE MECHANISM MAPS

We are now in a position to consider fracture over a range of temperatures and stresses drawing on the background developed for different types of failure mechanisms. A useful device is the fracture mechanism map, which is analogous to the deformation mechanism maps discussed in Chapter 20. Quinn and Matsui were apparently the first to construct fracture mechanism maps for specific engineering ceramics (Quinn, 1984a; 1986; Matsui et al., 1986; Quinn and Braue, 1990), although conceptual work was also done by others (Evans
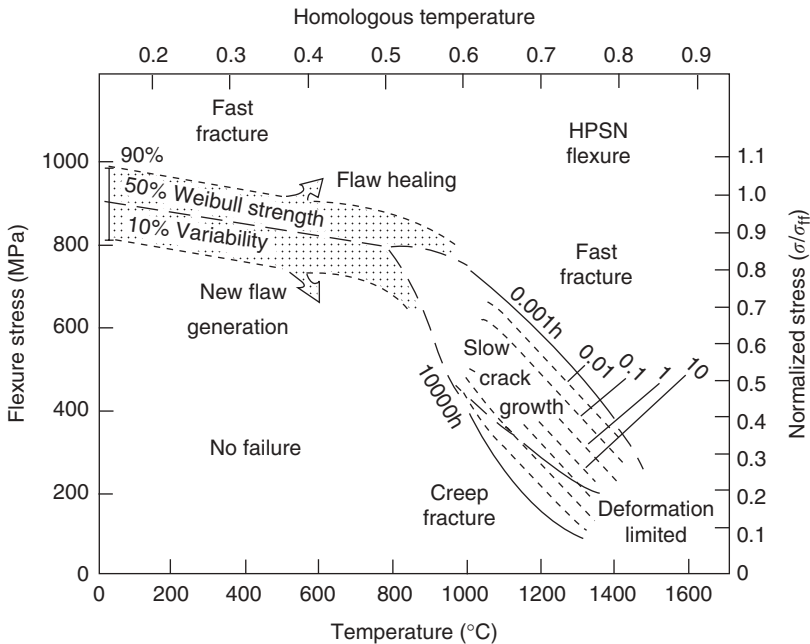
FIGURE 21.5   Fracture map for Mg-doped, hot-pressed silicon nitride in flexure in air. (From Quinn, 1990. Reprinted with permission of Springer-Verlag.)

Stress	Flaw
1023	MD
1011	I
972	MD
943	MD
941	–
927	I/MD
921	I
917	I/MD
916	–
915	–
889	–
883	MD
883	I/MD
876	MD
866	MD
784	–
781	MD

Mean = 909 MPa
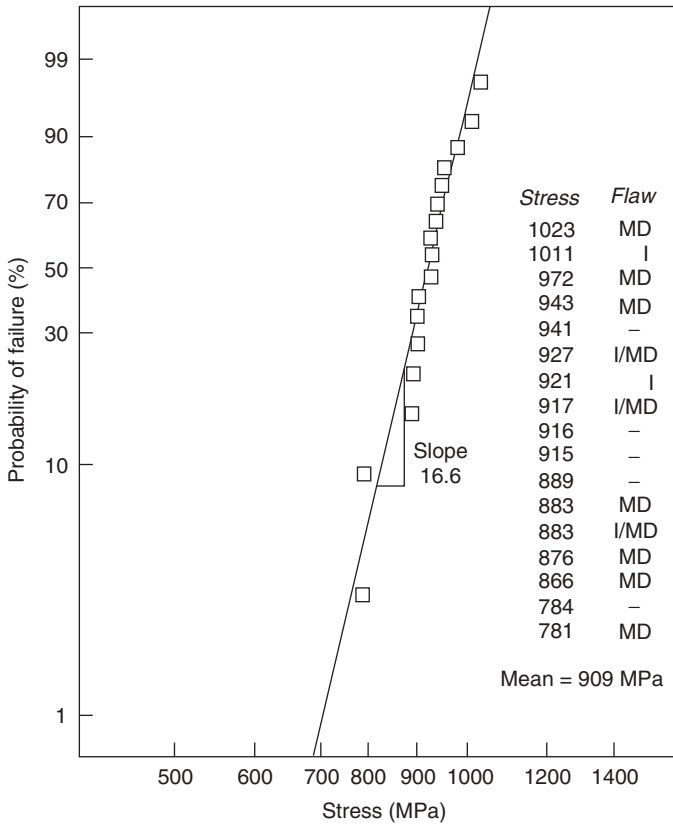
FIGURE 21.6 Weibull plot of flexure strength of MgO-doped silicon nitride: MD = machine damage; I = inclusion; I/MD = machine damage or inclusion;–, uncertain. (From Quinn, 1990. Reprinted with permission of Springer-Verlag.)

and Blumenthal, 1983; Evans and Dalgleish, 1987; and Grathwohl, 1984). In our summary we follow Quinn (1990), who gives the history including the first suggestion by Wray and subsequent early work by Ashby and his collaborators (Ashby et al., 1979; Gandhi and Ashby, 1979). Three fracture mechanisms are found in silicon nitride (and in polycrystalline ceramics in general). These are fast fracture (treated in Chapter 5), slow crack growth (treated in Chapter 8), and creep fracture (treated in Chapter 21). The stress required for fracture from either of the last two mechanisms depends on the time allowed for fracture so that lines of constant time to fracture are plotted. Figure 21.5 shows a fracture map constructed for Mg-doped, hot-pressed silicon nitride (Norton NC 132) based on measurements in flexure in air by Quinn. The stress values are those calculated assuming elastic deformation and the creep strains were calculated assuming an equal magnitude of strain on the tension and compression side of the flexure specimen. As noted earlier, these approximations are progressively

less good for increasing creep strain. Also, as discussed in Chapter 7, statistical effects lead to differences in strength in tension and bending in the fast-fracture regime. Despite these cautions, this fracture map is useful in displaying at a glance the approximate maximum permissible stress without failure for given times under load as a function of temperature. The map is plotted as fracture stress as a function of temperature (in degree celsius). A region of 90% strength variability in the fast-fracture regime is shown based on the value of 16.6 for the Weibull modulus of this material measured in flexure as shown in Figure 21.6. The measured values of flexure, failure stress as a function of time upon which the flexural failure map is based are shown in Figure 21.7.

Quinn used Weibull calculations and a comparison of failure times in tension with failure times in flexure to calculate a fracture map for the same silicon nitride in tension. His comparison of stress–failure lines in tension measured by Govila to those of his own in flexure is shown in Figure 21.8. A considerably lower allowable stress in tension at 1300°C for a given failure time is evident. Based on these data, Quinn constructed the tension fracture map shown in Figure 21.9. Scales of normalized stress (fracture stress divided by fast-fracture stress at room temperature) as a function of homologous temperature (absolute temperature divided by the melting temperature with the latter taken as 2123 K, the decomposition temperature) are used.

This type of map is evidently of great value in design with ceramics. Indeed, its attractiveness is so great that caution is urged in the use of such maps. First, the map is for a particular silicon nitride with a specific microstructure. Even apparently minor variations in sintering aids can alter creep behavior. Second, the map is based on data taken in air. A change in environmental conditions
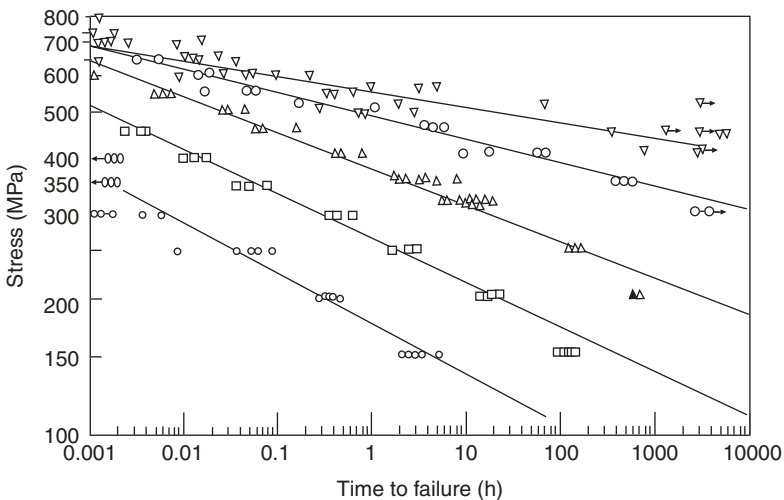
FIGURE 21.7 Flexural stress rupture results for MgO-doped, hot-pressed silicon nitride. (From Quinn, 1990. Reprinted with permission from Springer-Verlag.)
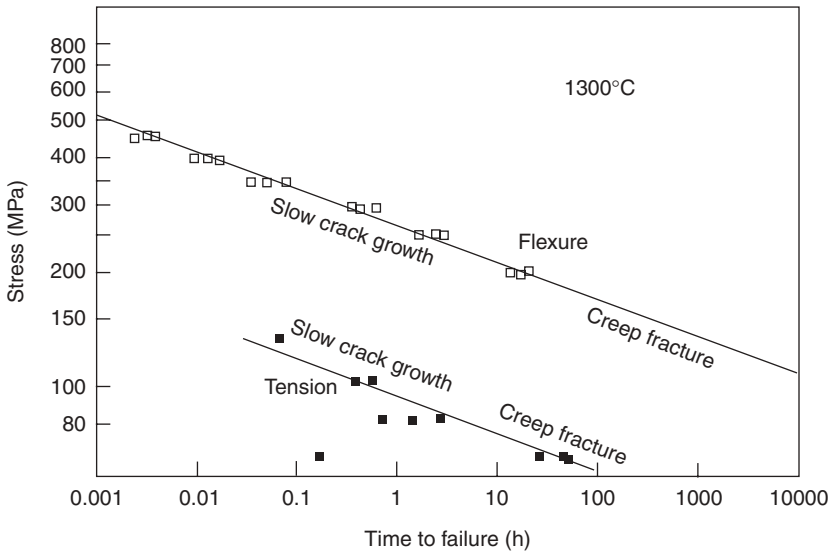
FIGURE 21.8   Comparison of tensile and flexural stress rupture data on MgO-doped, hot-pressed silicon nitride. (From Quinn, 1990. Reprinted with permission of Springer-Verlag.)
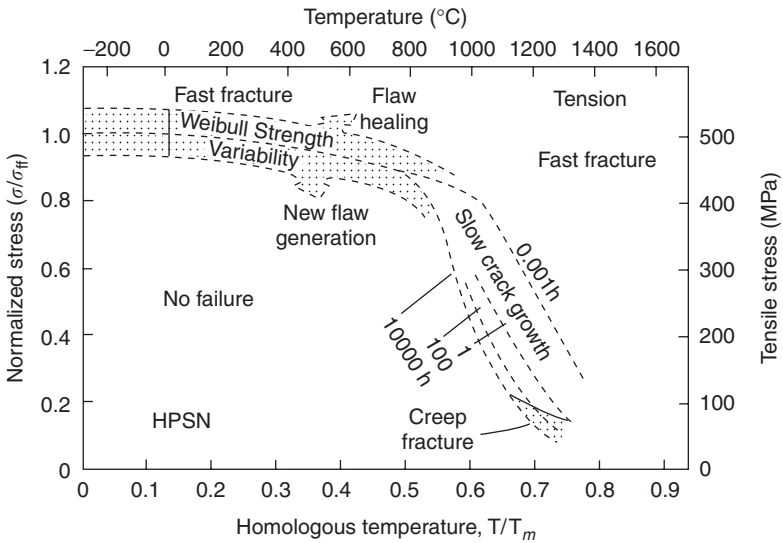
FIGURE 21.9   Fracture map for MgO-doped silicon nitride in air in tension. (From Quinn, 1990. Reprinted with permission of Springer-Verlag.)

can affect slow crack growth and perhaps creep rate. Third, this particular map is based in part on flexure data so that the calculated tensile behavior may not be accurate. Finally, the map takes no account of toughness and so gives no indication of degree of flaw sensitivity. The latter may be an important consideration in some applications. Also, in some applications deformation rather than failure may be the effective limitation. In summary, fracture mechanism maps provide an important and useful tool to be used as part of an overall consideration of materials behavior as part of design. They have been used in practice to design commercial turbocharger rotors (Matsui et al., 1986). An excellent discussion of the construction of fracture mechanism maps and their use in design is given by Wiederhorn et al. (1994).

PROBLEMS

1. Estimate the fraction of the grain boundary covered by cavities for alumina ($\rho = 4\,\text{g/cm}^3$) without a glassy phase (Figure 21.1) at $\varepsilon = 7.75\%$. Assume grain size $d = 30\,\mu\text{m}$ and the relationship between grain size and surface area is

$$\left(\frac{\text{m}^2}{\text{g}}\right) = \frac{6}{d(\mu\text{m})\rho(\text{g/cm}^3)}$$

This equation gives the grain boundary surface area per unit mass (assumes spherical grains) and ρ is the density. Units are shown in parentheses. The number of cavities per unit volume (m^{-3}) is obtained by graphically integrating the area under the curve.

2. In most cases ceramics exhibit very little primary or tertiary creep. Assume linear strain with time until failure. The table below lists time to creep failure for three different tests at each stress. Predict the time to failure at 10 MPa. Assume the stress exponent $n = 1$ in the equation $\dot{\varepsilon} = k\sigma^n$.

<div align="center">

TIME TO FAILURE AT CONSTANT STRESS

40 MPa	50 MPa	60 MPa
20 h	74 min	550 s
16.2 h	77 min	500 s
17.8 h	71.9 min	450 s

</div>

3. The creep failure times versus stress at 1300°C are as below:

Time to failure (h)	55	92	191	667
Stress (MPa)	200	150	100	50

Assuming that failure occurred by crack growth, what is the exponent N_c? Estimate the Monkman–Grant exponent M if the stress exponent for creep

$n = 1.2$. If the activation energy for crack growth is 500 kJ/mol, estimate the failure time at 1100°C. Again assume only steady-state creep.

4. Equations (21.4) and (21.5) are very similar to Eqs. (8.16) and (8.17), which describe subcritical crack growth, normally near room temperature. Two types of behavior were considered in Chapter 8, constant stress and constant strain rate.

   a. Comment on why these two categories are not considered here. Consider Eqs. (8.19)–(8.25).

   b. Are there any changes that need to be made in these equations if we consider the case of increasing the stress at a rate $\dot{\sigma}$ under high-temperature crack growth conditions.

   c. The final equation (8.25) is $\left(\sigma_{f1}/\sigma_{f2}\right)^{n+1} = \dot{\sigma}_1/\dot{\sigma}_2$. Is this equivalent to $\left(\sigma_{f1}/\sigma_{f2}\right)^{n+1} = \dot{\varepsilon}_1/\dot{\varepsilon}_2$? If not, what is the equivalent equation?

5. If the stress exponent of steady-state creep for MgO-doped hot-pressed silicon nitride in Figure 20.8 is $n = 2.1$, calculate the parameters C and M in the Monkman–Grant equation for tensile testing. Estimate the stress necessary to avoid creep fracture for two years.

22

HARDNESS AND WEAR

22.1   INTRODUCTION

Hardness, wear, erosion, and surface grinding all have in common that they occur by local deformation of the ceramic surface, usually over a region on the order of micrometers in width and depth. Under local deformation insufficient strain energy is available to entirely fracture the ceramic and cracks do not extend very far from their origin. Furthermore, under a sharp indenter stresses are sufficiently high to cause local plastic deformation from dislocations, twinning, and grain boundary shear. Because of the complex stress state around the localized deformation, the subject of hardness, wear, and so on, is not as straightforward to describe as fracture or yield strength. We will first treat the subject of hardness for which a large volume of literature is available and then briefly discuss wear. A comprehensive treatment of hardness of ceramics has been compiled by McColm (1990). Lawn (1993) presents a thorough discussion of indentation fracture. One might also refer to Tabor (1951) and Chandler (1999) for fundamental discussions of hardness testing in

metals. Three ASTM standards important in ceramics are ASTM E 384, C 1326-03, and C 1327-03. A mathematical treatment of contact mechanics is given by Johnson (1985).

Hardness, itself, is not uniquely defined. In the most general sense it refers to a materials resistance to penetration by a sharp object. The first attempt at quantifying hardness was to rank its scratch resistance as measured in Mhos, but later static hardness measured by the size of a permanent indentation became the standard method of quantifying hardness. As discussed in Section 6.6, Vickers hardness is generally given as the applied force on the indenter divided by the area between the four faces of the pyramid indenter and the surface (measured after the indenter is removed). The equation for calculating hardness is $H = 1.8544P/(2a)^2$, where a is $\frac{1}{2}$ the diagonal length. Tabor (1951), however, pointed out that the actual mean pressure that the surface experiences is the applied force to the indenter divided by the projected area of the indentation, that is, $H = 2.000P/(2a)^2$. This has led some in the ceramic community to use the projected area in defining the Vickers hardness, particularly Lawn and his colleagues, as pointed out in Chapter 6. In contrast, Knoop hardness, where one diagonal is seven times longer than the other, is always taken as the load divided by the projected area of the indentation. In reporting Vickers hardness it would be useful to state whether the projected area or the contact area is used since there is a 7.9% difference in hardness values.

22.2   SPHERICAL INDENTERS VERSUS SHARP INDENTERS

Spherical indenters are most often used to test the hardness of metals because ductile metals plastically yield under the concentrated stress of the spherical indenter whereas ceramics mostly crack under such a blunt indenter. When the applied force is slowly loaded onto the spherical indenter pressed against a metal surface, yielding of the surface begins between σ_y and $1.15\sigma_y$, where σ_y is the yield stress. As the spherical indenter is pressed further into the surface at a depth where hardness is usually measured, the metal surrounding the indentation confines the plastic zone and so measured hardness is much greater than the yield strength. In general the measured hardness can be written as

$$H = C\sigma_y \tag{22.1}$$

where C is the confinement parameter. For metals $C \simeq 3$ (Tabor relationship). Yield strength values in ceramic polycrystals are not readily available, but in the few cases where they are known, both larger and smaller values of C are reported (McColm, 1990).

Hertzian indentation refers to indentation from a spherical indenter. The following analysis shows why spherical indenters lead primarily to cracking in brittle materials. The explanation follows the treatment by Davidge (1979).

The contact radius of a spherical indentation is given by [same as Eq. (15.6)]

$$a^3 = \frac{4\kappa P R}{3E} \tag{22.2}$$

where P is the applied load, R is the radius of the spherical indenter, and κ is a term relating the stiffness of the material being tested with that of the indenter:

$$\kappa = \frac{9}{16}\left[(1-v^2) + \left(1-v'^2\right)\frac{E}{E'}\right] \tag{22.3}$$

The prime refers to the indenter properties. As noted above the point at which deformation begins is just greater than σ_y. Thus the hardness measured at this point is

$$H = \frac{\beta_1 P_d}{\pi a^2} \tag{22.4}$$

where β_1 corrects the projected area (πa^2) of the indent for the contact area and for the excess stress above the yield stress and P_d is the critical load for deformation. Substituting Eq. (22.2) into Eq. (22.4) gives

$$H = \frac{\beta_1 P_d}{\pi[4\kappa P_d R/(3E)]^{2/3}} \tag{22.5}$$

Thus the load necessary to initiate deformation under the indenter is

$$P_d = \frac{3.4 H^3 \kappa^2 R^2}{\beta_1 E^2} \tag{22.6}$$

Experimentally it is found that the force necessary to initiate a crack around a spherical indenter is

$$P_{cr} = \beta_2 R \tag{22.7}$$

where β_2 is a constant. Equating P_d to P_{cr} gives the critical indenter radius above which cracking will occur and below which deformation will occur:

$$R_{critical} = \frac{0.29\beta_1^3 \beta_2 E^2}{H^3 \kappa^2} \tag{22.8}$$

Since $R_{critical}$ varies inversely as H^3, ceramics, which have a much higher hardness than metals, require a very small $R_{critical}$ to avoid cracking. According to Davidge (1979) typical values for glass of $R_{critical}$ are 10–100 μm.

In order to achieve local deformation and minimize cracking beneath the indenter, diamond microhardness indenters with a sharp tip (but not perfectly sharp) are always used for ceramics.

22.3 METHODS OF HARDNESS MEASUREMENT

A brief discussion of two types of sharp-pointed hardness indenters, Vickers and Knoop, is found in Section 6.6. Here we describe these two in more detail and in addition describe a third type of indenter, the Berkovich indenter. Some properties of the indenters are listed in Table 22.1. The Vickers diamond pyramid indenter is very widely used for measuring hardness in ceramics. The indenter produces a symmetrical indentation whose diagonal is typically 50–200 μm long. A filer eyepiece on a microscope is used to measure the diagonal length, which is used to establish the Vickers hardness (HV) using the formula in Table 22.1. In practice the two diagonal lengths are not exactly equal and so their lengths are averaged. In Table 22.1 the equation uses the contact area rather than the projected area. Although in the past HV was given in kilograms per millimeter squared or HV numbers, Table 22.1 uses the SI units of gigapascals.

Only the long diagonal of the Knoop indentation is measured to determine the Knoop hardness (HK). Knoop hardness measurements are the preferred ones for very brittle ceramics such as SiC and loads, P, not exceeding 2 kg to avoid cracking. Knoop indenters are also used to measure hardness when a small penetration depth is desired, for instance, in measuring the hardness of a coating.

For even smaller depths nanoindenters whose depth can be as low as 20 nm are used. Nanoindentation measurements use Berkovich indenters which are three-sided indenters to achieve an almost perfectly sharp tip. Vickers and Knoop indenters normally form a chisel edge of approximately 1 μm in length. Berkovich indenters measure depth of penetration rather than diagonal length to determine the hardness.

The measure of depth of penetration to determine hardness has the advantage that the depth can be measured continually to produce a load–displacement (depth) curve such as the one shown in Figure 22.1. Such a

TABLE 22.1   Description of Diamond Indenters

Indenter (Shape)	Number of Sides	Angle with Vertical Axis	Diagonal-to-Depth Ratio	Formula for Hardness (GPa)
Vickers ◇	4	68° with faces	7:1	$0.001854 P/(2a)^2$
Knoop ◁▷	4	86.25° and 65° with edges	30:1	$0.014229 P/(2a)_K^2$
Berkovich △	3	65.3° with face	Area-to-depth ratio is same as for Vickers	$0.0408 P/\delta_c^2$

Note: $2a$ = Vickers diagonal; P is the force in newtons, $(2a)_K$ = Knoop long diagonal in millimeters; δ_c = depth in millimeters below surface under load (see Figure 22.1).
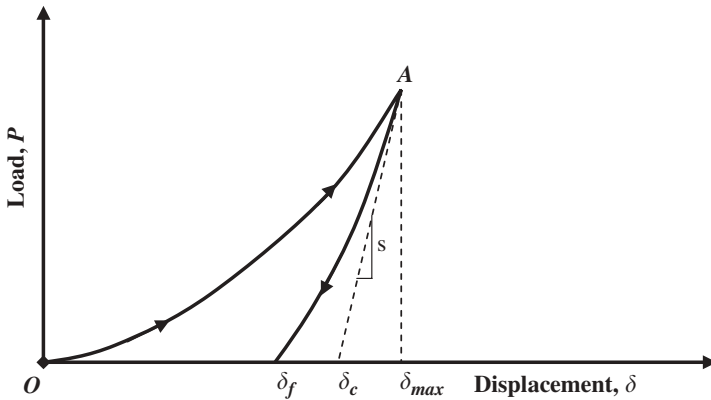
FIGURE 22.1   Typical load–displacement curve for instrumented hardness.

measurement is termed an "instrumented hardness" and is the type of measurement made by nanoindentation instruments. However, Vickers and Knoop instrumented indenters also exist.

Several features of hardness measurements can be illustrated from Figure 22.1. The indenter is loaded along OA and then unloaded along $A\delta_f$. Curvature in OA and $A\delta_f$ results because the contact area is increasing with increasing load along OA and decreasing as the load is removed along $A\delta_f$. Loading along OA produces both a hemispherical plastic zone directly beneath the indenter, as shown in Figures 6.13 and 22.2, and an elastic radial compression zone around the plastic zone. As the load is released, the elastically compressed zone pushes back on the plastically depressed indentation, causing spring-back. The slope s of $A\delta_c$ at A is the contact stiffness, which is related to the elastic modulus. Hardness is P/A_c, where A_c is the contact area of the indentation. This contact area is derived from the position of δ_c since this would be the depth of the indentation if the contact area had remained constant during the release of the load. The accuracy of nanohardness measurements is related to how accurately A_c can be determined by the position of δ_c. A correction is applied to δ_c for elastic displacement of the surface surrounding the indentation. It is given by

$$\delta_c = \delta_{\max} - \varepsilon \frac{P_{\max}}{s} \qquad (22.9)$$

where ε is a value between 0.72 and 1.0, according to Sneddon (1965) and Oliver and Pharr (1992). Much of the literature concerning accuracy of the nanoindentation technique is concerned with exact determination of the contact area. For a review of these issues see Mann (2005).
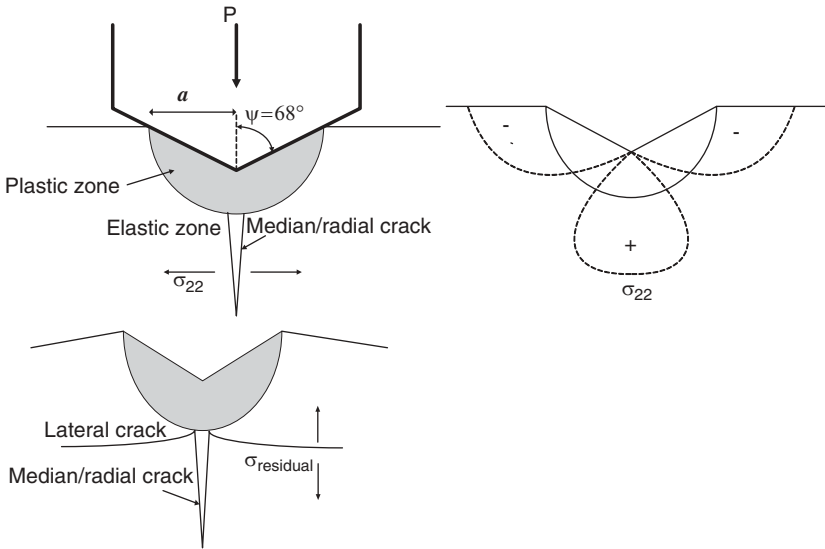
FIGURE 22.2 (a) Plastic zone and major cracks beneath Vickers indenter upon loading stress state producing crack (dashed line is isostress line). (b) Plastic zone and crack after unloading. (c) σ_{22} stress is tensile directly below indentation but changes to compression near surface.

According to Figure 22.1 the total energy stored after loading is $OA\delta_{max}$. The energy stored in the plastic and elastic deformation of the indentation after the load is released is $OA\delta_f$. The remaining area under the curve, $\delta_f A\delta_{max}$, is the elastic energy released upon releasing the load. The work of indentation (WOI) is given by

$$\text{WOI} = \frac{OA\delta_f}{OA\delta_{max}} \tag{22.10}$$

A residual stress is associated with the elastic zone beneath the indentation and results from the attempt of the material below the plastic zone to restore the flat surface. The WOI is higher for softer materials. For instance, according to Wilantewicz (2007) the WOI is 0.42 for sintered SiC (1 kg), as compared to 0.59 for Al_2O_3, which is less covalent and softer.

22.4   DEFORMATION AROUND INDENTATION

As the surface deforms under the indenter, a volume of material equal to the submerged indenter volume must relocate or material surrounding the indenter must become highly compressed. In a soft metal dislocation slip is easy and metal flows up along the sides of the indenter to pile up around the indenter's

perimeter. In ceramics more of the deformation is elastic and consequently the surface rises gradually as it approaches the indentation. The lateral crack shown in Figure 22.2(b), which will be more fully described in the next section, also contributes to the raising of the surface. However, even in covalent solids dislocation activity below the indentation is observed and contributes to the deformation. For instance, in SiC there is TEM evidence of dislocation activity by Hockey and Lawn (1975) below the indentation. In addition, extensive microcracking takes place in SiC directly beneath the indentation. Figures 22.3(a) and (b) show a cross section of an indentation in sintered SiC provided by Wilantewicz (2007). In the cleaved cross section of the indentation shown in Figure 22.3(a) the region beneath the indentation extensive microcracking has occurred. In Figure 22.3(b) an indentation made in the same material was polished to the center of the indentation. The polishing dislodged material is beneath the indentation where the material is so severely microcracked that the cracks are linked together allowing material to dislodge. A black line in Figure 22.3(a) and white line in Figure 22.3(b) indicate the original dimensions of the Vickers indenter. The size of the particles within the rubble from the micro-cracked region that was polished away is approximately the grain size but cracking is not always intergranular. The extent for which microcracking accounts for permanent deformation has not been quantitatively estimated as yet. Extensive microcracking beneath the indenter was not observed in aluminas and AlON, which are softer materials. Plastic deformation by grain boundary sliding without cracking occurs in nanocrystalline ceramics. It is thought to account for the decrease in hardness with decreasing grain size (inverse Hall–Petch effect) below ~ 100 nm grain size. Molecular dynamics simulations have supported the importance of grain boundary sliding and
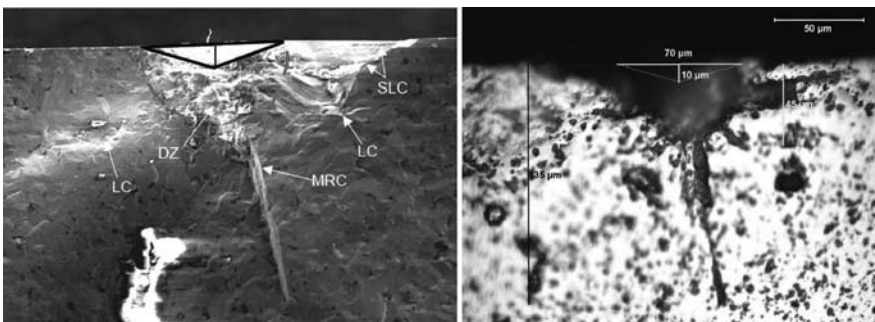
FIGURE 22.3 Knoop microhardness indentation cross section in sintered SiC (Hexaloy™): (a) cleaved cross section (black solid line is outline of indentation; (b) polished cross section of indentation in same specimen (white lines indicate original indentation). Polishing removed the damage zone since it was highly microcracked: LC = lateral crack; DZ = damaged zone; MRC = median radial crack; SLC = surface lateral crack (Wilantewicz, 2007).

rotation of grains beneath blunt indenters in nanocrystalline materials according to Szlufarska et al. (2005).

In glass displacement beneath an indentation occurs by two mechanisms: formation of shear faults and densification. Shear faults form when the shear stress reaches the theoretical shear stress of the glass along that plane. Bonds are broken, producing planes of shear which act in much the same way as dislocations. The shear faults expand as the indentation deepens. In anomalous glass (high-silica glasses) densification below the indentation under the high pressure accounts for an appreciable amount of permanent displacement. In this case there is sinking in rather than a pileup around the edges of the indenter.

22.5   CRACKING AROUND INDENTATION

In addition to microcracking under the indenter in the hardest ceramics, a set of characteristic major cracks form in all ceramics if a sufficiently high load is applied. The two characteristic cracks are the median/radial cracks and the lateral cracks (see Figure 22.2). The shape and location of these cracks are dictated by the stress state beneath a sharp indenter as the force is being applied and by the residual stresses produced in the elastic zone by the now misshaped plastic zone after the indenter is removed. Under load the stress state directly below the indentation is similar to the stress state around a particle with a low thermal expansion coefficient embedded in a matrix of high thermal expansion (see Chapter 11) though here the stress falls off with the square of the radial distance from the plastic zone rather than the cube of the radial distance from the particle. The radial stress beneath the indentation is strongly compressive, but the hoop stress is tensile. The stress state under point loading is designated as the Boussinesq field and is described by the stress trajectories of the three principal stresses where $\sigma_{11} \geq \sigma_{22} \geq \sigma_{33}$. For greater detail consult Johnson (1985), Lawn (1993), and McColm (1990). The σ_{33} stresses are the radial stresses below the indentation and are compressive. Figure 22.2(c) is a schematic of the σ_{22} stress which is tensile directly below the indentation but changes to compression near the surface. The tensile hoop stress directly below the indentation is responsible for propagation of the median crack [Figure 22.2(a)]. For a Vickers indentation two mutually perpendicular cracks form. During loading the median crack is driven down directly below the indentation. Upon release of the load radial surface cracks which are coplanar with the median cracks form and eventually combine with the median crack to form a half-penny crack or the median crack itself expands and breaks through to the surface [Figure 22.2(b)]. Also, as the load is released, the residual stress from the plastic region around the indentation produces a tensile stress in the radial direction below the indentation which is responsible for the propagation of the lateral crack.

The sequence of crack formation as described by Lawn (1993) and McColm (1990) is as follows:

1. Plastic deformation occurs below the indentation as force is applied to the sharp indenter.
2. At a critical load the median crack is initiated from an incipient flaw in the plastic zone beneath the indenter.
3. With increasing load the median crack propagates downward.
4. Upon release of the force on the indenter, the median crack closes but surface residual tensile stresses open up the radial crack at the surface (radial cracks have also been observed to form during loading).
5. Just prior to removal of the force on the indenter the tensile residual stress directly beneath the indentation at the interface between the plastic and elastic region is a maximum and initiates a lateral crack.
6. As the load is completely removed radial cracks expand downward, forming a fully developed half-penny crack and the lateral crack expands or, as mentioned above, the median crack expands to the surface.

22.6   INDENTATION SIZE EFFECT

Hardness measured by Vickers or Knoop indentation is often reported as a materials property; however, the measured value is strongly affected by two variables, the grain size for polycrystalline ceramics and the applied load. The Hall–Petch relationship discussed in Chapters 11 and 18 reasonably accurately predicts the grain size dependence of hardness. In this section the load dependence is discussed. Because hardness is dependent on the volume of material plastically deformed, load dependence is designated as an indentation size effect (ISE). Figure 22.4 illustrates the typical load dependence.

The indentation size dependence on the load is often described by Meyer's law:

$$P = k_P(2a)^{n_p} \tag{22.11}$$

where k_P and n_p are constants and a is one-half the diagonal length. If $n_p = 2$, hardness is constant with load. The value of n_p is almost always less than 2, which dictates a decreasing hardness with increasing applied load. Equation (22.11) predicts a continuously decreasing load with no plateau value of hardness. On the other hand, experimentally, Vicker hardness values often reach a plateau at some critical value of load, P_c. Although this plateau hardness could be taken as the intrinsic hardness, it appears that the plateau occurs when cracking around the indentation takes place at loads greater than P_c (Quinn and Quinn, 1997). The plateau behavior is shown as a dashed line in Figure 22.4.
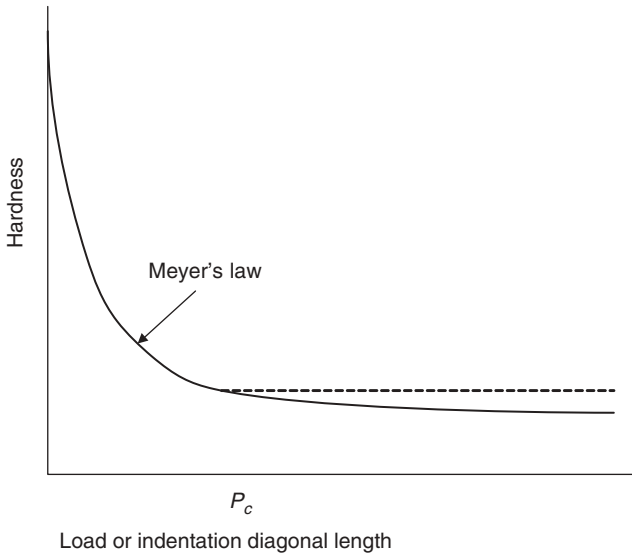
FIGURE 22.4   Indentation size effect curve.

A second problem with Eq. (22.11) is that it leads to no physical interpretation of the indentation size effect. These problems are both addressed by an alternate equation

$$P = A_1(2a) + A_2(2a)^2 \tag{22.12}$$

where A_1 and A_2 are constants. The total energy expended in forming the indentation is approximately $\frac{1}{2}P_{max}\delta_{max}$ (Figure 22.1). Because of the pyramidal shape, the diagonal length of the indentation is proportional to the depth and the work of indentation is

$$W \cong \alpha_I^* P^* 2a \tag{22.13}$$

where

$$\alpha_I = \frac{1}{2}\frac{\delta_{max}}{2a}$$

Multiplying Eq. (22.12) by $2a$ gives

$$P(2a) = \frac{W}{\alpha_I} = A_1(2a)^2 + A_2(2a)^3 \tag{22.14}$$

The first term on the right is directly proportional to the surface (or contact) area of the indentation and the second term to the volume of the deformed

indentation. It follows that A_1 is related to some sort of surface work and A_2 to the work of plastically creating the indentation volume. Originally it was thought that the surface energy term came from the creation of the new surface area of the indentation since the indented surface has a greater area than the original flat surface, but calculations showed that the total energy of new surface is not large enough. It has been proposed by Li and Bradt (1992) that a combination of friction energy and elastic resistance energy accounts for the surface term.

If Eq. (22.12) is multiplied by $k/(2a)^2$,

$$H = \frac{kP}{(2a)^2} = \frac{kA_1}{2a} + kA_2 \qquad (22.15)$$

where k is the geometric constant from Table 22.1 (Vickers: $k = 0.00185$; Knoop: $k = 0.014229$; Berkovich: $k = 0.0408$). Thus hardness can be thought of as having a surface and a volume contribution. The first term on the right controls the early part of the indentation size effect curve. At large loads hardness is dominated by the second term and is independent of load (diagonal length) and thus could be considered the true hardness. In the case where
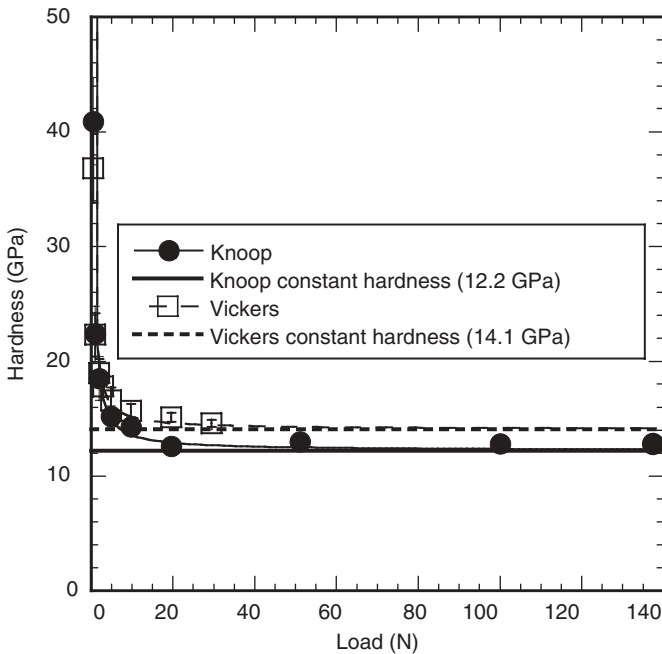
FIGURE 22.5   Equation (22.15) fit to experimental hardness measurements on poly-crystalline Al_2O_3 (AD995 Coortech Inc.) (Wilantewicz, 2007).

hardness follows Meyer's law (Figure 22.4) a constant value is never reached. Many attempts have been made to fit Eq. (22.15) to the experimental curve and thus estimate the true hardness kA_2. One example by Wilantewicz is shown below. Equation (22.15) is shown to fit the data quite well and the value of kA_2 is indicated by the solid and dashed horizontal lines for Knoop and Vickers, respectively. Figure 22.5 also shows that Knoop measurements yield a slightly lower value of hardness than Vickers. It is also important to note how rapidly the hardness values change at low load. It is cautioned that load values $< 20\,N$ for this particular curve should not be used if possible even if the load is specified since errors in the load strongly affect the hardness values.

22.7   WEAR RESISTANCE

Commercialization of structural ceramic parts has not entirely realized its potential because of their brittle nature. On the other hand, wear-resistant applications such as ball bearings, pump seals, prosthetic devices, and so on, have to a greater extent been successfully commercialized. As we shall see in this section, brittleness is still a problem when wear conditions are severe but not a problem under mild wear conditions. Therefore, commercial applications which are most successful are applications requiring only mild wear. Wear resistance is included in this chapter since under mild wear conditions wear is directly related to hardness.

The wear rate by abrasion of ductile materials depends on how deep grinding grit or asperities on one of the two rubbing surfaces penetrate into the other surface, which is also the definition of hardness. Thus the wear rate is directly related to the hardness. According to Archard (1953)

$$w' = k\frac{P}{H} \tag{22.16}$$

where w' is the wear rate in volume removed from the surface per unit sliding distance, k is the wear coefficient, P is the force of the asperity against the opposing surface, and H is the hardness. The wear resistance is $1/w'$.

There are a number of methods of measuring wear rates, but a simple and common method is a pin-on-disk method. The disk is rotated while the pin is pressed against it under a load P. The wear rate of the pin can be measured by the weight loss per unit length of travel along the disk but is usually reported as the volume loss v_{loss} per length of travel. The specific wear resistance w is

$$w = \frac{v_{loss}}{PL} \tag{22.17}$$

where P is the applied load and L is the distance traversed by the pin along the disk.

Wear rates are conveniently divided into "mild wear," "severe wear," and sometimes "very severe wear." The latter category is not so important for most practical applications where wear resistance is desired since these are in the mild-wear region. For grinding applications severe wear is more important. Severe wear is characterized by cracking along the wear track, a much increased surface roughness, a higher coefficient of friction, and a large increase in wear rates. The transition to severe wear is related to the onset of cracking and, in fact, is similar to the cracking at a high load under a microhardness indentation (Section 22.5). The onset of lateral cracking beneath an asperity leads to ceramic particles lifting out of the surface, causing very rapid wear rates. The transition from mild to severe occurs suddenly as the load, velocity, or travel length is increased above some critical value. For pin-on-disk wear tests the maximum specific wear rate in the mild-wear region is $w \approx 10^{-6}\,\mathrm{mm^3/N \cdot m}$. Specific wear rates in the severe-wear region are generally on the order of $w \approx 10^{-4}\,\mathrm{mm^3/N \cdot m}$ or greater.

Several estimates have been made of the critical conditions necessary for severe wear. Here we follow the analysis of Adachi et al. (1997). The transition can be estimated by determining whether, from the maximum tensile stress beneath an asperity, plowing through the surface is sufficient to cause cracking. The stress is assumed to be a Hertzian stress. The maximum tensile stress occurs on the rear edge of the contact and depends on the friction coefficient μ. Hamilton (1983) estimated the maximum tensile stress to be

$$\sigma_{\max} = \frac{3P}{2\pi a^2}\left(\frac{1-2\nu}{3} + \frac{4+\nu}{8}\pi\mu\right) \tag{22.18}$$

where the value of a is found from Eq. (22.2).

Equation (22.18) is simplified if we assume $\nu = 0.25$:

$$\sigma_{\max} = \frac{P(1+10\mu)}{4\pi a^2} \tag{22.19}$$

Cracking will not occur if

$$\frac{P(1+10\mu)}{4\pi a^2} \leq \frac{K_{IC}}{Y\sqrt{c}} \tag{22.20}$$

Rearranging Eq. (22.20) and estimating the flaw size as βd, where d is the grain diameter, give

$$\frac{P(1+10\mu)\sqrt{d}}{4\pi a^2 K_{IC}} = S_{c,m} \leq \frac{6}{Y\sqrt{\beta}} \tag{22.21}$$

All the parameters on the left side of Eq. (22.21) can be determined. Thus, if $S_{c,m}$ exceeds a certain value approximately $6/(Y\sqrt{\beta})$ wear will be severe.

Besides the mechanical stress from the asperity plowing through the surface, there is a thermal stress from rapid frictional heating. When the asperity temperature, designated as the flash temperature by Ashby et al. (1991), is sufficiently different from that below the surface, thermal stresses can lead to cracking. Considering that the asperities on the surface are at some high temperature and the temperature below the surface, which is the sink for heat flow, is ΔT lower, the stress is approximately [see Eq. (16.10)]

$$\sigma = \frac{E\alpha}{1 - 2\nu} \Delta T \tag{22.22}$$

The approach of Ashby et al. (1991) is used in order to estimate ΔT:

$$\frac{\mu P v}{A_r} = \Delta T \left(\frac{k_p}{l_p} + \frac{k_d}{l_d} \right) \tag{22.23}$$

The term on the left of Eq. (22.23) is the heat generated per second per unit area of real contact area, A_r; A_r is used rather than the total surface area since the surfaces are not perfectly flat but touch only at surface asperities; μ is the coefficient of friction; P is the force applied to the pin; and v is the velocity of the pin relative to the disc. The term on the right represents the heat dissipated out through the pin (first term in parentheses) and the disc (second term in parentheses). The subscript d stands for disk and p for pin, k is the thermal conductivity, and l is the distance from the contact to the heat sink just below the surface. Solving for ΔT and simplifying give

$$\Delta T = C_1 \frac{\mu P v}{A_r} \gamma \left(\frac{l}{2k} \right) \tag{22.24}$$

The term in parentheses on the right has been simplified by assuming that $k_p = k_d$ and $l_p = l_d$ but is compensated by a correction factor, the heat partition ratio γ, and the constant C_1.

The parameters A_r and l can be estimated from the following equations. The linear diffusion distance is dependent on the time of contact and therefore the velocity and can be estimated by

$$l = \sqrt{\frac{4\kappa A_r}{v}} \tag{22.25}$$

where $\kappa = k/(\rho c)$ is the thermal diffusivity, where ρ is the density and c is the heat capacity. Here, A_r can be estimated from the hardness H by

$$A_r = \frac{P}{H} \tag{22.26}$$

Combining these approximations to Eq. (22.24) gives

$$\Delta T = C_1 \gamma \mu \sqrt{\frac{vPH}{k\rho c}} \tag{22.27}$$

At some critical ΔT of magnitude ΔT_s, thermal stresses exceed the fracture stress. Thus

$$\Delta T = C_1 \gamma \mu \sqrt{\frac{vPH}{k\rho c}} \leq \frac{\sigma_f(1 - 2v)}{E\alpha} = \Delta T_s$$

The condition of failure dependent on thermal shock is more accurately determined by ΔT_s than by σ_f and so

$$S_{c,t} = \frac{1}{C_1} \leq \frac{\gamma \mu}{\Delta T_s} \sqrt{\frac{vPH}{k\rho c}} \tag{22.28}$$

where ΔT_s is the critical ΔT necessary for cracking.
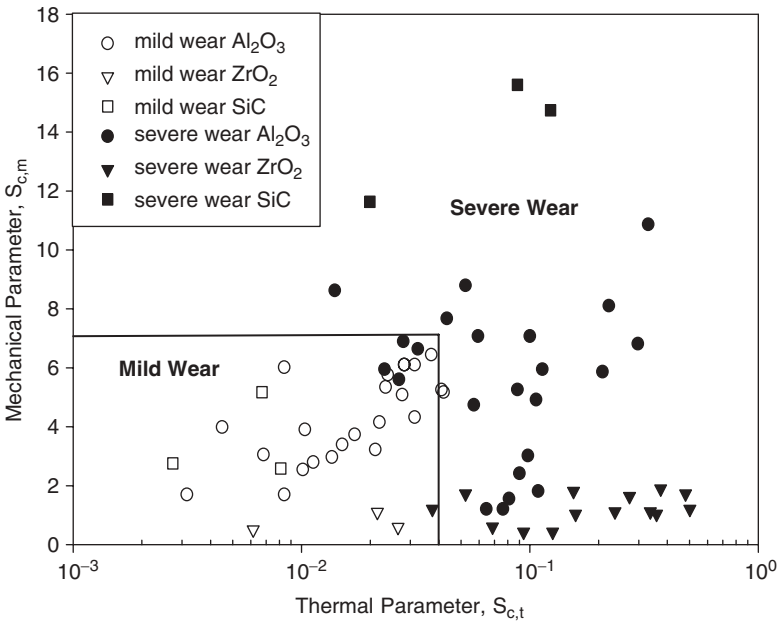
FIGURE 22.6   Experimental wear results (mild or severe) under dry sliding conditions for various combinations of thermal and mechanical parameter conditions. The limits for mild wear are $S_{c,t} = 4 \times 10^{-2}$ and $S_{c,m} = 6$. (From Adachi et al. 1997. Reprinted with permission of Elsevier).

Though this derivation contains some approximations, the parameters contained in Eqs. (22.21) and (22.28) have been successful in delineating the mild-wear region, as shown in Figure 22.6 from. From Figure 22.6 it is ascertained that $S_{c,m} \le 6$ and $S_{c,t} \le 0.04$ for mild wear.

It is important to emphasize that pressure and speed are the two experimental wear conditions most important to wear rates. Two other conditions are lubrication and sliding distance. For instance, under dry sliding conditions a transition from mild to severe wear rates for alumina worn against MgO–PSZ was observed after a sliding distance of 60 km. The transition occurred because of damage accumulated and specifically dislocation pileup at grain boundaries. This is similar to the Hall–Petch mechanism and like the Hall–Petch mechanism the sliding distance transition to severe wear was grain size dependent. Under lubrication conditions there was no transition to severe wear (Rainforth, 2004).

A second type of map is shown in Figure 22.7. It gives experimental wear transitions under various loading pressures and velocities with and without lubrication. Note that velocity and therefore thermal shock have much less effect under lubricating conditions.
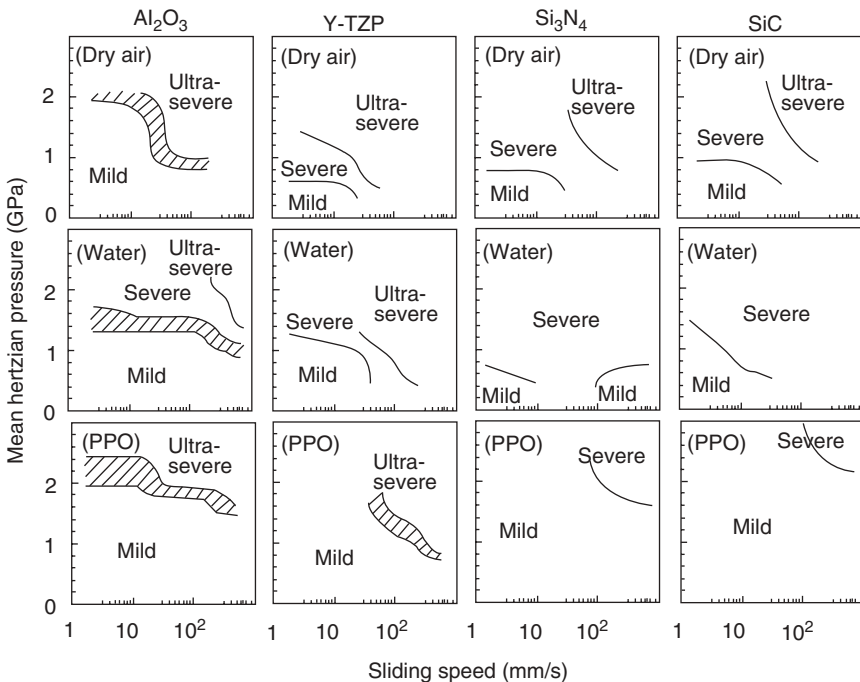
FIGURE 22.7 Wear transitions from mild to severe or ultra severe as function of mean Hertzian pressure and velocity: PPO = purified paraffin oil. Ball on three flats test measured after 5 min. [From Hsu and Shen (1996). Redrawn by Kato and Adachi (2002). Reprinted with permission of Elsevier].

The microstructural properties which have most effect on wear resistance are grain size and grain boundary composition. Surface finish is also important because it affects the coefficient of friction.

PROBLEMS

1. Calculate the mean diagonal length $2a$ of the Vickers indentation and the long diagonal length of the Knoop indentation measured at 4 kgf from Figure 22.5. Estimate the depth of a Berkovich nanoindentation if the load is $100\,\mu N$. Assume the hardness agrees with the hardness of the Knoop indentation at 4 kgf.

2. Calculate the total work of indentation of the Al_2O_3 (Figure 22.4) at 20 N load for a Knoop indenter.

3. The Si_3N_4 ($\rho = 3.2\,g/cm^3$) pin of a pin-on-disc wear test lost 35 mg in 1 h. The disc rotated at 50 rpm and the pin was at 5 cm radius from the center. The load on the pin was 50 N. Does this lie in the severe-wear regime?

4. Using the table below estimate the load that would cause severe wear due to mechanical stress for a 5-mm-diameter Al_2O_3 pin on an Al_2O_3 disc and a ZrO_2 pin on an Al_2O_3 disc. Then solve for the limiting velocity to avoid severe wear under the same load. Assume the coefficient of friction $\mu = 0.6$ and $d = 1.0\,\mu m$ in all cases. Assume $\gamma = k_d/k_p$.

	E	ν	K_{IC}	σ_f	α	H	k	ρ	c
Al_2O_3	380	0.23	6.0	500	7.4×10^{-6}	13	39	4.0	775
ZrO_2	230	0.31	4.0	800	9.6×10^{-6}	9	3.0	5.7	481
Units	GPa	—	$MPa \cdot m^{1/2}$	MPa	K^{-1}		GPa	W/mK	g/cm^3	J/kg K

23

MECHANICAL PROPERTIES OF GLASS AND GLASS CERAMICS

23.1   INTRODUCTION

Inorganic glasses make up a major category of materials from the point of view of applications (both traditional and advanced) and from the point of view of materials science. In American usage, glasses are considered a category of ceramic materials so that a chapter on their mechanical properties is included in the present book. Also, glassy phases are present in many nominally polycrystalline ceramics and have major effects on the high-temperature mechanical properties of these ceramics.

Good general references include Doremus (1982), Varshneya (1994), and Kurkjian (1983).

23.2   TYPICAL INORGANIC GLASSES

A number of oxides, sulfides, tellurides, and halides form glasses under appropriate conditions. However, most of the glass used in practice is based

TABLE 23.1   Important Categories of Silicate-Based Glasses

Type	Typical Composition	Typical Uses	Important Properties
Soda–lime	70–75% SiO_2, 12–16% Na_2O, 10–15% CaO	Bottles, glasses, windows	Optically clear, durable
Lead glasses	55–65% SiO_2, 18–38% PbO, 13–15% Na_2O or K_2O	Decorative items	High refractive index
Borosilicate	70–80% SiO_2, 7–13% Ba_2O_3, 4–8% Na_2O or K_2O, 2–7% Al_2O_3	Chemical apparatus, lamps and tubes	Chemical durability, low thermal expansion
Fused silica ("quartz")	100% SiO_2	High-temperature uses	High softening temperature, low thermal expansion

on silica as the glass former and is modified by the addition of other materials to give desired ranges of properties such as viscosity and elastic moduli. A summary of some of the most important categories of commercial silica glasses from Matthewson (1991) is given in Table 23.1.

23.3   VISCOSITY OF GLASS

Glass in a liquid condition responds to a constant shear stress σ_{xy} by deforming with a constant engineering shear strain rate $\dot{\gamma}_{xy}$ given by

$$\sigma_{xy} = \eta\,\dot{\gamma}_{xy} \tag{23.1}$$

where η is the viscosity. When the viscosity is independent of the strain rate, the deformation is said to be Newtonian. The SI unit of viscosity is the pascal-second, but the centimeter–gram–second (cgs) unit, the poise, is also widely used; it equals 1 $dyn \cdot s/cm^2$ or 0.1 $Pa \cdot s$. Viscosity in oxide glasses is usually taken to be Newtonian and this appears to be true for relatively low strain rates. At high strain rates deformation can depart from Newtonian behavior (Simmons and Simmons, 1989). The rate at which the departure becomes measurable depends on composition and microstructure of the glass, including the possibility of phase separation.

A useful analogy exists between purely Newtonian viscous deformation and purely linear elastic deformation. The equations developed from elasticity to describe **strain** resulting from stress for an incompressible isotropic elastic body can be used to calculate **strain rate** produced by stress in a viscous body. To do this, (i) the elastic equations are written in terms of the shear modulus and Poisson's ratio, (ii) Poisson's ratio is replaced by 0.5 to represent incompressible behavior, and (iii) strain components are replaced by the corresponding

strain rates (or deformation is replaced by deformation rate) and the shear modulus by the viscosity.

As a typical inorganic glass is cooled, the viscosity increases from values as low as 10 Pa·s to as high as 10^{13} Pa·s in the measurable range and presumably continues to increase as the temperature is further reduced. Several temperatures important in the technology of making glass and glass articles are defined in terms of viscosity values and given names. These names and the corresponding viscosities are working point 10^3 Pa·s, softening point $10^{6.65}$ Pa·s, annealing point 10^{12} Pa·s, and strain point $10^{13.5}$ Pa·s. All of the foregoing are ASTM definitions except the working point.

The viscosity η of inorganic glasses (and many other viscous materials) can be described by the inverse Arrhenius equation

$$\eta = A \, \exp\!\left(\frac{Q}{RT}\right) \tag{23.2}$$

where Q, the activation energy for viscous flow, and A are empirically determined constants, R is the gas constant, and T is absolute temperature. While this equation describes the behavior reasonably well, it often does not accurately describe the behavior over a very broad range of temperature. A more accurate description is given by the empirical Vogel–Fulcher–Tammann equation, usually termed the Fulcher equation in the ceramic community (Fulcher, 1925):

$$\eta = A \, \exp\!\left(\frac{B}{T - T_0}\right) \tag{23.3}$$

where A, B, and T_0 are constants for a given glass. This equation can be derived from free-volume theory as summarized by Scherer (1992).

23.4   ELASTICITY OF INORGANIC GLASSES

At temperatures below the strain point glasses typically are elastic until brittle failure, except for limited inelastic deformation under pointed indenters, as discussed later. The high strength of glass with a pristine surface causes the elastic strain to failure to be as high as 17% for fused silica. Above a few percent strain deviations from linear elasticity become evident and can be detected at lower strains with careful measurements. Silica is found to have a higher elastic modulus at higher strains while vitreous germanium oxide and vitreous boric oxide have a lower modulus at higher strain than at low strain (Doremus, 1982). For silica the strain dependence of Young's modulus is given approximately by $E \approx E_0(1 + 3\varepsilon)$, where E_0 is the modulus in the limit of zero strain (Glaesemann et al. 1988). A more accurate polynomial approximation was given by Krause et al. (1979).

23.5   STRENGTH AND FRACTURE SURFACE ENERGY OF INORGANIC GLASSES

Silicate glass was used by Griffith (1920) in his classic work on strength of brittle materials and today is generally considered to typify brittle behavior, although some degree of local inelastic behavior can occur under concentrated loads (Marsh, 1964; Holloway, 1983). This inelastic deformation in high-silica glasses appears to consist of two different types: (1) a densification that recovers completely upon subsequent heating and (2) shear deformation along fault lines. Doremus (1982) summarizes work by Hagan on this type of shear deformation of glass under a concentrated load and describes it as consisting of faults or flow lines separated by regions in which there is only elastic strain. He points out that it resembles geologic faults and is quite different from plastic deformation in ductile crystals. Additional studies summarized by Kurkjian (1988) show that under pointed indenters a different type of behavior occurs in "anomalous" glasses (i.e., high-silica glasses) and "normal" glasses (i.e., glasses having greater than 15% network modifier). In the latter a true volume-conserving shear flow is possible. Mechanisms and theories of inelastic deformation are discussed further in a review by Argon (1980).

Many experiments indicate that glass with a normal surface usually fails from the surface and that flaws are responsible for its ordinary strength. The contemporary view is that Griffith's theory correctly describes the strength of glass having significant surface flaws. However, glass can be prepared without surface flaws (having a so-called "pristine" surface) and then has very high strength. Carefully prepared silica fibers have strengths as high as 14 GPa, which is about $E/5$, with $E = 72$ GPa (Kurkjian, 1988). Applying the Griffith–Irwin fracture mechanics with $K_{IC} = 0.81$ MPa·m$^{1/2}$ as determined from experiments with long cracks requires a crack length of 1 nm to account for a strength of 14 GPa. Such a short crack is probably outside the range of validity of the Griffith–Irwin theory and so 14 GPa is thought to be the theoretical strength of silica.

Carefully prepared silica fibers can have not only a high average strength but also a small scatter about the mean strength. Schonhorn et al. (1976) drew silica fibers about 110 μm in diameter and coated them with an epoxy–acrylate film. The resulting fibers had an average strength of 3.5 GPa and a Weibull modulus m of about 25. Improvement in manufacturing methods means that the Weibull modulus of the strength of fused silica optical fibers now routinely reaches or exceeds 100. The strength distribution is so narrow that it is not possible to distinguish between real variability in the strength and small-diameter fluctuations causing an apparent variability in strength. France et al. (1980) measured the flexural strength of silica fibers at liquid nitrogen temperature, which eliminates stress corrosion due to moisture, and measured a strain to failure of ~17%, which is close to the theoretical strength. All these results suggest that an essentially flaw-free surface can be produced and then maintained by application of polymer layers.

Several questions arise: What is the origin of flaws in normal glass surfaces? How can glass with a pristine surface be protected from strength degradation? What can be done to strengthen glasses with normal surfaces? Some of the surface flaws are evidently caused by mechanical damage. Studies using blunt indenters show a reduction of postindentation strength with increasing load on the indenter (Kurkjian, 1988). The processes taking place depend on both the cleanliness of the indenter and the initial state of the surface. Thus dust particles of small radius on the blunt indenter can be the actual indenter so that the stresses acting are greater than those calculated from the equation for the maximum stress under a ball (Lawn, 1993):

$$\sigma_{rr} = \frac{1 - 2\nu}{2} \frac{P}{\pi a^2} \tag{23.4}$$

where

$$a = 1.1 \left(\frac{PR}{E} \right)^{1/3} \tag{23.5}$$

Here P is the load on the ball and R is its radius and a is the radius of contact and σ_{rr} is the maximum tensile stress, which is in the radial direction and occurs at the contact edge, $r = a$. A question is whether the concentrated local stress is initiating a surface flaw or causing growth of a small preexisting flaw. For glasses with nonpristine surfaces (including chemically polished glass) the latter is probably the case. The tensile stress causes small preexisting flaws in nonpristine surfaces to grow stably once a threshold stress is exceeded. This threshold stress is independent of flaw size and distribution unless the number of flaws is very small. Details of the process of mechanical damage of glass surfaces are complex and not yet completely understood but certainly involve local stresses from contact sometimes combined with chemical reactions. The tensile stress caused by a ball contact on a surface can be considerably larger than that given by the above equation if there is a component of force on the ball parallel to the surface (Hamilton and Goodman, 1966).

23.6   ACHIEVING HIGH STRENGTH IN BULK GLASSES

The strength of bulk glass is typically far below the theoretical strength (usually a factor of 100 or more) unless special treatment has been used to remove surface flaws or render them less effective in initiating fracture. Removal of flaws can be done to a large extent by careful flame polishing or chemical polishing. Carefully flame-polished rods can have high strengths, as high as 1.4 GPa at liquid nitrogen temperature. However, such glass surfaces readily degraded by chemical or mechanical action and the high strength is then lost. A more useful approach in practice is to induce a compressive stress in a surface layer by thermal tempering, ion exchange, or other methods (Doremus, 1973;

TABLE 23.2   Factors by Which Glasses Can Be Strengthened by Various Treatments

Treatment	Approximate Maximum Strengthening Factor
Quench hardening (thermal tempering)	6
Ion exchange	10
Surface crystallization	17
Ion exchange and surface crystallization	22
Etching	30
Fire polishing	200
Second-phase particles	2

Source: From Doremus (1973).

Kirchner, 1979; Schaeffer, 1983; Matthewson, 1991). The maximum strengthening factors achievable by various techniques have been summarized by Doremus and are given in Table 23.2.

The term "tempered" glass derives from the process of tempering steel in that a suitable thermal treatment can produce strengthening of either (Gardon, 1980). However, the process is quite different in terms of the basic mechanisms involved. In steel, carbides are precipitated and both hardness and toughness are changed. Thermal tempering leaves glass a single-phase material with no significant change in hardness. The increase in strength of thermally tempered glass results from a compressive stress at and near the surface balanced by a tensile stress within the body. Failure of glass typically takes place by propagation of surface cracks so that compressive prestressing produced by thermal tempering must be overcome by applied stress before cracks can propagate. The process of thermal tempering causes strain energy to be stored in the glass. When failure does occur in tempered glass, this energy is released, resulting in shattering into many small fragments whose size and shape make them less dangerous than typical broken fragments of untempered glass.

The origin of a surface compressive stress caused by thermal tempering is qualitatively easy to understand. When glass is held for sufficient time above the annealing temperature, the stresses anneal out. If the glass is subsequently cooled rapidly, the temperature of the center lags behind that of the surface. As the surface drops below the annealing temperature, it can no longer undergo viscous flow, but the hotter center still can flow so that it adjusts to the thermal contraction of the surface, relieving any stresses until the center also passes through the annealing temperature. Thereafter the center and surface contract together without any significant stress developing until the surface reaches room temperature. At this point, the center continues to cool toward room temperature and attempts to contract further, causing the surface to go into compression. Stated differently, a nonuniform temperature distribution with a uniform (zero) stress distribution is converted to a nonuniform stress distribution when the temperature distribution becomes uniform. The surface compression of fully tempered glass is typically about 100 MPa (Gardon,

1980). The actual process of tempering is more complicated because the spatial and temporal distribution of temperature and stress must be treated quantitatively and because some degree of structural compaction as well as viscous flow must be taken into account. The theoretical situation is surveyed by Gardon (1980). Bartholomew and Garfinkel (1980) state that the minimum sample thickness for effective thermal tempering is about 0.3 cm and that the achievable maximum strength is typically 170 MPa, while annealed glass typically has a strength of about 55 MPa.

Chemical strengthening can produce somewhat greater strengthening. Bartholomew and Garfinkel classify chemical strengthening into three types: compound glass, ion exchange, and surface crystallization. A compound glass made of surface layers of low thermal expansion on a core of high thermal expansion can produce high compressive surface stresses but suffers from edge effects. Ion exchange of Li for Na at high temperature has produced strength as high as 482 MPa. Surface crystallization of a low expansion phase at high temperature has produced strength in excess of 690 MPa.

23.7 GLASS CERAMICS

The controlled crystallization of certain glasses can be used to produce fine-grain-sized polycrystalline ceramics with some amount of residual glassy phase that are termed glass ceramics (McMillan, 1979; Beall, 1992). High strength can be achieved if the final grain size is small. Obtaining fine grain size requires forming many nuclei from which the individual crystalline grains grow. Multiple nucleation is achieved by using a suitable nucleating agent combined with a heat treatment in an appropriate temperature range. Crystal growth is then accomplished by holding at a higher temperature.

McMillan gives typical ranges of values for the modulus of rupture as 55–70 MPa for glasses and 70–350 MPa for glass ceramics. For a Li_2O–SiO_2 glass he gives 30–50 MPa. The same base glass made into a glass ceramic by using P_2O_5 as a nucleating agent gave 110–398 MPa.

PROBLEMS

1. The viscosity of a certain glass is 10^{11} Pa·s at 600°C and 10^9 Pa·s at 660°C. Assuming it follows inverse Arrhenius behavior, Eq. (23.2), what is the activation energy for viscous flow? What is the viscosity at 720°C? Determine the working point, softening point, annealing point, and strain point for this glass.

2. Show that when a mass m is suspended from the end of a thin elastic vertical fiber of length l and radius a, the end extends by a distance δ given by

$$\delta = \frac{mgl}{\pi E a^2}$$

where E is Young's modulus. By drawing an analogy between the deformation of an elastic body and the deformation of a viscous incompressible liquid, derive an expression relating the extension rate $d\delta/dt$ to the applied weight W for a fiber which deforms by viscous flow. A glass fiber (length 20 cm, radius 62.5 μm) is heated to 700°C. When a 3-kg weight is suspended from its end, it is found to extend at a rate of 2 mm/min. What is the viscosity of the glass at this temperature?

24

MECHANICAL PROPERTIES OF POLYCRYSTALLINE CERAMICS IN GENERAL AND DESIGN CONSIDERATIONS

24.1 INTRODUCTION

Polycrystalline ceramics comprise an extensive variety of materials with a wide range of mechanical properties. In the present chapter we present a brief overview to give perspective on their broad categories and corresponding mechanical properties. In subsequent chapters we present more detailed discussions of selected important families of ceramics.

Ceramics are conveniently considered as traditional and advanced (Phelps and Wachtman, 1986). There is no absolute distinction between these two categories; a particular ceramic such as an aluminum oxide with a silicate phase may appropriately be considered as one or the other depending on the degree of property optimization that has been accomplished through control of composition and processing to achieve a special microstructure. Nevertheless, the distinction is useful up to a point. Traditional ceramics are usually made in bulk from relatively inexpensive (usually natural) starting materials and tend to have low to modest strength values and creep resistance. Advanced ceramics are usually made from more highly refined or synthetic starting materials and

often have microstructures designed to optimize mechanical or other functional properties.

24.2 MECHANICAL PROPERTIES OF POLYCRYSTALLINE CERAMICS IN GENERAL

Research intended to improve understanding of basic factors controlling mechanical properties is usually done on specimens with carefully controlled compositions and microstructures. One or at most a few features are systematically varied while other features are kept as constant as possible. The composition and microstructure are usually chosen to be as simple as possible consistent with the effect being studied. The result is that most of the basic research results available are on advanced ceramics or model materials rather than on traditional ceramics. Basic data on many advanced ceramics have been presented in previous chapters. Engineering data on mechanical behavior of conventional ceramics are available, often from manufacturers, and a sample is given here to indicate a range of properties. Table 24.1 summarizes typical ranges of elastic moduli and strength of several classes of traditional ceramics and two (electrical porcelain and capacitor electronic ceramics) that can be considered advanced.

The mechanical property data that one would like to have available for a particular ceramic ideally include a considerable list as follows: (1) elastic moduli as a function of temperature; (2) average strength and Weibull

TABLE 24.1   Some Mechanical Properties of Ceramic Materials in Common Use

Material	Young's Modulus (GPa)	Flexural Strength (MPa)	Compressive Strength (MPa)
Brick	5–20	5–10	10–25
Roof tile	5–20	8–15	10–25
Steatite	1–3	140–160	850–1000
Silica refractories	96–97% SiO_2	8–14	30–80
Fireclay refractories, 10–44% Al_2O_3	20–45	5–15	10–80
Corundum refractories, 75–90% Al_2O_3	30–120	10–150	40–200
Forsterite refractories	25–30	5–10	20–40
Magnesia refractories	30–35	8–200	40–100
Zircon refractories	35–40	80–200	30–60
Whiteware	10–20	20–25	30–40
Stoneware	30–70	20–40	40–100
Electrical porcelain	55–100	90–145	55–100
Capacitor ceramics	—	90–160	300–1000

parameters, both as a function of temperature; (3) values of toughness as a function of temperature (actually, knowledge of the full R-curve is desirable at each temperature); (4) data characterizing slow crack propagation for each temperature of possible use (these should include curves of slow crack propagation rate as a function of applied stress intensity factor for each combination of environment and temperature of interest); (5) data on cyclic fatigue behavior for a range of amplitudes of the time-varying applied stress intensity factor and the static component; and (6) creep curves and stress rupture data at high temperatures.

Apart from the elastic moduli all these data typically depend on composition and microstructure and in some cases depend strongly on them. Evidently any sensible body of mechanical property data should be accompanied by a degree of characterization for each material sufficient to determine the mechanical properties being listed. Also, some mechanical property values depend on the test method so that accepted and specified test methods should be used. Both adequate characterization and good testing are much harder to do than is generally realized. A standard system of classifying ceramics and accepted standards for the measurement of mechanical properties and behavior are thus important. The general problem was recognized (Schneider, 1989) by the Versailles Project on Advanced Materials and Standards, and a system of classifying advanced ceramics was recently established in ASTM standard C 1286-95. Activities on standardization in Europe, Japan, and the United States were summarized by Padgett (1989), and the following list of organizations developing standards and recommendations for fine ceramics was given by the International Organization for Standardization (ISO, 1994):

1. Divisional Council on Ceramics of Japanese Industrial Standards (JIS)
2. Committee C-28 on Advanced Ceramics of the American Society for Testing and Materials (ASTM Committee C-28)
3. Technical Committee on Advanced Technical Ceramics of European Committee for Standards (CEN/TC 184)
4. Versailles Project on Advanced Materials and Standards (VAMAS)
5. Cooperative Programme on Ceramics for Advanced Engines and Other Conservation Applications (Annex II) of International Energy Agency (IEA)

The Versailles Project on Advanced Materials and Standards has defined advanced ceramics as "a highly engineered, high performance, predominately non-metallic, inorganic, ceramic material having specific functional attributes" and has proposed a classification system for advanced technical ceramics in terms of four independent fields: application, chemical character (including form), processing, and property data (CIAC, 1994).

ASTM Committee C-28 on Advanced Ceramics has completed several standards, many of which are listed in Table 24.2.

TABLE 24.2   ASTM Standards Completed by Committee C-28 for Mechanical Properties

C-28.01: Mechanical Properties and Performance (Monolithic)

C 1161-02	Standard test method for flexural strength of advanced ceramics at ambient temperature
C 1198-08	Standard test method for dynamic Young's modulus, shear modulus, and Poisson's ratio for advanced ceramics by sonic resonance
C 1211-02	Standard test method for flexural strength of advanced ceramics at elevated temperatures
C 1259-01	Test method for dynamic Young's modulus, shear modulus, and Poisson's ratio for advanced ceramics by impulse excitation of vibration
C 1273-05	Test method for tensile strength of monolithic advanced ceramics at ambient temperatures
C 1291-00	Standard test method for elevated temperature tensile creep strain, creep strain rate, and creep time to failure for advanced monolithic ceramics
C 1326-03	Standard test method for Knoop indentation hardness of advanced ceramics
C 1327-03	Standard test method for Vickers indentation hardness of advanced ceramics
C 1361-01	Standard practice for constant-amplitude, axial, tension–tension cyclic fatigue of advanced ceramics at ambient temperatures
C 1366-04	Standard test method for tensile strength of monolithic advanced ceramics at elevated temperatures
C 1368-06	Standard test method for determination of slow-crack-growth parameters of advanced ceramics by constant-stress-rate flexural testing at ambient temperature
C 1421-01	Standard test methods for the determination of fracture toughness of advanced ceramics (formerly PS 070-97)
C 1424-04	Standard test method for monotonic compressive strength testing of advanced ceramics at ambient temperatures
C 1465-00	Standard test method for determination of slow-crack-growth parameters of advanced ceramics by constant-stress-rate flexural testing at elevated temperatures
C 1499-05	Standard test method for monotonic biaxial flexural strength testing of advanced ceramics at ambient temperature
C 1525-04	Standard test method for determination of thermal shock resistance for advanced ceramics by water quenching
C 1576-05	Standard test method for determination of slow-crack-growth parameters of advanced ceramics by constant-stress flexural testing stress rupture at ambient temperature
C 1624-05	Standard test method for adhesion strength and mechanical failure modes of ceramic coatings by quantitative single-point scratch testing

C-28.02: Reliability

C 1239-07	Practice for reporting uniaxial strength data and estimating Weibull distribution parameters for advanced ceramics

TABLE 24.2 (*Continued*)

C 1256-93	Standard practice for interpreting glass fracture surface features
C 1322-05	Practice for fractography and characterization of fracture origins in advanced ceramics
C 1678-07	Standard practice for fractographic analysis of fracture mirror sizes in ceramics and glasses

C-28.07: Ceramic Matrix Composites

C 1275-00	Standard practice for monotonic tensile strength testing of continuous fiber-reinforced advanced ceramics with solid rectangular cross section at ambient temperatures
C 1292-00	Standard test method for shear strength of continuous fiber-reinforced advanced ceramics at ambient temperatures
C 1337-96	Standard test method for creep and creep rupture of continuous fiber-reinforced ceramic composites under tensile loading at elevated temperature
C 1341-06	Standard test method for flexural properties of continuous fiber-reinforced advanced ceramic composites
C 1358-05	Standard test method for monotonic compressive strength testing of continuous fiber-reinforced advanced ceramics with solid rectangular cross-sectional specimens at ambient temperatures
C 1359-05	Standard test method for monotonic tensile strength testing of continuous fiber-reinforced advanced ceramics with solid rectangular cross-sectional specimens at elevated temperatures
C 1360-01	Standard practice for constant-amplitude, axial, tension–tension cyclic fatigue of continuous fiber-reinforced advanced ceramics at ambient temperatures
C 1425-05	Standard test method for interlaminar shear strength of continuous fiber-reinforced advanced ceramics at elevated temperatures
C 1468-06	Standard test method for trans-thickness tensile testing of continuous fiber-reinforced advanced ceramics at ambient temperature
C 1469-00	Standard test method for shear strength of joints in advanced ceramics at ambient temperature
C 1557-03	Standard test method for tensile strength and Young's modulus of fibers

Note: The four-digit number is the number of the standard; the two-digit number is the year last updated. Standards are reviewed and updated from time to time. These are the latest versions at the time of writing, but the reader should check for the availability of more up-to-date versions.

The Japan Institute for Standards has established standards for measurement of bending strength at room temperature, modulus of elasticity, bending strength at high temperatures, and elastic modulus at high temperature and is at work on many other tests (Japan Fine Ceramics Association, 1987).

A strong note of caution is therefore appropriate in the use of any mechanical property data from tables. With this caution in mind we mention some of the existing tabulations. An early and still useful series of reports was produced by Battelle Memorial Institute for the Air Force (Battelle, 1979).

A report on structural ceramics produced in 1984 includes data on the strength and creep rate of many then-current materials as a function of temperature (Larson and Adams, 1984). A handbook series begun by the National Physical Laboratory provides an introduction and surveys data on high-alumina ceramics (Morrell, 1985, 1987). A survey of the principal families of structural ceramics as of 1989 including silicon nitride, silicon carbide, and zirconia is available (Wachtman, 1989).

Several computerized databases on ceramics exist and continue to be developed (Munro, 1991). A database on mechanical properties of ceramics studied in the Ceramic Technology Project of the Department of Energy is maintained by Oak Ridge National Laboratory (Keyes, 1994). Emphasis is on silicon-based ceramics and transformation-toughened ceramics. Data include computerized plots and scanned microstructures.

A computerized database on structural ceramics can be obtained from the National Institutes of Standards and Technology (Munro and Hubbard, 1989; Munro et al., 1989; R. G. Munro, personal communication, 1994). Both the database and a set of programs to use it are available on a computer disk. Both research materials and commercial materials are included when either meets stringent standards of quality regarding characterization and test methods. This database includes carbides (SiC, TiC, B_4C, etc.), nitrides (Si_3N_4, AlN, BN, etc.), oxides (Al_2O_3, ZrO_2, BeO, mullite, etc.), oxynitrides (sialon, silicon oxynitride, etc.), and borides (TiB_2, ZrB_2, etc.). The property data include a full range of thermal and mechanical properties and crystallography and corrosion property data are being added.

Another computerized database on ceramics contains only data on commercial ceramics as supplied by manufacturers. This is available from the Ceramic Information Center of the American Ceramic Society (C. Schnitzer, personal communication, 1994).

24.3 DESIGN INVOLVING MECHANICAL PROPERTIES

The brittle failure typical of ceramics requires special care in design of structures or devices using ceramic components. If ceramics and their properties are taken as given, the problem becomes one of designing the device to survive within the properties available and under the service conditions. If modification of the ceramic to better serve the function required is included in consideration, the question of design of the microstructure to provide optimum properties, especially mechanical properties, becomes of interest. In either situation much of the material of the present book is pertinent to design. In a still broader consideration design can be taken to include economic factors, in which case consideration of mechanical properties still plays a role.

In the present section we briefly discuss the use of mathematical techniques for the analysis of stress and how the considerations of several earlier chapters come into play. Again we emphasize that mathematical sophistication in formal

modeling should be supplemented by commonsense consideration of practical experience.

Within the general question of design with ceramics some particular situations have been developed into a theoretical model with a mathematical framework, which is complete within its assumptions. Examples include safe life design for subcritical crack propagation and design for a desired probability of survival. How well the assumptions underlying these theoretical models fit the real behavior is always an important consideration. Knowledge of actual behavior of ceramics in comparable practical situations and judgment in application of formal treatments are evidently very important to design with ceramics.

Systematic qualitative discussions of design with ceramics including consideration of processing have been given by Creyke et al. (1982), Morrell (1987), and Richerson (1992). Design for survival from a stress distribution and statistical point of view has been reviewed in full mathematical detail by McLean and Hartsock (1989, 1991), who provide a completely worked-out example. These excellent papers present an extensive discussion that is too long and complex to summarize here; they are highly recommended to the reader concerned with design for reliability with ceramics.

Design of ceramics with improved properties through control of composition and microstructure has been mentioned by various authors but is often focused only on some particular aspect of microstructure or some particular aspect of mechanical survival. Treatments of design of ceramic microstructures from a mechanical point of view with particular consideration of toughness, strength, and reliability include Becher (1991) and Lawn (1993).

Probabilistic design of ceramic components with the assistance of computer programs is discussed by Nemeth and Gyekenyesi (1991). Their basic model deals with overall fast-fracture failure but is being modified to include subcritical crack growth. The initial step in their procedure is to use a computer program based on a finite element model. This model uses boundary conditions including loading and thermal conditions to obtain the stress distribution throughout the specimen or structure under consideration. The results from this model are input to a program called CARES (Ceramics Analysis and Reliability Evaluation of Structures) that combines three major elements: (1) linear elastic fracture mechanics, (2) extreme-value fracture statistics to obtain the characteristic flaw size distribution function, and (3) material microstructure. The CARES program first statistically analyzes the data obtained from the fracture of simple specimens such as uniaxial tensile specimens or flexural specimens. The Weibull and Batdorf material parameters are then estimated from these data. A probability of failure by fast fracture is then done by taking into account the probability of failure of each volume element (or surface element) of the specimen or structure. Nemeth and Gyekenyesi (1991) give an example of a rotating annular disk and calculate the probability of failure as a function of the angular speed in revolutions per minute. Life prediction methodologies and data for ceramic materials have recently been reviewed in a conference proceedings book (Brinkman and Duffy, 1994).

REFERENCES

Abramowitz, M., and Stegun, I. A., *Handbook of Mathematical Functions with Formulas, Graphs, and Mathematical Tables*, Applied Mathematics Series 55, National Bureau of Standards, Washington, DC, June 1964.

Adachi, K., Kato, K., and Chen, N., "Wear Map of Ceramics," *Wear*, Vols. 203–204, 291–301, 1997.

Amazigo, J. C., and Budiansky, B., "Interaction of Particulate and Transformation Toughening," *J. Mech. Phys. Solids*, Vol. 36, 581–595, 1988.

American Society for Testing and Materials (ASTM), "Biaxial Flexure Strength (Modulus of Rupture) of Ceramic Substrates," pp. 783–789 in *1978 Annual Book of ASTM Standards, Part 43, Electronics*, ANSI/ASTM F394-78, ASTM, Philadelphia, 1978.

American Society for Testing and Materials (ASTM), "Standard Test Method for Dynamic Young's Modulus, Shear Modulus, and Poisson's Ratio for Advanced Ceramics by Sonic Resonance," ASTM C 1198-91, ASTM, Philadelphia, 1991.

Anderson, O. L., "A Proposed Law of Corresponding States for Oxide Compounds," *J. Geophys. Res.*, Vol. 70, 4963–4971, 1966a.

Anderson, O. L., "Derivation of Wachtman's Equation for the Temperature Dependence of Elastic Moduli of Oxide Compounds," *Phys. Rev.*, Vol. 144, 553–557, 1966b.

Anderson, O. L., *Equations of State of Solids for Geophysics and Ceramic Science*, Oxford University Press, New York, 1995.

Andreasen, J. G., "Statistics of Brittle Failure in Multiaxial Stress States," *J. Am. Ceram. Soc.*, Vol. 76, 2933–2935, 1993.

Anstis, G. R., Chantikul, P., Lawn, B. R., and Marshall, D. B., "A Critical Evaluation of Indentation Techniques for Measuring Fracture Toughness: I, Direct Crack Measurements," *J. Am. Ceram. Soc.*, Vol. 64, 533–538, 1981.

Archard, J. F., "Contact and Rubbing of Flat Surfaces," *J. Appl. Phys.*, Vol. 24, 981–988, 1953.

Argon, A. S., "Inelastic Deformation and Fracture in Oxide, Metallic, and Polymeric Glasses," pp. 79–132 in Uhlmann, D. R., and Kreidl, N. J., Eds., *Glass Science and Technology*, Vol. 5: Elasticity and Strength in Glasses, Academic, New York, 1980.

Ashby, M. F., "First Report on Deformation Maps," *Acta Metall*, Vol. 20, 877–897, 1972.

Ashby, M. F., Abulawi, J., and Kong, M. S., "Temperature Maps for Frictional Heating," in *Dry Sliding, Tibol. Trans.*, Vol. 34, 577–587, 1991.

Ashby, M. F., Gandhi, C., and Taplin, D. M. R., "Fracture Mechanism Maps and Their Construction for F.C.C. Metals and Alloys," *Acta Metall.*, Vol. 27, 699–720, 1979.

Ashby, M. F., and Verrall, R. A., "Diffusion Accomodated Flow and Superplasticity," *Acta. Metall.*, Vol. 21, 149–163, 1973.

Ashby, M. F., and Verrall, R. A., "Micromechanisms of Flow and Fracture and Their Relevance to the Rheology of the Upper Mantle," *Philos. Trans. R. Soc. Lond.*, Vol. 288A, 59–95, 1978.

Ashkin, D., Haber, R. A., and Wachtman, J. B., "Elastic Properties of Porous Silica Derived from Colloidal Gels," *J. Am. Ceram. Soc.*, Vol. 73, 3376–3381, 1990.

Aveston, J., Cooper, G. A., and Kelly, A., "Single and Multiple Fracture," pp. 15–26 in *Proceedings of the Conference on the Properties of Fibre Composites*, National Physical Laboratory, IPC Science & Technology Press, Guildford, UK, 1971.

Badwal, S. P. S., Bannister, M. J., and Hannink, R. H. J., *Science and Technology of Zirconia*, Vol. 5, Technomic Publishing, Lancaster, PA, 1993.

Baratta, F. I., "Requirements for Flexure Testing of Brittle Materials," pp. 194–222 in Freiman, S., and Hudson, C., Eds., *Methods for Assessing the Structural Reliability of Brittle Materials*, ASTM STP 844, American Society for Testing and Materials, Philadelphia, 1982.

Bartholomew, R. F., and Garfinkel, H. M., "Chemical Strengthening of Glass," pp. 217–270 in Uhlmann, D. R., and Kreidl, N. J., Eds., *Glass Science and Technology*, Vol. 5: *Elasticity and Strength in Glasses*, Academic, New York, 1980.

Batdorf, S. B., and Chang, D. J., "On the Relation between the Fracture Statistics of Volume Distributed and Surface-Distributed Cracks," *Int. J. Fract.*, Vol. 15, 191–199, 1979.

Batdorf, S. B., and Crose, J. G., "A Statistical Theory for the Fracture of Brittle Structures Subjected to Nonuniform Polyaxial Stresses," *J. Appl. Mech.*, June, 459–464, 1974.

Batdorf, S. B., and Heinisch, H. L. Jr., "Weakest-Link Theory Reformulated for Arbitrary Fracture Criterion," *J. Am. Ceram. Soc.*, Vol. 61, 355–358, 1978.

Batdorf, S. B., and Sines, G., "Combining Data for Improved Weibull Parameter Estimation," *J. Am. Ceram. Soc.*, Vol. 63, 214–218, 1980.

Battelle Memorial Institute, *Engineering Property Data on Selected Ceramics;* Vol. 1: *Nitrides*, Vol. 2: *Carbides*, Vol. 3: *Single Oxides*, Metals and Ceramics Information Center, Battelle Columbus Division, report MCIC-HB-07, August 1979. Reprinted July 1987, American Ceramic Society, Westerville, OH.

Beall, G. H., "Design and Properties of Glass-Ceramics," *Annu. Rev. Mater. Sci.*, Vol. 22, 91–119, 1992.

Becher, P. F., "Transient Thermal Stress Behavior in ZrO_2-Toughened Al_2O_3," *J. Am. Ceram. Soc.*, Vol. 64, 37–39, 1981.

Becher, P. F., "Microstructural Design of Toughened Ceramics," *J. Am. Ceram. Soc.*, Vol. 73, 255–269, 1991.

Becher, P. F., Fuller, E. R. Jr., and Angelini, P., "Matrix-Grain-Bridging Contributions to the Toughenss of Whisker-Reinforced Ceramics," *J. Am. Ceram. Soc.*, Vol. 74, 2131–2135, 1991.

Becher, P. F., Hsueh, C.-H., Angelini, P., and Tiegs, T. N., "Toughening Behavior of Whisker-Reinforced Ceramic Matrix Composites," *J. Am. Ceram. Soc.*, Vol. 71, 1050–1061, 1988.

Becher, P. F., Hsueh, C. H., Angelini, P., and Tiegs, T. N., "Theoretical and Experimental Analysis of the Toughening Behavior of Whisker Reinforcement in Ceramic Matrix Composites," *Mater. Sci. Eng., A*, Vol. A107, 257–259, 1989.

Becher, P. F., Painter, G. S., Sun, E. Y., Hsueh, Ch. H., and Lance, M. J., "The Importance of Amorphous Films in Self-Reinforced Si_3N_4 Ceramics," *Acta Mater.*, Vol. 48, 4493–4499, 2000.

Becher, P. F., Sun, E. Y., Plucknett, K. P., Alexander, K. B., Hsueh, C.-H., Lin, H.-T., Waters, S. B., and Westmoreland, C. G., "Microstructural Design of Silicon Nitride with Improved Fracture Toughness: I, Effects of Grain Shape and Size," *J. Am. Ceram. Soc.*, Vol. 81, 2821–2830, 1998.

Becher, P. F., and Swain, M. V., "Grain-Size Dependent Transformation Behavior in Polycrystalline Tetragonal Zirconia," *J. Am. Ceram. Soc.*, Vol. 75, 493–502, 1992.

Becher, P. F., and Tiegs, T. N., "Toughening Behavior Involving Multiple Mechanisms: Whisker Reinforcement and Zirconia Toughening," *J. Am. Ceram. Soc.*, Vol. 70, 651–654, 1987.

Bennison, S. J., and Lawn, B. R., "Role of Interfacial Grain-Bridging Sliding Friction in the Crack-Resistance and Strength Properties of Nontransforming Ceramics," *Acta Metall.*, Vol. 37, 2659–2671, 1989.

Beyerle, D. S., Spearing, S. M., and Evans, A. G., "Damage Mechanisms and the Mechanical Properties of a Laminated 0/90 Ceramic/Matrix Composite," *J. Am. Ceram. Soc.*, Vol. 75, 3321–3330, 1992.

Bilde-Sørenson, J. B., Lawler, B. F., Geipel, T., Pirouz, P., Heuer, A. H., and Lagerlöf, K. P. D., "On Basal Slip and Twinning in Sapphire (α-Al_2O_3): I. Basal Slip Revisited," *Acta Mater.*, Vol. 44, 2145–2152, 1996.

Birch, J. M., Wilshire, B., and Godfrey, D. J., "Deformation and Fracture Processes During Creep of Reaction Bonded and Hot Pressed Silicon Nitride," *Proc. Br. Ceram. Soc.*, Vol. 26, 141–154, 1978.

Bleise, D., and Steinbrech, R. W., "Flat *R*-Curve from Stable Propagation of Indentation Cracks in Coarse-Grained Alumina," *J. Am. Ceram. Soc.*, Vol. 77, 315–322, 1994.

Blumenthal, W., and Evans, A. G., "High-Temperature Failure of Polycrystalline Alumina: II, Creep Crack Growth and Blunting," *J. Am. Ceram. Soc.*, Vol. 67, 751–759, 1984.

Bogatyrjov, V. A., Bubnov, M. M., Dianov, E. M., Rumyantsev, S. D., and Semjonov, S. L., "Mechanical Reliability of Polymer-Coated and Hermetically Coated Optical Fibers Based on Proof Testing," *Opt. Eng.*, Vol. 30, 690–699, 1991.

Boley, B. A., and Weiner, J. H., *Theory of Thermal Stresses*, Wiley, New York, 1960.

Born, M., and Huang, K., *Dynamical Theory of Crystal Lattices*, Oxford University Press, New York, 1954.

Bradt, R. C., Evans, A. G., Hasselman, D. P. H., and Lange, F. F., *Fracture Mechanics of Ceramics*, Vol. 5: *Concepts, Surface Flaws, Statistics, and Microcracking*, Plenum, New York, 1983a.

Bradt, R. C., Evans, A. G., Hasselman, D. P. H., and Lange, F. F., *Fracture Mechanics of Ceramics*, Vol. 6: *Concepts, Measurements, Transformations, and High-Temperature Fracture*, Plenum, New York, 1983b.

Bradt, R. C., Hasselman, D. P. H., and Lange, F. F., *Fracture Mechanics of Ceramics*, Vol. 1: *Concepts, Flaws and Fractography*, Plenum, New York, 1973a.

Bradt, R. C., Hasselman, D. P. H., and Lange, F. F., *Fracture Mechanics of Ceramics*, Vol. 2: *Microstructure, Materials, and Applications*, Plenum, New York, 1973b.

Bradt, R. C., Hasselman, D. P. H., and Lange, F. F., *Fracture Mechanics of Ceramics*, Vol. 3: *Flaws and Testing*, Plenum, New York, 1978a.

Bradt, R. C., Hasselman, D. P. H., and Lange, F. F., *Fracture Mechanics of Ceramics*, Vol. 4 : *Crack Growth and Microstructure*, Plenum, New York, 1978b.

Bradt, R. C., Hasselman, D. P. H., Munz, D., Sakai, M., and Shevchenko, V. Y., Eds., *Fracture Mechanics of Ceramics*, Vol. 10: *Fracture Fundamentals, High-Temperature Deformation, Damage, and Design*, Plenum, New York, 1992.

Bradt, R. C., and Tressler, R. E., *Fractography of Glass*, Plenum, New York, 1994.

Brennan, J. J., and Prewo, K. M., "Silicon Carbide Fiber Reinforced Glass-Ceramic Matrix Composites Exhibiting High Strength and Toughness," *J. Mater. Sci.*, Vol. 17, 2371–2383, 1982.

Brinkman, C. R., and Duffy, S. F., Eds., *Life Prediction Methodologies and Data for Ceramic Materials*, ASTM Publication Code Number 04–12010-09, American Society for Testing and Materials, Philadelphia, 1994.

Broek, D., *Elementary Engineering Fracture Mechanics*, 4th ed., Martinus Nijhoff, Dordrecht, 1987.

Brown, W. F. Jr., and Srawley, J. E. pp. 12–14 in *Plane Strain Crack Toughness Testing of High Strength Metallic Materials*, ASTM Special Technical Publication 410, American Society for Testing and Materials, Philadelphia, 1966.

Brückner-Foit, A., and Munz, D., "Statistical Analysis of Flexure Strength Data," International Energy Agency Annex II, Subtask 4, University of Karlsruhe, Karlsruhe, Germany, June 1989.

Budiansky, B., "On the Theoretical Toughness and Strength of Ceramic Composites," pp. 197–212 in Baker, C. and Karihaloo, B. L., Eds., *Fracture of Brittle Disordered Materials: Concrete, Rock, and Ceramics*. Chapman & Hall, London, 1994.

Budiansky, B., and Amazigo, J. C., "Toughening by Aligned, Frictionally Constrained Fibers," *J. Mech. Phys. Solids,*, Vol. 37, 93–109, 1989.

Budiansky, B., Amazigo, J. C., and Evans, A. G., "Small-Scale Crack Bridging and the Fracture Toughness of Particulate-Reinforced Ceramics," *J. Mech. Phys. Solids,*, Vol. 36, 167–187, 1988.

Budiansky, B., Hutchinson, J. W., and Evans, A. G., "Matrix Fracture in Fiber-Reinforced Ceramics," *J. Mech. Phys. Solids*, Vol. 34, 167–189, 1986.

Budiansky, B., Hutchinson, J. W., and Lambropoulos, J. C., "Continuum Theory of Dilatant Transformation Toughening in Ceramics," *Int. J. Solids Struct.*, Vol. 19, 337–355, 1983.

Budiansky, B., and Stump, D. M., "Theory of Ceramic/Zirconia Composites: Toughening, Strengthening and Synergism," pp. 317–325 in Vincenzini, P., Ed., *Advanced Structural Inorganic Composites*, Elsevier Science, Amsterdam, 1991.

Budiansky, B., and Truskinovsky, L., "On the Mechanics of Stress-Induced Phase Transformation in Zirconia," *J. Mech. Phys. Solids*, Vol. 41, 615–630, 1993.

Butler, E. P., and Fuller, E. R. Jr., "Ceramic-Matrix," pp. 77–108 in *Kirk–Othmer Encyclopedia of Chemical Technology*, Vol. 7: *Composite Materials*, 4th ed., Wiley, New York, 1993.

Cahn, R. W., "Twinned Crystals," *Adv. Phys.*, Vol. 3, 363–445, 1954.

Cai, H., Kalceff, M. A. S., and Lawn, B. R., "Deformation and Fracture of Mica-Containing Glass-Ceramics in Hertzian Contacts," *J. Mater. Res.*, Vol. 9, 121–129, 1994.

Campbell, G. H., Ruhle, M., Dalgleish, B. J., and Evans, A. G., "Whisker Toughening: A Comparison between Aluminum Oxide and Silicon Nitride Toughened with Silicon Carbide," *J. Am. Ceram. Soc.*, Vol. 73, 521–530, 1990.

Cannon, R. M., "Mechanical Properties of MgO and Al_2O_3," pp. 818–838 in Kingery, W. D., Ed. *Structure and Properties of MgO and Al_2O_3 Ceramics*, American Ceramic Society, Columbus, OH, 1984.

Cannon, R. M., Rhodes, W. H., and Heuer, A. H., "Plastic Deformation of Fine-Grained Alumina (Al_2O_3): I, Interface-Controlled Diffusional Creep," *J. Am. Ceram. Soc.*, Vol. 63, 46–53, 1980.

Cannon, W. R., "Transformation Toughened Ceramics for Structural Aplications," pp. 195–288 in Wachtman, J. B. Jr., Ed., *Structural Ceramics*, Vol. 29 of *Treatise on Materials Science and Technology*, edited by H. Herman, Academic, Orlando, FL, 1989.

Cannon, W. R., and Langdon, T. G., "Review: Creep of Ceramics: Part 1 Mechanical Characteristics," *J. Mater. Sci.*, Vol. 18, 1–50, 1983.

Cannon, W. R., and Langdon, T. G., "Review: Creep of Ceramics: Part 2, An Examination of Flow Mechanisms," *J. Mater. Sci.*, Vol. 23, 1–20, 1988.

Cao, H., and Thouless, M. D., "Tensile Tests of Ceramic-Matrix Composites: Theory and Experiment," *J. Am. Ceram. Soc.*, Vol. 73, 2091–2094, 1990.

Cao, H. C., Bischoff, E., Sbaizero, O., Ruhle, M., Evans, A. G., Marshall, D. B., and Brennan, J. J., "Effect of Interfaces on the Properties of Fiber-Reinforced Ceramics," *J. Am. Ceram. Soc.*, Vol. 73, 1691–1699, 1990.

Carlsson, R., Johansson, T., and Kahlman, L., *4th International Symposium on Ceramic Materials and Components for Engines*, Elsevier Applied Science, London, 1992.

Carniglia, S. C., "Reexamination of Experimental Strength-vs Grain-size Data for Ceramics," *J. Am. Ceram. Soc.*, Vol. 55, 243–249, 1972.

Carroll, D. F., and Tressler, R. E., "Accumulation of Creep Damage in a Siliconized Silicon Carbide," *J. Am. Ceram. Soc.*, Vol. 71, 472–477, 1988.

Carroll, D. F., and Tressler, R. E., "Effect of Creep Damage on the Tensile Creep Behavior of a Siliconized Silicon Carbide," *J. Am. Ceram. Soc.*, Vol. 72, 49–53, 1989.

Carroll, D. F., Wiederhorn, S. M., and Roberts, D. E., "Technique for Tensile Testing of Ceramics," *J. Am. Ceram. Soc.*, Vol. 72, 1610–1614, 1989.

Carslaw, H. S., and Jaeger, J. C., *Conduction of Heat in Solids*, 2nd ed., Oxford University Press, Oxford, 1959.

Carter, C. H. Jr., Davis, R. F., and Bentley, J., "Kinetics and Mechanisms of High-Temperature Creep in Silicon Carbide: II, Chemically Vapor Deposited," *J. Am. Ceram. Soc.*, Vol. 67, 732–740, 1984.

Chan, K. S., and Page, R. A., "Creep Damage Development in Structural Ceramics," *J. Am. Ceram. Soc.*, Vol. 76, 803–826, 1993.

Chandler, H., *Hardness Testing*, ASM International, Materials Park, OH, 1999.

Chantikul, P., Anstis, G. R., Lawn, B. R., and Marshall, D. B., "A Critical Evaluation of Indentation Techniques for Measuring Fracture Toughness: II, Strength Method," *J. Am. Ceram. Soc.*, Vol. 64, 539–543, 1981.

Chantikul, P., Bennison, S. J., and Lawn, B. R., "Role of Grain Size in the Strength and *R*-Curve Properties of Alumina," *J. Am. Ceram. Soc.*, Vol. 72, 2419–2427, 1990.

Chao, L.-Y., and Shetty, D. K., "Equivalence of Physically Based Statistical Fracture Theories for Reliability Analysis of Structural Ceramics in Multiaxial Loading," *J. Am. Ceram. Soc.*, Vol. 73, 1917–1921, 1990.

Chao, L.-Y., and Shetty, D. K., "Reliability Analysis of Structural Ceramics Subjected to Biaxial Flexure," *J. Am. Ceram. Soc.*, Vol. 74, 333–344, 1991.

Charalambides, P. G., "Steady-State Mechanics of Delamination Cracking in Laminated Ceramic-Matrix Composites," *J. Am. Ceram. Soc.*, Vol. 74, 3066–3080, 1991.

Charalambides, P. G., and Evans, A. G., "Debonding Properties of Residually Stressed Brittle-Matrix Composites," *J. Am. Ceram. Soc.*, Vol. 72, 746–753, 1989.

Charles, R. J., and Hillig, W. S., pp. 511–527 in *Symposium on Mechanical Strength of Glass and Ways of Improving It*, Florence, Italy, Sept. 25–29, 1962, Union Scientifique Continentale du Verre, Charleroi, Belgium, 1962.

Chawla, K. K., *Ceramic Matrix Composites*, Chapman & Hall, London, 1993.

Chen, C.-F., and Chuang, T.-J., "Improved Analysis for Flexural Creep with Application to Sialon Ceramics," *J. Am. Ceram. Soc.*, Vol. 73, 2366–2373, 1990.

Chen, C.-F., Wiederhorn, S. M., and Chuang, T.-J., "Cavitation Damage during Flexural Creep of SiAlON—YAG Ceramics," *J. Am. Ceram. Soc.*, Vol. 74, 1658–1662, 1991.

Chen, I. W., "Model of Transformation Toughening in Brittle Materials," *J. Am. Ceram. Soc.*, Vol. 74, 2564–2572, 1991.

Chen, I.-W., and Chiao, Y. H., "Martensitic Nucleation in ZrO_2," *Acta Metall*, Vol. 31, 1627–1638, 1983.

Chen, I. W., and Xue, S. A., "Develpoment of Superplastic Structural Ceramics," *J. Am. Ceram. Soc.*, Vol. 73, 2585–2609, 1990.

Chen, Z., and Mecholsky, J. J. Jr., "Toughening by Metallic Lamina in Nickel/Alumina Composites," *J. Am. Ceram. Soc.*, Vol. 76, 1258–1264, 1993.

Cho, C., Holmes, J. W., and Barber, J. R., "Distribution of Matrix Cracks in a Uniaxial Ceramic Composite," *J. Am. Ceram. Soc.*, Vol. 75, 316–324, 1992.

Chokshi, A. H., and Langdon, T. G., "Characteristics of Creep Deformation in Ceramics," *Mater. Sci. Technol.*, Vol. 7, 577–584, 1991.

Chou, T.-W., *Microstructural Design of Fiber Composites*, Cambridge University Press, New York, 1992.

Chou, Y.-S., and Green, D. J., "Silicon Carbide Platelet/Alumina Composites: III, Toughening Mechanisms," *J. Am. Ceram. Soc.*, Vol. 76, 1985–1992, 1993.

Christensen, R. M., and Waal, F. W., "Effective Stiffness of Randomly Oriented Fiber Composites," *J. Comp. Mater.*, Vol. 6, 518–532, 1972.

Chuang, T.-J., "A Diffusive Crack Growth Model for Creep Fracture," *J. Am. Ceram. Soc.*, Vol. 65, 93–103, 1982. "Correction," Vol. 65, 226, 1982.

Chuang, T.-J., "Estimation of Power-Law Creep Parameters from Bend Test Data," *J. Mater. Sci.*, Vol. 21, 165–175, 1986.

Chuang, T.-J., Tressler, R. E., and Minford, E. J., "On the Static Fatigue Limit at Elevated Temperatures," *Mater. Sci. Eng.*, Vol. 82, 187–195, 1986.

Chuang, T-J, and Wiederhorn, S. M., "Damage-Enhanced Creep in a Siliconized Silicon Carbide: Mechanics of Deformation," *J. Am. Ceram. Soc.*, Vol. 71, 595–601, 1988.

CIAC Newsletter, *Ceramics Information Analysis Newsletter*, Vol. 4, No. 3, CINDAS Purdue University, June 1994.

Clarke, D. R., "Microfracture in Brittle Solids Resulting from Anisotropic Shape Changes," *Acta Metall.*, Vol. 28, 913–924, 1980.

Clarke, F. J. P., "Residual Strain and the Fracture Stress—Grain Size Relationship in Brittle Solids," *Acta Metall.*, Vol. 12, 139–143, 1964.

Claussen, N., "Fracture Toughness of Al_2O_3 with an Unstabilized ZrO_2 Dispersed Phase," *J. Am. Ceram. Soc.*, Vol. 59, 49–51, 1976.

Claussen, N., "Microstructural Design of Zirconia-Toughened Ceramics," pp. 325–351 in Claussen, N., Ruhle, M., and Heuer, A., Eds., *Science and Technology of Zirconia II, Advances in Ceramics*, Vol. 12: American Ceramic Society, Westerville, OH, 1983.

Claussen, N., and Jahn, J., "Mechanical Properties of Sintered, In Situ-Reacted Mullite-Zirconia Composites," *J. Am. Ceram Soc.*, Vol. 63, 228–229, 1980.

Claussen, N., Ruhle, M., and Heuer, A., Eds., *Science and Technology of Zirconia II, Advances in Ceramics*, Vol. 12: American Ceramic Society, Westerville, OH, 1983.

Claussen, N., Steeb, J., and Pabst, R. F., "Effect of Induced Microcracking on the Fracture Toughness of Ceramics," *Am. Ceram. Soc. Bull.*, Vol. 56, 559–562, 1977.

Coble, R. L., "A Model for Boundary Diffusion Controlled Creep in Polycrystalline Materials," *J. Appl. Phys.*, Vol. 34, 1679–1682, 1963.

Coble, R. L., "Thermal Grooving in Polycrystalline Ceramics and Initiation of Brittle Failure," *J. Am. Ceram. Soc.*, Vol. 54, 59–60, 1971.

Cook, R. F., and Clarke, D. R., "Fracture Stability, *R*-Curves and Strength Variability," *Acta Metall.*, Vol. 36, 555–562, 1988.

Cook, R. F., and Lawn, B. R., "A Modified Indentation Toughness Technique," *J. Am. Ceram. Soc.*, Vol. 66, C200–C201, 1983.

Cook, R. F., Lawn, B. R., and Fairbanks, C. J., "Microstructure–Strength Properties in Ceramics: I, Effect of Crack Size on Toughness," *J. Am. Ceram. Soc.,* Vol. 68, 604–615, 1985a.

Cook, R. F., Lawn, B. R., and Fairbanks, C. J., "Microstructure–Strength Properties in Ceramics: II, Fatigue Relations," *J. Am. Ceram. Soc.*, Vol. 68, 616–623, 1985b.

Cook, R. F., Liniger, E. G., Steinbrech, R. W., and Deuerler, F., "Sigmoidal Indentation—Strength Characteristics of Polycrystalline Alumina," *J. Am. Ceram. Soc.*, Vol. 77, 303–314, 1994.

Cook, R. F., and Pharr, G. M., "Direct Observation and Analysis of Indentation Cracking in Glasses and Ceramics," *J. Am. Ceram. Soc.*, Vol. 73, 787–817, 1990.

Corman, G. S., "Creep of 6 H α-Silicon Carbide Single Crystals," *J. Am. Ceram. Soc.*, Vol. 75, 3421–3424, 1992.

Cottrell, A. H., *Dislocations and Plastic Flow in Crystals*, Clarendon, Oxford, 1953.

Courtney, T. H., *Mechanical Behavior of Materials*, McGraw-Hill, New York, 1990.

Cox, B. N., "Extrinsic Factors in the Mechanics of Bridged Cracks," *Acta Metall. Mater.*, Vol. 39, 1189–1201, 1991.

Cox, B. N., and Lo, C. S., "Load Ratio, Notch, and Scale Effects for Bridged Cracks in Fibrous Composites," *Acta Metall. Mater.*, Vol. 40, 69–80, 1992.

Cox, B. N., Marshall, D. B., and Thouless, M. D., "Influence of Statistical Fiber Strength Distribution on Matrix Cracking in Fiber Composites," *Acta Metall.*, Vol. 37, 1933–1943, 1989.

Creyke, W. E. C., Sainsbury, I. E. J., and Morrell, R., *Design with Non-Ductile Materials*, Applied Science, London, 1982.

Cui, Y. L., "Interaction of Fiber Toughening and Transformation Toughening," *J. Mech. Phys. Solids,*, Vol. 40, 1837–1850, 1992.

Cui, Y. L., and Budiansky, B., "Steady-State Matrix Cracking of Ceramics Reinforced by Aligned Fibers and Transforming Particles," *J. Mech. Phys. Solids,*, Vol. 41, 615–630, 1993.

Dalgleish, B. J., Johnson, S. M., and Evans, A. G., "High-Temperature Failure of Polycrystalline Alumina: I, Crack Nucleation," *J. Am. Ceram. Soc.*, Vol. 67, 741–750, 1984.

Darroudi, T., Tressler, R. E., and Kasprzyk, M. R., "Low-Cost Melt-Formed Siliconized Silicon Carbide Radiant Tube Materials," *J. Am. Ceram. Soc.*, Vol. 76, 173–179, 1993.

Dauskardt, R. H., James, M. R., Porter, J. R., and Ritchie, R. O., "Cyclic Fatigue-Crack Growth in a SiC-Whisker-Reinforced Alumina Ceramic Composite: Long- and Short-Crack Behavior," *J. Am. Ceram. Soc.*, Vol. 75, 759–771, 1992.

Dauskardt, R. H., Marshall, D. B., and Ritchie, R. O., "Cyclic Fatigue-Crack Propagation in Magnesia-Partially Stabilized Zirconia Ceramics," *J. Am. Ceram. Soc.*, Vol. 73, 893–903, 1990.

Davidge, R. W., "Mechanical Properties of Reaction Bonded Silicon Nitride," pp. 541–560 in Riley, F. L., Ed., *Nitrogen Ceramics*, Nordhoff International, Leyden, 1977.

Davidge, R. W., *Mechanical Behavior of Ceramics*, Cambridge University Press, New York, 1979.

Davidge, R. W., McLaren, J. R., and Tappin, B., "Strength–Probability–Time (SPT) Relationships in Ceramics," *J. Mater. Sci.*, Vol. 8, 1699–1705, 1973.

Davidge, R. W., and Tappin, G., "Thermal Shock and Fracture in Ceramics," *Trans. Br. Ceram. Soc.*, Vol. 68, 405–422, 1967.

Davidge, R. W., and Tappin, G., "Internal Strain Energy and the Strength of Brittle Materials," *J. Mater. Sci.*, Vol. 3, 297–301, 1968.

de With, G., and Wagemans, H. H. M., "Ball-on-Ring Test Revisited," *J. Am. Ceram. Soc.*, Vol. 72, 1538–1541, 1989.

Dickson, R. W., and Wachtman, J. B., "An Alumina Standard Reference Material for Resonance Frequency and Dynamic Elastic Moduli Measurement I. For Use at 25 °C," *J. Res. Natl. Bur. Stand.*, Vol. 75A, 155–162, 1971.

Dieter, G. E., *Mechanical Metallurgy*, 3rd ed., McGraw-Hill, New York, 1986.

Doremus, R. H., "Fracture and Fatigue of Glass," pp. 169–239 in Tomozawa, M., and Doremus, R. H., Eds., *Treatise on Materials Science and Technology,* Vol. 22: *Glass III*, Academic Press, New York, 1982.

Doremus, R. H., *Glass Science*, Wiley, New York, 1973.

Dörre, E., and Hubner, H., *Alumina*, Springer-Verlag, Berlin, 1984.

Duclos, R., "Direct Observation of Grain Rearrangement during Superplastic Creep of a Fine-Grained Zirconia," *J. Eur. Ceram. Soc.*, Vol. 24, 3103–3110, 2004.

Ekstrom, T., and Nygren, M., "SiAlON Ceramics," *J. Am. Ceram. Soc.*, Vol. 75, 259–276, 1992.

Evans, A. G., "The Strength of Brittle Materials Containing Second Phase Dispersions," *Philos. Mag.*, Vol. 26, 1327–1344, 1972.

Evans, A. G., "A Simple Method for Evaluating Slow Crack Growth in Brittle Materials," *Intl. J. Fract.*, Vol. 9, 267–275, 1973.

Evans, A. G., "A General Approach for the Statistical Analysis of Multiaxial Fracture," *J. Am. Ceram. Soc.*, Vol. 61, 302–308, 1978a.

Evans, A. G., "Microfracture from Thermal Expansion Anisotropy—I. Single Phase Systems," *Acta. Metall.*, Vol. 26, 1845–1853, 1978b.

Evans, A. G., "A Dimensional Analysis of the Grain-Size Dependence of Strength," *J. Am. Ceram. Soc.*, Vol. 63, 115–116, 1980.

Evans, A. G., "Perspective on the Development of High-Toughness Ceramics," *J. Am. Ceram. Soc.*, Vol. 73, 187–206, 1990.

Evans, A. G., and Blumenthal, W., "High Temperature Failure in Ceramics," pp. 423–448 in Bradt, R. C., Evans, A. G., Hasselman, D. P. H., and Lange, F. F., Eds., *Fracture Mechanics of Ceramics*, Vol. 6: Plenum, New York, 1983.

Evans, A. G., and Cannon, R. M., "Toughening of Brittle Solids by Martensitic Transformations," *Acta Metall.*, Vol. 34, 761–800, 1986.

Evans, A. G., and Charles, E. A., "Fracture Toughness Determinations by Indentation," *J. Am. Ceram. Soc.*, Vol. 59, 371–373, 1976.

Evans, A. G., and Dalgleish, B. J., "Some Aspects of the High Temperature Performance of Ceramics and Ceramic Composites," pp. 929–955 in Wilshire, B., and Evans, R. W., Eds., *Creep and Fracture of Engineering Materials and Structures*, Institute of Metals, London, 1987.

Evans, A. G., Domergue, J.-M., and Vagaggini, E., "Methodology for Relating the Tensile Constitutive Behavior of Ceramic-Matrix Composites to Constituent Properties," *J. Am. Ceram. Soc.*, Vol. 77, 1425–1435, 1994.

Evans, A. G., and Faber, K. T., "Crack-Growth Resistance of Microcracking Brittle Materials," *J. Am. Ceram. Soc.*, Vol. 64, 255–260, 1984.

Evans, A. G., and Fuller, E. R., "Crack Propagation in Ceramic Materials Under Cyclic Loading Conditions," *Metall. Trans.*, Vol. 5, 27–33, 1974.

Evans, A. G., and Heuer, A. H., "Review—Transformation Toughening in Ceramics: Martensitic Transformations in Crack-Tip Stress Fields," *J. Am. Ceram. Soc.*, Vol. 68, 241–253, 1980.

Evans, A. G., and Langdon, T. G., "Structural Ceramics," *Prog. Mater. Sci.*, Vol. 21, 171–441, 1976.

Evans, A. G., and Marshall, D. B., "The Mechanical Behavior of Ceramic Matrix Composites," *Acta Metall.*, Vol. 37, 2567–2583, 1989.

Evans, A. G., and McMeeking, R. M., "On Toughening of Ceramics by Strong Reinforcements," *Acta Metall.*, Vol. 34, 2435–2441, 1986.

Evans, A. G., and Wiederhorn, S. M., "Proof Testing of Ceramic Materials—An Analytical Basis for Failure Prediction," *Int. J. Fract.*, Vol. 10, 379–392, 1974.

Evans, R. W., and Wilshire, B., *Introduction to Creep*, Institute of Metals, London, 1993.

Faber, K. T., and Evans, A. G., "Crack Deflection Processes—I. Theory," *Acta Metall.*, Vol. 31, 565–576, 1983a.

Faber, K. T., and Evans, A. G., "Crack Deflection Processes—II. Experiment," *Acta Metall.*, Vol. 31, 577–584, 1983b.

Ferber, M. K., Jenkins, M. G., Nolan, T. A., and Yeckley, R. L., "Comparison of the Creep and Creep Rupture Performance of Two HIPed Silicon Nitride Ceramics," *J. Am. Ceram. Soc.*, Vol. 77, 657–665, 1994.

Ferber, M. K., Tennery, V., Waters, S., and Ogle, J., "Fracture Strength Characterization of Tubular Ceramic Materials Using a Simple C-ring Geometry," *J. Mater. Sci.*, Vol. 21, 2628–2632, 1980.

Fett, T., and Munz, D., "Subcritical Crack Growth of Macrocracks in Alumina with *R*-Curve Behavior," *J. Am. Ceram. Soc.*, Vol. 75, 958–963, 1992.

Fett, T., and Munz, D., "Lifetime Prediction for Ceramic Materials Under Constant and Cyclic Load," pp. 161–174 in Brinkman, C. R., and Duffy, S. F., Eds., *Life Prediction Methodologies and Data for Ceramic Materials* ASTM STP 1201, American Society for Testing and Materials, Philadelphia, 1994.

Firestone, R. F., and Heuer, A. H., "Creep Deformation of $0°$ Sapphire," *J. Am. Ceram. Soc.*, Vol. 59, 24–29, 1976.

Flinn, B. D., Lo, C. S., Zok, F. W., and Evans, A. G., "Fracture Resistance Characteristics of a Metal-Toughened Ceramic," *J. Am. Ceram. Soc.*, Vol. 76, 369–375, 1993.

France, P. W., Paradine, M. J., Reeve, M. H., and Newns, G. R., "Liquid Nitrogen Strengths of Coated Optical Glass Fibres," *J. Mater. Sci.*, Vol. 15, 825–830, 1980.

Frank, F. C., "Crystal Dislocations—Elementary Concepts and Definitions," *Phil. Mag.*, Vol. 42, 809–819, 1951.

Fréchette, V. D., *Failure Analysis of Brittle Materials*, American Ceramic Society, Westerville, OH, 1990.

Frenkel, J., "Zur Theorie der Elastizitatsgrenze und der Festigkeit kristallinischerKorper," *Z. Phys.*, Vol. 37, 572–609, 1926.

Frost, H. J., and Ashby, M. F., *Deformation-Mechanism Maps—The Plasticity and Creep of Metals and Ceramics*, Pergamon, New York, 1982.

Fulcher, G. S., "Analysis of Recent Measurements of the Viscosity of Glasses," *J. Am. Ceram. Soc.*, Vol. 8, 339–355, 1925.

Fuller, E. R. Jr., Freiman, S. W., Quinn, J. B., Quinn, G. D., and Carter, W. C., "Fracture Mechanics Approach to the Design of Glass Aircraft Windows: A Case Study," *Proc. Soc. Photo-Opt. Instrum. Eng.*, Vol. 2286, 419–430, 1994.

Fuller, E. R., Lawn, B. R., and Cook, R. F., "Theory of Fatigue for Brittle Flaws Originating from Residual Stress Concentrations," *J. Am. Ceram. Soc.*, Vol. 66, 314–321, 1983.

Fuller, E. R. Jr., Wiederhorn, S. M., Ritter, J. E. Jr., and Oates, P. B., "Proof Testing of Ceramics, Part 2 Theory," *J. Mater. Sci.*, Vol. 15, 2282–2295, 1980.

Fullman, R. L., "Measurement of Particle Sizes in Bodies," *Trans. AIME.*, Vol. 197, 447–452, 1953.

Gandhi, C., and Ashby, M. F., "Fracture Mechanism Maps for Materials which Cleave: F.C.C., B.C.C. and H.C.P. Metals and Ceramics," *Acta Metall.*, Vol. 27, 1565–1602, 1979.

Gardon, R., "Thermal Tempering of Glass," pp. 145–216 in Uhlmann, D. R., and Kreidl, N. J., Eds., *Glass Science and Technology*, Vol. 5: *Elasticity and Strength in Glasses*, Academic, New York, 1980.

Garvie, R. C., Hannink, R. H., and Pascoe, R. T., "Ceramic Steel?" *Nature (London)*, Vol. 285(5537), 703–704, 1975.

Garvie, R. C., Hannink, R. H. J., and Pascoe, R. T., "Ceramic Materials," U.S. Patent 4,067,745, 1978.

Garvie, R. C., Hannink, R. H. J., and Urbani, C., *Ceramurgia Int.*, Vol. 6, 19–24, 1980.

Geipel, T., Bilde-Sørensen, J. B., Lawler, B. F., Pirouz, P., Lagerlöf, K. D. P., and Heuer, A. H., "On Basal Slip and Basal Twinning in Sapphire (α-Al$_2$O$_3$): III. HRTEM of the Twin/Matrix Interface," *Acta Mater.*, Vol. 44, 2165–2174, 1996.

Geipel, T., Lagerlof, K. P. D., and Heuer, A. H., "Zonal Dislocation Mechanism for Rhombohedral Twinning in Sapphire (α-Al$_2$O$_3$)," *Acta Metal. et Mater.*, Vol. 42, 1367–1372, 1994.

Geller, R. F., and Yavorsky, P. J., "Effects of Some Oxide Additions on the Thermal Length Changes of Zirconia," *J. Res. Natl. Bur. Stand.*, Vol. 35, 87–110, 1945.

Giannakopoulos, A. E., and Breder, K., "Synergism of Toughening Mechanisms in Whisker-Reinforced Ceramic-Matrix Composites," *J. Am. Ceram. Soc.*, Vol. 74, 194–202, 1991.

Gibson, L. J., and Ashby, M. F., *Cellular Solids—Structure and Properties*, Pergamon, New York, 1988.

Gilman, J. J., "The Strength of Ceramic Crystals," p. 240 in Klingsberg, C., Ed., *The Physics and Chemistry of Ceramics*, Gordon & Breach, New York, 1963.

Gilman, J. J., and Johnston, W. G., "Behavior of Individual Dislocations in Strain-Hardened LiF Crystals," *J. Appl. Phys.*, Vol. 31, 687–692, 1960.

Glaesemann, G. S., Gulati, S. T., and Helfinstine, J. D., "Effect of Strain and Surface Composition on Young's Modulus of Optical Fibers," p. 48 in *Digest of Conference on Optical Fiber Communication*, 1988 OSA Technical Digest Series, Optical Society of America, Washington, DC, 1988.

Gordon, R. S., "Mass Transport in the Diffusional Creep of Ionic Solids," *J. Am. Ceram. Soc.*, Vol. 56, 147–152, 1973.

Gordon, R. S., "Ambipolar Diffusion and Its Application to Diffusional Creep," pp. 445–464 in Cooper, A. R., and Heuer, A. H., Eds., *Mass Transport Phenomena in Ceramics*, Plenum, New York, 1975.

Grain, C. F., "Phase Relations in the ZrO_2–MgO System," *J. Am. Ceram. Soc.*, Vol. 50, 288–290, 1967.

Grathwohl, G., "Creep and Fracture of Hot-Pressed Silicon Nitride with Natural and Artificial Flaws," pp. 565–577 in Wilshire, B., and Owen, R., Eds., *Creep and Fracture of Engineering Materials and Structures*, Pineridge, Swansen, UK, 1984.

Green, D. J., "Critical Microstructures for Microcracking in Al_2O_3–ZrO_2 Composites," *J. Am. Ceram. Soc.*, Vol. 65, 610–614, 1982.

Green, D. J., Hannink, R. H. J., and Swain, M. V., *Transformation Toughening of Ceramics*, CRC Press, Boca Raton, FL, 1989.

Green, D. J., Nicholson, P. S., and Embury, G. H., "Fracture of a Brittle Particulate Composite—Part 2 Theoretical Aspects," *J. Mater. Sci.*, Vol. 14, 1657–1661, 1979.

Griffith, A. A., "The Phenomena of Rupture and Flow in Solids," *Philos. Trans. R. Soc. Lond.,* Vol. A221, 163–198, 1920.

Griffith, A. A., "The Theory of Rupture," p. 55 in Biezeno, C. B., and Burgers, J. M., Eds., *Proceedings of the First International Congress on Applied Mechanics*, ICTAM, Delft, Netherlands, 1924.

Groves, G. W., and Kelly, A., "Independent Slip Systems in Crystals," *Philos. Mag.*, Vol. 8, 877–887, 1963.

Gui, F., Li, M., and Reece, M. J., "Role of Crack-Bridging Ligaments in the Cyclic Fatigue Behavior of Alumina," *J. Am. Ceram. Soc.*, Vol. 75, 2976–2984, 1992.

Guiberteau, F., Padture, N. P., Cai, H., and Lawn, B. R., "Indentation Fatigue: A Simple Cyclic Hertzian Test for Measuring Damage Accumulation in Polycrystalline Ceramics," *Philos. Mag.,* Vol. A68, 1003–1016, 1993.

Guiberteau, F., Padture, N. P., and Lawn, B. R., "Effect of Grain Size on Hertzian Contact Damage in Alumina," *J. Am. Ceram. Soc.*, Vol. 77, 1825–1831, 1994.

Hall, E. O., "The Deformation and Ageing of Mild Steel: III Discussion of Results," *Proc. Phys. Soc.,* Vol. B64, 747–753, 1951.

Hamilton, G. M., "Explicit Equation for Stresses Beneath a Sliding Spherical Contact," *Proc. Inst. Mech. Engrs.*, Vol. 1976, 53–58, 1983.

Hannink, R. H. J., "Microstructural Development of Sub-Eutectoid Aged MgO–ZrO_2 Alloys," *J. Mater. Sci.*, Vol. 18, 457–470, 1983.

Hannink, R. H. J., and Swain, M. V., "Magnesia—Partially Stabilized Zirconia: The Influence of Heat Treatment on Thermomechanical Properties," *J. Aust. Ceram. Soc.*, Vol. 18, 53–62, 1983.

Hannink, R. H. J., and Swain, M. V., "Progress in Transformation Toughening of Ceramics," pp. 359–408 in Flemings, M. C., Wachtman, J. B. Jr., Kaufmann, E. N., and Giordmaine, J. A., Eds., *Annual Review of Materials Science, Keynote Topic: Structural Materials*, Vol. 24, Annual Reviews, Palo Alto, CA, 1994.

Hashida, T., and Li, V. C., "New Development of the J-Based Fracture Testing Technique for Ceramic-Matrix Composites," *J. Am. Ceram. Soc.*, Vol. 77, 1553–1561, 1994.

Hashin, Z., and Rosen, B. W., "The Elastic Moduli of Fiber-Reinforced Materials," *J. Appl. Mech.*, Vol. 33, 223, 1964.

Hasselman, D. P. H., "On the Porosity Dependence of the Elastic Moduli of Polycrystalline Refractory Materials," *J. Am. Ceram. Soc.*, Vol. 45, 452, 1962.

Hasselman, D. P. H., "Unified Theory of Thermal Shock Fracture Initiation and Crack Propagation in Brittle Ceramics," *J. Am. Ceram. Soc.*, Vol. 52, 600–604, 1969.

Hasselman, D. P. H., "Thermal Stress Crack Stability and Propagation in Severe Thermal Environments," pp. 89–103 in Kriegel, W. W., and Palmour, Hayne III., Eds., *Ceramics in Severe Environments*, Plenum, New York, 1971.

Hasselman, D. P. H., "Thermal Stress Resistance of Engineering Ceramics," *Mater. Sci. Eng.*, Vol. 71, 251–264, 1985.

Hasselman, D. P. H., and Fulrath, R. M., "Proposed Fracture Theory of Dispersion-Strengthened Glass Matrix," *J. Am. Ceram. Soc.*, Vol. 49, 68–72, 1966.

Hasselman, D. P. H., and Venkateswaran, A., "Effect of Cracks on Mechanisms and Kinetics of Creep Deformation of Brittle Ceramics," pp. 525–546 in Tressler, R. E., and Bradt, R. C., Eds., *Deformation of Ceramic Materials*, Vol. 2, Plenum, New York, 1984.

Hayhurst, D., Leckie, F. A., and Evans, A. G., "Component Design-Based Model for Deformation and Rupture of Tough Fiber-Reinforced Metal and Ceramic-Matrix Composites," *Proc. R. Soc. Lond. A*, Vol. A434, 369–381, 1991.

Hazzledine, P. M., "Work Hardening in Easy Glide," *Can. J. Phys.*, Vol. 45, 765–775, 1967.

He, M.-Y., and Hutchinson, J. W., "Kinking of a Crack Out of an Interface," *J. Appl. Mech., (Trans. ASME)*,, Vol. 56, 270–278, 1989.

Hearmon, R. F. S., *An Introduction to Applied Anisotropic Elasticity*, Oxford University Press, New York, 1961.

Hearmon, R. F. S., *The Elastic Constants of Nonpiezo Crystals*, Landolt–Bornstein Tables, New Series, Group III, Vol. I, Springer-Verlag, Berlin, 1966.

Herring, C., "Diffusional Viscosity of a Polycrystalline Solid," *J. Appl. Phys.*, Vol. 21, 437–445, 1950.

Hertzberg, R. W., *Deformation and Fracture Mechanics of Engineering Materials*, 3rd ed., Wiley, New York, 1989.

Heuer, A. H., "Deformation Twinning in Corundum," *Philos. Mag.*, Vol. 13, 379–393, 1966.

Heuer, A. H., "Transformation Toughening in ZrO_2-Containing Ceramics," *J. Am. Ceram. Soc.*, Vol. 70, 689–698, 1987.

Heuer, A. H., Claussen, N., Kriven, W. M., and Ruhle, W. M., "Stability of Tetragonal ZrO_2 Particles in Ceramic Matrices," *J. Am. Ceram. Soc.*, Vol. 65, 642–650, 1982.

Heuer, A. H., and Hobbs, L. W., *Science and Technology of Zirconia, Advances in Ceramics*, Vol. 3. American Ceramic Society, Westerville, OH, 1981.

Heuer, A. H., Lange, F. F., Swain, M. V., and Evans, A. G., "Transformation Toughening: An Overview," *J. Am. Ceram. Soc.*, Vol. 69, i–iv, 1986.

Heuer, A. H., Lanteri, V., and Dominguez-Rodriguez, A., "High Temperature Precipitation Hardening of Y_2O_3 Partially-Stabilized ZrO_2 (Y-PSZ) Crystals," *Acta Metall.*, Vol. 37, 559–567, 1989.

Heuer, A. H., Tighe, N. J., and Cannon, R. M., "Plastic Deformation of Fine-Grained Alumina (Al_2O_3): II, Basal Slip and Nonaccommodated Grain-Boundary Sliding," *J. Am. Ceram. Soc.*, Vol. 63, 53–58, 1980.

Hillig, W. S., "A Methodology for Estimating the Mechanical Properties of Oxides at High Temperatures," *J. Am. Ceram. Soc.*, Vol. 76, 129–138, 1993.

Hillig, W. S., and Charles, R. J., "Surfaces, Stress-dependent Surface Reactions and Strength," pp. 682–705 in Zackay, V. F., Ed., *High Strength Materials*, Wiley, New York, 1965.

Hirth, J. P., and Lothe, J., *Theory of Dislocations*, Ch. 12, pp. 376–397, McGraw-Hill, New York, 1968.

Hirth, J. P., and Lothe, J., *Theory of Dislocations*, 2nd ed., Wiley, New York, 1982.

Hockey, B. J., "Plastic Deformation of Aluminum Oxide by Indentation and Abrasion," *J. Am. Ceram. Soc.*, Vol. 54, 223–231, 1971.

Hockey, B. J., and Lawn, B. R., "Electron Microscopy of Microcracking about Indentations in Aluminum Oxide and Silicon Carbide," *J. Mater. Sci.*, Vol. 10, 1275–1284, 1975.

Hockey, B. J., and Wiederhorn, S. M., "Effect of Microstructure on the Creep of Siliconized Silicon Carbide," *J. Am. Ceram. Soc.*, Vol. 75, 1822–1830, 1992.

Hollenberg, G. W., Terwilliger, G. R., and Gordon, R. S., "Calculation of Stresses and Strains in Four-Point Bending Creep Tests," *J. Am. Ceram. Soc.*, Vol. 54, 196–199, 1971.

Holloway, D. G., "A Look at the History of Glass Strength," pp. 1–18 in Kurkjian, C. R., Ed., *Strength of Inorganic Glass*, NATO Conference Series, VI, *Materials Science*, Vol. 11, Plenum, New York, 1983.

Hori, S., Yoshimura, M., and Somiya, S., "Strength–Toughness Relations in Sintered and Isostatically Hot-Pressed ZrO_2-Toughened Al_2O_3," *J. Am. Ceram. Soc.*, Vol. 69, 169–172, 1986.

Hsu, S. M., and Shen, M. C., "Ceramic Wears Maps," *Wear*, Vol. 200, 154–175, 1996.

Hu, X.-Z., and Mai, Y.-W., "Crack-Bridging Analysis for Alumina Ceramics Under Monotonic and Cyclic Loading," *J. Am. Ceram. Soc.*, Vol. 75, 848–893, 1992.

Hu, X.-Z., Mai, Y.-W., and Cotterell, B., "A Statistical Theory of Time-Dependent Fracture for Brittle Materials," *Philos. Mag. A*, Vol. 58, 299–324, 1988.

Hüebner, H., and Jillek, W., "Sub-Critical Crack Extension and Crack Resistance in Polycrystalline Alumina," *J. Mater. Sci.*, Vol. 12, 117–125, 1977.

Hull, D., *Introduction to Dislocations*. Pergamon, New York, 1965.

Hull, D., *Fractography*, Cambridge University Press, Cambridge, 1999.

Hull, D., and Bacon, D. J., *Introduction to Dislocations*, 3rd ed., Pergamon, New York, 1982.

Hutchinson, J. W., *On Steady Quasistatic Crack Growth*, Harvard University Report, DEAP S-8, Division of Applied Sciences, Cambridge, MA, 1974.

Hutchinson, J. W., "Crack Tip Shielding by Micro-Cracking in Brittle Solids," *Acta Metall*, Vol. 35, 1605–1619, 1987.

Ingel, R. P., Lewis, D., Bender, B. A., and Rice, R. W., "Physical, Microstructural, and Thermomechanical Properties of ZrO_2 Single Crystals," pp. 408–414 in Claussen, N., Ruhle, M., and Heuer, A., Eds., *Science and Technology of Zirconia II, Advances in Ceramics*, Vol. 12, American Ceramic Society, Westerville, OH, 1983.

Inglis, C. E., "Stresses in a Plate Due to the Presence of Cracks and Sharp Corners," *Trans. Inst. Nav. Archit.*, Vol. 55, 219–230, 1913.

International Organization for Standardization, ISO Doc. ISO/TC 206, Strategic Policy Statement, April 4, 1994.

Irwin, G. R., "Analysis of Stresses and Strains Near the End of a Crack Traversing a Plate," *J. Appl. Mech.*, Vol. 24, 361–364, 1957.

Islam, R. A., "Structure-Property Relationship in High-Tension Ceramic Insulator Fired at High Temperature," *Mater. Sci. Eng. B*, Vol. B106, 132–140, 2004.

Iwasa, M., and Bradt, R. C., "Fracture Toughness of Single-Crystal Alumina," pp. 767–779 in Kingery, W. D., Ed., *Structure and Properties of MgO and Al_2O_3 Ceramics*, American Ceramic Society, Columbus, OH, 1984.

Jack, K. H., and Wilson, W. I., "Ceramics Based on the Si-Al-O-N and Related Systems," *Nature (London)*, Vol. 238, 28–29, 1977.

Jackman, E. A., and Roberts, J. P., "Strength of Single-Crystal and Polycrystalline Corundum," *Philos. Mag.*, Vol. 46, 809–811, 1955.

Jacobs, D. S., and Chen, I.-W., "Mechanical and Environmental Factors in the Cyclic and Static Fatigue of Silicon Nitride," *J. Am. Ceram. Soc.*, Vol. 77, 1153–1161, 1994.

Jakus, K., "Proof Testing—A Tool for Quality Assurance," pp. 195–204 in Boyd, D. C., and MacDowell, J. F., Eds., *Commercial Glasses, Advances in Ceramics*, Vol. 18, American Ceramic Society, Westerville, OH, 1986.

Jakus, K., Coyne, D. C., and Ritter, J. E. Jr., "Analysis of Fatigue Data for Lifetime Prediciton for Ceramic Materials," *J. Mater. Sci.*, Vol. 13, 2071–2080, 1978.

Jakus, K., and Ritter, J. E. Jr., "Lifetime Prediction for Ceramics Under Random Loads," *Res. Mechan.*, Vol. 2, 39–52, 1981.

Jakus, K., Ritter, J. E. Jr., Service, T., and Sonderman, D., "Evaluation of Bimodal Concurrent Flaw Distributions," *J. Am. Ceram. Soc.*, Vol. 64, C-174–C-175, 1981.

Jakus, K., Ritter, J. E. Jr., and Sullivan, J. M., "Dependency of Fatigue Predictions on the Form of the Crack Velocity Equation," *J. Am. Ceram. Soc.*, Vol. 64, 372–374, 1981.

Jakus, K., and Wiederhorn, S. M., "Creep Deformation of Ceramics in Four-Point Bending," *J. Am. Ceram. Soc.*, Vol. 71, 832–836, 1988.

Japan Fine Ceramics Association, *FC Annual Report for Overseas Readers*, JFCA, Tokyo, Japan, 1987.

Jayatilaka, A. de S., *Fracture of Engineering Brittle Materals*. Applied Science Publishers, London, 1979.

Jimenez-Melendo, M., Dominguez-Rodriguez, A, Bravo-Leon, A. "Superplastic Flow of Fine-Grained Yttria-Stabilized Zirconia Polycrystals: Constitutive Equation and Deformation Machanisms," *J. Amer. Ceram. Soc.*, Vol. 81, 2761–2776, 1998.

Johnson, C. A., "Fracture Statistics of Multiple Flaw Distributions," pp. 365–386 in Bradt, R. C., Evans, A. G., Hasselman, D. P. H., and Lange, F. F., Eds., *Fracture Mechanics of Ceramics*, Vol. 5: *Surface Flaws, Statistics, and Microcracking*, Plenum, New York, 1983.

Johnson, C. A., and Tucker, W. T., "Weibull Estimators for Pooled Fracture Data," pp. 250–264 in Brinkman, C. R., and Duffy, S. F., Eds., *Life Prediction Methodologies and Data for Ceramic Materials*, ASTM STP 1201, American Society for Testing and Materials, Philadelphia, 1993.

Johnson, K. L., *Contact Mechanics*, Cambridge University Press, Cambridge, 1985.

Johnson, S. M., Dalgleish, B. J., and Evans, A. G., "High-Temperature Failure of Polycrystalline Alumina: III, Failure Times," *J. Am. Ceram. Soc.*, Vol. 67, 759–763, 1984.

Johnston, W. G., and Gilman, J. J., "Dislocation Velocities, Dislocation Densities, and Plastic Flow in Lithium Fluoride Crystals," *J. Appl. Phys.*, Vol. 30, 129–144, 1959.

Kajihara, K., Yoshizawa, Y., and Sakuma, T., "Superplastic Behavior of a Fine-Grained Yttria-Stabilized, Tetragonal Zirconia Polycrystal," *Acta Metall. Mater.*, Vol. 38, 1121, 1990.

Karandikar, P. G., Chou, T.-W., and Parvizi-Majidi, A., "Mechanical Properties," in Lehman, R. L., technical editor, El-Rahaiby, S. K., managing editor, and Wachtman, J. B., American Ceramic Society editor, *Handbook on Continuous Fiber Reinforced Ceramic Matrix Composites*, jointly published by Purdue University and the American Ceramic Society, Westerville, OH, 1996.

Kato, K., and Adachi, K., "Wear of Ceramics," *Wear*, Vol. 253, 1097–1104, 2002.

Kelly, A., and MacMillan, N. H., *Strong Solids*, 3rd ed., Oxford University Press, Oxford, 1986.

Kendall, K., Alford, N. M., and Birchall, J. D., "Weibull Modulus of Toughened Ceramics," *Mater. Res. Soc. Symp. Proc.*, Vol. 78, 181–187, 1987.

Keyes, B. L. P., "Ceramic Technology Project Database: September 1993 Summary Report," Oak Ridge National Laboratory Report ORNL/M-3155, Jan. 1994. Also personal communication with the author, Aug. 1994.

Kim, B. N., Hiraga, K., Morita, K., and Sakka, Y., "A High-Strain-Rate Superplastic Ceramic," *Nature*, Vol. 413, 288–291, 2001.

King, A. G., and Yavorsky, P. J., "Stress Relief Mechanisms in Magnesia- and Yttria-Stabilized Zirconia," *J. Am. Ceram. Soc.*, Vol. 51, 38–42, 1968.

Kirchner, H. P., *Strengthening of Ceramics—Treatments, Tests and Design Applications*. Marcel Dekker, New York, 1979.

Kirchner, H. P., and Conway, J. C. Jr., "Criteria for Crack Branching in Cylindrical Rods: I, Tension," *J. Am. Ceram. Soc.*, Vol. 70, 413–418, 1987a.

Kirchner, H. P., and Conway, J. C. Jr., "Criteria for Crack Branching in Cylindrical Rods: II, Flexure," *J. Am. Ceram. Soc.*, Vol. 70, 419–425, 1987b.

Kirchner, H. P., and Kirchner, J. W., "Fracture Mechanics of Fracture Mirrors," *J. Am. Ceram. Soc.*, Vol. 62, 198–202, 1979.

Kittel, C., *Introduction to Solid State Physics*. Wiley, New York, 1968.

Knehans, R., and Steinbrech, R., "Memory Effect of Crack Resistance during Slow Crack Growth in Notched Al_2O_3 Bend Specimens," *J. Mater. Sci. Lett.*, Vol. 1, 327–329, 1982.

Knowles, K. M., and Yang, X. F., "Mathematical Modeling of the Strength and Toughness of Unidirectional Fiber-Reinforced Ceramics," *Ceram. Eng. Sci. Proc.*, Vol. 12, 1387–1388, 1991.

Knudsen, F. P., "Effect of Porosity on Young's Modulus of Alumina," *J. Am. Ceram. Soc.*, Vol. 45, 94–95, 1962.

Kovar, D., and Readey, M. J., "Role of Grain Size in Strength Variability of Alumina," *J. Am. Ceram. Soc.*, Vol. 77, 1928–1938, 1994.

Krause, J. T., Testardi, L. R., and Thurston, R. N., "Deviations from Linearity in the Dependence of Elongation upon Force for Fibres of Simple Glass Formers and of Glass Optical Lightguides," *Phys. Chem. Glasses*, Vol. 20, 135–139, 1979.

Krause, R. F. Jr., "Rising Fracture Toughness from the Bending Strength of Indented Alumina Beams," *J. Am. Ceram. Soc.*, Vol. 71, 338–343, 1988.

Kriven, W. M., "Possible Alternative Transformation Tougheners to Zirconia: Crystallographic Aspects," *J. Am. Ceram. Soc.*, Vol. 71, 1021–1030, 1988.

Krohn, D. A., and Hasselman, D. P. H., "Relation of Flaw Size to Mirror in the Fracture of Glass," *J. Am. Ceram. Soc.*, Vol. 54, 411, 1971.

Kronberg, M. L., "Plastic Deformation of Single Crystals of Sapphire: Basal Slip and Twinning," *Acta Metall*, Vol. 5, 507–524, 1957.

Kronberg, M. L., "Dynamical Flow Properties of Single Crystals of Sapphire: I," *J. Am. Ceram. Soc.*, Vol. 45, 274–279, 1962.

Kurkjian, C. R., *Strength of Inorganic Glass*, NATO Conference Series VI, *Materials Science*, Vol. 11, Plenum, New York, 1983.

Kurkjian, C. R., "Mechanical Stability of Oxide Glasses," *J. Non-Crystall. Solids*, Vol. 102, 71–81, 1988.

Kuszyk, J. A., and Bradt, R. C., "Influence of Grain Size on Effects of Thermal Expansion Anisotrophy on $MgTi_2$," *J. Am. Ceram. Soc.*, Vol. 56, 420–423, 1973.

Lagerlof, K. P. D., Heuer, A. H., Castaing, J., Riviere, J. P., and Mitchell, T. E., "Slip and Twinning in Sapphire (α-Al_2O_3)," *J. Am. Ceram. Soc.*, Vol. 77, 385–397, 1994a.

Lagerlof, K. P. D., Lawlor, B. F., Geipel, T., Pirouz, P., Heuer, A. H., and Bilde-Sorensen, J. B., "Basal Twinning in Sapphire (α-Al_2O_3)," *Solid State Phenom.*, Vol. 35/36, 607–612, 1994b.

Lamon, J., "Statistical Approaches to Failure for Ceramic Reliability Assessment," *J. Am. Ceram. Soc.*, Vol. 71, 106–112, 1988.

Langdon, T. G., "Deformation Mechanism Maps for Applications at High Temperatures," *Ceramurgia Int.*, Vol. 6, 11–88, 1980.

Langdon, T. G., "The Mechanical Properties of Superplastic Materials," *Metall. Trans. A,* Vol. 13A, 689–701, 1982.

Langdon, T. G., "Superplastic Ceramics," *JOM*, Vol. 42, 8–13, 1990.

Langdon, T. G., "The Physics of Superplastic Deformation," *Mater. Sci. Eng.,* Vol. A137, 1–11, 1991a.

Langdon, T. G. "Superplasticity: An Historical Perspective," pp. 3–12 in Hori, S., Tokizane, M., and Furushiro, N., Eds., *Superplasticity in Advanced Materials*, Japan Society for Research on Superplasticity, Tokyo, 1991b.

Langdon, T. G., "The Role of Grain Boundaries in High Temperature Deformation," *Mater. Sci. Eng.,* Vol. A166, 67–79, 1993a.

Langdon, T. G., "The Mechanical Properties of Superplastic Materials," pp. 265–281 in Vincenzini, P., Ed., *Innovative Materials, Prospects and Problems in a Competitive Industrial Context*, Techna, Faenza, 1993b.

Langdon, T. G., "An Evaluation of the Strain Contributed by Grain Boundary Sliding in Superplasticity," *Mater. Sci. Eng.*, Vol. A174, 225–230, 1994a.

Langdon, T. G., "A Unified Approach to Grain Boundary Sliding in Creep and Superplasticity," *Acta Metall. Mater.*, Vol. 42, 2437–2443, 1994b.

Langdon, T. G., and Mohamed, F. A., ''Deformation Mechanism Maps for Ceramics,'' *J. Mater. Sci.*, Vol. 11, 317–327, 1976.

Langdon, T. G., and Mohamed, F. A., ''Deformation Mechanism Maps for Ceramics,'' *J. Mater. Sci.*, Vol. 13, 473–482, 1978.

Lange, F. F., ''The Interaction of Crack Front with Second-Phase Dispersion,'' *Philos. Mag.*, Vol. 22, 983–992, 1970.

Lange, F. F., ''Fracture Energy and Strength Behavior of a Sodium Borosilicate Glass–Al_2O_3 Composite System,'' *J. Am. Ceram. Soc.*, Vol. 54, 614–620, 1971.

Lange, F. F., ''Transformation Toughening, Part 4 Fabrication, Fracture Toughness and Strength of Al_2O_3–ZrO_2 Composites,'' *J. Mater. Sci.*, Vol. 17, 247–254, 1982a.

Lange, F. F., ''Transformation Toughening, Part 5 Effect of Temperature and Alloy on Fracture Toughness,'' *J. Mater. Sci.*, Vol. 17, 255–263, 1982b.

Lange, F. F., ''Powder Processing Science and Technology for Increased Reliability,'' *J. Am. Ceram. Soc.*, Vol. 71, 3–15, 1989.

Larson, D. C., and Adams, J. W., ''Property Screening and Evaluation of Ceramic Turbine Materials,'' Air Force Materials Laboratory Report AFWAL-TR-83-4141, Apr. 1984.

Larson, D. R., Coppola, J. A., Hasselman, D. P. H., and Bradt, R. C., ''Fracture Toughness and Spalling Behavior of High-Al_2O_3 Refractories,'' *J. Am. Ceram. Soc.*, Vol. 57, 417–421, 1974.

Lathabai, S., Rödel, J., and Lawn, B. R., ''Cyclic Fatigue from Frictional Degradation at Bridging Grains in Alumina,'' *J. Am. Ceram. Soc.*, Vol. 74, 1340–1348, 1991.

Lawn, B. R., *Fracture of Brittle Solids*, Cambridge University Press, Cambridge, 1993.

Lawn, B. R., Evans, A. G., and Marshall, D. B., ''Elastic/Plastic Indentation Damage in Ceramics: The Median/Radial Crack System,'' *J. Am. Ceram. Soc.*, Vol. 63, 574–581, 1980.

Lawn, B. R., Freiman, S. W., Baker, T. L., Cobb, D. D., and Gonzalez, A. C., ''Study of Microstructural Effects in the Strength of Alumina Using Controlled Flaws,'' *J. Am. Ceram. Soc.*, Vol. 67, 667–669, 1984.

Lawn, B. R., Padture, N. P., Cai, H., and Guiberteau, F., ''Making Ceramics Ductile,'' *Science*, Vol. 263, 1114–1116, 1994a.

Lawn, B. R., Padture, F., Guiberteau, F., and Cai, H., ''A Model for Microcrack Initiation and Propagation Beneath Hertzian Contacts in Polycrystalline Ceramics,'' *Acta Metall. Mater.*, Vol. 42, 1683–1693, 1994b.

Lawn, B. R., and Wilshaw, T. R., ''Indentation Fracture; Principles and Applications,'' *J. Mater. Sci.*, Vol. 10, 1049–1081, 1975.

Lehman, R. L., technical editor, El-Rahaiby, S. K., managing editor, and Wachtman, J. B., American Ceramic Society editor, *Handbook on Continuous Fiber Reinforced Ceramic Matrix Composites*, jointly published by Purdue University and the American Ceramic Society, Westerville, OH, 1996.

Lewis, D. III, ''Continuous Fiber Reinforced Ceramic Matrix Composites: A Historical Review,'' in Lehman, R. L., technical editor, El-Rahaiby, S. K., managing editor, and Wachtman, J. B., American Ceramic Society editor, *Handbook on Continuous Fiber Reinforced Ceramic Matrix Composites,* jointly published by Purdue University and the American Ceramic Society, Westerville, OH, 1996.

Lewis, D., and Rice, R. W., "Thermal Shock Fatigue of Monolithic Ceramics and Ceramic–Ceramic Particulate Composites," *Ceram. Eng. Sci. Proc.*, Vol. 2, 712–718, 1981.

Li, H., and Bradt, R. C., "The Microhardness Indentation Size-Load Effect (ISE) in Hard Ceramic Materials," *J. Hard Mater*, Vol. 3, 403–419, 1992.

Li, C.-W., and Yamanis, J., "Super-Tough Silicon Nitride with *R*-Curve Behavior," *Ceram. Eng. Sci. Proc.*, Vol. 10, 632–645, 1989.

Li, Y.-Z., Wang, C., Chan, H. M., and Harmer, M. P., "Codoping of Alumina to Enhance Creep Resistance," *J. Am. Ceram. Soc.*, Vol. 82, 1497–1509, 1999.

Liu, S.-Y., and Chen, I. W., "Fatigue of Yttria-Stabilized Zirconia: II, Crack Propagation Fatigue Striations, and Short-Crack Behavior," *J. Am. Ceram. Soc.*, Vol. 74, 1206–1216, 1991.

Lutz, E. H., Claussen, N., and Swain, M. V., "K^R-Curve Behavior of Duplex Ceramics," *J. Am. Ceram. Soc.*, Vol. 74, 11–18, 1991a.

Lutz, E. H., Swain, M. V., and Claussen, N., "Thermal Shock Behavior of Duplex Ceramics," *J. Am. Ceram. Soc.*, Vol. 74, 19–24, 1991b.

Ma, Y., and Langdon, T. G., "An Examination of the Implications of Void Growth in Submicrometer and Nanocrystalline Structures," *Mater. Sci. Eng.*, Vol. A168, 225–230, 1993.

Mackenzie, J. K., "The Elastic Constants of a Solid Containing Spherical Holes," *Proc. Phys. Soc.*, Vol. B63, 2, 1950.

Maehara, Y., and Langdon, T. G., "Review Superplasticity in Ceramics," *J. Mater. Sci.*, Vol. 25, 2275–2286, 1990.

Mai, Y.-W., and Lawn, B. R., "Crack-Interface Grain Bridging as a Fracture Resistance Mechanism in Ceramics: II, Theoretical Fracture Mechanics Model," *J. Am. Ceram. Soc.*, Vol. 70, 289–294, 1987.

Mandelbrot, B. B., *The Fractal Geometry of Nature*, W. H. Freeman, New York, 1982.

Mann, A. B., "Nanomechanical Properties of Solid Surfaces & Thin Films," pp. 575–622 in Bhushan, B., Ed., *An Introduction to Nanotribology and Nanomechanics*, Springer-Verlag, Berlin, 2005.

Marsh, D. M., "Plastic Flow in Glass. *Proc. R. Soc.*, London, Vol. A279, 420–435, 1964; "Plastic Flow and Fracture of Glass," *Proc. R. Soc.*, London, Vol. A282, 33–43, 1964.

Marshall, D. B., "An Improved Biaxial Flexure Test for Ceramics," *Am. Ceram. Soc. Bull.*, Vol. 59, 551–553, 1980.

Marshall, D. B., "Strength Characteristics of Transformation-Toughened Zirconia," *J. Am. Ceram. Soc.*, Vol. 69, 173–180, 1986.

Marshall, D. B., Cox, B. N., and Evans, A. G., "The Mechanics of Matrix Cracking in Brittle-Matrix Fiber Composites," *Acta Metall*, Vol. 33, 2013–2021, 1985.

Marshall, D. B., and Evans, A. G., "Failure Mechanisms in Ceramic-Fiber/Ceramic-Matrix Composites," *J. Am. Ceram. Soc.*, Vol. 68, 225–231, 1985.

Marshall, D. B., and Evans, A. G., "The Tensile Strength of Uniaxially Reinforced Ceramic Fiber Composites," pp. 1–15 in Bradt, R. C., Evans, A. G., Lange, F. F., and Hasselman, D. P. H., Eds., *Fracture Mechanics of Ceramics*, Vol. 7, Plenum, New York, 1986.

Marshall, D. B., and Evans, A. G., "The Influence of Residual Stress on the Toughness of Reinforced Brittle Materials," *Mater. Forum*, Vol. 11, 304–312, 1988.

Marshall, D. B., Evans, A. G., and Drory, M. D., "Transformation Toughening in Ceramics," pp. 289–307 in Bradt, R. C., Evans, A. G., Hasselman, D. P. H., and Lange, F. F., Eds., *Fracture Mechanics of Ceramics*, Vol. 6: *Measurements, Transformations, and High-Temperature Fracture*, Plenum, New York, 1983.

Marshall, D. B., Lawn, B. R., and Chantikul, P., "Residual Stress Effects in Sharp-Contact Cracking: I. Indentation Fracture Mechanics, II. Strength Degradation," *J. Mater. Sci.*, Vol. 14, 2110–1012, 2225–2235 1979.

Martinez-Fernandez, J., Jimenez-Melendo, M., Dominguez-Rodriguez, A., Cordier, P., Lagerlof, K. P. D., and Heuer, A. H., "High-Temperature Precipitation Hardening in Y_2O_3 Partially Stabilized ZrO_2 (Y-PSZ) Single Crystals—III. Effect of Solute Composition and Orientation on the Hardening," *Acta Metall. Mater.*, Vol. 43, 2469–2484, 1995.

Martinez-Fernandez, J., Jimenez-Melendo, M., Dominguez-Rodriguez, A., Lagerlof, K. P. D., and Heuer, A. H., "High-Temperature Precipitation Hardening in Y_2O_3 Partially-Stabilized ZrO_2 (Y-PSZ) Single Crystals—II. A Quantitative Model for the Hardening," *Acta Metall. Mater.*, Vol. 41, 3171–3180, 1993.

Matsui, M., Ishida, Y., Soma, T., and Oda, I., "Ceramic Turbocharger Rotor Design Considering Long Term Durability," pp. 1043–1062 in Bunk, W., and Hausner, H., Eds., *Ceramic Materials and Components for Engines—Proceedings of the Second International Symposium*, Verlag Deutsche Keramische Gesellschaft, Bad Honnef, 1966.

Matsuo, Y., and Sasaki, H., "Effect of Grain Size on Microcracking in Lead Titanate Ceramics," *J. Am. Ceram. Soc.*, Vol. 49, 229–230, 1966.

Matthewson, M. J., "Design Practices for Glass and Glass Fibers," pp. 741–745 in Schneider, S. J., volume chairman, *Engineered Materials Handbook*, Vol. 4: Ceramics and Glasses, ASM International, Materials Park, OH, 1991.

Matthewson, M. J., *Optical Fiber Mechanical Testing Techniques, Critical Reviews of Optical Science and Technology*, Vol. CR50, Society of Photo-Optical Instrumentation Engineers, Bellingham, WA, 1994.

Matthewson, M. J., "Strength-Probability-Time Diagrams Using Power Law and Exponential Kinetics Models for Fatigue," pp. 61.9301-1–11 in Limberger, H. G., and Matthewson, M. J., Eds., *Reliability of Optical Fiber Components, Devices, Systems, and Networks*, Vol. 3, Proceedings of SPIE, Vol. 6193, SPIE, Bellingham, WA, 2006.

Matthewson, M. J., Kurkjian, C. R., and Gulati, S. T., "Strength Measurement of Optical Fibers by Bending," *J. Am. Ceram. Soc.*, Vol. 69, 815–821, 1986.

McCartney, L. N., "Mechanics of Matrix Cracking in Brittle-Matrix Fiber-Reinforced Composites," *Proc. R. Soc. Lond.*, Vol. A409, 329–350, 1987.

McColm, I. J., *Ceramic Hardness*, Plenum, New York, 1990.

McLean, A. F., and Hartsock, D. L., "Design with Structural Ceramics," pp. 27–98 in Wachtman, J. B. Jr., Ed., *Structural Ceramics*, Academic, New York, 1989.

McLean, A. F., and Hartsock, D. L., "An Overview of the Ceramic Design Process," pp. 676–689 in Schneider, S. J., volume chairman, *Engineered Materials Handbook*, Vol. 4: *Ceramics and Glasses*, ASM International, Materials Park, OH, 1991.

McMeeking, R. M., and Evans, A. G., "Mechanics of Transformation-Toughening in Brittle Materials," *J. Am. Ceram. Soc.*, Vol. 65, 242–246, 1982.

McMillan, P. W., *Glass Ceramics*, 2nd ed., Academic, New York, 1979.

Mecholsky, J. J., "Fracture Surface Analysis of Optical Fibers," pp. 663–668 in Schneider, S. J., volume chairman, *Engineered Materials Handbook*, Vol. 4: *Ceramics and Glass*, ASM International, Materials Park, OH, 1991.

Mecholsky, J. J., private communication, 1995.

Mecholsky, J. J. Jr., and Freiman, S. W., "Relationship between Fractal Geometry and Fractography," *J. Am. Ceram. Soc.*, Vol. 74, 3136–3138, 1991.

Mecholsky, J. J., Freiman, S. W., and Morey, S. M., "Fractographic Analysis of Optical Fibers," *Am. Ceram. Soc. Bull.*, Vol. 56, 1016–1017, 1977.

Mecholsky, J. J., Gonzalez, A. C., and Freiman, S. W., "Fractographic Analysis of Delayed Failure in Soda-Lime Glass," *J. Am. Ceram. Soc.*, Vol. 62, 577–580, 1979.

Mecholsky, J. J., and Powell, S. R. Jr., *Fractography of Ceramic and Metal Failures*, ASTM STP 827 American Society for Testing and Materials, Philadelphia, 1984.

Mecholsky, J. J., Rice, R. W., and Freiman, S. W., "Prediction of Fracture Energy and Flaw Size in Glasses from Measurements of Mirror Size," *J. Am. Ceram. Soc.*, Vol. 57, 440–443, 1974.

Michalske, T. A., "Quantitative Fracture Surface Analysis," pp. 652–662 in Schneider, S. J., volume chairman, *Engineered Materials Handbook*, Vol. 4: *Ceramics and Glass*, ASM International, Materials Park, OH, 1991.

Michalske, T. A., and Freiman, S. W., "A Molecular Mechanism for Stress Corrosion in Vitreous Silica," *J. Am. Ceram. Soc.*, Vol. 66, 284–288, 1983.

Monkman, F. C., and Grant, N. J., "An Empirical Relationship between Rupture Life and Minimum Creep Rate in Creep-Rupture Tests," *Proc. ASTM*, Vol. 56, 593, 1956.

Monroe, L. D., and Smyth, J. R., "Grain Size Dependence of Fracture Energy of Y_2O_3," *J. Am. Ceram. Soc.*, Vol. 61, 538–539, 1978.

Morrell, R., *Handbook of Properties of Technical & Engineering Ceramics Part 1 An Introduction for the Engineer and Designer*, Her Majesty's Stationery Office, London, 1985.

Morrell, R., *Handbook of Properties of Technical & Engineering Ceramics Part 2 Data Reviews Section 1 High-Alumina Ceramics*, Her Majesty's Stationery Office, London, 1987.

Morrell, R., and Ashbee, K. H. G., "High Temperature Creep of Lithium Zinc Silicate Glass-Ceramics, Part I, General Behavior and Creep Mechanisms," *J. Mater. Sci.*, Vol. 8, 1253–1270, 1973.

Morscher, G. N., and DiCarlo, J. A., "A Simple Test for Thermomechanical Evaluation of Ceramic Fibers," *J. Am. Ceram. Soc.*, Vol. 75, 136–140, 1992.

Munro, R. G., "Ceramic Properties Database Systems," pp. 690–693 in Schneider, S. J., volume chairman, *Engineered Materials Handbook*, Vol. 4: *Ceramics and Glasses*, ASM International, Materials Park, OH, 1991.

Munro, R. G., and Hubbard, C. R., "Property Database for Gas-Fired Applications of Ceramics," *Ceram. Bull.*, Vol. 68, 2084–2090, 1989.

Munro, R. G., Hwang, F. Y., and Hubbard, C. R., "The Structural Ceramics Database: Technical Foundations," *J. Res. Natl. Inst. Stand. Tech.*, Vol. 94, 37–47, 1989.

Munz, D., Bubsey, R. T., and Shannon, J. L. Jr., "Fracture Toughness Determination of Al_2O_3 Using Four-Point-Bend Specimens with Straight-Through and Chevron Notches," *J. Am. Ceram. Soc.*, Vol. 63, 300–305, 1980.

Munz, D., Himsolt, G., and Eschweiler, J., "Effect of Stable Crack Growth on Fracture Toughness Determination for Hot-Pressed Silicon Nitride at Elevated Temperatures," pp. 69–84 in Freiman, S. W., and Fuller, E. R., Ed., *Fracture Mechanics Methods for Ceramics, Rocks, and Concrete*, ASTM Special Technical Publication 745, American Society for Testing and Materials, Philadelphia, 1981.

Murakami, Y., *Stress Intensity Factors Handbook*, Pergamon, New York, 1986.

Nabarro, R. R. N., p. 75 in *Report of a Conference on Strength of Solids*, Physical Society, London, 1948.

Nabarro, R. R. N., Ed., *Dislocations in Solids*, Vols. 1–8, North-Holland, Amsterdam, 1979–1989.

Nemeth, N. N., and Gyekenyesi, J. P., "Probabilistic Design of Ceramic Components with the NASA CARES Computer Program," pp. 700–708 in Schneider, S. J., volume chairman, *Engineered Materials Handbook*, Vol. 4: *Ceramics and Glasses*, ASM International, Materials Park, OH, 1991.

Newman, J. C. Jr., and Raju, I. S., "An Empirical Stress-Intensity Factor Equation for the Surface Crack," *Eng. Fract. Mech.*, Vol. 15, 185–192, 1981.

Nieh, T. G., and Wadsworth, J., "Superplastic Behavior of a Fine-Grained Yttria-Stabilized, Tetragonal Zirconia Polycrystal," *Acta Metall. Mater.*, Vol. 38, 1121, 1990a.

Nieh, T. G., and Wadsworth, J., "Superplastic Ceramics," *Annu. Rev. Mater. Sci.*, Vol. 20, 117–140, 1990b.

Nielsen, L. F., "Elastic Properties of Two-Phase Materials," *Mater. Sci. Eng.*, Vol. 52, 39–62, 1982.

Nielsen, L. F., "Elasticity and Damping of Porous Materials and Impregnated Materials," *J. Am. Ceram. Soc.*, Vol. 67, 93–98, 1984.

Nishida, T., Hanaki, Y., and Pezzotti, G., "Effect of Notch-Root Radius on the Fracture Toughness of a Fine-Grained Alumina," *J. Am. Ceram. Soc.*, Vol. 77, 606–608, 1994.

Nishida, T., Hanaki, Y., and Pezzotti, G., "Effect of Notch-Root Radius on the Fracture Toughness of a Fine-Grained Alumina," *J. Am. Ceram. Soc.*, Vol. 77, 606–608, 2006.

Nixon, R. D., and Davis, R. F., "Diffusion-Accommodated Grain Boundary Sliding and Dislocation Glide in the Creep of Sintered Alpha Silicon Carbide," *J. Am. Ceram. Soc.*, Vol. 75, 1786–1795, 1992.

Nye, J. F., *Physical Properties of Crystals*, Oxford University Press, New York, 1985.

O'Brian, M. H., and Coon, D. N., "Mechanistic Analysis of Time-Dependent Failure of Oxynitride Glass-Joined Silicon Nitride below 1000°C," *J. Am. Ceram. Soc.*, Vol. 74, 103–108, 1991.

Oliver, W. C., and Pharr, G. M., "An Improved Technique for Determining Hardness and Elastic Modulus Using Load and Displacement Sensing Indentation Experiments," *J. Mater Res.*, Vol. 7, 1564–1580, 1992.

Orowan, E., "Fracture and Strength of Solids," *Rep. Prog. Phys.*, Vol. 12, 185–232, 1949.

Ostrowski, T., and Rödel, J., "Evolution of Mechanical Properties of Porous Alumina during Sintering and Hot Pressing," *J. Am. Ceram. Soc.*, Vol. 82, 3080–3086, 1999.

Padgett, G. C., "Review of the National and International Standardization of Advanced Ceramics," pp. 363–370 in de With, G., Terpstra, R. A., and Metselaar, R., Eds., *Euro-Ceramics*, Vol. 3, Elsevier Applied Science, London, 1989.

Palaniswamy, A., and Knauss, W. G., "On the Problem of Crack Extension in Brittle Solids Under General Loading," *Mech. Today*, Vol. 4, 87–148, 1978.

Paluszny, A., Proceedings of the Workshop on Ceramics for Advanced Heat Engines, Orlando, FL, Jan. 24–26, 1977, pp. 231–246 in *Energy Research and Development Report*, ERDA Rep. CONF-770110, 1977.

Pasto, A. E., Van Schalkwyk, W. C., and Mahoney, F. M., "Creep Behavior of Yttria- and Alumina-Doped Silicon Nitride," pp. 776–785 in Tennery, V. J., Ed., *Third International Symposium on Ceramic Components and Materials for Engines*, American Ceramic Society, Westerville, OH, 1989.

Petch, N. J., "The Cleavage Strength of Polycrystals," *J. Inst. Sci. Technol.*, Vol. 173, 25–28, 1953.

Petch, N. J., "Metallographic Aspects of Fracture," p. 351 in Liebowitz, H., Ed., *Fracture*, Vol. 173, Academic, New York, 1968.

Peterson, I. M., and Tien, T.-Y., "Effect of the Grain Boundary Thermal Expansion Coefficient on the Fracture Toughness in Silicon Nitride," *J. Am. Ceram. Soc.*, Vol. 78, 2345–2352, 1995.

Phani, K. K., and Niyogi, S. K., "Young's Modulus of Porous Brittle Materials," *J. Mater. Sci.*, Vol. 22, 257–263, 1987.

Phelps, G. W., and Wachtman, J. B., "Ceramics General Survey," pp. 1–42, in *Ullmann's Encyclopedia of Industrial Chemistry*, Vol. A6, 1–42, Wiley-VCH, Weinheim, Germany, 1986.

Poirier, J.-P., *High Temperature Deformation Processes in Metallurgy, Ceramics, and Minerals*, Cambridge University Press, Cambridge, 1985.

Porter, D. L., and Heuer, A. H., "Microstructural Development in MgO–Partially Stabilized Zirconia (Mg-PSZ)," *J. Am. Ceram. Soc.*, Vol. 62, 298–305, 1979.

Prewo, K. M., "Fiber-Reinforced Ceramics: New Opportunities for Composite Materials," *Ceram. Bull.*, Vol. 68, 395–400, 1989.

Prewo, K. M., and Brennan, J. J., "High Strength Silicon Carbide Fibre Reinforced Glass Matrix Composites," *J. Mater. Sci.*, Vol. 15, 463, 1980.

Pyzik, A. J., and Carroll, D. F., "Technology of Self-Reinforced Silicon Nitride," *Annu. Rev. Mater. Sci.*, Vol. 24, 189–214, 1994.

Quinn, G. D., "Review of Static Fatigue in Silicon Nitride and Silicon Carbide," *Ceram. Eng. Sci. Proc.*, Vol. 3, 77–98, 1982.

Quinn, G. D., *Static Fatigue in High-Performance Ceramics*, ASTM Special Technical Testing Publication 844, American Society for Testing and Materials, Philadelphia, 1984a. Report of a conference in San Francisco in 1982.

Quinn, G. D., "Fracture Mechanism Map for Hot-Pressed Silicon Nitride," *Ceram. Eng. Sci. Proc.*, Vol. 5, 596–602, 1984b.

Quinn, G. D., "Fracture Mechanism Maps for Silicon Nitride," pp. 931–939 in Bunk, W., and Hausner, H., Eds., *Ceramic Materials and Components for Engines—Proceedings of the Second International Symposium*, Verlag Deutsche Keramische Gesellschaft, Bad Hannef, 1986.

Quinn, G. D., "Delayed Failure of a Commercial Vitreous Bonded Alumina," *J. Mater. Sci.*, Vol. 22, 2309–2316, 1987.

Quinn, G. D., "Fracture Mechanism Maps for Advanced Structural Ceramics," *J. Mater. Sci.*, Vol. 25, 4361–4376, 1990.

Quinn, G. D., *Fractography of Ceramics and Glasses*, NIST Special Publication 960-17. National Institute of Standards and Technology, Washington, DC, 2007.

Quinn, G. D., and Braue, W. R., "Fracture Mechanism Maps for Advanced Structural Ceramics, Part 2, Sintered Silicon Nitride," *J. Mater. Sci.*, Vol. 25, 4377–4392, 1990.

Quinn, G. D., and Gettings, R. J., "Fracture Toughness by the Surface Crack in Flexure (SCF) Method: Results of the Vamas Round Robin," *Ceram. Eng. Sci. Proc.*, Vol. 15, 846–855, 1994.

Quinn, G. D., and Morrell, R., "Design Data for Engineering Ceramics: A Review of the Flexure Test," *J. Am. Ceram. Soc.*, Vol. 74, 2037–2066, 1991.

Quinn, J. B., and Quinn, G. D., "Indentation Brittleness in Ceramics, a Fresh Approach," *J. Mater. Sci.*, Vol. 32, 4331–4346, 1997.

Quinn, G. D., Swab, J. J., and Slavin, M., *Fractography and Characterization of Fracture Origins in Advanced Structural Ceramics*, Military Handbook 790, U.S. Government Printing Office, Washington, DC, July 1, 1992.

Rainforth, W. M., "The Wear Behavior of Oxide Ceramics, a Review," *J. Mater. Sci.*, Vol. 39, 6705–6721, 2004.

Raj, R., "Separation of Cavitation-Strain and Creep-Strain During Deformation," *J. Am. Ceram. Soc.*, Vol. 63, C-46, 1982.

Raj, R., and Dang, C. H., "De-Adhesion by Growth of Penny-Shaped Bubbles in an Adhesive Layer," *Philos. Mag.*, Vol. 32, 909–922, 1975.

Ramakrishnan, N., and Arunachalam, V. S., "Effective Elastic Moduli of Porous Ceramic Materials," *J. Am. Ceram. Soc.*, Vol. 76, 2745–2752, 1993.

Rao, S. S., Tsakalakos, T., and Cannon, W. R., "Stress Distributions in Ceramic Composites Containing Faceted Inclusions," *J. Am. Ceram. Soc.*, Vol. 75, 1807–1817, 1992.

Rawson, H., *Glasses and Their Applications*, Institute of Metals, London, 1991.

Read, W. T. Jr., *Dislocations in Crystals*, McGraw-Hill, New York, 1953.

Reece, M., and Guiu, F., "Indentation Fatigue of High-Purity Alumina in Fluid Environments," *J. Am. Ceram. Soc.*, Vol. 74, 148–154, 1991.

Reichl, A., and Steinbrech, R. W., "Determination of Crack-Bridging Forces in Alumina," *J. Am. Ceram. Soc.*, Vol. 71, C299–C301, 1988.

Rice, J. R., "A Path-Independent Integral and the Approximate Analysis of Strain Concentration by Notches and Cracks." *J. Appl. Mech.*, *Trans. ASME*, Vol. 35, 379–386, 1968a.

Rice, J. R., "Mathematical Analysis in the Mechanics of Fracture," pp. 192–308 in Liebowitz, H., Ed., *Fracture, An Advanced Treatise*, Vol. 2, Academic, New York, 1968b.

Rice, J. R., "Elastic Fracture Mechanics Concepts for Interfacial Cracks," *J. Appl. Mech. (Trans. ASME)*, Vol. 55, 98–103, 1988.

Rice, R. J., Wu, C. C., and Borchelt, F., "Hardness-Grain-Size Relations in Ceramics," *J. Am. Ceram. Soc.*, Vol. 77, 2539–2554, 1994.

Rice, R. W., "Microstructural Dependence of Mechanical Properties," p. 199 in McCrone, R. K., Ed., *Treatise on Materials Science and Technology*, Vol. 11: Properties and Microstructure, Academic, New York, 1977.

Rice, R. W., "Mechanisms of Toughening in Ceramic Matrix Composites," *Ceram. Eng. Sci. Proc.*, Vol. 2, 661–701, 1981.

Rice, R. W., "Evaluating Porosity Parameters for Porosity-Property Relations," *J. Am. Ceram. Soc.*, Vol. 76, 1801–1808, 1993.

Rice, R. W., "Mechanically Reliable Ceramics," *J. Phys. Chem. Solids*, Vol. 45, 1033–1050, 1984.

Rice, R. W., "Ceramic Matrix Composite Toughening Mechanisms: An Update," *Ceram. Eng. Sci. Proc.*, Vol. 6, 589–607, 1985.

Rice, R. W., "Grain Size and Porosity Dependence of Ceramic Fracture Energy and Toughness," *J. Mater Sci.*, Vol. 31, 1969–1983, 1996.

Rice, R. W., *Mechanical Properties of Ceramics and Composites: Grain and Particle Effects*, Marcel Dekker, New York, 2000.

Rice, R. W., "Effects of Environment and Temperature on Ceramic Tensile Strength–Grain Size Relations," *J. Mater. Sci.*, Vol. 32, 3071–3087, 1997.

Rice, R. W., Freiman, S. W., and Becher, P. F., "Grain-Size Dependence of Fracture Energy in Ceramics: I, Experiment," *J. Am. Ceram. Soc.*, Vol. 64, 345–350, 1981.

Richerson, D. W., "Failure Analysis of Ceramics," pp. 755–757 in Metals Handbook, Vol. 11, 9th ed., ASM International, Materials Park, OH, 1986.

Richerson, D. W., *Modern Ceramic Engineering*, 2nd ed., Marcel Dekker, New York, 1992.

Riley, F. L., *Nitrogen Ceramics*. Nordhoff International, Leyden, 1977.

Ripperger, A., and Davids, N., "Critical Stresses in a Circular Ring," *Trans. Am. Soc. Civ. Eng.*, Vol. 112, 619–628, 1947.

Ritchie, R. O., and Dauskardt, R. H., "Cyclic Fatigue of Ceramics: A Fracture Mechanics Approach to Subcritical Crack Growth and Life Prediction," *J. Ceram. Soc. Japan Int. Ed.*, Vol. 99, 1009–1023, 1991.

Ritter, J. E. Jr., "Engineering Design and Fatigue Failure of Brittle Materials," pp. 667–686 in Bradt, R. C., Hasselman, D. P. H., and Lange, F. F., Eds., *Fracture Mechanics of Ceramics*, Vol. 4: *Crack Growth and Microstructure*, Plenum, New York, 1978.

Ritter, J. E., Jr., Bandyopadhyay, N., and Jakus, K., "Statistical Reproducibility of the Crack Propagation Parameter N in Dynamic Fatigue Tests," *J. Am. Ceram. Soc.*, Vol. 62, 542–543, 1979.

Ritter, J. E., Jr., Bandyopadhyay, N., and Jakus, K., "Statistical Reproducibility of the Dynamic and Static Fatigue Experiments," *Bull. Am. Ceram. Soc.*, Vol. 60, 798–806, 1981.

Ritter, J. E., Jr., Jakus, E., Batakis, A., and Bandyopadhyay, N., "Appraisal of Biaxial Strength Testing," *J. Non-Crystal. Solids*, Vol. 38/39, 419–424, 1980.

Rodel, J., "Interaction between Crack Deflection and Crack Bridging," *J. Eur. Ceram. Soc.*, Vol. 10, 143–150, 1992.

Rödel, J., Kelly, J. F., and Lawn, B. R., "In Situ Measurements of Bridged Crack Interfaces in Scanning Electron Microscope," *J. Am. Ceram. Soc.*, Vol. 73, 3313–3318, 1990.

Ruhle, M., Claussen, N., and Heuer, A. H., "Transformation and Microcrack Toughening as Complementary Processes in ZrO_2 Toughened Al_2O_3," *J. Am. Ceram. Soc.*, Vol. 69, 195, 1986.

Russo, C. J., Harmer, M. P., Chan, H. M., and Miller, G. A., "Design of a Laminated Ceramic Composite for Improved Strength and Toughness," *J. Am. Ceram. Soc.*, Vol. 75, 3396–3400, 1992.

Sakai, M., and Bradt, R. C., "Fracture Toughness Testing of Brittle Materials," *Int. Mater. Rev.*, Vol. 38, 53–78, 1993.

Sakai, M., and Kouzou, Y., "Numerical Fracture Analysis of Chevron-Notched Specimens: I, Shear Correction Factor, k," *J. Am. Ceram. Soc.*, Vol. 66 No. 5, 371–375, 1983; "Numerical Fracture Analysis of Chevron-Notched Specimens II, Stability Condition for Crack Growth," *J. Am. Ceram. Soc.*, Vol. 66, No. 5, 376–379, 1983.

Sambell, R. A., Bowen, D., and Phillips, D. C., "Carbon Fiber Composites with Ceramic and Glass Matrices, Part I, Discontinuous Fibers," *J. Mater. Sci.*, Vol. 7, 663–675, 1972.

Sbaizero, O., and Evans, A. G., "Tensile and Shear Properties of Laminated Ceramic Matrix Composites," *J. Am. Ceram. Soc.*, Vol. 69, 481–486, 1986.

Schaeffer, H. A., "Thermal and Chemical Strengthening of Glass—Review and Outlook," pp. 469–483 in Kurkjian, C. R., Ed., *Strength of Inorganic Glass*, NATO Conference Series VI, *Materials Science*, Vol. 11, Plenum, New York, 1983.

Scherer, G. W., "Editorial Comments on a Paper by Gordon S. Fulcher," *J. Am. Ceram. Soc.*, Vol. 75, 1060–1062, 1992.

Schneider, S. J., "Advanced Ceramics—What's in a Name," *ASTM Standardization News*, pp. 28–30, 1989.

Schneider, S. J., volume chairman, *Engineered Materials Handbook*, Vol. 4, *Ceramics and Glasses*, ASM International, Materials Park, OH, 1991.

Schonhorn, H., Kurkjian, C. R., Jaeger, R. E., Vazirani, H. N., Albarino, R. V., and DiMarcello, F. V., "Epoxy-Acrylate-Coated Fused Silica Fibers with Tensile Strengths 500 ksi ($3.5\,GN/m^2$) in 1-km Gauge Lengths," *Appl. Phys. Lett.*, Vol. 29, 712–714, 1976.

Scott, W. D., and Orr, K. K., "Rhombohedral Twinning in Alumina," *J. Am. Ceram. Soc.*, Vol. 66, 27–32, 1983.

Service, T. H., Ritter, J. E. Jr., Jakus, K., and Sonderman, D., "Bimodal Strength Populations," *Bull. Am. Ceram. Soc.*, 64, 1276–1280, 1985.

Shaffer, P. T. B., "Engineering Properties of Carbides," pp. 804–811 in Schneider, D. J., volume chairman, *Engineered Materials Handbook*, Vol. 4: *Ceramics and Glasses*, ASM International, Materials Park, OH, 1991.

Shah, S. P., and Ouyang, C. O., "Mechanical Behavior of Fiber-Reinforced Cement-Based Composites," *J. Am. Ceram. Soc.*, Vol. 74, 2727–2738, 2947–2953, 1991.

Shalek, P. D., Petrovic, J. J., Hurley, G. F., and Gac, F. D., "Hot-Pressed SiC Whisker/ Si_3N_4 Matrix Composites," *Am. Ceram. Soc. Bull.*, Vol. 65, 351–356, 1986.

Shetty, D. K., Rosenfield, A. R., Duckworth, W. H., and Held, P. R., "A Biaxial-Flexure Test for Evaluating Ceramic Strengths," *J. Am. Ceram. Soc.*, Vol. 66, 36–42, 1983.

Shetty, D. K., and Wang, J.-S., "Crack Stability and Strength Distribution of Ceramics That Exhibit Rising Crack-Growth-Resistance (*R*-Curve) Behavior," *J. Am. Ceram. Soc.*, Vol. 72, 1158–1162, 1989.

Sigl, L. S., and Evans, A. G., "Effects of Residual Stress and Frictional Sliding on Cracking and Pull-Out in Brittle Matrix Composites," *Mech. Mater.*, Vol. 8, 1–9, 1989.

Simmons, J. H., and Simmons, C. J., "Nonlinear Viscous Flow in Glass Forming," *Ceram. Bull.*, Vol. 68, 1949–1955, 1989.

Simpatico, A., Cannon, W. R., and Matthewson, M. J., "Comparison of Hydraulic-Burst and Ball-on-Ring Tests for Measuring Biaxial Strength," *J. Am. Ceram. Soc.*, Vol. 82, 2737–2744, 1999.

Sines, G., *Elasticity and Strength*, Allyn & Bacon, Boston, 1969.

Singpurwalla, N. D., Wilson, S. P., and Fuller, E. R. Jr., "Statistical Aspects of Failure Processes in Ceramics," in Bernardeo, J. M., Berger, J. O., David, A. P., and Smith, A. F. M., Eds., *Bayesian Statistics*, Oxford University Press, New York, 1995.

Smith, S. M., and Scattergood, R. O., "Crack-Shape Effects for Indentation Fracture Toughness Measurements," *J. Am. Ceram. Soc.*, Vol. 75, 305–315, 1992.

Sneddon, I. N., "The Relation between Load and Penetration in the Axisymmetric Boussinesq Problem for a Punch of Arbitrary Profile," *Int. J. Eng. Sci.*, Vol. 3, 47–57, 1965.

Sneddon, I. N., and Lowengrub, M., *Crack Problems in the Classical Theory of Elasticity*. Wiley, New York, 1969.

Snow, J. D., and Heuer, A. H., "Slip Systems in Al_2O_3," *J. Am. Ceram. Soc.*, Vol. 56, 153–157, 1973.

Somiya, S., Yamamoto, N., and Yanagida, H., *Science and Technology of Zirconia III, Advances in Ceramics*, Vol. 24B, American Ceramic Society, Westerville, OH, 1986.

Sonderman, D., Jakus, K., Ritter, J. E. Jr., Yuhaski, S. Jr., and Service, T. H., "Maximum Likelihood Estimation Techniques for Concurrent Flaw Subpopulations," *J. Mater. Sci.*, Vol. 20, 207–212, 1985.

Sprackling, M. T., *The Plastic Deformation of Simple Ionic Crystals*. Academic, London, 1976.

Spriggs, R. M., "Expression for Effect of Porosity on Elastic Modulus of Polycrystalline Refrectory Materials, Particularly Aluminum Oxide," *J. Am. Ceram. Soc.*, Vol. 45, 628–629, 1961.

Spriggs, R. M., and Brissette, L. A., "Expressions for Shear Modulus and Poisson's Ratio of Porous Refractory Oxides," *J. Am. Ceram. Soc.*, Vol. 45, 198, 1962.

Spriggs, R. M., Brissette, L. A., and Vasilos, T., "Effect of Porosity on Elastic and Shear Moduli of Polycrystalline Magnesium Oxide," *J. Am. Ceram. Soc.*, Vol. 45, 400, 1962.

Srawley, J. E., and Brown, W. F. Jr., "Fracture Toughness Testing Methods," pp. 133–198 in *Fracture Toughness Testing and Its Applications*. ASTM Special Technical Publication 381, American Society for Testing and Materials, Philadelphia, 1965.

Sridhar, N., Yang, W., Srolovitz, D. J., and Fuller, E. R. Jr., "Microstructural Mechanics Model of Anisotropic-Thermal-Expansion-Induced Microcracking," *J. Am. Ceram. Soc.*, Vol. 77, 1123–1138, 1994.

Srinivasan, M., "The Silicon Carbide Family of Structural Ceramics," pp. 99–159 in Wachtman, J. B. Jr., Ed., *Structural Ceramics*, Vol. 29 *of Treatise on Materials Science and Technology*, edited by H. Herman, Academic, Orlando, FL, 1989.

Srinivasan, M., and Seshadri, S. G., "Application of Single Edge Notched Beam and Indentation Techniques to Determine Fracture Toughness of Alpha Silicon Carbide," pp. 46–68 in Freiman, S. W., and Fuller, E. R., Eds., *Fracture Mechanics Methods for Ceramics, Rocks, and Concrete*, ASTM Special Technical Publication 745, American Society for Testing and Materials, Philadelphia, 1981.

Stein, D. F., and Low, J. R. Jr., "Mobility of Edge Dislocations in Silicon-Iron Crystals," *J. Appl. Phys.*, Vol. 31, 362–369, 1960.

Steinbrech, R. W., "Toughening Mechanisms for Ceramic Materials," *J. Eur. Ceram. Soc.*, Vol. 10, 131–142, 1992.

Steinbrech, R. W., Reichl, A., and Schaarwaechter, W., "*R*-Curve Behavior of Long Cracks in Alumina," *J. Am. Ceram. Soc.*, Vol. 73, 2009–2015, 1990.

Steinbrech, R. W., and Schmenkel, O., "Crack-Resistance Curves of Surface Cracks in Alumina," *J. Am. Ceram. Soc.*, Vol. 71, C271–C272, 1988.

Stevens, R., "Engineering Properties of Zirconia," pp. 775–786 in Schneider, S. J., volume chairman, *Engineered Materials Handbook*, Vol. 4: Ceramics and Glasses, ASM International, Materials Park, OH, 1991.

Stokes, R. J., "Dislocation Sources and the Strength of Magnesium Oxide Single Crystals," *Trans. Metall. Soc. AIME*, Vol. 222, 1227–1237, 1962.

Stokes, R. J., "Thermal-Mechanical History and the Strength of Magnesium Oxide Single Crystals: I, Mechanical Tests," *J. Am. Ceram. Soc.*, Vol. 48, 60–67, 1965.

Stokes, R. J., "Thermal-Mechanical History and the Strength of Magnesium Oxide Single Crystals: II, Etch Pit and Electron Transmission Studies," *J. Am. Ceram. Soc.*, Vol. 49, 39–46, 1966a.

Stokes, R. J., "The Role of Defects on the Mechanical Properties of Nonfissionable Ceramics," p. 3 in *Nuclear Applications of Non-Fissionable Ceramics*, American Nuclear Society, Hinsdale, IL, 1966b.

Stokes, R. J., "Mechanical Behavior of Polycrystalline Ceramics," p. 379 in Fulrath, J. M., and Pask, J. A., Eds., *Ceramic Microstructures*, Wiley, New York, 1968.

Stokes, R. J., "Microscopic Aspects of Fracture in Ceramics," p. 157 in *Fracture*, Vol. VII, Academic, New York, 1972.

Stokes, R. J., and Li, C. H., "The Sodium Chloride–Silver Chloride Alloy System," *Acta Metall*, Vol. 10, 535–542, 1962.

Stokes, R. J., and Li, C. H., "The Anisotropic Extension of Microcracks by Plastic Flow in Semi-Brittle Solids," p. 289 in Drucker, D. C., and Gilman, J. J., Eds., *Fracture of Solids*, Wiley-Interscience, New York, 1963.

Stokes, R. J., and Li, C. H., "Dislocation Configurations and the Initiation of Yielding in Magnesium Oxide," *Discuss. Faraday Soc.*, No. 38, 233–242, Butterworth, London, 1964.

Stokes, R. J., Johnston, T. L., and Li, C. H., "Environmental Effects of the Mechanical Properties of Ionic Solids with Particular Reference to the Joffe Effect," *Trans. Metall. Soc. AIME*, Vol. 218, 655–662, 1960.

Stump, D. M., "Toughening and Strengthening of Ceramics Reinforced by Dilatant Transformations and Ductile Particles," *Int. J. Solids*, Vol. 28, 669–689, 1991.

Suresh, S., *Fatigue of Materials*. Cambridge University Press, New York, 1991.

Suresh, S., Shih, C. F., Morrone, A., and O'Dowd, N. P., "Mixed Mode Fracture Toughness of Ceramic Materials," *J. Am. Ceram. Soc.*, Vol. 73, 1257–1267, 1990.

Suresh, S., and Tschegg, E. K., "Combined Mode I–Mode III Fracture of Fatigue-Precracked Alumina," *J. Am. Ceram. Soc.*, Vol. 70, 726–733, 1987.

Swab, J. J., and Quinn, G. D., "Fractography of Advanced Structural Ceramics: Results from Topic #2 of the VAMAS Round Robin Exercise," *Ceram. Eng. Sci. Proc.*, Vol. 16, 929–938, 1995.

Swain, M. V., "*R*-Curve Behavior and Thermal Shock Resistance of Ceramics," *J. Am. Ceram. Soc.*, Vol. 73, 621–628, 1990.

Swain, M. V., and Hannink, R. H. J., "*R*-Curve Behavior in Zirconia Ceramics," pp. 225–239 in Claussen, N., Ruhle, M., and Heuer, A., Eds., *Science and Technology of Zirconia II, Advances in Ceramics*, Vol. 12, American Ceramic Society, Westerville, OH, 1983.

Swain, M. V., Hannink, R. H. J., and Garvie, R. C., "The Influence of Precipitate Size and Temperature on the Fracture Toughness of Calcia— and Magnesia—Partially Stabilized Zirconia," pp. 339–354 in Bradt, R. C., Evans, A. G., Hasselman, D. P. H., and Lange, F. F., Eds., *Fracture Mechanics of Ceramics*, Vol. 6: *Concepts, Measurements, Transformations, and High-Temperature Fracture*, Plenum, New York, 1983.

Swanson, P. L., Fairbanks, C. J., Lawn, B. R., Mai, Y.-W., and Hockey, B. J., "Crack-Interface Grain Bridging as a Fracture Resistance Mechanism in Ceramics: I, Experimental Study on Alumina," *J. Am. Ceram. Soc.*, Vol. 70, 279–289, 1987.

Szlufarska, I., Nakano, A., and Vashishta, P., "A Crossover in the Mechanical Response of Nanocrystalline Ceramics," *Science*, Vol. 309, 911–913, 2005.

Tabor, D., *The Hardness of Metals*, Clarendon, Oxford, 1951, pp. 6–8.

Tada, H., Paris, P., and Irwin, G., *The Stress Analysis Handbook*, Del Research Corporation, St. Louis, MO, 1985.

Tandon, R., Green, D. J., and Cook, R. F., "Strength Variability in Brittle Materials with Stabilizing and Destabilizing Resistance Fields," *Acta Metall. Mater.*, Vol. 41, 399–408, 1993.

Tennery, V. J., Ed., *Third International Symposium on Ceramic Materials and Components for Engines*, American Ceramic Society, Westerville, OH, 1989.

Thiemeier, T., and Bruckner-Foit, A., "Influence of the Fracture Criterion on the Failure Prediction of Ceramics Loaded in Biaxial Flexure," *J. Am. Ceram. Soc.*, Vol. 74, 48–52, 1991.

Thoman, D. R., Bain, L. J., and Antle, C. E., "Inferences on the Parameters of the Weibull Distribution," *Technometrics*, Vol. 11, 445–460, 1969.

Thouless, M. D., Sbaizero, O., Sigl, L. S., and Evans, A. G., "Effect of Interface Mechanical Properties in a SiC-Fiber Reinforced Lithium Aluminum Silicate Glass-Ceramic," *J. Am. Ceram. Soc.*, Vol. 72, 525–532, 1989.

Thouless, M. D., and Evans, A. G., "Effects of Pull-Out on the Mechanical Properties of Ceramic-Matrix Composites," *Acta Metall*, Vol. 36, 517–522, 1988.

Timoshenko, S., and Goodier, J. N., *Theory of Elasticity*, 2nd ed., McGraw-Hill, New York, 1951.

Tomozawa, M., "Fracture of Glasses," *Annu. Rev. Mater. Sci.*, Vol. 26, 43–74, 1996.

Tressler, R. E., and Barber, D. J., "Yielding and Flow of *c*-Axis Sapphire Filaments," *J. Am. Ceram. Soc.*, Vol. 57, 13–19, 1974.

Tsai, R. L., and Raj, R., "Creep Fracture in Ceramics Containing Small Amounts of a Liquid Phase," *Acta Metall*, Vol. 30, 1043–1058, 1982.

Tsukuma, K., Kubota, Y., and Tsukidate, T., "Thermal and Mechanical Properties of Y_2O_3-Stabilized Tetragonal Zirconia Polycrystals," pp. 382–390 in Claussen, N., Ruhle, M., and Heuer, A., Eds., *Science and Technology of Zirconia II, Advances in Ceramics*, Vol. 12, American Ceramic Society, Westerville, OH, 1983.

Tsukuma, K., and Ueda, K., "Strength and Fracture Toughness of Isostatically Hot-Pressed Composites of Al_2O_3 and Y_2O_3–Partially-Stabilized ZrO_2," *J. Am. Ceram. Soc.*, Vol. 68, C-4–C-5, 1985.

Tsukuma, K., Ueda, K., Matsushita, K., and Shimada, M., "High-Temperature Strength and Fracture Toughness of Y_2O_3–Partially Stabilized ZrO_2/Al_2O_3 Composites," *J. Am. Ceram. Soc.*, Vol. 68, C-56, 1985.

Tucker, W. T., and Johnson, C. A., "The Multiaxial Equivalent of Stressed Volume," pp. 265–279 in Brinkman, C. R., and Duffy, S. F., Eds., *Life Prediction Methodologies and Data for Ceramic Materials*, ASTM STP 1201, American Society for Testing and Materials, Philadelphia, 1993.

Tvergaard, V., and Hutchinson, J. W., "Microcracking in Ceramics Induced by Thermal Expansion or Elastic Anisotropy," *J. Am. Ceram. Soc.*, Vol. 71, 157–166, 1988.

Varner, J. R., "Descriptive Fractography," pp. 635–644 in Schneider, S. J., volume chairman, *Engineered Materials Handbook*, Vol. 4: *Ceramics and Glasses*, ASM International, Materials Park, OH, 1991.

Varshneya, A. K., *Fundamentals of Inorganic Glass*. Academic, San Diego, CA, 1994.

Veknis, G., Ashby, M. F., and Beaumont, P. W. R., "*R*-Curve Behavior of Al_2O_3 Ceramics," *Acta Metall. Mater.*, Vol. 38, 1151–1162, 1990.

Venkinis, G., Ashby, M. F., and Beaumont, P. W. R., "*R*-Curve Behavior of Al_2O_3 Ceramics," *Acta. Metall. Mater.*, Vol. 38, 1151–1162, 1990.

Virher, A. V., and Matsumoto, R. L. K., "Ferroelastic Domain Switching as a Toughening Mechanism in Tetragonal Zirconia," *J. Am. Ceram. Soc.*, Vol. 69, C224, 1986.

Wachtman, J. B. Jr., "Elastic Deformation of Ceramics and Other Refractory Materials," pp. 139–168 in Wachtman, J. B. Jr., Ed., *Mechanical and Thermal Properties of Ceramics*, NBS Special Publication 303, U.S. Government Printing Office, Washington, DC, 1969.

Wachtman, J. B. Jr., "Highlights of Progress in the Science of Fracture of Ceramics and Glass," *J. Am. Ceram. Soc.*, Vol. 57, 509–519, 1974.

Wachtman, J. B. Jr., Ed., *Structural Ceramics*, Vol. 29 *of Treatise on Materials Science and Technology*, edited by H. Herman, Academic, Orlando, FL, 1989.

Wachtman, J. B. Jr., Capps, W., and Mandel, J., "Biaxial Flexure Tests of Ceramic Substrates," *J. Mater.*, Vol. 7, 188–194, 1972.

Wachtman, J. B. Jr., and Lam, D. G. Jr., "Young's Modulus of Various Refractory Materials as a Function of Temperature," *J. Am. Ceram. Soc.*, Vol. 42, 254–260, 1959.

Wachtman, J. B. Jr., and Maxwell, L. H., "Plastic Deformation of Ceramic-Oxide Single Crystals," *J. Am. Ceram. Soc.*, Vol. 37, 291–299, 1954.

Wachtman, J. B. Jr., and Maxwell, L. H., "Plastic Deformation of Ceramic-Oxide Single Crystals, II," *J. Am. Ceram. Soc.*, Vol. 40, 377–385, 1957.

Wachtman, J. B. Jr., and Maxwell, L. H., "Strength of Synthetic Single Crystal Sapphire and Ruby as a Function of Temperature and Orientation," *J. Am. Ceram. Soc.*, Vol. 42, 432–433, 1959.

Wachtman, J. B. Jr., Tefft, W. E., Lam, D. G. Jr., and Apstein, C. S., "Elastic Constants of Synthetic Single Crystal Corundum at Room Temperature," *J. Res. Natl. Bur. Stand.*, Vol. 64A, 213–228, 1960.

Wachtman, J. B. Jr., Tefft, W. E., Lam, D. G. Jr., and Apstein, C. S., "Exponential Temperature Dependence of Young's Modulus for Several Oxides," *Phys. Rev.*, 122, 1754, 1961.

Wagner, W. R., "Characterization of Fiber Damage Affecting the Reliability of Terminated Optical Fiber," pp. 231–243 in Tekippe, V. J. and Varachi, J. P., Eds., *Passive Fiber Optic Components and Their Reliability*, *Proc. Soc. Photo-Opt. Instrum. Eng.*, Vol. 1973, 231–243, SPIE, Bellingham, WA, 1993.

Walsh, J. B., "Effect of Cracks on the Compressibility of Rock," *J. Geophys. Res.*, Vol. 70, 382–389, 1965.

Wang, C. M., Cargill, G. S., Chan, H. M., and Harmer, M. P., "Structure of Y and Zr Segregated Grain Boundaries in Alumina," *Interface Sci.*, Vol. 8, 243–255, 2000.

Weertman, J., "Steady-State Creep of Crystals," *J. Appl. Phys.*, Vol. 28, 1185–1189, 1957.

Weertman, J., and Weertman, J. R., "Mechanical Properties, Strongly Temperature Dependent," pp. 1039–1340 in Kahn, R. W., Ed., *Physical Metallurgy*, 3rd ed., North-Holland, Amsterdam, 1983.

Weertman, J., and Weertman, J. R., *Elementary Dislocation Theory*. Oxford University Press, New York, 1992.

Weibull, W., "A Statistical Theory of the Strength of Materials," *Ingenioersvetenskapsakad. Handl*, Vol. 151, 1–45, 1939.

Weiss, J., "Silicon Nitride Ceramics: Composition, Fabrication Parameters, and Properties," *Annu. Rev. Mater. Sci.*, Vol. 11, 381–389, 1981.

Westergaard, H. M., "Bearing Pressures and Cracks," *J. Appl. Mech.*, Vol. 6, A49–53, 1939.

White, K. W., and Guazzone, "Elevated-Temperature Toughening Mechanisms in a SiC_w/Al_2O_3 Composite," *J. Am. Ceram. Soc.*, Vol. 74, 2280–2285, 1991.

Wiederhorn, S. M., "Fracture of Sapphire," *J. Am. Ceram. Soc.*, Vol. 52, 485–491, 1969.

Wiederhorn, S. M., and Bolz, L. H., "Stress Corrosion and Static Fatigue of Glass," *J. Am. Ceram. Soc.*, Vol. 53, 543–548, 1970.

Wiederhorn, S. M., "Influence of Water Vapor on Crack Propagation in Soda-Lime Glass," *J. Am. Ceram. Soc.*, Vol. 50, 407–414, 1967.

Wiederhorn, S. M., "Subcritical Crack Growth in Ceramics," pp. 613–646 in Bradt, R. C., Hasselman, D. P. H., and Lange, F. F., Eds., *Fracture Mechanics of Ceramics*, Plenum, New York, 1974.

Wiederhorn, S. M., "Brittle Fracture and Toughening Mechanisms in Ceramics," *Annu. Rev. Mater. Sci.*, Vol. 14, 374–403, 1984.

Wiederhorn, S. M., and Fuller, E. R. Jr., "Structural Reliability of Ceramic Materials," *Mater. Sci. Eng.*, Vol. 71, 169–186, 1985.

Wiederhorn, S. M., and Hockey, B. J., "High Temperature Degradation of Structural Composites," pp. 365–380 in Vincenzini, P., Ed., *Advanced Structural Ceramics*, Elsevier Science, New York, 1991.

Wiederhorn, S. M., Hockey, B. J., and Chuang, T.-J., "Creep and Creep Rupture of Structural Ceramics," pp. 555–575 in Shah, S. P., Ed., *Toughening Mechanisms in Quasi-Brittle Materials*, Kluwer Academic, Norwell, MA, 1991.

Wiederhorn, S. M., and Johnson, H., "Effect of Electrolyte pH on Crack Propagation in Glass," *J. Am. Ceram. Soc.*, Vol. 56, 192–197, 1973.

Wiederhorn, S. M., Johnson, H., Diness, A. M., and Heuer, A. H., "Fracture of Glass in Vacuum," *J. Am. Ceram. Soc.*, Vol. 57, 8, 1974.

Wiederhorn, S. M., Roberts, D. E., Chuang, T.-J., and Chuck, L., "Damage-Enhanced Creep in a Siliconized Silicon Carbide: Phenomenology," *J. Am. Ceram. Soc.*, Vol. 71, 602–608, 1988.

Wiederhorn, S. M., Quinn, G. D., and Krause, R., "Fracture Mechanism Maps: Their Applicability to Silicon Carbide," pp. 36–61 in Brinkman, C. R., and Duffy, S. F., Eds., *Life Prediction Methodologies and Data for Ceramic Materials*, ASTM STP 1201, American Society for Testing and Materials, Philadelphia, 1994.

Wilantewicz, T., private communications, 2007.

Wilkinson, D. S., "Creep Damage Mechanisms in Structural Ceramics," pp. 349–366 in Bradt, R. C., Hasselman, D. P. H., Munz, D., Sakai, M., and Shevchenko, V. Y., Eds., *Fracture Mechanics of Ceramics*, Vol. 10: *Fracture Fundamentals, High-Temperature Deformation, Damage, and Design*, Plenum, New York, 1992.

Woodilla, D., Buonomo, M., Bar-On, I., Katz, R. N., and Whalen, T., "Elevated-Temperature Behavior of High-Strength Silicon Carbide," *J. Am. Ceram. Soc.*, Vol. 76, 249–252, 1993.

Xu, A., and Solomon, A. A., "Diffusional Creep and Cavitational Strains in High-Purity Alumina Under Tension and Subsequent Hydrostatic Compression," *J. Am. Ceram. Soc.*, Vol. 75, 985–995, 1992.

Yajima, S., Hayashi, J., Omori, M., and Okamura, K., "Development of a Silicon Carbon Fibre with High Tensile Strength," *Nature (London)*, Vol. 261, 683–685, 1976.

Yang, S. F., and Knowles, K. M., "The One-Dimensional Car Parking Problem and Its Application to the Distribution of Spacings between Matrix Cracks in Unidirectional Fiber-Reinforced Brittle Materials," *J. Am. Ceram. Soc.*, Vol. 75, 141–147, 1992.

Yavuz, B. O., and Tressler, R. E., "Threshold Stress Intensity for Crack Growth in Silicon Carbide Ceramics," *J. Am. Ceram. Soc.*, Vol. 76, 1017–1024, 1993.

Young, W. C., *Roark's Formulas for Stress and Strain*, 6th ed., McGraw-Hill, New York, 1989.

Zelin, M. G., and Mukherjee, A. K., "Geometric Aspects of Superplastic Flow," *Mater. Sci. Eng. A*, Vol. A208, 210–225, 1996.

Zeng, J., Tanaka, I., Miyamoto, Y., Yamada, O., and Niihara, K., "High-Temperature Strength and Cavitation Threshold of Silicon Nitride-Silica Ceramics," *J. Am. Ceram. Soc.*, Vol. 75, 195–200, 1992.

Zimmermann, A., Hoffman, M., Flinn, B. D., Bordin, R. K., Chuang, T., Fuller, E. R., and Raedel, J., "Fracture of Alumina with Controlled Pores," *J. Am. Ceram. Soc.*, Vol. 81, 2449–2457, 1998.

Zok, F. W., Evans, A. G., and Mackin, T. J., "*The Mechanical Properties of Fiber-Reinforced Ceramic-Matrix Composites*," in Lehman, R. L., technical editor, El-Rahaiby, S.-K., managing editor, and Wachtman, J. B., American Ceramic Society editor, *Handbook on Continuous Fiber Reinforced Ceramic Matrix Composites*, jointly published by Purdue University and the American Ceramic Society, Westerville, OH, 1996.

INDEX